Microwave thermal emission from Saturn's icy moons

Léa Bonnefoy

PSL
UNIVERSITÉ PARIS

THÈSE DE DOCTORAT
DE L'UNIVERSITÉ PSL

Préparée à l'Observatoire de Paris

Emission thermique micro-ondes des lunes glacées de Saturne

Thermal micro-wave emission from Saturn's icy moons

Soutenue par
Léa Bonnefoy
Le 18 septembre 2020

Ecole doctorale n° 127
Ecole Doctorale Astronomie et Astrophysique d'Île de France

Spécialité
Astronomie et Astrophysique

Composition du jury :

Daniel, HESTROFFER Astronome, OBSPM – IMCCE	*Président*
Cécile, FERRARI Professeur, IPGP	*Rapportrice*
Jérémie, LASUE Astronome adjoint, IRAP	*Rapporteur*
Catherine, PRIGENT Directeur de recherche, OBSPM – LERMA	*Examinatrice*
Paul, HARTOGH Staff scientist, MPI für Solar System Research	*Examinateur*
Aurélie, GUILBERT-LEPOUTRE Chargé de recherche, LGL – TPE	*Examinatrice*
Emmanuel, LELLOUCH Astronome, OBSPM – LESIA	*Directeur de thèse*
Alice, LE GALL Maître de conférences, SU/UVSQ/IUF	*Co-directrice de thèse*

Invité :

Cédric, LEYRAT Astronome adjoint, OBSPM – LESIA	*Co-directeur de thèse*

l'Observatoire de Paris | PSL

RÉSUMÉ

Les satellites sans atmosphère de Saturne ont connu des évolutions divergentes liées notamment à leur environnement proche (position dans la magnétosphère de Saturne, interaction avec les anneaux de poussières etc.). Une partie de cette histoire est contenue dans leur régolithe de glace et un moyen d'y accéder est de mesurer leur émission thermique dans le domaine micro-onde. A partir des données du Radar/radiomètre de Cassini et d'observations de radiotélescopes terrestres, l'objectif de cette thèse est de caractériser la composition et structure des sous-surfaces des satellites glacés de Saturne, notamment Rhéa, Dioné et Japet, les trois plus grands satellites Saturniens après Titan. L'étude des variations intra- (en particulier entre les faces avant et arrière de ces satellites synchrones) et inter-satellites de ces propriétés nous renseigne sur les processus qui façonnent ces surfaces glacées.

La première partie de cette thèse décrit l'étalonnage, la réduction et l'analyse des observations actives (radar) et surtout passives (radiométriques) du Radar à bord de la sonde Cassini (2004-2017). Les données radar montrent le rôle clé de l'anneau E de Saturne (alimenté par les geysers d'Encelade) dans le degré de pureté des régolithes glacés des satellites intérieurs de la planète (de Mimas à Rhéa) – contenant bien moins de contaminants non-glacés que les régolithes Galiléens. L'ajustement des observations radiométriques à une combinaison de modèles thermiques, radiatifs, et d'émissivité apporte de nouvelles contraintes sur les propriétés thermiques, structurelles et compositionnelles de Rhéa et Dioné. Cette étude révèle des anomalies thermiques régionales associées à la couverture d'éjectas du jeune cratère Inktomi sur Rhéa et à la dichotomie avant/arrière sur Dioné. Les données radar et radiométriques confirment la présence de structures de taille probablement centimétriques dans les sous-surfaces des satellites intérieurs de Saturne qui rendent ces objets particulièrement diffusifs et peu émissifs aux micro-ondes.

Le second volet de cette thèse porte sur Japet et la construction du spectre micro-onde de ce satellite connu pour sa spectaculaire dichotomie avant/arrière. Les données de Cassini et des radiotélescopes SMA et GBT ont été complétées par des observations inédites depuis deux grands radiotélescopes terrestres : le 30-m de l'IRAM (1-2 mm) et le VLA (0.7-3 cm). Le spectre de la face arrière (brillante) de Japet montre une possible figure d'absorption sans doute liée à la taille des grains du régolithe (quelques mm). Le spectre de la face avant (sombre), proche de celui de Phœbé, conforte l'idée que l'anneau diffus de Phœbé est la source du matériau sombre de Japet. Enfin, les spectres avant et arrière se rapprochent aux plus grandes longueurs d'onde (c'est-à-dire aux plus grandes profondeurs) suggérant que l'épaisseur du dépôt sombre sur la face avant de Japet n'excède pas quelques décimètres.

MOTS CLÉS

Radiométrie micro-ondes, Satellites glacés, Rhéa, Japet, Dioné, thermique, radiotélescope, radar

ABSTRACT

Saturn's atmosphere-less satellites have followed divergent evolution paths associated with their environment (position in Saturn's magnetosphere, interaction with dust rings etc). Part of this history is contained in their icy regolith, and a way to access it is to measure their thermal microwave emission. Using observations from the Cassini Radar/radiometer and Earth-based radiotelescopes, the goal of this thesis is to characterize the composition and structure of the subsurfaces of Saturn's icy satellites, especially Rhea, Dione, and Iapetus, the three largest Saturnian moons after Titan. Studying inter- and intra-satellite variations (e.g., between the leading and trailing sides of these synchronous satellites) of these properties informs on the processes which shape these icy surfaces.

The first part of this thesis describes the calibration, reduction, and analysis of active (radar) and especially passive (radiometry) observations of the Radar instrument on the Cassini probe (2004–2017). The radar data highlight the key role of Saturn's E ring (fed by the geysers of Enceladus) in the degree of purity of the icy regoliths of Saturn's inner moons (from Mimas to Rhea) — containing much fewer non-icy contaminants than Jupiter's satellites. Fitting the Cassini radiometry to a combination of thermal, radiative, and emissivity models provides new constraints on the thermal, structural, and compositional properties of Rhea and Dione. This study reveals regional thermal anomalies associated with the ejecta blanket of the young crater Inktomi on Rhea and to the leading/trailing dichotomy on Dione. The radar and radiometry data both confirm the presence of likely centimeter-scale structures in the subsurfaces of Saturn's inner moons, scattering microwaves and causing the high radar brightness and low emissivity of these objects.

The second part of this thesis is dedicated to the construction of the microwave spectrum of Iapetus, a satellite known for its dramatic leading/trailing dichotomy. We complemented the data gathered by the Cassini probe and the SMA and GBT telescopes with new observations from two radio telescopes: the 30-m IRAM antenna (1–2 mm) and the VLA (0.7–3 cm). The spectrum of the trailing (bright) face of Iapetus indicates a possible absorption feature likely due to the grain size in the regolith (of the order of millimeters). The spectrum of the leading (dark) side, similar to Phoebe's, supports the theory that the diffuse Phoebe ring is the source of the dark material on Iapetus. Finally, the spectra of the leading and trailing sides become closer at the longest wavelengths (that is, at the largest depths), suggesting that the depth of the leading side's dark layer is at most a few decimeters.

KEYWORDS

Microwave radiometry, icy satellites, Rhea, Iapetus, Dione, thermal, radiotelescope, radar

Contents

Acknowledgements

These last three years have been a wonderful adventure, full of fascinating new experiences, encounters, and discussions. Countless people have brought me to where I am today, and have taught me what it means to be a scientist.

First and foremost, I thank my three PhD advisors Alice Le Gall, Emmanuel Lellouch, and Cédric Leyrat for guiding me throughout my thesis. Their complementary expertise in Cassini data, Earth-based observations, and thermal modeling (and more of course) brought me the tools and knowledge necessary to undergo this project, while their enthusiasm and friendship made the work both interesting and fun. I also thank them for writing the IRAM, VLA (and ALMA) proposals that provided new data for Iapetus and gave me the opportunity to observe with the IRAM 30 meter telescope.

I wish to thank the members of my defense committee for their interest in my work, their presence at my thesis defense in such great numbers in spite of the circumstances, and their insightful comments and questions, which helped improve the final version of this document.

The existence and quality of the data used herein have been made possible by many people around the world; researchers, technicians, engineers, administrators, operators, and more.

I therefore thank the Cassini radar team and especially those involved in the design, calibration, and observations of the radiometer. The help of Michael Janssen and Lauren Wye especially has been crucial to my understanding and calibration of the Cassini radiometry and scatterometry.

I warmly thank the IRAM NIKA2 team for accepting our proposals and doing everything possible to observe Iapetus, including organizing an additional observation run after bad weather in 2018. I especially thank Jean-François Lestrade who helped enormously with the calibration, and Bilal Ladjelate for going above and beyond when organizing and conducting the observations, but also Nicolas Ponthieu, Carsten Kramer, and Laurence Perotto. I thank the observers, technicians, operators, and cooks at the 30 meter telescope for making this experience so fantastic, even on the windy, snowy nights when we had to terraform Mars or settle on Catan.

I thank the VLA team and the NRAO for obtaining precious centimetric Iapetus data. In particular, Bryan Butler's help was crucial in every step of requesting, acquiring, and calibrating this dataset. Raphaël Moreno's help was also instrumental for both the VLA and IRAM datasets, thank you!

For their re-calibration of the SMA data and their help understanding and using it, I thank Mark Gurwell and Arielle Moullet.

I am grateful to the astronomy and planetary science community in general, which I love meeting and learning from, especially at conferences. In particular, I would like to thank my past advisors, Gordon Stacey, Alex Hayes, and Christopher Hamilton, who gave their trust and projects to an enthusiastic inexperienced student. I also wish to thank my new advisors for my first postdoctoral position, Antoine Lucas, Sébastien Rodriguez, and Alex Hayes, and I look forward to the fascinating projects we will work on together!

For teaching me how to teach, I am grateful to the DU LU, DU ECU, and Observatory M1 teams and students, especially Cédric Leyrat, Jérémie Vaubaillon, Thierry Fouchet, and Clément Hottier. And Nicolas Nio, thank you so much for your help with quantum (you saved me!).

For an unforgettable week of science outreach, I send my warmest thanks to SpaceBus France, its president, the team, and the C2 2019 volunteers.

I thank the ED127, including Thierry Fouchet, Jacques Le Bourlot, Alain Doressoundiram, Géraldine Gaillant, and Jacqueline Plancy for hosting my PhD and helping me navigate its administrative side. I thank the DIM ACAV+ for funding my PhD.

I thank everybody at the LATMOS and LESIA for welcoming me: administration staff, IT, engineers, scientists. To the doctoral and post-doctoral students of the LESIA and the LATMOS — Yann, Audrey, Nicolas (Oudart), Lora, Loïc, Aurélien (Stcherbinine), Margaux, Aurélien (Stolzenbach), Elisabeth, Ana, Rimal, Maxence (LMD but you still fit in this list), Pedro (and Alice Bernard!), Océane, Alice (Praet), Christophe, Nicolas (Bott), Doriann, Desh, Jules: thank you for some great board games/RPGs/lunches/coffee breaks/random chats/other events. Thanks also to my two internship students, Robin Sultana and Marie Azevedo, who unknowingly taught me a lot while I was teaching them!

I thank all my friends. Whether I met them at the LFB, LFM, Cornell, U of A, or in Paris, it has been great to chat and/or meet up. Gabriela, Nicolle, Dama, Pratiti, Caroline, Shereen, Lia, Max, Hal, the list is too long, but if we saw each other or talked during these last three years, know that I thought of you while writing this! Brian from the Abbey Bookshop, thank you also for the books, coffee, and tote bags.

And of course, I thank my family. My housemates in Vitry, and in Entraigues during the first COVID confinement have all my gratitude for helping me write my thesis without forgetting the most important things in life. Thank you to my parents, grandmothers, brother, sisters, nieces, nephews, and all my cousins, aunts, uncles, and extended family. Of course, I also thank Raphaël, he is super cool!

And I thank dandelions, whose seemingly infinite numbers kept me sane and gave me a much-needed daily break from writing.

I dedicate this thesis to my niece Ylona, who is almost exactly the same age as my PhD and accompanied me every step of the way, giving me a reason to sing my beautiful songs as often as I wanted to.

Acronyms

ALMA Atacama Large Millimeter/submillimeter Array

ASI Italian Space Agency

AU astronomical unit

CAPS Cassini Plasma Spectrometer

CBE Coherent Backscattering Effect

CDA Cosmic Dust Analyser

CEB Combined Emissivity-Backscatter

CIRS Composite Infrared Spectrometer

CMB Cosmic Microwave Background

CR Cassini Regio

CRST Cassini Radar Science Team

DEM Digital Elevation Model

ESA European Space Agency

FSL far sidelobes

FWHM full width at half maximum

GBT Green Bank Telescope

IEBR Inktomi Ejecta Blanket Region

INMS Ion Neutral Mass Spectrometer

IRAM Institut de Radioastronomie Millimétrique

ISS Imaging Science Subsystem

JPL Jet Propulsion Laboratory

JUICE JUpiter ICy moons Explorer

LH Leading Hemisphere

LHT Leading Hemisphere Terrain

LPI Lunar and Planetary Institute

MAG Cassini Magnetometer

NASA National Aeronautics and Space Administration

NIKA2 New IRAM KIDs Array

NRCS normalized radar cross-section

PDS the Planetary Data System

RAR Real Aperture Radar

RT Ronceveaux Terra

SAR Synthetic Aperture Radar

SMA Sub-Millimeter Array

SPT Enceladus South Polar Terrain

SSI Space Science Institute

ST Saragossa Terra

TH Trailing Hemisphere

TNO Trans-Neptunian Object

UV ultraviolet

UVIS Ultraviolet Imaging Spectrograph

VIMS Visual and Infrared Mapping Spectrometer

VLA Karl G. Jansky Very Large Array

Introduction

What would it be like to walk on Saturn's icy moons Rhea, Iapetus, or Dione? How fluffy and snow-like are their surfaces, and to what depth? How much non-icy material is present in the top few meters of the subsurface, and where does it come from? The answers to these questions, beyond helping us imagine icy extraterrestrial landscapes, offer insights into the formation and evolution of the surfaces of Saturn's icy moons.

The mid-sized satellites of Saturn — in order of increasing distance to their planet: Mimas, Enceladus, Tethys, Dione, Rhea, and, much further from Saturn, Iapetus — are all tidally locked with Saturn, featuring a leading side (toward the direction of movement) and a trailing side. During its 13.5 years in orbit around Saturn (2004–2017), the Cassini probe revealed the intricate interactions between distinct regions of the satellites and their orbital environment, including Saturn's magnetosphere and dust rings. The deposition of Phoebe ring optically dark dust preferentially onto the leading hemisphere of Iapetus is the root cause of its albedo dichotomy, the most dramatic in the Solar System. Meanwhile, the inner moons (within Titan's orbit) are brightened by water ice particles spewed into the E ring by Enceladus. Impacts by dust ring particles and micrometeoroids process the surface into a loose, unconsolidated regolith. On Mimas, Tethys, and Dione, the surface of the equatorial regions of the leading hemisphere is further altered by high-energy electrons.

Although most of the processes affecting Saturn system bodies have been identified, their relative contribution and the time for which they have been active remain largely unknown. The age of the inner moons is a standing question, with some arguments such as the limited sustainability of Enceladus's hydrothermal activity and the rings' low non-icy contaminant content indicating young (of the order of a hundred million years old) bodies, while conflicting observations like high crater densities point to a formation within the Saturn subnebula (of the order of four billion years old). Knowing the vertical structure of the satellites' subsurfaces can help understand to what depth they have been affected by different processes such as incoming icy or non-icy material.

Centimetric to decametric depths can be probed by microwave radar and radiometry, which thereby offer complimentary information to other wavelengths. In particular, the Cassini 2.2-cm Radar/radiometer was able to measure the temperature and backscattering properties of the top few meters of icy surfaces. In passive radiometry mode, the instrument measured the microwave thermal radiation emitted by the satellite. This passive emission depends on the emissivity and temperature of the subsurface, thus informing on its thermal, structural, and compositional properties. Meanwhile, in active radar mode, a microwave signal was sent to the satellite and scattered in all directions, including back toward the Cassini spacecraft. The amplitude and time delay of the received backscatter provide clues to the structure and composition of the subsurface, independent of thermal properties.

The primary objective of the work described herein is to use microwave radiometry to derive the subsurface properties of Saturn's mid-sized icy moons, thus adding new elements to our understanding of the processes which have shaped and continue to affect these icy landscapes. To this end, the first step has been the calibration of the complete Cassini radar and radiometry datasets on these

satellites. Then, a combination of thermal, radiative transfer, and emissivity models inspired from previous work was used to simulate the radiometry observations. By fitting the simulated temperatures to the ones observed by the Cassini spacecraft, it is possible to derive the thermal inertia, emissivity, and effective dielectric constant of the subsurface. This method was applied in priority to Rhea, the satellite of Saturn where the most and highest-resolution radiometry data have been acquired (after Titan), then to Dione and Iapetus.

The second, shorter part of this thesis, which was conducted in parallel to the analysis of Cassini data, was the collection and interpretation of Earth-based radiometry observations of Iapetus and Phoebe. Indeed, microwave radar and radiometry data can also be obtained from Earth: although only the day side of Saturn's satellites can be seen, it can be examined at multiple different wavelengths. Longer wavelengths generally probe deeper into the subsurface, and are sensitive to larger particle sizes than shorter wavelengths. Multi-wavelength microwave radiometry can therefore examine the vertical structure of the subsurface. This is particularly relevant for Iapetus, where a layer of optically dark material covers the leading side: long (centimetric) wavelengths are expected to probe the underlying icy substrate. If the dark material on Iapetus's leading hemisphere originates from Phoebe and its ring, then their microwave properties are expected to be similar, especially at shallow depth. Meanwhile, the icy trailing hemisphere of Iapetus should be more similar to other little-contaminated icy surfaces of the Saturn system, unless unusual structures or non-icy materials are present.

This manuscript is divided into seven chapters. Chapter 1 traces the history of discovery and exploration of Saturn's mid-sized icy moons, providing the scientific context of this study. Chapter 2 details the theoretical background of microwave radar and radiometry exploration and presents some of its applications to planetary science, especially to the study of icy satellites. Chapter 3 examines the complete dataset of Cassini radar observations of Saturn's atmosphere-less icy satellites and its scientific implications. In chapter 4, the 2.2-cm radiometry data gathered on these bodies by the Cassini spacecraft are calibrated and some preliminary interpretations are drawn; however, further analysis of these data requires the use of a thermal model. Chapter 5 describes the combination of thermal, radiative transfer, and emissivity models we developed to simulate the radiometry data. Chapter 6 compares the simulated temperatures to those measured on Rhea, Dione, and Iapetus by the Cassini radiometer, and discusses the scientific implications of this study. Lastly, chapter 7 is dedicated to the complimentary Earth-based radiotelescope observations of Iapetus, which complete part of the microwave spectra of its leading and trailing hemispheres, bringing to light vertical variations in subsurface thermo-physical properties.

This work was performed at the LESIA (Laboratoire d'Études Spatiales et d'Instrumentation en Astrophysique, UMR 8109) laboratory at the Observatoire de Paris-Meudon, and at the LATMOS (Laboratoire Atmosphères, Milieux, Observations Spatiales, UMR 8190) laboratory at the Sorbonne Université. It was funded by the Île-de-France region through a DIM-ACAV (Domaine d'Intêret Majeur – Astrophysique et Conditions d'Apparition de la Vie) grant. This work is also the fruit of several collaborations, including with scientists at the IRAM (Institut de Radioastronomie Millimétrique), LERMA (Laboratoire d'Etudes du Rayonnement et de la Matière en Astrophysique et Atmosphères), and NRAO (National Radio Astronomy Observatory), especially for the collection and calibration of new radiometry observations from Earth.

Chapter 1

Saturn's icy satellites: discovery and exploration

1.1 First discoveries

Saturn being such a beautiful celestial body and the furthest Solar System object easily visible to the naked eye, it was often among the first observed each time telescope techniques were improved. In consequence, and also due to its large number of moons (82, and still counting), the history of the discovery and exploration of Saturn's system can be traced to the progression of telescope technology.

A couple years after its invention, the refracting telescope was already used to observe the Saturn system: in 1610, Galileo Galilei wondered at the odd symmetrical protuberances on either side of Saturn. These "arms", shifting in brightness and disappearing at Saturn's equinoxes, were only identified as rings in 1655 by Christiaan Huygens thanks to a 57-mm-diameter refracting telescope, with a 3.7-m-long focal length (Huygens, 1659). This instrument also led to the discovery of Saturn's largest satellite Titan, whose orbit could be derived from its observed movement around Saturn from day to day (Fig. 1.1).

Larger, "aerial" telescopes, i.e. without a tube (illustrated in Fig. 1.2), were used by Jean-Dominique Cassini at the newly founded Paris Observatory. A string was held from the lens to the eyepiece, and the focal point had to be found by trial and error, a painstaking process that nonetheless led Cassini to the discovery of Saturn's four largest satellites after Titan: Iapetus (1671), Rhea

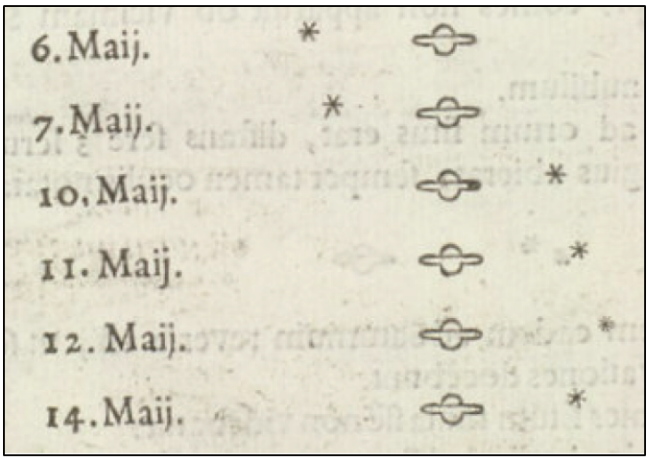

Figure 1.1 – Schematic representation of the May 1655 observations leading to the discovery of Titan (Huygens, 1659)

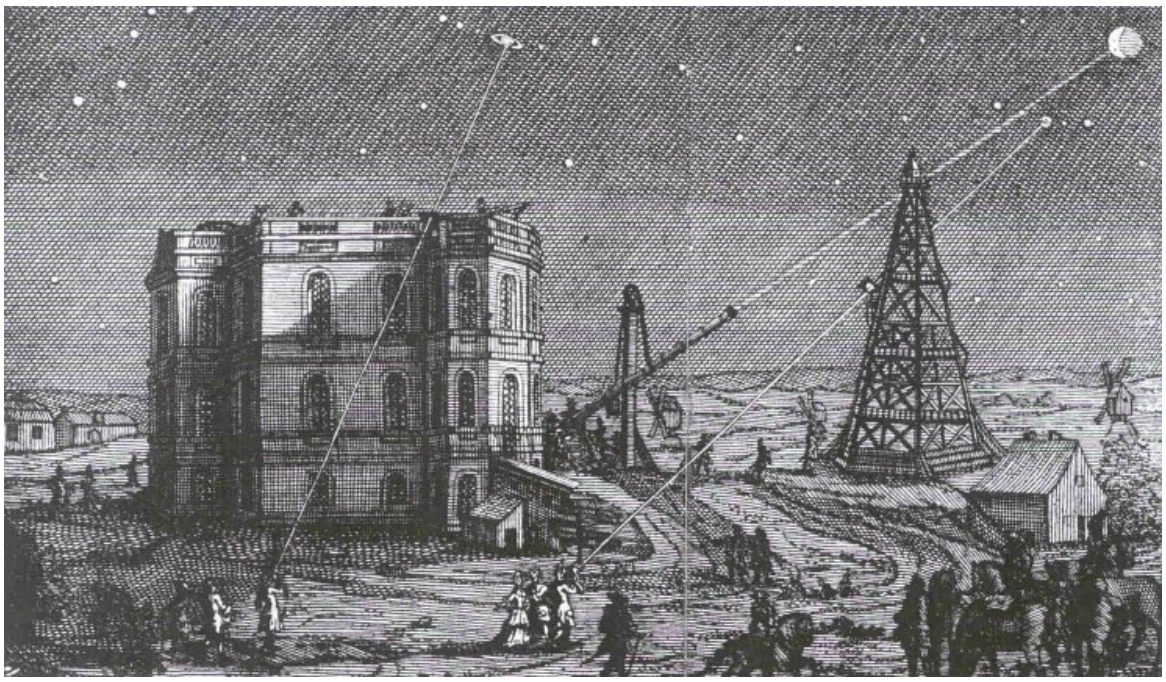

Figure 1.2 – The Paris observatory in 1705, in an engraving by Coquart. Note the Marly tower on the right, which was used to hold lenses with very large focal lengths. A thread was pulled from the lens to the eyepiece to aid in finding the telescope's focal point, a difficult and pain-staking process which led to the discovery of four satellites of Saturn.

(1672), Tethys (1684), and Dione (1684). In 1671, Jean-Dominique Cassini was only able to see Iapetus on one side of Saturn, whereas he could not detect it at its predicted position on the other side of Saturn. He correctly theorized that it was tidally locked to Saturn, and that its trailing side was much brighter than its leading side. It took over thirty years for him to develop a telescope powerful enough to observe Iapetus's leading side, which is almost two magnitudes fainter than its trailing side in the visible domain (e.g., Squyres et al., 1984; Harland, 2007). Observations of Saturn's moons are generally easier near Saturn's equinox every 15 years, when the rings, seen edge-on, are considerably less bright: this explains the 12-year gap between the discoveries of Iapetus and Rhea, and the ~two thirds smaller moons Tethys and Dione.

Meanwhile, Isaac Newton, James Gregory, and Laurent Cassegrain had invented three different versions of the reflecting telescope, using mirrors instead of lenses and thus avoiding chromatic aberrations. Difficulty in creating and polishing large mirrors largely delayed the reflector's utility to the 18th century, when William Herschel started constructing large mirrors of polished copper and tin (an alloy called speculum). His 40-foot telescope, with its 120-cm primary mirror, was financed by King George III after the discovery of Uranus in 1781 (this telescope was, like many of its successors would be, both late and over-budget). It remained the largest and most powerful telescope for over 50 years, and allowed the discovery of Saturn's moons Mimas and Enceladus in 1789 (Herschel, 1790).

By the mid 19th century, the chromatic and spherical aberrations of refracting telescopes had been fixed, while equatorial mounts had been invented and mirror polishing techniques had improved. Thus Hyperion was discovered simultaneously in 1848 by William Lassel on an equatorial reflector near Liverpool and by William Cranch Bond and his son George Phillips Bond on a refractor at Harvard (Bond, 1848; Lassell, 1848). Further improvements on the telescope, such as the construction of large glass mirrors with a lasting metal covering and, crucially, the invention of photography led William Henry Pickering to discover Phoebe on photographic plates in 1899 (Pickering, 1905).

The 20th century witnessed the construction of large telescopes around the world, and countless improvements in their performance. The existence of a satellite near the rings was suspected as an explanation for the gaps in the rings; a dedicated search by Audouin Dollfus during the 1966 equinox revealed Janus (Dollfus, 1968). The difficulty in calculating its orbit was explained a decade later by the presence of Epimetheus, surprisingly sharing the same orbit (Fountain and Larson, 1977). Observations of the Saturn system during the following (1980) equinox, which benefited from the invention of the CCD (Charge-Coupled Device) camera, confirmed this deduction and revealed Dione's trojan Helene and Tethys's trojans Telesto and Calypso (Lecacheux et al., 1980; Seidelmann et al., 1981). Trojan satellites lie within the same orbit as a larger satellite (Tethys or Dione) at its L4 or L5 Lagrange points, i.e., 60° ahead or behind it. A year earlier, Pioneer 11 had flown through the Saturn System, imaging and almost colliding with Epimetheus, and inaugurating a new age of Saturn satellite exploration.

1.2 Spacecraft exploration

With the arrival of the space age and the development of interplanetary probes, the exploration of the Saturn system was largely taken over by spacecraft.

1.2.1 Before Cassini

The first human-made object to fly through the Saturn system was the Pioneer 11 probe on September 1, 1979 (launched in 1973), which discovered the thin F ring. It was followed by Voyager 1 in 1980 and 2 in 1981, which confirmed the existence of the small co-orbital satellites and uncovered the small shepherd moons Atlas, Prometheus, Pandora, and Pan, which constantly interact with Saturn's rings.

Although Titan's surface remained veiled behind its thick haze, the Voyager 1 and 2 spacecraft did reveal the surfaces of Saturn's icy satellites. The normal reflectance in the Voyager clear filter (0.47 μm) was mapped, as well as the orange/violet color ratio, for the inner mid-sized icy satellites (Mimas, Enceladus, Tethys, Dione, and Rhea); Iapetus and Phoebe were also mapped at 0.47 μm (Smith et al., 1981, 1982; Squyres et al., 1984; Buratti et al., 1990; Simonelli et al., 1999). These data showed heavily cratered terrains, with leading/trailing albedo dichotomies, especially on Iapetus. Bright, probably icy fractures called wispy terrain were observed on both Dione's and Rhea's trailing sides, while a rift system was noted on Tethys (Ithaca Chasma) (Moore and Ahern, 1983; Moore, 1984; Moore et al., 1985). The uniqueness of Enceladus was clear from its Bond albedo near unity, a scarcity of craters, signs of recent tectonic and cryovolcanic activity, and its location in the highest-density region of the E ring (e.g., Buratti and Veverka, 1984; Hill, 1984; Buratti, 1988). The irregular shape and high vertical relief of Hyperion identified it as a likely collisional fragment, while Phoebe's photometric and orbital properties were consistent with an outer Solar System origin.

1.2.2 The Cassini-Huygens mission

The Cassini-Huygens mission was the fruit of a collaboration between the National Aeronautics and Space Administration (NASA), the European Space Agency (ESA), and the Italian Space Agency (ASI). It launched from Cape Canaveral, in Florida (USA) on October 15, 1997. After a 7-year cruise including flybys of Venus, the Earth, and Jupiter, the Cassini spacecraft discovered Saturn's 3- and 5-km moons Methone and Pallene, flew by Phoebe, and finally began orbiting Saturn on July 1, 2004. The Huygens descent probe landed on Titan on January 14, 2005, revealing its unique surface featuring complex drainage networks and rounded pebbles (Tomasko et al., 2005). Though the Cassini

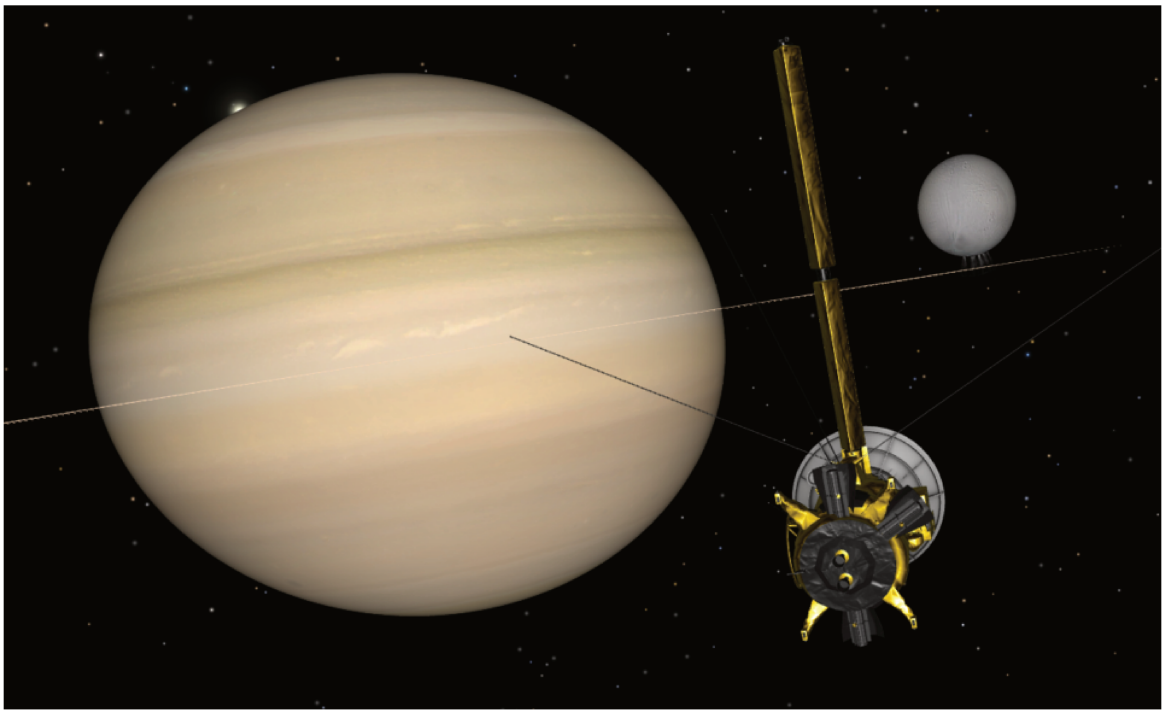

Figure 1.3 – Simulated view of the Cassini radar/radiometer observing Enceladus on November 6, 2011. Notice Saturn's polar flattening and the Sun setting behind Saturn. (Credit: NASA's Eyes on the Solar System)

nominal mission ended in June 2008, it was extended first to 2010 ("Equinox mission") then to 2017 ("Solstice mission"), thus spanning 13 years of orbit around Saturn, corresponding to about 2 seasons in the Saturn system (a Saturn year is 29.5 Earth years). During this time, the Cassini spacecraft flew by Titan 127 times and icy satellites 38 times, as pictured for Enceladus in Fig. 1.3.

The Cassini spacecraft, which was about the size (and the color) of a schoolbus, weighed six tons and was powered by three Radioisotope Thermoelectric Generators (RTGs). It was equipped with a diverse suite of instruments designed to fully characterize Saturn and its rings, satellites, and magnetosphere. The Ion Neutral Mass Spectrometer (INMS), Cassini Plasma Spectrometer (CAPS), and Cassini Magnetometer (MAG) instruments probed the plasma environment *in situ* around Saturn and its satellites (Waite. et al., 2004; Young et al., 2004; Dougherty et al., 2004). Images, including of Saturn's icy moons, were obtained in the ultraviolet (UV) from the Ultraviolet Imaging Spectrograph (UVIS) (Esposito et al., 2004), in the visible and near-infrared (IR) with the Imaging Science Subsystem (ISS) (Porco et al., 2004), and in the near- to mid-IR with the Visual and Infrared Mapping Spectrometer (VIMS) (Brown et al., 2004). The Composite Infrared Spectrometer (CIRS), which observed Saturn and its satellites in the mid- to far-IR, could function both as a high-resolution spectrometer and a radiometer (Flasar et al., 2004). Finally, the Cassini radar/radiometer, operating at a wavelength of 2.2 cm (13.8 GHz, Ku band Elachi et al., 2004), was primarily designed to see through Titan's thick haze and image its surface, but also collected data on the icy satellites (e.g. Ostro et al., 2006; Ostro et al., 2010). The rings, which were observed throughout the mission, were of particular interest during its last phase, the Grand Finale, which consisted in 22 orbits passing between Saturn and its rings before an ultimate dive into the planet's atmosphere.

The Cassini-Huygens mission thus revolutionized our understanding of the Saturn system, revealing the intricacy of interactions between Saturn, its satellites, its magnetosphere, and its rings.

1.2.3 After Cassini

On September 15, 2017, the Cassini spacecraft plunged into Saturn's atmosphere and was finally destroyed in order to avoid any possible contamination of a satellite. Yet, during its 13.5 years around Saturn, it collected a wealth of data, which can still yield new and surprising discoveries. Now that all data has been acquired, we have a comprehensive view of the instruments' performances and the science that results: the calibration procedures can be finalized and perfected. New, more complex approaches are being put into place, such as radiative transfer methods correcting for Titan's atmosphere in the VIMS dataset (e.g., Rodriguez et al., 2018; Le Mouélic et al., 2019), super-resolution techniques applied to Radar altimetry (e.g., Mastrogiuseppe et al., 2018), or topography derivation from overlapping beam patterns or stereo-radargrammetry (e.g., Stiles et al., 2009; Hayes et al., 2017).

In parallel, observations of the Saturn system are being conducted from Earth-based telescopes (on the ground or in Earth orbit), at multiple wavelengths. Such Earth-based data complemented those of the Cassini spacecraft while it was still active, and continue today. For instance, observations from the infrared Spitzer Space Telescope revealed the large, diffuse Phoebe ring (Verbiscer et al., 2009). Astrometry observations at optical wavelengths led to the discovery of 20 new irregular moons orbiting Saturn, as announced by S. Sheppard in 2019. Cloud activity on Titan is regularly monitored from infrared telescopes, and informs on seasonal changes (Corlies et al., 2019). Millimeter observations of Titan with the Atacama Large Millimeter/submillimeter Array (ALMA) resulted in the recent discovery of a thermospheric jet (Lellouch et al., 2019). As described within the present thesis, millimetric and centimetric ground-based observations can also teach us a lot about Saturn's icy satellites.

Finally, spacecraft-based remote sensing remains unique in resolution and geometry, while also allowing *in situ* experiments. After the end of the Cassini-Huygens mission and its myriad discoveries, several future missions will explore icy moons. The Dragonfly mission (Lorenz et al., 2018), which will send a rotorcraft to Titan's equatorial regions by 2034, will conduct *in situ* compositional, thermal, physical, and meteorological characterization of a region comprising extensive dune fields as well as a recent crater. The moons of Jupiter, although they are in a different environment from those of Saturn, also feature icy atmosphere-less surfaces. Europa will be explored by NASA's Europa Clipper mission (mid-2020s launch), while Ganymede will be investigated by ESA's JUpiter ICy moons Explorer (JUICE) mission (2022 launch expected). These three missions will considerably advance our understanding of the icy moons of the Solar System.

1.3 A variety of worlds

Saturn's nine largest satellites are all unique worlds. Their orbital characteristics are described in Table 1.1 and illustrated in Fig. 1.4. In spite of their different orbits, sizes, origins, and evolution, they all have bulk densities significantly lower than rocks, indicating compositions dominated by water ice (hence the denomination "icy moons"). Their surfaces especially are primarily composed of water ice, with varying quantities of silicate, metallic, or organic contaminants. The largest seven satellites (by order of increasing distance to Saturn: Mimas, Enceladus, Tethys, Dione, Rhea, Titan, and Iapetus) are all synchronous, featuring sub-Saturn and anti-Saturn sides. The leading hemisphere (in the direction of movement of the satellite, centered at -90°E) and the trailing hemisphere (centered at 90°E) interact differently with the Saturn system, more specifically its rings, magnetosphere, meteorites, and planetocentric dust. Meanwhile, Phoebe has a short rotation period, and Hyperion's is chaotic. The satellites are dynamically locked into their orbits by resonances: Hyperion is in a 4:3 resonance with Titan, while the Mimas-Tethys and Enceladus-Dione pairs are both in 2:1 mean motion resonances.

Table 1.1 – Orbital characteristics and density of Saturn's nine largest satellites, from Castillo-Rogez et al. (2018) and Thomas et al. (2018). Geometric albedos from Verbiscer et al. (2007), Blackburn et al. (2011), and Miller et al. (2011) are also given, as recorded in Verbiscer et al. (2018). Note that most moons are synchronous, i.e. they have identical orbital and rotation periods.

Satellite	Mean Radius (km)	Semi-major axis (R_{Saturn})[a]	Orbital period (days)	Rotation period (days)	Geometric albedo	Mean Density (kg m^{-3})
Mimas	198.2 ± 0.4	3.2	0.94	0.94	0.962 ± 0.004	1149 ± 7
Enceladus	252.1 ± 0.2	4.1	1.37	1.37	1.375 ± 0.008	1609 ± 5
Tethys	531.0 ± 0.6	5.1	1.89	1.89	1.229 ± 0.005	985 ± 3
Dione	561.4 ± 0.4	6.5	2.74	2.74	0.998 ± 0.004	1478 ± 3
Rhea	763.5 ± 0.6	9.1	4.52	4.52	0.949 ± 0.003	1237 ± 3
Titan	2574.7 ± 0.09	21.0	15.95	15.95		1880 ± 4
Hyperion	135.0 ± 4.0	25.4	21.28	chaotic	0.44 ± 0.13	544 ± 50
Iapetus	734.3 ± 2.8	61.1	79.33	79.33	0.04 to 0.45	1088 ± 13
Phoebe	106.5 ± 0.7	221.0	548.02	0.39	0.086 ± 0.002	1642 ± 18

[a] The average Saturn radius is R_{Saturn} = 58232 km.

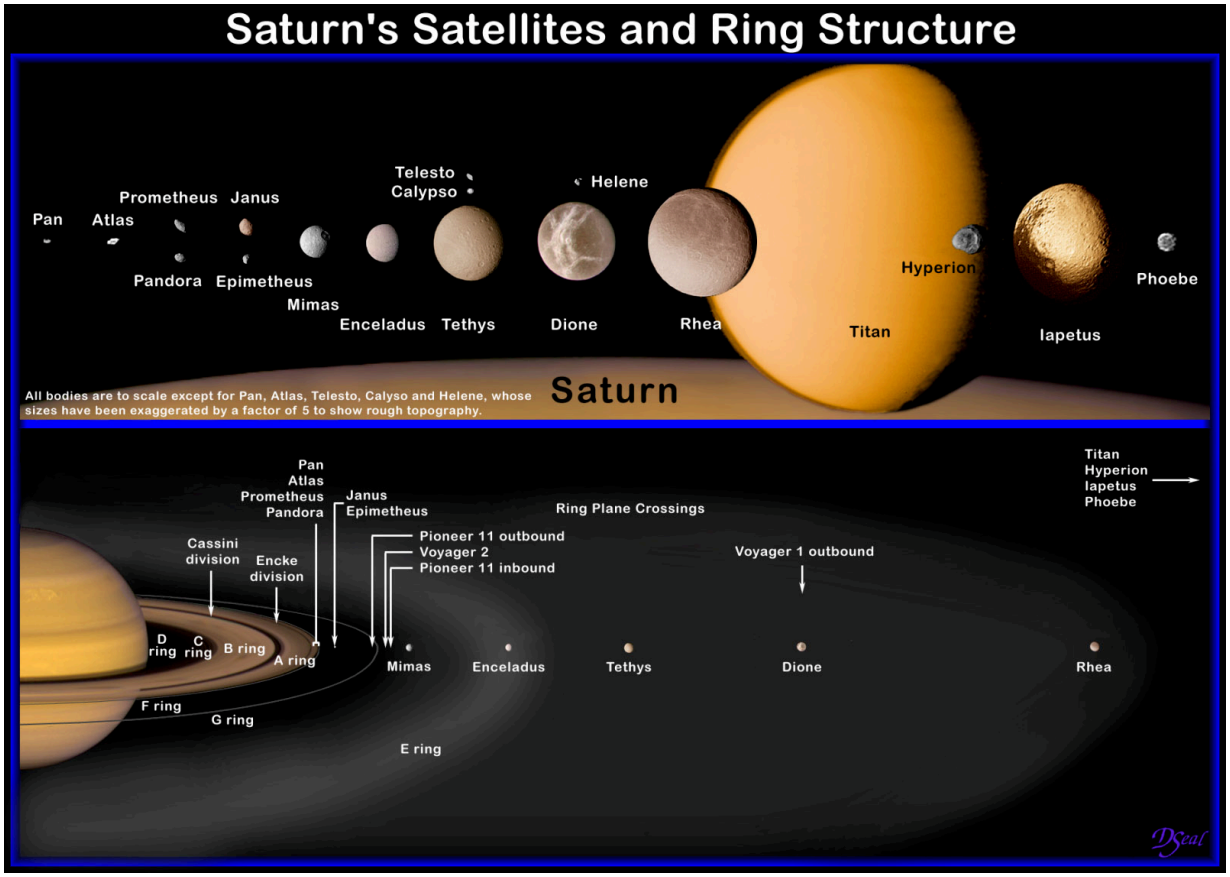

Figure 1.4 – Saturn's satellites and rings structure. Top: The 18 moons of Saturn known before the Cassini spacecraft arrived at Saturn, to scale, in order of increasing distance to Saturn (Saturn would be on the left). Bottom: Saturn, its rings and satellites up to Rhea. Note that the E ring, while densest at Enceladus, extends from Mimas to Rhea. Similarly but not shown here, the large, diffuse ring around Phoebe extends to Hyperion; Phoebe ring particles may also reach Titan and possibly Rhea. (Credit: NASA/Jet Propulsion Laboratory (JPL)-CalTech/David Seal)

Second largest moon after Jupiter's satellite Ganymede, Titan is the only Solar system satellite to have a substantial atmosphere, which is mainly composed of nitrogen (~98% N_2) and methane (2–5% CH_4). Liquid methane and ethane are stable at surface pressures (1.45 bar) and temperatures (93 K). The Cassini-Huygens mission has revealed the presence of methane-ethane lakes, seas, rivers, clouds, and rain (e.g., Tomasko et al., 2005; Stofan et al., 2007; Turtle et al., 2009, 2011), as well as extensive plains, dune fields, mountains, and labyrinthic terrains (e.g., Elachi et al., 2005; Lorenz et al., 2006; Radebaugh et al., 2007; Malaska et al., 2010).

Because this thesis work is dedicated to Saturn's mid-sized icy satellites, we will not describe Titan in more detail, in spite of its complexity and beauty. Similarly, we will not mention further the inner small icy satellites such as Tethys's and Dione's trojans, the shepherd moons, the main ring satellites, and the co-orbitals Janus and Epimetheus, though we recognize the intricacy of their dynamics and their importance to our understanding of the Saturn system as a whole. Instead, we concentrate on the mid-sized icy satellites, especially Iapetus, Rhea, and Dione.

1.4 Outer system satellites: Phoebe, Iapetus, and Hyperion

We define the outer Saturn system as beyond the orbit of Titan. The three largest satellites of the outer Saturn system (Phoebe, Iapetus, and Hyperion) have different compositions, orbital characteristics, and origins. Yet their interactions justify examining them together.

1.4.1 Phoebe

Phoebe's retrograde orbit, high inclination (orbital inclination of 176°), and low albedo suggest it was likely captured, rather than formed in the Saturn nebula (Pollack et al., 1979). Cassini's close flyby of Phoebe in 2004 supports this interpretation, as Phoebe's albedo, composition, and mean density are also very different from that of Saturn's regular satellites (Johnson and Lunine, 2005; Denk et al., 2018). Cassini VIMS and UVIS observations indicate a diverse surface composition, including organics, water ice, iron-bearing minerals, and trapped H_2 and CO_2, generally consistent with an origin in the Kuiper belt (Clark et al., 2005; Coradini et al., 2008; Cruikshank et al., 2008; Hendrix and Hansen, 2008b). Phoebe is heavily cratered, dark (bolometric Bond albedo of 0.023 to 0.1; Simonelli et al. 1999; Flasar et al. 2005; Buratti et al. 2008), and features brighter ice-rich material in craters and scarps. Low thermal inertias (20 to 25 $Jm^{-2}K^{-1}s^{-1/2}$) point to a porous surface down to millimeter depths (Flasar et al., 2005; Howett et al., 2010).

Phoebe is located far from Saturn, near the center of the so-called Phoebe ring, a gigantic diffuse, dusty torus about 170 R_{Saturn} wide, with a vertical thickness of 40 R_{Saturn} (Verbiscer et al., 2009; Hamilton et al., 2015; Tamayo et al., 2016). The particles within this ring most likely originate from dust ejected from Phoebe itself during impacts; like Phoebe, they are most likely retrograde (e.g., Tamayo et al., 2011). Retrograde dust particles larger than 1–5 μm within the Phoebe ring progressively migrate inwards in the Saturn system, and eventually encounter Iapetus, Hyperion, or maybe even Titan (Burns et al., 1996; Tosi et al., 2010; Tamayo et al., 2011).

1.4.2 Iapetus

Iapetus is a heavily cratered icy satellite with many large impact basins, most likely formed within the Saturn subnebula 4.3 billion years ago, though its high inclination (7.5°with respect to the Laplace plane; Mosqueira et al., 2010) and low density (1088 ± 13 kg m^{-3}) remain difficult to

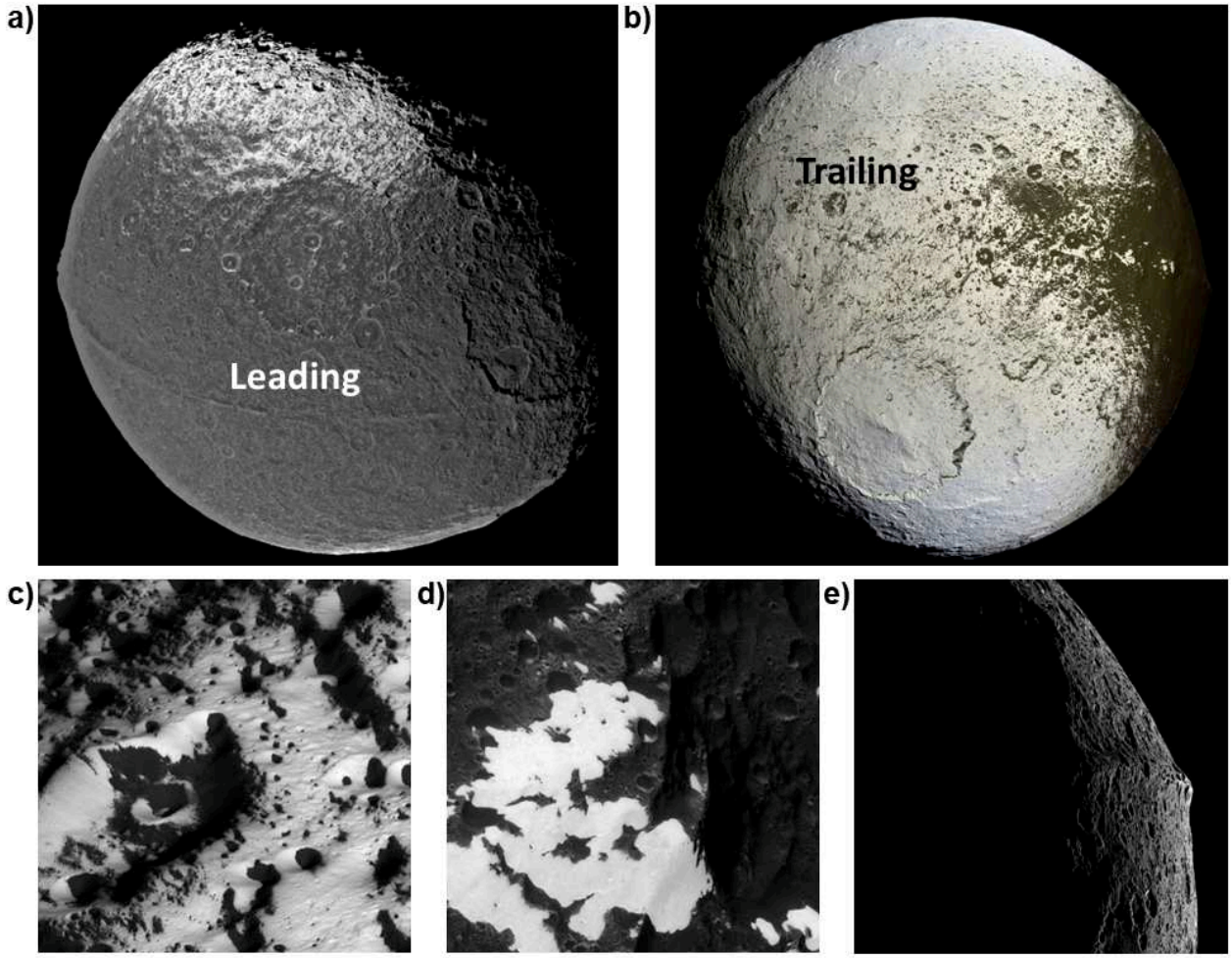

Figure 1.5 – Cassini ISS views of **Iapetus**. a) Leading hemisphere view: the dark terrain (Cassini Regio) does not extend to the North pole. Note also the equatorial ridge. (PIA06166) b) Trailing hemisphere view: the dark terrain extends to part of the trailing at the equator. (PIA08384) c) and d) Close-up views of the boundary between bright and dark terrains near the equator. (PIA08373 and PIA08375) e) Limb view of the equatorial ridge. (Credit: NASA/ESA/JPL/Space Science Institute (SSI)/Cassini Imaging Team)

explain (Mosqueira et al., 2010; Castillo-Rogez et al., 2018). Its low density points to a composition dominated by water ice, with low silicate content. Iapetus's strong flattening (equatorial radius of 745.7 ± 2.9 km vs polar radius of 712.1 ± 1.6 km; Thomas 2010) suggests that it cooled down early in its history. It would thus have preserved a shape corresponding to hydrodynamical equilibrium with a very fast rotation (8.5–15 h), in spite of its 79-day current period (Castillo-Rogez et al., 2007; Robuchon et al., 2010). The high topography contrasts and the quasi-lack of crater relaxation show that Iapetus has remained dynamically inert, in agreement with the lack of tidal heating expected that far from Saturn (White et al., 2013).

Iapetus also features an enigmatic equatorial ridge (Fig. 1.5e). Up to 20 km high, this discontinuous mountain chain extends over 75% of the circumference, but is heavily eroded by cratering, indicating its ancient age (Porco et al., 2005; Giese et al., 2008; Schenk et al., 2018, and references therein). Many different theories, both endogenous and exogenous, have been proposed for the origin of the ridge (Schenk et al., 2018, and references therein), though the most favored today is the infall of a ring around Iapetus. This theory is supported by the ridge's narrowness and its discontinuity, both of which are difficult to explain with endogenous processes. The presence of a discontinuous

equatorial color feature on Rhea (Schenk et al., 2011), which likely formed in a similar manner, as well as rings around the Centaur Chariklo (Braga-Ribas et al., 2014) and Kuiper Belt Object Haumea (Ortiz et al., 2017), lend credibility to the possibility of small-body ring systems.

Nonetheless, the most salient attribute of Iapetus is its leading/trailing hemispheric albedo dichotomy (Fig. 1.5a and b), the most dramatic one in the Solar System. At $61R_{Saturn}$, Iapetus circulates near the edge of the Phoebe ring, whose particles spiral toward Saturn. Thus Iapetus's leading hemisphere accumulates a coating of dark material, while its trailing side remains mostly icy and bright. As a result, at optical wavelengths, Iapetus's trailing hemisphere is 10 to 20 times brighter than its leading hemisphere, as seen by J.-D. Cassini when he first observed it (visible albedos of $0.3 - 0.6$ vs $0.02 - 0.03$; Squyres et al. 1984). The deposition of exogenous dark material associated with Phoebe was first proposed by Soter (1974), and is supported by the results of the Cassini mission. The distribution of dark material at a local scale, which for instance covers only the leading-facing slopes of craters at intermediate longitudes, supports an exogenous origin (Porco et al., 2005). The trailing hemisphere has a mainly icy composition with the presence of some CO_2, while the dark terrain presents spectral features of metallic iron and iron-bearing minerals (hematite), CO_2, and water ice, similar to Phoebe's surface (Fink et al., 1976; Buratti et al., 2005; Pinilla-Alonso et al., 2011; Clark et al., 2012). More recent studies show the presence of aromatic and aliphatic hydrocarbons on Phoebe, Iapetus's leading hemisphere, and Hyperion, consistent with a dust coating from Phoebe (Cruikshank et al., 2014; Hendrix et al., 2018). The fact that large Iapetus leading hemisphere craters do not expose the icy substrate underneath the dark layer, in spite of its <1-m thickness detected by radar (Black et al., 2004; Ostro et al., 2006; Le Gall et al., 2014), indicates that the deposition of dark material is an ongoing process. However, the dark material on Iapetus extends slightly beyond the leading hemisphere at equatorial latitudes, and is absent from the poles (Fig. 1.5a and b). Furthermore, in some places the dark material seems to cover an icy substrate (e.g., Fig. 1.5c) whereas in other places it is the opposite (e.g., Fig. 1.5d). This distribution is consistent with thermal segregation: albedo differences cause significant temperature contrasts, which lead to migration of water ice from dark, warmer regions to bright, colder ones, in particular toward the poles (Hendrix and Hansen, 2008a; Spencer and Denk, 2010; Kimura et al., 2011).

1.4.3 Hyperion

Hyperion is a small, heavily cratered, irregular satellite in a 4:3 resonance with Titan, with a chaotic rotation and a sponge-like appearance. Its unusual rotation, irregular shape, and very low density indicate that it is likely the remnant from a larger moon after a violent collision (e.g., Matthews, 1992). Its low mean density (544 ± 50 kgm^{-3}), i.e., about a third of Phoebe's mean density) indicates a porosity of at least ~40%. In such high-porosity media, impacts dig deeper craters, with little ejecta, consistent with the unusual crater morphologies observed on Hyperion (Thomas et al., 2007a). Mass wasting, accelerated by the sublimation of CO_2 ice, then widens these craters, smooths the surface, and destroys small craters (Howard et al., 2012). At the bottom of the large craters is a dark material, of composition apparently similar to Phoebe and Iapetus's leading hemisphere: it likely also originates in large part from the Phoebe ring, although other sources of contaminants are possible (Cruikshank et al., 2007; Dalton et al., 2012). However, at an orbital distance of 25 R_{Saturn}, Hyperion receives much less Phoebe ring dust than Iapetus.

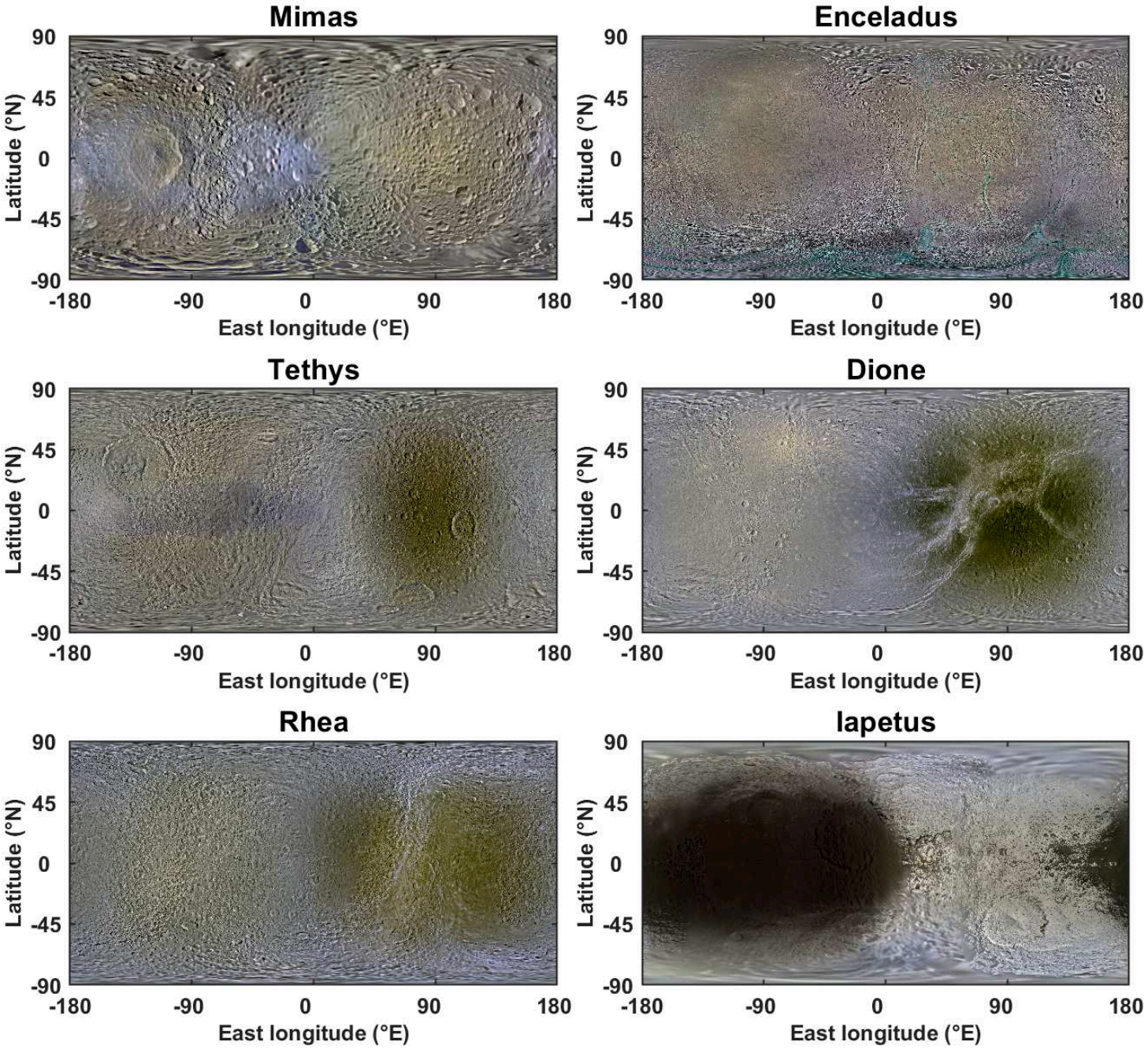

Figure 1.6 – Enhanced 3-color mosaics of Saturn's mid-sized icy satellites, in equidistant projection. For all maps shown within the present manuscript, the leading hemisphere is on the left and the trailing hemisphere on the right (the sub-Saturn point is at 0° longitude). The leading side is most likely brightened by E-ring particles on Tethys, Dione, and Rhea, but darkened by Phoebe ring particles on Iapetus. Note the equatorial UV-bright ellipses on Mimas and Tethys, the tiger stripes on Enceladus's South pole, the dark trailing hemisphere terrain on Tethys, Dione, and Rhea, and the wispy terrains on Dione's and Rhea's trailing sides. From left to right and top to bottom, references for these maps are: PIA18437, PIA18435, PIA18439, PIA18434, PIA18438, PIA18436. (Credit: NASA/JPL-CalTech/SSI/LPI/Schenk et al. 2018)

1.5 Inner mid-sized icy satellites

The five inner mid-sized icy satellites, from Mimas to Rhea, form a fascinating family of bodies with multiple similarities and key differences. Tides with Saturn and resonances among the satellites lead to tectonic and volcanic past and present activity. Enhanced 3-color mosaics of the inner mid-sized icy satellites, as well as Iapetus, are displayed in Fig. 1.6. As they are all in synchronous rotation, their leading and trailing hemispheres are differently affected by exogenous processes, which also vary with distance to Saturn. Their surfaces are all primarily composed of water ice, with minor non-icy contaminants (Clark et al., 1984; Cruikshank et al., 2005). Their age and formation mechanism remains one of the key mysteries of the Saturn system. We will first examine them one by one, in order of decreasing distance to Saturn, then we will summarize the different processes affecting their surfaces.

1.5.1 Rhea

Rhea is the largest of Saturn's icy satellites, including Iapetus (see Table 1.1). Moment of inertia and mean density derived from close Rhea flybys are consistent with an undifferentiated interior of about 25% rock-metal and 75% water ice (Anderson and Schubert, 2007; Tortora et al., 2016). Like Iapetus, Rhea is heavily cratered and presents no hints of recent resurfacing. Nonetheless, Rhea has fewer large impact basins, and their topography is relaxed, indicating a past heat flow up to 30 mW m^{-2}, likely originating from radioactive decay and/or tidal resonances (White et al., 2013; Beddingfield et al., 2015; Schenk et al., 2018). Rhea also shows extensive scarps, ridges, and troughs, constituting grabens up to 30 km wide and 3 km deep and faults up to 100 km in length (see Fig. 1.7a for an example) (Moore et al., 1985; Hammond et al., 2011). Although some of these features appear ancient, the trailing hemisphere graben system ("wispy terrain") seems relatively recent, indicating a complex tectonic and thermal history, including likely recent global extension.

The bright 49-km-wide crater Inktomi (14.1°S, −112.1°E), shown in Fig. 1.7d, is likely one of the youngest craters of the Saturn system, with age estimates between 8 and 280 Ma old (Wagner et al., 2011; Stephan et al., 2012; Dalle Ore et al., 2015). Its ejecta mantles the pre-existing cratered landscape near the crater, and bright discontinuous ejecta rays extend hundreds of km, in a butterfly pattern indicative of an oblique impact from the East. Inktomi has the strongest water ice signature on Rhea (Fig. 1.7b; Stephan et al., 2012; Scipioni et al., 2014).

Rhea's surface composition, examined by VIMS, is dominated by water ice, with some contamination by as yet unidentified non-icy optically dark materials of uncertain origin (Roatsch et al., 2009; Stephan et al., 2012; Scipioni et al., 2014). This material is mainly present on the trailing hemisphere (see Fig. 1.6 and Fig. 1.7b). Especially high-purity water ice is exposed in the fractures of the trailing hemisphere, along the high slopes at the edges of some craters, and in the ejecta blanket of the young impact crater Inktomi (Fig. 1.7b and d). These observations point to a clean water ice crust for the top few km of Rhea, whereas surface dark materials must be of exogenic origin (Schenk et al., 2011; Stephan et al., 2012; Tortora et al., 2016). Schenk et al. (2011) also describes infrared-dark spots almost aligned along the equator. These "blue pearls" (shown in Fig. 1.7c), associated with high topography, were most likely produced by infalling debris from a former ring around Rhea.

A tenuous exosphere, composed of CO_2 and O_2, has been detected from CAPS and INMS observations (Teolis et al., 2010; Simon et al., 2012). This exosphere, less present in the nighttime and the winter pole, is temperature dependent, indicating adsorption and possibly condensation in the colder regions (temperatures as low as ~25 K have been observed at Rhea's South pole; Howett et al., 2016), especially for CO_2 which is less volatile than O_2 (Teolis and Waite, 2016; Teolis et al., 2018).

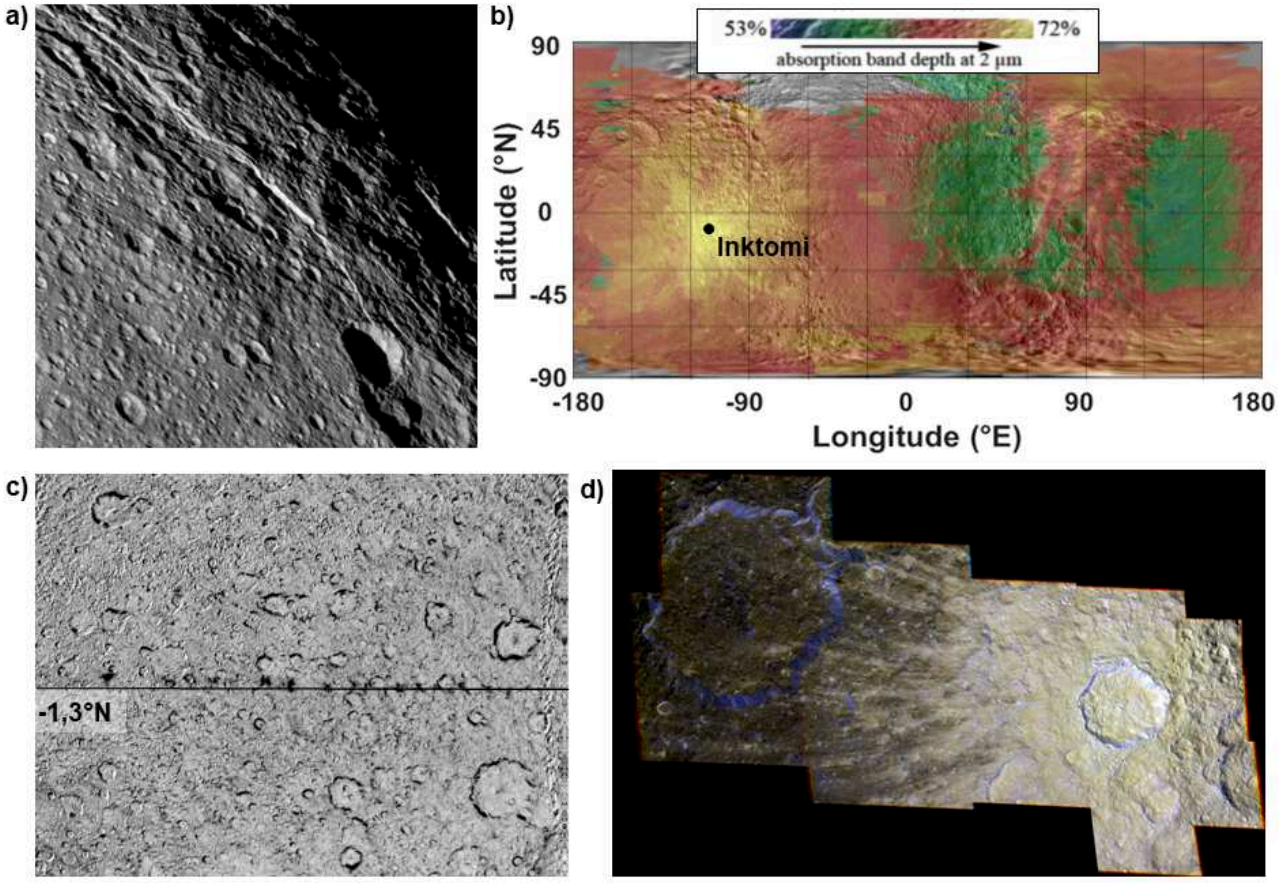

Figure 1.7 – Cassini views of **Rhea**. a) ISS image of graben systems on Rhea. Note also the heavily cratered surface (PIA14654). b) Map of the absorption band depth at 2 µm as seen by VIMS. Deeper band depth is linked to increased abundance in water ice, whereas lower values indicate the presence of non-icy contaminants (silicates or organics). The bright yellow region is centered at Inktomi crater (14.1°S, 112.1°W). Map from Stephan et al. (2012). c) IR/UV ratio image of equatorial patches. The thin black line marks a latitude of −1.3°N. The image extends from 50 to 100°W and from 20°S to 20°N. Figure from Schenk et al. (2011). d) Enhanced 3-color composite of the 40-km-wide Inktomi crater and part of its ejecta blanket. (Credit: NASA/ESA/JPL-CalTech/SSI/LPI/Cassini Imaging Team/Paul Schenk.)

1.5.2 Dione

Although it is considerably smaller (R_{Dione} = 561 km and R_{Rhea} = 764 km; Table 1.1) and denser (indicating ~50% rock fraction), Dione presents many similarities with Rhea (Castillo-Rogez et al., 2018). Indeed, Dione's trailing hemisphere is also coated with dark exogenic material interrupted by large fault systems ("wispy terrain") (Moore, 1984). Dione's surface is dominantly composed of water ice, which is depleted in the dark trailing hemisphere terrain, as shown in Fig. 1.8b. The water ice signatures are particularly strong within the fractures and near the bright young ray crater Creusa (49°N, 76°W; see Fig. 1.8a), which is analogous to Rhea's Inktomi crater, with a likely age of a few tens to a few hundred million years (Stephan et al., 2010; Scipioni et al., 2013; Hirata and Miyamoto, 2016). Like Rhea, Dione features a tenuous, seasonally varying exosphere, best explained by adsorption/desorption and condensation/sublimation cycles (Tokar et al., 2012; Teolis et al., 2018).

Nonetheless, Dione seems younger and more endogenically evolved than Rhea. Dione's tectonic features are more extensive (as obvious in Fig. 1.6), collectively extending to ~ 1300 km (Schenk et al., 2018). Cross-cutting relationships with craters and lack of erosion, shown for example

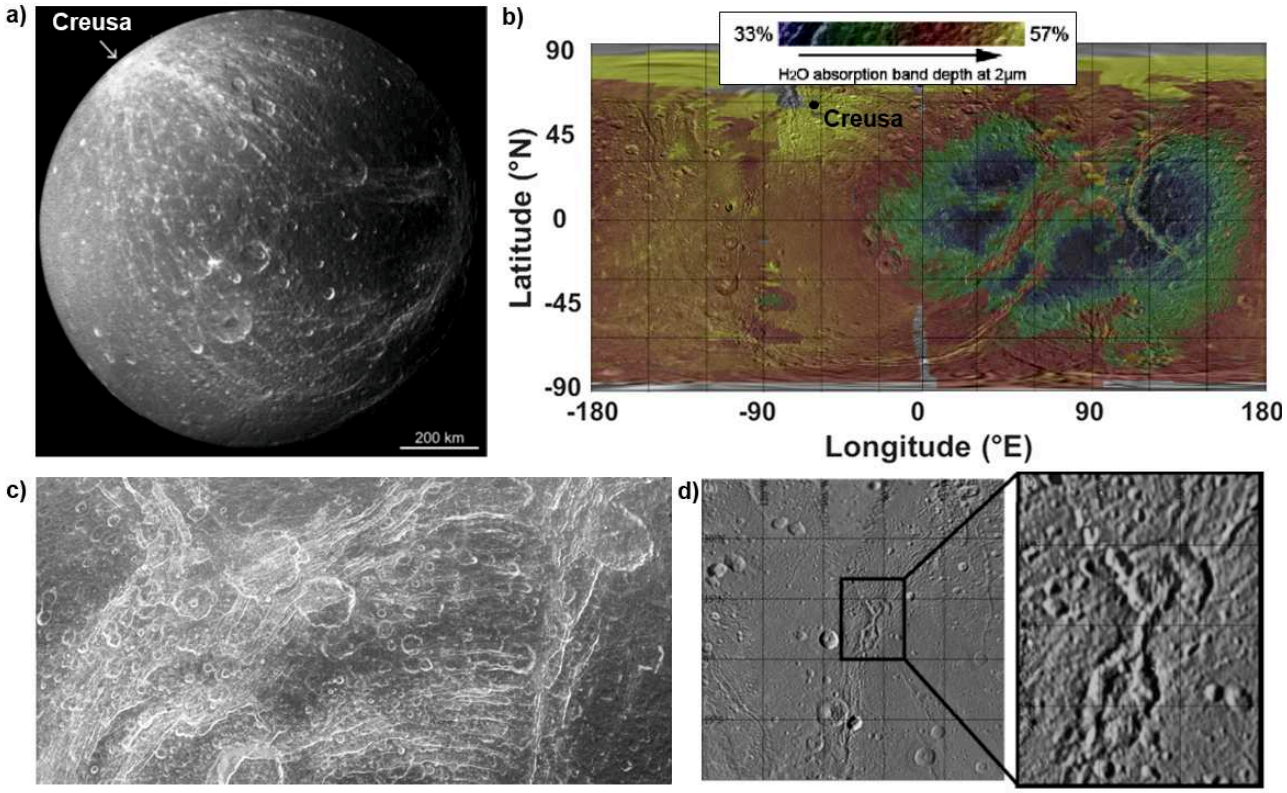

Figure 1.8 – Cassini views of **Dione**. a) ISS image of Dione's sub-Saturn hemisphere (centered on 0°N, 350°W). The location of Creusa crater (49°N, 76°W) is indicated. Figure from Hirata (2016b). b) Map of the absorption band depth at 2 μm as seen by VIMS. Deeper band depth is linked to increased abundance in water ice, whereas lower values indicate the presence of non-icy contaminants (silicates or organics). Map from Stephan et al. (2010). c) ISS image of graben systems on Dione's trailing hemisphere (wispy terrain). (PIA18327) d) Smooth plains of Dione's leading hemisphere, with a close-up of unusual walled depressions. Figure from Kirchoff and Schenk (2015).

in Fig. 1.8c, indicate that these extensional faults are relatively young (at most half of Dione's age), and that their formation may still be ongoing (Beddingfield et al., 2015; Kirchoff and Schenk, 2015; Hirata, 2016b). Dione's leading hemisphere features smooth plains, first noticed on Voyager images (Moore, 1984), in the center of which unusual walled depressions were found (Fig. 1.8d; Schenk and Moore, 2009; Kirchoff and Schenk, 2015). Cryovolcanism is a likely explanation for these features, as well as for extensional and compressional landforms observed in this region, though no current endogenic activity has been detected (Hammond et al., 2013; Kirchoff and Schenk, 2015; Howett et al., 2018; Buratti et al., 2018). Dione's craters are also more relaxed than Rhea's, especially on the leading hemisphere, indicating past heat flux of 50 to 60 mW m^{-2}, consistent with that indicated by the lithosphere elastic thickness (Hammond et al., 2013; White et al., 2017). These high heat fluxes point to either the (past or current) presence of a subsurface ocean on Dione, or stronger tidal forces in the past (Hammond et al., 2013; Schenk et al., 2018). Gravity and topography point to a differentiated interior, and support the presence of a subsurface ocean today (Beuthe et al., 2016; Hemingway et al., 2016).

1.5.3 Tethys

Tethys is very close in size to Dione (R_{Tethys} = 531 km; Table 1.1), and also features a darkened trailing hemisphere, as seen in Fig. 1.6. Its low bulk density indicates a mainly icy composition, with rock fraction varying between 7 and 20% depending on the assumed bulk porosity (Matson et al.,

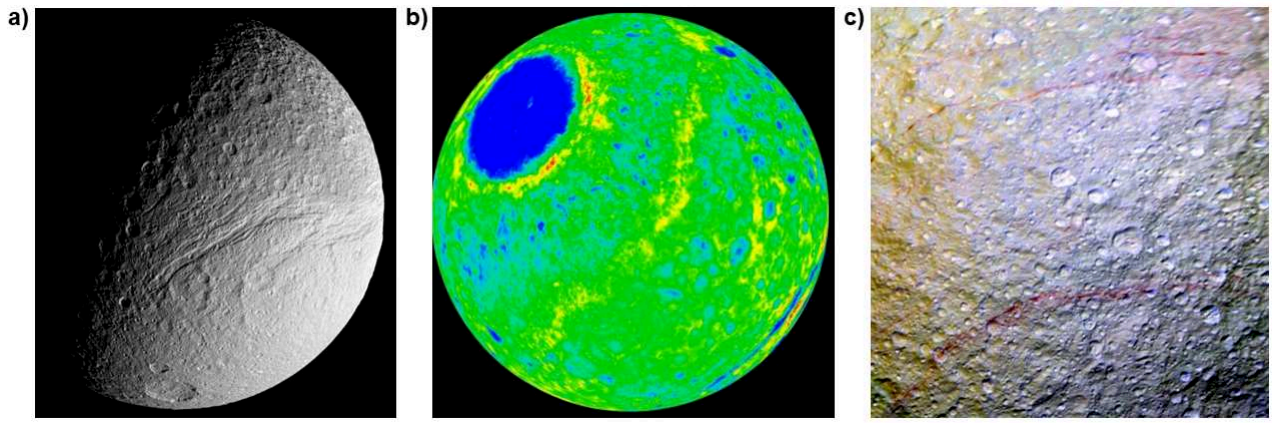

Figure 1.9 – Cassini views of **Tethys**. a) ISS view of Ithaca Chasma (PIA09918). b) Stereo-derived Digital Elevation Model (DEM) of Tethys's leading hemisphere, showing the Odysseus impact basin in the upper left. Total relief is ~ 10 km. (PIA13701) c) Enhanced-color mosaic of the unusual red streaks of Tethys (PIA19637). (Credit: NASA/ESA/JPL-CalTech/SSI/LPI/Cassini Imaging Team/Universities Space Research Association.)

2009). Tethys features a 1000-km-long extensional rift called Ithaca Chasma centered on its sub-Saturn side and shown in Fig. 1.9a. The 425-km-diameter Odysseus impact basin (32.8°N, 128.9°W), shown in Fig. 1.9b, is among the largest in the Saturn System. Tethys also has a relatively smooth plains unit, as well as some unusual red streaks (Fig. 1.9c), whose origin remains unexplained (Smith et al., 1982; Moore and Ahern, 1983; Schenk et al., 2011; Schenk et al., 2018). The significant relaxation of its craters indicates heat fluxes of the same order as Dione's (Giese et al., 2007; White et al., 2017). The history of Tethys, which must account for and possibly relate the formation of Ithaca Chasma, Odysseus crater, smooth plains, and muted topography, remains largely unclear, but likely includes expansion related to global cooling, tidal stresses linked to past resonances, and seismic waves from the Odysseus impact (Castillo-Rogez et al., 2018; Schenk et al., 2018, and references therein).

An elliptically shaped region centered on Tethys's leading side is slightly darker, bluer, and more UV-bright than its surroundings, as apparent in Fig. 1.6 (Buratti et al., 1990; Schenk et al., 2011). The CIRS instrument, by observing diurnal temperature variations, can constrain the thermal inertia (in J m^{-2} K^{-1} $s^{-1/2}$, hereafter referred to as MKS), which describes the surface's ability to store and release heat. These data revealed that the blue region exhibits a higher thermal inertia than its surroundings (25 ± 3 MKS, vs 5 ± 1 MKS outside the anomaly; Howett et al., 2012). Surface alteration by megaelectronvolt electrons accelerated by Saturn's magnetosphere, which preferentially hit equatorial regions of the leading side, is the best explanation for these features (Howett et al., 2012; Paranicas et al., 2014; Howett et al., 2018).

1.5.4 Enceladus

The discovery of water jets from the fractures at the South pole of Enceladus, first by the MAG instrument (Dougherty et al., 2006) then confirmed by multiple instruments aboard the Cassini spacecraft, made it a high-priority target during the Cassini mission as well as for future missions, especially regarding the search for habitable environments or even life in the Solar System. The South Polar Terrain (SPT) of Enceladus is an extremely young region associated with multiple tectonic rifts (including four parallel fractures called the "tiger stripes"), warm temperatures up to ~200 K (Fig. 1.10d, Goguen et al., 2013), high thermal emission (15.8 ± 3.1 GW; Howett et al., 2011b; Le Gall et al., 2017), and jets of icy particles which supply Saturn's E ring (Fig. 1.10a and b; Porco et al.,

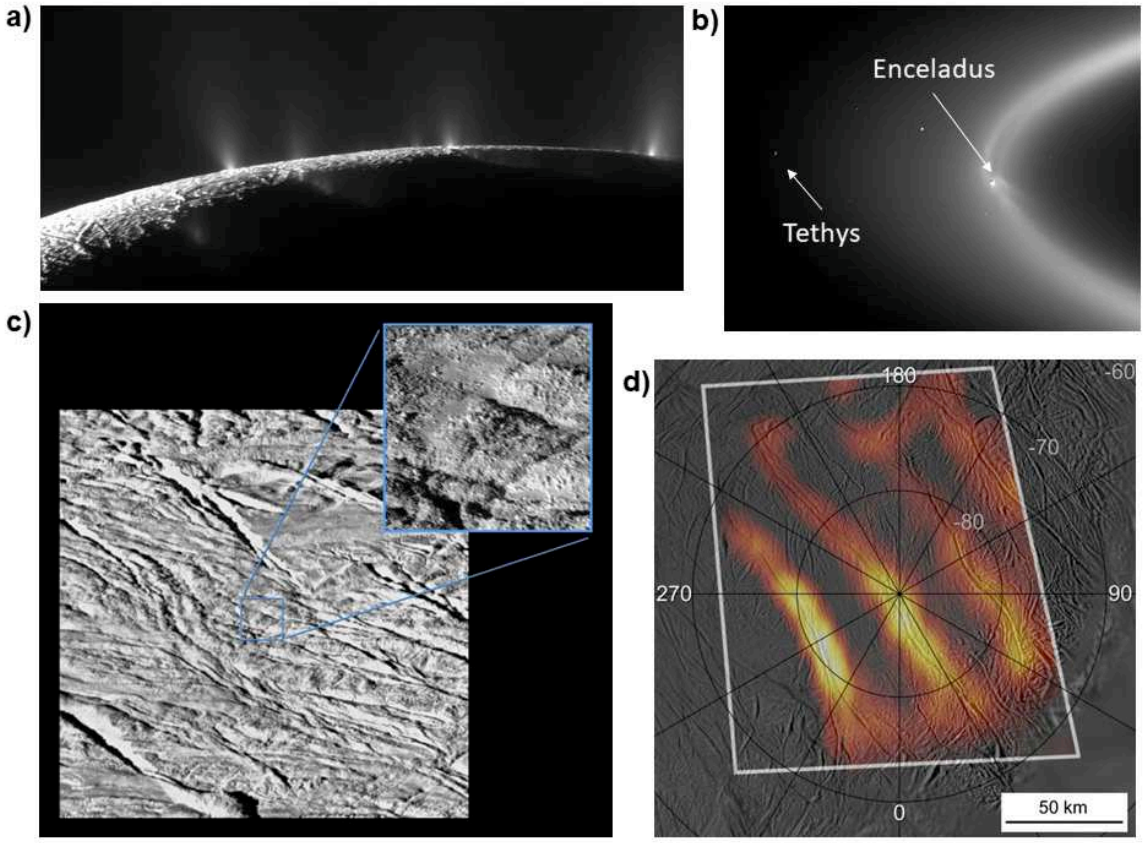

Figure 1.10 – Cassini views of **Enceladus**. a) ISS image of the water ice plumes at Enceladus's South pole, from Porco et al. (2014) (PIA11688). b) Cassini ISS backlit view of Enceladus within the E ring. Tethys is also visible (PIA08321). c) ISS high-resolution observation of the Enceladus South Polar Terrain (SPT), at resolutions of ~ 37 m/pixel and (inset) ~ 4 m/pixel (PIA06251 and PIA06252). d) Heat map of the active SPT obtained by Cassini CIRS, superimposed on an ISS mosaic (PIA10361). (Credit: NASA/ESA/JPL-CalTech/SSI/LPI/Cassini Imaging Team)

2006; Spencer et al., 2006; Abramov and Spencer, 2009; Bland et al., 2015). Radioactive activity and tidal heating on a fully differentiated Enceladus do not provide sufficient energy to sustain this intense activity over long periods of time, which therefore requires periodic activity, a porous core, a varying Saturn dissipation factor Q, or a young Enceladus (e.g., Běhounková et al., 2012; Choblet et al., 2017; Nimmo et al., 2018).

Being largely covered by fresh ice from its South polar jets, Enceladus has the highest albedo of the solar system (geometric albedo of 1.38, Verbiscer et al., 2007, and bolometric Bond albedo of 0.85 ± 0.11, Pitman et al., 2010). It features three fractured regions: the currently active SPT and the young (with few craters and likely formerly active) Leading and Trailing Hemisphere Terrains (LHT and THT). The rest of Enceladus is heavily cratered while still displaying troughs, cracks, and pit chains (Spencer et al., 2009; Crow-Willard and Pappalardo, 2015), its estimated age lies between 0.6 and 4.6 Ga (Kirchoff and Schenk, 2009). The tectonic structures of the fractured regions are fairly complex, including compressional, extensional, and shear features such as ridges, troughs, strike-slip faults, and parallel fractures with different sets of orientations (Patthoff and Kattenhorn, 2011; Yin and Pappalardo, 2015; Crow-Willard and Pappalardo, 2015; Patterson et al., 2018). The highest-resolution Enceladus Cassini imagery (~4 m/pixel) was obtained over the SPT, showing an abundance of meter-sized ice blocks, as shown in Fig. 1.10c (Martens et al., 2015; Helfenstein and Porco, 2015; Patterson et al., 2018).

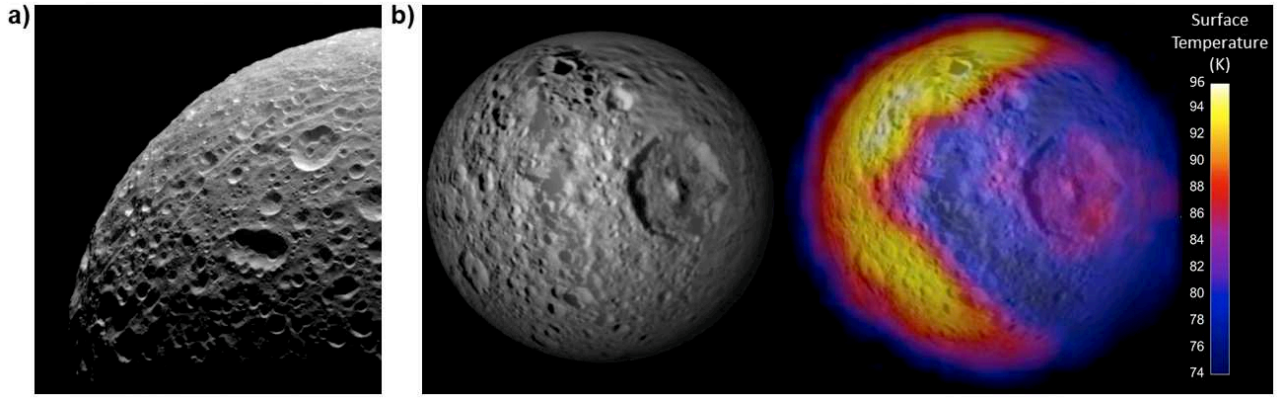

Figure 1.11 – Cassini views of **Mimas**. a) ISS image of Mimas's trailing hemisphere, showing linear grooves (PIA18292.) b) Left: ISS mosaic of Mimas. The large impact basin is Herschel crater (0°N, 100°W). Right: Daytime temperatures measured by CIRS overlain on the ISS mosaic. The low-temperature region ("PacMan") corresponds to the lens-shaped blue region in Fig. 1.6. Low daytime temperatures in spite of similar albedos are due to high thermal inertia (PIA12867). Credit: NASA/JPL-CalTech/GSFC/SWRI/SSI

Although the surface of Enceladus is mainly composed of high-purity water ice, variations in grain size and minor contaminant (e.g., CO_2, NH_3, CH_4) abundance can be seen in VIMS observations (Jaumann et al., 2008; Filacchione et al., 2010; Scipioni et al., 2017; Combe et al., 2019). The predicted distribution of the plume particles falling back onto Enceladus matches the UV-bright regions noted by Schenk et al. (2011) and the regions with larger ice grain sizes seen in the VIMS dataset (Jaumann et al., 2008; Kempf et al., 2010; Scipioni et al., 2017; Southworth et al., 2019).

Enceladus has a relatively high density (1609 kg m^{-3}; Table 1.1), pointing to a higher rock fraction than on Saturn's other icy satellites (Charnoz et al., 2011). Gravity, topography, and libration data show the presence of a global liquid water ocean under an icy crust tens of km thick (Hemingway et al., 2018, and references therein). The Cosmic Dust Analyser (CDA) and INMS instruments aboard Cassini revealed the presence of salts and organics in the ice grains of the plume, as well as molecular hydrogen in the gas component of the plume, indicating that the ocean is in direct contact with the rocky core, with hydrothermal activity at the ocean floor (Postberg et al., 2011; Hsu et al., 2015; Waite et al., 2017; Glein et al., 2018; Postberg et al., 2018). The ocean floor of Enceladus may therefore be a habitable environment, analogous to hydrothermal vents on Earth, making this small icy moon a prime target for the search for life (McKay et al., 2018, and references therein).

1.5.5 Mimas

Unlike the other four inner mid-sized satellites of Saturn, there is no evidence of resurfacing or crater relaxation on Mimas, and the only signs of tectonic activity are some linear grooves shown in Fig. 1.11a (Schenk et al., 2018). The grooves may be linked to the large impact basin Herschel, or could have formed as a result of global expansion as an inner ocean cooled (Tajeddine et al., 2014; Rhoden et al., 2017; Schenk et al., 2018).

Like Tethys, Mimas features a UV-bright region on its leading side (the so-called Mimas "Pac-Man"; Howett et al., 2011a). Fig. 1.11b shows daytime temperatures are lower within this elliptical region, due to a higher thermal inertia (98 ± 42 MKS, vs 34 ± 32 MKS outside the anomaly; Howett et al., 2011a, 2020). As on Tethys, this anomaly is most likely caused by high-energy electron altering

the surface (Schenk et al., 2011; Paranicas et al., 2014; Nordheim et al., 2017; Howett et al., 2018; Howett et al., 2020).

1.6 Inner icy satellite formation and age

There are three leading models, each with different variants and caveats, of the formation of Saturn's inner icy moons. First, they may have formed in place about 4.5 Ga years ago, within Saturn's subnebula; this model cannot, however, explain the variations in density between satellites (e.g. Mosqueira and Estrada, 2003a,b; Canup and Ward, 2006). Second, they may have formed from a larger ring system (Charnoz et al., 2011), itself originating from the disruption of a large satellite entering the Roche zone of Saturn (e.g. Canup, 2010). Third, they may have formed from the reaccretion of debris from a collision between two satellites (Sekine and Genda, 2012; Asphaug and Reufer, 2013; Ćuk et al., 2016; Hyodo and Charnoz, 2017). The accretion from rings and from debris models can both be compatible with very young icy satellites, whereas the subnebula model implies old satellites. However, the age of the icy moons of Saturn is remarkably difficult to constrain.

Various clues indicate that the inner mid-sized icy satellites of Saturn could be relatively young, of the order of 100 million years old. More specifically, these clues include Saturn's low tidal Q implying a fast orbital expansion of the satellites (e.g., Lainey et al., 2012), high past heat fluxes on Tethys, Dione, and Rhea indicating past resonances between different satellites (e.g., Ćuk et al., 2016), the scarcity of large impact basins on the inner moons compared to Iapetus (e.g., Charnoz et al., 2011; Schenk et al., 2018), the anomalously high heat flow from Enceladus (e.g., Spencer and Nimmo, 2013), and the low mass and low non-icy contaminant fraction of Saturn's main rings as possible evidence of their youth (Iess et al., 2019). Together, these observations suggest that the satellites formed either from a large ring system or from reaccretion of collisional debris.

Using crater densities to date the surfaces of Saturn's icy satellites is particularly difficult, as crater statistics in the outer Solar System are not well known (e.g., Zahnle et al., 2003). This is especially true within the Saturn system, where the dominant source of impactors may be planetocentric debris, i.e., objects orbiting Saturn rather than the Sun. Furthermore, secondary and sesquinary (ejecta that escapes into Saturn orbit before re-impacting the surface) impacts may contribute a significant amount of craters on the mid-sized icy satellites (Alvarellos et al., 2005; Bierhaus et al., 2012; Alvarellos et al., 2017; Bierhaus et al., 2018). Although crater statistics do not allow absolute aging of the inner icy moons, the presence of several large impact basins such as Mimas's Herschel and Tethys's Odysseus, which likely formed from comets, seems to indicate an ancient ($\sim$ 4 billion years ago) formation (e.g., Kirchoff et al., 2018). Relative crystalline and amorphous ice fractions near the apparently recent (relative to the rest of the surface) Obatala crater on Rhea lead to an age of ~450 Ma for this crater, implying that the rest of the surface is significantly older (Dalle Ore et al., 2015). Thus the cratering record, though not robust enough to clearly discern between the old and young satellite models, does point towards old surfaces (Kirchoff et al., 2018; Castillo-Rogez et al., 2018).

1.7 Icy satellite surface processes

The processes that altering the (sub)surfaces of Saturn's icy satellites are summarized hereafter; the depths affected are illustrated in Fig. 1.12.

- **Endogenic activity**, namely tectonic, cryovolcanic, and relaxation processes, has modified all of Saturn's mid-sized icy satellites to varying degrees, as described above.

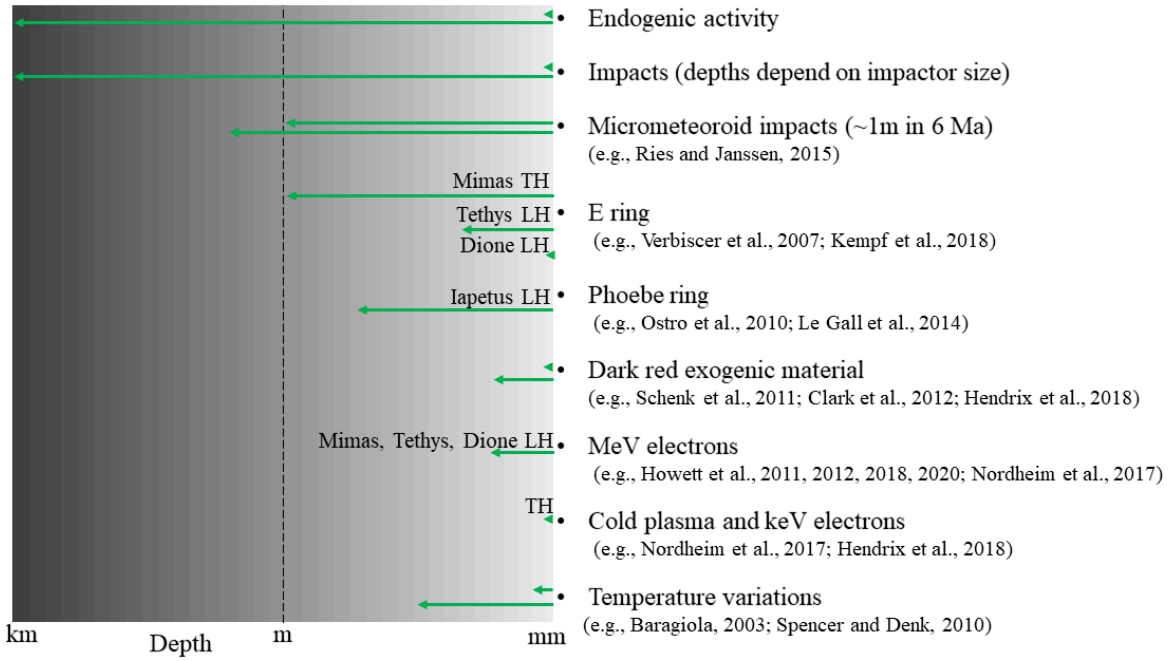

Figure 1.12 – Schematic representation of the depths affected by different processes acting on Saturn's icy satellites. When relevant, the hemisphere (leading, LH, or trailing, TH) most affected is indicated.

- **Impacts** clearly have affected these surfaces throughout their histories, although cratering history in the Saturn system is not robust enough to allow confident surface dating from crater statistics (see discussion above). Heliocentric impactors dominantly affect the leading hemisphere; however, little to no apex-antapex asymmetry impact crater density has been found, implying either crater saturation or a dominantly nonheliocentric impactor population (Kirchoff and Schenk, 2010; Leliwa-Kopystynski et al., 2012; Hirata, 2016a; Kirchoff et al., 2018). Planetocentric impactors would be more uniformly distributed (Kirchoff et al., 2018).

- **Micrometeoroid impacts** likely contribute to the formation of a loose regolith (impact "gardening"), and would dominantly affect the leading hemisphere (e.g., Buratti et al., 1990; Ries and Janssen, 2015). The Cassini Cosmic Dust Analyzer (CDA; Srama et al., 2004) measured an important dust population in the ring plane, as well as interplanetary particles (Srama et al., 2006; Altobelli et al., 2016). While these particles very likely affect the satellites' surfaces, this effect is difficult to disentangle from others (in particular E ring particles and high-energy electrons) and has not been clearly observed (Szalay et al., 2018). Micrometeoroid impacts also introduce non-icy materials to the surface.

- **Deposition of E ring particles**, which are mainly composed of high-purity water ice from Enceladus's subsurface ocean, bombard the moons of the inner Saturn system (Kempf et al., 2010; Schenk et al., 2011). The mean visual geometric albedos of the inner mid-sized satellites are well correlated with the expected E ring flux at their orbits (Verbiscer et al., 2007); infrared water ice band depths (Filacchione et al., 2012) and radar brightness (Ostro et al., 2006; Le Gall et al., 2019) follow the same trend. E ring brightening affects preferentially the trailing hemisphere of Mimas and the leading hemispheres of Tethys, Dione, and Rhea, and is therefore the likely cause of hemispheric dichotomies (e.g., Hamilton and Burns, 1994; Schenk et al., 2011; Royer and Hendrix, 2014; Howett et al., 2018), although recent work indicates that the distribution of infalling E ring particles may be more complex (Juhasz and Horanyi, 2015; Kempf et al., 2018). E ring material dominantly affects the satellites closest to Enceladus (Mimas, Enceladus itself, and Tethys), whereas as at most millimeter depths are expected on Dione, and less on Rhea (Juhasz and Horanyi, 2015; Hendrix et al., 2018).

- **Deposition of Phoebe ring particles** are the most likely origin for the dark material on Iapetus and Hyperion (see Section 1.4). It is also a possible origin for the dark material on the trailing hemispheres of Rhea, Dione, and Tethys, although Phoebe dust is expected to be considerably more rare in the inner Saturn system (Clark et al., 2012).

- **Deposition of a dark red material** seems to be affecting the trailing hemispheres of Tethys, Dione, and Rhea, and to a lesser degree their leading hemispheres as well as Mimas and Enceladus (Clark et al., 2008; Stephan et al., 2010; Schenk et al., 2011; Stephan et al., 2012; Hendrix et al., 2018). The nature and origin of this material are not clear; candidates include complex organic dust (tholins) (e.g., Hendrix et al., 2018), nano-sized iron particles (Clark et al., 2008, 2012), and processed salts from the E ring (Hendrix et al., 2018).

- **High-energy (MeV) electrons** circulating in Saturn's magnetosphere are the best explanation for the thermal inertia anomaly and UV-bright lens-shaped regions on the leading sides of Tethys (Howett et al., 2012; Howett et al., 2019), Mimas (Fig. 1.11b; Howett et al., 2011a, 2020), and possibly Dione (Howett et al., 2014; Howett et al., 2018). These MeV electrons penetrate up to centimeter depths into the subsurface, which may lead to physical (sintering, amorphization) and/or chemical (new molecules, coloring) changes detectable both in the UV and in the thermal infrared (Schenk et al., 2011; Paranicas et al., 2014; Schaible et al., 2017; Howett et al., 2018).

- **Cold plasma (ions and keV electrons) bombardment** would affect preferentially the icy satellites' trailing sides (Nordheim et al., 2017; Howett et al., 2018; Verbiscer et al., 2018). Like MeV electrons, keV electrons may affect the structure of the surface (through annealing or sputtering), but as they would only affect the top millimeters of the surface, their effect should often be obscured by other processes such as infalling E ring grains (Nordheim et al., 2017; Howett et al., 2018). Radiolysis of silicates and organics by keV electrons may however be reddening and darkening the trailing hemispheres, though this effect is also competing with infalling clean E ring grains, especially for Mimas and Enceladus (Hendrix et al., 2012; Hendrix et al., 2018). Further, cold plasma may play a role in the presence of CO_2 and O_3 on all five inner mid-sized moons (Johnson et al., 2008; Hendrix et al., 2018).

- **Temperature variations** lead to winter adsorption and condensation and summer desorption and sublimation of CO_2 at Rhea's and Dione's poles (Teolis and Waite, 2016). On Iapetus, the long day length and stark temperature contrasts between bright and dark regions lead to thermal migration of water ice (e.g., Spencer and Denk, 2010). Thermal stresses likely also modify the structure of the surface, possibly creating stresses and cracks (Baragiola, 2003).

1.8 Conclusion

In the last four hundred years, we have progressed from discovering Saturn's icy satellites to investigating their surfaces in detail. The Cassini-Huygens mission, during its 13.5 years in the Saturn system, revealed diverse and complex worlds, interacting with each other and with the rings and magnetosphere of their planet. Yet, the formation and evolution of the icy satellites remains largely mysterious, as contradictory information points to young or old systems. A variety of processes affect the composition and structure of the satellites' surfaces: these processes come into competition both in space (depths and regions) and over time, and their relative contributions are still unconstrained. The thesis work described herein aims to contribute to our understanding of Saturn's icy satellite subsurfaces, informing on their thermal, physical, and compositional properties down to metric depths.

Chapter 2

Microwave remote sensing: from theory to icy satellite observations

Microwaves, which can peer under the icy surfaces of Saturn's satellites, offer unique information on their properties, history, and evolution.

This chapter begins by reviewing the principles of microwave remote sensing and the way microwaves propagate through matter. We then describe both the active (radar) and passive (radiometry) modes of microwave observations. Finally, this chapter details the microwave radar and radiometry observations of Jupiter's and Saturn's icy satellites.

2.1 Principles of microwave remote sensing

2.1.1 Advantages of microwave remote sensing

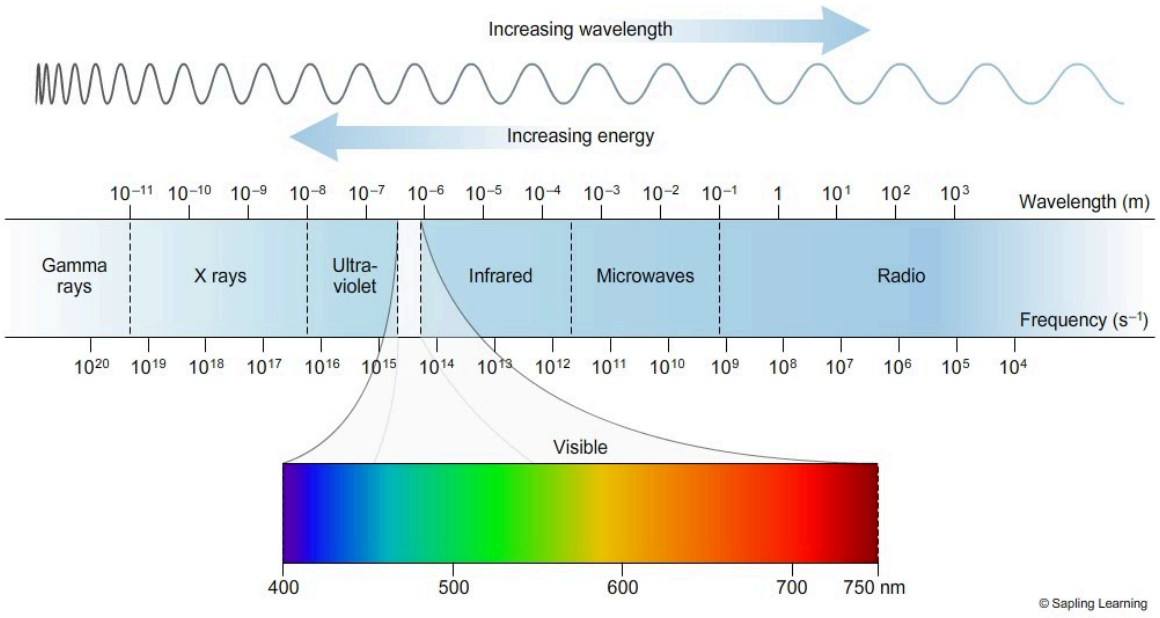

Figure 2.1 – The electromagnetic spectrum. (Credit: Sapling learning)

By convention, the microwave region of the electromagnetic spectrum includes wavelengths from 1 mm to 1 m (i.e., frequencies from 300 GHz to 3 GHz; Fig. 2.1). Just beyond the far infrared

(also called sub-millimeter), it encompasses the high-frequency end of the radio spectrum: the (confusingly named) Ultra High Frequency (UHF, 0.3–3 GHz), Super High Frequency (SHF, 3–30 GHz), and Extremely High Frequency (EHF, 30–300 GHz) bands. Common uses of microwaves include communication systems, microwave ovens, cellular telephone, TV broadcasting, radar, radio astronomy, and surface remote sensing. The latter three applications are particularly of interest to planetary science.

Microwave remote sensing observations, which can be both active (radar) and passive (radiometry), offer information complementary to observations at other wavelengths (including UV, optical, and IR). Microwave radiometry measures the passive continuum blackbody emission of an object (e.g., a surface) in the microwave domain, which gives an indication of its thermal, physical, and to some extent compositional properties. Especially at shorter (millimetric) wavelengths, microwave radiometry can also observe gas emission and absorption bands from atmospheres. Radars observe the signal scattered by a medium from a transmitter to a receiver; it informs on the target's geometry and its absorbing and scattering properties. Both active and passive observations can be obtained regardless of target illumination from the Sun. This offers a considerable advantage with respect to UV and optical wavelengths: the possibility to "see" the surface during the night and polar winter.

In the case of planetary bodies with an atmosphere opaque to most wavelengths, microwaves permit to peer through the clouds and haze to examine the surface. This is the case of Venus and Titan, whose surfaces were revealed in unprecedented detail by, respectively, the Magellan Venus Radar Mapper and the Cassini radar/radiometer. Observing the surface is also possible within several infrared windows, although these observations generally include a greater atmospheric contribution: the Cassini VIMS and ISS instruments, for example, mapped Titan's surface in the near- and mid-infrared.

Microwave radiometry is also particularly well adapted to the study of very cold objects ($\sim$ 20 – 70 K), whose thermal radiation is difficult or impossible to detect in the infrared. Furthermore, in most cases, UV to IR wavelengths only give information on the top few nanometers to millimeters of the surface, although in a few cases meter depths can be probed as well (i.e., with very long observation timescales in polar regions where daily temperature variations are negligible; Howett et al., 2016). Meanwhile, microwaves can generally penetrate down to several meters under the surface. They can thus access key pages in a surface's history, providing insight into thermal, compositional, and structural variations with depth.

Microwave instruments are, however, hampered by their low spatial resolution, which can only be improved by building large antennas. There are consequently few microwave instruments able to resolve Saturn's icy satellites from Earth. Spaceborne radars and radiometers, which can achieve better resolutions from their proximity to the target, are large and heavy. Their use on space missions has therefore been limited, and the Cassini radar/radiometer is one of the most complex, multi-faceted, and high-performance microwave instruments on any interplanetary mission.

2.1.2 Radar/radiometer antennas

Both radars and radiometers include antennas and receivers but radars differ from radiometers in that they include a transmitter as well. Radar/radiometer antennas can take many different shapes, best suited to their wavelength, polarization, modes of operation, and target. The data used in this thesis were obtained either from the Cassini radar/radiometer, the Karl G. Jansky Very Large Array (VLA), or the Institut de Radioastronomie Millimétrique (IRAM) 30m telescope, which all consist in parabolic dish antennas. The main characteristics of such antennas are described herein.

The **gain** of an antenna in a given direction is the ratio of the antenna radiation intensity relative to a lossless isotropic antenna. Although the energy radiated or received is maximal at the boresight (the pointing direction), it is generally significant in other directions. The antenna **beam pattern** $G(\theta, \phi)$ describes variations of the gain intensity with the azimuth and zenith angles. A schematic representation of a typical beam pattern in given in Fig. 2.2. The beam pattern consists in a Gaussian main beam surrounded by smaller near side lobes. The sidelobes greatly decrease with angular distance from the boresight: these far side lobes are generally much less significant but often not negligeable for radiometry measurements.

The half-power **beamwidth** β, or full width at half maximum (FWHM), is defined as the angular width at which the magnitude of the radiation intensity is half of its peak value (-3dB on a decibel scale). For a circularly symmetric antenna pattern, the beamwidth β (in radians) is related to the wavelength λ and the antenna diameter D as follows:

$$\beta \approx \lambda / D_{\text{antenna}} \tag{2.1}$$

The antenna pattern solid angle Ω_p describes the equivalent width of the main lobe of the antenna pattern. It is defined as the integral of the normalized beam pattern $G(\theta, \phi)$ over a sphere (Ulaby and Long, 2015):

$$\Omega_p = \iint_{4\pi} G(\theta, \phi) d\Omega \tag{2.2}$$

For a circularly symmetric antenna, Ω_p can be approximated as the square of the half-power beamwidth:

$$\Omega_p = \beta^2 = \frac{\lambda^2}{D^2_{\text{antenna}}} \tag{2.3}$$

For a real aperture radar or a radiometer, the beamwidth is a good proxy for the resolution of the antenna. Eq. 2.1 implies that, to keep the same resolution, an antenna observing at longer wavelengths must be proportionally larger. Thus Earth-based radio telescopes are among the largest astronomical instruments in the world, with very large single-dish antennas, such as 100-m Green Bank Telescope (GBT) in West Virginia (USA), the 300-m Arecibo telescope in Puerto Rico or Five-hundred-meter Aperture Spherical Telescope (FAST) in China.

Instead of single antenna dishes several kilometers in diameter (impossible to build or steer), equivalent resolutions can be reached with **interferometry**, a technique also used at optical and infrared wavelengths consisting in combining signal from multiple antennas. By observing the phase difference of the signal received from a single source at each antenna (whose position is known), an interferometer array obtains a synthezied beam, whose half power beamwidth is dependent on the maximum distance between antennas, the baseline D_{baseline}:

$$\beta \approx \lambda / D_{\text{baseline}} \tag{2.4}$$

The synthetic beamwidth corresponds to the diffraction limit of the interferometer, and therefore to its best possible resolution. The peak sensitivity (in the pointing direction) of the instrument is dependent on the total collecting area of the antenna array. Microwave interferometers used in planetary science include the cm-wavelength Karl G. Jansky Very Large Array (VLA) in New Mexico (USA), the Atacama Large Millimeter/submillimeter Array (ALMA) in the Llano de Chajnantor (Chile), and the Northern Extended Millimeter Array (NOEMA) at the Plateau de Bure (France). Longer baseline

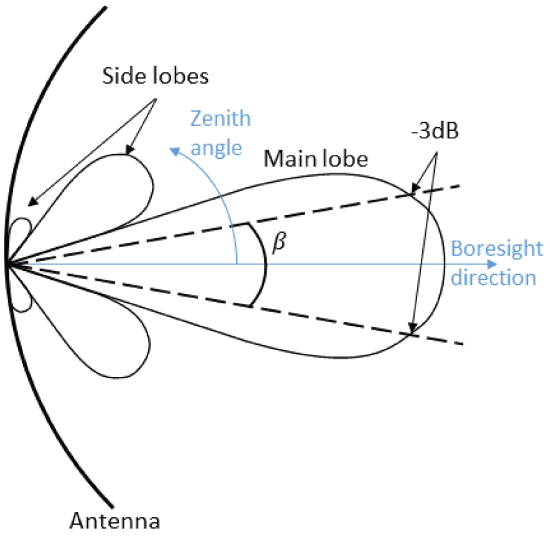

Figure 2.2 – Schematic representation of an antenna radiation pattern. The main lobe and some side lobes are shown. The half-power beamwidth β is plotted.

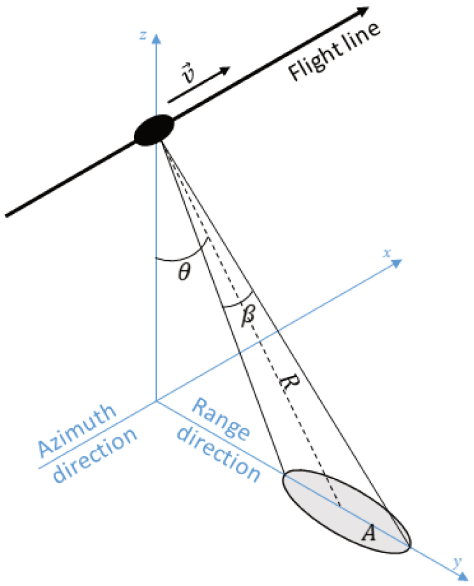

Figure 2.3 – Schematic representation of an oblique radar/radiometer observation geometry from a spacecraft moving at velocity $\vec{v}$ over a flat surface. The incidence angle θ and the range R are shown for the center of the fooprint (antenna boresight point). A circular main beam of width β projected onto a flat surface yields an elliptical footprint in an oblique viewing geometry.

interferometry is possible with the Very Large Baseline Interferometry (VLBI) network, which uses telescopes on different continents. Interferometer arrays also exist for both longer (e.g., the Giant Metrewave Radio Telescope (GMRT) in India, the Low Frequency Array (LOFAR) in Europe, or the Square Kilometer Array (SKA) in South Africa and Australia) and shorter (e.g., the SubMillimeter Array (SMA) in Hawaii, USA) wavelengths.

Spaceborne antennas are more limited in size, but their proximity to the target generally guarantees better resolutions, while also permitting a variety of observation angles and local times. The geometry of oblique incidence angle observations from a radar/radiometer aboard a spacecraft is illustrated in Fig. 2.3. The receiver measures the signal returned from an area corresponding to the antenna beam pattern projected onto the surface, called the real-aperture footprint (by opposition to the synthetic aperture resolution, see Section 2.3.1). In the case of a circular main beam observing a flat surface, the footprint is elliptical, as in Fig. 2.3. In practice, the surface may be curved (if a planetary body is observed at a distant range), and the near and far side lobes of the beam pattern may also contribute to the received signal, especially in passive mode. Several examples of spaceborne radars and radiometers will be discussed in Section 2.4.1.

2.2 Interactions of microwaves with matter

Before discussing the microwave radar/radiometry observations on Saturn's icy satellites, this section reviews the ways in which electromagnetic waves interact with matter.

2.2.1 Medium electromagnetic properties

We describe the properties of a medium, while focusing on how an electromagnetic wave propagates through them.

The **magnetic permeability** μ, in Henry per meter (H/m), describes the medium magnetization in the presence of a magnetic field. In practice, all materials considered in this thesis (water ice, tholins, and small quantities of silicates and CO_2 ice) are **non-magnetic**, and we can consider that $\mu = \mu_0 = 4\pi \times 10^{-7}$ H/m., where μ_0 is the magnetic permeability of vacuum.

The **electrical permittivity** ε, in Farad per meter (F/m), describes the local redistribution and absorption of charges due to polarization in the presence of an electric field. Its value depends on the composition, structure, porosity, and temperature of the medium, as well as on the considered wavelength. In the frequency domain, it is a complex quantity:

$$\varepsilon = \varepsilon' - j\varepsilon'' \tag{2.5}$$

The permittivity of a medium is generally expressed relative to that of the void, $\varepsilon_0 = 8.85 \times 10^{-12}$ F/m. The **relative permittivity** is therefore given by:

$$\varepsilon_r = \varepsilon/\varepsilon_0 = \varepsilon'_r - j\varepsilon''_r \tag{2.6}$$

The materials considered herein are all **dielectric**: they can be polarized by an applied electric field, but do not transport electrical charges (as opposed to electrical conductors). For such media, the real part of the complex relative permittivity is the **dielectric constant** ε'_r; it controls the velocity of electromagnetic waves in the medium and the magnitude of the reflectivity at an interface between two media. The imaginary part of the complex permittivity corresponds to losses due to absorption by the medium, which dissipates this energy as heat. These losses are generally expressed through the **loss tangent**, which is the ratio between the imaginary and real parts of the permittivity:

$$\tan\delta = \varepsilon''_r/\varepsilon'_r \tag{2.7}$$

The dielectric properties of a few materials are given in Table 2.1. Freshwater and (even more so) saltwater contain dissolved ions, leading to relatively high conductivity which increases the imaginary part of the permittivity ε''_r (Mätzler, 2006; Ulaby and Long, 2015). High porosity significantly decreases the dielectric constant ε'_r, with values reaching 1.3 for 80% porosities (Mätzler, 1996).

2.2.2 Electromagnetic waves in a homogeneous medium

For an electromagnetic wave propagating in a homogeneous, non-dispersive, stationary, and isotropic medium and assuming a sinusoidal time-varying electric field $\vec{E}$ with angular frequency ω, the homogeneous wave equation is:

$$\vec{\nabla}^2\vec{E} + \omega^2\mu\varepsilon_r\varepsilon_0\frac{\partial^2}{\partial t^2}\vec{E} = 0 \tag{2.8}$$

$$\vec{\nabla}^2\vec{E} + k^2\frac{\partial^2}{\partial t^2}\vec{E} = 0 \tag{2.9}$$

Table 2.1 – Dielectric properties of a few representative materials, at frequencies close to that of the Cassini radar/radiometer (13.78 GHz). Water ice, CO_2 ice, tholins, and hematite (an iron oxide) have all been detected in the Saturn system. Note also that a material's dielectric properties can vary significantly with its porosity and degree of compaction.

Material	**Frequency (GHz)**	ε'_r	ε''_r ($\times 10^{-3}$)	$\tan\delta$ ($\times 10^{-3}$)	**Reference**
Water ice	13	3.13	1.3	0.41	Paillou et al., 2008
CO_2 ice	13	1.55	0.3	0.19	Paillou et al., 2008
Tholins	13	2.03 – 2.33	20.6 – 22.0	8.8 – 10.8	Paillou et al., 2008
Silicates	35	5 – 8	50 – 500	6 – 100	Campbell and Ulrichs, 1969
Carbonates	15	~ 8	~ 200	~ 25	Thomas, 2004
Hematite	22	2 – 11	50 – 500	~ 50	Nelson et al., 1989; He et al., 2015
Liquid water (20°C)	13.78	66	29000	1300	Ulaby and Long, 2015

where the complex wavenumber k is defined as follows:

$$k = 2\pi/\lambda = \omega\sqrt{\mu\varepsilon_r\varepsilon_0} = \beta - j\alpha/2 \tag{2.10}$$

where α is the medium attenuation (or extinction) coefficient in power and β is its propagation, or phase, constant. The solution to the above form of the wave equation, for a plane wave propagating in the $\hat{z}$ direction, is given by:

$$\vec{E}(t,z) = \vec{E}_0 e^{j\omega t} e^{-jkz} \tag{2.11}$$

$$\vec{E}(t,z) = \vec{E}_0 e^{j(\omega t - \beta z)} e^{-z\alpha/2} \tag{2.12}$$

A plane wave is characterized by electric and magnetic fields that are perpendicular to each other, perpendicular to the direction of propagation and have uniform properties in the plane orthogonal to this direction (the wavefront plane). In the far-field domain (far away from the emitting source), waves can be regarded as locally plane.

The amplitude of the electric field decreases exponentially with z as the energy transported by the wave is converted into heat. We thus define the **electrical skin depth** $\delta_{\text{el}} = 1/\alpha$ as the depth at which the power of the signal is reduced by a factor of $e^{-1} \approx 0.37$. The electrical skin depth is commonly used as a proxy of the distance to which the wave can propagate into a medium.

A low-loss medium is a high-transparency medium through which an electromagnetic signal of wavelength λ can propagate along great distance (typically >100 wavelengths) before being significantly attenuated. It has a low value of $\tan\delta$ (< 0.01) and is associated with a large electrical skin depth δ_{el}. In this thesis, only low-loss media composed primarily of water ice ($\tan\delta = 1.3 \times 10^{-3}$; Paillou et al., 2008) are considered. For such media and assuming all losses are due to absorption (by opposition to losses by scattering), the electrical skin depth is related to the loss tangent, the wavelength λ, and the dielectric constant ε'_r by the following equation:

$$\delta_{\text{el}} = \frac{\lambda}{2\pi\sqrt{\varepsilon'_r}\tan\delta} \tag{2.13}$$

We note that, assuming that ε'_r and $\tan\delta$ vary little with wavelength (generally true at GHz wavelengths for dielectric media), the electrical skin depth is directly proportional to the wavelength. This

illustrates the fact that, the longer the observation wavelength, the deeper under the surface the instrument can probe.

For plane waves, the **polarization** describes the manner in which the direction of the electric field changes with time. For a wave propagating in the $\hat{z}$ direction, the electric field vector has a component aligned with each of the $\hat{x}$ and $\hat{y}$ axes. The polarization is then described as the phase shift ϕ between these two components of the electric field:

$$\vec{E} = (E_{0x}\hat{x} + E_{0y}\hat{y}e^{j\phi})e^{j(\omega t-\beta z)}e^{-z\alpha/2} \tag{2.14}$$

For $\phi = 0$ or π, the x- and y-components are in phase. The electric field has a constant inclination with respect to the $\hat{x}$ axis: the wave is linearly polarized. For $\phi = \pm\pi/2$, the wave is circularly polarized. However, in most cases, the wave is elliptically polarized and can be described as the superposition of two orthogonal linearly polarized waves, perpendicular and parallel to the plane of incidence (defined as the plane containing the surface normal and the direction of propagation of the wave), as illustrated in Fig. 2.4.

2.2.3 Wave reflection and transmission

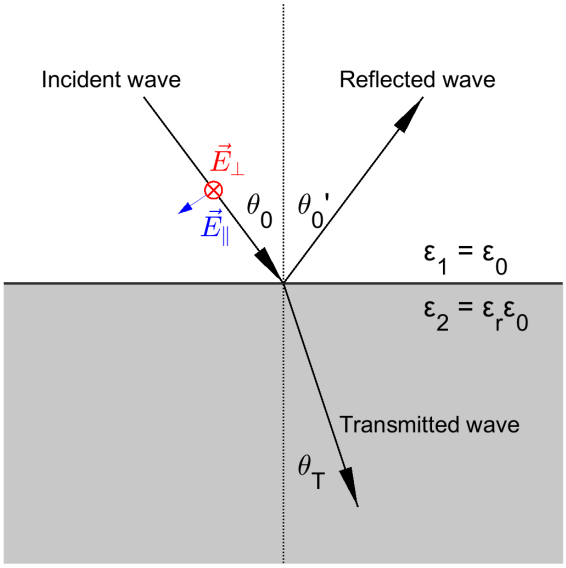

Figure 2.4 – Ray representation of wave reflection and transmission from vacuum into a perfectly smooth and uniform surface at oblique incidence. The electric field of the incident wave is divided into its components perpendicular and parallel to the plane of incidence.

A radar or radiometry signal generally examines a surface, which is defined as a transition between two media of different electromagnetic properties, namely a solid medium and air or space, as illustrated in Fig. 2.4. The transmission and reflection of electromagnetic waves at such interfaces are described by the Snell-Descartes law:

$$\theta_0' = \theta_0 \tag{2.15}$$

$$\frac{\sin\theta_T}{\sin\theta_0} = \sqrt{\frac{\varepsilon_1'}{\varepsilon_2'}} \tag{2.16}$$

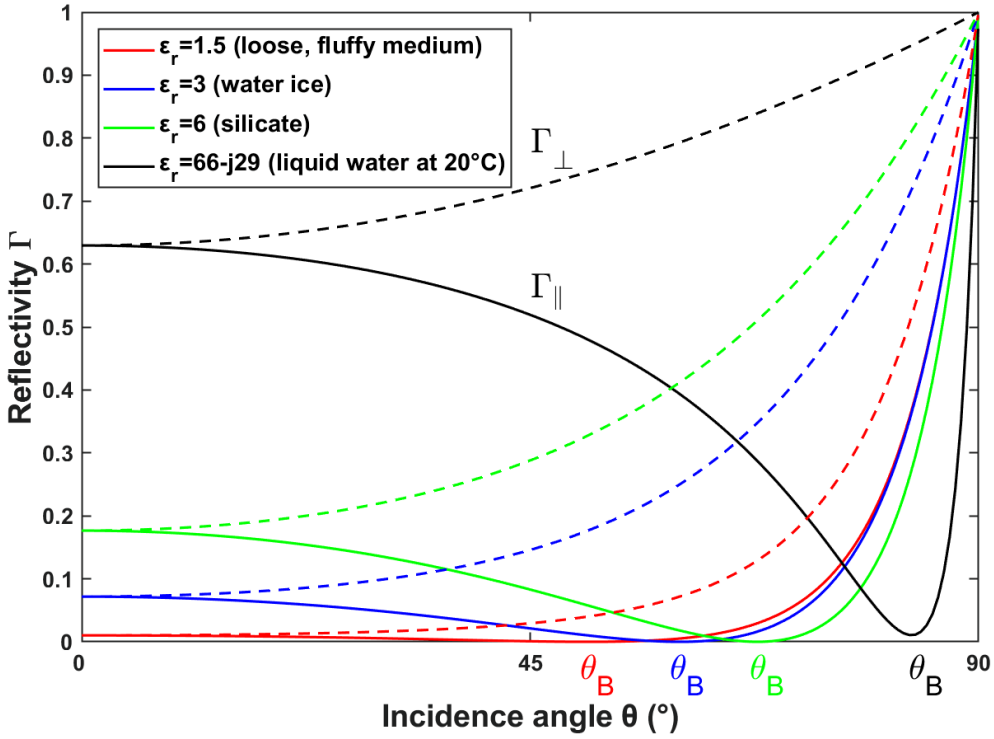

Figure 2.5 – Reflectivity Γ in parallel (continuous lines) and perpendicular (dashed lines) polarizations, as a function of incidence angle for four different values of the dielectric constant (near 13.78 GHz), typical of four different media (liquid water at 20°C, a silicate, water ice, and a loose, high-porosity medium). At the Brewster angles θ_B, the parallel polarization reflectivity $\Gamma_\parallel$ is null.

where θ_0 is the angle of incidence, θ_0' the angle of reflection and θ_T the angle of transmission as given in Fig. 2.4. For a perfectly smooth non-magnetic surface, the ratios of reflected power to the incident power, also called the **reflectivity** Γ, for parallel and perpendicular polarizations, is given by the Fresnel coefficients. Applied to the boundary described in Fig. 2.4 and using the Snell-Descartes law to simplify their expression, they are formulated as follows:

$$\begin{aligned}\Gamma_\perp &= \left|\frac{\cos\theta_1 - \sqrt{\varepsilon_r - \sin^2\theta_1}}{\cos\theta_1 + \sqrt{\varepsilon_r - \sin^2\theta_1}}\right|^2 \\ \Gamma_\parallel &= \left|\frac{\varepsilon_r\cos\theta_1 - \sqrt{\varepsilon_r - \sin^2\theta_1}}{\varepsilon_r\cos\theta_1 + \sqrt{\varepsilon_r - \sin^2\theta_1}}\right|^2\end{aligned} \tag{2.17}$$

At normal incidence, the reflectivity in both polarizations reduces to:

$$\Gamma = \left|\frac{\sqrt{\varepsilon_r} - 1}{\sqrt{\varepsilon_r} + 1}\right|^2 \tag{2.18}$$

Conservation of energy implies that the ratio of the transmitted power to the incident power, also called the transmissivity, is given by:

$$\begin{aligned}\mathbb{T}_\perp &= 1 - \Gamma_\perp \\ \mathbb{T}_\parallel &= 1 - \Gamma_\parallel\end{aligned} \tag{2.19}$$

Fig. 2.5 illustrates the angular variations of the reflectivity in parallel and perpendicular polarizations, for dielectric constants typical of four different materials. The parallel polarization reflectivity $\Gamma_\parallel$ goes

to zero at an angle called the **Brewster angle** θ_B, for which all the wave's energy is transmitted into the medium:

$$\theta_B = \tan^{-1} \sqrt{\frac{\varepsilon_2}{\varepsilon_1}} = \tan^{-1} \sqrt{\varepsilon_r} \tag{2.20}$$

In practice, measuring the position of the Brewster angle on a planetary surface can provide a direct measure of its effective dielectric constant.

For a low-loss medium (i.e., $\varepsilon_r'' \ll \varepsilon_r'$), Eq. 2.17–2.20 can be simplified by assuming that the imaginary part of the permittivity is negligible: $\varepsilon_r = \varepsilon_r'$.

2.2.4 Wave scattering

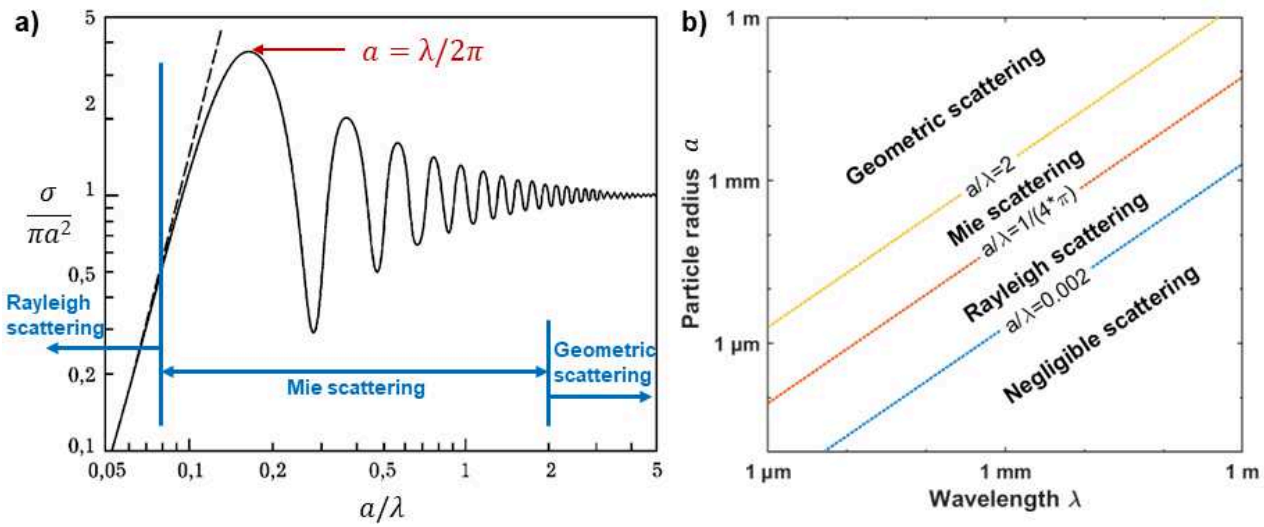

Figure 2.6 – (a) Monostatic radar cross-section of a perfectly conducting sphere as a function of the radius-to-wavelength ratio a/λ. Figure from Kostylev (2007). (b) Scattering regimes for different wavelengths and particle sizes. Scattering from a perfectly conducting sphere peaks at $a/\lambda = 1/2\pi$, within the Mie regime. The boundaries between the different regimes shown here are indicative; the borders are not actually strictly defined.

When an electromagnetic wave encounters a particle, the amplitude of scattering changes with particle size a and wavelength λ of the incident wave in the medium of propagation ($\lambda = \lambda_0/\sqrt{\varepsilon_r}$, where λ_0 is the wavelength in vacuum). The monostatic radar backscattering cross-section σ_b describes the fraction of an incident wave scattered back towards the direction of incidence. For a spherical particle of radius a, the backscattering efficiency ξ_b is (Ulaby and Long, 2015):

$$\xi_b = \frac{\sigma_b}{\pi a^2} \tag{2.21}$$

The three regimes of scattering are briefly described below and illustrated in Fig. 2.6.

- $a < \lambda/4\pi$: For small particle sizes, Rayleigh scattering dominates. In this regime, ξ_b varies as $(a/\lambda)^4$, leading to negligible scattering for small particle sizes and long wavelengths. This Rayleigh scattering law is generally valid for $a < n\lambda/4\pi$, where n is the index of refraction between the propagation medium and the particle. Rayleigh scattering of sunlight by the Earth's atmosphere famously gives our sky its blue color and sunsets their red color.

- $a \sim \lambda$: If the particle size is of the same order as the wavelength, scattering enters the Mie regime. Resonance between the particle size and the wavelength leads to oscillations in backscattering efficiency (see Fig. 2.6a). Mie scattering by micrometer-sized dust in Mars's atmosphere is responsible for its blue sunsets.

- $a \gg \lambda$: At particle sizes larger than the wavelength, geometric optics apply. The incident wave is reflected and transmitted at each boundary between the particles and the propagation medium, as described in Section 2.2.3. The wavelength dependence of the angle of scattering by water droplets causes rainbows.

The top few millimeters of icy satellite surfaces are often composed of a loose, fine-grained regolith. Dominant surface particle sizes of the order of tens of μm have been derived for Saturn's icy satellites from infrared band depths and using the Hapke scattering model (Newman et al., 2009; Filacchione et al., 2010; Ciarniello et al., 2011). However, such particles sizes have a negligible scattering effect in the microwaves, which are sensitive to greater depths and to larger inhomogeneities.

2.2.5 Subsurface scattering

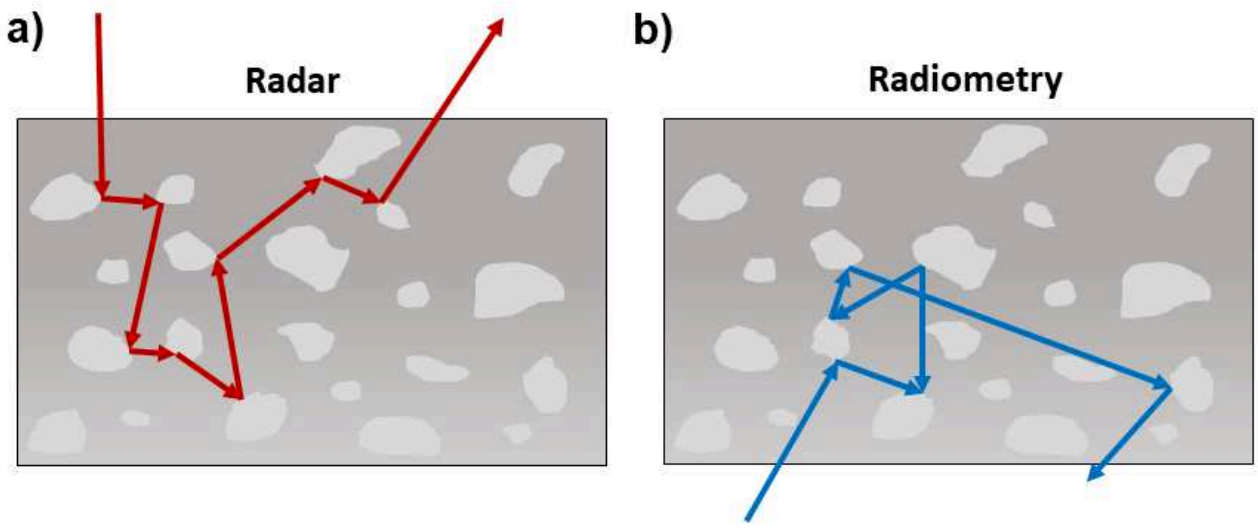

Figure 2.7 – Schematic representation of the effect of volume scattering on (a) an incoming radar signal and (b) an outgoing radiometry signal.

A planetary near subsurface generally consists in an inhomogeneous medium, containing structural and/or compositional variations such as pores or non-icy material inclusions, causing discontinuities in the subsurface. At scales comparable to or larger than the wavelength, Mie and geometric scattering on these discontinuities scatter both incoming radar signals and outgoing thermal emission (radiometry). This **subsurface (or volume) scattering** thereby increases the backscattered radar signal (both albedo and backscattering cross-section) and decreases the amount of emitted radiation (leading to low emissivities) (e.g., Hewison and English, 1999; Lellouch et al., 2016, 2017b). Volume scattering thus further amplifies the anti-correlation between radar and radiometry data implied by Kirchhoff's thermal radiation law (Eq. 2.32). Volume scattering is most significant in weakly absorbing media such as water ice, where the long photon path length increases the number of opportunities for reflection.

Multiple subsurface scattering can lead to exceptionally high reflectivities, both at optical and radar wavelengths depending on the scattering structures' size. This process is described by the **Coherent Backscattering Effect (CBE)** (also called the Coherent Backscattering Opposition Effect, or CBOE, at optical wavelengths), which was initially invoked to explain opposition peaks in the optical (e.g., MacKintosh and John, 1988; Mishchenko, 1992; Mishchenko and Dlugach, 2017). The CBE was first applied to microwave observations of Jupiter's moons by Hapke (1990), and was later refined by laboratory, numerical, analytical, and observational studies (e.g., Hapke and Blewett, 1991; Peters, 1992; Black et al., 2001b; Dlugach et al., 2011; Pitman et al., 2017). The CBE argues that multiple scattering by randomly oriented dielectric inhomogeneities embedded within a low-absorption medium creates an opposition effect, which increases scattering back towards the source of the incident wave (i.e., toward the radar transmitter). For coherent backscattering to be effective, the scattering inhomogeneities must be about wavelength-sized, and separated by distance of the order of a wavelength (Hapke, 1990; Peters, 1992; Black et al., 2001b).

A subsurface may also contain ordered rather than random structures, which can change its radar and radiometric properties. Possible ordered subsurface structures similarly-sized round pebbles (such as on a riverbed; e.g., Le Gall et al., 2010), buried craters (Eshleman, 1986), or buried ice pipes (Rignot, 1995). Vertical stratification can be important, especially on Earth where precipitation is important (adding horizontally uniform layers), but also on airless bodies where porosity can vary with depth, or where past events (impacts, endogenic activity) can be buried by a loose regolith (e.g., Ries and Janssen, 2015). Radiative transfer models and emissivity have been proposed to simulate the effects of scattering within solid surfaces (e.g., Kuga et al., 1991; Wiesmann and Mätzler, 1999; Mishchenko et al., 1999; Moroz, 2005; Liang et al., 2008; Ulaby and Long, 2015) on the outgoing radiation.

While the exact size of subsurface inhomogeneities cannot easily be constrained from radar and radiometry data, they must generally be larger than $\lambda/4\pi$ to cause significant scattering. Section 2.5 describes microwave observations of outer Solar System icy satellites, and how volume scattering is invoked to explain both the passive and active data.

2.3 Radars for planetary exploration

The term radar is originally an acronym for RAdio Detection And Ranging. The basic principle of a radar is to emit a radio signal from a transmitter, and measure the signal scattered by the target toward a receiver. The transmitter and receiver can be at different positions (bistatic radar) or use the same antenna system (monostatic radar). Even though radar technology was originally used mainly for military purposes, such as aircraft detection and ranging, it has since been widely applied to remote sensing for scientific purposes.

2.3.1 Types of radars used in planetary exploration

Radars have a wide range of possible applications, including within planetary science. The basic information that a radar can provide is an object's or surface's position (in the antenna pointing direction, at a range determined by the light travel time), speed (by measuring the shift in frequency due to the Doppler effect), and radar scattering cross section in different polarizations (by comparing the amplitude of the emitted and received signals). Shorter wavelengths are sensitive to shallower depths into a medium, and to smaller scales of surface roughness (i.e., topographic variations at the scale of the wavelength). Depending on their application, radars can operate from the ground or from an airborne or spaceborne platform.

Ground-based radar

During the 1940s to 1960s, radar echos were obtained from Mars, Venus, Mercury, and the Moon, enabling for instance precise calculation of Venus's and Mercury's rotation state (e.g., Dyce et al., 1967), a fourth test of General Relativity (Shapiro et al., 1968), and early mapping of the Moon in preparation for the Apollo missions. Radar observations have been obtained for all planets and large moons up to the Saturn system, providing clues to the structure and composition of their near subsurfaces (e.g., Neish and Carter, 2014). Saturn's rings have also been observed from ground-based radars at several wavelengths and ring plane tilt angles, revealing high-purity water ice particles of sizes of the order of a meter (e.g., Goldstein and Morris, 1973; Cuzzi and Pollack, 1978; Ostro et al., 1980; Nicholson et al., 2005; Zhang et al., 2019).

The Arecibo radar system and Goldstone Solar System Radar (GSSR) are especially useful for planetary exploration, and can map (using Synthetic Aperture Radar processing) the surface of the Moon at ~200–400-m resolutions (Campbell et al., 2007, 2014), and those of the inner planets at ~km resolutions (Carter et al., 2004; Harmon et al., 2011, 2012). These data have for instance revealed water ice in Mercury's permanently shadowed polar craters (Fig. 2.8b; Harmon et al., 2001; Harmon et al., 2011), buried structures on the Moon (Campbell et al., 2014), and dust and lava deposits on Mars (Fig. 2.8c; Harmon et al., 2012; Harmon and Nolan, 2017). The Arecibo radar system measured the polarization properties of Venus's surface, revealing likely buried rough surfaces and mantling by impact ejecta (Carter et al., 2004; Campbell et al., 2015). Earth-based radar systems have also proved to be particularly valuable in the study of small bodies, allowing determination of the orbit, rotation, and shape of comets and asteroids with Doppler imaging (e.g., Ostro, 1985).

Oblique-looking radars: Real and Synthetic Aperture Radar

For spaceborne radars observing at oblique incidence, smooth surfaces reflect the signal in a different direction and therefore appear dark, while rough surfaces show up as bright features. Real Aperture Radar (RAR) examines the signal returned from the whole footprint of the beam pattern. RAR systems can yield low-resolution imaging, but are also used on Earth to measure wave heights, wind speed, or rain rate, among other applications (Ulaby and Long, 2015). A RAR system used as a scatterometer measures the radar scattering coefficient for a variety of incidence angles.

When observing at oblique angles, examining the return time and the Doppler delay (due to the relative movement between the target and the spacecraft) of a modulated signal can allow a significant improvement in the along-track resolution, a technique called Synthetic Aperture Radar (SAR). SAR processing allows high-resolution imaging, and has been used extensively on Earth as well as on Venus and Titan, whose atmospheres are opaque to optical and most infrared wavelengths. SAR images acquired at different polarizations and incidence angles can inform on surface composition, roughness, and slope (and to a lesser extent, on the subsurface properties). SAR images of Solar System bodies have been obtained from Earth (as mentioned above) as well as from dedicated instruments aboard spacecraft.

Venus's optically opaque atmosphere is transparent to radar wavelengths, which therefore permit a characterization of surface properties. After initial radar exploration by Pioneer Venus (NASA, 1978) and Venera 15 and 16 (Lavochkin, 1982), the Magellan mission (NASA, 1990–1994) focused primarily on SAR imaging. The Magellan Radar Mapper mapped 98% of Venus's surface at a wavelength of 12.6 cm and a resolution of 150 m, revealing varied and extensive volcanic activity (Fig. 2.8a), as well as signs of tectonism (Fig. 2.8a), mass wasting, aeolian processes (dunes, wind streaks, yardangs), and a sparsity of impact craters (Saunders et al., 1992). The Magellan mission also obtained crucial information on topography and dielectric properties (e.g., Campbell, 1994). Both the VERITAS and EnVision missions recently proposed and (pre)selected respectively in the NASA Dis-

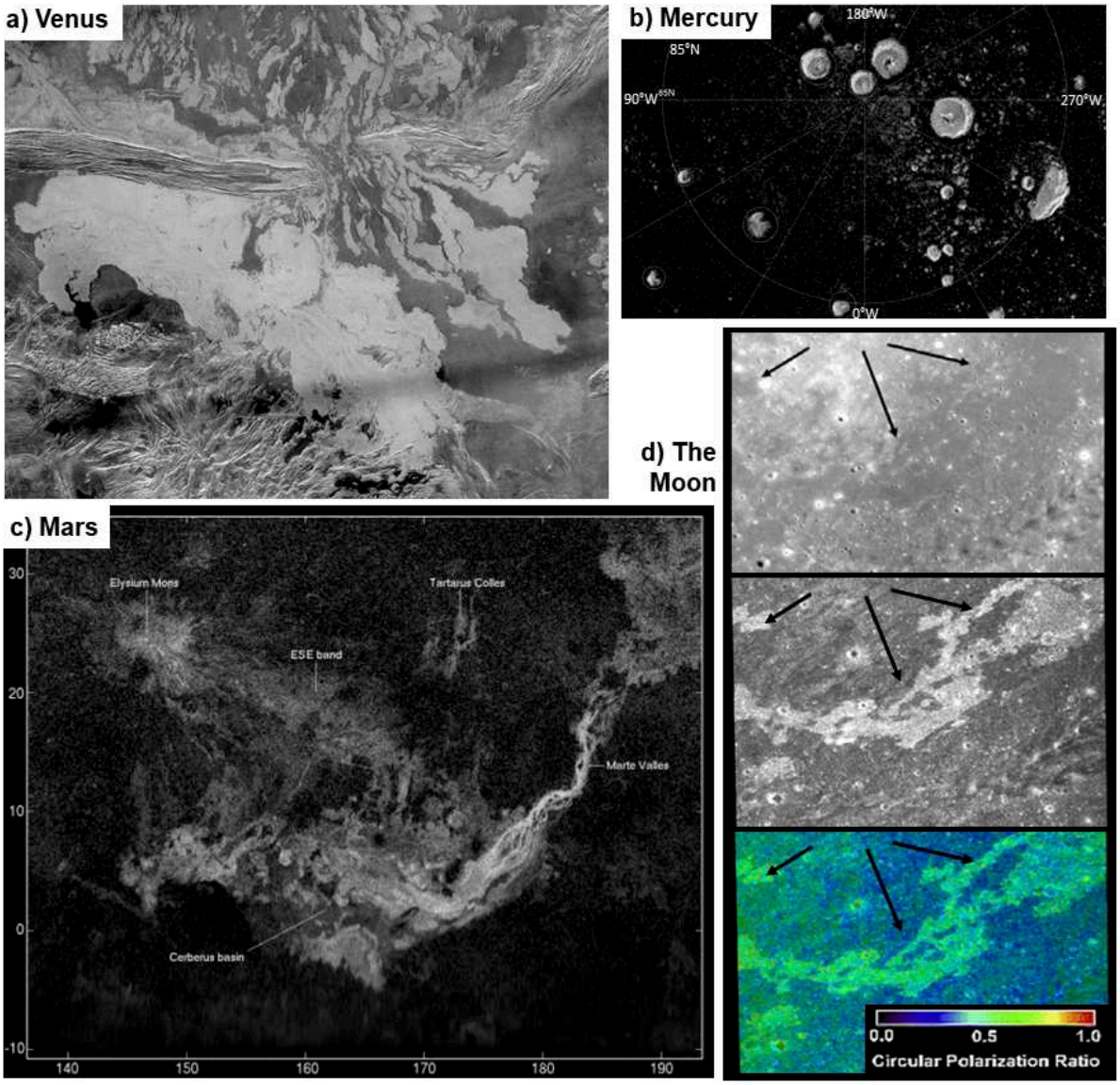

Figure 2.8 – SAR images of rocky Solar System surfaces a) Magellan SAR image of lava flows crossing a ridge belt on Venus, centered at (25°E, 47°S; North is to the right) (PIA00486). Credit: NASA/JPL b) Arecibo radar image of Mercury's North polar region, showing higher radar backscatter from water ice in permanently shadowed craters. Figure from Harmon et al. (2011). c) Arecibo radar image of the Elysium region, including radar-bright rough lava flows. Figure from Harmon et al. (2012). d) Top: Kaguya (JAXA) Terran Camera image of barely apparent impact melt flows northeast of Aristillus, on the Moon. Middle: Mini-RF total power SAR image featuring clearly visible radar-bright impact melt. Bottom: Mini-RF circular polarization ratio (CPR) overlaid on the total power image; impact melts have higher CPR than surrounding terrains. Arrows point to the impact melt flows. Figure adapted from Carter et al. (2012).

covery and ESA Cosmic Vision (M5) programs include advanced radar for surface characterization (e.g., Hensley et al., 2015; Ghail et al., 2017).

Titan, which also has a thick and optically opaque atmosphere, is similarly a natural target for radar exploration. The Titan Radar Mapper on board the Cassini mission conducted SAR, altimetry, and scatterometry observations. It was designed primarily to explore Titan's surface (Elachi et al., 2004), and successfully mapped 45% of it at $\leq$ 1 km/pixel resolution (Lopes et al., 2019), while also examining Saturn's rings and its icy satellites. An example SAR image of Titan's second largest hydrocarbons sea, Ligeia Mare, is pictured in Fig. 2.9b. Cassini radar observations of Titan and other Saturnian satellites are further discussed in Section 2.5.

The Mini-SAR and Mini-RF radars aboard the Chandrayaan-1 (ISRO) spacecraft and the Lunar Reconnaissance Orbiter (LRO, NASA) respectively, operating at 4.2 and 12.6 cm, have mapped the Moon (including its far side and polar regions, inaccessible to ground-based radars) in left and right circular polarizations (Spudis et al., 2009; Nozette et al., 2010). Among other results, these data allowed confirmation of water ice at the poles (Spudis et al., 2013), characterization of surficial structures (Neish et al., 2011), and detection of buried impact melts (Fig. 2.8d and Carter et al., 2012).

Nadir-looking radars: radar altimeters and sounding radars

A radar altimeter observes at nadir (i.e., at 0° incidence) and measures the signal travel time with high precision and accuracy, in order to assess the range between the instrument antenna and the target, thereby giving access to surface topography. In this geometry of observation, smooth surfaces return especially high echoes, while rough or inclined surfaces scatter the signal away from the radar. Most imaging radars aboard spacecraft (including the Magellan and Cassini radars) can operate as altimeters and obtain topography profiles.

If the wavelength is long enough to penetrate into the surface material (>m wavelengths into some solid soils; cm wavelengths into ice and liquid hydrocarbons), it becomes possible to examine the vertical structure of the subsurface. These sounding, or ground-penetrating, radars (GPR) are especially useful in high-transparency media (i.e., with a large skin depth and a low loss tangent) such as water ice. GPRs can be either space-borne or operate directly on the surface. In order to probe down to kilometer depths, sounding radars often operate at radio wavelengths; the applications of these instruments is summarized herein.

Sounding radars have been used on the Moon since the Apollo 17 mission, which included two such instruments designed to investigate the electromagnetic and structural properties of the top kilometer of the lunar subsurface: SEP (Surface Electrical Properties Experiment) and ALSE (Apollo 17 Lunar and Sounder Experiment), operating at wavelengths of 2–60 meters (e.g., Olhoeft and Strangway, 1975). The SEP data showed a lack of subsurface water and a porosity decreasing with depth (Simmons, 1974), while ALSE provided accurate topography (Elachi et al., 1976). The 2007 SELENE (JAXA) spacecraft also carried a 60-m (5 MHz) lunar radar sounder (LRS; Ono et al., 2008), which investigated subsurface structures and found hidden lava tubes down to a depth of 1 km (Pommerol et al., 2010; Kaku et al., 2017). The Chang'E 3 and 4 rovers (CNSA) both included a GPR (the Lunar Penetrating Radar, LPR, Fang et al., 2014) operating at 5, 15, and 150 MHz (60, 20, and 0.6 m wavelengths). These missions identified and characterized the lunar porous and granular regolith and underlying terrains, including on the far side of the Moon (e.g., Xiao et al., 2015; Dong et al., 2017; Li et al., 2020).

Similarly to the Moon, most radar exploration of Mars has been undergone by sounding radars. More specifically, MARSIS (Mars Advanced Radar for Subsurface and Ionosphere Sounding) on Mars express (ESA) operated at 1.5—5.5 MHz frequencies (55—230 m) (Jordan et al., 2009), and SHARAD (the Mars SHAllow RADar sounder) on the Mars Reconnaissance Orbiter (MRO, NASA)

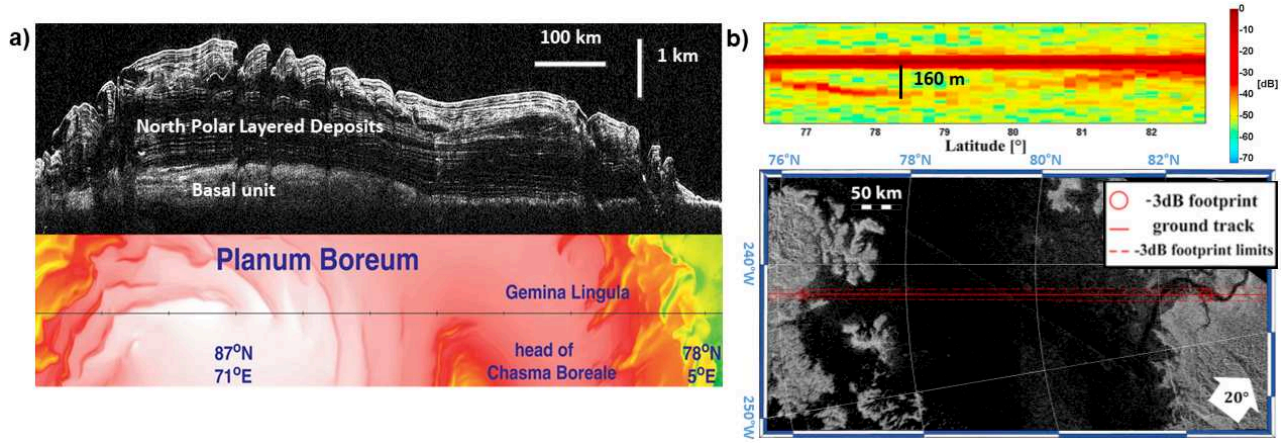

Figure 2.9 – a) Top: Radargram of the North Polar layered deposits of Mars from SHARAD orbit 5192. Bottom: Ground track of SHARAD (orbit 5192) shown on a Digital Elevation Model (DEM) derived from Mars Orbiter Laser Altimeter (MOLA) data. Elevation range is −4.5 (green) to −2 km (white). Figure from Phillips et al. (2008). b) Top: Radargram of Titan's Ligeia Mare from Cassini orbit T91. Bottom: Radar altimeter ground track during Cassini orbit T91, shown on the T29 SAR image of Ligeia Mare. Figure from Mastrogiuseppe et al. (2014).

at 20 MHz (15 m) (Seu et al., 2007), both of which are outside the common definition of microwaves. Among other results, these instruments revealed the layered structure of Mars' ice caps (shown in Fig. 2.9) and helped quantify the volatile inventory on Mars (e.g., Phillips et al., 2008; Selvans et al., 2010). The Mars 2020 (NASA) and ExoMars (ESA) rovers, expected to launch in 2020 and 2022 respectively, both include GPRs: RIMFAX (the Radar Imager for Mars' Subsurface Experiment) and WISDOM (Water Ice and Subsurface Deposit Observation on Mars), which will characterize the subsurface at depths of 3–10 m (Hamran et al., 2015; Ciarletti et al., 2017).

The Rosetta mission (ESA) included a unique bistatic radar sounder (the Comet Nucleus Sounding Experiment by Radiowave Transmission, CONSERT), which transmitted a signal from the Philae lander, through the comet nucleus, and to the Rosetta spacecraft (Kofman et al., 2007). This experiment revealed a low dielectric constant (~1.27), indicative of a very high porosity, increasing with depth (Kofman et al., 2015; Ciarletti et al., 2015).

Finally, the Cassini radar included an altimetry mode, providing topography with a vertical resolution of the order of meters. Mastrogiuseppe et al. (2014) and Mastrogiuseppe et al. (2016) revealed that radar sounding was also possible with the Cassini radar altimeter through Titan's high-transparency liquid methane/ethane lakes and seas. This novel analysis of the Cassini radar altimetry allowed these authors to calculate the depth and methane/ethane content of several seas of Titan, as shown in Fig. 2.9b (Mastrogiuseppe et al., 2014; Mastrogiuseppe et al., 2018).

2.3.2 Fundamental radar equation

The present manuscript hereafter concentrates on monostatic real aperture radar observations, whose basic principles are described below. These concepts will be applied to Cassini radar observations in Chapter 3 (Section 3.3).

In a monostatic mode of operation, the radar measures the amount of energy scattered back ("backscattered") toward it. A radar antenna transmits a signal of power P_t, which is backscattered by a point source towards the receiver, which measures a return power P_r. A point target is a target whose physical dimensions are such that the solid angle it subtends (from where the radar is located) is much smaller than the solid angle of the radar beam. The received power is then related to the target range and characteristics as described by the **point target monostatic radar equation** (Ulaby

and Long, 2015):

$$P_r = \frac{P_t G^2 \lambda^2}{(4\pi)^3 R^4} \sigma \tag{2.22}$$

where G is the gain of the antenna (squared because the wave is emitted then received by the antenna), λ is the instrument's operating wavelength, R is the range to the target, and σ is the target radar cross-section (RCS) in m^2. The monostatic radar equation for a point target can be extended to a distributed target (such as a planetary surface) by integrating the backscattered power over the illuminated area A:

$$\langle P_r(\theta_{\text{eff}}) \rangle = \int_A \frac{P_t G^2 (dA) \lambda^2}{(4\pi)^3 R^4 (dA)} \sigma^0 (dA) dA \tag{2.23}$$

where $G(dA)$ is the gain of the antenna pattern at surface element dA, and $R(dA)$ is the range to that surface element. θ_{eff} is the effective incidence angle over the antenna footprint, relative to normal incidence. The **normalized radar cross-section (NRCS)** σ^0, also called the backscattering coefficient, represents the ability of an object or a surface to backscatter the received signal with respect to an isotropic surface. More specifically, it is defined as the ratio of the energy received by the sensor over the energy that the sensor would have received if the target/surface had backscattered the energy incident on it in an isotropic fashion. It depends on the observation geometry, polarization, and wavelength but also on the surface properties and is thus of high interest to investigate the surface variations in terms of composition and texture. SAR and RAR are primarily designed to map σ^0 variations across a surface.

In a RAR observation, the antenna observes a planetary surface at an oblique incidence angle, with the antenna beam pattern projected onto the surface (see Fig. 2.3). The variations in antenna gain and range to target within this area can be predicted; however, variations in σ^0 being unknown and inaccessible to measurement, it is replaced by its weighted average over the footprint, σ^0_{avg}:

$$\sigma^0_{\text{avg}} = \frac{\int_A \frac{g^2(dA)\sigma^0(dA)dA}{R^4(dA)}}{\int_A \frac{g^2(dA)dA}{R^4(dA)}} \tag{2.24}$$

where $g(dA)$ is the normalized gain of the antenna pattern. We then obtain the following form of the radar equation (Wye, 2011):

$$P_r = \frac{P_t G^2 \lambda^2}{(4\pi)^3} \sigma^0_{avg} \int_A \frac{g^2(dA)dA}{R^4(dA)} \tag{2.25}$$

σ^0_{avg} is derived for each observation from the measured received power knowing the geometry, the transmitted power, and the antenna gain.

2.3.3 Radar albedo

Ground-based radars such as the Arecibo telescope and the GSSR cannot resolve Saturn's satellites, and instead measure a disk-integrated radar albedo, which is a measure of how reflective the surface of the target's visible hemisphere is in the backscatter direction compared to a reference surface. More specifically, the radar albedo is a dimensionless quantity derived by normalizing the radar cross section σ of a target by its projected geometric area. By definition, a perfectly reflective and isotropic surface (such as a smooth metallic sphere) has a radar albedo of 1. The radar albedo of a surface can exceed unity if the surface or, more accurately, if the depths probed at the operating wavelength, are

such that the radar waves are preferentially scattered back toward their source (i.e., in the backscatter direction). Radar albedos measured by the Cassini radar are discussed in Chapter 3 (Section 3.2)

Depending on the polarization of the electromagnetic wave sent and received by the radar, which can be linear or circular, in the same or opposite sense, four different polarizations can be measured. For conciseness, we use the following common abbreviations: A_{TP} for total power albedo, OC and SC for opposite- and same-sense circular polarization, and OL and SL for opposite- and same-sense linear polarization, with $A_{\mathrm{TP}} = A_{\mathrm{SC}} + A_{\mathrm{OC}} = A_{\mathrm{SL}} + A_{\mathrm{OL}}$. An ideal metal sphere would yield $A_{\mathrm{TP}} = 1$ and $A_{\mathrm{SC}} = A_{\mathrm{OL}} = 0$ (Kofman et al., 2010; Ostro et al., 2010). The circular and linear polarization ratios μ_C and μ_L are then given as follows:

$$\mu_C = A_{\mathrm{SC}}/A_{\mathrm{OC}} \tag{2.26}$$

$$\mu_L = A_{\mathrm{OL}}/A_{\mathrm{SL}} \tag{2.27}$$

Rocky bodies typically have total power albedos of $A_{\mathrm{TP}} \sim 0.1$, and low circular polarization ratios near $\mu_C \sim 0.3$, caused by a strong direct reflection relative to scattering by the surface and subsurface (Kofman et al., 2010).

2.4 Microwave radiometry

A microwave radiometer measures the thermal emission from a source in the microwave domain. In addition to insights into the structure and composition, it thus provides clues on the thermal properties of a planetary surface and near-surface, which are not accessible to an active radar.

2.4.1 Planetary exploration with microwave radiometry

Radiotelescopes

Radiotelescopes, thanks to which the cosmic microwave background (CMB) radiation at 2.7 K was discovered (Penzias and Wilson, 1965), are able to measure very high redshift radiation from the early universe, and are therefore widely used in cosmology. They are also especially useful to study strong radio sources such as pulsars, quasars and masers, although most stars and galaxies also emit at radio frequencies. Radiotelescopes are also powerful tools to explore the Solar System, as detailed herein.

Spectrometry and atmospheric sounding

At millimeter wavelengths, microwave spectrometry allows the detection of absorption and emission lines, rather than passive thermal emission. In planetary science, sub-mm to mm wavelength spectrometry has thus been used to derive atmospheric constituent abundances on Venus, Mars, Titan, Io, Pluto, and the giant planets (e.g., Pollack and Morrison, 1970; Shah et al., 1991; Muhleman and Clancy, 1995; Fouchet et al., 2011; Lellouch et al., 2017a, 2019). Microwave radiometry observations have also examined atmospheric opacity on the giant planets, ever since their detection in the 1950s and increasingly as radiotelescopes and interferometers improved (Janssen et al., 2013, and references therein).

Radiometers on spacecraft have further pursued atmospheric characterization. Thus the Cassini radiometer has been used to observe Saturn's atmosphere (Janssen et al., 2013) as well as Jupiter's (Moeckel et al., 2019). The Juno (ESA) mission to Jupiter carries a microwave radiometer (MWR) designed to study Jupiter's deep atmosphere, especially the abundance of ammonia (Janssen et al.,

2017; Li et al., 2017). The New Horizons (NASA) spacecraft is equipped with a 4.2-cm radiometer (REX, Tyler et al., 2009), which measured the surface pressure and the low-altitude temperature structure of Pluto's atmosphere (Hinson et al., 2017). The Rosetta (ESA) mission to comet 67P Churyumov-Gerasimenko carried a microwave spectrometer/radiometer (the Microwave Instrument for the Rosetta Orbiter, MIRO; Gulkis et al., 2007), which included a sub-mm band (0.5 mm) and a microwave band (1.6 mm). MIRO permitted identification of parent molecules in the comet (Biver et al., 2019).

Because the work presented herein focuses on microwave remote sensing of icy surfaces, both microwave spectrometry and atmospheric sounding will not be described in more detail.

Surface thermal and physical properties

Radiometers can detect the surface thermal emission of satellites and rocky planets, which can provide indications of the surface temperature, thermal inertia, bolometric albedo, emissivity, dielectric constant, structure, and composition (depending on the complementary information obtained from other wavelengths or active radar observations). Such studies have been conducted from Earth-based radiotelescopes at a variety of microwave wavelengths on Mercury (e.g., Morrison, 1969; Mitchell and de Pater, 1994), Venus (e.g., Pollack and Sagan, 1965; Kuzmin, 1983; Butler et al., 2001), Mars (e.g., Morrison et al., 1969; Cuzzi and Muhleman, 1972), the Moon (e.g., Piddington and Minnett, 1949; Heiles and Drake, 1963; White and Cogdell, 1973), comets (de Pater et al., 1998), asteroids (e.g., Webster and Johnston, 1989; Redman et al., 1998; Leyrat et al., 2012), Saturn's rings as shown in Fig. 2.10 (e.g., Cuzzi et al., 1980; de Pater and Dickel, 1991; Zhang et al., 2019), Pluto (Altenhoff et al., 1988), and outer Solar System satellites (discussed in Section 2.5). Millimeter observations of Kuiber Belt Objects (KBOs) and Centaurs have also been conducted using ALMA, allowing the derivation of their size, thermal inertia, and emissivity (e.g., Lellouch et al., 2017b; Gerdes et al., 2017; Brown and Butler, 2017).

There have been few dedicated microwave radiometers; however, many radar instruments on space missions, such as the Magellan and Cassini radars, incorporate a radiometer using the same receiving antenna. Spaceborne radiometers have two considerable advantages over earth-based radiotelescopes: higher resolutions and the possibility for observations of regions and local times invisible from Earth. Night-time observations of outer Solar System objects are inaccessible from Earth, and are crucial to accurately constrain their thermal properties.

The first radiometer ever sent to another planet than Earth was on board Mariner 2, which encountered Venus in December 1962. The Mariner 2 microwave radiometer confirmed the high temperatures observed from ground-based radio-telescope and showed conclusively that the surface of Venus was hot, ruling out an ionosphere origin for the surprisingly high measured thermal emission (Pollack and Sagan, 1967). Later (1990–1994), in its passive mode, the Magellan radar mapped Venus's thermal emission at resolutions varying from 15 to 85 km (Pettengill et al., 1992).

Microwave radiometry of the Moon from space has only been conducted by the Chang'E 1 and 2 (CNSA) probes, which for instance identified variations in thermal properties associated with Titanium abundance (e.g., Fa and Jin, 2010; Gong et al., 2015; Zhu et al., 2019).

The MIRO instrument on the Rosetta mission measured the night-time surface temperature (Fig. 2.10), revealing very low temperatures (25–50 K) and thermal inertias (10–30 MKS) (Choukroun et al., 2015; Schloerb et al., 2015).

Finally, the Cassini radiometer examined Titan (Janssen et al., 2009, 2016), Saturn's rings (Zhang et al., 2017b,a), and its icy satellites (Section 2.5 and Chapters 4 and 6).

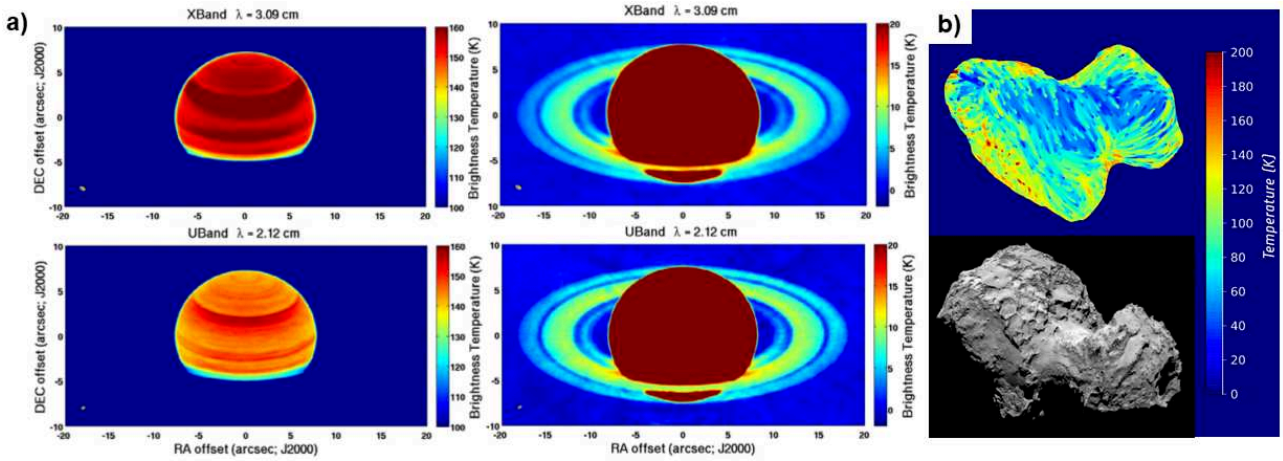

Figure 2.10 – a) Thermal emission from Saturn (left) and its rings (right) in the X-band (~3 cm; top) on 25 January 2015 and in the U-band (~2 cm; bottom) on 24 January 2015, as measured by the VLA. Figure adapted from Zhang et al. (2019). b) Thermal emission from comet 67P Churyumov-Gerasimenko at 1.6 mm by the Microwave Instrument for the Rosetta Orbiter (MIRO), with an image of illuminated side of this comet's nucleus by the Rosetta/OSIRIS instrument for reference. Credits: ESA/Rosetta/MPS/MIRO/NASA/JPL-Caltech/Choukroun et al., 2015.

2.4.2 Thermal emission from a surface and near subsurface

Thermal emission from a surface

Planetary bodies are primarily heated by electromagnetic radiation from the Sun. Kirchhoff's law of thermal radiation states that a body at thermal equilibrium emits the same amount of energy that it absorbs from its environment. For an ideal blackbody, which absorbs all incident radiation (without reflection), the spectral radiance B_ν (in $\mathrm{Wm^{-2}sr^{-1}Hz^{-1}}$) or B_λ (in $\mathrm{Wm^{-3}sr^{-1}}$) emitted is given by **Planck's blackbody radiation law**:

$$\begin{aligned} B_\nu(T) &= \frac{2h\nu^3}{c^2}\left(\frac{1}{e^{h\nu/k_BT}-1}\right) \\ B_\lambda(T) &= \frac{2hc^2}{\lambda^5}\left(\frac{1}{e^{hc/\lambda k_BT}-1}\right) \end{aligned} \tag{2.28}$$

where $h = 6.63\times10^{-34}$ Js is Planck's constant, $k_B = 1.38\times10^{-23}$ $\mathrm{JK^{-1}}$ is Boltzman's constant, T is the blackbody's temperature (in K), ν is the frequency (in Hz), $\lambda = c/\nu$ is the wavelength (in m), and c is the velocity of light in the medium ($c = 3\times10^8/\sqrt{\varepsilon'_r}$ m/s). The wavelength at which B_λ is maximum decreases with T, as apparent in Fig. 2.11.

Natural planetary surfaces, with temperatures generally between 30 K (Eris) and 735 K (Venus surface), emit thermal radiation primarily in the thermal infrared; however, their thermal radiation extends into the microwaves. Microwave radiometers thus detect the Rayleigh-Jeans tail of Planck's backbody radiation curve.

Planetary surfaces are so-called graybodies: they absorb and emit less energy than an ideal blackbody. A body's **brightness temperature** T_B is thus defined as the temperature that a blackbody emitting the same amount of radiation as the considered body for equal size would have, given its emission at the observation wavelength λ. The brightness temperature can be derived directly from the measured radiance using Eq. 2.28. In the microwave regime (where $h\nu \ll k_BT$), Planck's law can be simplified into the **Rayleigh-Jeans law**:

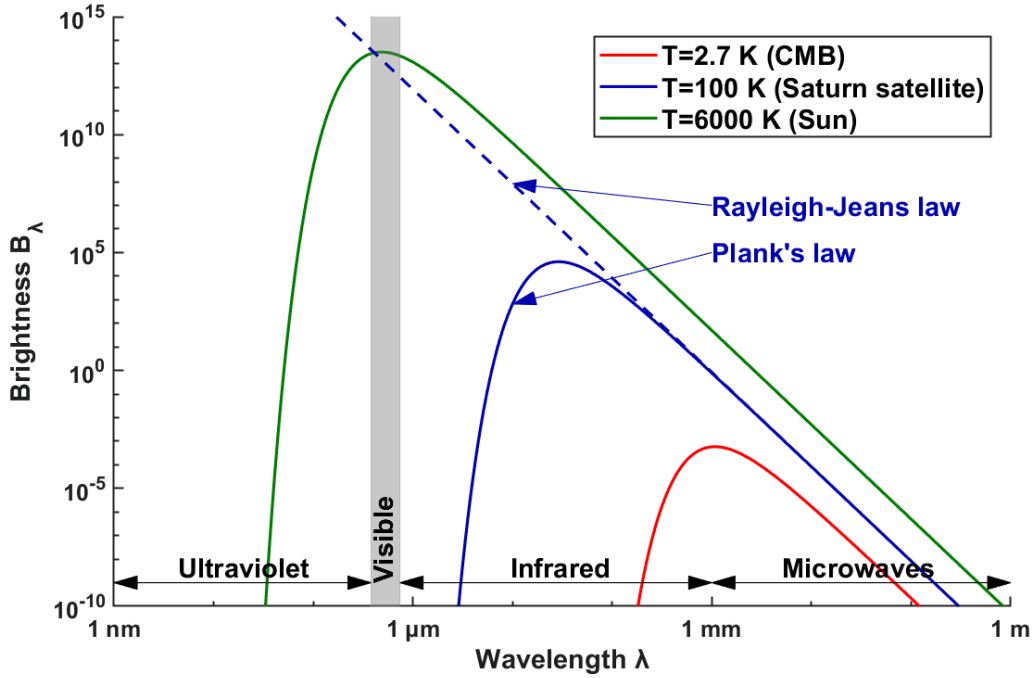

Figure 2.11 – Planck's blackbody radiation law for the Cosmic Microwave Background (CMB), a typical Saturn satellite, and the Sun. The Rayleigh-Jeans law is also indicated for the typical Saturn satellite.

$$\begin{aligned} B_\nu(T) &\approx \frac{2\nu^2 k_B T}{c^2} \\ &\approx \frac{2k_B T}{\lambda^2} \end{aligned} \tag{2.29}$$

Nevertheless, for millimeter wavelengths and cold objects, the Rayleigh-Jeans approximation leads to significant errors (e.g., a 7.6% error for a 1-mm observation of a 100-K body). In practice, the fractional deviation of the Rayleigh-Jeans law from Planck's law is less than 1% if $\lambda T > 0.77$ Km. Fig. 2.11 displays both the Planck and Rayleigh-Jeans laws for a blackbody of 100 K, illustrating the fact that they give the same result at most microwaves wavelengths.

For graybodies, the measured brightness temperature T_B is smaller than the actual surface temperature. The ratio of the observed brightness intensity B_ν to that of an ideal blackbody of same physical effective temperature T_{eff} (see below) B_ν^{bb} is defined as the **emissivity** e:

$$e = \frac{B_\nu}{B_\nu^{bb}} \tag{2.30}$$

In the microwaves, due to the Rayleigh-Jeans approximation, the emissivity can be expressed in terms of a temperature ratio:

$$e = \frac{T_B}{T_{\text{eff}}} \tag{2.31}$$

The emissivity is unitless and comprised between 0 and 1. It varies with the geometry of observation (especially the emission angle), the wavelength, and the surface properties (dielectric constant, roughness, etc). For a smooth, uniform, dielectric surface observed at an emission angle θ, the emissivity

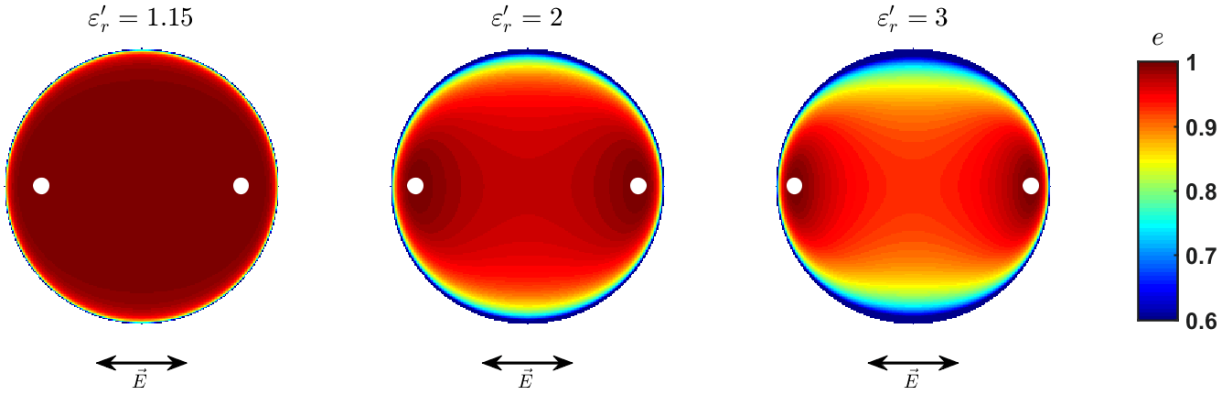

Figure 2.12 – Emissivity maps given by Fresnel's equations for an ideal smooth, uniform, dielectric, spherical surface, for dielectric constants of $\varepsilon'_r = 1.15$, 2, and 3. The direction of the electric field sensed by the antenna $\vec{E}$ is indicated. Polarization parallel to $\vec{E}$ is therefore left–right, whereas perpendicular polarization is top–bottom. The Brewster highlights peak at the Brewster angles θ_B, which are marked with a black dot.

depends only on the dielectric constant ε'_r, and is related to the Fresnel coefficients as follows:

$$e_p(\theta) = \mathbb{T}_p = 1 - \Gamma_p \tag{2.32}$$

where p is the polarization of the antenna (parallel or perpendicular), and $\mathbb{T}$ and Γ are, respectively, the transmissivity and reflectivity, obtained from Fresnel's equations (Eq. 2.17, in Section 2.2.3). The emissivity, like the transmissivity, peaks at its maximum value of 1 at the Brewster angle θ_B in parallel polarization.

When observing a mostly spherical object such as a natural satellite, the emissivity at any azimuthal and emission angle can be derived from that at parallel ($e_\parallel$) and perpendicular ($e_\perp$) polarizations. If δ is the angle between the parallel polarization direction and the azimuthal position of a point, and θ is its emission angle, then the emissivity at this point is given by the following formula (Heiles and Drake, 1963):

$$e(\theta, \delta) = e_\parallel(\theta) \cos^2 \delta + e_\perp(\theta) \sin^2 \delta \tag{2.33}$$

Example emissivity maps for ideal smooth, uniform, dielectric spheres derived from this equation using dielectric constants in the range expected for icy satellites are shown in Fig. 2.12. The "Brewster highlights" are the high-emissivity regions near parallel polarizations centered at the Brewster angle. Increasing the dielectric constants yields lower disk-integrated emissivities but makes the Brewster highlights much more obvious. If the dielectric constant is very low, the Brewster highlights are practically invisible, and the global emissivity is high. Detection of the amplitude and position of the Brewster highlights of a planetary body can therefore inform on the dielectric constant of its surface.

Radiative transfer through the subsurface

Microwave radiometers do not only sense the signal radiated by the surface, but also by the subsurface. In order to estimate the brightness temperature T_B sensed by the radiometer, it is necessary to consider processes of radiative transfer through the subsurface.

Radiative transfer in a medium involves loss in brightness intensity I due to extinction, and increase in I due to emission. Propagation of the signal over a thickness dz therefore results in

a change in intensity $dI = dI_{\text{emission}} - dI_{\text{extinction}}$. The power extinction, or attenuation coefficient $\kappa_e = \alpha + \kappa_s$ (in dB/m) is composed of an absorption coefficient (α, already mentioned in Section 2.2.2) and a scattering extinction coefficient κ_s. For outgoing radiation traveling through the subsurface, the optical depth τ is defined as:

$$\tau(z) = \int_0^z \kappa_e(l) dl \tag{2.34}$$

such that $d\tau = \alpha dz$, while accounting for variations of the attenuation coefficient $\kappa_e(l)$ with depth l. For energy propagating at an angle θ' from the vertical, the radiative transfer equation is:

$$\cos\theta' \frac{dI}{d\tau} + I = J \tag{2.35}$$

where $J_\lambda(z) = B_\lambda(T(z))$ is the total source function, corresponding to the thermal emission originating from the subsurface layers beneath depth z. If we consider a scatter-free medium ($\kappa_s = 0$), the solution to Eq. 2.35 is:

$$I_\lambda = \sec\theta' \int_0^\infty B_\lambda(T(\tau)) e^{-\tau \sec\theta'} d\tau \tag{2.36}$$

In the microwave domain, by virtue of the Rayleigh-Jeans law, $B_\lambda(T) \propto T$ and $I \propto T_{\text{eff}}$. We can therefore derive the **effective temperature** T_{eff} sensed by a radiometer:

$$\begin{aligned} T_{\text{eff}} &= \alpha \sec\theta' \int_0^\infty T(z) e^{-\alpha \sec\theta' z} dz \\ &= \frac{\int_0^\infty T(z) e^{-\alpha \sec\theta' z} dz}{\int_0^\infty e^{-\alpha \sec\theta' z} dz} \end{aligned} \tag{2.37}$$

We recall that the electrical skin depth $\delta_{\text{el}} = 1/\alpha$ is proportional to the radiometer wavelength (Eq. 2.13), and is a proxy for the depth probed by the antenna.

For heterogeneous media, the emitted signal is also attenuated by scattering in the subsurface, especially by **volume scattering**. The magnitude of volume scattering depends on parameters such as porosity, the size and density of inclusions, the dielectric contrast between the inclusions and the substrate, and the structure of the medium. We propose a model for this phenomenon in Chapter 5.

2.4.3 Microwave radiometers

Fundamental equation of radiometry

Radiometers measure a receiver power P_A (in W), which relates to the instrument characteristics as follows (Ulaby and Long, 2015):

$$P_A = \frac{1}{2} A_r \int_{\nu_1}^{\nu_2} \iint_{4\pi} B_\nu(\theta, \phi) G(\theta, \phi) \, d\Omega \, d\nu \tag{2.38}$$

where $A_r = D^2$ is the effective aperture area of the antenna (D is the antenna diameter or the interferometer baseline), $G(\theta, \phi)$ is its directional radiation pattern (see Section 2.1.2), $\Delta\nu = \nu_2 - \nu_1$ is its bandwidth, and $B_\nu(\theta, \phi)$ is the spectral radiance from direction (θ, ϕ). The factor of $1/2$ originates from the fact that the radiometer generally measures incoming unpolarized electromagnetic radiation

in only one polarization, in average equivalent to half of the total incoming energy.

If the instrument bandwidth is sufficiently narrow ($\Delta\nu \ll \nu$), then B_ν is approximately constant over $\Delta\nu$:

$$P_A = \frac{1}{2} A_r \Delta\nu \iint_{4\pi} B_\nu(\theta, \phi) G(\theta, \phi)\, d\Omega \tag{2.39}$$

In the microwave domain, the spectral radiance B_ν is given by the Rayleigh-Jeans law (Eq. 2.29), yielding:

$$P_A = k_B \Delta\nu \frac{A_r}{\lambda^2} \iint_{4\pi} T_B(\theta, \phi) G(\theta, \phi)\, d\Omega \tag{2.40}$$

Recognizing the antenna solid beam angle (Eq. 2.2), we finally obtain the **fundamental equation of radiometry**:

$$P_A = k_B \Delta\nu T_A \tag{2.41}$$

where the lossless **antenna temperature** T_A is the integrated value of the brightness temperature distribution weighted by the antenna radiation pattern, normalized by the antenna solid beam angle (i.e., the integral of the weighting function):

$$T_A = \frac{\iint_{4\pi} T_B(\theta, \phi) G(\theta, \phi) d\Omega}{\iint_{4\pi} G(\theta, \phi) d\Omega} \tag{2.42}$$

By analogy both with observations of a thermal source (as above) and with the similar behavior of a resistor at temperature T (Nyquist, 1928; Johnson, 1928), Eq. 2.41 is the definition of the antenna temperature regardless of whether the Rayleigh-Jeans approximation applies or not.

Receiver transfer function

In practice, the power P_{SYS} measured by a radiometer incorporates the signal from the target P_A as well as self-emitted energy P_{REC} contributed by the antenna structure and electronics. Each of these powers can be related to corresponding temperatures from Eq. 2.41:

$$P_{\mathrm{SYS}} = P_A + P_{\mathrm{REC}} = k_B \Delta\nu T_{\mathrm{SYS}} = k_B \Delta\nu (T_A + T_{\mathrm{REC}}) \tag{2.43}$$

The antenna is also not lossless: part of the energy received is absorbed by the antenna material and converted into heat. This phenomenon is expressed through the receiver gain G_{REC}. Most radiometers measure a voltage V_{out} in counts, which is the product of the receiver gain and the system temperature T_{SYS}:

$$V_{\mathrm{OUT}} = G_{\mathrm{REC}} T_{\mathrm{SYS}} = G_{\mathrm{REC}} (T_A + T_{\mathrm{REC}}) \tag{2.44}$$

The antenna temperature can then be derived from the gain, voltage, and receiver temperature according to the **receiver transfer function**:

$$T_A = \frac{V_{\mathrm{out}}}{G_{\mathrm{REC}}} - T_{\mathrm{REC}} \tag{2.45}$$

T_{REC} thus corresponds to a temperature offset. Both T_{REC} and G_{REC} vary on the short term (due to temperature and power supply voltage variations) and the long term (due to aging of the components), and must therefore be determined as often as possible, by measurements on warm and cold sources of known temperatures.

Uncertainties

The **accuracy**, or absolute uncertainty, of a radiometer depends primarily on the knowledge of its receiver transfer function, and on the quality of its calibration. It generally primarily depends on the long term variations of gain.

The **precision**, or relative uncertainty, is primarily caused by random photon noise, which decreases with longer integration times t_{int}, following $\Delta T_N = T_{\text{SYS}}/\sqrt{Bt_{\text{int}}}$. Short term variations in the gain also contribute an error of $\Delta T_G = T_{\text{SYS}}\Delta G_{\text{REC}}/G_{\text{REC}}$. These independent sources of uncertainty combine to give the total rms uncertainty ΔT_A:

$$\Delta T_A = T_{\text{SYS}}\left[\frac{1}{Bt_{\text{int}}} + \left(\frac{\Delta G}{G}\right)^2\right]^{1/2} \tag{2.46}$$

Flux density

Most ground-based radiotelescopes measure a flux density S (in Jy = 10^{-26}W m^{-2} Hz^{-1}), which is the integral of the spectral radiance B_ν over the solid angle, weighted by the gain of the antenna pattern. It therefore relates to the above equations as follows:

$$S = \frac{2P_r}{\eta A_r \Delta\nu} = \iint_{4\pi} B_\nu G(\theta,\phi)d\Omega \tag{2.47}$$

where η is the antenna efficiency (between 0 and 1). For a source of solid angle Ω_s and of total flux density S_s, the disk-integrated brightness temperature T_B^{disk} can be derived from the following equation, using either Planck's law or the Rayleigh-Jeans approximation if it applies:

$$S_s = B_\nu(T_B^{\text{disk}})\Omega_s \tag{2.48}$$

2.5 Icy satellite microwave observations

Both active and passive microwave observations have been conducted throughout the Solar System, as described in Sections. 2.3.1 and 2.4.1. This section focuses on studies of Jupiter's and Saturn's icy satellites from ground-based and spacecraft radars and radiometers.

Although this thesis concentrates on the satellites of Saturn, it is important to review the microwave properties of the Jovian icy satellites (Europa, Ganymede, and Callisto), which have been observed from ground-based radars and radiotelescopes on more occasions than the Saturnian satellites. These observations have led to new models of radar backscatter.

2.5.1 Icy Galilean satellites: radiometry observations

Passive radiometry measurements of the brightness temperatures of the icy Galilean satellites (by increasing distance from Jupiter: Europa, Ganymede, and Callisto) have been conducted at multiple μm–cm wavelengths, and are plotted in Fig. 2.13 (Ulich et al., 1984; de Pater et al., 1989; Muhleman and Berge, 1991, and references therein). The brightness temperature visibly decreases as the observation wavelength increases. Although the longest wavelengths are expected to probe deeper than the diurnal thermal skin depth and therefore to exhibit lower temperatures (for daytime observations), this effect alone is insufficient to explain the low mm–cm values of T_B, especially on Europa

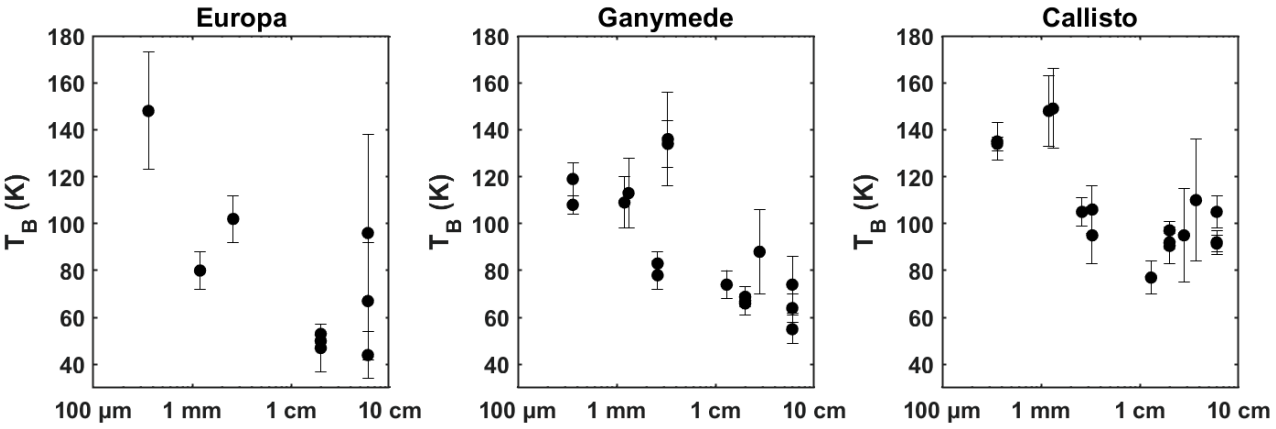

Figure 2.13 – Disk-integrated brightness temperatures T_B, from de Pater et al. (1989), Muhleman and Berge (1991), and references therein. All observations are taken from ground-based radiotelescopes, and therefore correspond to the local day (near noon at the disk center). Centimeter wavelength observations were obtained with the VLA.

and Ganymede (de Pater et al., 1984). Estimating the effective physical temperature with a simplified (temperature equilibrium) model yields low emissivities, around 0.5–0.8, for Europa and Ganymede at mm–cm wavelengths (Muhleman and Berge, 1991; Trumbo et al., 2018), to be compared with the emissivity of 0.8–0.95 of most terrestrial surfaces.

Similarly low microwave emissivities have been reported on other icy bodies, more specifically Trans-Neptunian Objects TNO) (Fornasier et al., 2013; Lellouch et al., 2017b; Brown and Butler, 2017) including Pluto and Charon (Lellouch et al., 2000, 2016), comets (Boissier, J. et al., 2011), and thick snow and lake ice on Earth (Wiesmann et al., 1998; Hewison and English, 1999). Low asteroid sub-millimeter to millimeter emissivities have also been detected (e.g., Redman et al., 1998; Gulkis et al., 2010), but for most asteroids (except perhaps Vesta; Redman et al., 1992; Leyrat et al., 2012) this likely results from large dielectric constants, surface roughness, and subsurface sounding of colder night-time temperatures (Keihm et al., 2013). This explanation remains insufficient for Earth snow and TNOs, as for the Galilean satellites (Lellouch et al., 2016, 2017b). Instead, the preferred explanation is subsurface scattering, by subsurface voids or inhomogeneities on scales comparable to the wavelength (see Section 2.2.5).

For the Galilean satellites, the low microwave emissivities are most likely caused by buried mm–cm-sized scattering inhomogeneities; because of their size, these scatterers affect more centimetric than millimetric wavelengths. It is also possible that the top few mm of the surface probed at shorter (submillimeter) wavelengths are smoother and more uniform than greater depths probed at centimeter wavelengths, where the scattering inhomogeneities would be buried (Muhleman and Berge, 1991; Wiesmann et al., 1998). It is likely that these subsurface inhomogeneities also cause the Galilean satellites' unusual radar properties (discussed below), as high radar reflectivities are generally associated with low emissivities (Eq. 2.32; de Pater et al., 1984; Muhleman and Berge, 1991).

Recent re-reduction of the VLA data presented in Fig. 2.13 shows, contrary to earlier studies, an increase in Europa brightness temperatures with wavelength at mm–cm wavelengths, with a minimum at sub-mm wavelengths (Butler, 2012). This would indicate that, if the low sub-mm brightness temperature is caused by subsurface scattering, either the particle size must be relatively small (tens to hundreds of microns at most) such that scattering is less efficient at longer wavelengths, and/or there is an emissive contaminant present at cm–m depths. On Ganymede and Callisto, Butler (2012) only finds a slight increase in brightness temperature at cm wavelengths, where scattering therefore

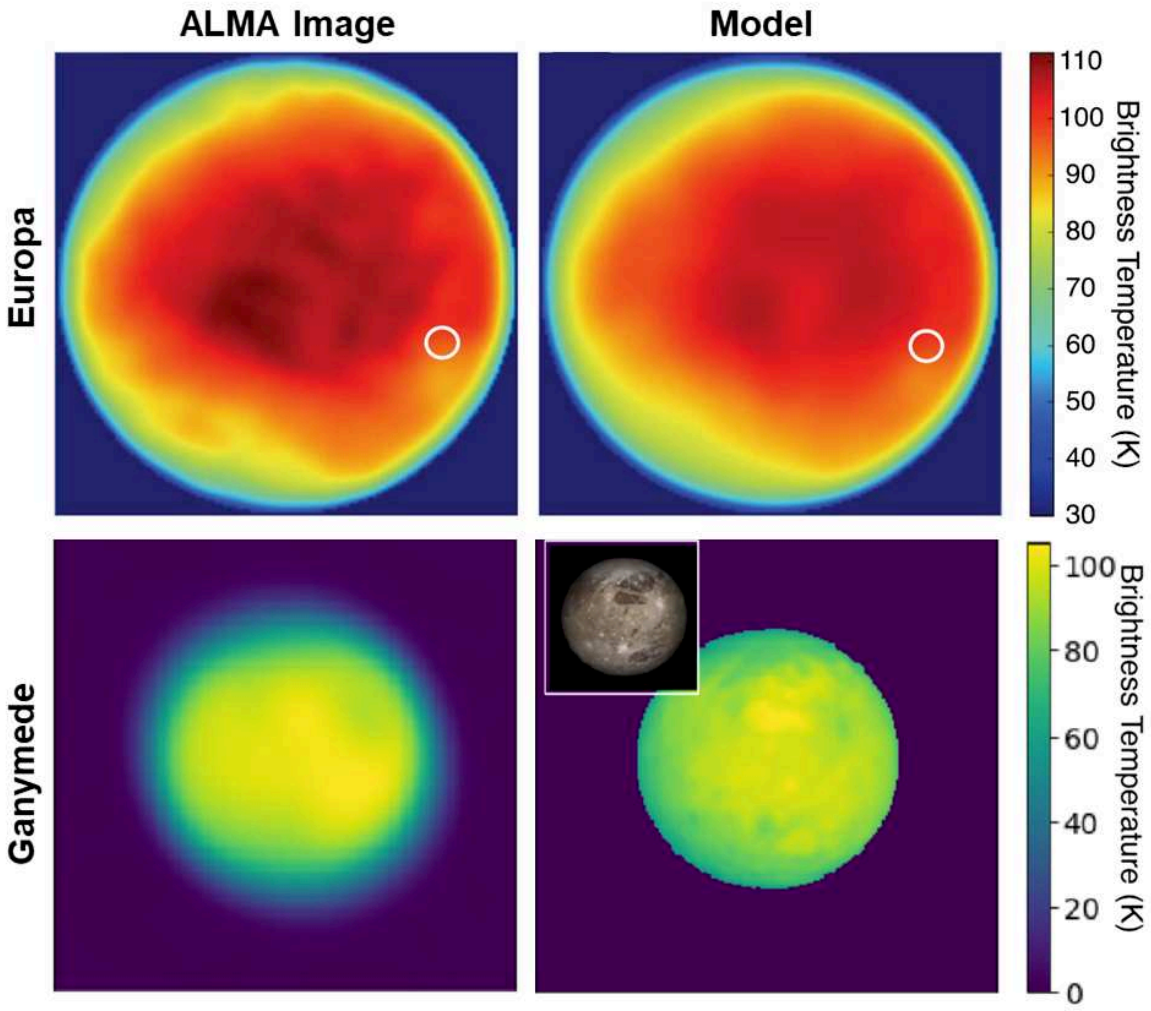

Figure 2.14 – Brightness temperature images of Europa (top) and Ganymede (bottom) as observed by ALMA at 1.3-mm (left) and predicted using a thermal model including an albedo map (right). For Europa, the location of the potential plume source region and Galileo thermal anomaly is circled in white, where the size of the circle corresponds to the size of the ALMA resolution element. Europa data is from Trumbo et al., 2017 and Ganymede data from de Kleer et al., 2019. Ganymede (2630 km diameter) and Europa (1560 km diameter) are not to scale. For Europa but not for Ganymede, the thermal model output has been convolved with the beam pattern.

seems more active.

More recently, ALMA has been used to obtain resolved maps of Europa's (Trumbo et al., 2017, 2018) and Ganymede's (de Kleer et al., 2019) mm-wavelength brightness temperatures, shown in Fig. 2.14. On Europa, brightness temperature measurements were used to investigate a putative thermal anomaly (located near Pwyll crater) associated with plume activity. The observations were found to be consistent with thermal surface models without any endogenic flux. Instead of a hotspot, the Pwyll crater region exhibits a locally high thermal inertia (105 ± 10 MKS compared to 70–90 MKS elsewhere; Rathbun and Spencer, 2020), which may result from larger particle sizes in its ejecta blanket (Trumbo et al., 2017; Rathbun and Spencer, 2020). ALMA observations of Europa were also used to derive partial thermal inertia and emissivity maps, identifying a low emissivity and/or high-thermal inertia region which may be linked to increased water ice purity or larger grain sizes (Trumbo et al., 2018).

2.5.2 Galilean satellites: radar observations

The Arecibo (13 cm and 70 cm) and Goldstone (3.5 cm) radar systems are the only two radar systems powerful and sensitive enough to observe outer Solar System satellites. The resulting radar properties of the three outer Galilean satellites (Europa, Ganymede, and Callisto) have been assembled by Ostro et al. (1992) and Ostro et al. (2006) and are summarized in Table 2.2.

Table 2.2 – Radar properties of icy satellites, summarized from Ostro et al. (2006, and references therein) for the Galilean satellites, Lorenz and Lunine (1997) and Black et al. (2011) for Titan, Black et al. (2004) for Iapetus, and Black et al. (2007) for Saturn's other icy satellites. LH and TH indicate the leading and trailing hemispheres, respectively.

Satellite	**Wavelength** λ	**Total power albedo** A_{TP}	**Circular polarization ratios** μ_C	**Linear polarization ratios** μ_L
Europa	3.5 cm	2.31 ± 0.36	1.43 ± 0.24	
	13 cm	2.60 ± 0.22	1.53 ± 0.03	0.47 ± 0.07
	70 cm	$\leq 0.95 \pm 0.36$	1.70 ± 0.40	
Ganymede	3.5 cm	1.55 ± 0.20	1.40 ± 0.10	
	13 cm	1.39 ± 0.14	1.43 ± 0.06	0.47 ± 0.08
	70 cm	0.62 ± 0.20	1.44 ± 0.19	
Callisto	3.5 cm	0.72 ± 0.06	1.20 ± 0.08	
	13 cm	0.69 ± 0.06	1.17 ± 0.04	0.55 ± 0.10
	70 cm	$\leq 0.18 \pm 0.06$	> 2.2	
Enceladus	13 cm	1.94 ± 0.31	0.83 ± 0.25	
Enceladus (LH)	13 cm	2.55 ± 0.42	1.28 ± 0.41	
Enceladus (TH)	13 cm	0.78 ± 0.28	≤ 0.56	
Tethys	13 cm	1.45 ± 0.13	1.22 ± 0.21	
Dione	13 cm	0.74 ± 0.10	0.81 ± 0.21	
Rhea	13 cm	1.31 ± 0.05	1.17 ± 0.09	
Titan	3.5 cm	0.16 to 0.43	0.3 to 0.5	
Titan (average)	13 cm	0.235 ± 0.001	0.46 ± 0.07	
Iapetus (LH)	13 cm	0.13 ± 0.04	0.33 ± 0.07	
Iapetus (TH)	13 cm	0.17 ± 0.04	0.46 ± 0.10	

The radar properties of the icy Galilean moons were quickly recognized as anomalous (e.g., Campbell et al., 1978). Their circular polarization ratios μ_C are indeed considerably higher (> 1) than those of rocky regoliths ($\mu_C \sim 0.1 - 0.4$). Furthermore, compared to the commonly encountered reflectivity of 0.1 in the inner Solar System, their surfaces show very high total power albedo. The radar albedo increases from Callisto, to Ganymede, and to Europa (see Table 2.2), with the highest radar return correlated to the youngest and most ice-rich surfaces (Ostro et al., 1992; Black et al., 2001a). Although the circular polarization ratios are high both at 3.5 to 70 cm wavelengths, this is not true for the reflectivity, which decreases at 70 cm, indicating that the mechanism that causes it is less active at this wavelength. The returned radar echoes also follow a diffuse scattering law, exhibiting no quasi-specular reflections.

Similar radar properties (high reflectivities and circular polarization ratios) have been observed within the icy permanently shadowed craters at Mercury's poles (Harmon et al., 2001; Harcke, 2005),

the polar ice caps of Mars (Muhleman et al., 1991; Butler, 1993), the Greenland ice sheet (Rignot et al., 1993; Rignot, 1995), and high-altitude ices (Haldemann and Muhleman, 1999). Although these four environments differ in their temperatures, atmospheric properties, and erosion processes, they have in common a water ice composition. It is therefore likely that different ice modification processes (e.g., melting/refreezing, thermal stresses, seasonal layering...) lead to common radar properties.

A variety of subsurface properties and structures have been suggested as the cause for the Galilean moons' unusual radar properties, but none is fully satisfactory. Surface scatterers such as hemispherical craters (Ostro and Pettengill, 1978) or randomly oriented facets (Goldstein and Green, 1980) are an unlikely explanation for a high-transparency medium like water ice. Instead, buried craters have been theorized by Eshleman, 1986, but would not lead to the observed radar properties (Baron et al., 2003). Hagfors et al. (1985, 1997) proposed that the incoming signal was being refracted (rather than reflected) by subsurface meter-sized lenses of higher refractive index (due to higher density and/or presence of powdered silicates); however, it remains unclear how such structures would form in sufficient numbers (Baron et al., 2003). Multiple reflections on solid ice pipes and ice layers within a snowy medium, forming from seasonal melt, are a good explanation for the radar properties within the Greenland ice sheet and high-altitude ices, but would not form at icy satellite surface temperatures (Rignot et al., 1993; Rignot, 1995; Haldemann and Muhleman, 1999).

The mechanism which best reproduces the Galilean satellites' radar behavior (high radar brightness, diffuse scattering, and high circular polarization ratio) is the Coherent Backscattering Effect (CBE), described in Section 2.2.5 (Hapke, 1990; Peters, 1992; Black et al., 2001b). Ganymede and Callisto's radar properties are consistent with 2% and 5% volume fractions of such scattering inhomogeneities in their subsurface. Europa's high radar albedo, however, requires a scatterer volume density as high as 80% (Black et al., 2001b). The drop in radar reflectivity from 13-cm to 70-cm observations indicates that the scattering inhomogeneities are more numerous at cm scales than at decimeter or meter scales, supporting the power-law size distribution proposed by Black et al. (2001b). However, the CBE does not predict the specific shape and formation mechanism of these subsurface inhomogeneities.

Resolved observations of Ganymede and Callisto have also been possible using a 3.5-cm bistatic aperture synthesis radar system, with Goldstone as the transmitter and the VLA as the receiver (Harcke, 2005). Harcke (2005) mapped the radar backscatter for these two moons, finding radar albedos and polarization ratios within error of previous measurements. The apparently youngest regions of Ganymede (sulci and recent craters) are brighter than their surroundings, most likely due to excavation of high-purity water ice. On Callisto, the large impact crater Valhalla is radar-bright, consistent with the results of Ostro et al. (1992). This study concluded that the leading hemispheres of Ganymede and Callisto were 20% ± 5% more radar-bright than their trailing hemispheres, which Harcke (2005) attributed to increased micrometeoroid gardening on the leading side, roughening its surface and near subsurface.

2.5.3 Galilean satellites: future microwave exploration

The importance of radar studies for icy satellite exploration has been widely recognized, and both icy satellite missions currently in preparation will carry high-priority radar instruments. ESA's JUICE mission, launching nominally in 2022 for a 2030 arrival at Jupiter, will carry a 9-MHz (30-m wavelength) sounding radar (the Radar for Icy Moon Exploration, RIME; Bruzzone et al., 2013). NASA's Europa Clipper mission, which will be launched around 2025, will carry a dual frequency sounding radar (the Radar for Europa Assessment and Sounding: Ocean to Near-surface, REASON)

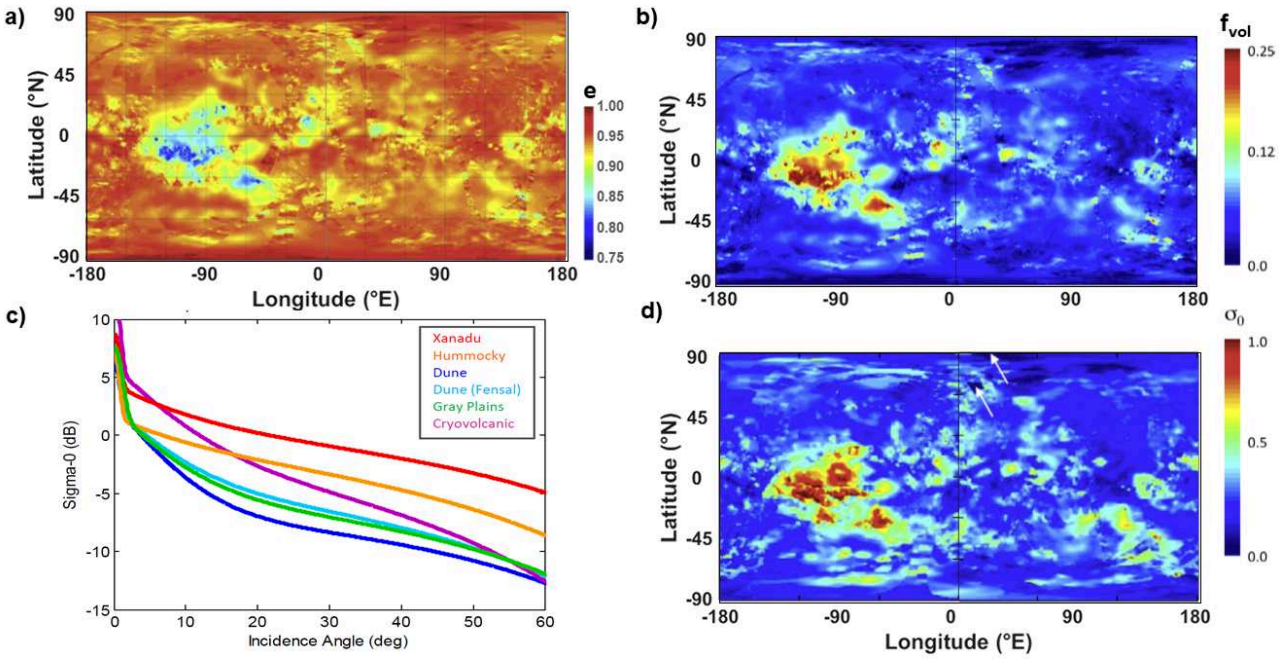

Figure 2.15 – a) Global emissivity map of Titan obtained from Cassini radiometry. b) Amplitude of volume scattering derived from the emissivity data. f_{vol} is the probability that a photon entering the surface scatters and escapes from the subsurface before it is absorbed (where 0.25 corresponds to 25% probability). c) Comparison of Titan feature backscatter curves. Xanadu and hummocky terrains are the most radar-bright terrains on Titan, whereas dunes and plains are the most radar-dark after methane lakes and seas. The "cryovolcanic" terrain, which may also correspond to evaporite deposits (MacKenzie et al., 2014), seems to have a different scattering mecanism than elsewhere. Figure from Wye (2011). d) NRCS σ^0 measured by the Cassini radar in scatterometry mode. The large low-emissivity and radar-bright region centered on 110°W in longitude and the Equator is Xanadu. Figure adapted from Janssen et al. (2016).

to examine Europa's sub-surface, and hopefully detect its ocean (Blankenship et al., 2009). This radar will operate at two frequencies, 9 and 60 MHz (33 and 5 m wavelengths), allowing both good vertical resolution and deep sounding (Heggy et al., 2017; Kalousová et al., 2017). Both the RIME and REASON radars should also be able to perform passive measurements, which in Jupiter's high radiation environment may allow subsurface sounding (Schroeder et al., 2016). The JUICE spacecraft will also carry a submillimeter radiometer (SWI; Hartogh et al., 2013), which will provide new thermal information at 600 and 1200 GHz (0.5 and 0.25 mm) on icy surfaces. These future missions focused on icy satellites have also motivated the Juno (NASA) microwave radiometry (MWR) team to propose Europa observations at 1–50 cm wavelength for the extended mission, providing the first resolved centimetric data on this satellite.

In parallel, a ground-based observation campaign is ongoing. To complement the ALMA data already collected on Europa and Ganymede (Trumbo et al., 2017, 2018; de Kleer et al., 2019), these authors have proposed resolved centimetric observations with the VLA. At these longer wavelengths, radiometry would help characterize the subsurface medium while being able to detect buried anomalies, similar to what has been possible on Saturn's icy satellites using Cassini radiometry for this thesis.

2.5.4 Titan radar/radiometry observations

Titan, which is the only Solar System satellite with a thick and optically opaque atmosphere, is well suited to radar/radiometry exploration but is difficult to detect from Earth (due to its small angular size and proximity to Saturn). Prior to the Cassini-Huygens mission, radar echoes had been obtained on Titan at 3.5 and 13 cm using the Arecibo and Goldstone radars (see Table 2.2). The radar albedo, slightly lower than Callisto's, varied with the phase of Titan, pointing to a rough, "dirty", heterogeneous icy surface and ruling out the hypothesis of a global ocean (Muhleman et al., 1995; Lorenz and Lunine, 1997). Campbell et al. (2003) detected specular echoes at 13 cm using Arecibo, which they interpreted as indicative of liquid hydrocarbons in equatorial or mid-latitude regions; however, these were most likely caused by flat paleoseas, as the Cassini radar only detected liquids at high latitudes (Hofgartner et al., 2020).

Beyond revealing the geomorphology of the surface, the Cassini 2.2 cm radar/radiometer instrument has been used in multiple different ways on Titan, for instance to measure dune height through radarclinometry (Lorenz et al., 2006) and by combining data from overlapping radar beams (SARTopo; Stiles et al., 2009), to estimate sea depth from double echos in altimetry (Mastrogiuseppe et al., 2014), or to map the surface dielectric constant and the degree of volume scattering in the subsurface (Janssen et al., 2016).

Le Gall et al. (2010) and Janssen et al. (2011) identified regions of Titan, namely the IR- and radar-bright mountainous Xanadu region, radar-bright hummocky terrains, channels, and alluvial fans, exhibiting very high radar backscatter (σ^0 between 0.5 and 2). The coherent backscattering effect (see Section 2.2.5) is insufficient to explain simultaneously the high radar backscatter and the relatively high emissivities (0.75 to 0.9 for Xanadu and the hummocky terrains) of these regions. Instead, multiple scattering by ordered subsurface structures is invoked (Janssen et al., 2011). In the radar-bright channels and alluvial fans, the presence of rounded icy pebbles larger than the wavelength like those observed at the Huygens landing site is likely and would account for the high radar return (Le Gall et al., 2010). As displayed in Fig. 2.15, low emissivity and high radar backscatter are well correlated, and both are likely explained by volume scattering in the subsurface (Janssen et al., 2016). Water ice is a low-loss medium (allowing long path lengths and multiple scattering) and has a higher dielectric constant (3.13) than organics ($\sim$ 2), perhaps allowing high dielectric contrasts with embedded voids or inhomogeneities. High volume scattering regions are therefore likely associated with high degrees of water ice purity in the near subsurface of Titan (Janssen et al., 2016). This interpretation is consistent with the high radar brightness and low emissivity of crater ejecta, where we expect the impact to have excavated high-purity water ice from the underlying icy bedrock.

2.5.5 Saturn's icy satellite radar/radiometry observations

Microwave observations of Saturnian satellites are rare and recent. Until the 2004 through 2007 opposition of the Saturn system, Earth-based radar measurements in the outer Solar System have been limited to Galilean satellites and Titan. Black et al. (2004) and Black et al. (2007) observed, respectively, both hemispheres of Iapetus and the mid-sized Saturnian satellites Rhea, Dione, Tethys, and Enceladus with the Arecibo Observatory's 13 cm wavelength (2.38 GHz) radar system. The other Earth-based planetary radar system, Goldstone (equipped with a 3.5 cm transmitter (X-band)), has never been used to observe these objects or other Saturnian airless satellites yet. In addition, passive microwave observations of Saturnian moons from Earth are difficult due to confusion with thermal emission from the planet, the faintness of some targets, and their small apparent size. That is the reason why, with the exception of Titan and Iapetus, they have never been conducted. In that regards, the Cassini radar and radiometry observations of Saturn's icy moons are pioneer.

The Arecibo 13 cm observations of Black et al. (2004) and Black et al. (2007) are summarized in Table 2.2, besides similar observations of the Galilean satellites for comparison. Saturn's inner icy moons (Enceladus, Tethys, Dione, and Rhea; Mimas ground-based observations have not been undergone) display a similar radar behavior as the Galilean moons at 13 cm: high reflectivity (> 0.6 and up to 2.55) and polarization ratios (generally around 1). They are also cold, quasi-atmosphereless icy bodies, and are exposed to mostly the same processes (though Jupiter's magnetic field is stronger, and Saturn's E ring influences its moons). It therefore seems likely that similar subsurface properties and scattering processes lead to this radar behavior (Black et al., 2007; Ostro et al., 2006). The radar albedo values found for Iapetus, though still higher than those of rocky surfaces such as the Moon, are remarkably lower than those of the inner Saturnian satellites, indicating the likely presence of absorptive contaminants such as ammonia in the subsurface (Black et al., 2004).

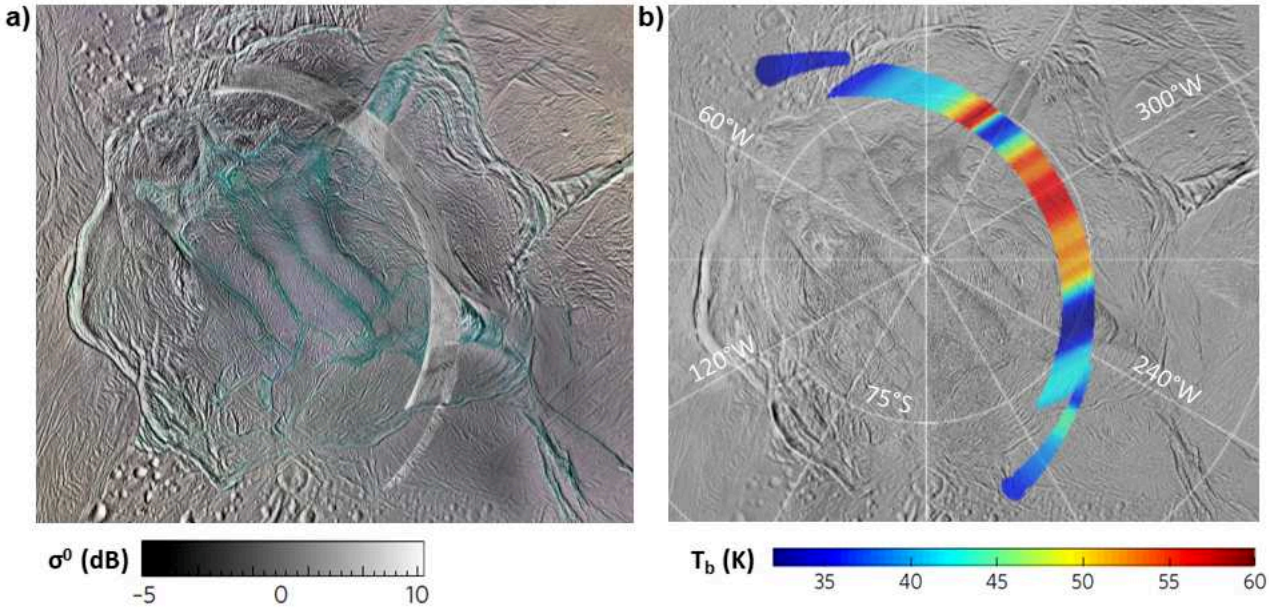

Figure 2.16 – a) Stereographic polar projection of active and passive radar observations of Enceladus's South Polar Terrain acquired during the closest approach of flyby E16. a) E16 SAR image overlaying an ISS color mosaic (PIA18435). b) E16 brightness temperature map overlaying a visible-light ISS mosaic (PIA14937). Figure from Le Gall et al. (2017).

Before the work presented in this thesis, microwave ground-based radiometry observations of Saturn's mid-sized icy satellites had only been performed for Iapetus, by Ries (2012) and Hagen et al. (2014). Their observations and results will be described in detail in Chapter 7, before presenting the complementary data obtained and analyzed during my thesis.

The Cassini radar measured the radar albedo in same-sense linear polarization, A_{SL}, of Saturn's icy satellites. The resulting disk-integrated albedos of Saturn's icy satellites have been analyzed by Ostro et al. (2006), Ostro et al. (2010), and Le Gall et al. (2019). As I have contributed to this last work as part of my dissertation, these data and their interpretation will be discussed in detail in Chapter 3. Resolved scatterometry and concurrent radiometry was also obtained on Rhea (Wye, 2011, and described in Chapter 3), Dione (Le Gall et al., 2019 and described in Chapter 3), Iapetus (Le Gall et al., 2014), and Enceladus (Ries and Janssen, 2015; Le Gall et al., 2017). An Enceladus flyby was even dedicated to the radar instrument, yielding a high-resolution SAR image near the South Polar region, displayed in Fig. 2.16a (Mitchell et al., 2012). From the concurrent resolved radiometry pictured in Fig. 2.16b, Le Gall et al. (2017) detected thermal anomalies associated with prominent fractures, implying high heat flux even relatively far from the tiger stripes themselves. Partially resolved radiometry in the equatorial regions revealed a 30% decrease in emissivity on the leading hemisphere of Enceladus, likely related to a geologically young (and therefore locally clean) terrain (Ries and Janssen, 2015).

Chapter 3

Saturn's icy satellites seen by the Cassini radar

The Cassini radar/radiometer is a complex, multi-modal instrument; at 2.2 cm it is the only instrument aboard the Cassini spacecraft able to probe up to several meters into an icy surface. This chapter begins by describing the Cassini radar/radiometer and its observation strategy, applicable to both active and passive modes of observation. We then focus on the icy satellite radar observations, first the distant radar data, then the resolved scatterometry on Dione and Rhea.

3.1 The radar/radiometer on the Cassini spacecraft

The Titan Radar Mapper on the Cassini spacecraft was jointly developed by NASA's Jet Propulsion Laboratory (JPL), the Italian Space Agency (ASI), and the Cassini Radar Science Team (CRST) (Elachi et al., 2004). This instrument, which could operate both in active and passive modes, is referred to herein as the Cassini radar/radiometer. While it was primarily designed to characterize Titan's surface by peering through its optically thick haze, it also observed Jupiter (Moeckel et al., 2019), Saturn (Janssen et al., 2013), its rings (Zhang et al., 2017a,b), and its icy satellites (Ostro et al., 2006; Ostro et al., 2010; Le Gall et al., 2014; Ries and Janssen, 2015; Le Gall et al., 2017).

3.1.1 Characteristics

The Cassini radar/radiometer operated at 2.17 cm (13.78 GHz frequency), within the Ku-band. It measured linearly polarized radiation, with the receiver's electric field lying along the x-axis of the spacecraft. The polarization of the received signal thus depended on the angle between the incidence (emission for radiometry) plane and the x-axis. The radar/radiometer antenna was not articulated separately from the Cassini spacecraft; therefore, changing pointing direction or polarization orientation implied rotating the whole spacecraft.

The radar/radiometer had 5 distinct transmitters and receivers, each with its own beam pattern. The instrument properties are provided in Table 3.1. The central beam (beam 3) was circular, while the others were elliptical. All data considered in this thesis were obtained using beam 3, whose radiation pattern, which is identical for both passive and active modes, is shown out to 2° from the boresight (thus including near side lobes (NSL) around the main beam) in Fig. 3.1. This beam pattern was obtained by Janssen et al. (2009) by combining a scan of the Sun obtained in 2001 with the preflight characterization of the main beam. The main beam, which is Gaussian, has a full width at half maximum (FWHM) of $\beta = 0.373°$, while the near side lobes extend to 2°from the boresight. The sidelobes beyond this point, hereafter called the far sidelobes (FSL), are too weak to be measurable

Table 3.1 – Properties of the Cassini radar/radiometer, from Elachi et al. (2004), West et al. (2009), and Janssen et al. (2009). Note the theoretical measurement noise has been corrected from the value in Janssen et al. (2009).

Antenna diameter	4 m
Frequency	13.78 GHz
Wavelength	2.17 cm
Polarization	Linear
Number of beams	5 (1, 2, 4, and 5 are elliptical; 3 is circular)
Beam width at half power (beam 3)	0.373° (circular)
Peak radar power	46.2 W
Radiometer bandwidth	135 MHz
Radiometer measurement noise	0.075 K/ $\sqrt{Hz}$

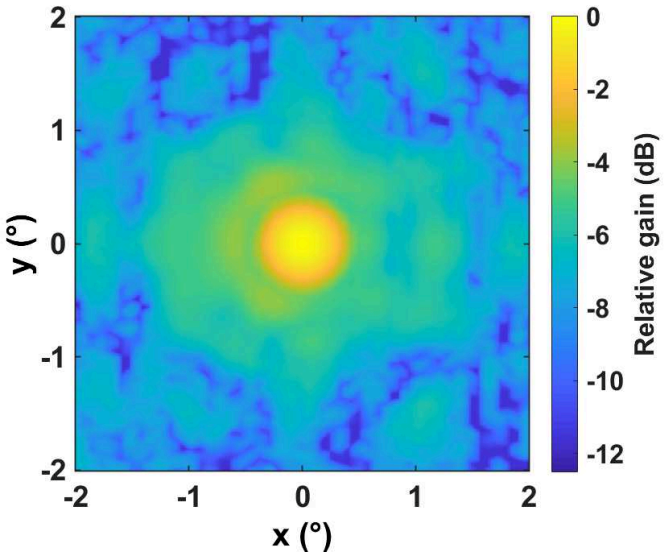

Figure 3.1 – Cassini radar/radiometer beam 3 pattern out to 2°, obtained by combining a 2001 Sun scan and preflight main beam characterization (Janssen et al., 2009; West et al., 2009). Within the half power beam width of 0.373°, the main beam is Gaussian. The x and y directions correspond to the spacecraft coordinates.

with a distant scan of the Sun. Instead, they were determined out to 90° from high-resolution Titan scans, where the far sidelobes contributed a significant part of the signal (Janssen et al., 2009).

3.1.2 Observation strategy

A typical Titan flyby dedicated to the radar/radiometry instrument had the observation sequence pictured in Fig. 3.2. When the spacecraft was still far from Titan, it only obtained passive radiometry data, by scanning the disk with its central, circular beam (beam 3). The small angular size of the target allowed regular sky observations, which are needed for the radiometer calibration. Ideally, two scans were obtained in orthogonal polarizations by rotating the Cassini probe by 90° in-between the scans. Observing at orthogonal polarizations allows the calculation of the surface dielectric constant (Janssen et al., 2009, 2016).

Once the Cassini probe was only 40000 km from Titan, the radar transmitter was turned ON and scatterometry data was obtained by scanning Titan's surface. At closer range, the instrument

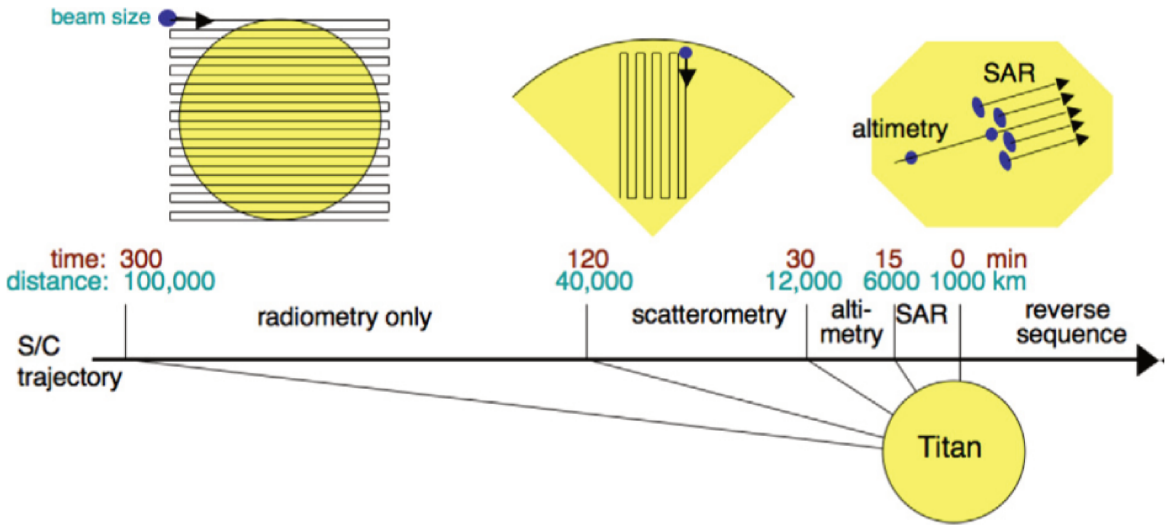

Figure 3.2 – Schematic spacecraft trajectory (not to scale) for a Titan pass illustrating the different radar/radiometer modes. Figure from Janssen et al. (2009)

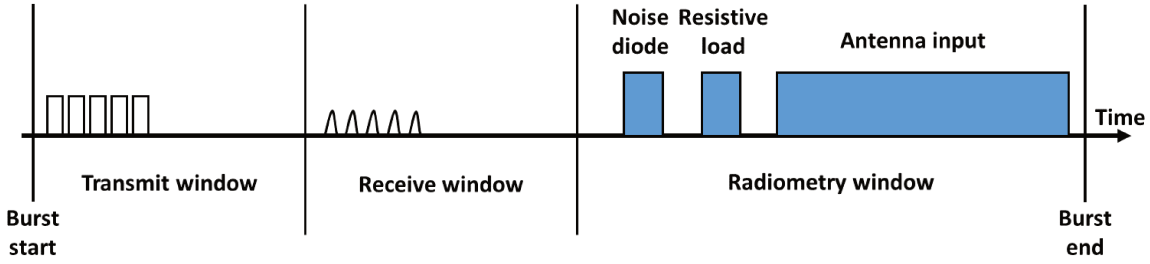

Figure 3.3 – Illustration of a typical burst cycle, including both its radar (transmit and receive) and radiometry components. Adapted from West et al. (2009).

concentrated on radar altimetry, by observing at nadir (0° incidence angle). At closest approach, all five beams transmitted and received signals at oblique incidence angles in order to map the surface in SAR mode. After closest approach, as the spacecraft was receding from Titan, the reverse observation sequence was conducted, ending with passive radiometry (Elachi et al., 2004).

A single radar/radiometry observation, called a burst, consisted in the timeline shown in Fig. 3.3. A burst began with the radar transmit window, when a modulated signal (of shape depending on the type of observation) was sent towards the target. After a short time delay, taking into account the 2-way travel time of the signal, the receive window began, during which the antenna measured the backscatter from the target. The radiometry portion of the burst followed. Before observing the target, during each burst, the radiometer underwent two calibration measurements by sampling the noise diode and resistive load temperatures. Finally, the thermal radiation from the target was measured, over an integration time t_{int} (length during which the antenna input is measured). If only passive radiometry observations were used, the burst only included the radiometry window.

Saturn's icy satellites are significantly smaller than Titan (at most a third of its diameter), and radiometry data was taken at ranges $R > 8000$ km (typically $R > 50000$ km), except in the case of the dedicated Enceladus flyby, during which SAR data and concurrent high-resolution radiometry could be obtained from an altitude of 500 km (Mitchell et al., 2012; Le Gall et al., 2017). As a consequence, icy satellites required a modified radar/radiometry observation sequence. Most of radiometry scans were unresolved (ie. with a beam size greater than the size of the target disk) and therefore designed to provide disk-integrated brightness temperature (Section 4). Polarized radiometry data were acquired

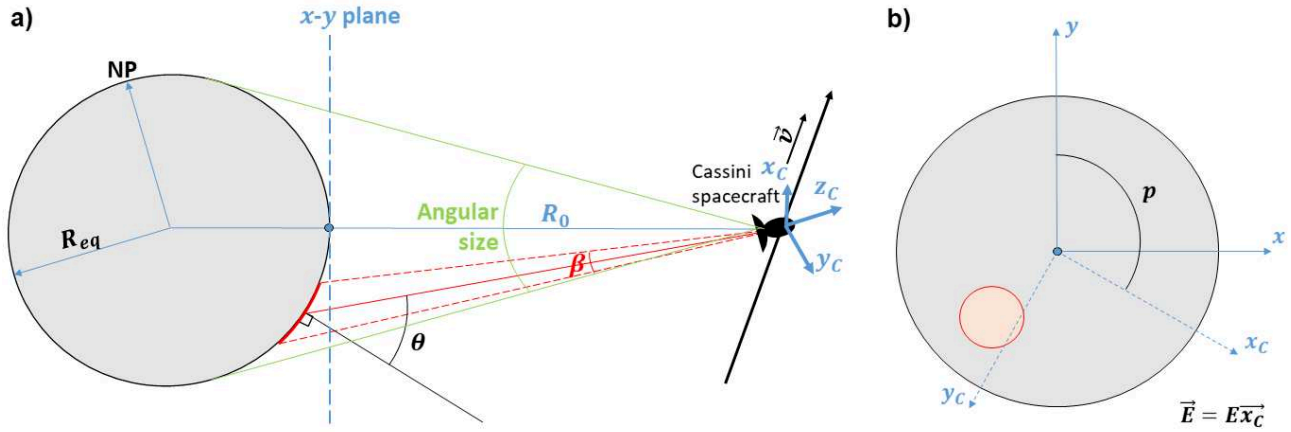

Figure 3.4 – Geometry of an icy satellite resolved radiometry/scatterometry observation. In order to take into account foreshortening, polar flattening, and variable spacecraft orientations, all data are projected onto the x-y plane pictured here. (a) Side view. Note that the antenna points in the spacecraft $-z_C$ direction (b) Projected view on the x-y plane. In these coordinates, the antenna footprint is circular. The angle p gives the direction of the electric field (along the x-axis of the Cassini spacecraft, x_C), which is the direction of parallel polarization.

at only rare instances. Resolved scatterometry and concurrent radiometry were obtained in four cases (on Enceladus, Dione, Rhea, and Iapetus), as described in Section 3.3. When the target was too distant for scatterometry, disk-integrated radar albedos were instead measured using a different observation strategy, called a "stare", described in Section 3.2. A few SAR images have been derived both from scatterometry and stare data (Ostro et al., 2010; Wye, 2011).

3.1.3 Observation geometry recalculation

The radar and radiometry data files (Long and Short Burst Data Record, LBDR and SBDR), which are publicly available on the Planetary Data System (PDS), include observation geometry, timing, spacecraft position and orientation, and calibration data. However, several errors and inaccuracies have since been noticed in the method to generate some of this information. For instance, all main beam footprints projected onto the surface were assumed elliptical, which is only true at very close range when the target's curvature is negligible. Foreshortening and polar flattening were also not taken into account. The first step of my analysis has therefore been to recalculate all useful information using the correct geometry. For these purposes, I used the SPICE toolkit developed by NASA's Navigation and Ancillary Information Facility (NAIF) (Acton, 1996). SPICE, which stands for Spacecraft, Planet, Instrument, Camera-matrix Events, uses ancillary data (planet, moon, spacecraft, and instrument positions, orientations, sizes, and reference frames) expressed in kernels in order to calculate the precise geometry at a given time t.

The geometry of a resolved icy satellite observation is given in Fig. 3.4; an unresolved observation has the same geometry but with a footprint size larger than the target disk. The range R from the Cassini spacecraft to the sub-spacecraft point on the icy satellite is easily calculated with SPICE. We then need to project all data into a coordinate system which corresponds to the spacecraft's view of the satellite, but does not change with spacecraft orientation. An orthographic projection, which is straightforward to compute from latitude/longitude coordinates for a spherical object viewed from infinity, can be applied only if the spacecraft is sufficiently far from its target of observation. However, the conversion to orthographic coordinates is complex for non-spherical bodies such as Saturn's icy satellites. Indeed, Iapetus exhibits significant polar flattening, while the other icy satellites have a triaxial shape, elongated by tides in the Saturn–satellite direction (i.e., perpendicular to satellite's

movement on its orbit) (Thomas, 2010). Moreover, in many cases, the Cassini probe was close enough to the target for foreshortening to be significant: objects nearer to the spacecraft have a larger angular size, which changes the aspect of the target seen by the radar/radiometer antenna. Instead, the vertical perspective projection is used. The coordinates are fixed relative to the orientation of the target, unlike the Cassini spacecraft coordinates (x_C, y_C, and z_C), which change with polarization and radiometer pointing.

We define the x-y plane (hereafter called "spacecraft view coordinates") as the plane tangent to the surface at the sub-spacecraft point, with the $\overrightarrow{y}$-direction corresponding to the projection of vector from the sub-spacecraft point to the North Pole, as pictured in Fig 3.4. The spacecraft's angular view of the target is projected onto this plane (Fig 3.4b); the main antenna beam remains circular in these coordinates. There is no simple direct formula to convert from latitude/longitude planetocentric coordinates to the vertical perspective projection. Instead, I used SPICE to built look-up tables of the correspondence between both coordinate systems, for every 0.5° in latitude/longitude, and for a 201 by 201 grid in x-y coordinates, while taking into account the shape of the satellite and the correct spacecraft distance.

Once the coordinate system is defined, the observation geometry is characterized from the following variables. The angle p, between the y-axis and the projected Cassini spacecraft x_C-axis, gives the direction of the sensed electric field, which is the direction of parallel polarization. The latitude/longitude and x-y coordinates of the pointing direction (antenna boresight) are recorded, as well as the emission angle θ (the same as the incidence angle in active radar mode) at that point.

A systematic beam 3 pointing offset has been noticed in radiometer scans of Saturn (Janssen et al., 2013), Iapetus (Le Gall et al., 2014), Saturn's rings (Zhang et al., 2017a), and Jupiter (Moeckel et al., 2019). This offset, which has an amplitude of about 0.036° (i.e., a tenth of the main beam diameter), strongly affects the poorly resolved icy satellite radar/radiometry. Following Zhang et al. (2017a), this systematic offset was taken into account by modifying the radar/radiometer (Ku-band) instrument boresight direction in the Cassini frame definitions kernel, to match the X- and Ka-band boresights, whose kernels had already been corrected by the Cassini Radio Science team from the spacecraft $-z_C$ axis [0,0,-1] to [0.0004900,0.0004500,-0.9999998]. Indeed, the Cassini Radar and Radio Science Experiment use the same antenna, and should therefore have the same pointing direction.

3.2 Distant radar observations: Disk-integrated radar albedos

As part of my thesis, I participated in the interpretation of the distant icy satellite Cassini radar data, which has been published in *Geophysical Research Letters* (Le Gall et al., 2019). The analysis of the distant radar observations is summarized herein.

3.2.1 Observations and derivation of the disk-integrated radar albedo

Throughout the Cassini mission, the Cassini radar performed a total of 97 distant active observations, also called "active stares." During these active stares, the radar transmitted 46 W through the 4-meter dish antenna. The receiver operated with a relatively high noise temperature around 900 K, and the received echo power was well below the noise floor for a single measurement. To overcome the low signal strength, the radar stared at the target body while accumulating echo measurements (Fig. 3.5). Spacecraft power constraints limited the Radar to a 7% transmit duty cycle, so the actual integration time was less than the total staring time which usually ran 5 to 10 minutes for a single observation. In order to maximize the signal to noise ratio (SNR), the echo data is Fourier-transformed

and then summed in the frequency domain. The transmit events consist of bursts of single frequency pulses at 13.78 GHz. The received echo power is spread out in the frequency domain by Doppler variation which arises from a combination of the relative motion of the spacecraft and the rotation of the target body (Fig. 3.5b). For the icy satellites, the Doppler variation ranges from a few hundred Hz up to about 4 kHz. The pulsed nature of the transmit events introduces grating lobes spaced at the pulse repetition frequency (PRF). The PRF is set to a frequency higher than the Doppler spread of the target, so the central spectral peak is separated from the grating lobes and shows the natural variation of the echo power over the target body.

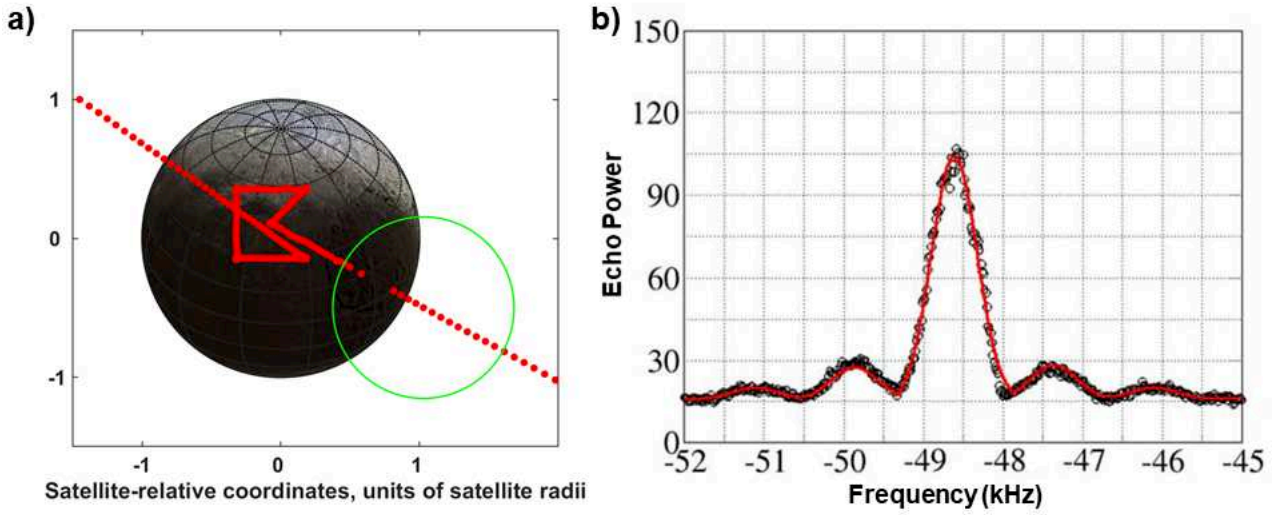

Figure 3.5 – (a) Boresight pointing directions (red points) during the five-point IA00B active stare observation, shown over the projected ISS 3-color composite of Iapetus (PIA18436). The beam size at the beginning of the observation is indicated in green. (b) Cassini 2.2-cm radar echo power spectrum (black circle symbols) acquired during the IA00B stare observation and best-fit model (red line); extracted from Ostro et al. (2006).

The sum of the echo power in the power spectrum is then scaled by the radar equation to derive the disk-integrated radar albedo of the target body. More specifically, the radar equation is applied assuming azimuthal homogeneity and a diffuse surface scattering function given by $\sigma^0(\theta) = A\cos^n\theta$ where θ is the incidence angle. The values of A and n are obtained from a least-square fit of the observed power spectrum with a model consisting of the above surface scattering function and the antenna gain pattern integrated over the illuminated area (Fig. 3.5b). The resulting disk-integrated radar albedo is the uniform normalized backscattering value which best reproduces the observed integrated power assuming that the fit model is correct. Therefore, it is derived from the best-fit values of A and n as follows:

$$A_{\mathrm{SL-2}}^{\mathrm{disk}} = \frac{2\pi R^2 \int_0^{\pi/2} \sigma^0(\theta)\sin\theta d\theta}{\pi R^2} = 2\int_0^{\pi/2} A\cos^n\theta\sin\theta d\theta \tag{3.1}$$

Where the subscript SL – 2 indicates same-sense linear polarization (see Section 2.3.3) measured at 2 cm. It results:

$$A_{\mathrm{SL-2}}^{\mathrm{disk}} = \frac{2A}{n+1} \tag{3.2}$$

For comparison with total-power albedos measured on the Galilean satellites (Table 2.2 in Section 2.5.2), we convert the same-sense linear disk-integrated radar albedos into total-power albedos

$A^{\text{disk}}_{\text{TP}-2}$ following empirical formula proposed for icy satellites by Ostro et al. (2006) and Ostro et al. (2010):

$$A^{\text{disk}}_{\text{TP}-2} = (1.52 \pm 0.13) \times A^{\text{disk}}_{\text{SL}-2} \tag{3.3}$$

More details can be found in Ostro et al. (2006), Ostro et al. (2010), Wye (2011), and Le Gall et al. (2019).

We note that many stare observations are resolved (i.e., the beam size is smaller than the satellite diameter). Because of the way they are calculated, the values derived here are disk-integrated radar albedos regardless of the resolution. Nonetheless, these radar albedos are only representative of the radar properties in the region observed at that moment (i.e., within the radar footprint). Thus, resolved multi-point stares allow the detection of regional variations in radar albedo.

3.2.2 Results

The choice of a diffuse cosine law for the surface scattering function is supported by the shape of the measured spectra (Fig. 3.5). As stated in Ostro et al. (2006), "none of them, and none of the ground-based echo spectra from any of our targets or the icy Galilean satellites, show any hint of the specular (narrowband) scattering expected if the echoes were dominated by single backreflections from surface elements that are large and smooth at scales near the wavelength. Rather, the spectral shapes are broad, indicating diffuse scattering from structural complexity at some scale(s) comparable to the wavelength or larger." As discussed in Section 2.5, diffuse scattering is also consistent with the high radar brightness and relatively low emissivities of the icy Galilean and Saturnian satellites.

The details of each observation and the derived parameters A, n, $A^{\text{disk}}_{\text{SL}-2}$, and $A^{\text{disk}}_{\text{TP}-2}$ are provided in Le Gall et al. (2019). The resulting radar albedos, averaged both globally and for the leading and trailing hemispheres of each satellite, are summarized in Table 3.2 and plotted in Fig. 3.6. All of Saturn's inner moons have extremely high radar albedos with values above unity even when accounting for all possible sources of uncertainties. Enceladus is the most radar-bright satellites of Saturn, followed by Tethys, Mimas, Rhea, Dione, Iapetus, Phoebe, and Titan, in that order.

We also note that the derived values for the shape parameter n range from about 1 to 5 (with a standard error typically $< 0.1 - 0.2$; see Le Gall et al., 2019). This parameter characterizes the rate at which the radar backscatter decreases with the incidence angle. More specifically, it quantifies how focused diffuse scattering from the surface is. $n > 2$ implies that the measured diffuse scatter is more focused than that of a Lambertian surface (i.e., a perfectly rough surface that scatters uniformly in all directions). The very high values obtained for Titan ($n = 2.7 - 9.8$) and their associated large standard errors suggest that the diffuse scattering model does not apply well to the surface of this satellite. However, because n is a semi-empirical parameter it cannot be more explicitly related to the surface properties.

The spatial distribution of radar albedos on each satellite is pictured in Fig. 3.7. On Iapetus, the leading/trailing dichotomy is cleary apparent at 2.2 cm. On Mimas and Dione, the leading side has not been observed, so no dichotomy can be detected. On Enceladus, partial coverage and poor resolutions also do not permit the detection of regional anomalies. On Tethys, the unique leading hemisphere observation is brighter than the two trailing hemisphere data points, consistent with the dichotomy observed at optical wavelengths (Section 1.5). Finally, significant variations in Rhea's radar albedo seem to occur at different scales, and are difficult to discern at the resolution of the stares.

These results and their interpretations are further discussed in Section 3.4.

Table 3.2 – Summary of the radar properties of Saturn's satellites as derived from Cassini radar distant stare observations. The range of values extracted for the parameters A and n are given. The details for each observation are included in the supplementary material of Le Gall et al. (2019). The Galilean satellites Europa, Ganymede, and Callisto are included for reference.

Satellite	**Number of stares**	n	A	**Average** $A^{\text{disk}}_{\text{SL}-2}$	**Leading** $A^{\text{disk}}_{\text{SL}-2}$	**Trailing** $A^{\text{disk}}_{\text{SL}-2}$	**Average** $A^{\text{disk}}_{\text{TP}-2}$ [a]
Mimas	4	1.23 – 2.04	2.56 – 3.94	2.44 ± 0.18		2.27	3.71 ± 0.59
Enceladus	10	1.08 – 2.09	3.03 – 4.89	2.97 ± 0.35	3.01 ± 0.27	3.15	4.51 ± 0.92
Tethys	3	1.63 – 2.16	3.52 – 4.85	2.84 ± 0.23	3.10	2.66	4.32 ± 0.72
Dione	18	1.07 – 4.91	1.39 – 3.70	1.65 ± 0.29	1.51	1.37 ± 0.12	2.55 ± 0.66
Rhea	26	0.94 – 5.54	1.94 – 3.41	1.88 ± 0.38	1.63 ± 0.77	2.00 ± 0.44	2.86 ± 0.86
Titan	8	2.71 – 9.77	0.28 – 0.98	0.19 ± 0.06			0.29 ± 0.12
Iapetus	18	0.31 – 3.36	0.29 – 1.21	0.53 ± 0.21	0.34 ± 0.05	0.80 ± 0.13	0.81 ± 0.39
Phoebe	2	0.92 – 1.42	0.28 – 0.38	0.30 ± 0.01			0.46 ± 0.05
							$A^{\text{disk}}_{\text{TP}-3.5}$ [b]
Europa							2.31 ± 0.36
Ganymede							1.55 ± 0.20
Callisto							0.72 ± 0.06

[a] For comparison with measurements made on the Galilean satellites at 3.5-cm ($A^{\text{disk}}_{\text{TP}-3.5}$), we have converted Cassini same-sense linear disk-integrated radar albedos into total-power albedos $A^{\text{disk}}_{\text{TP}-2}$ using the formula proposed in Ostro et al. (2006) and Ostro et al. (2010).

[b] Total-power 3.5-cm radar albedos of the Galilean satellites are repeated here (from Table 2.2) for convenience.

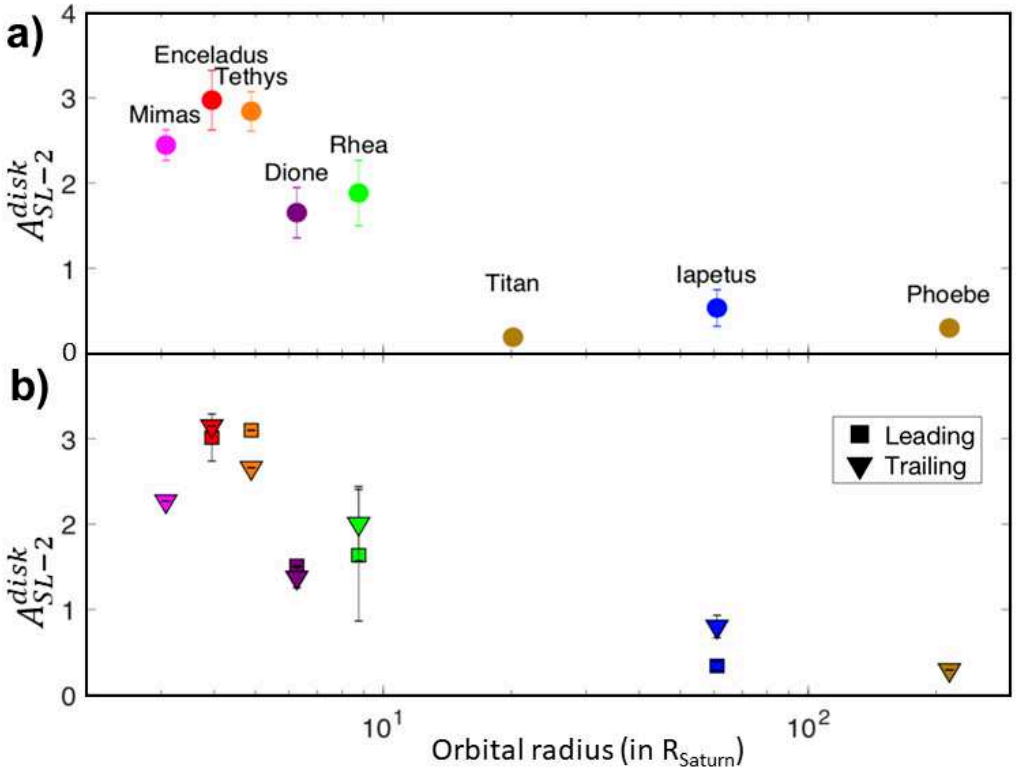

Figure 3.6 – (a) Averaged 2.2-cm disk-integrated radar albedos $A^{\text{disk}}_{\text{SL}-2}$ of Saturn's major satellites. The error bars show the dispersion of the data set for each satellite, whereas the statistical uncertainties on the derived albedos (inferred from the goodness of the fit) are smaller than the size of the symbols. (b) $A^{\text{disk}}_{\text{SL}-2}$ measured on the leading and trailing hemispheres of each of Saturn's satellites. Note that the large uncertainty on Rhea's leading hemisphere is due to the strong contrast between the radar-bright ejecta blanket of the Inktomi crater and the radar-darker rest of Rhea's leading side.

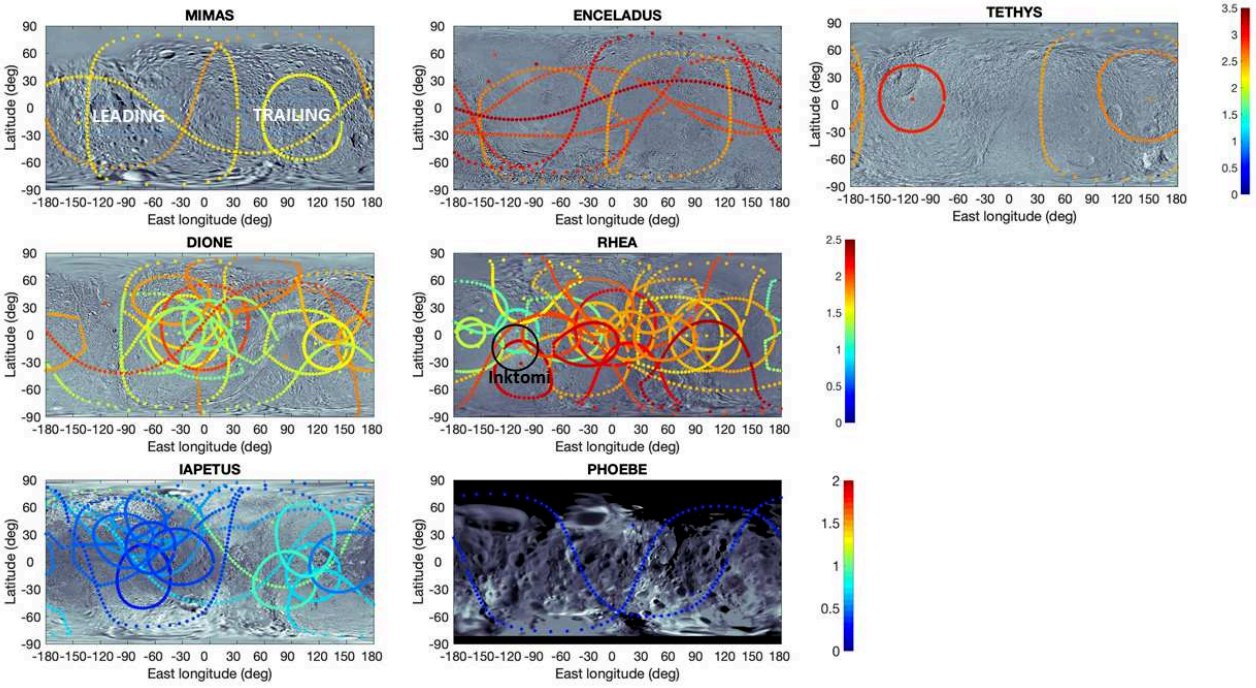

Figure 3.7 – Radar footprints on each targeted icy satellite, for all active distant stare observations. The color code indicates the value of the derived radar albedo $A^{\text{disk}}_{\text{SL}-2}$ for each line of observations. The Inktomi ejecta blanket is indicated on Rhea. For all satellites except Phoebe (which is not synchronous), the leading side is centered at -90°E and the trailing side at 90°E.

3.3 Resolved radar observations: scatterometry

As part of my thesis, I re-calibrated the available Cassini scatterometry data of Rhea and Dione in order to take into account the aforementioned radar antenna pointing offset (see Section 3.1.3), then examined the backscattering behavior of different regions on these icy satellites. This work has been published as part of the comprehensive analysis of the icy satellite Cassini radar data (Le Gall et al., 2019). The updated calibration process is detailed hereafter, and our results and interpretations are summarized in Section 3.4.

3.3.1 Observations

Active spatially resolved data were acquired during one close flyby of Iapetus (Wye, 2011; Le Gall et al., 2014), two close flybys of Enceladus (one partially remaining to be analyzed; Wye, 2011; Le Gall et al., 2017), one close flyby of Rhea (Wye, 2011; reanalyzed herein), and one close flyby of Dione (this work). These observations are briefly described below and their characteristics are provided in Table 3.3.

Iapetus

During Cassini's 49th orbit around Saturn (IA049, Sept. 9–10, 2007), the radar was assigned a time slot while the spacecraft was at a range of ~20 000 km from Iapetus. The SAR image obtained during this close encounter is described in Ostro et al. (2010) while the scatterometry data were processed and analyzed by Wye (2011) and the radiometry data by Le Gall et al. (2014). Both the spatially-resolved scatterometry and radiometry images acquired during IA049 are shown in Le Gall et al. (2014). The scatterometry analysis yields a same-sense linear polarization radar albedo $A^{\text{disk}}_{\text{SL}-2}$ = 0.29 ± 0.01 for the dark leading side of Iapetus and $A^{\text{disk}}_{\text{SL}-2}$ = 0.53 ± 0.05 for the bright polar regions

Table 3.3 – Cassini icy satellite scatterometry observations.

Satellite	Observation ID	Date	Beam size (diameter) min–max	Center Lon (°E), Lat (°N)	Range (10^3 km) min–max
Iapetus	IA049_3	10 SEP 2007	0.07 – 0.11	[-77,11]	16 – 24
Enceladus	EN120	01 NOV 2007	0.39 – 1.1	[35,-1]	30 – 82
Enceladus	EN156	05 NOV 2011	0.006 – 0.53	variable[a]	0.5 – 42
Rhea	RH127	02 MAR 2010	0.11 – 0.23	[-166,1]	26 – 56
Dione	DI163	27 MAR 2012	0.32 – 0.56	[-4 to -34,-1]	59 – 97

[a] Scatterometry during EN156 covers the sub-Saturn, anti-Saturn, and South polar regions.

(Wye, 2011).

Enceladus

Wye (2011) describes the scatterometry analysis of the resolved data collected during Cassini's 120th orbit around Saturn (called EN120 or E7) in November 2009. The observation occurred at a range between 30 000 and 57 000 km and yields $A^{\text{disk}}_{\text{SL}-2} = 3.14 \pm 0.08$ for a sub-spacecraft point at 36°E longitude and -25°N latitude (Wye, 2011). Another scatterometry observation occurred in November 2011 (called EN156 or E16) but remains to be analyzed. The corresponding SAR images are shown in the supplementary material of Le Gall et al. (2017).

Rhea

Wye (2011) describes the scatterometry analysis of spatially resolved data collected during flyby RH127 (March 2, 2010). This observation occurred with a sub-spacecraft point centered at (-157.4°E, 0°N). These data were re-reduced for this work in order to take into account the pointing offset discovered since the work by Wye (2011).

Dione

For this work we conducted the analysis of the spatially-resolved active observations acquired during flyby DI163 (March 28, 2012) following the approach described in Wye (2011) and accounting for the boresight offset. This observation occurred with a sub-spacecraft point centered at (-18.5°E, -0.9°N).

3.3.2 Data reduction

The scatterometry data available on PDS have originally been reduced and calibrated according to the method of Wye (2011) with the following form of the Real Aperture Radar equation (derived from Eq. 2.24):

$$\sigma^0_{\text{avg}} = \frac{(4\pi)^3}{P_r P_t G^2 \lambda^2} \left(\int_A \frac{g^2(dA) dA}{R^4(dA)} \right)^{-1} \tag{3.4}$$

where P_t and P_r are the transmitted and returned power, λ is the instrument's operating wavelength, G is the peak gain of the antenna, $g(dA)$ is the normalized gain of the antenna pattern at surface element dA, $R(dA)$ is the range to this surface element, and σ^0_{avg} is the NRCS, averaged over the footprint, as defined in Section 2.3.2. The integral is evaluated numerically by projecting the beam pattern onto

the surface, where the range and area of each surface element are known.

However, as mentioned in Section 3.1.3, a boresight pointing offset has since been discovered, which affects the results of the integral in Eq. 3.4. A small residual pointing offset, of varying amplitude, is also present: it is derived from the radiometry data as detailed in Section 4.2.4. Once the offset was found, rather than redoing the entire reduction (which is complicated for example by ITAR restrictions on the codes), I corrected this inaccuracy by evaluating the integral with and without accounting for the offset:

$$\sigma^0_{\text{avg}} = \sigma^0_{\text{avg,no offset}} \left(\int_A \frac{g^2(dA)dA}{R^4(dA)} \right)_{\text{no offset}} \left(\int_A \frac{g^2(dA)dA}{R^4(dA)} \right)^{-1}_{\text{with offset}} \tag{3.5}$$

The correct values of σ^0_{avg} are thus obtained.

Similarly, the effective incidence angle θ_{eff} over the footprint is weighted by the beam pattern and the range, but also by σ^0 itself, since regions of locally high reflectivity (such as those observed with a small incidence angle) return more signal than others. The iterative method used by Wye (2011) in order to derive θ_{eff} is summarized hereafter. She modeled the backscatter as a cosine power law: $\sigma^0(\theta) = A\cos^n(\theta)$, consistent with diffusely scattering surfaces such as icy satellites (Ostro et al., 2006; Ostro et al., 2010). Knowing the incidence angle $\theta(dA)$ at each surface element dA, she computed the simulated average backscatter $\sigma^0_{\text{avg,sim}}$:

$$\sigma^0_{\text{avg,sim}} = \frac{\displaystyle\int_A \frac{g^2(dA)A_0\cos^{n_0}(\theta(dA))dA}{R^4(dA)}}{\displaystyle\int_A \frac{g^2(dA)dA}{R^4(dA)}} \tag{3.6}$$

for a given (A_0,n_0) pair. The modeled effective incidence angle can then be found for this (A_0,n_0) pair by inverting the cosine backscatter law:

$$\theta_{\text{eff,sim}} = \cos^{-1}\left(\frac{\sigma^0_{\text{avg,sim}}}{A_0} \right)^{1/n_0} \tag{3.7}$$

Note that A_0 can be taken out of the integral in Eq. 3.6, and consequently cancels out in Eq. 3.7. Therefore only n_0 needs to be found in order to find the correct value of θ_{eff}. Wye (2011) thus iterated on different possible values of n_0. For each n_0, she derived θ_{eff}, and plotted the corresponding observed values of σ^0_{avg}, as shown in Fig. 3.8–3.9. She then fit σ^0_{avg} as a function of θ_{eff} by a cosine power law and derive a new value of n, which we call n_f. This process is iterated upon until the input and output n are the same ($n_f = n_0$); θ_{eff} is then calculated using this value. This process is illustrated in Figs. 3.8–3.9.

In order to account for the pointing offset in the derivation of θ_{eff}, the same method is used as by Wye (2011), while adjusting the beam pattern distribution for the correct pointing direction. On Rhea, a radar-bright region was identified around Inktomi crater, a young crater (located at 14.1°S, 112.1°W) surrounded by an optically bright ejecta blanket (see Section 1.5.1 for details). All data within 25° in latitude/longitude from the Inktomi crater were therefore examined separately from the rest of the scatterometry data, as pictured in Fig. 3.8. Similarly, on Dione, the leading and trailing hemispheres exhibit different radar behaviors, with the leading hemisphere appearing more radar-bright. Data to the East or West of 0°E were examined separately, as illustrated in Fig. 3.9.

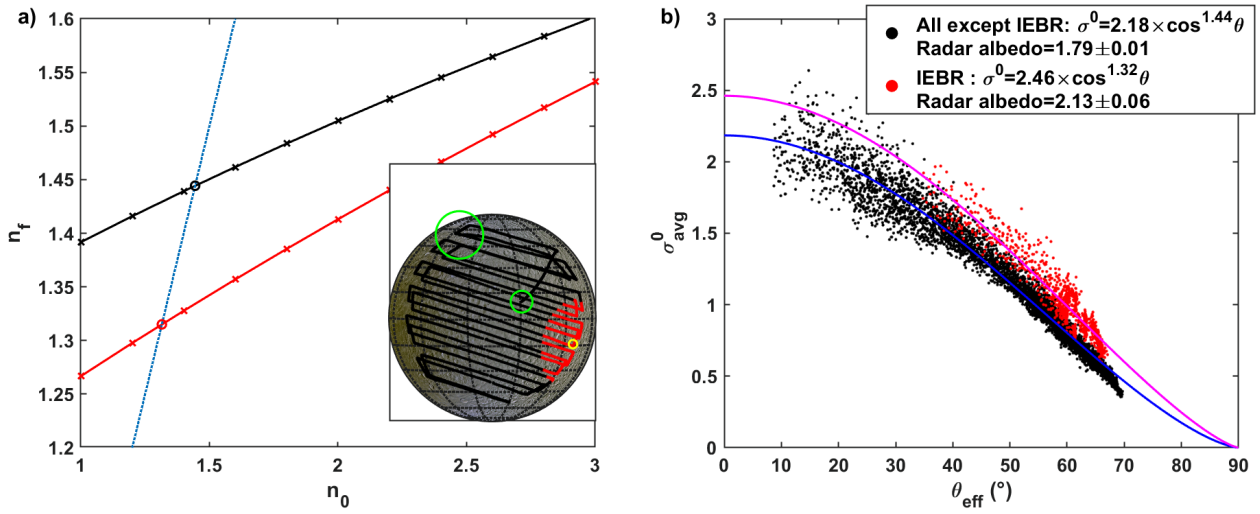

Figure 3.8 – (a) Determination of the backscatter model parameter n for the **Rhea** scatterometry observation (flyby RH127). Best-fitting values n_f are plotted for each initial assumed value n_0, for the Inktomi Ejecta Blanket Region (IEBR) (red) and for the rest of Rhea (black). The $n_f = n_0$ line is plotted in blue. The inset displays the projected ISS 3-color composite of Rhea (PIA18438); the boresight pointing direction is shown with a red dot for IEBR observations and a black dot for the remaining Rhea scatterometry observations. The FWHM beam size is shown in green at the beginning (larger beam size) and end (smaller beam size) of the RH127 scan. The Inktomi crater is circled in yellow. (b) The Rhea backscatter data σ^0_{avg} is plotted against the effective incidence angle θ_{eff}, and the best fit diffuse backscatter model is plotted in magenta for the IEBR and blue for the remaining data. The parameters of each fit (a, n) are given, as well as the derived radar albedo.

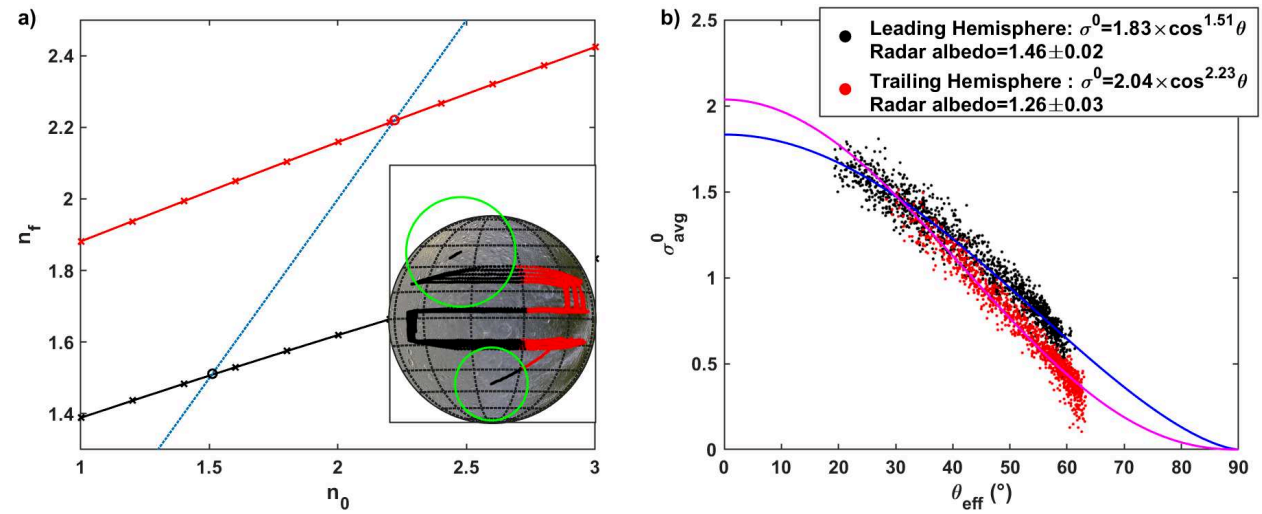

Figure 3.9 – Same as Fig. 3.8 for the **Dione** scatterometry observation (flyby DI163). The leading (black) and trailing (red) hemispheres are examined separately.

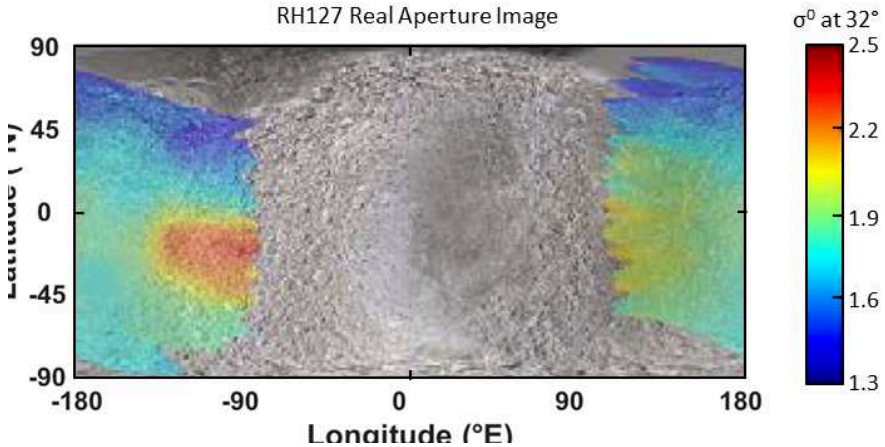

Figure 3.10 – Real aperture radar image built by Wye (2011) from the RH127 resolved scatterometry, corrected for incidence effects. Unlike the image presented in Fig. 3.11, this data has not been corrected for the pointing offset.

Once the data are correctly calibrated and the best fitting values of A and n have been found, it is possible to calculate the radar albedo $A^{\text{disk}}_{\text{SL}-2}$ using Eq. 3.2; all three variables are given for Rhea and Dione in Figs. 3.8–3.9. These values are nicely consistent with those found from distant stare observations (Section 3.2).

3.3.3 Results

The fully calibrated normalized backscattering cross-section σ^0 is mapped in Figs. 3.11–3.12 for Rhea and Dione, respectively. To represent the scattering behavior over the whole observed region, we correct for incidence angle effects by calculating σ^0 for $\theta = 32°$, using the scattering laws described above and given in Figs. 3.8–3.9.

On Rhea, the real aperture radar image produced by Wye (2011) (shown in Fig. 3.10), showed locally high radar brightness on the trailing hemisphere and the Inktomi ejecta blanket, while the Northern high latitudes appeared particularly radar-dark. After re-reducing this dataset while taking the pointing offset into account (Fig. 3.11), we see neither a leading/trailing dichotomy nor a clear difference between the northern and southern high latitudes; these effects were most likely caused by the antenna pointing offset. The high-latitude regions appear slightly less radar-bright than lower latitudes; however, this effect is of low amplitude and may be caused by inaccuracies (the incidence angle correction, for instance, is less reliable near the limbs). The Inktomi Ejecta Blanket Region (IEBR), however, remains very radar-bright, as expected from the analysis of backscattering curves (Fig. 3.8).

Dione is globally less radar-bright than Rhea (Fig. 3.9), consistent with distant radar data (Table 3.2). A leading/trailing radar albedo dichotomy is apparent in both the backscatter images (Fig. 3.12) and the scatterometry curve (Fig. 3.9). Indeed, the leading side is brighter than the trailing side, which mirrors the optical dichotomy (see Fig. 1.6). This dichotomy is not obvious in the stare data, most likely due to the scarcity of observations on the leading hemisphere (Fig. 3.7). We note that the pointing offset is particularly challenging to determine for the DI163 flyby due to confusion with real surface temperature variations (see Section 4.2.4). The scatterometry data was reprocessed using three different values of pointing offset (from none to 0.02°in the $\hat{x}$-direction). The leading/trailing dichotomy was always obvious, though its amplitude varied. Consequently, this dataset allows for a qualitative interpretation but calls for caution before quantitative analysis.

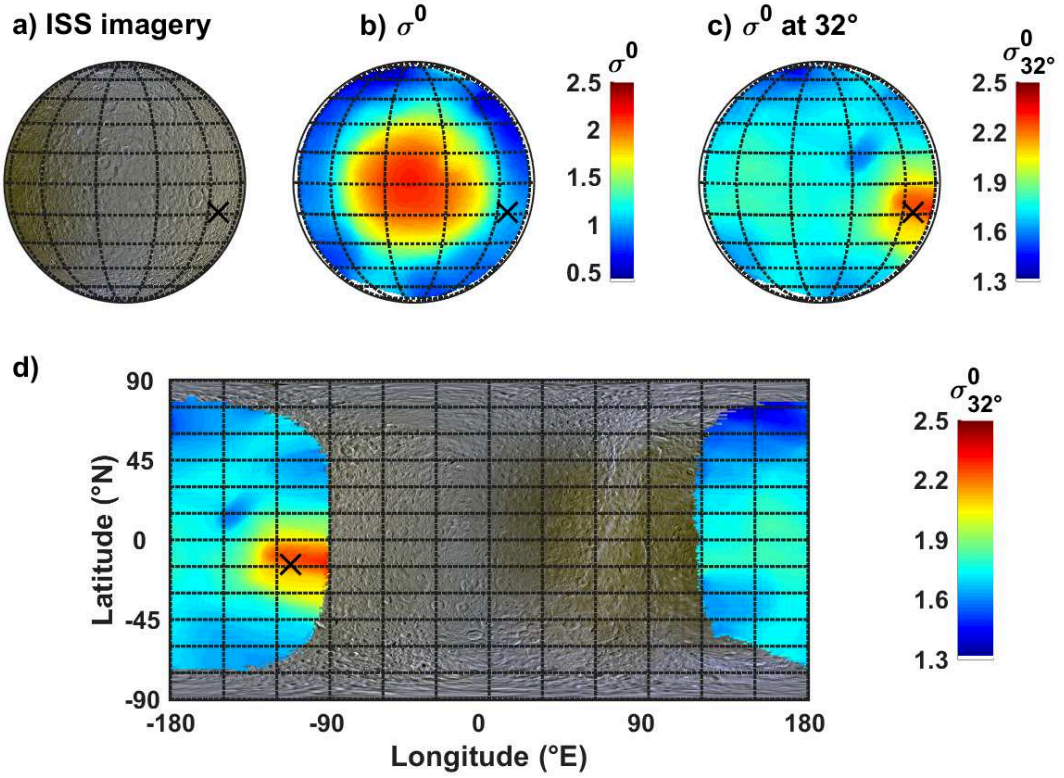

Figure 3.11 – (a) Cassini view of **Rhea** during flyby RH127. (b) Normalized backscattering cross sections σ^0 mapped over the disk of Rhea; notice the sharp decrease in radar brightness at high incidence angles. (c) σ^0 corrected to an incidence angle of $\theta = 32°$, using the diffuse scattering laws given in Fig. 3.8. (d) Same as (c), projected onto the ISS map of Rhea (PIA18438). Inktomi crater is marked with a black ×.

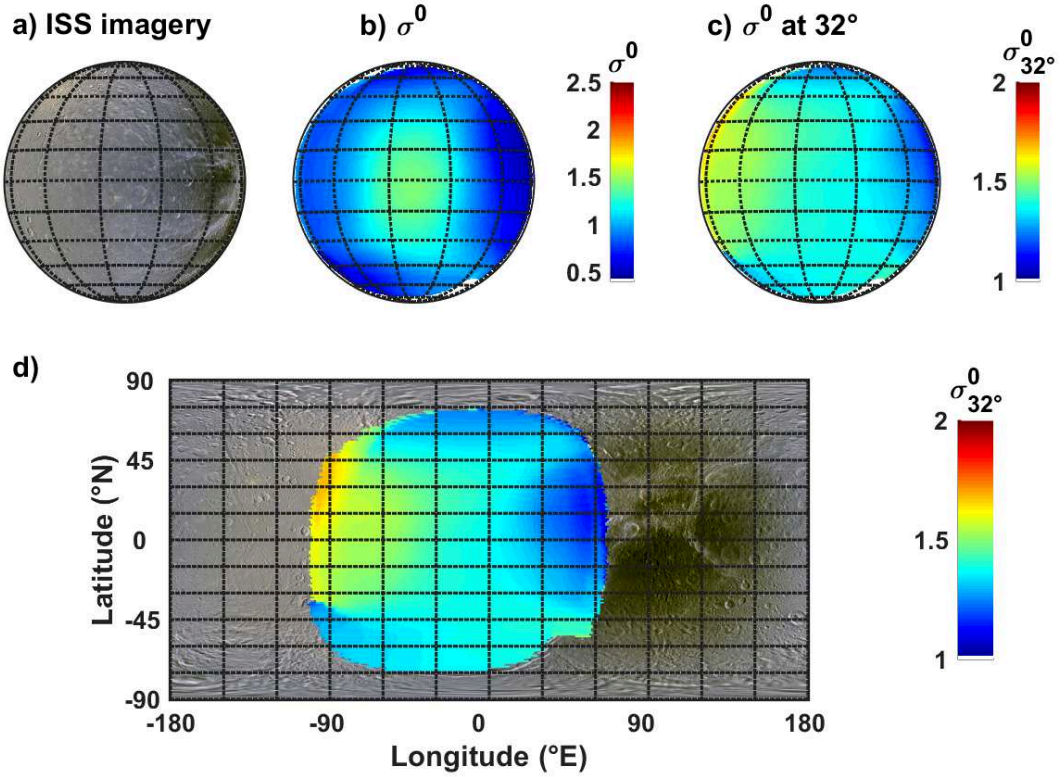

Figure 3.12 – Same as Fig. 3.11 for the **Dione** scatterometry observation (flyby DI163). The range of σ^0 is narrower than for Fig. 3.11; note that Dione is in average less radar-bright than Rhea.

3.4 Interpretations

3.4.1 Radar albedo and water ice purity

Diffuse subsurface scattering is generally associated with high water ice purity. Indeed, a transparent medium such as water ice allows for large ($> 10 - 100$ times the wavelength) penetration depths of the incident waves, which therefore have many opportunities for multiple scattering by voids and inhomogeneities in the subsurface (see Section 2.5). Conversely, the presence of non-icy contaminants, which absorb the signal and thus decrease the probed depths, reduces the opportunities for scattering and consequently decreases the radar albedo. At first order, the radar albedos of Saturn's moons can therefore be regarded as a measure of the degree of purity of their regoliths or, inversely, as a measure of their degree of contamination by non-ice compounds. A further argument for the association between high radar albedo and high water ice purity is that the satellite-to-satellite variability in radar albedo closely follows (with a Pearson correlation coefficient of 0.91) that of the optical geometric albedo (Fig. 3.13).

The fact that Saturn's inner moons are more radar-bright than the Galilean moons (Table 3.2) therefore points to a "cleaner" icy regolith on the former, consistent with their generally higher bolometric Bond albedos (Howett et al., 2010). The surfaces of Saturn's inner icy moons are thus primarily composed of high-purity water ice, more so than the outer satellites (Iapetus and Phoebe) which are more radar-dark. The low average radar brightness of Titan (Table 3.2), the lowest in the Saturn system, is explained by the abundance of likely optically dark organic matter on top of its icy crust (e.g., Janssen et al., 2016). As discussed in Section 2.5.4, regionally high radar scattering on Titan is often associated with the presence of water ice, e.g. in crater ejecta blankets. The same interpretation holds for the radar-bright Inktomi ejecta blanket, on Rhea, where high-purity water ice was likely excavated by the impact. On Iapetus, the leading hemisphere is subjected to contamination by an optically dark non-icy material from the Phoebe ring (Section 1.4.2), causing a dichotomy at optical wavelengths. The fact that the radar observations at 2.2 cm exhibit a similar dichotomy implies that the thickness of the dark deposits is at least of few centimeters (Fig. 3.7 and Le Gall et al., 2014), consistent with results from CIRS (Rivera-Valentin et al., 2011).

Meanwhile, in the inner Saturn system, water ice purity is primarily controlled by the deposition of E-ring particles.

3.4.2 Interactions with Saturn's E ring

The optical and radar albedos both decrease with distance to Enceladus. The variations in optical geometric albedo have been attributed to the surface abundance of water ice, which for the inner satellites is controlled by the deposition of icy E ring particles (Section 1.7; Fig. 3.6d; Verbiscer et al., 2007).

Simulating the dynamics of E ring particles as their orbit evolves (due to Saturn's gravity, plasma drag, radiation pressure and electromagnetic forces) has allowed Juhasz and Horanyi (2015) to derive the spatial distribution of particles impacting the icy satellites, presented in Fig. 3.14, from Kempf et al. (2018). These deposition maps match both the optical–IR data (e.g., Fig 1.4, from Schenk et al., 2018) and the available radar brightness measurements (Fig. 3.7) fairly well (with the exception of Rhea). Thus, the leading/trailing radar albedo dichotomies of Dione (resolved observation, Section 3.3.3) and Tethys (distant observations, Section 3.2.2) are consistent with varying water ice purity caused by ultra-clean water ice particles from the E ring, which are expected to be deposited preferentially on their leading sides.

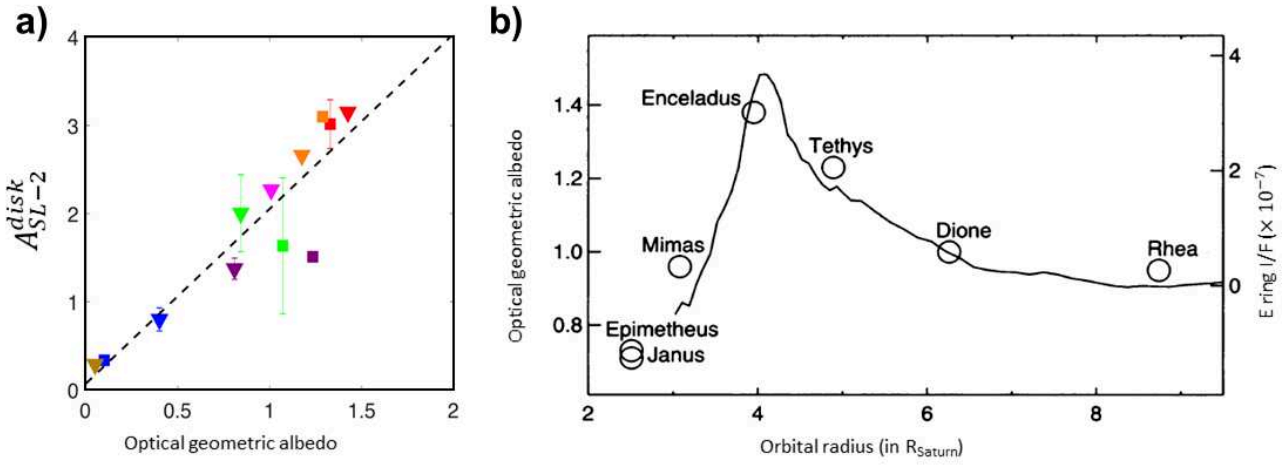

Figure 3.13 – (a) Averaged 2.2-cm disk-integrated radar albedos $A^{\mathrm{disk}}_{\mathrm{SL}-2}$ versus optical geometric albedo p (from Morrison et al., 1986; Verbiscer et al., 2007; Hendrix et al., 2018). The best linear fit between these quantities is indicated (black dashed line); it relates p to $A^{\mathrm{disk}}_{\mathrm{SL}-2}$ as follows: $A^{\mathrm{disk}}_{\mathrm{SL}-2} = 1.98p + 0.07$. Figure from Le Gall et al. (2019). (b) The mean visual geometric albedo of the inner icy satellites and pole-on reflectance profile of the E ring (continuous line), from Verbiscer et al. (2007).

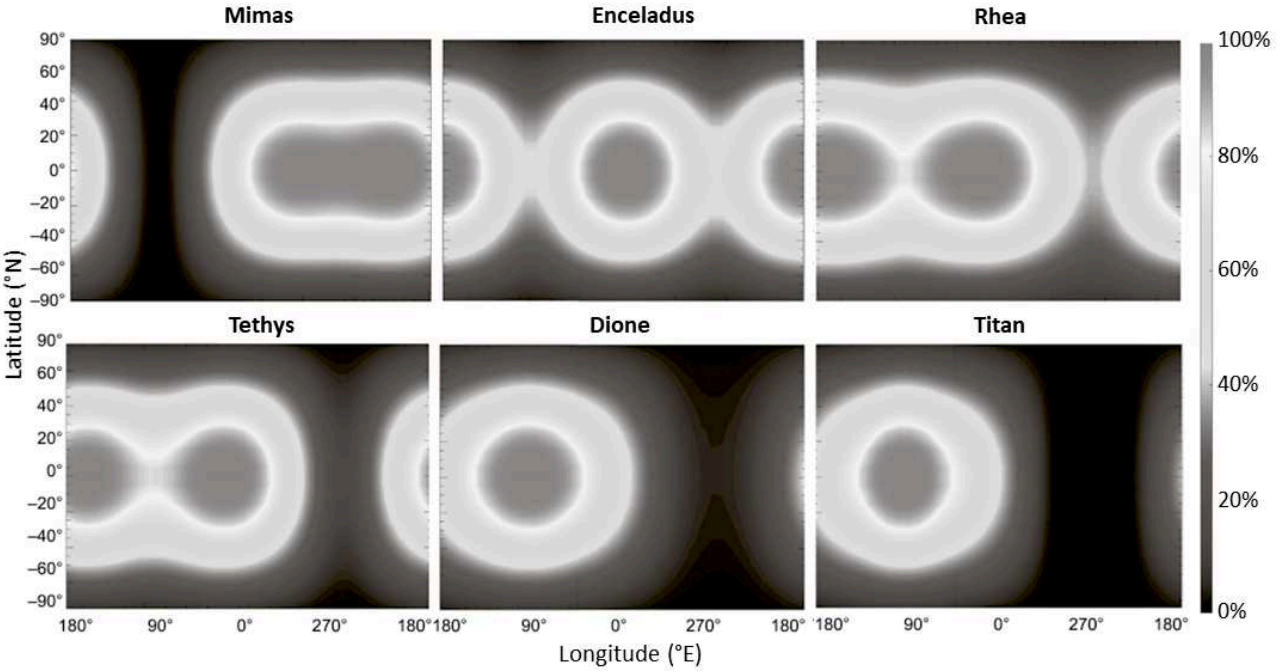

Figure 3.14 – E ring mass influx maps onto the surfaces of Mimas, Enceladus, Tethys, Dione, Rhea, and Titan. In each case the color code represents the mass influx normalized to its maximum value. 90°W and 270°W are on the leading and trailing side of the moons, respectively. Figure from Kempf et al. (2018).

Rhea, being further from Enceladus and receiving less E-ring material than Dione, should be more radar-dark than Dione. Instead, the radar stares (Fig. 3.7 and Table 3.2) and the resolved scatterometry (Fig. 3.11–3.12) both show a higher average 2.2-cm radar albedo on Rhea than on Dione. Rhea is also brighter than Dione in the infrared (Scipioni et al., 2014) and at 13 cm (Black et al., 2007). Possible explanations include the fresh water ice in the Inktomi ejecta blanket (which increases the average global albedo of Rhea), decreased space weathering at Rhea's orbit (Scipioni et al., 2014), and increased contamination by an optically and radar-dark exogenic agent on Dione, especially on its trailing side (e.g., Clark et al., 2008). Furthermore, the lack of a leading/trailing dichotomy at radar wavelengths (although one is apparent in the optical, see Fig. 1.4) on Rhea indicates that both the optically dark layer of contaminants on the trailing hemisphere and the possible bright layer of E ring water ice on the leading hemisphere must be thin (at most a few centimeters), making both sides similar at radar wavelengths.

On Dione and Mimas, the hemispherical dichotomy is obvious in the radar observations. At least a decimeter of E-ring material must therefore be present to guarantee a significant effect on the degree of scattering and hence on the measured radar albedos (e.g., Black et al., 2001b). Yet, current models predict a layer of at best a few centimeters for Mimas and less than a millimeter for Rhea and Dione (assuming a porosity of 50%) of E-ring material mantling these surfaces after 100 Myr, which is likely a strict upper limit for the age of the E-ring and cryovolcanism on Enceladus (Juhasz and Horanyi, 2015; Hendrix et al., 2018).

Rather than a low-velocity deposition process, the E-ring particles may impact the icy satellites at high velocities (> 5 km/s) and "sandblast" the surface. This "sandblasting" would excavate the clean subsurface water ice, which would fall back to coat the surface (Verbiscer et al., 2007; Howett et al., 2018). While such a process would affect the structure and porosity of the surface, it would only very slightly increase the purity of the water ice over the several meters probed by the Cassini radar. It therefore remains likely that the influx of icy E-ring particles is the root cause for the higher radar brightness, independent of their impact velocity.

The discrepancy between model predictions of E-ring material influx and observations has already been reported by Hirata et al. (2014); based on the analysis of depositional features on Helene (a co-orbital moon of Dione), they estimate the E-ring deposits to be tens to hundreds of meters thick. Thomas et al. (2013) and Thomas et al. (2018) estimate similarly deep deposits of loose, icy debris on all trojans (Helene, Callisto, Telesto, and Polydeuces), but consider the E-ring to be an unlikely source. Instead, they suggest that ejecta from large impacts on the primary (Tethys or Dione) may reach the Trojans at low velocities (Dobrovolskis et al., 2010; Thomas et al., 2013; Thomas et al., 2018). On Enceladus, however, the evidence for buried craters (Kirchoff and Schenk, 2009) and pit chains (Martin et al., 2017) point to a much thicker regolith than predicted by models of plume-sourced regolith deposition. Radar observations thus raise the question of the intensity and age of Enceladus's cryovolcanic activity and suggests that current models underestimate the rate of deposition of particles from the E-ring at the surface of Enceladus's neighbors.

3.4.3 Structure of the regoliths

Although the degree of purity of the water ice regolith controls the significance of high-order scattering in the near surface, the composition alone cannot explain the extremely high albedos recorded by the Cassini radar. Like the Galilean satellites (Section 2.5), the inner satellites of Saturn must contain scattering structures that are especially efficient in returning waves in the backscattering direction. The Coherent Backscattering Effect (CBE) has therefore been invoked as a likely subsurface scattering process on Saturn's inner moons (Ostro et al., 2006; Ostro et al., 2010). These authors

also noted that the 13 cm radar albedos (Table 2.2) are lower than those at 2.2 cm (Table 3.2). This decreasing radar albedo with increasing wavelength can be explained either by i) the presence of an absorbing component such as ammonia at depths of 10–100 m (Ostro et al., 2006), ii) the subsurface scattering process being less active at these depths (few or no scattering structures at 10–100-m-depths), or iii) the subsurface scattering being less active at these wavelengths (the size and spacing of the structures both need to be of the order of the wavelength for the CBE to be efficient; Hapke, 1990; Black et al., 2001b and Section 2.5.2).

Yet even compared to those of Jupiter's satellites, the 2.2-cm radar albedos of Saturn's inner icy satellites are exceptionally high, implying higher densities of backscattering structures. Dione, the most radar-dark inner satellite ($A^{\mathrm{disk}}_{\mathrm{TP-3.5}} = 2.55 \pm 0.66$; Table 3.2), is about as radar-bright as Europa ($A^{\mathrm{disk}}_{\mathrm{TP-3.5}} = 2.31 \pm 0.36$; Table 2.2), the most radar-bright Galilean satellite. The capacity of the CBE model to boost the intensity in the backscattering direction is limited and an extremely high density of scatterers (as much as 80% of the scattering layer must be occupied by scatterers rather than the propagation medium) is already required for Europa (Black et al., 2001a), which is twice as faint as Enceladus. The density, shape, and origin of the scattering structures leading to the extreme radar albedos of Saturn's inner icy moons remain to be determined, for instance with numerical models or field and laboratory studies of water ice dielectric and scattering properties at cm wavelengths.

The Cassini radiometry observations of Saturn's icy satellites, by investigating their thermal behavior and probing down to larger depths than the active radar, can offer insights complementary to that of the radar into the structure and composition of the subsurface of Saturn's icy moons.

Chapter 4

Saturn's icy satellites seen by the Cassini radiometer

Cassini 2.2 cm radiometry of Saturn's icy satellites constitutes a heterogeneous dataset, with unequal resolutions, spatial coverage, and temporal sampling. Nonetheless, it provides unique clues to the structure and composition of the top few meters of the surface, which no other Cassini instrument can probe. This chapter provides the observational and data processing details, including the deconvolution method used to produce maps of the microwave brightness temperature of the main icy satellites of Saturn.

4.1 Observations

There are three different types of Cassini radiometry icy satellite data: the "resolved scans" collected concurrently with the scatterometry (Section 3.3), the "stares" acquired concurrently with active radar stares (Section 3.2), and the "distant scans", dedicated to the radiometer and during which the radar transmitter was OFF. All three types of observation are shown in Fig. 4.1 on the example of the RH127 Rhea flyby that occurred on March 2, 2010. The geometry of all icy satellite radiometry observations is summarized in Table 4.1.

Distant scans were designed for radiometry: the antenna scanned the target, regularly moving off-target for baseline calibration. Despite their primary objective being the measurement of the disk-integrated brightness temperatures, the distance to the target could significantly vary from one scan to another (from 40000 to 400000 km), and several distant scans do resolve features at the surface, with beam radii of at best $0.3R_{target}$ (where R_{target} is the radius of the observed icy satellite; see Table 4.1). In addition, the integration time was longer (about 1 s) during distant observations than during stares, implying low photon noise (see Section 2.4.3).

Resolved scans were performed on Rhea (RH127 flyby), Dione (DI163), Iapetus (IA049), and Enceladus (EN156), during which active scatterometry and passive radiometry data were simultaneously collected (with the same viewing geometry and spatial resolution) from distances of 5000 to 100000 km. Resolved radiometry observations are particularly useful as they can be analyzed jointly with concurrent scatterometry. However, they are also especially difficult to calibrate i) because the radar transmitter was ON during these scans, leading to instrument warming, ii) due to the lack of a "cold sky" observation during or, in the case of Rhea, after the scan.

Stares were intended for calculation of the average radar albedo of the observed hemisphere, as described in Section 3.2. Radiometry measurements were performed in-between burst cycles, with a shorter integration time (< 0.3 s) than during distant scans, leading to a higher noise level. Calibration

of the radiometry data acquired during stares is particularly challenging because i) the antenna does not move off-target, therefore a baseline calibration during the stare is impossible and ii) the fact that the transmitter is ON affects the receiver temperatures, especially if the integration time is short (long integration times let the receiver cool down in-between bursts). We therefore use caution whenever interpreting these data. Furthermore, they are only moderately useful as coverage is restricted to a few points on the target.

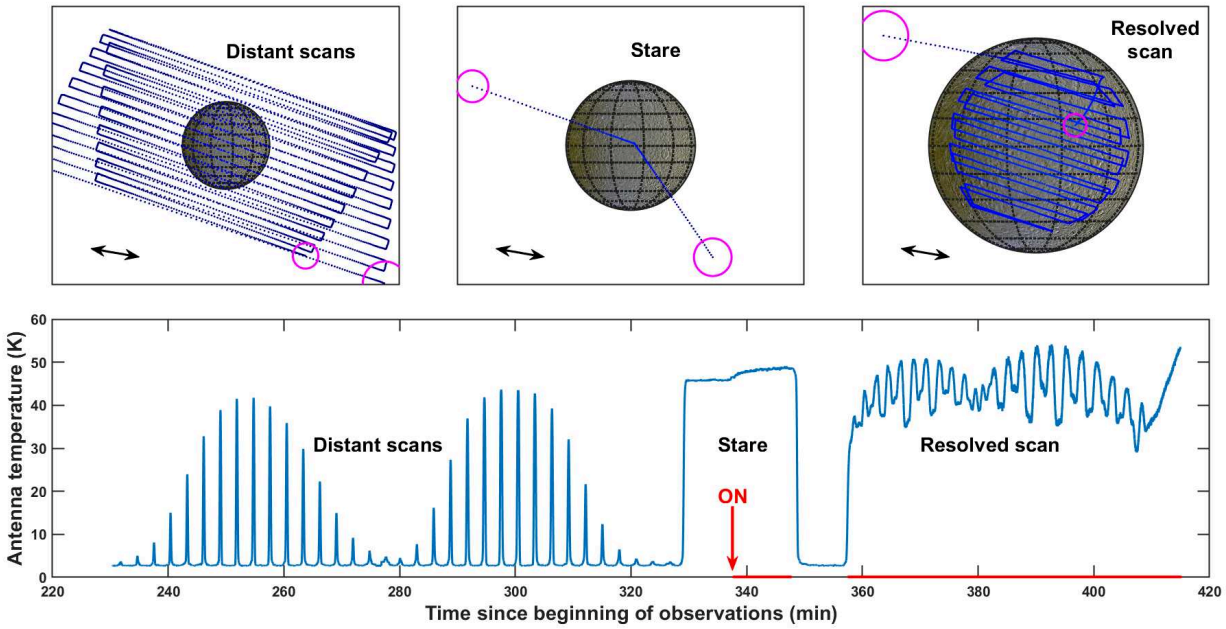

Figure 4.1 – Observations of Rhea on March 2, 2010 (flyby RH127), showing all three types of radiometry observations. Top: image of the disk of Rhea as seen by the Cassini spacecraft during each type of observation. The boresight pointing direction is shown with a blue dot for each observation. The half-power beamwidth at the beginning and end of each sequence is shown with a magenta circle. The direction of the electric field (direction of parallel polarization) is indicated with a black double arrow. The background Rhea map is the global enhanced 3-color Rhea mosaic (PIA18438), projected to spacecraft view coordinates. Bottom: Calibrated antenna temperatures during the RH127 observation. The baseline is set to the CMB temperature (2.7 K). The moment the radar transmitter turns ON is indicated with a red arrow. Periods when the radar transmitter was ON and the integration time was shorter than 0.3 s are indicated in red: during these observations, the background temperature is higher due to heating of the receiver. We therefore only use the resolved scan data acquired after minute 366, when the receiver temperature is stable (see Section 4.2.3).

Table 4.1 – Cassini icy satellite radiometry observations. Distant scans are identified with a "u" in the observation IDs, stares with an "s", and resolved scans with an "r". The center (i.e., sub-spacecraft) point coordinates are given in °E longitude and °N latitude. Unusable data (due to temperature changes caused by the radar transmitter being ON or to lack of baseline observations for calibration) are indicated with the symbol ×, whereas the data that were successfully reduced are indicated with the symbol ✓. Disk-integrated brightness temperatures T_B^{disk} are derived following the method described in Section 4.3. When calculating T_B^{disk}, the usable part of stares are if possible included in the distant scan data.

Satellite	**Observation ID**	**Date**	**Beam size (diameter)**	**Center Lon (°E), Lat (°N)**	**Local time (hh:mm)**	**Range (10^3 km)**	T_B^{disk} **(K)**
Mimas	MI047_1s ×	28 JUN 2007	3.4 – 3.8	[−50,−2]	10:40	212 – 234	
Mimas	MI047_2u ✓	28 JUN 2007	3.8 – 3.9	[−53,−2]	11:04	231 – 242	45.0 ± 1.2
Mimas	MI053_1u ✓	03 DEC 2007	4.8 – 4.3	[−93,16]	20:26	267 – 293	39.7 ± 1.2
Mimas	MI053_2s ✓	03 DEC 2007	4.0 – 3.9	[−97,17]	20:47	241 – 247	40.7 ± 1.2
Mimas	MI064_1s ×	11 APR 2008	1.7 – 1.9	[−140,−53]	1:30	107 – 115	
Mimas	MI064_2u ✓	11 APR 2008	1.9 – 2.2	[−161,−70]	0:38	120 – 135	44.2 ± 0.7
Mimas	MI126_1u ✓	13 FEB 2010	0.8 – 0.7	[96,−4]	23:33	44 – 50	45.0 ± 0.6
Mimas	MI126_2s ✓	13 FEB 2010	0.7 – 0.5	[89,−5]	23:29	34 – 44	
Enceladus	EN003_1s ×	17 FEB 2005	1.8 – 2.9	[144,1]	0:35	144 – 225	
Enceladus	EN003_2u ✓	17 FEB 2005	3.0 – 3.5	[128,1]	0:49	235 – 274	38.4 ± 1.3
Enceladus	EN004_1s ✓	09 MAR 2005	0.9 – 1.0	[−65,0]	3:18	74 – 76	34.4 ± 0.4
Enceladus	EN004_2u ✓	09 MAR 2005	1.2 – 1.4	[−74,0]	3:33	93 – 107	33.9 ± 0.5
Enceladus	EN028_1s ✓	10 SEP 2006	1.9 – 2.2	[150,57]	17:06	150 – 174	38.0 ± 0.7
Enceladus	EN032_1s ✓	09 NOV 2006	1.2 – 1.2	[116,−35]	10:33	90 – 90	38.4 ± 0.9
Enceladus	EN032_2u ✓	09 NOV 2006	1.2 – 1.2	[113,−16]	10:48	93 – 97	40.2 ± 0.6
Enceladus	EN050_1s ✓	30 SEP 2007	1.5 – 1.6	[−124,17]	7:56	117 – 122	
Enceladus	EN050_2u ✓	30 SEP 2007	1.6 – 1.6	[−130,17]	8:02	122 – 127	31.8 ± 0.7
Enceladus	EN061-1_1u ✓	12 MAR 2008	2.5 – 2.1	[−108,69]	1:45	161 – 198	35.5 ± 0.7
Enceladus	EN061-1_2s ✓	12 MAR 2008	2.1 – 1.8	[−112,70]	1:56	138 – 161	
Enceladus	EN061-2_1s ✓	12 MAR 2008	0.9 – 0.9	[26,−71]	14:11	67 – 70	44.2 ± 0.6
Enceladus	EN088_1u ×	09 OCT 2008	4.8 – 4.8	[−36,67]	2:53	374 – 378	
Enceladus	EN088_2u ✓	09 OCT 2008	4.5 – 4.3	[−43,65]	3:16	332 – 349	37.9 ± 1.2
Enceladus	EN088_3s ×	09 OCT 2008	4.2 – 3.8	[−47,65]	3:29	298 – 330	
Enceladus	EN120_1u ✓	02 NOV 2009	2.1 – 1.9	[62,−1]	23:16	149 – 165	41.8 ± 0.8
Enceladus	EN120_2u ✓	02 NOV 2009	1.8 – 1.6	[56,−1]	23:34	127 – 143	41.0 ± 0.6
Enceladus	EN120_3s ×	02 NOV 2009	1.1 – 0.4	[35,−1]	0:19	30 – 82	
Enceladus	EN156_1u ×	06 NOV 2011	0.7 – 0.6	[172,−0]	22:15	48 – 53	
Enceladus	EN156_2u ×	06 NOV 2011	0.6 – 0.5	[167,−0]	22:12	36 – 43	
Enceladus	EN156_3r ×	06 NOV 2011	0.5 – 0.3	[164,−0]	22:10	26 – 36	
Enceladus	EN156_4r ×	06 NOV 2011	0.3 – 0.2	[158,−1]	22:06	17 – 24	
Enceladus	EN156_5r ×	06 NOV 2011	0.2 – 0.04	[151,−2]	21:56	3 – 15	
Enceladus	EN156_6r ×	06 NOV 2011	0.01 – 0.02	[57,−30]	15:52	0.5 – 2	
Enceladus	EN156_7r ×	06 NOV 2011	0.04 – 0.3	[−32,−2]	10:22	4 – 26	
Enceladus	EN156_8r ✓	06 NOV 2011	0.3 – 0.4	[−38,−1]	10:17	26 – 32	
Enceladus	EN156_9r ✓	06 NOV 2011	0.5 – 0.5	[−42,−1]	10:17	37 – 42	

Table 4.1 – (continued)

Satellite	Observation ID	Date	Beam size (diameter)	Center Lon (°E), Lat (°N)	Local time (hh:mm)	Range (10^3 km)	T_B^{disk} (K)
Enceladus	EN156_10u ✓	06 NOV 2011	0.5 – 0.6	[−44,−1]	10:18	42 – 49	38.9 ± 1.5
Enceladus	EN156_11u ✓	06 NOV 2011	0.7 – 0.8	[−48,−1]	10:21	54 – 61	39.2 ± 1.7
Enceladus	EN250_1s ×	27 NOV 2016	2.5 – 1.4	[−57,78]	20:11	108 – 199	
Tethys	TE015_1s ✓	24 SEP 2005	0.7 – 0.9	[158,−0]	0:54	115 – 144	
Tethys	TE015_2u ✓	24 SEP 2005	0.9 – 1.0	[152,−0]	0:55	144 – 165	34.4 ± 0.5
Tethys	TE021_1s ×	25 FEB 2006	1.4 – 1.5	[112,−1]	18:26	232 – 254	
Tethys	TE048_1s ✓	20 JUL 2007	0.6 – 0.6	[−109,2]	5:13	96 – 96	31.5 ± 0.5
Dione	DI016_1s ✓	11 OCT 2005	0.6 – 1.0	[−18,0]	0:56	102 – 181	
Dione	DI016_2u ✓	11 OCT 2005	1.0 – 1.2	[−24,0]	1:03	178 – 210	55.6 ± 0.7
Dione	DI016_3s ✓	11 OCT 2005	1.2 – 1.2	[−25,0]	1:06	210 – 213	
Dione	DI027_1s ×	16 AUG 2006	1.0 – 1.0	[94,−31]	1:40	167 – 172	
Dione	DI033_1s ✓	21 NOV 2006	0.4 – 0.5	[−1,32]	2:26	75 – 91	53.9 ± 0.6
Dione	DI050_1u ✓	30 SEP 2007	0.7 – 0.6	[152,−13]	19:52	101 – 120	53.6 ± 0.7
Dione	DI050_2s ✓	30 SEP 2007	0.6 – 0.4	[137,−13]	19:18	74 – 101	
Dione	DI163_1r ✓	28 MAR 2012	0.6 – 0.3	[−17,−1]	19:54	59 – 97	55.3 ± 1.1
Dione	DI163_2u ✓	28 MAR 2012	0.3 – 0.3	[−37,−1]	18:53	55 – 59	55.1 ± 1.5
Dione	DI163_3s ✓	28 MAR 2012	0.3 – 0.3	[−41,−1]	18:40	53 – 55	
Dione	DI177_1s ✓	23 DEC 2012	1.3 – 1.3	[−97,40]	6:17	232 – 234	47.3 ± 0.6
Dione	DI177_2u ✓	23 DEC 2012	1.3 – 1.4	[−95,46]	6:36	234 – 235	47.9 ± 0.7
Dione	DI177_3u ✓	23 DEC 2012	1.7 – 1.4	[−94,49]	6:51	237 – 238	47.5 ± 0.6
Rhea	RH011_1s ✓	14 JUL 2005	0.8 – 0.8	[−67,−77]	19:41	191 – 200	46.8 ± 1.0
Rhea	RH011_2u ✓	14 JUL 2005	0.8 – 0.8	[−48,−75]	21:08	185 – 190	47.8 ± 0.7
Rhea	RH018_1s ×	27 NOV 2005	0.5 – 0.7	[−18,0]	0:01	111 – 162	
Rhea	RH018_2u ✓	27 NOV 2005	0.7 – 0.8	[−22,0]	0:04	163 – 187	50.1 ± 0.6
Rhea	RH022_1s ×	21 MAR 2006	0.4 – 0.4	[−114,1]	0:29	93 – 106	
Rhea	RH022_2u ✓	21 MAR 2006	0.5 – 0.6	[−135,1]	23:29	108 – 134	47.4 ± 0.7
Rhea	RH022_3u ✓	21 MAR 2006	0.6 – 0.7	[−152,1]	22:47	141 – 159	48.2 ± 0.6
Rhea	RH022_4s ✓	21 MAR 2006	0.7 – 0.7	[−161,1]	22:28	170 – 171	
Rhea	RH027_1s ×	17 AUG 2006	0.8 – 0.7	[41,24]	9:07	177 – 189	
Rhea	RH045_1u ✓	27 MAY 2007	0.9 – 0.8	[−58,−44]	18:36	197 – 202	48.4 ± 0.6
Rhea	RH045_2s ✓	27 MAY 2007	0.8 – 0.8	[−64,−45]	18:19	188 – 197	49.2 ± 0.6
Rhea	RH047_1s ×	28 JUN 2007	0.6 – 0.7	[104,−3]	8:03	145 – 160	
Rhea	RH049_1u ✓	29 AUG 2007	0.5 – 0.5	[15,−0]	20:38	111 – 129	50.2 ± 0.7
Rhea	RH049_2s ×	29 AUG 2007	0.5 – 0.4	[12,−0]	20:37	88 – 111	
Rhea	RH127_1u ✓	02 MAR 2010	0.5 – 0.4	[−159,0]	0:05	98 – 123	47.9 ± 0.7
Rhea	RH127_2u ✓	02 MAR 2010	0.4 – 0.3	[−162,0]	0:06	70 – 96	48.3 ± 0.8
Rhea	RH127_3s ✓	02 MAR 2010	0.3 – 0.3	[−163,1]	0:06	70 – 70	48.5 ± 0.5
Rhea	RH127_4r ✓	02 MAR 2010	0.2 – 0.1	[−167,1]	0:05	26 – 56	50.6 ± 1.8
Rhea	RH177_1u ✓	22 DEC 2012	0.4 – 0.4	[−102,−76]	5:58	88 – 99	44.6 ± 0.7
Rhea	RH177_2u ✓	22 DEC 2012	0.4 – 0.3	[−92,−77]	6:46	73 – 83	45.0 ± 0.8
Rhea	RH177_3s ×	22 DEC 2012	0.3 – 0.2	[−74,−77]	8:02	50 – 72	
Iapetus	IA00B_1s ✓	31 DEC 2004	0.7 – 0.7	[−73,38]	14:33	159 – 161	75.3 ± 1.1

Table 4.1 – (continued)

Satellite	Observation ID	Date	Beam size (diameter)	Center Lon (°E), Lat (°N)	Local time (hh:mm)	Range (10^3 km)	T_B^{disk} (K)
Iapetus	IA00B_2u ✓	31 DEC 2004	0.7 – 0.7	[−72,40]	14:37	153 – 159	73.1 ± 0.9
Iapetus	IA00B_3s ×	31 DEC 2004	0.7 – 0.6	[−70,43]	14:46	147 – 152	
Iapetus	IA00C_1s ✓	01 JAN 2005	0.8 – 0.9	[57,49]	23:42	191 – 216	56.8 ± 1.1
Iapetus	IA00C_2u ✓	01 JAN 2005	1.0 – 1.0	[61,44]	23:58	217 – 226	58.6 ± 0.7
Iapetus	IA00C_3u ✓	01 JAN 2005	1.0 – 1.0	[62,42]	0:02	228 – 236	58.6 ± 0.7
Iapetus	IA00C_4s ✓	01 JAN 2005	1.0 – 1.0	[62,42]	0:04	237 – 238	59.1 ± 0.6
Iapetus	IA017_1s ✓	12 NOV 2005	1.8 – 1.8	[−0,39]	18:26	419 – 419	67.2 ± 1.1
Iapetus	IA017_2u ✓	12 NOV 2005	1.8 – 1.8	[1,40]	18:34	420 – 421	65.1 ± 0.8
Iapetus	IA049-1_1u ✓	09 SEP 2007	1.1 – 1.1	[−65,12]	21:52	251 – 258	77.5 ± 0.9
Iapetus	IA049-1_2s ✓	09 SEP 2007	1.1 – 1.1	[−66,12]	21:52	248 – 251	78.4 ± 0.8
Iapetus	IA049-2_1u ✓	10 SEP 2007	0.5 – 0.5	[−69,12]	21:49	110 – 118	77.5 ± 0.9
Iapetus	IA049-2_2s ✓	10 SEP 2007	0.5 – 0.4	[−70,12]	21:49	99 – 110	
Iapetus	IA049-3_1r ✓	10 SEP 2007	0.1 – 0.1	[−77,11]	21:27	16 – 24	80.1 ± 3.1
Iapetus	IA049-4_1s ×	11 SEP 2007	0.5 – 0.5	[107,−12]	9:55	109 – 114	
Iapetus	IA049-4_2u ✓	11 SEP 2007	0.5 – 0.5	[107,−12]	9:54	114 – 123	62.5 ± 0.8
Phoebe	PH002_1u ✓	11 JUN 2004	3.4 – 2.8	[133,−25]	6:06	95 – 115	84.2 ± 3.0
Phoebe	PH002_2s ✓	11 JUN 2004	2.8 – 2.7	[113,−25]	6:04	91 – 95	
Phoebe	PH002_3s ✓	11 JUN 2004	1.4 – 3.0	[12,25]	17:38	47 – 102	
Phoebe	PH002_4u ✓	11 JUN 2004	3.0 – 3.3	[−48,25]	17:56	102 – 111	75.7 ± 2.0
Phoebe	PH002_5u ✓	12 JUN 2004	3.3 – 3.5	[−66,25]	17:55	113 – 121	76.1 ± 2.2
Phoebe	PH002_6s ✓	12 JUN 2004	3.9 – 4.0	[−97,25]	17:46	133 – 137	76.6 ± 1.7

4.2 Calibration

4.2.1 Radiometry calibration

We follow the calibration method developed for Titan described in Janssen et al. (2009), updated to account for temporal gain drift by Janssen et al. (2016), and adapted to airless icy satellites (i.e., removing absorption in Titan's atmosphere). The antenna temperature T_A at time t is given by the following equation (similar to Eq. 2.45):

$$T_A(t) = \left(\frac{V_{\text{out}}(t)}{G_{\text{rec}}(t)} - T_{\text{sys}}(t) - T_{\text{FSL}}(t) - T_{\text{zero}}(t) \right) \times F_{\text{cal}}(t_y) \times F_{\text{airless}} \tag{4.1}$$

where V_{out} is the normalized counts measured, G_{rec} is the radiometer gain, T_{sys} is the system temperature, T_{FSL} is the far sidelobe contribution, T_{zero} is a baseline offset (due to instrumental noise) obtained from observing the empty sky (including both the instrumental temperature background and the CMB temperature of 2.7 K), and F_{cal} is the correction factor introduced by Janssen et al. (2016) to account for gain drift over time over the course of the Cassini mission. The calibration by Janssen et al. (2009, 2016) was fine-tuned for Titan, whose atmosphere absorbs a small part of the signal even at a wavelength of 2.2 cm. A final correction factor of $F_{\text{airless}} = 1/0.9945$ is necessary to apply these calibration values to airless icy satellites (Janssen et al., 2016; Zhang et al., 2017a).

The system temperature $T_{\rm sys}(t)$ varies with time during each flyby; it is calculated from the resistive load temperature $T_{\rm rl}$ while taking into account the receiver attenuation $a_0 = 0.8$ and the receiver temperature $T_{\rm rec} = 550$ K:

$$T_{\rm sys}(t) = \frac{(1 - a_0)T_{\rm rl}(t) + T_{\rm rec}}{a_0} \tag{4.2}$$

Because the reference load signal has a very short integration time (generally about 0.02 s) leading to important noise, a one-minute moving average is applied to stabilize it. The gain also varies on relatively short timescales, and is calculated as follows (Janssen et al., 2009):

$$G_{\rm rec}(t) = \frac{CN_{\rm rl}(t)}{T_{\rm rec} + T_{\rm rl}(t)} \tag{4.3}$$

where $N_{\rm rl}$ is the normalized counts on the reference load (measured during each burst cycle; see Fig. 3.3) and C is a calibration constant. The gain also varies on longer timescales due to aging of the receiver components: this variation is accounted for in $F_{\rm cal}(t_y)$ as follows:

$$F_{\rm cal}(t_y) = \Big[0.9743 + 0.0029 \times (t_y - 2004)\Big] \times \Big[1 - (t_y - 2009.61) \times 0.002\Big] \times 0.998 \tag{4.4}$$

where the observation time t_y is expressed here in years. This unwieldy expression has been updated multiple times over the course of the Cassini mission. The derivation of and adjustments to these factors are detailed in Janssen et al. (2009, 2013, 2016) and Zhang et al. (2017a). Finally, we note that the correction factors $F_{\rm cal}(t)$ and $F_{\rm airless}$ must be applied *after* removing the far sidelobe contribution and baseline offset, because the factors were determined that way.

The derivation of both $T_{\rm FSL}$ and $T_{\rm zero}$ are described hereafter. The calibration process is illustrated in Fig. 4.2.

4.2.2 Removal of the far sidelobe contribution

As detailed in Section 3.1.1, the radiometer beam pattern is composed of a Gaussian main beam with a half-power width of 0.373° and near sidelobes up to 2° which are well characterized (Fig. 3.1), and far sidelobes (FSL) extending from 2° to 90°, all of which are given in Janssen et al. (2009). The FSL contribution $T_{\rm FSL}$ and the calibrated $0 - 2°$ antenna temperature T_A thus correspond to the convolution of the normalized beam pattern $g(\theta_z, \phi)$ with the brightness temperature $T_B(\theta_z, \phi)$ over the ranges of θ_z corresponding to the desired angle from the boresight, as follows:

$$T_A(t) = \int_{0°}^{180°} \int_{0°}^{2°} T_B(\theta'_z, \phi') g(\theta'_z - \theta_z(t), \phi' - \phi(t)) \sin\theta'_z d\theta'_z d\phi' \tag{4.5}$$

$$T_{\rm FSL}(t) = \int_{0°}^{180°} \int_{2°}^{90°} T_B(\theta'_z, \phi') g(\theta'_z - \theta_z(t), \phi' - \phi(t)) \sin\theta'_z d\theta'_z d\phi' \tag{4.6}$$

where $\theta_z(t)$si the zenith angle and $\phi(t)$ the azimuth angle, defining the antenna boresight pointing direction at time t. In order to estimate the FSL contribution $T_{\rm FSL}(t)$ as a function of time t throughout each scan, we assume a brightness temperature model comprising a disk of constant temperature $T_{\rm disk}$, against a 2.7 K sky background. If Saturn is present in the FSL, we also include it as a disk with the latitudinal 2.2-cm temperature profile derived by Janssen et al. (2013).

The disk temperature $T_{\rm disk}$ is initially assumed to be 50 K to calculate a first estimate of $T_{\rm FSL}$ using Eq. 4.6. $T_{\rm FSL}$ is removed and the calibration is completed as described above (Section 4.2.1) to obtain a fully calibrated T_A. We then simulate the antenna temperatures by convolving a limb-darkened disk of uniform temperature $T_{\rm disk}$ with the beam pattern along the scan path, following

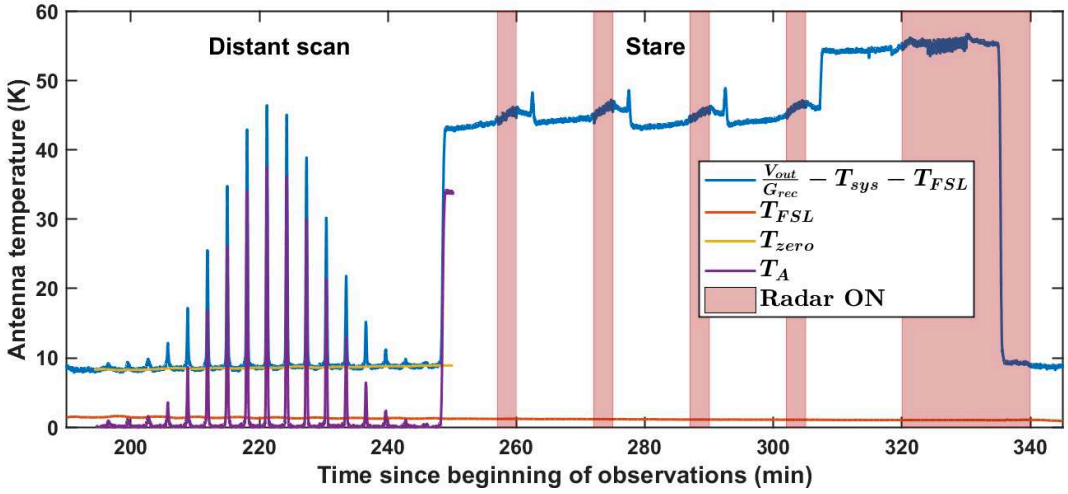

Figure 4.2 – Illustration of the calibration process for Dione flyby DI050, which consists in a distant scan followed by a five-point stare. The radiometry data can only be used before the radar transmitter turns ON, as the baseline zero level T_{zero} cannot be known after. Note the far sidelobes contribute very little to the signal during this flyby.

Eq. 4.5. The limb-darkening consists in a simple $cos^{0.04}(\theta)$ brightness taper, where θ is the emission angle, as described in Le Gall et al. (2014). We fit these simulated antenna temperatures to the observed calibrated T_A to obtain the best value of T_{disk} for each distant scan. The value for T_{disk}, which ranges from 31.7 K for Tethys's early morning to 86.1 K for Phoebe, is then used to recalculate the FSL (without limb-darkening). For resolved scans and stare observations, we assume the same disk temperature as the distant scan(s) undergone during the same flyby (because they are close enough in time that they observed the same region at the same local time). Overall, the observation resolution is low enough that the FSL always contribute less than 5% to the signal; it is therefore not necessary to include surface temperature variations when calculating T_{FSL}.

4.2.3 Determination of the baseline offset

The temperature baseline offset T_{zero} is determined after having subtracted the FSL contribution. During a **distant scan**, the antenna regularly moves away from the satellite disk and observes the sky for baseline calibration, leading to a comb-shaped time sequence (Fig. 4.1). Each time the radiometer points away from the target, the antenna temperatures of the 20 points with the least target contribution are averaged, and this level is interpolated linearly when pointing at the target. The zero level is mainly influenced by the instrument physical temperature, but if the antenna does not move far enough from the target, it may also include a contribution from the near sidelobes. This is taken into account by subtracting a zero level in the exact same way whenever we compute a simulated T_A.

The **stares** and **resolved scans**, which were acquired while the Cassini radar transmitter was ON, are more challenging to calibrate. Indeed, the transmitter causes an increase in the receiver temperature, which plateaus at 2–3 K after 10–20 minutes (depending on the integration time); for example, a temperature increase can be seen during the RH127_3s stare in Fig. 4.1. In addition, in some instances, the transmitter was turned successively ON and OFF during the stares, causing jumps in the radiometry temperature measurements. Similarly, for longer integration times, the receiver cools down in-between bursts, leading to lower temperatures. Thus, if the integration time changes, the observation is too short, or the transmitter turns OFF before the temperature is stable, we simply cannot use the radiometry data.

Several stares include radiometry data collected before the transmitter is turned ON: these data

can be used without specific caution, but are only moderately useful as they only cover a single observation point. The baseline T_{zero} in this case is simply a linear interpolation of the baseline before the stare began and/or after it ended, if the temperature is stable. This is the case of all stare observations that were used for radiometry.

Because the radar transmitter had been ON for long enough, the temperature is stable during the **resolved scans** of Dione (DI163_1r) and Iapetus (IA049_3r). The baseline offset T_{zero} is therefore estimated by interpolating the sky observations before and after the resolved scan. During the inbound part of the Enceladus EN156 flyby (EN156_1u to EN156_5r), Saturn and its rings are behind Enceladus, rendering this data difficult to calibrate as a very accurate Saturn and ring effective temperature model has to be used to subtract their contribution.

Similarly, the temperature is stable during part of the resolved scan of Rhea RH127_4r. The cold sky observation directly before the resolved scan is only partially affected by the instrument warming because while the transmitter was ON, the integration time was 0.9 s, which is long enough for the receiver to cool down in-between bursts. The integration time then dropped at the beginning of the resolved scan (at minute 358 in Fig. 4.1), leading to a warming of the receiver over the first few minutes of resolved data. In order to assess the amplitude of the receiver heating and estimate after how long the system temperature stabilized, we applied the following steps. We first deconvolved (see Section 4.4 for the deconvolution method) the last half of the resolved data (minutes 380–415 in Fig. 4.1) which, >20 min after the integration time drop, have a stable receiver temperature. The temperature map thus obtained was then convolved with the beam pattern to obtain a simulated time-sequence. We find that the residual between the simulated time-sequence and the resolved observation stabilizes after 8 minutes; we therefore only kept the data acquired after this time (minute 366 in Fig. 4.1). We then calculated the disk-integrated temperature for these data and the two distant scans performed during the same flyby (i.e., on the same disk between minutes 230 and 325, see Fig. 4.1). Lastly, the difference in disk-integrated brightness temperature was subtracted from the resolved data, ensuring that this dataset is consistent with the unresolved and less noisy one.

4.2.4 Pointing and time offset correction

In addition to the aforementioned systematic pointing offset (Section 3.1.3), there is a higher-order fluctuating offset, which has to be derived independently for each observation (Moeckel et al., 2019). There is also a small error $t_{\text{offset}} < 0.6$ s in the timing of each observation. The offset in time t_{offset} and in the x and y directions (defined in Section 3.1.3), x_{offset} and y_{offset}, are found for radiometry scans using a method very similar to Le Gall et al. (2014) and described below. The offsets derived from radiometry scans are then applied to all active and passive data taken during the same flyby.

In order to find the offsets, a simple temperature model (called here T_{LM} for latitudinal model) is applied. This model allows for latitudinal temperature variations (with colder polar regions):

$$T_{\text{LM}}(\phi) = T_{\text{equator}} - \Delta T \times \frac{1 - \cos 2\phi}{2} \tag{4.7}$$

where ϕ is the latitude and T_{equator} is the temperature at the equator ($\phi = 0°$). These temperatures are projected into spacecraft view coordinates. A simple emissivity map e_{map} is then derived from Fresnel's equations as described in Section 2.4.2, assuming a dielectric constant of $\varepsilon'_r = 1.15$. This value was chosen for the dielectric constant because, as will be shown later, it fits most data best; it is so low that the main effect of the resulting emissivity map is to add a small amount of limb darkening. The modeled brightness temperature map in spacecraft view coordinates is then given by $T_B = e_{\text{map}} \times T_{\text{LM}}$.

For each scan, the icy moon's angular size, antenna polarization, and pointing direction calculated using the SPICE toolkit can be interpolated from their values at a time t, to a time $t + t_{\text{offset}}$.

The pointing direction is adjusted to [$x_0 + x_{\text{offset}}$,$y_0 + y_{\text{offset}}$]. The beam pattern (main beam and near sidelobes up to 2°) is convolved with T_B (Eq. 4.5), with the center of the beam lying at coordinates [$x_0 + x_{\text{offset}}$,$y_0 + y_{\text{offset}}$], for all times $t + t_{\text{offset}}$. We thus obtain a simulated antenna temperature time sequence, which can be directly compared with the observed antenna temperature T_A. The model is fit to the data using the Levenberg–Marquardt algorithm for non-linear least squares parameter estimation (Levenberg, 1944; Marquardt, 1963), with the five parameters (x_{offset}, y_{offset}, t_{offset}, T_{equator}, ΔT). The observations near the center of the icy satellite disk may capture real surface effective temperature variations that are not included in this model (e.g., caused by differences in local time or regional emissivity anomalies); consequently, only the data near the limbs is included in the fit (within one half-power beam width of the circle of radius 1.3 satellite radii). This process is illustrated for two example flybys in Fig. 4.3.

4.2.5 Measurement uncertainties

The uncertainty σ associated with our final value of the antenna temperature T_A is composed of i) random Gaussian noise σ_G including the instrumental noise and photon noise decreasing as the inverse square root of integration time with an added constant (Fig. 4.4), and ii) a 1% calibration uncertainty that globally takes into account uncertainties in the gain and the calibration factors (Janssen et al., 2009, 2016). The uncertainty on the antenna temperatures T_A is then given by the following equation:

$$\sigma = \sqrt{\sigma_G^2 + (0.01 T_A)^2} \tag{4.8}$$

We determine σ_G empirically by examining the standard deviation of the sky observations for each flyby as follows.

For each flyby, observations with constant average temperatures are selected: these are either observations of the sky or of a fixed point on the target during stares. The calibrated antenna temperatures are smoothed over 20 consecutive bursts. The difference between the observed and smoothed antenna temperatures, plotted in Fig. 4.4a for an example flyby, provides an estimate of the noise level. For each flyby and for each integration time, the standard deviation of the noise is calculated. As expected, we find that the amplitude of the Gaussian noise is inversely proportional to the square root of the integration time, with an added offset taking into account the constant instrument read noise: $\sigma_G = 0.058/\sqrt{t_{\text{int}}} + 0.045$ (Fig. 4.4b). Because the noise level varies, especially near 0.8 to 1 s integration times, we use the empirically determined value of σ_G for each flyby. We note that, for an integration time of $t_{\text{int}} = 1$ s, we find a measurement noise of ~0.1 K, which is about four times higher than the theoretical value 0.026 K given in (Janssen et al., 2009, 2016). After re-examination of this previous work, an error of a factor $\sqrt{10}$ has been found in the calculation of the measurement noise, which should therefore be 0.075 K for $t_{\text{int}} = 1$ s (Janssen, personal communication), that is, much closer to the value found here empirically (~0.1 K). The small error found here does not affect previously published results, for which the calibration uncertainty dominates.

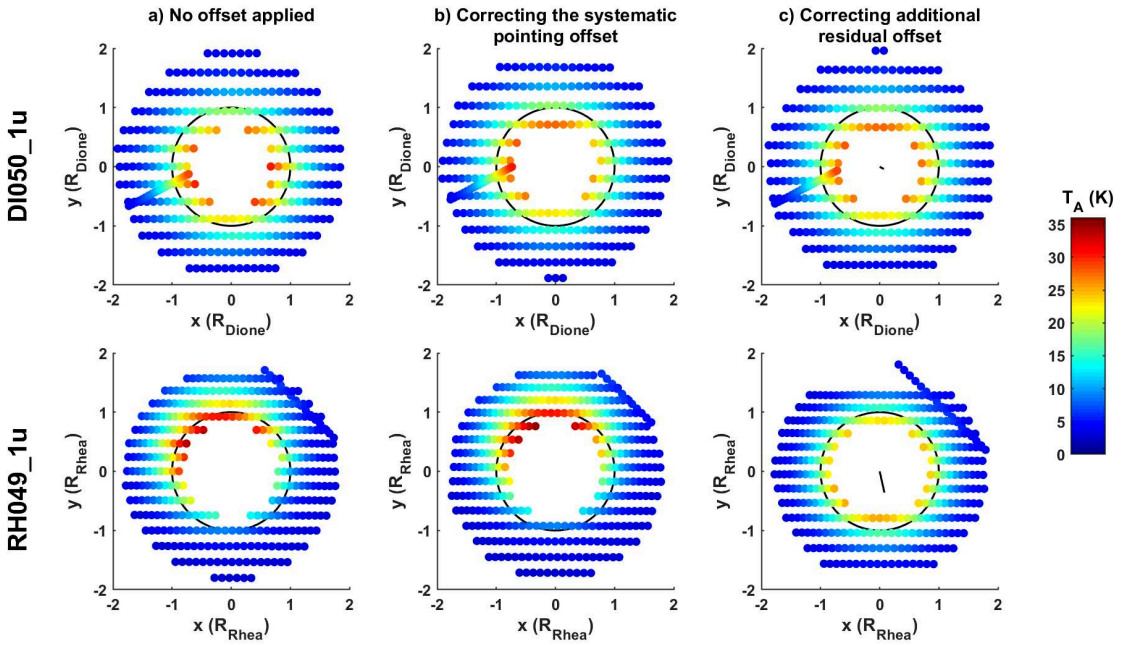

Figure 4.3 – Illustration of the method used to find the x- and y-offsets for scans DI050_1u (top) and RH049_1u (bottom). The antenna temperatures T_A are given only for the points where the fit is applied, close to the limbs, where we expect a uniform decrease in T_A away from the disk. The outline of the icy satellite's disk is shown in black and the data are projected in spacecraft view coordinates. (a) Pointing offsets are not corrected. (b) The systematic pointing offsets from Zhang et al. (2017a) are corrected in the SPICE kernels. (c) After correcting the systematic offsets to the kernels, the data are fitted by the model described herein and a small residual offset is inferred. This offset is drawn with a black line at the center of the disk; it is of $+0.07\mathrm{R_{Dione}}\hat{\mathrm{x}}$ and $-0.04\mathrm{R_{Dione}}\hat{\mathrm{y}}$ for DI050_1u, and $+0.08\mathrm{R_{Rhea}}\hat{\mathrm{x}}$ and $-0.36\mathrm{R_{Rhea}}\hat{\mathrm{y}}$ for RH049_1u. Note that the RH049_1u offset is anomalously large, even after fixing the spacecraft pointing direction in the SPICE kernels; all other inferred residual offsets are of the order of the one found for DI050_1u.

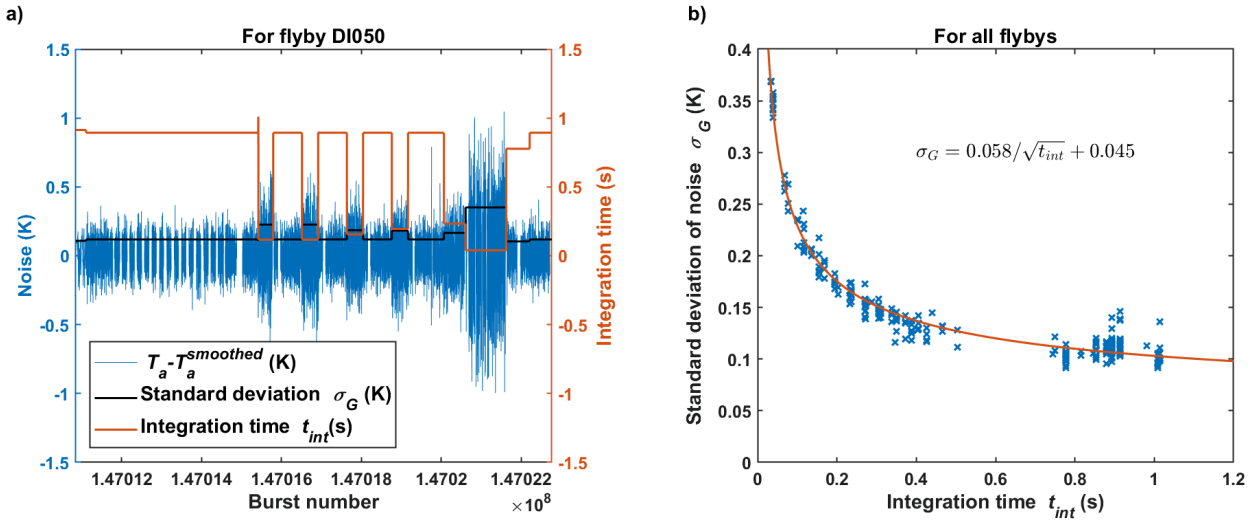

Figure 4.4 – (a) Example of the extraction of the Gaussian uncertainty σ_G for flyby DI050. The difference between smoothed antenna temperatures and observed antenna temperatures, when the average temperature remains constant, is the Gaussian component of the noise. Gaps in the data correspond to rapidly changing antenna temperatures. The distant scan occurs during the first third of the scan, while the rest is a series of five stares, with very short integration times (see Fig. 4.2). (b) The standard deviation of the noise is calculated for each integration time of each flyby. The best fit of the form $y = a/\sqrt{x} + b$ is plotted and its equation is given.

4.3 Preliminary analysis: disk-integrated temperatures

4.3.1 Extraction of disk-integrated temperatures

The disk-integrated brightness temperatures of the icy satellites are obtained using the same fitting method as when searching for the pointing and time offsets (Section 4.2.4): by fitting the latitude-dependent temperature model $T_{\rm LM}$. There are only two differences: when applying the fit to find disk-integrated temperatures, i) we use all data over the disk, up to one FWHM away from the limbs, and ii) the offsets are now fixed to the values found with the method described above (Section 4.2.4). The disk-integrated temperature $T_B^{\rm disk}$ is then the average of the best-fit brightness temperature model map $T_{\rm LM}$ map (Le Gall et al., 2014):

$$T_B^{\rm disk} = \frac{1}{\Omega_{\rm disk}} \int T_{\rm LM} d\Omega \tag{4.9}$$

where $\Omega_{\rm disk}$ is the disk solid angle.

Including a latitudinal variation in temperature generally yields much better fits for partially resolved observations (i.e., observations where the angular size of the satellite is at least as large as the beam size). For unresolved observations, the latitudinal variation derived by the fit is null, which makes the model equivalent to a disk of uniform temperature. The resulting disk-integrated temperatures are shown in Fig. 4.5, with the observations centered on the leading and trailing hemispheres indicated with different symbols (sub-spacecraft point latitude <50°; longitude of ±90°E ±50). The error estimate is the quadratic sum of a 1% calibration uncertainty (Section 4.2.5) and of the reduced χ^2 value, calculated from the best fit residual R as $\chi^2 = \sqrt{\sum_N R^2}/N$

4.3.2 Results

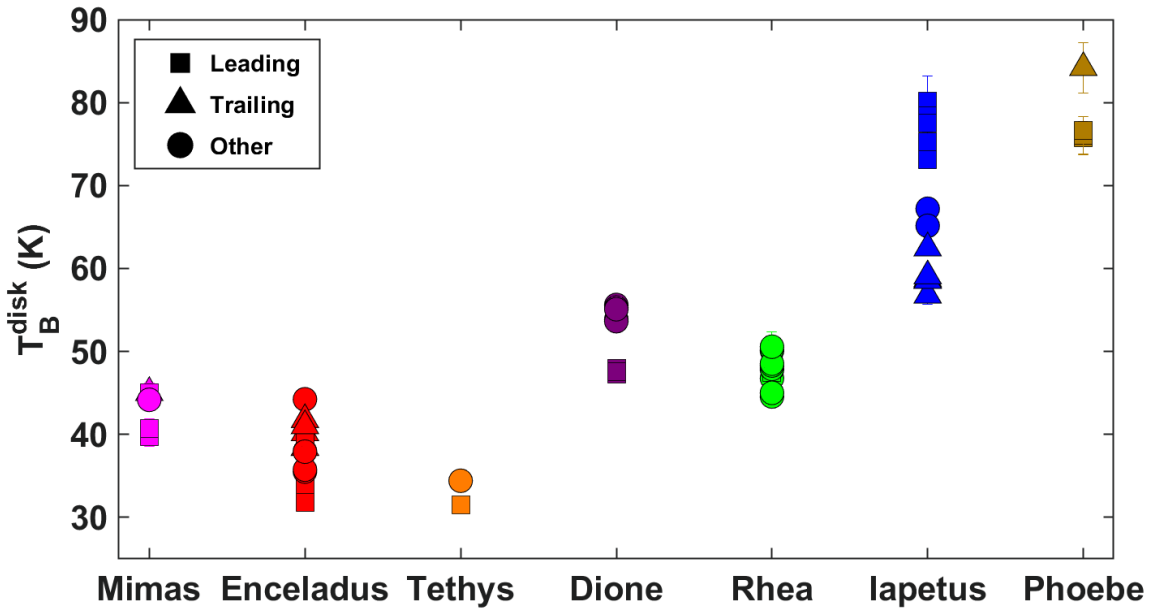

Figure 4.5 – Disk-integrated brightness brightness temperatures $T_B^{\rm disk}$. The leading (latitude <50°; longitude of −90±50°E) and trailing (latitude <50°; longitude of +90±50°E) hemisphere observations are symbolized by squares and triangles, respectively, while all other data are symbolized by a circle. The error bars derived from the fit are of the order of 1–2 K.

Satellite-to-satellite variations in brightness temperatures follow the opposite pattern as those in radar albedo (Section 3.2.2 and Fig. 3.6), with Enceladus and Tethys being the coldest icy satellites, and Iapetus and Phoebe the warmest. The trend of increasing temperatures with distance to Enceladus is thus consistent with the generally expected anti-correlation between emissivity and radar albedo (from Kirchhoff's law; see Section 2.4.2). Low emissivities are expected for surfaces enriched in high-purity water ice, where subsurface scattering reduces the outgoing radiation.

Meanwhile, intra-satellite variations such as hemispherical dichotomies are difficult to examine simply from disk-integrated brightness temperatures, except for Iapetus. The trailing (optically bright) hemisphere of Iapetus is always colder than its leading hemisphere, regardless of the local time, consistent with higher leading hemisphere emissivities and/or temperatures. However, large variations in brightness temperature (of 5 to 20 K) are observed for each satellite (except Tethys, where little data was obtained). This is likely caused not by emissivity variations but rather by changes in temperature due to varying local times, seasons, latitudes, thermal properties, and albedos. A thermal model, which simulates the surface and near-subsurface temperatures, is therefore required to go further in the analysis of the derived disk-integrated brightness temperatures.

4.4 Towards a resolved analysis: deconvolution

4.4.1 Deconvolution method

The goal of deconvolution is to map the brightness temperature distribution on the target at the resolution of the projected main beam size (given in Table 4.1). Once the FSL contribution and the baseline level are removed, the calibrated antenna temperatures correspond to the antenna beam pattern (up to 2°) convolved with the brightness temperature map of the target, following Eq. 4.5.

We follow the iterative deconvolution approach applied by Zhang et al. (2017a) on the Cassini radiometry data acquired on Saturn's C ring, adapted for icy satellite observations (i.e., with a different shape than the rings). We initially assume that the icy satellite is a disk of uniform temperature of 50 K (the initial value has no impact on the final result), to build a uniform surface brightness temperature distribution $T_{B,\mathrm{map}}$ as seen from the instrument. We then convolve the antenna beam pattern with this map using Eq. 4.5 in order to compute a simulated antenna temperature $T_{A,\mathrm{sim}}$. The residual $\Delta T = T_A - T_{A,\mathrm{sim}}$ is mapped by computing an average, weighted by the beam pattern, of all residuals. The residual map is then added to the initial temperature map $T_{B,\mathrm{map}}$. We reiterate until the standard deviation of the residual is smaller than the mean theoretical noise level (Eq. 4.8). The resolution of the map thus obtained is equal to the antenna main beam size, whose half-power width is 0.373°(Section 3.1.1). Any details below this resolution are artifacts of the deconvolution, originating from spatially overlapping data with different temperatures.

For scans with partial coverage or variable resolutions, the parts of the disk that are poorly observed are interpolated. During subsequent iterations, the algorithm attempts to correct for uncertainties by adjusting the remainder of the data, and the uncertainty thus propagates to the observations near the gap in coverage. Consequently, only full-disk scans with fairly homogeneous sampling are appropriate for the deconvolution method.

4.4.2 Deconvolution results

The results of the iterative deconvolution method are shown in Fig. 4.6 for all icy satellite observations with a beam size $\leq$ 1.1 satellite diameter. Most of these observations were acquired on

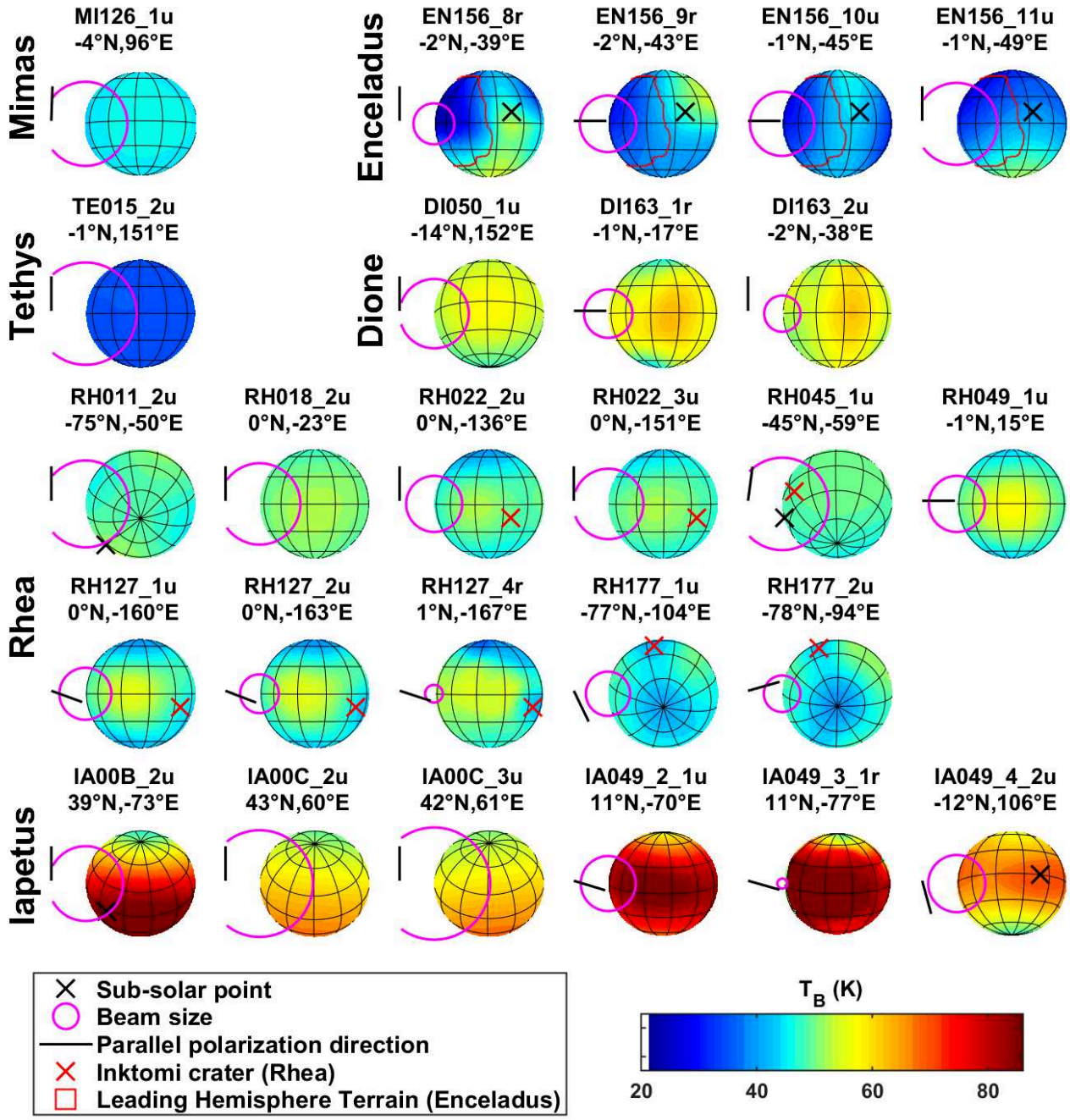

Figure 4.6 – Deconvolved radiometry observations of Saturn's icy satellites, with the sub-spacecraft coordinates provided for each scan. For daytime observations, the sub-solar point is indicated by a black ×. Note that, apart for Enceladus and Iapetus observations (IA00B and IA049_4), all partially resolved radiometry data were obtained on the night side or in the polar regions. For Rhea, the location of Inktomi crater is marked by a red ×; it is generally associated with lower brightness temperatures. The direction of the antenna electric field (parallel polarization) is shown by a black line. For Enceladus, the outline of the Leading Hemisphere Terrain (LHT) as defined by Crow-Willard and Pappalardo (2015) is drawn; Ries and Janssen (2015) found a 30% decrease in thermal emission within this region.

the night side, although Enceladus and Iapetus were also observed during the local day. The brightness temperature ranges are consistent with the disk-integrated analysis of these and unresolved data (Fig. 4.5), but display regional variations. Temperature changes with latitude are clearly visible on all satellites except Mimas and Tethys, which were poorly resolved. In scans of Rhea and Dione that do not include the poles, we notice a significant limb darkening, caused by emissivity variations with emission angle, averaged over the beam size. The direction of polarization is indicated in Fig. 4.6; however, there generally seems to be little variation in the distribution of T_B with polarization direction, indicating most likely depolarized surfaces.

Enceladus

During the Enceladus EN156 flyby (also called E16, as it was the 16th flyby of Enceladus), a total of 10 scans with a resolution high enough for deconvolution were acquired. The first (inbound) half of these observations were obtained on the anti-Saturn side, with either Saturn or its rings in the background, such that their contribution to the signal has to be removed. This calibration has been applied by Ries and Janssen (2015), however the remaining baseline variations after Saturn decontamination are still too large to allow for quantitative analysis. The deconvolution of these data is therefore not shown herein.

Meanwhile, the outbound part of the EN156 flyby is not contaminated by Saturn. All four deconvolved EN156 scans have inhomogeneous coverage, with the poles and limbs being less observed than the center of the disk. This is the most likely explanation for the apparent inconsistency between the results in these fours scans, although the varying polarization, resolutions, and local times may also contribute. EN156_8r has both the best coverage and resolution, so it yields the most reliable image; the sub-solar point exhibits a locally high temperatures. While the southern latitudes seem to exhibit locally high temperatures in this dataset, the partial coverage (especially at high latitudes) and possible thermal inertia and seasonal effects do not permit an interpretation regarding the eventuality of endogenic flux. An excess in the emitted heat flux has, however, been detected by Le Gall et al. (2017) in the high-resolution scan over the southern region, during the same flyby.

Analysis of the outbound EN156 radiometry by Ries and Janssen (2015) has exposed a large-scale emissivity anomaly on the leading hemisphere, with an emissivity decrease of approximately 30%. This anomaly is not associated with any albedo change, and its shape best matches a geologically young region featuring tectonic faults and a scarcity of craters, termed the Leading Hemisphere Terrain (LHT) and mapped by Crow-Willard and Pappalardo (2015). This region is outlined on the deconvolved EN156 radiometry in Fig. 4.6, and matches well with a locally low brightness temperature near 20 K, the lowest value found in all of Saturn's icy satellites. Ries and Janssen (2015) attribute this low emissivity to increased subsurface scattering in the younger, fractured, and less processed regolith of the LHT.

Dione

The two DI163 Dione resolved radiometry observations, taken concurrently with scatterometry (Fig. 3.12), also have inhomogeneous coverage: the high latitudes ($>\sim 45°$) especially are partially covered in DI163_1r and not at all in DI163_2u. While the differences between these two successive scans seem to point to a polarization effect (higher T_B aligned with the direction of parallel polarization, where the Brewster highlights are expected to lie), they may also be caused by the lack of polar data in DI163_2u.

Nonetheless, these observations exhibit longitudinal variations in antenna temperatures, with the leading hemisphere (left half) appearing colder than the trailing hemisphere (right half). The

local time is in the late afternoon for the colder leading side, and in the night for the warmer trailing side: the opposite observation (warmer afternoon temperatures) would be expected for a uniform surface and subsurface. The data are therefore consistent with a leading/trailing dichotomy, which may be caused by differences in a variety of parameters, including bolometric Bond albedo, thermal inertia, and emissivity. The optical and infrared observations of Dione clearly show a lower albedo on the trailing hemisphere (e.g., Blackburn et al., 2012). In order to know if an albedo dichotomy is sufficient or if it is associated with an emissivity or thermal inertia anomaly, a thermal model is necessary. However, the presence of a radar backscatter dichotomy in the concurrent scatterometry (Section 3.3) strongly suggests at least increased scattering in the subsurface of the leading side, and therefore a locally lower emissivity.

Rhea

On Rhea, there is a locally cold area spatially correlated with the ejecta blanket of the young impact crater Inktomi (best visible in the higher-resolution data RH127 and RH177). Using CIRS observations which probe at most a few millimeters into the subsurface, Howett et al. (2014) found that the Inktomi Ejecta Blanket Region (IEBR) has a thermal inertia higher than its surroundings ($\sim$ 20 MKS near Inktomi versus $\sim$ 10 MKS elsewhere). However, at 2.2 cm with the Cassini radiometer, this area stands out (especially in the resolved data) as a cold spot during the night; the exact opposite behavior would be expected for a high thermal inertia region with equal albedo and emissivity properties. This suggests that the Inktomi ejecta blanket is associated with a locally low emissivity and/or high Bond albedo, that overwhelms the thermal inertia effect. The high radar backscatter of the IEBR discussed in Section 3.3.3 and shown in Fig. 3.11 consistently points to efficient subsurface scattering, which increases the radar backscatter and decreases the emissivity.

Iapetus

The leading/trailing dichotomy of Iapetus (see Sections 1.4.2 and 3.3.3) is clearly apparent in the radiometry observations, as reported by Le Gall et al. (2014). The leading hemisphere (centered at $-90°$E) is the radiometrically warmest region of this satellite, followed by the trailing hemisphere (centered at $+90°$E) consistent with the distribution of optically dark material at the surface (Spencer and Denk, 2010). This remains true even during the IA049_4_2u daytime observation, in support of the high thermal inertia found from the resolved radiometry scan (IA049_3_1r) on Iapetus by Le Gall et al. (2014). The poles are the coldest area, because i) they receive less incident flux than the lower latitudes, ii) they feature less optically dark material than equatorial regions, and ii) thermal segregation brings bright water ice from the equatorial region to the poles, where it condenses (Spencer and Denk, 2010).

4.5 Conclusion

Preliminary analysis of the fully calibrated and deconvolved Cassini radiometry observations of Saturn's icy satellites led to identification of both inter- and intra-satellite variations consistent with the results from active radar data (Chapter 3). The brightness temperature is found to increase with distance from Enceladus and show, like visible and radar observations, leading/trailing dichotomies on Iapetus and possibly on Dione. A locally low thermal emission is recorded on Enceladus's Leading Hemisphere Terrain (LHT) (consistent with the results of Ries and Janssen, 2015) and in the Rhea Inktomi Ejecta Blanket Region (IEBR). However, these anomalies cannot be fully characterized without the use of a thermal model. Comparison with such a model can also exploit the observations at different seasons, latitudes, and local times in order to derive the thermo-physical properties of the subsurface.

Chapter 5

Simulation of microwave radiometry observations

In order to extract new constraints on the chemical and thermophysical properties of icy satellites surfaces, we compare radiometry observations to a model simulating the microwave thermal emission from an icy surface. This chapter describes the different steps of the model, their parameters, and their outputs. For the work presented herein, the model was applied to Saturn's three largest airless icy satellites (Dione, Rhea, and Iapetus), as well as on Enceladus.

The model closely follows the one presented in Le Gall et al. (2014), which we summarize here while detailing some modifications. As in Le Gall et al. (2014), our modeling approach is divided into three steps: a thermal model providing the vertical temperature profile within the subsurface $T(z)$, a radiative transfer model calculating the effective temperature T_{eff}, and an emissivity model. As detailed in Section 5.2, the effective temperature is the solution of the radiative transfer equation in the assumed purely absorptive subsurface and would represent the brightness temperature of the surface in the absence of any emissivity effects. In the microwave domain, the Rayleigh-Jeans approximation applies and the surface brightness temperature T_B is simply the product of the emissivity e and the effective temperature T_{eff}. Convolution of T_B with the beam pattern yields the simulated antenna temperature T_A, which can be directly compared to the Cassini radiometer observations.

5.1 Thermal model

The thermal model used here to calculate a temperature profile with depth was originally designed by Ferrari and Leyrat (2006) and Leyrat (2006) to examine Saturn's rings. It has since been applied to the asteroids Steins (Leyrat et al., 2011) and Vesta (Leyrat et al., 2012), Saturn's satellites Iapetus (Le Gall et al., 2014) and Enceladus (Le Gall et al., 2017), comet 67P Churyumov-Gerasimenko (Leyrat et al., 2015), and Pluto (Leyrat et al., 2016).

5.1.1 Incident flux

The physical temperature profile results from the energy balance between the incident solar flux, energy re-radiated into space, and heat conduction in the subsurface. Rhea and Iapetus both have heavily cratered surfaces with no signs of recent resurfacing or tectonic activity (see Chapter 1). On Dione, no hot spots have been found from Cassini/CIRS observations, which have better resolutions coverage than Cassini radiometry (Howett et al., 2018). We can therefore safely assume the absence of endogenic flux on all three satellites.

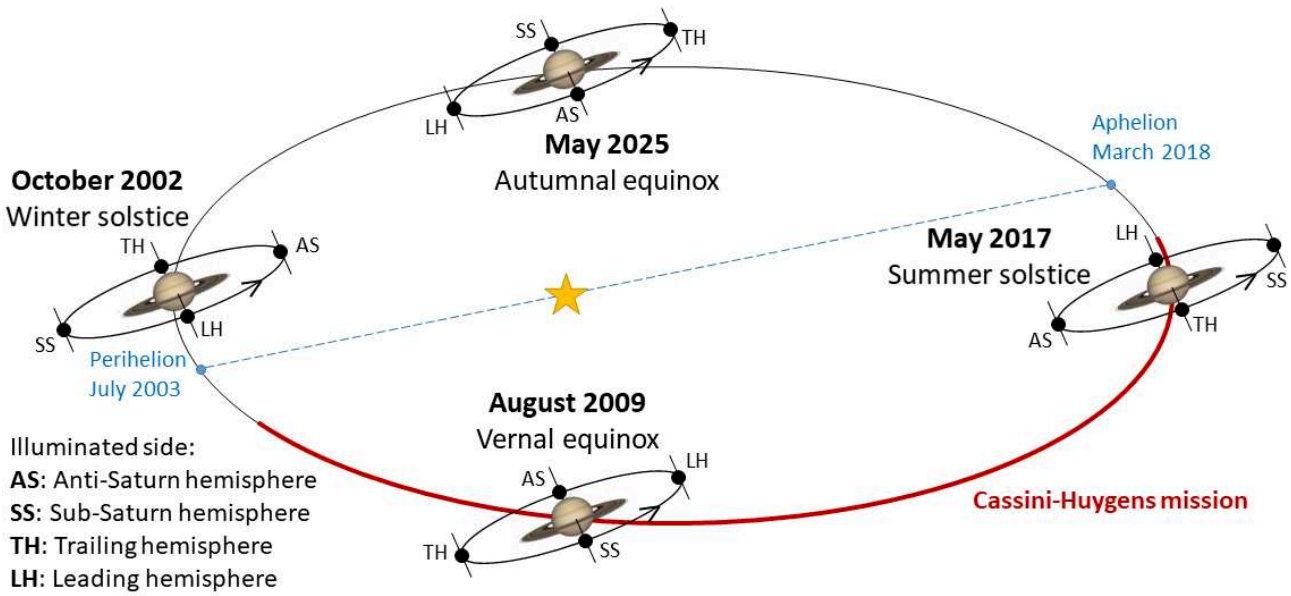

Figure 5.1 – Diagram of an orbit of Saturn around the Sun (in 29.36 Earth years), showing the orbit of a Saturn satellite with low inclination (e.g., Dione or Rhea). The side of the satellite illuminated by the Sun is indicated at each solstice and equinox, for four positions of the satellite. Saturn's northern winter solstice currently almost coincides with its perihelion. The diagram is not to scale.

Table 5.1 – Triaxial satellite shapes (in kilometers) used to calculate the incident solar flux. Values are from (Thomas et al., 2007b).

Satellite	**Saturn-facing radius (a) (km)**	**Orbit-facing radius (b) (km)**	**Polar radius (c) (km)**
Mimas	207.4	196.8	190.6
Enceladus	256.6	251.4	248.3
Tethys	540.4	531.1	527.5
Dione	563.8	561.0	560.3
Rhea	767.2	762.5	763.1
Iapetus	747.4	747.4	712.4

The incident solar flux is computed using SPICE/NAIF libraries (Acton, 1996) for each time step over a full orbit of Saturn (29.36 Earth years), while accounting for solar eclipses by Saturn. An example of this incident flux during an eclipse is shown in Fig. 5.2.

The global patterns of the incident flux already give an indication on how the surface and sub-surface temperature should vary. At a sufficient depth (larger than the seasonal thermal skin depth), the temperature should depend only on the yearly averaged flux, and be constant with time. We therefore examine the incident solar flux, averaged over a year, as shown for latitudes of 50°N and 50°S in Fig. 5.2. The causes of latitudinal, longitudinal, and inter-satellite variation in the yearly averaged incident flux are the following:

- **Eclipses:** Near the equinoxes, the inner satellites (which lie near Saturn's equatorial plane) pass through Saturn's shadow. These eclipses, apparent in Fig. 5.2d, decrease the yearly flux on the sub-Saturn side, which would otherwise be illuminated at these times. Satellites closer to Saturn are eclipsed for a larger fraction of their orbit than satellites further away from the planet,

explaining the lower fluxes at the sub-Saturn point (0°E longitude) on Dione than on Rhea, as seen in Fig. 5.2a and b. Iapetus is much more distant from Saturn and its orbit is inclined (by 7.5°) relative to the Laplace plane: it is therefore eclipsed only on four brief occasions, which barely affect the flux on the sub-Saturn side.

- **Solar distance:** A more significant effect on Iapetus is the difference in solar distance. Because the mid-sized icy satellites of Saturn are tidally locked, the anti-Saturn side is always illuminated when the satellite is closest to the Sun, whereas the opposite is true for the sub-Saturn side, as illustrated in Fig. 5.1. This effect is more important for Iapetus, which has a large orbital radius around Saturn, than for the inner satellites such as Rhea and Dione.

- **Eccentricity of Saturn's orbit:** Fig. 5.1 also illustrates the effect of the ellipticity of Saturn's orbit. With an eccentricity of 0.0565, Saturn's aphelion (10.04 astronomical unit (AU)) is over 1 AU larger than its perihelion (9.03 AU), leading to asymmetrical seasons (e.g. Aharonson et al., 2009; Lorenz et al., 2010). Saturn's northern winter solstice almost coincides with perihelion, leading to shorter and colder winters in the northern hemisphere of each satellite than in the southern hemisphere. Averaged over a Saturn year, this asymmetry leads to slightly higher average northern fluxes, as seen for instance in Fig. 5.2a–c. However, the insolation peak is reached in the southern hemisphere, causing the distribution of lakes on Titan (Aharonson et al., 2009, e.g.,).

- **Satellite triaxial shape:** Saturn's inner mid-sized icy satellites have an ellipsoidal triaxial shape, elongated by tides in the sub- and anti-Saturn directions. These satellites shapes, summarized in Table 5.1, lead to higher incidence angles on the mid-latitudes of the sub- and anti-Saturn sides than on those of the leading and trailing hemispheres. The incident flux is proportional to the cosine of the incidence angle. Thus the ellipsoidal satellite shape causes the peak in incident flux at 90°E and -90°E on Dione and Rhea (Fig. 5.2a and b). Iapetus, being much further from Saturn, is less influenced by tides and is not elongated in the sub-Saturn direction. The effect of solar distance therefore dominates over the satellite shape, and the leading and trailing sides receive less sunlight than the anti-Saturn side (Fig. 5.2c).

- **Satellite inclination:** The orbits of Dione and Rhea lie within the equatorial plane of Saturn, and therefore endure the same seasonal changes. Meanwhile, Iapetus is inclined by 15.5°relative to Saturn's equator (itself at a 29° axial tilt angle from the ecliptic). Consequently, Iapetus has a lower inclination relative to the Sun than the inner icy satellites, causing less intense seasons on Iapetus. Averaged over a year, the incident flux on Iapetus high latitudes (e.g., 50°, see Fig. 5.2c) is lower than on the inner moons.

- **Thermal infrared emission from Saturn:** At an effective temperature of 95 K, Saturn constantly heats the sub-Saturn side of synchronous satellites. The amplitude of the infrared flux from Saturn depends primarily on the angular size of Saturn as seen from the satellite (and thus on the Saturn–satellite distance), which is 17.1° from Dione, 12.4° from Rhea, and 1.87° from Iapetus. For large angular sizes of Saturn, the anti-Saturn side is also affected by Saturn's emission, especially at high latitudes. The thermal IR flux from Saturn is constant, both in coverage and in time; it does not depend on day/night cycles.

- **Saturnshine:** The portion of Saturn's disk that is illuminated by the Sun reflects part of the incident solar flux toward the icy satellites. Like the thermal Saturn flux, Saturnshine affects primarily the sub-Saturn side, and is more significant for satellites with small orbital radii. The amplitude of Saturnshine, however, also varies with local time: it is null at noon (sub-Saturn side facing the night side of Saturn) and maximal during the satellite's local night (sub-Saturn side facing the day side of Saturn).

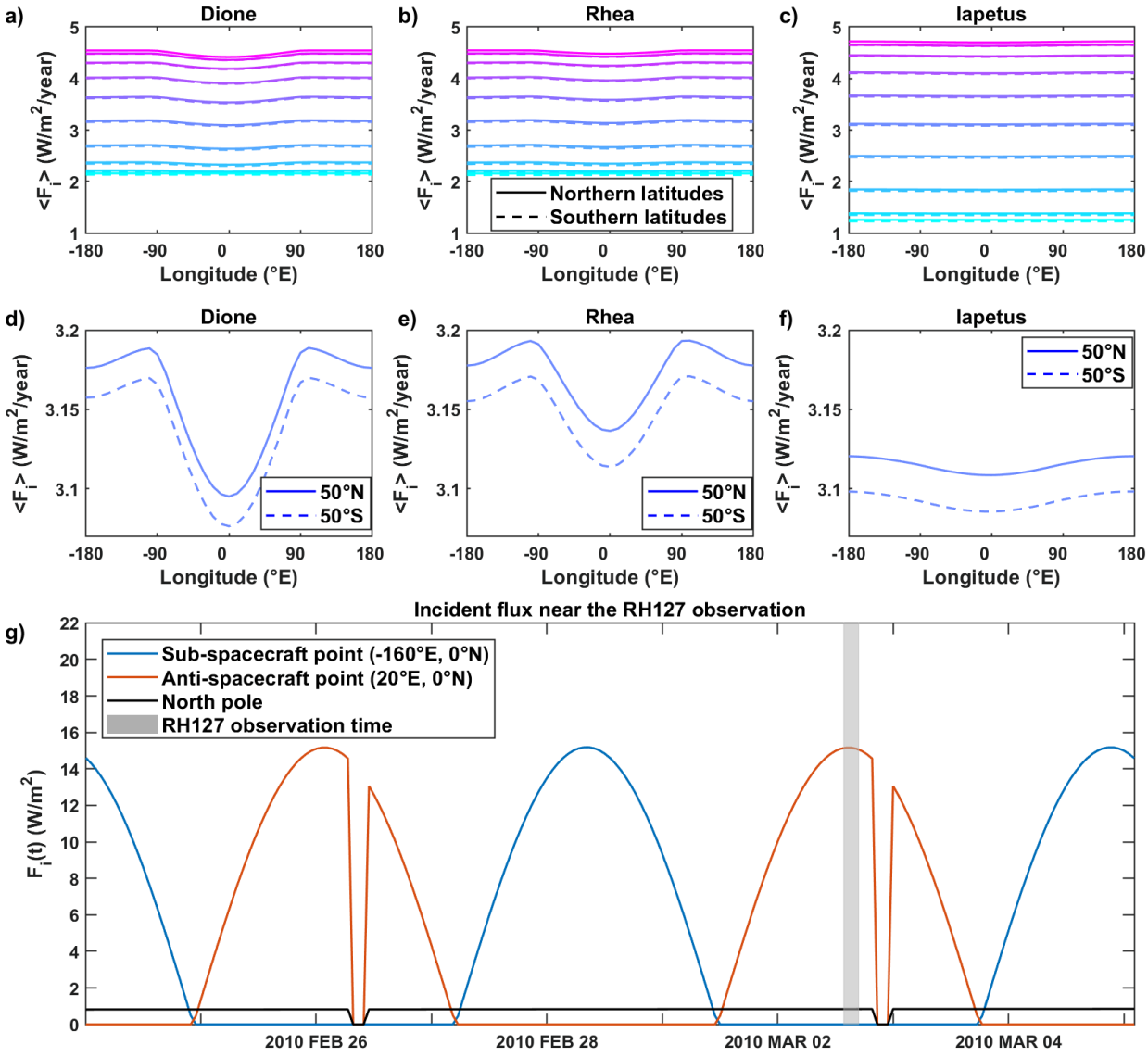

Figure 5.2 – Yearly average of the incident solar flux at all latitudes (with a latitudinal step of 10°), on (a) Dione, (b) Rhea, and (c) Iapetus. Close-up of the yearly average of the incident flux at 50°N and 50°S, on (d) Dione, (e) Rhea, and (f) Iapetus. (g) Incident flux F_i at three different locations on Rhea's surface for two Rhea days (4.52 Earth days; see Table 1.1), including at the time of RH127 observation, which is outlined in gray. The Northern spring equinox was on August 11, 2009, less than a year before this observation; the South pole is therefore in permanent shadow and receives zero solar flux. For about a year before and after the equinox, Rhea passes through Saturn's shadow, causing the dips in solar flux seen here on February 26 and March 2. These eclipses only affect the sub-Saturn side of Rhea.

Iapetus is far enough from Saturn that only direct solar illumination is significant. On Rhea and Dione, most past analyses of CIRS data using a thermal model have neglected both Saturnshine and thermal infrared emission from Saturn (Howett et al., 2014; Howett et al., 2016), though Howett et al. (2018) accounted for radiation from Saturn. With a Saturn bolometric Bond albedo of $A_B^{\text{Saturn}} = 0.34$, an icy satellite infrared albedo $A_{\text{IR}}^{\text{icysat}} = 0.95$, and the icy satellite bolometric Bond albedo values discussed hereafter (Section 5.1.3), the thermal and visible fluxes from Saturn contribute respectively a yearly average of 2.0% and 0.8% of the total flux absorbed by Rhea's surface. We therefore considered that only direct solar illumination was significant, and chose not to account for Saturn reflected and thermal radiation. This would later prove to be a mistaken assumption, especially for Dione, where the thermal and visible Saturn fluxes contribute respectively 6.4% and 1.7% of the total absorbed flux. The importance of Saturn's contribution is further discussed in Chapter 6.

If Saturn's contribution is neglected, the absorbed flux F_{absorbed} is related to the bolometric Bond albedo A_B and the incident solar flux $F_\odot$ by:

$$F_{\text{absorbed}} = (1 - A_B) F_\odot \cos i(t) \tag{5.1}$$

where $i(t)$ is the time-varying incidence angle of the solar flux. The values used for the bolometric Bond albedo are discussed in Section 5.1.3.

5.1.2 Derivation of the temperature profile below the surface

Heat equation

The temperature profile is derived at a given latitude/longitude point by solving the 1-dimensional time-dependent heat equation:

$$\rho C \frac{\partial T(z,t)}{\partial t} = \frac{\partial}{\partial z}\left[K_E \frac{\partial T(z,t)}{\partial z}\right] \tag{5.2}$$

where z is the depth under the surface, ρ is the effective density of the medium (in kg/m^3), K_E is the effective thermal conductivity (in Wm^{-1}K), and C is the bulk heat capacity (in Jkg^{-1}K^{-1}). The thermal model that we used considers uniform thermal properties with depth, thus permitting the following simplification of the heat equation:

$$\frac{\rho C}{K_E} \frac{\partial T(z,t)}{\partial t} = \frac{\partial^2 T(z,t)}{\partial z^2} \tag{5.3}$$

Boundary conditions

The surface boundary condition imposes radiative equilibrium, where the outgoing flux is given by the Stefan-Boltzman law and the incident flux from the Sun varies along the satellite's orbit as detailed above:

$$-K_S \left.\frac{\partial T}{\partial z}\right|_{z=0} = F_{\text{emitted}}(t) - F_{\text{absorbed}}(t) = e_{IR}\sigma T_s^4(t) - (1 - A_B) F_{\text{incident}}(t) \tag{5.4}$$

where $\sigma = 5.67 \times 10^{-8}$ Wm^{-2}K^{-4} is the Stefan constant, and e_{IR} is the infrared emissivity, which was fixed at unity, as found by Howett et al. (2016).

The boundary condition at the bottom of the computational layer assumes no internal source of heating and therefore a zero temperature gradient at depth. The lower boundary is taken at a depth of six seasonal thermal skin depths ($\delta_{\text{th}}^{\text{season}}$, see Eq. 5.11) and below:

$$\left.\frac{\partial T}{\partial z}\right|_{z=6\delta_{\text{th}}^{\text{season}}} = 0 \tag{5.5}$$

Dimensionless form

The heat equation can be expressed in dimensionless form using the following parametrization, following Spencer et al. (1989):

$$\begin{aligned} T' &= T/T_{SS} \\ t' &= \omega t \\ z' &= z/\delta_{\text{th}}^{\text{day}} \\ F'_{\odot}(t') &= F_{\odot}(t')/F_{\odot,SS} \end{aligned} \tag{5.6}$$

where ω is the rotation rate of the satellite, $\delta_{\text{th}}^{\text{day}}$ is the diurnal thermal skin depth defined in Section 5.1.3, $F_{\odot,SS}$ is the sub-solar insolation, and T_{SS} is the sub-solar equilibrium temperature, defined as follows:

$$e_b \sigma T_{SS}^4 = (1 - A_B) F_{\odot}/R^2 \tag{5.7}$$

.

with $F_{\odot}$ the solar constant at 1 AU, R the heliocentric distance in AU, and e_b the bolometric emissivity. The heat equation and its top boundary conditions then become dimensionless (Spencer et al., 1989):

$$\begin{aligned} 2\frac{\partial T'(z',t')}{\partial t'} &= \frac{\partial^2 T'(z',t')}{\partial z'^2} \\ \sqrt{2}\Theta \left.\frac{\partial T'(z',t')}{\partial z'}\right|_{z'=0} &= T'^4(0,t') - F'_{\odot,SS}(t') \end{aligned} \tag{5.8}$$

where the thermal parameter Θ is defined as follows:

$$\Theta = \frac{I\sqrt{\omega}}{e_b \sigma T_{SS}^3} \tag{5.9}$$

Note that the factors of 2 and $\sqrt{2}$, not present in Spencer et al., 1989, account for our slightly different definition of the thermal skin depth (by a factor $\sqrt{2}$). The temperature profile therefore depends on only two parameters: the bolometric Bond albedo A_B and the thermal inertia $I = \sqrt{K_E \rho C}$.

Step sizes

The 1-dimensional heat equation is solved numerically by discretizing time and space (with respective steps Δt and Δz) and using the Crank-Nicolson method, a semi-implicit algorithm which is unconditionally stable.

Lateral heat conduction (i.e., parallel to the surface) is neglected, and we only take into account heat conduction through depth. This assumption is valid as long as the step in the horizontal direction (10° in latitude and longitude, equivalent to tens to hundreds of kilometers) is much larger than the seasonal thermal skin depth (at most ~ 100 m, for a thermal inertia of 2000 MKS).

The discretized spatial step in depth Δz must be small enough to sense periodic variations of the temperature near the surface, i.e. where the thermal gradients are the largest. We choose $\Delta z = \delta_{\mathrm{th}}^{\mathrm{day}}/5$.

Meanwhile, the temporal step Δt must be small enough to track abrupt incident flux variations, especially around the eclipse events. The time step was therefore chosen such that there are 100 points over a diurnal cycle. Given their orbital periods (Table 1.1), this is equivalent to times steps of 0.66, 1.08, and 19 hours for Dione, Rhea, and Iapetus respectively. One full thermal cycle contains must include an orbit of Saturn (29.5 years) and thus tens to hundreds of thousands of points.

The thermal model was run for every 10° in latitude and longitude, providing a resolution similar to the resolved observations of each satellite.

The thermal model begins with all layers at the equilibrium temperature, then iteratively recalculates the temperature profile for a full Saturn year (29.5 years), for at least 4 iterations. Convergence is reached when the Pearson correlation coefficient between input and output temperature profiles is over 0.999, which generally occurs after 6 iterations. For a single thermal inertia value, in a 10°×10° latitude and longitude block, the computation time is of about six to seven minutes. Thus, the thermal model requires about three weeks to run for the whole surface of a satellite and for seven thermal inertia values.

Model limitations

The thermal model of Ferrari and Leyrat (2006) and Leyrat (2006) considers heat transfer only by conduction. This assumption is reasonable for the depths probed by the Cassini radiometer (at least meters into an icy surface). A thin isolating layer may exist near the surface, with high porosity and poor grain contact quality leading to important heat transfer by radiation. Given that the radiative component of the thermal conductivity is proportional to the temperature cubed ($K_R \propto T^3$), such an isolating layer may amplify the observed short-term temperature changes. However, it would retain little effect on the temperature profile at depths much larger than the daily thermal skin depth.

More importantly, however, the model used here assumes that the thermal inertia is constant with depth. In fact, it is expected to increase with depth as the medium becomes more compact, as has been confirmed by the comparison of Cassini radiometry and CIRS observations on Iapetus (Howett et al., 2010; Le Gall et al., 2014). Modeling an increase in thermal inertia with depths, as did Howett et al. (2016) for Rhea, requires the introduction of additional parameters (e.g., the amplitude of these variations and the depth at which they occur), which the data are insufficient to constrain. Instead, we opted for a simple, single-layer, uniform model, which can be fitted to the dataset to derive a depth-averaged value of the thermal inertia. This model has the additional advantage of being the same used on Iapetus and Enceladus by Le Gall et al. (2014, 2017), providing consistency to the treatment of the Cassini radiometry dataset.

5.1.3 Model parameters

Bolometric Bond albedo A_B

The bolometric Bond albedo A_B governs the amount of incident radiation absorbed by the surface (Eq. 5.1).

For **Iapetus**, a global bolometric Bond albedo map has been derived by Blackburn et al. (2011) from Cassini VIMS, Cassini ISS, and Voyager ISS observations. As in Le Gall et al. (2014), this map

was used as an input for the thermal model, and is shown in Fig. 5.3.

For **Dione**, only a partial bolometric Bond albedo map exists, derived from a combination of Cassini VIMS and ISS measurements (Blackburn et al., 2012). The partial map mainly covers equatorial regions, below 45° latitude. Missing data were filled with the average leading and trailing hemisphere values for each latitude. When no data was available (i.e., at the poles), the average leading hemisphere albedo was used, since the higher latitudes are not expected to be affected by the trailing hemisphere dark material (see Chapter 1). For each $10 \times 10°$square in latitude and longitude, the bolometric Bond albedo is averaged and the thermal model is applied to calculate the temperature profile.

For **Rhea**, there is unfortunately no bolometric Bond albedo map yet. The bolometric Bond albedo is not straightforward to compute from ISS and VIMS data at different wavelengths and phase angles, and such a derivation is beyond the scope of the present thesis. Spatial variations of the visible albedo, although present on optical images (Schenk et al., 2011; Schenk et al., 2018), thus cannot be explicitly taken into account. More specifically, the brightness of the Inktomi Ejecta Blanket Region (IEBR) varies considerably with wavelength (Schenk et al., 2011), and even its appearance in 3-color composite maps changes with the color ratios chosen. Indeed, the IEBR is much brighter than its surroundings in the map of Schenk et al. (2011), but is indistinguishable in the updated map of Schenk et al. (2018) (PIA18438; Fig. 1.6). From CIRS thermal infrared data, Howett et al. (2014) do not find a clear albedo change near Inktomi either.

We therefore tested four different values of albedo (constant over the disk), inspired from literature (Table 5.2): 0.42, 0.55, 0.63, and 0.72. This last value was derived from Cassini CIRS data over Rhea's poles (Howett et al., 2016).

Thermal inertia I

The thermal inertia I of a material describes its capacity to resist temperature changes. A material with low thermal inertia quickly reaches thermal equilibrium after a perturbation, whereas for a high thermal inertia material it can take much longer. The bulk thermal inertia of crystalline water ice is of the order of 2000 $\mathrm{Jm^{-2}K^{-1}s^{-1/2}}$ (units referred to as MKS herein) and varies little with temperature (Ferrari and Lucas, 2016); however, thermal inertia decreases along with thermal conductivity for porous media:

$$I = \sqrt{K_E \rho C} \tag{5.10}$$

The thermal inertia that enters the model does not in general represent the thermal inertia of the surface/subsurface bulk material. As we will find, best fit thermal inertia are much smaller than expected values for compact ices, which we interpret as due primarily to a large porosity of the medium. The inferred values are therefore "effective" thermal inertias. We note that, other than porosity, several structural characteristics of an icy surface can also decrease the thermal inertia, such as small grain sizes, loose contacts between particles, the presence of amorphous (rather than crystalline) ice, and low temperatures (Gundlach and Blum, 2013; Ferrari and Lucas, 2016). These different parameters are difficult to separate given their often similar effects to structural and compositional properties.

Thermal inertia has been derived for Saturn's icy satellites from thermal infrared observations, using primarily Cassini CIRS data; the resulting values are summarized in Table 5.2. The thermal inertia of Saturn's icy moons is generally around 10–20 MKS and always below 100 MKS in the thermal infrared (e.g., Howett et al., 2010; Howett et al., 2014; Howett et al., 2016)). However, at cm wavelengths (which probe deeper into the subsurface), Le Gall et al. (2014) found higher values,

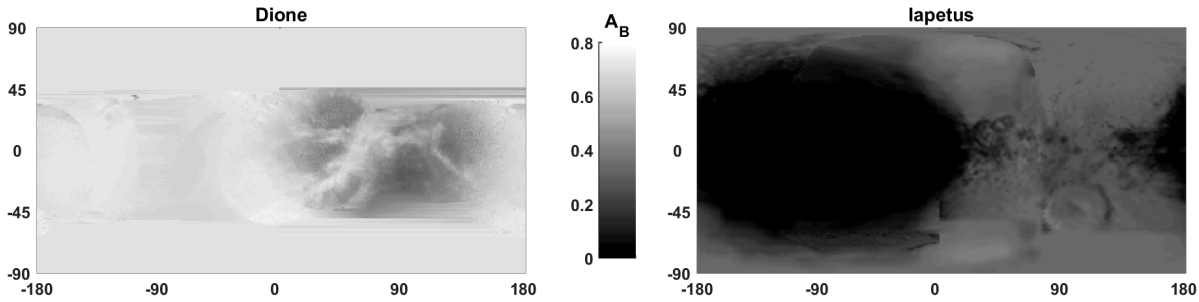

Figure 5.3 – Bolometric Bond albedo maps of Dione (adapted from Blackburn et al., 2012) and Iapetus (Blackburn et al., 2011).

Table 5.2 – Thermal inertias I (MKS) and bolometric Bond albedos A_B of the icy satellites of Saturn as inferred during the Cassini mission. Pitman et al. (2010) derived the bolometric Bond albedo from VIMS data (near-infrared), Blackburn et al. (2011) and Blackburn et al. (2012) used both VIMS and ISS (visible wavelengths) observations. The other articles cited in this table derived I and A_B from CIRS data (thermal infrared, typically 30 – 200 µm); their values are thus valid for the top few millimeters to centimeters of the surface. All thermal inertias shown here are diurnal, except the one measured by Howett et al. (2016) on Rhea's poles, which is seasonal.

Satellite	**Bolometric Bond albedo A_B**		**Thermal inertia I (MKS)**		**Reference**
	Leading	Trailing	Leading	Trailing	
Mimas	0.65 ± 0.13	0.72 ± 0.10			Pitman et al., 2010
	$0.49^{+0.05}_{-0.14}$		19^{+57}_{-9}		Howett et al., 2010
	Partial map (0.3 – 0.6)		Partial map (2 – 200)		Howett et al., 2011a, 2020
Enceladus	0.80 – 0.82		12 – 25		Spencer et al., 2006
	0.77 ± 0.09	0.93 ± 0.11			Pitman et al., 2010
	0.81 ± 0.04		15^{+24}_{-9}		Howett et al., 2010
Tethys	0.67 ± 0.09	0.52 ± 0.08			Pitman et al., 2010
	0.67 ± 0.11		9^{+10}_{-4}		Howett et al., 2010
	Partial map (0.5 – 0.8)		Partial map (5 – 50)		Howett et al., 2012
Dione	0.63 ± 0.05	0.37 ± 0.08			Pitman et al., 2010
	0.63 ± 0.15		11^{+18}_{-6}		Howett et al., 2010
	Partial map (0.2 – 0.65)		Partial map (3 – 15)		Howett et al., 2014
	Partial map (0.29 – 0.8)				Blackburn et al., 2012
Rhea	0.55 ± 0.08	0.42 ± 0.10			Pitman et al., 2010
	$0.63^{+0.11}_{-0.12}$	$0.57^{+0.20}_{-0.26}$	9^{+9}_{-5}	8^{+12}_{-5}	Howett et al., 2010
	Partial map (0.4 – 0.8)		Partial map (5 – 25)		Howett et al., 2014
	Poles (0.70 – 0.74)		Poles (1 – 46)		Howett et al., 2016
Iapetus			30		Spencer et al., 2005
	0.10	$0.31^{+0.15}_{-0.17}$	14^{+7}_{-8}	20^{+13}_{-8}	Howett et al., 2010
	Global map (0.01 – 0.41)				Blackburn et al., 2011
			11 – 14.8	15 – 25	Rivera-Valentin et al., 2011
Phoebe	0.1		25		Flasar et al., 2005
	0.023 ± 0.07				Buratti et al., 2008
	0.1		20		Howett et al., 2010

of the order of 100–200 MKS, pointing to increasing compaction with depth.

In order to derive the thermal inertia, the thermal model was run for seven values of I from 10 to 1000 MKS (10, 20, 50, 100, 250, 500, and 1000 MKS), and results were interpolated for intermediate thermal inertia values.

Thermal skin depth δ_{th}

The thermal skin depth δ_{th} is defined as the depth at which the amplitude of temperature variations (due to diurnal or seasonal variations of the incident flux) has decreased by a factor of 1/e = 37%. It is related to the thermal inertia I as follows:

$$\delta_{\mathrm{th}} = \sqrt{\frac{2K_E}{\rho C \omega}} = \frac{I}{\rho C}\sqrt{\frac{P}{\pi}} = \frac{I}{(1-p)\rho_0 C}\sqrt{\frac{P}{\pi}} \tag{5.11}$$

where $P = 2\pi/\omega$ is the thermal wave period (a satellite day for $\delta_{\mathrm{th}}^{\mathrm{day}}$ or year for $\delta_{\mathrm{th}}^{\mathrm{season}}$), p is the porosity, ρ_0 is the bulk density (918 kg/m^3 for crystalline water ice), and $C = 7.49 \times T_0 + 90$ Jkg^{-1}K^{-1} is the bulk heat capacity calculated for a temperature of $T_0 = 75$ K using the formulas for crystalline water ice proposed in Klinger (1981). From the adimensional form of the heat equation (Eq. 5.8), the values assumed for C and p do not influence the derived value of the thermal inertia; however, they do affect the derived thermal skin depths (Eq. 5.11). A low thermal inertia surface quickly changes temperature, and the thermal wave penetrates very little. Conversely, for a high thermal inertia surface, the thermal skin depth is high. Because of the orbital periods of each satellite, assuming similar thermal inertia and porosity at diurnal and seasonal thermal skin depths, $\delta_{\mathrm{th}}^{\mathrm{season}} = 62.6\delta_{\mathrm{th}}^{\mathrm{day}}$ on Dione, $\delta_{\mathrm{th}}^{\mathrm{season}} = 48.7\delta_{\mathrm{th}}^{\mathrm{day}}$ on Rhea, and $\delta_{\mathrm{th}}^{\mathrm{season}} = 11.7\delta_{\mathrm{th}}^{\mathrm{day}}$ on Iapetus.

5.1.4 Model outputs

The output of the thermal model is the vertical temperature profile $T(z)$ for different assumed thermal inertias and albedos, over the whole surface. The model assumes homogeneous properties with depth: the parameters should therefore be regarded as an average over the sensed depth (that is, the electrical skin depth δ_{el} at the instrument wavelength, see Section 5.2). In particular, the thermal inertia is expected to increase with depth as the medium becomes more compact.

The amplitude and phase of the temperature variations with depth both depend strongly on the thermal inertia, as illustrated in the modeled temperature profiles shown in Fig. 5.4. Fig. 5.5 illustrates the variations of the modeled temperature distribution with depth, for Rhea and Dione. At the surface, local time dominates, with the sub-solar region being the warmest region on each satellite. The northern vernal equinox was in August 2009 (see Fig. 5.1); temperatures are mapped in March 2010 for Rhea (RH127 observation) and March 2012 for Dione (DI163 observation). Because the Dione map is shown later in the spring (closer to the northern solstice) than the Rhea map, it exhibits warmer northern temperatures than Rhea at the surface and the diurnal skin depth. At the seasonal skin depth, however, the buried cold northern temperatures of the previous winter appear. On Dione, the bolometric Bond albedo map plays an important role in the temperature distribution, especially under the diurnal skin depth.

Once thermal equilibrium is reached (e.g., at 6 times the seasonal thermal skin depth in Fig. 5.5), the effects of the yearly averaged fluxes described in Section 5.1.1 are apparent. The South pole, where winter is longer but less intense due to Saturn's eccentricity, is then about 3 K colder than

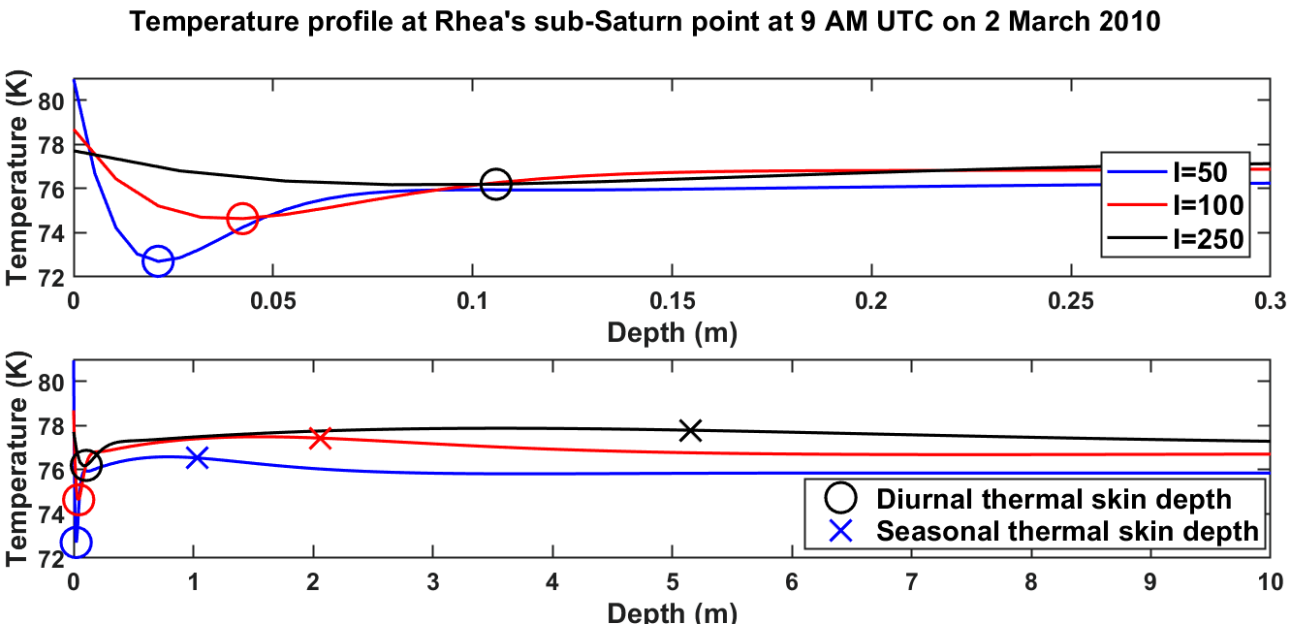

Figure 5.4 – Temperature profile with depth at the sub-Saturn point (0°E, 0°N) on Rhea on 2 March 2010 (during the RH127 observation), for three different values of the thermal inertia I. The profile extends down to (top) 0.3 m into the subsurface to highlight the diurnal thermal wave and (bottom) 10 m to highlight the seasonal thermal wave. At 0°E longitude, the local time is just before noon, hence the high surface temperature. The diurnal thermal skin depth is marked with a circle and the seasonal skin depth with a cross for each thermal inertia. When the thermal inertia increases, the diurnal dip in temperature is located at a greater depth and is wider but also less strong.

the North pole for both Dione and Rhea for a thermal inertia of 10 MKS. On Rhea, eclipses lead to a 0.2-K-dip in temperature at the sub-Saturn point relative to the anti-Saturn point (at the time of this observation, i.e., less than one Earth year after the equinox and while eclipses still occur). The satellites' elongation in the Saturn-facing direction causes a 0.15-K-peak in the leading and trailing hemispheres relative to the anti-Saturn side (unaffected by eclipses).

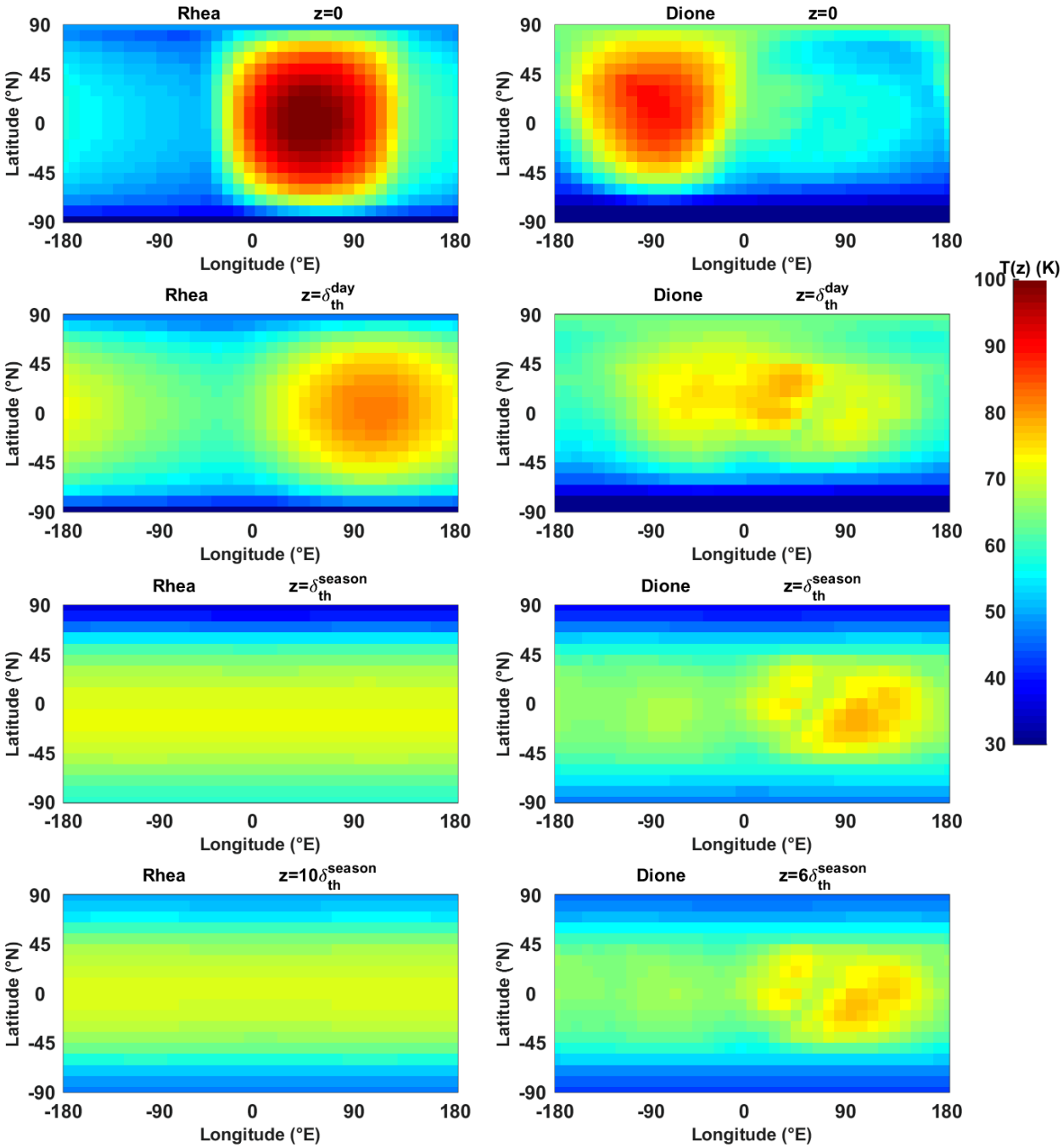

Figure 5.5 – Temperature maps at four different depths, for a thermal inertia of $I = 10$ MKS, for (left) Rhea on 2 March 2010 (RH127 observation) and (right) Dione on 27 March 2012 (DI163 observation). On Dione, the bolometric Bond albedo map shown in Fig. 5.3 is used, whereas on Rhea a uniform bolometric Bond albedo of $A_B = 0.55$ is assumed.

5.2 Radiative transfer model

5.2.1 Model hypotheses

The theory of microwave transfer through the subsurface is summarized in Section 2.4.2. In order to simulate the effective temperature T_{eff} sensed by the Cassini radiometer, we do not explicitly include scattering in the radiative transfer equation, even though both the radar properties of Saturn's icy moons (Chapter 3) and pre-existing analyses of the Cassini radiometry (Chapter 4 and Le Gall et al., 2010; Janssen et al., 2011; Le Gall et al., 2014) have demonstrated that multiple scattering in the subsurface is actually very significant on icy satellites.

To limit both the complexity of the model and the number of parameters we have made the choice of a scatter-free single-layer radiative transfer model, like Le Gall et al. (2014) (see also Keihm et al., 2013 for asteroids). As we will see, such models require the introduction of surface emissivities to fit the observed brightness temperatures. In the next step of the model, we interpret these lower than 1 surface emissivities in terms of the scattering properties of the subsurface. The degree of scattering and its regional variations are thus estimated afterward from the derived emissivity. The backscatter measured during the resolved scatterometry (Section 5.3) also provides an independent insight into the degree of scattering in the subsurface.

5.2.2 Calculating the effective temperature T_{eff}

The radiative transfer model used herein therefore applies the following form of Eq. 2.37, valid for a scatter-free medium (repeated here for convenience):

$$T_{\text{eff}}(I, \delta_{\text{el}}) = \frac{1}{\delta_{\text{el}} \cos\theta'} \int_0^\infty T(z, I) e^{-z/(\delta_{\text{el}} \cos\theta')} dz \tag{5.12}$$

where δ_{el} is the electrical skin depth sensed by the radiometer (Eq. 2.13) and $T(z, I)$ is the temperature profile for a thermal inertia I computed from the thermal model. The effective temperature sensed by the Cassini radiometer is thus a weighted function of the physical temperature profile, along the line of sight within the subsurface. The angle of transmission θ' in the subsurface is defined as follows:

$$\cos\theta' = \sqrt{1 - \frac{\sin^2\theta}{\varepsilon'_r}} \tag{5.13}$$

where θ is the angle of emission at which the Cassini radiometer observes the surface locally, and ε'_r is the effective relative dielectric constant of the subsurface. Its value in the radiative transfer model is fixed at $\varepsilon'_r = 1.15$ (the value that will be determined from the emissivity model; see Chapter 6). The dielectric constant has a small influence on the effective temperature, and only near the limbs. Changing this value from $\varepsilon'_r = 1.15$ to $\varepsilon'_r = 2$ in Eqs 5.12 and 5.13 affects the results discussed in Chapter 6 to a negligible degree. The dielectric constant plays a much more important role in the emissivity, as detailed in Section 5.3.

Using the same substitution as in Eq. 5.8 and defining the skin depth ratio $r = \delta_{\text{el}}/\delta_{\text{th}}^{\text{day}}$, Eq. 5.12 becomes:

$$T_{\text{eff}}(I, r) = \frac{1}{r \cos\theta'} \int_0^\infty T(z', I) e^{-z'/(r \cos\theta')} dz' \tag{5.14}$$

The derived effective temperature is therefore a function of only two parameters: the thermal inertia I and the skin depth ratio r.

5.2.3 Model parameters

Thermal inertia I

The radiative transfer model uses the temperature profile $T(z, I)$ output by the thermal model as an input. It therefore inherits the thermal inertia I as a parameter (Section 5.1.3). The effective temperature is calculated for the same values of I as the temperature profile (7 values from 10 MKS to 1000 MKS).

Skin depth ratio r

As detailed above, the signal sensed by the radiometer is in fact a function of the ratio between the electrical skin depth and the thermal skin depth, and we therefore consider the parameter $r = \delta_{\rm el}/\delta_{\rm th}^{\rm day}$. A low ratio $r \leq 1$ indicates that the radiometer only probes the diurnal variations in temperature of the subsurface, whereas a high ratio $r \gg 1$ implies that the radiometer also captures seasonal variations in temperature. In other words, a high ratio r is indicative of a medium very transparent to microwaves, likely porous and with very little contamination by non-ice impurities, whereas a low value of r points to the presence of absorbing materials.

The effective temperature was calculated for 66 values of r ranging from $r = 0.01$ (very shallow) to $r = 1000$ (over ten times the seasonal thermal skin depth, for all icy satellites considered). The highest value of the ratio corresponds to electrical skin depths of at least (for null porosity and $I = 10$ MKS) 200 times the wavelength.

5.2.4 Numerical application

The temperature profile $T(z, I)$ output by the thermal model is interpolated in time to provide a point every 5 UT minutes. It is then projected to the spacecraft view coordinates defined in Section 3.1.3, with a sampling of 200 points over the satellite diameter. The integral in Eq. 5.12 is integrated numerically for each point in this grid, yielding the effective temperature maps shown in Fig. 5.6.

For low ratios ($r < 1$), the temperatures near the surface are given more weight than for large ratios. Thus, the sampling in depth of only $\Delta z = \delta_{\rm th}^{\rm day}/5$ (Section 5.1.2) is insufficient for accurate numerical integration with $r < 1$. In these cases, the sampling in depth is interpolated on a 100 times finer grid, down to 20 diurnal skin depths $\delta_{\rm th}^{\rm day}$, thus allowing for numerical integration.

5.2.5 Model outputs

Examples of effective temperature maps output by the radiative transfer model are displayed in Fig. 5.6 for Rhea and Dione, during the RH127 and DI163 observations (the same as in Fig. 5.5). This figure shows that, at low skin depth ratios and thermal inertias, the effective temperature is controlled by local time effects, with the western (late afternoon) side of the disk being warmer. Meanwhile, at high skin depth ratios and thermal inertias, the temperature is controlled primarily by albedo and seasonal effects. By comparing these maps to the radiometry data (Figs. 4.5 and 4.6), it is obvious that the modeled effective temperatures are much higher (about 60 – 80 K) for all (I,r) combinations than the observed brightness temperatures (about 45 – 55 K), for both Rhea and Dione. The emissivity of the subsurface, which corresponds to the ratio between observed brightness temperature and modeled effective temperature, clearly has a large influence on the brightness temperatures, and an emissivity model is required.

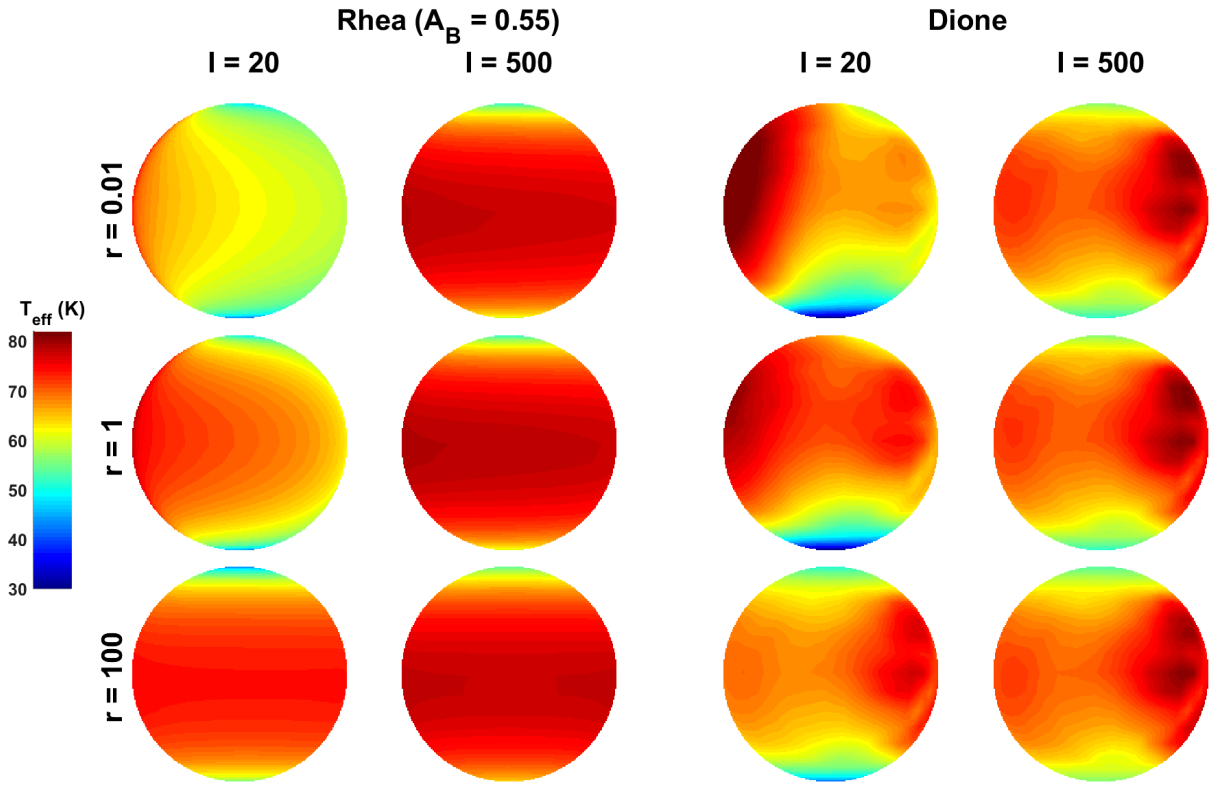

Figure 5.6 – Effective temperature maps in spacecraft view coordinates, for (left) Rhea during the RH127 observation, with a uniform bolometric Bond albedo of 0.55, and (right) Dione during the DI163 observation, using the albedo map pictured in Fig. 5.3. The effective temperatures are shown for a low ($I = 20$ MKS) and a high ($I = 500$ MKS) value of the thermal inertia, and for three different values of the skin depth ratio $r = \delta_{\rm el}/\delta_{\rm th}^{\rm day}$. Both observations are centered at 0°latitude, but RH127 covers the anti-Saturn side whereas DI163 is on the sub-Saturn side (the optically dark trailing hemisphere is on the right). Local times at the center of the disk are midnight for Rhea and 8 PM for Dione.

5.3 Emissivity model

5.3.1 Combined emissivity-backscatter model

We use the Combined Emissivity-Backscatter (CEB) model initially proposed by Janssen et al. (2011) for Titan and since then applied on Iapetus and Enceladus by Le Gall et al. (2014, 2017). This model relies on Kirchhoff's law of thermal radiation (emissivity=1-reflectivity; see Section 2.4.2) using the formulation proposed by Peake (1959), which relates emissivity to radar backscatter. The benefit of such a model is to exploit the normalized radar cross-section (NRCS) (defined in Section 2.3.2) σ^0 measured during the active scatterometry observations (see Section 3.3) to provide constraints on the emissivity level and regional variations.

The emissivity model has two components: a quasi-specular component, which accounts for polarization and limb-darkening, and a diffuse component, which takes into account multiple scattering in the subsurface as well as regional reflectivity/emissivity variations:

$$e(\theta,\phi) = 1 - \underbrace{R(\varepsilon'_r,\theta,\phi)}_{\text{Quasi-specular component}} - \underbrace{\left(\frac{1+\mu_L}{2nf_{\text{CBE}}}\right)\frac{\sigma^0(\theta,\phi)}{\cos^n\theta_{\text{eff}}}}_{\text{Diffuse component}} \tag{5.15}$$

where (θ,ϕ) defines the angular coordinates, relative to the vector from the Cassini spacecraft to the sub-spacecraft point. The parameters of the model are defined hereafter.

Diffuse component

This model assumes that the NRCS σ^0 measured in the scatterometry data obeys a diffuse scattering law of the form $\sigma^0(\theta_{\text{eff}}) = A\cos^n\theta_{\text{eff}}$, as found in Chapter 3. The power coefficient n is derived as described in Section 3.3.2, by fitting the function $\sigma^0(\theta_{\text{eff}}) = A\cos^n\theta_{\text{eff}}$ through the scatterometry data (separately for Dione's leading and trailing hemispheres, and for Rhea's Inktomi ejecta blanket), where θ_{eff} is the effective incidence angle for each scatterometry observation. Dividing the NRCS by $\cos^n\theta_{\text{eff}}$ removes the dependence on incidence angle.

The emissivity-backscatter model includes diffuse subsurface scattering with the factor f_{CBE}, which enhances radar backscatter (and decreases the emissivity) according to the Coherent Backscattering Effect (CBE) (Hapke, 1990; Janssen et al., 2011). The CBE can boost the radar return in the backscattering direction by a factor of up to 2 for a low-loss medium hence: $1 \leq f_{\text{CBE}} \leq 2$.

The linear polarization ratio μ_L (defined in Section 2.3.3) is assumed to be independent of viewing geometry, which is likely for an unpolarized surface. By definition $0 \leq \mu_L \leq 1$. μ_L is null for a smooth homogeneous surface while it equals 1 when the surface is very rough or when multiple/volume scattering occurs in the subsurface.

Quasi-specular component

Although the near subsurface of most of Saturn's icy satellites are primarily diffusely scattering media (e.g., Ostro et al., 2006; Ostro et al., 2010), the emissivity model also includes a quasi-specular component: $1 - R(\varepsilon'_r,\theta,\phi)$ where $R(\varepsilon'_r,\theta,\phi)$ is the reflectivity of a smooth surface as given by the Fresnel equations (see Section 2.2.3). $R(\varepsilon'_r,\theta,\phi)$ depends on the incidence and polarization angles, with limb darkening and the position and amplitude of the Brewster highlights varying with the dielectric constant ε'_r. ε'_r can therefore be estimated using observations acquired over all incidences and azimuthal angles.

Using the Fresnel equations to model the quasi-specular component of the emissivity assumes a smooth surface. Important surface roughness, similarly to subsurface inhomogeneities, would tend to

depolarize the signal and lead to lower derived dielectric constants (e.g., White and Cogdell, 1973). Therefore, the dielectric constants are effective ones, implicitly accounting for surface roughness.

5.3.2 Model parameters

Dielectric constant ε'_r

For very diffuse scattering surfaces such as those of the icy satellites, the effective dielectric constant is mostly a measure of the degree of depolarization of the incident waves by the regolith. It thus provides insight into the subsurface structure (porosity, heterogeneity) rather than composition (although a pure water ice regolith will favor scattering in the subsurface volume by allowing large penetration depth). This is why very low effective dielectric constants are possible for a depolarized water ice medium, even though the bulk dielectric constant of water ice is 3.13 at cm wavelengths (e.g., Mätzler, 1996; Paillou et al., 2008).

Scattering parameter f

The parameter $f = (1 + \mu_L)/f_{\mathrm{CBE}}$ is derived by finding the value which yields the best fit for each combination of thermal inertia I, skin depth ratio r, and effective dielectric constant ε'_r. Small values of f indicate important scattering in the subsurface volume. Given the boundaries of μ_L and f_{CBE}, f should be bounded between 0.5 ($f_{\mathrm{CBE}} = 2$ and $\mu_L = 0$) and 2 ($f_{\mathrm{CBE}} = 1$ and $\mu_L = 1$). However, we always find $f < 0.5$, which implies that the CBE is not sufficient to explain the high recorded backscattering cross sections; this is further discussed in Chapter 6.

5.3.3 Application to Rhea, Dione, and Iapetus

Previous work applied this model only to radiometry taken concurrently with the scatterometry, thus taking advantage of the identical coverage and geometry (Janssen et al., 2011; Le Gall et al., 2014, 2017). As detailed in Chapter 3, there is only one resolved scatterometry observation each for Dione, Rhea, and Iapetus, which therefore only covers a restricted area on each satellite. In order to apply the CEB model to other observations of varying coverage, geometry, and resolution, we implement the following adjustments.

Rhea

The RH127 scatterometry data only cover the anti-Saturn side of Rhea, including a large part of the Inktomi Ejecta Blanket Region (IEBR) (Section 3.3.3 and Fig. 3.11). We create a simplified map $\sigma^0_{\mathrm{map}}(\theta,\phi) = (\sigma^0(\theta,\phi))/(2ncos^n\theta_{\mathrm{eff}})$ by averaging all values far (>30°in latitude/longitude away) from Inktomi crater and assigning the resulting value to the entire disk, except for the region near Inktomi where a 2-dimensional Gaussian fit is applied to the data. The resulting map is displayed in Fig. 5.7.

Dione

The DI163 scatterometry data only cover the sub-Saturn side of Dione, and exhibits a leading/trailing dichotomy (Section 3.3.3 and Fig. 3.12). For our initial analysis of the Dione radiometry, we preferred not to use this dataset, which is plagued by an uncertainty in the pointing offset. Instead, we divide Dione into 45° latitude and longitude bins, a size large enough to contain enough data for a fit and small enough to take into account spatial variations and in particular the leading/trailing dichotomy. In each of these areas and for each set of parameters (I,r,ε'_r), we find the best-fit value of f, assuming $\sigma^0/(2n\cos^n\theta_{\mathrm{eff}}) = 0.529$, the mean value from the Dione scatterometry. We then combine

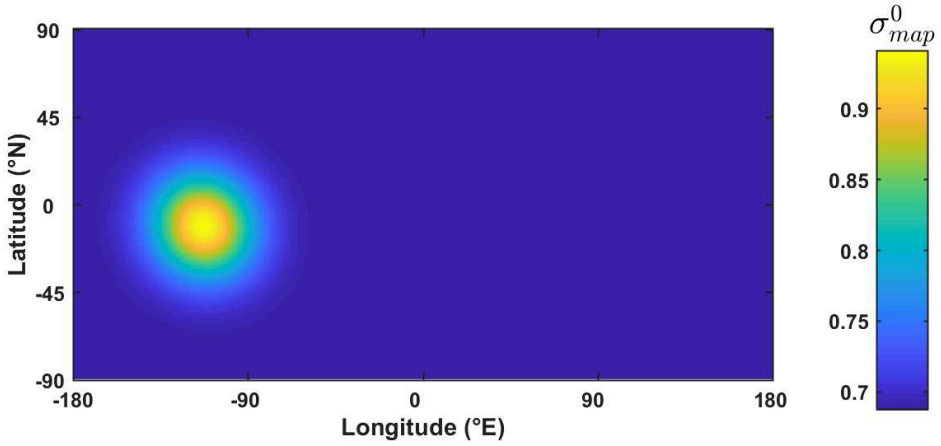

Figure 5.7 – Simplified map of the backscatter over Rhea. The IEBR is modeled as a 2-dimensional Gaussian increase in backscatter.

the data over all of Dione to derive the three other parameters (I,r,ε'_r). We expect the extracted emissivity to display a leading/trailing dichotomy, anti-correlated with the variations of the NRCS with longitude (i.e., a lower emissivity on the leading than the trailing side).

Iapetus

The IA049-3 scatterometry data covers the leading hemisphere of Iapetus, and shows a strong contrast between the optically dark Cassini Regio and the optically brighter polar regions, Ronceveaux Terra and Saragossa Terra. This data has been examined by Wye (2011) and Le Gall et al. (2014). Le Gall et al. (2014) applied the same emissivity model described herein on Iapetus, while also including a quasi-specular component of the backscattering cross-section, which is necessary for an accurate fit of the backsatter response with incidence angle:

$$\sigma^0(\theta,\phi) = a\cos^n\theta + \sigma^0_{p_{qs}}(\theta,\phi) \tag{5.16}$$

Le Gall et al. (2014) used the distant observations to adjust the ratio $(1+\mu_L)/f_{\mathrm{CBE}}$, and derived the emissivity of each radiometry burst from the concurrent scatterometry data. They then proceeded to finding the best-fitting values of the thermal inertia and skin depth ratio from the IA049-3r radiometry data independently in Cassini Regio and the polar terrains (Ronceveaux and Saragossa Terra). Le Gall et al. (2014) did not, however, jointly fit consecutive distant scans of the same regions: this analysis was therefore undergone as part of my thesis.

The scatterometry data samples only Cassini Regio well enough to derive accurately its scattering properties: the polar regions were only observed at high incidence angles, and the optically bright trailing hemisphere terrain was not scanned. We opted against using the scatterometry data in the emissivity model, which simplifies the model and makes it applicable to the whole surface. We therefore use a uniform value of $\sigma^0/(2n\cos^n\theta_{\mathrm{eff}}) = 0.1$, the average value in Cassini Regio, before finding the factor $f = (1+\mu_L)/f_{\mathrm{CBE}}$. In reality, $\sigma^0/(2n\cos^n\theta_{\mathrm{eff}})$ is likely to be much higher than 0.1 at the poles and in the trailing hemisphere: the values of f derived are therefore only valid for the leading hemisphere. Even within Cassini Regio, Le Gall et al. (2014) detected local variations in the backscatter, probably caused by a large impact crater named Falsaron. Because such variations are not accounted for in the uniform emissivity model, we expect them to appear in the residuals between our model and the observations.

5.4 Simulating the antenna temperature

5.4.1 Obtaining the brightness temperature

At this point, we can produce a simulated brightness temperature map using the following formula:

$$T_B(I, r, \varepsilon'_r, f, \theta, \phi) = e(\varepsilon'_r, f, \theta, \phi) \times T_{\text{eff}}(I, r, \theta, \phi) \tag{5.17}$$

which depends on the observation geometry (θ, ϕ), two thermal/electrical parameters (I,r), and two emissivity parameters (ε'_r,f). An example of simulated emissivity, effective temperature and brightness temperature maps is shown in Fig. 5.8.

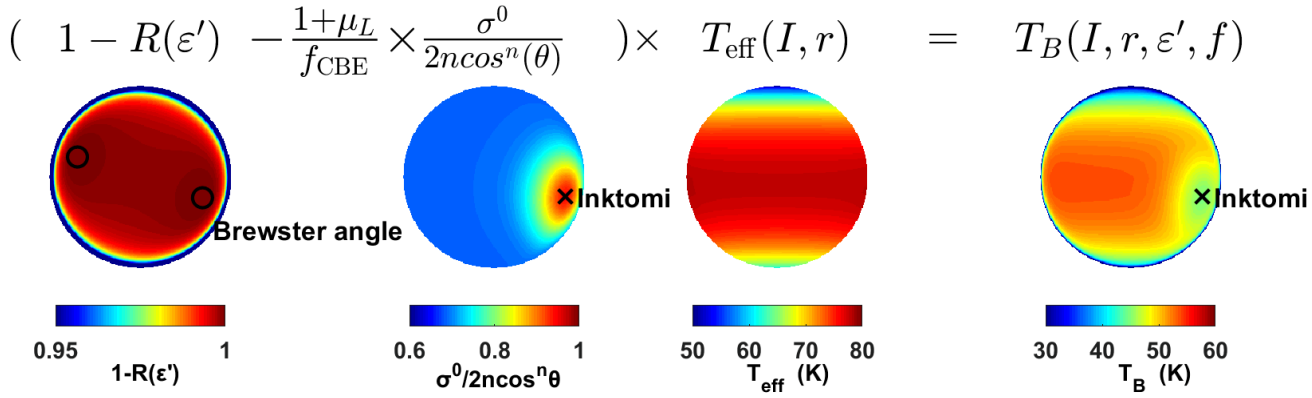

Figure 5.8 – Visualization of the Combined Emissivity-Backscatter (CEB) model for the following parameter values: $\varepsilon'_r = 1.15$, $I = 250$ MKS and $r = 100$. The quasi-specular component $1 - R(\varepsilon'_r)$ and the simplified scatterometry map $\sigma^0/(2n\cos^n\theta_{\text{eff}})$ used in the diffuse component of the emissivity model are shown in the first two diagrams, followed by the effective temperature map $T_{\text{eff}}(I, r)$ and the resulting brightness temperature distribution $T_B(I, r, \varepsilon'_r, f) = e(\varepsilon'_r, f) \times T_{\text{eff}}(I, r)$. The positions of the Brewster angles (where $R(\varepsilon'_r) = 0$) are shown with circles; Inktomi is marked with an ×. All maps are shown as seen by the Cassini spacecraft at the time of the RH127 observation (the sub-spacecraft latitude was 0°N).

5.4.2 Convolution with the beam pattern

The final step in simulating antenna temperatures consists in convolving the brightness temperature map with the beam pattern. We separate the diffuse and quasi-specular components of the emissivity before convolution, yielding the following equation for the antenna temperature $T^{\text{model}}_{A,0}$:

$$T^{\text{model}}_{A,0}(I, r, \varepsilon'_r, f) = \iint_{4\pi} (1 - R(\varepsilon'_r))\, T_{\text{eff}}(I, r) g d\Omega - f \iint_{4\pi} \sigma^0_{\text{map}} T_{\text{eff}}(I, r) g d\Omega \tag{5.18}$$

where g is the normalized beam pattern and $d\Omega = \sin\theta d\theta d\phi$ is the solid angle in the viewing direction (θ, ϕ); all variables, except f, are functions of the viewing direction. Because the integral does not have to be calculated for each value of f, separating the two components of the emissivity reduces computation time. We apply this convolution with the beam pattern for the geometry of each time step, thus obtaining a time sequence which can be directly compared to the calibrated antenna temperatures measured by the Cassini radiometer (e.g., Fig. 4.1).

Before being able to compare the modeled antenna temperatures to the observations, there is one last required step: the baseline must be subtracted from the simulated data. Indeed, during

the distant scans, the icy satellite (Rhea or Dione) is almost always present in the near sidelobes during the cold sky observations, and the modeled temperature thus does not reach zero. Since this contribution was removed from the observed T_A when subtracting the radiometer temperature baseline (see Section 4.2.3), the exact same method must be applied to the modeled $T_{A,0}^{\text{model}}$ in order to obtain final modeled antenna temperature time sequence T_A^{model}.

5.4.3 Data fitting method

Deriving the factor f

Although Eq. 5.18 may suggest that f could be derived directly by comparison to the data for each combination of (I,r,ε'_r), this is in fact not possible because the baseline must be subtracted after calculation of f. Instead, for each combination of the parameters I, r, and ε'_r and for 15 values of f from 0 to 1, we compute T_A^{model} and the reduced weighted chi-squared statistic χ_r^2, as follows:

$$\chi_r^2 = \frac{\sum_{t_0}^{t_f} w \times \left(\frac{T_A^{\text{obs}} - T_A^{\text{model}}}{\sigma} \right)^2}{\sum_{t_0}^{t_f} w} \tag{5.19}$$

where σ is the measurement uncertainty defined in Chapter 4 (Eq. 4.8), t_0 and t_f are the start and end time of the observation, and w is a weight calculated from the distance between consecutive observations (described below). Plotting χ_r^2 versus f as in Fig. 5.9 yields a parabolic curve, whose minimum indicates the best value for f.

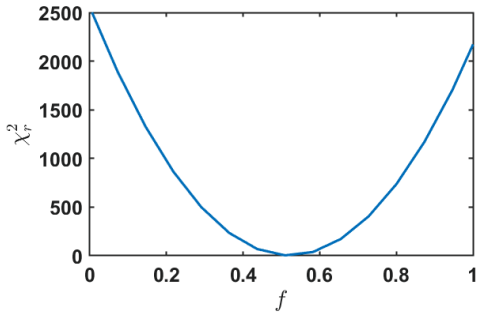

Figure 5.9 – Example of the relation between χ_r^2 and f, for a fit on the South pole of Rhea with a thermal inertia of $I = 250$ MKS and a skin depth ratio of $r = 69$. In this case, the minimal value of χ_r^2 is found for $f = 0.49$.

Calculating the weights w

When we include the stares or the resolved scan in the fit, the observations are not uniformly distributed in time and space. For example, stares observe a unique point at the satellite's surface many times during tens of minutes. These consecutive observations of the same region are thus not independent, and should not be given more weight than the observations of the same region during a much faster but independent distant scan. This also poses a problem for the resolved datasets (RH127_4r, DI163_1r, and IA049-3_1r), which have repetitive coverage near the limbs but not near nadir. In order to take into account the varying resolution and spatial coverage, each observation is weighted by the angular distance Δd separating it from the previous observation:

$$w = \Delta d \tag{5.20}$$

The best fitting value for each parameter (I,r,ε'_r) is the one giving the smallest χ^2_r ($\chi^2_{\mathrm{r,min}}$), for the best value of f determined above. The 2-σ error bars on the parameters are found using the 95% confidence intervals from the χ^2 statistics, taking into account the number of DOF (degrees-of-freedom).

On Rhea and Iapetus, there is an additional weighting factor accounting for possible regional variations in subsurface properties; these weights are described in Section 5.4.5.

Mapping f and e

For each satellite, we first fit all data simultaneously, regardless of expected regional differences in surface and subsurface properties. This fit is generally poor; however, mapping its residuals allows us to examine which regions appear to behave differently from the others at 2.2 cm wavelengths. These regions are then fitted independently to determine their subsurface properties.

If we assume uniform thermal inertia, skin depth ratio, and dielectric constant over the whole surface of a satellite, then we can attribute the large residuals to changes in emissivity (and albedo in the case of Rhea). In this approach, the satellite's surface is divided into 45° latitude and longitude bins, a size large enough to contain enough data to constrain f and small enough to account for most spatial variations. In each of these areas and for each set of parameters (I,r,ε'_r), we find the best-fit value of f following the method described above. We then combine the data over all of the satellite and calculate a global χ^2_r. The value of f found within each 45×45° region is used to calculate the emissivity e (Eq. 5.15), assuming a uniform value of $\sigma^0(\theta,\phi)/(2ncos^n\theta_{\mathrm{eff}})$. An emissivity map results, which is most reliable where repeat observations have been acquired.

On Iapetus, observations of the Northern polar regions during the IA00B, IA00C, and IA017 scans include signals from both the leading and trailing hemispheres, which exhibit very different behaviors. Thus, the data poleward of 60°latitude are excluded from the emissivity map, and 30° latitude and longitude bins were used globally. For the resolution and coverage of the Iapetus radiometry dataset, this is still a large enough region size to derive the emissivity map.

On Rhea, the bolometric Bond albedo was assumed constant over the surface (see Section 5.1.3), even though it should actually be higher on the leading than the trailing side (Howett et al., 2010; Pitman et al., 2010; Howett et al., 2014). Emissivity and albedo are largely degenerate parameters in our model (this is observed and discussed in Section 6.2.2). Thus regions with low emissivity in the "emissivity" map can be explained by lower emissivity and/or higher albedo than their surroundings (i.e., their brightness temperature is colder, due either to low emissivity and/or high albedo). On Dione and Iapetus, however, a bolometric Bond albedo map was used for the thermal model and should take into account most temperature variations due to albedo. On these satellites, the emissivity map does represent emissivity, assuming that I,r,ε'_r are uniform.

5.4.4 Deriving subsurface thermal, physical, and compositional properties

As detailed above, the best-fit parameters I, $r = \delta_{\mathrm{el}}/\delta^{\mathrm{day}}_{\mathrm{th}}$, ε'_r, and $f = (1+\mu_L)/f_{\mathrm{CBE}}$ are those that provide the best fit, i.e., the lowest value of $\chi^2_{\mathrm{r,min}}$. To obtain the 95% confidence interval on each parameter, we first adjust the uncertainties on the time-sequence data such that $\chi^2_{\mathrm{r,min}} = 1$. The maximum allowed χ^2_r values within a 95% confidence interval are obtained using a χ^2 table (available online, e.g. at https://www.medcalc.org/manual/chi-square-table.php), where the number of degrees of freedom is determined by the number of observations, minus 4 (the number of free parameters). The asymmetrical 2-σ error bars correspond to the minimum and maximum values of each parameter

allowed within the 95% confidence interval.

The best-fit parameters and their uncertainties are then converted into diurnal, seasonal (Eq. 5.11), and electrical skin depths (Eq. 2.13), assuming a temperature of $T_0 = 75$ K when calculating the specific heat capacity. Using a lower T_0 would yield higher thermal and electrical skin depths and a lower loss tangent. The emissivity e is derived from the dielectric constant ε'_r and the factor f (Eq. 5.15). For a low-loss medium like porous water ice and assuming all losses are due only to absorption (i.e., no scattering loss), the loss tangent is derived from the wavelength λ (2.2 cm), the electrical skin depth $\delta_{\rm el}$, and the dielectric constant ε'_r according to Eq. 2.13, given again here for clarity:

$$\tan\delta \approx \frac{\lambda}{2\pi\sqrt{\varepsilon'_r}\delta_{\rm el}} \tag{5.21}$$

From $\tan\delta$ we can then derive the imaginary component of the permittivity, ε''_r (Eq. 2.7). We recall that a low value of ε''_r (and of $\tan\delta$) corresponds to a low-loss, transparent medium, through which the signal can travel easily: it is therefore associated with a large electrical skin depth $\delta_{\rm el}$. However, the low inferred dielectric constants and high measured radar brightness suggest important losses due to scattering (in addition to absorption). Thus the derived values for the loss tangent are strict upper bounds.

5.4.5 Application to Rhea, Dione, and Iapetus

Rhea

From the RH127 scatterometry data (Fig. 3.11) and the concurrent deconvolved brightness temperature map (RH127_4r in Fig. 4.6), it is obvious that areas near or within the Inktomi Ejecta Blanket Region (IEBR) are more radar-bright and radiometrically cold than their surroundings, strongly suggesting different thermal properties and/or emissivity in this region. The thermal emission model we have developed only accounts for differences in emissivity (using the scatterometry observations, see Section 5.3.3), while the local thermal inertia, ratio, and albedo may also be different. Due to the lack of a bolometric Bond albedo map and because there is not sufficient radiometry coverage in local hours or seasons, we cannot constrain the properties of the IEBR independently from those of its surroundings.

Instead, we treat the IEBR in two different ways: i) using the backscattering cross-section map $\sigma^0_{\rm map}$ as described in Section 5.3 while assuming all other parameters equal, or ii) fitting only the data with no Inktomi contribution and weighting the rest of the data to account for the contribution of the IEBR in the near sidelobes. To calculate the percent contribution of the IEBR to the antenna temperature, we first delineated this region using the enhanced three color global map of Rhea from Schenk et al. (2011), as shown in Fig. 5.10. We then convolved this map with the beam pattern to obtain the Inktomi crater filling fraction $\nu_{\rm IEBR}$ for each particular observation. Data "with no Inktomi contribution" are defined as those where the Inktomi areal filling factor is $\nu_{\rm IEBR} < 0.02$ (<2%). Because even these data are not entirely devoid of Inktomi contribution, we weighted them with the factor $(0.02 - \nu_{\rm IEBR})$. The final weights applied when calculating χ^2_r (from Eq. 5.19) on Rhea are therefore:

$$w = \Delta d \times (0.02 - \nu_{\rm IEBR}) \tag{5.22}$$

The results and interpretations of applying this method to Rhea are detailed in Section 6.2.

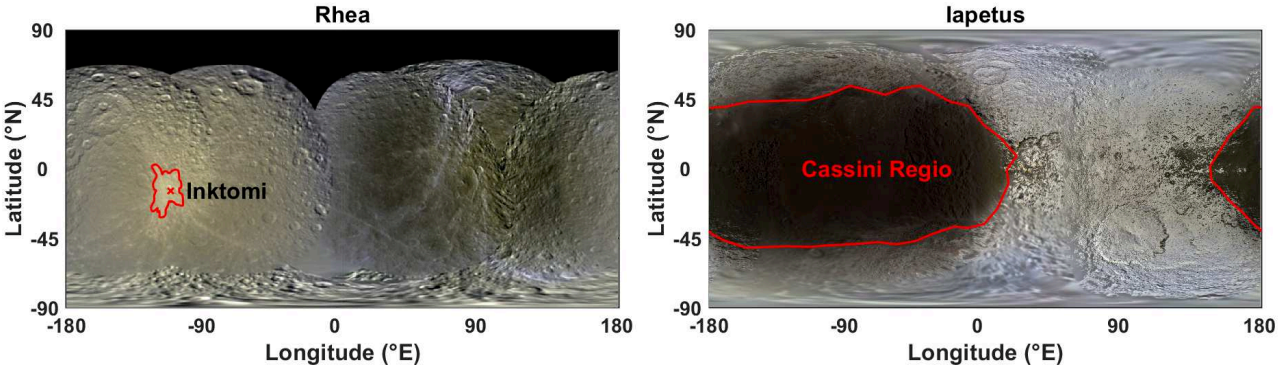

Figure 5.10 – Left: Outline of the IEBR, overlain on the enhanced three-color Rhea ISS mosaic from Schenk et al. (2011). The position of Inktomi crater is indicated. Right: Outline of Cassini Regio, overlain on the enhanced three-color Iapetus ISS mosaic from Schenk et al. (2018) (PIA 18436).

Dione

On Dione, the scarcity of the data and its poor resolution do not permit the detection of regional anomalies clearly correlated with geological or albedo features. We therefore used the weights and methods described above (Eq. 5.20) for the general case. The results and interpretations of applying this method to Dione are detailed in Section 6.3.

Iapetus

On Iapetus, there is a strong leading/trailing dichotomy apparent at all observed wavelengths, including in the 2 cm radar/radiometry data (Chapters 3 and 4). The emissivity cannot be mapped from the scatterometry data, which only covers a section of the leading hemisphere. Furthermore, different thermal properties are expected within the leading hemisphere optically dark terrain called Cassini Regio and the rest of Iapetus, as suggested by the best-fitting thermal inertias and skin depths found by Le Gall et al. (2014). Consequently, the data inside and outside of Cassini Regio are fitted separately, using a weighting method similar to the one applied to the IEBR on Rhea.

The outline of Cassini Regio is delineated from the enhanced three-color mosaic of Schenk et al. (2018), as illustrated in Fig. 5.10. As for Rhea, this map is then convolved with the beam pattern during each scan to obtain ν_{CR}, the Cassini Regio filling fraction. The cut-off value to select data within Cassini Regio was fixed at $\nu_{\mathrm{CR}} > 0.7$ (70%), whereas the cut-off value for data outside of Cassini Regio (i.e., the trailing hemisphere optically bright terrain, divided into Ronceveaux Terra in the Northern hemisphere and Saragossa Terra in the Southern hemisphere) is $\nu_{\mathrm{CR}} < 0.3$ (30%). The data selected within Cassini Regio is weighted as follows:

$$w = \Delta d \times \nu_{\mathrm{CR}} \tag{5.23}$$

Meanwhile, the data selected outside of Cassini Regio is given the following weights:

$$w = \Delta d \times (0.7 - \nu_{\mathrm{CR}}) \tag{5.24}$$

The results and interpretations of applying this method to Iapetus are detailed in Section 6.4.

5.4.6 Model limitations

Like most models, the ones used here have several limitations, which are important to keep in mind before examining the results of the parameter derivations. These assumptions and limitations have been detailed above, and are summarized here for convenience:

- Only heat transfer through conduction is considered (Section 5.1.2).
- Thermal properties are assumed uniform with depth and with temperature (Section 5.1.2).
- No physical model of thermal inertia and thermal conductivity is used, thus the physical properties of the subsurface (e.g., grain size, contact quality) cannot be derived (Section 5.1.3).
- Scattering is not physically accounted for in the radiative transfer model, although it is estimated in the emissivity model (Section 5.2.1).
- The model parameters (and the bolometric Bond albedo for Rhea) are assumed uniform in each fitted region, even though they are expected to vary regionally (Section 5.4.3).

These simplifications are necessary to keep a small number of free parameters, which can be derived from the data available, which is limited in resolution, spatial coverage, and temporal sampling.

5.5 Conclusion

By combining a thermal model, a radiative transfer model, and an emissivity-backscatter model, we derive simulated antenna temperatures for the Cassini radiometry observations of Saturn's icy satellites. The bolometric Bond albedo assumed is either mapped (according to Blackburn et al., 2011; Blackburn et al., 2012) or assumed constant when no map is available (on Rhea). The parameters of the model are the thermal inertia I, the ratio of electrical skin depth to diurnal thermal skin depth $r = \delta_{\mathrm{el}}/\delta_{\mathrm{th}}^{\mathrm{day}}$, the dielectric constant ε'_r, and the scattering factor $f = (1 + \mu_L)/f_{\mathrm{CBE}}$. The antenna temperature time sequence obtained can then be directly compared to the calibrated Cassini radiometry observations to determine the best fitting parameters.

Chapter 6

Derivation of thermal, physical, and compositional subsurface properties from Cassini radiometry

Once the radiometry data have been calibrated and processed (Chapter 4) and a model has been developed to simulate them (Chapter 5), the modeled antenna temperatures can be fitted to those observed. A simple comparison of disk-integrated antenna and effective temperatures yields a first estimate of the emissivity for Iapetus, Enceladus, Rhea, and Dione. Including the emissivity model and analyzing jointly all available data leads to new thermo-physical constraints for the subsurfaces of Rhea, Dione, and Iapetus.

6.1 Disk-integrated emissivities

Disk-integrated emissivities have been derived for the mid-sized icy satellites of Saturn by Ostro et al. (2006) from the early Cassini radiometry observations. These authors derived the emissivity from the disk-integrated temperatures by comparing them to the isothermal equilibrium temperature $T_{\rm eq} = 91.4(1 - A_B)^{1/4}$, where A_B is the bolometric Bond albedo, as a first approximation. Herein, we derive disk-integrated emissivities from all available Cassini radiometry data on Enceladus, Dione, Rhea, and Iapetus, using the thermal and radiative transfer models described in Chapter 5, which provide a much better estimate of the effective temperature sensed by the radiometer. This approach has been applied to Iapetus by Le Gall et al. (2014) and to Dione, Rhea, and Enceladus by Robin Sultana during his Master's internship in 2018 (co-supervised by Alice Le Gall and myself). These results, updated using the most recent calibration, processing, and thermal model described in previous chapters, are presented in this section.

This analysis yields some constraints on the thermal inertia, probed depths, and emissivity variations. However, it remains very limited: both an emissivity model and a comprehensive analysis of all overlapping observations is necessary. The results of applying the complete model and fitting method are described in Section 6.2 for Rhea, Section 6.3 for Dione, and Section 6.4 for Iapetus.

6.1.1 Method

For each combination of the thermal inertia I and the skin depth ratio $r = \delta_{\rm el}/\delta_{\rm th}^{\rm day}$ (parameters described in Chapter 5), we average the effective temperature map, obtained as detailed in Section 5.2, over the disk, yielding $T_{\rm eff}^{\rm disk}(I, r)$. In parallel, we determine the disk-integrated brightness temperatures for each scan $T_B^{\rm disk}$ as described in Section 4.3.1. Stare observations, which do not have global

coverage, are excluded from this analysis. The disk-integrated emissivity for each set of parameters is then given by:

$$e^{\text{disk}}(I, r) = \frac{T_B^{\text{disk}}}{T_{\text{eff}}^{\text{disk}}(I, r)} \tag{6.1}$$

This method is the same as that used by Le Gall et al. (2014) on Iapetus. Because these emissivities are integrated over the satellite disk and are obtained from global scans, the dependence of the emissivity on emission angle and polarization is also averaged over the disk. Note that, although we explore a wide parameter space (r from 0.01 to 1000 and I from 10 to 1000 MKS), implying a large range of electrical skin depths, electrical skin depths below 10 cm (<5 times the wavelength) are unlikely in a transparent medium such as a water-ice regolith. The thermal inertia / ratio combinations corresponding to such short skin depths, which generally yield very high emissivities (sometimes even higher than the unity which is not physical), are therefore very unlikely; they are grayed out in the figures shown herein.

The results of applying this method to the Enceladus, Dione, Rhea, and Iapetus Titan are given hereafter. We have not yet applied this method to Tethys and Mimas, where few Cassini radiometry observations have been acquired. Indeed, the short orbital period of Tethys and above all Mimas imposes a very short time step for the thermal model to accurately sample a day on these moons, leading to very long computation times and large file sizes. Moreover, Saturnshine (sunlight reflected by Saturn) and Saturn's thermal emission must be taken into account for these moons, which adds to flux computation times. These complications are also true of Enceladus, which was prioritized over Mimas and Tethys due to its current activity and more numerous Cassini radiometry observations. Furthermore, Le Gall et al. (2017) had already calculated the incident fluxes over Enceladus when examining the high-resolution observation.

6.1.2 Application to Iapetus

Previous work by Le Gall et al. (2014)

All Cassini observations of Iapetus have already been analyzed by Le Gall et al. (2014). These data have been re-reduced following the method described in Chapter 4. Although the systematic antenna pointing offset we corrected within the SPICE kernels was not known at the time, Le Gall et al. (2014) adjusted the pointing offset for each scan. The main difference between the re-reduction of the Iapetus radiometry and the data they presented is caused by the disk-integrated temperature fitting method, described in Section 4.3.1. Fitting a latitudinally varying temperature model yields better fits (lower χ^2 values) than with a uniform temperature model, leading to lower uncertainties in our brightness temperatures (Table 4.1) than in those of Le Gall et al. (2014). Nonetheless, even this difference in method is small, and we expect to find the same emissivities as Le Gall et al. (2014).

After deriving the emissivity values for each flyby, Le Gall et al. (2014) adjusted the thermal model to the resolved leading hemisphere observation (namely IA049-3 in Table 4.1), using the emissivity model described in Section 5.3 with an additional quasi-specular component in the backscattering cross-section σ^0. During this resolved observation, data were acquired on the optically dark equatorial terrain Cassini Regio (CR) and the optically bright mid-to-high latitude regions of Ronceveaux Terra (RT) in the North and Saragossa Terra (ST) in the South. These authors applied their fitting method separately to CR and jointly to RT and ST. Their results are summarized in Table 6.1. The thermal inertia they derived is higher than in the thermal infrared (15 – 30 MKS; Table 5.2; Spencer et al., 2005; Howett et al., 2010; Rivera-Valentin et al., 2011), indicating a likely increased

degree of compaction of the regolith at meter depths. The differences in thermal inertia, probed depth, and emissivity between the optically bright and dark terrains are most likely caused by the leading hemisphere optically dark material, which is emissive (high leading side emissivity) at 2.2 cm; Le Gall et al. (2014) favor tholins over iron oxides as a candidate for this leading hemisphere material.

Table 6.1 – Inferred parameters for Iapetus's optically dark terrain Cassini Regio (CR) and optically bright terrains Saragossa Terra (ST) and Saragossa Terra (ST), from Le Gall et al. (2014). The lower (LCL) and upper (UCL) confidence limits are given for the two model parameters, I and $r = \delta_{\rm el}/\delta_{\rm th}^{\rm day}$. See Le Gall et al. (2014) for further detail.

Region	I **(MKS)**			$r = \delta_{\rm el}/\delta_{\rm th}^{\rm day}$			$\delta_{\rm th}^{\rm day}$ **(cm)**	$\delta_{\rm el}$ **(m)**	e
	Mean	LCL	UCL	Mean	LCL	UCL			
CR	>200	50	1000	~7.0	0.5	100	59 (>15)	4.1 (>1.2)	0.87 (>0.85)
RT+ST	163	48	~560	3.6	0.7	9.5	48 (>14)	1.7 (>1.4)	0.78 (>0.74)

Updated results

Fig. 6.1 displays the derived emissivities for each (I, r) combination, on each scan of Iapetus. Both the I and $r = \delta_{\rm el}/\delta_{\rm th}^{\rm day}$ axes are shown in log scale to improve legibility. For some (I, r) combinations of several flybys (all except IA049-4 and IA017), the effective temperatures are actually lower than the disk-integrated brightness temperature. According to Eq. 6.1, this would yield $e^{\rm disk}(I, r) > 1$, which is not a physical value. These (I, r) combinations, which are portrayed in black in Fig. 6.1, must therefore be discarded. From the IA049-1, IA049-2, and IA049-3 observations, this implies that the leading hemisphere thermal inertia must be strictly larger than 20 MKS, consistent with the result of Le Gall et al. (2014) (Table 6.1). The leading/trailing dichotomy, already reported from this dataset by Ostro et al. (2006) and Le Gall et al. (2014), is also apparent in this visualization. The minimum emissivity derived on the leading side (flyby IA049-2) is $e^{\rm disk} > 0.86$, whereas on the trailing side (IA00C and IA049-4) we find (excluding probing depths below 10 cm) $0.71 < e^{\rm disk} < 0.90$, both consistent with Table 6.1 and Le Gall et al. (2014).

On the trailing side, radiometry data were acquired during the local night (IA00C; near midnight on 01 January 2005) and the local day (IA049-4; 10 AM on 10 September 2007). Both observed regions consist in mostly the optically bright trailing hemisphere terrain, and we can assume that they have similar thermophysical properties, including emissivity. In this case, the only possible (I,r) combinations are those which give the same emissivity within error for both flybys. The difference in emissivity is shown in Fig. 6.2 up to the uncertainty in emissivity. This simple method, much quicker than fitting modeled antenna temperatures jointly to both datasets, nevertheless yields some constraints for the skin depths, although the thermal inertia remains undetermined. We thus confirm that the electrical skin depth $\delta_{\rm el}$ must be larger than 1 m, with depths between 1 and 10 m being best. This result is consistent with those of Le Gall et al. (2014), from an in-depth analysis of only flyby IA049-3r (Table 6.1).

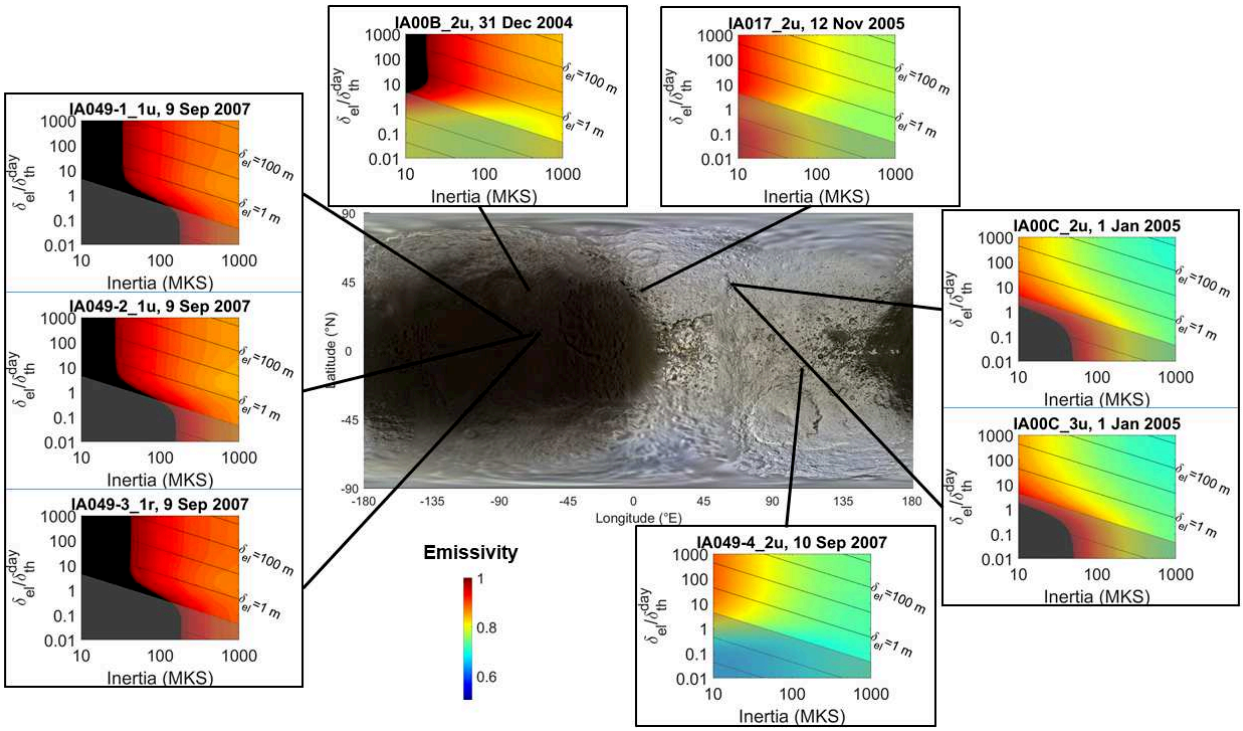

Figure 6.1 – Disk-integrated emissivities for different combinations of thermal inertia and skin depth ratio derived from all scans of **Iapetus**. Oblique lines indicate constant values of the electrical skin depths δ_{el}. Electrical skin depths below 10 cm (<5 times the wavelength), which often yield high emissivities, are unlikely in a water-ice regolith; they are therefore grayed out. The sub-Saturn point is at 0°E and the anti-Saturn point at +/-180°E. The background map is the global enhanced 3-color Iapetus mosaic (PIA 18436). The bolometric Bond albedo map shown in Fig. 5.3 is used as input to the thermal model. As in Le Gall et al. (2014), these data require a higher leading than trailing hemisphere emissivity.

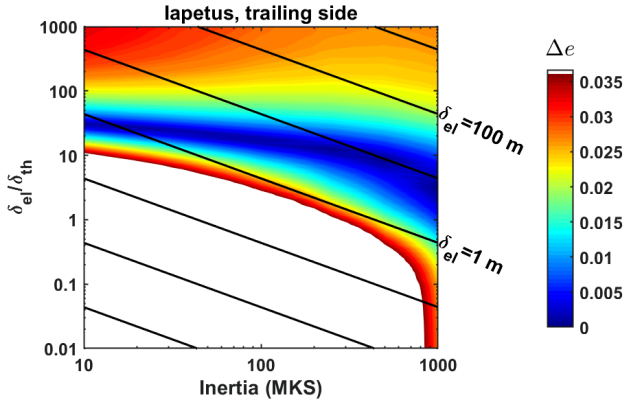

Figure 6.2 – Absolute value of the difference between the disk-integrated emissivities on the trailing side of Iapetus, inferred from the IA00C (January 2005, midnight local time) and IA049-4 (September 2007, 10 AM local time) scans. Because both regions observed are dominated by the optically bright trailing hemisphere terrain, they should have very similar 2-cm emissivities. The difference in emissivities between flybys is shown up to the quadratic sum of the 1-σ uncertainties on the emissivities of each scan (see Section 4.2.5).

6.1.3 Application to Enceladus

Previous work by Ries and Janssen (2015) and Le Gall et al. (2017)

The resolved radiometry observations acquired during flyby EN156 (also called E16, as it was the 16th flyby of Enceladus) have been examined by Ries and Janssen (2015) on the leading and sub-Saturn sides, and by Le Gall et al. (2017) in the high Southern latitudes. Their results have been summarized in Sections 2.5.5 and 4.4.2, and include the discovery of a low-emissivity terrain on the leading hemisphere associated with a geologically young region (Ries and Janssen, 2015) and the detection of excess heat flux in the South polar region (Le Gall et al., 2017).

Incident fluxes on Enceladus

The orbit of Enceladus lies at only $4.1 R_{\text{Saturn}}$ from the planet's center. Saturn as seen from Enceladus thus has an angular size of 26.8°. In consequence, the thermal infrared emission from Saturn $F_{\text{S,IR}}$ and the visible solar flux reflected off Saturn $F_{\text{S,VIS}}$ are not negligible at Enceladus. The flux absorbed at Enceladus then takes the following form:

$$F_{\text{absorbed}} = (1 - A_B) \times (F_{\odot} \cos \delta_{\odot} + F_{\text{S,VIS}} \cos \delta_{\text{S}}) + (1 - A_{\text{IR}}) \times F_{\text{S,IR}} \cos \delta_{\text{S}} \tag{6.2}$$

where A_B is the bolometric Bond albedo of Enceladus, $A_{\text{IR}} = 0.05$ is the infrared reflectivity of Enceladus, and $\delta_{\odot}$ and δ_{S} are the incidence angle of the solar and Saturn flux, respectively. In the model computing the incoming flux on Enceladus, Saturn was divided into a 15 by 15° grid. The solar flux reflected on Saturn was integrated on the illuminated side of the planet visible from each surface point on Enceladus, assuming a bolometric Bond Saturn albedo of $A_B^{\text{Saturn}} = 0.34$ (Hanel et al., 1983). The thermal infrared component, meanwhile, is integrated over the full disk of Saturn with effective temperature 95 K, and is assumed to be homogeneous with Saturn latitude and longitude. Once the absorbed flux is calculated, the remaining steps of the thermal and radiative transfer models are as described in Chapter 5. The infrared flux from Saturn, which permanently affects the sub-Saturn side of Enceladus regardless of time or season, has an important heating effect in this region. The visible solar flux reflected on Saturn (the so-called Saturnshine) also heats only the sub-Saturn side, though only during the local night at the satellite, i.e. when Saturn's facing side is illuminated.

Le Gall et al. (2017) found that accounting for Saturn's visible and infrared contribution to the absorbed flux is indeed mandatory at Enceladus. During the E16 high-resolution scan on the southern high latitudes, they found that Saturn flux could contribute > 5 K of heating on the sub-Saturn side, as shown in Fig. 6.3. Due to Saturn's large angular side, it also affects, to a lesser but non-negligible degree, temperatures on the anti-Saturn high-latitudes.

Results

Fig. 6.4 displays the derived emissivities for each (I, r) combination, on each scan of Enceladus. Here, we assume a uniform bolometric Bond albedo of $A_B = 0.85$, the same value used by Ostro et al. (2006) and within the range of estimates from infrared data (see Table 5.2). In reality, the albedo is expected to be fairly variable over the surface (e.g., Pitman et al., 2010; Howett et al., 2010). To first order, modeled physical temperatures are proportional to $(1 - A_B)^{1/4}$. Thus, lower values of A_B would yield lower derived emissivities than shown here. The leading hemisphere, which already features some of the lowest derived emissivities, is expected to have a lower albedo than the rest of Enceladus (Pitman et al., 2010), which would result in even lower emissivities. This is consistent with the large-scale low-emissivity leading hemisphere terrain detected by Ries and Janssen (2015), and also apparent in the deconvolved maps of Fig. 4.6.

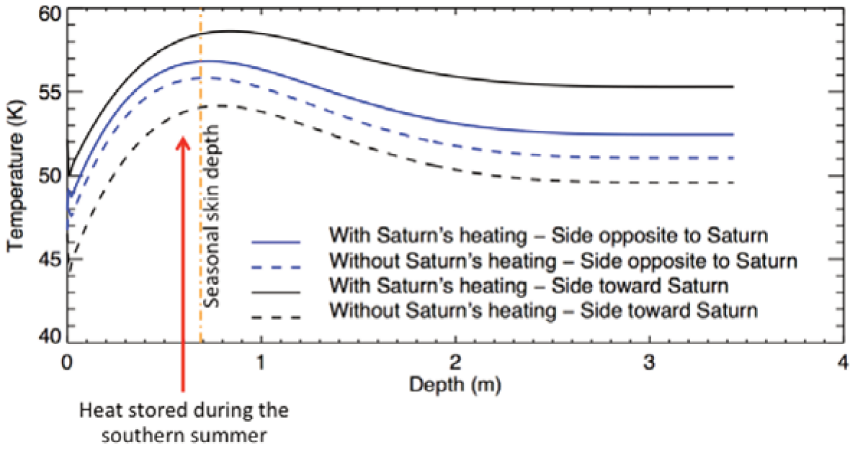

Figure 6.3 – Temperature profile below the surface at a latitude of 60°S, on the sides toward and opposite to Saturn, at the epoch of the E16 closest approach as predicted by the thermal model accounting or not for Saturn's heating (both due to Saturn's infrared radiation and to the reflection of the sunlight on Saturn). The subsurface was here assumed to have a thermal inertia of 20 MKS. Around the seasonal skin depth (~70 cm for a thermal inertia of 20 MKS), the temperature rises due to the heat stored during the past southern summer. Figure from the Supplementary Materials of Le Gall et al. (2017).

Globally, the emissivities are always comprised within 0.5 and 0.7, although this range may be extended in case of large albedo variations. Such low microwave emissivities are most likely caused by subsurface scattering on buried void or inhomogeneities (as detailed in Section 2.5.1). The exceptionally low leading hemisphere emissivities would then be caused by increased subsurface scattering, due either to increased purity of water ice (Le Gall et al., 2019) or to backscatter from structures buried under a relatively thin regolith (Ries and Janssen, 2015). Both hypotheses point to a geologically young terrain.

As on Iapetus, two successive observations of mostly the same region occurred at the same season but different local times: EN003 (~1 AM on 17 February 2005) and EN032 (~11 AM on 8 November 2006). While the lowest emissivity difference between these two flybys, displayed in Fig. 6.5, suggests thermal inertias under 500 MKS and probed depths around 0.1 – 10 m, the uncertainty on the emissivity does not allow us to derive any reliable constraints within this region.

To properly exploit the Enceladus observations, an emissivity model and a joint fit over several scans would be necessary, as used in the following sections on Rhea, Dione, and Iapetus. However, such an analysis is more complex in the case of Enceladus due to i) unknown variations in bolometric Bond albedo (as on Rhea), ii) the necessity for very short time steps in the thermal model to properly sample the eclipses (especially for flyby EN156, which occurs during an eclipse), substantially increasing both computation times and file sizes, iii) the difficult calibration of flyby EN156, with Saturn and its rings in the background, and iv) the particularity of the leading hemisphere terrain, which must be modeled or fitted separately.

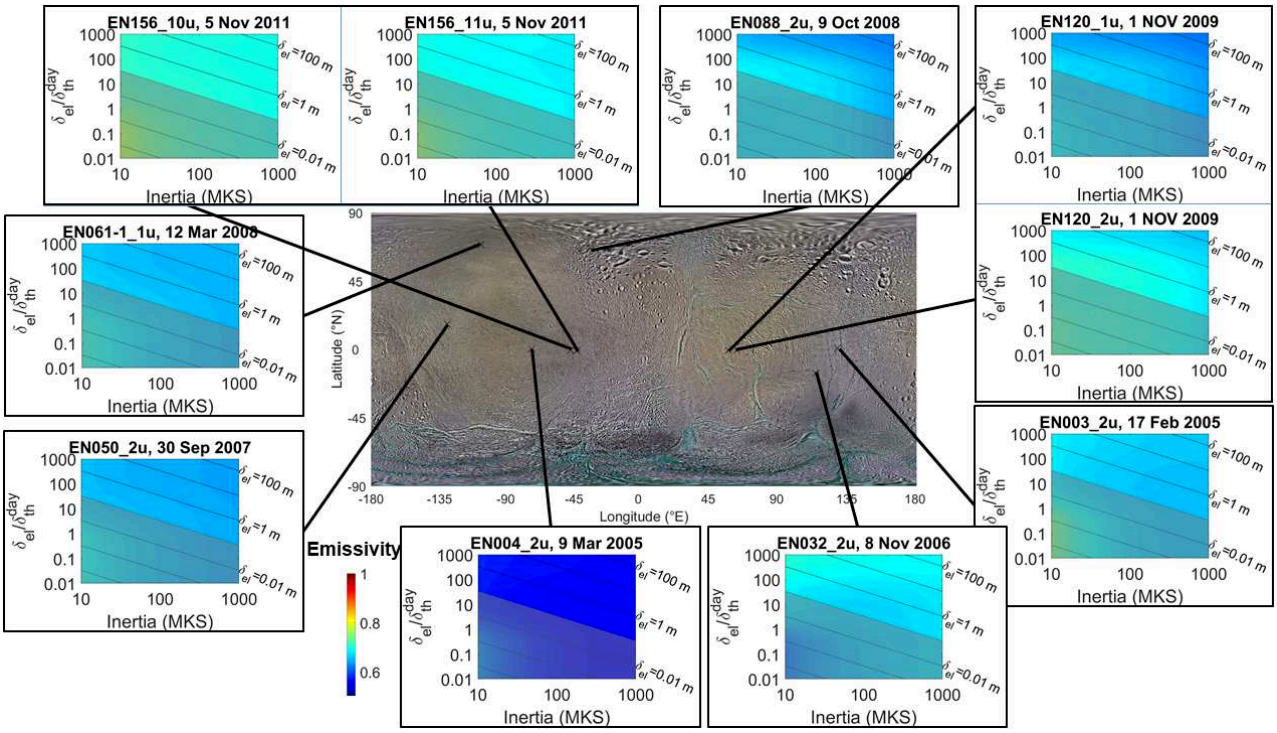

Figure 6.4 – Same as Fig; 6.1, for **Enceladus**. The background map is the global enhanced 3-color Enceladus mosaic (PIA 18435). In the absence of bolometric Bond albedo map, a uniform bolometric Bond albedo of 0.85 is assumed. In reality, the albedo is expected to be fairly variable over the surface (see Table 5.2). An albedo lower than 0.85 would yield lower emissivities than shown here.

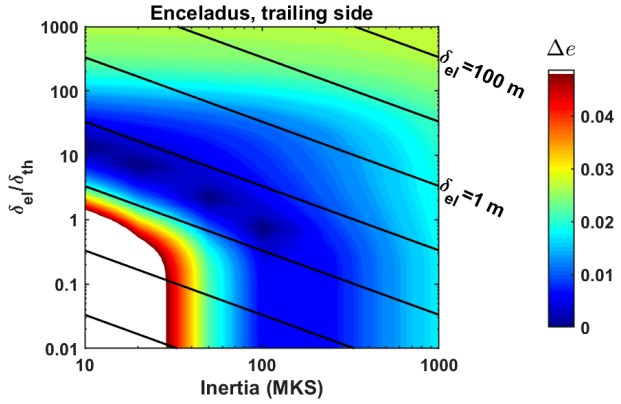

Figure 6.5 – Absolute value of the difference between the disk-integrated emissivities at the Sub-Saturn side inferred from the EN003 (February 2005, ~1 AM local time) and EN032 (November 2006, ~11 AM local time) scans. The difference in emissivities between flybys is shown up to the quadratic sum of the 1-σ uncertainties on the emissivities of each scan.

6.1.4 Application to Dione

Fig. 6.6 displays the derived emissivities for each (I, r) combination, on each scan of Dione. The emissivities measured during flybys DI177 (near the geologically young Creusa crater) and DI050 (near the optically dark trailing hemisphere terrain) are very similar, and always within $0.695 < e^{\text{disk}} < 0.808$, a little higher than those on Enceladus, most likely due to the presence of more non-icy contaminants on Dione than on Enceladus. However, we would expect the optically dark trailing hemisphere material to exhibit a high emissivity (as on Iapetus) and the icy, blocky crater ejecta to have a low emissivity. The fact that the emissivities of both of these regions are similar despite their sampling different terrains suggests that, in both regions, the radiometer probes the icy substrate.

Meanwhile, for flybys DI016 and DI163, both of which sample the sub-Saturn side, the emissivities are $e^{\text{disk}} > 0.786$, and can reach values above unity. This is an unexpected result, since there is no obvious reason for the sub-Saturn side to be compositionally or structurally different from the rest of Dione. Although local variations in emissivity are possible, it is likely that the thermal model underestimates the sub-Saturn temperatures on Dione. Indeed, we did not account for Saturn's heating (i.e., both the sunlight reflected by Saturn and the infrared thermal emission from the planet) when computing the incident fluxes on Dione, assuming that they would be negligible at an orbital radius of $6.5R_{\text{Saturn}}$. The abnormally high derived sub-Saturn disk-integrated emissivities suggest that Saturn's contribution to the incident flux is actually not negligible for Dione. This is further discussed in Section 6.3.3.

Fig. 6.7 examines the difference in derived emissivity between flybys DI016 (October 2005, 1 AM local time) and DI163 (March 2012, 7 PM local time). Apart from excluding electrical skin depths below 10 cm for $I < 100$ MKS (which is already strongly suspected as we expect to probe deeper than ~ 5 times the wavelength), this technique cannot constrain the subsurface properties of the sub-Saturn region. This is most likely because the difference in local time only affects subsurface temperatures down to shallow depths, and seasonal temperature variations have little effect at the equator.

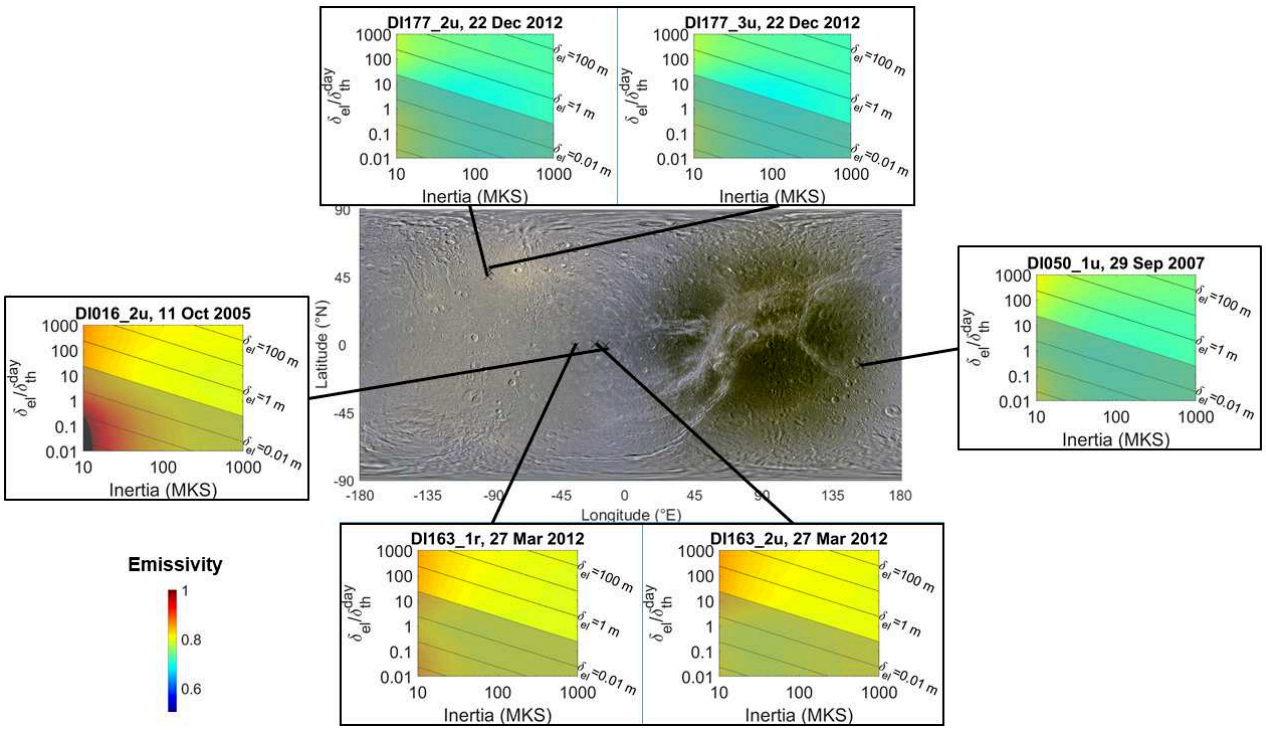

Figure 6.6 – Same as Fig; 6.1, for **Dione**. The background map is the global enhanced 3-color Dione mosaic (PIA 18434). The bolometric Bond albedo map shown in Fig. 5.3 is used as input to the thermal model.

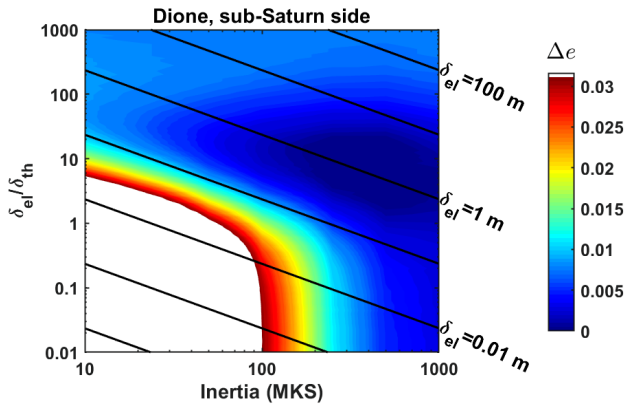

Figure 6.7 – Absolute value of the difference between the disk-integrated emissivities at the Sub-Saturn side inferred from the DI016 (October 2005, 1 AM local time) and DI163 (March 2012, 7 PM local time) scans. The difference in emissivities between flybys is shown up to the quadratic sum of the 1-σ uncertainties on the emissivities of each scan.

6.1.5 Application to Rhea

Fig. 6.8 displays the derived emissivities for each (I, r) combination, on each scan of Rhea. A uniform bolometric Bond albedo of $A_B = 0.55$ was assumed; as for Enceladus, decreasing the albedo would correspondingly decrease the emissivities. Globally, emissivities are on average lower on Rhea than on Dione, although they can vary significantly with thermal inertia, ratio, and albedo. For the same parameters (I,r), we find slightly higher emissivities for flybys RH018 and RH049, observations which are centered on the sub-Saturn side, than on the rest of Rhea. As on Dione, this may be caused by Saturn's contribution to the incident flux, which, although much less significant at an orbital radius of $9.1 R_{\mathrm{Saturn}}$, still has a non-negligible effect on subsurface temperatures. Alternately, the high sub-Saturn emissivities may be due to the presence of a high-emissivity or low-albedo anomaly in this region.

In the South pole, data were collected during the Southern summer (RH011 in July 2005) and during the southern fall (RH177 in December 2012), both centered at a latitude of 77°S. Fig. 6.8 shows that, for most combinations of thermal inertia I and skin depth ratio r, very different emissivities are found for RH011_2u and RH045_1u (southern summer) than for RH177_1u and RH177_2u (southern fall). Yet, the near-surface emissivity is presumably independent of the season, implying that most of the (I, r) combinations can be excluded. Instead, the parameters for which the summer and fall datasets agree in terms of emissivity must be representative of the South pole's subsurface: as shown in Fig. 6.9a, this occurs for skin depth ratios near $r = 100$, yielding electrical skin depths around $\delta_{\mathrm{el}} = 0.5$ to 15 m i.e., 25 to 700λ. A large probing depth indicates a very transparent medium, and therefore a high degree of purity of the water ice regolith in this region; this is further discussed in Section 6.2.3. This result also implies that the 2.2 cm emissivity of Rhea's South pole must range from $e = 0.62$ to 0.72, for an albedo of $A_B = 0.55$.

In the anti-Saturn side, data were acquired in March 2006 (RH022) and in March 2010 (RH127). However, in the equatorial regions, the temperature does not change enough over these four years for any constraints to be derived using this simple method, as shown in Fig. 6.9b. Local time is very similar during these flybys (~23:00 and midnight; see Table 4.1), so daily temperature variations also cannot be detected. Going further requires the use of an emissivity model and simultaneous fitting on several scans, as in Section 6.2.

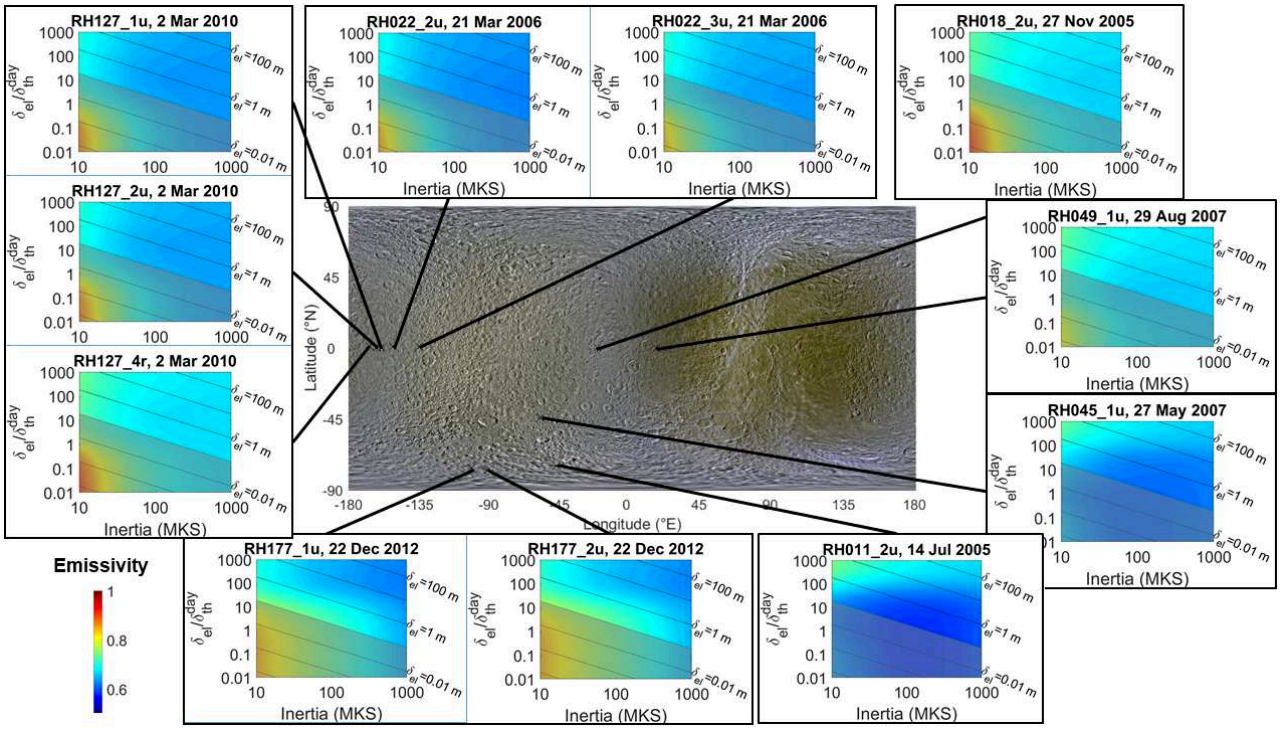

Figure 6.8 – Same as Fig; 6.1, for **Rhea**. The background map is the global enhanced 3-color Rhea mosaic (PIA 18438). A uniform bolometric Bond albedo of $A_B = 0.55$ is assumed.

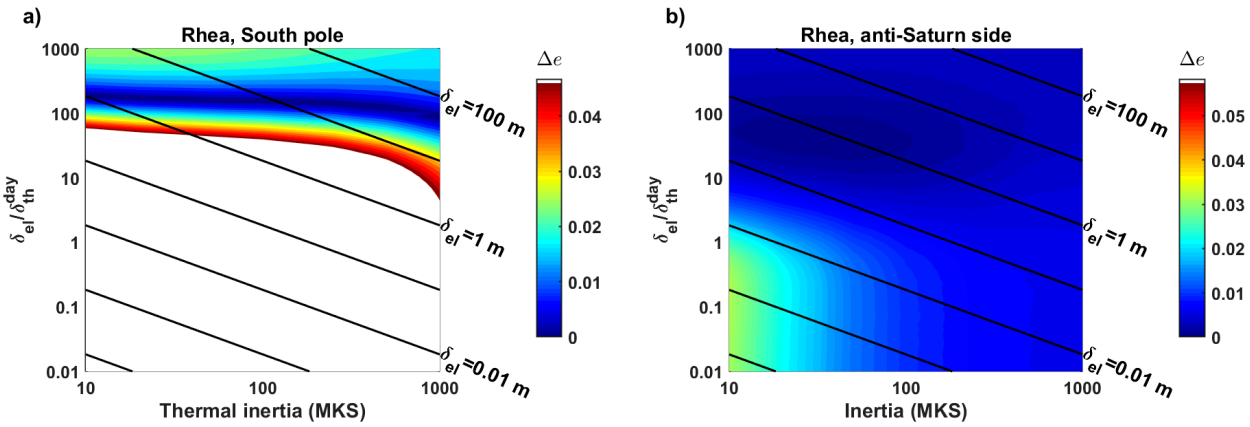

Figure 6.9 – Absolute value of the difference between the disk-integrated emissivities at (a) the South pole inferred from the RH011 (July 2005) and RH177 (December 2012) scans; (b) the Anti-Saturn side inferred from the RH022 (March 2006, 11:30 PM local time) and RH127 (March 2010, midnight local time) scans. The difference in emissivities between flybys is shown up to the quadratic sum of the 1-σ uncertainties on the emissivities of each scan. On the South pole, the skin depth ratio must lie approximately between 100 and 1000. On the anti-Saturn side, the seasonal temperature variations are insufficient to permit the derivation of any constraints with this method.

6.2 Thermal, structural, and compositional properties of Rhea's subsurface

After Titan, Rhea is the satellite which the Cassini radiometer observed the most; yet this dataset had so far not been exploited. I therefore focused primarily on Rhea during my thesis. The results and interpretations described herein have been published in Bonnefoy et al. (2020a).

6.2.1 Method

Radiometry observations have been acquired on Rhea during 9 flybys, including repeated observations of the sub-Saturn, anti-Saturn, and South polar regions. To investigate the thermal and electrical properties of different regions of interest of Rhea, we apply the fitting method described in Section 5.4 first to all data jointly (with and without including the poles). Regional differences in albedo and emissivity are taken into account together as described in Section 5.4.3; the IEBR is either masked or modeled as an emissivity anomaly (Section 5.4.5). Then, the fitting method is applied separately for each well-sampled region: the South pole (latitudes poleward of 50°S), the sub-Saturn side (0 ± 45°E; <50°latitude), and the anti-Saturn side (180±°E; <50°latitude). There is too little coverage on the North pole and the trailing hemisphere for their analysis, and the leading hemisphere is contaminated by the Inktomi crater ejecta blanket, which clearly has very specific chemical and/or thermophysical properties.

6.2.2 Results

We recall that the Inktomi Ejecta Blanket Region (IEBR) was either modeled as an emissivity anomaly or masked while the remainder of the data was weighted according to distance to Inktomi crater (Section 5.4.5). The results obtained in both cases are reported in Table 6.2 when Inktomi is within the region of interest (i.e., not for the sub-Saturn side), assuming a bolometric Bond albedo of $A_B = 0.55$. Fig. 6.10 illustrates the 2-σ confidence regions in the (I,r) space, for best fit values of ε'_r and f. We note that the electrical skin depths are generally larger than or comparable to the seasonal thermal skin depths (Table 6.2), indicating that the Cassini radiometer is sensitive to seasonal, rather than only diurnal, temperature variations on icy satellites.

For the emissivity e, we find values in the range $0.62 - 0.76$ assuming $A_B = 0.55$. This range is extended to $0.59-0.84$ if the albedo is allowed to vary from 0.42 to 0.72. These emissivities are largely consistent with the value of 0.59 derived by Ostro et al. (2006) using fewer observations, a Bond albedo of $A_B = 0.45$, and a very simple temperature model. For the ranges of (I,r) shown in Fig. 6.10 and for the flybys in each considered region, the disk-integrated emissivity from Section 6.1.5 is within error of the values given in Table 6.1. For example, on the South pole, the emissivity within the 2-σ best fitting ellipses in the (I,r) domain extends from 0.62 to 0.68, within error of the value shown in Table 6.2 ($0.65^{+0.03}_{-0.03}$) for a bolometric Bond albedo of 0.55. Slightly smaller disk-integrated emissivities (by $\sim$ 0.02) are generally obtained in regions including Inktomi and its ejecta blanket. The constraints on the thermal inertia and skin depth ratio obtained using the emissivity-backscatter model and fitting all available South polar data (Table 6.2 and Fig. 6.10) are also perfectly within the range of those obtained from the disk-integrated emissivities on the South pole (Fig. 6.9).

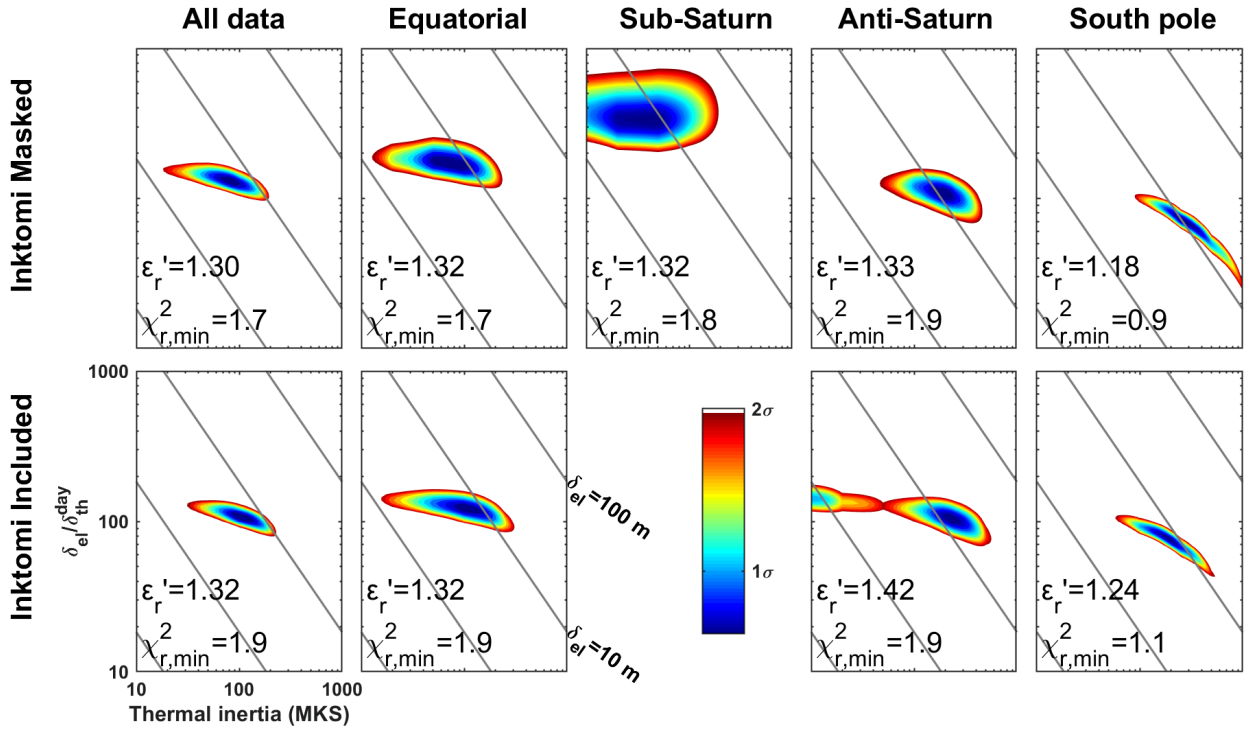

Figure 6.10 – 2-σ best fitting ellipses in the (I,r) domain, for best-fit values of ε'_r (see Table 6.1 for the other parameters) for each of the 5 regions where the fitting method was applied on Rhea, and for each of the two different ways to treat the Inktomi ejecta blanket (masked or not). The minimum reduced χ^2 value ($\chi^2_{r,\mathrm{min}}$) is indicated for each fit. The bolometric Bond albedo used is $A_B = 0.55$. Note that, while the thermal inertia and skin depth ratio vary, the best-fit electrical skin depth δ_{el} always remains within 5–15 m.

Table 6.2 – Best-fit parameters and associated 2-σ error bars in different regions of **Rhea**, assuming a uniform global bolometric Bond albedo of $A_B = 0.55$. A higher albedo yields lower scattering factors f and higher emissivities e, but barely changes the other derived parameters. The Inktomi ejecta blanket region is handled with two different methods: either it is masked and the fit is applied to the rest of the region ("Masked"), or it is included but treated as an emissivity anomaly, with a Gaussian dependence with distance to Inktomi itself ("Included"); see Section 5.3.3 for details. Note that Inktomi being located on the anti-Saturn Southern hemisphere, it has no influence on the sub-Saturn data. When the error bars reach the boundaries of the range of tested values for the thermal inertia ($10 < I < 1000$), the actual error bars cannot be known, and *MIN* or *MAX* are indicated instead. The electric and thermal skin depths were calculated assuming zero porosity; their actual values for non-zero porosities are likely larger ($\propto 1/(1-p)$). The loss tangent, inversely proportional to the electrical skin depth, would be lower for higher porosities.

	Inktomi	$\chi^2_{\mathrm{r,min}}$	I **(MKS)**	$r = \frac{\delta_{\mathrm{el}}}{\delta_{\mathrm{th}}^{\mathrm{day}}}$	ε'_r	$f = \frac{1+\mu_L}{f_{\mathrm{CBE}}}$	δ_{el} [c] **(m)**	e **(at nadir)**	$\delta_{\mathrm{th}}^{\mathrm{day}}$ [c] **(cm)**	$\delta_{\mathrm{th}}^{\mathrm{season}}$ [c] **(m)**	$\tan\delta$ [c] **$\times 10^{-3}$**
All data[a]	Masked	1.7	83^{+107}_{-64}	132^{+34}_{-32}	$1.30^{+0.06}_{-0.06}$	$0.45^{+0.02}_{-0.05}$	$6.0^{+5.4}_{-4.4}$	$0.69^{+0.03}_{-0.01}$	$4.5^{+5.9}_{-3.5}$	$2.2^{+2.9}_{-1.7}$	< 1.9
	Included	1.9	114^{+104}_{-82}	105^{+27}_{-22}	$1.32^{+0.06}_{-0.06}$	$0.46^{+0.02}_{-0.04}$	$6.6^{+4.3}_{-4.3}$	$0.68^{+0.02}_{-0.01}$	$6.3^{+5.7}_{-4.5}$	$3.0^{+2.8}_{-2.2}$	< 1.3
Equatorial[a]	Masked	1.7	72^{+157}_{-59}	174^{+77}_{-54}	$1.32^{+0.06}_{-0.06}$	$0.45^{+0.02}_{-0.07}$	$6.8^{+12.0}_{-5.5}$	$0.69^{+0.04}_{-0.01}$	$4.0^{+8.5}_{-3.2}$	$1.9^{+4.2}_{-1.6}$	< 2.1
<50°S/N	Included	1.9	105^{+197}_{-89}	120^{+38}_{-33}	$1.32^{+0.08}_{-0.06}$	$0.46^{+0.02}_{-0.07}$	$6.9^{+8.9}_{-5.7}$	$0.68^{+0.04}_{-0.01}$	$5.7^{+10.8}_{-4.8}$	$2.8^{+5.2}_{-2.4}$	< 2.5
Sub-Saturn	Absent	1.8	50^{+140}_{-MIN}	331^{+393}_{-122}	$1.32^{+0.18}_{-0.12}$	$0.42^{+0.02}_{-0.09}$	$9.1^{+38.4}_{-MIN}$	$0.70^{+0.06}_{-0.01}$	$2.7^{+7.7}_{-MIN}$	$1.3^{+3.7}_{-MIN}$	–[b]
0°E±45°											
Anti-Saturn	Masked	1.9	209^{+228}_{-159}	105^{+47}_{-36}	$1.33^{+0.07}_{-0.07}$	$0.48^{+0.01}_{-0.02}$	$11.9^{+11.9}_{-8.6}$	$0.67^{+0.01}_{-0.004}$	$11.4^{+12.4}_{-8.7}$	$5.5^{+6.0}_{-4.2}$	< 0.9
180°E±45°	Included	1.9	229^{+320}_{-MIN}	105^{+69}_{-36}	$1.42^{+0.07}_{-0.07}$	$0.47^{+0.01}_{-0.09}$	$13.1^{+11.8}_{-12.4}$	$0.67^{+0.06}_{-0.003}$	$12.5^{+17.5}_{-MIN}$	$6.1^{+8.5}_{-MIN}$	–[b]
South pole	Masked	0.9	275^{+MAX}_{-184}	69^{+36}_{-44}	$1.18^{+0.12}_{-0.10}$	$0.50^{+0.04}_{-0.04}$	$10.4^{+MAX}_{-5.4}$	$0.65^{+0.03}_{-0.03}$	$15.0^{+MAX}_{-12.0}$	$11.4^{+MAX}_{-5.8}$	< 0.6
>50°S	Included	1.1	200^{+325}_{-139}	76^{+34}_{-32}	$1.24^{+0.14}_{-0.10}$	$0.49^{+0.04}_{-0.04}$	$8.3^{+4.8}_{-4.8}$	$0.66^{+0.03}_{-0.02}$	$10.9^{+17.7}_{-7.6}$	$5.3^{+8.6}_{-3.7}$	< 0.9

[a] For the global and equatorial fits, we calculate the factor f separately in bins of 45 by 45° before fitting all data jointly. The value given here is the global average.
[b] No upper bound can be extracted for $\tan\delta$ if no lower bound was found for the thermal inertia.
[c] The values given herein were calculated for a bulk density of $\rho_0 = 992\mathrm{kg/m^3}$. The correct value for crystalline water ice is $\rho_0 = 918\mathrm{kg/m^3}$, leading to an 8% underestimation of depths, and overestimation of $\tan\delta$.

Effect of surface roughness

We further note that these results are obtained while neglecting surface roughness. However, we have checked that this assumption does not change the results by also deriving the quasi-specular component of the emissivity according to the model proposed by White and Cogdell (1973), which includes large-scale surface roughness as a new parameter. For a representative sub-section of the data (only one scan for each flyby, thus ignoring repeat scans and the resolved observation), we always obtain the same best-fitting thermal inertias I and skin depth ratios r as with the smooth model (as given in Table 6.2). For the South pole and the anti-Saturn side the derived dielectric constant remains the same and the best-fitting roughness is minimal (1° rms slope). On the anti-Saturn side, the highest tested value of roughness (35°rms slope) yields the best fit, with a correspondingly higher dielectric constant (1.75 instead of 1.3 – 1.4). The large number of parameters of this model leads to degeneracy between several parameters and overfitting of the model; consequently, error bars should be very high and interpretations on surface roughness would be speculative. Nonetheless, the fact that we always find the same best I and r while the dielectric constant ε'_r remains < 2 provides confidence in the robustness of the results obtained assuming a smooth surface.

Effect of the bolometric Bond albedo

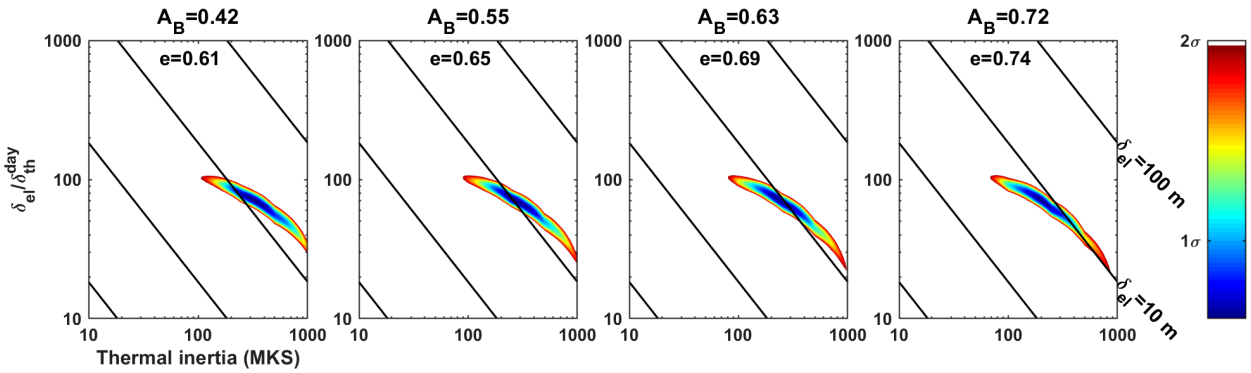

Figure 6.11 – 2-σ best fitting ellipses in the (I,r) domain for the South pole (> 50°S), for four different values of the bolometric Bond albedo A_B and for $\varepsilon'_r = 1.2$. Note that the derived ratio remains the same, but the inferred thermal inertia and the electrical skin depth $\delta_{\rm el}$ decrease with increasing albedo. The value of the emissivity at nadir for the best fit parameters is indicated; as expected it increases with albedo.

Modifying the albedo uniformly across Rhea mostly affects the absolute values of the brightness temperature, rather than its spatial or temporal variations. A higher albedo leads to colder modeled physical temperatures (at first approximation they are proportional to $(1 - A_B)^{1/4}$) and therefore the emissivity required to fit the observations must be higher (Fig. 6.11), which further implies a higher scattering factor f. Thus f and the bolometric Bond albedo A_B are essentially degenerate parameters, while the remaining parameters change little with albedo. This is true only to first order: we note a small difference in the derived thermal inertias, and consequently in the electrical skin depth and loss tangent, as a function of A_B (see Fig. 6.11 for the case of the South Pole). Including the influence of the global value of the albedo would increase the error bars on the derived parameters by about 10%, but would not change the overall results (except for the scattering factor f and emissivity e) which is why we only show the case where $A_B = 0.55$ in Table 6.1.

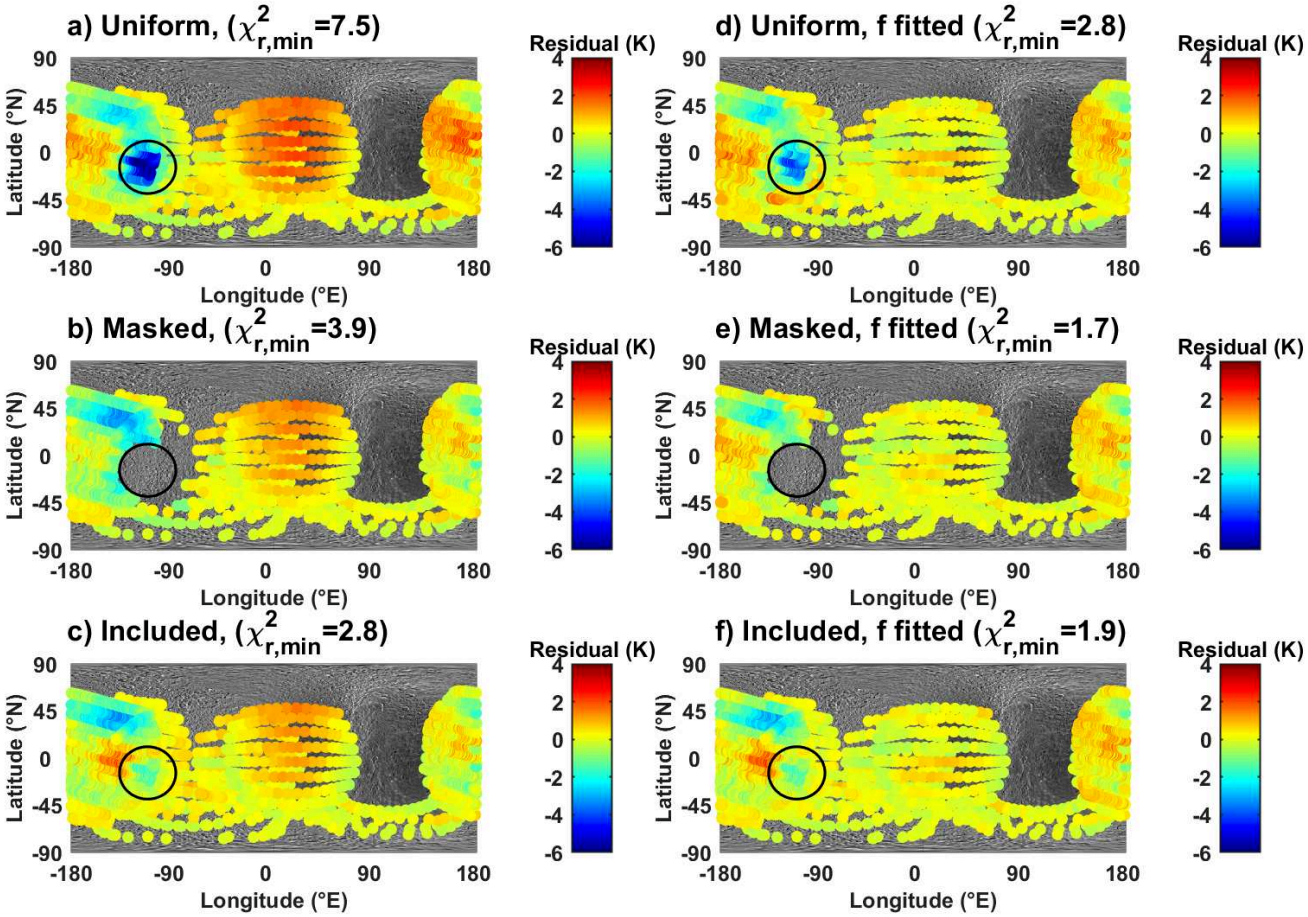

Figure 6.12 – Residual maps after fitting the model to all Rhea data, (a) Assuming emissivity is uniform over the whole satellite (b) Excluding data with an Inktomi contribution > 2% (c) Modeling the Inktomi ejecta blanket as a change in emissivity, Gaussian with distance from Inktomi. (d), (e), and (f) use the same treatment of Inktomi as (a), (b), and (c), respectively, while dividing f into 45° latitude and longitude bins. In each map, the position of the Inktomi ejecta blanket is indicated by a black circle.

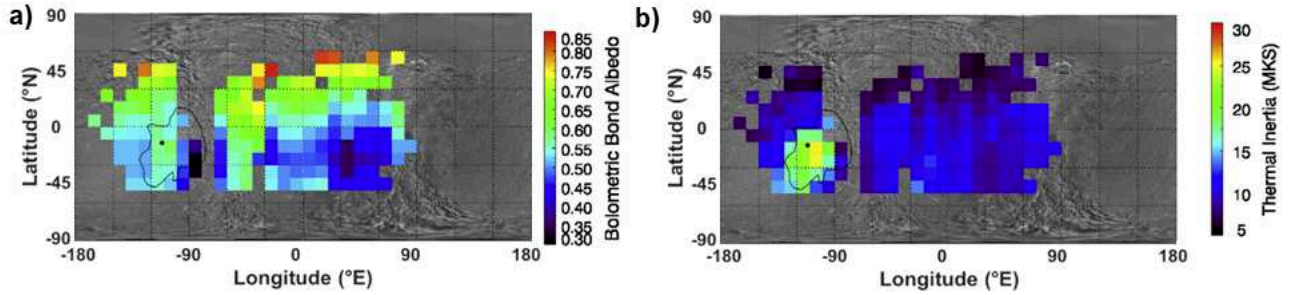

Figure 6.13 – Maps of thermophysical properties for Rhea derived from CIRS data by Howett et al. (2014). The base-map is the Rhea ISS map PIA08343. The black solid contour shows the approximate edge of the Inktomi ejecta blanket, whilst the dark circle at 14.1°S and 112.1°W shows the location of the Inktomi crater. Note that the positions of the leading and trailing hemispheres are inverted in these maps as compared to other maps herein. (a) Bolometric Bond albedo map of Rhea. (b) Thermal inertia map of Rhea.

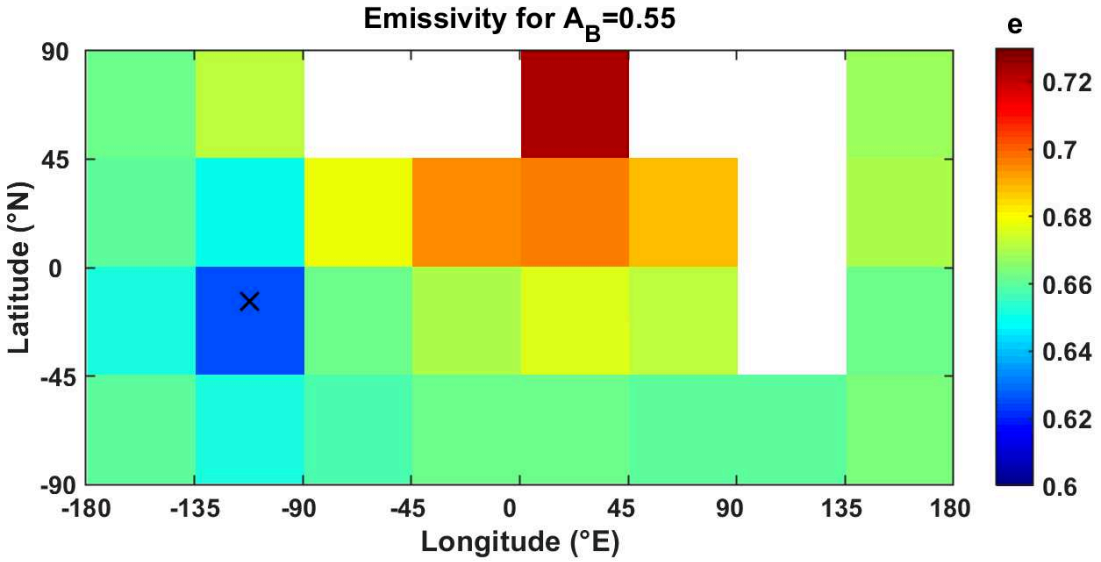

Figure 6.14 – Emissivity map assuming a uniform albedo $A_B = 0.55$, using all available data. The emissivity is assumed constant in every 45×45° latitude/longitude bin. There is no data available in the white regions; the emissivities between 45 and 65°N are based on a few limb observations and are less reliable. Because emissivity and albedo cannot be separated, apparent lower emissivity regions observed in this map may instead be caused by locally higher bolometric Bond albedos (and vice versa for high emissivity regions).

Regional albedo/emissivity variations

The local value of the albedo, however, may have a significant influence on the observed temperature map. Indeed, applying our fitting methods to the data from all flybys at once yields imperfect fits ($\chi^2_r > 2.8$), with the residual clearly showing, whether Inktomi is masked or not, an anomaly on the sub-Saturn side (longitude of 0°E; Fig. 6.12b and c). More localized anomalies are also apparent on the leading hemisphere (longitudes of -180 to 0°E). At first order, these poor fits may be explained by albedo and/or emissivity variations at the surface of Rhea.

Interestingly, the model degeneracy between the subsurface scattering parameter f and the bolometric Bond albedo A_B allows us to account for the variations in both parameters simultaneously by fitting f separately in 45° latitude by 45° longitude regions, using the method detailed in Section 5.4.3. The parameters (I,r,ε'_r) are assumed uniform over all of Rhea, while the subsurface scattering and albedo are allowed to vary spatially (but cannot be disentangled). With this method, much better fits are obtained; the residuals $\chi^2_{r,\min}$ are indicated in Fig. 6.12e & f for both different ways of treating the IEBR (masked or included and modeled using the scatterometry data), with and without dividing f into smaller regions. This method is applied to all data at once, and to the equatorial data only (i.e, at latitude within ±50°), with and without Inktomi (Table 6.1). Once f has been calculated in each 45° region, we can compute the emissivity in each region using Eq. 5.15, assuming a constant albedo; the resulting map is shown in Fig. 6.14. We recall that, as discussed in Section 5.4.3, emissivity and albedo effects cannot be disentangled using this method.

We find a low-emissivity/high-albedo anomaly spatially correlated with the IEBR (Fig. 6.14). To examine the influence of the IEBR, Fig. 6.12 shows the residual of a global fit obtained assuming the emissivity is uniform over Inktomi, without (Fig. 6.12a) then with (Fig. 6.12d) dividing f into 45° squares. The strong negative residual near Inktomi and the poor quality of the fit testify of the necessity to either i) mask the IEBR (Fig. 6.12b & e) or ii) model the IEBR as an emissivity anomaly (Fig. 6.12c & f). Figs. 6.12c & f also show a positive residual to the West of Inktomi: this is because

the Inktomi crater ejecta is, in fact, butterfly-shaped rather than circular as was modeled.

We also find a high-emissivity/low-albedo anomaly on the sub-Saturn side, especially in the northern hemisphere (see Fig. 6.14). Conversely, the partial bolometric Bond albedo map derived from CIRS observations by Howett et al. (2014) (pictured in Fig. 6.13) shows an increase in albedo from -30°N to 60°N. This contradiction is partially explained by the scarcity of radiometry data at northern latitudes, while the southern latitudes were observed on several occasions, causing an artificial North/South asymmetry (especially given the large 45° step size). On the other hand, our results are consistent with a higher albedo at the South pole than at the Equator (except near Inktomi), as also found by Howett et al. (2016). Lastly, Fig. 6.12 reveals another cold spot to the North-west of Inktomi (-180 – -100°E, 45°N), which is associated with a slight increase in the backscatter image. This cold spot is not correlated to any optical or IR anomaly, but does coincide with a large part of Tirawa crater, the largest crater on Rhea. Further interpretation of this anomaly would require more high-resolution data which cannot be obtained in the foreseeable future; it thus remains to be interpreted.

Regional variations in terms of thermal and dielectric properties

Because all of the observations were taken during the local night (sub-spacecraft point between 20:00 and 00:30 local time, see Table 5.2), the thermal inertia of the equatorial regions can only be approximately constrained. However, at high latitudes, seasonal variations in temperature are much more prevalent. In particular, at the South pole of Rhea, radiometry data were collected during the southern summer and fall. Combining summer and fall observations provides reliable constraints on the thermal properties of the near-subsurface. Fits for the South pole are especially good ($\chi^2_{r,\min} \sim 1$), and are shown in Fig. 6.15, where the effects of the different parameters are illustrated separately. Lower values of the thermal inertia yield warmer modeled temperatures in the summer (2005), and colder in fall (2012), as the subsurface retains less heat (Fig. 6.15f). The same is true for the skin depth ratio: small ratios only probe the top layers, where the temperature changes more quickly with incoming solar flux, leading to warm summer temperatures and cold fall temperatures (Fig. 6.15g). The χ^2_r maps (Fig. 6.15a, b, & c) show that the derived thermal inertia ($I = 70 - 850$ MKS), ratio ($r = 20 - 100$), and dielectric constant ($\varepsilon'_r = 1.09 - 1.35$) are still somewhat correlated, while the best determined parameter is the electrical skin depth (4 – 12 m).

While constraining thermal properties requires to have a sample of data collected at different times of the day (especially for the equatorial region) or of the year (especially for the poles), the determination of the dielectric constant requires observations at different emission and polarization angles. As expressed in Eq. 5.15 and described in Section 5.3.2, the dielectric constant mainly intervenes in the quasi-specular component of the emissivity model, described by Fresnel's coefficients. More specifically, the dielectric constant controls both limb darkening and the emissivity variations around the Brewster angle. However, observing either of these characteristics and deriving the effective dielectric constant is possible only with relatively high-resolution observations such as RH127 (sub-Saturn; resolution of $0.1-0.5R_{\mathrm{Rhea}}$) and RH177 (South pole; resolution of $0.3-0.4R_{\mathrm{Rhea}}$). As seen in Fig. 6.15e, only the last two flybys (RH127 and RH177) show changes of the modeled temperature with ε'_r, and are therefore useful for the derivation of this parameter.

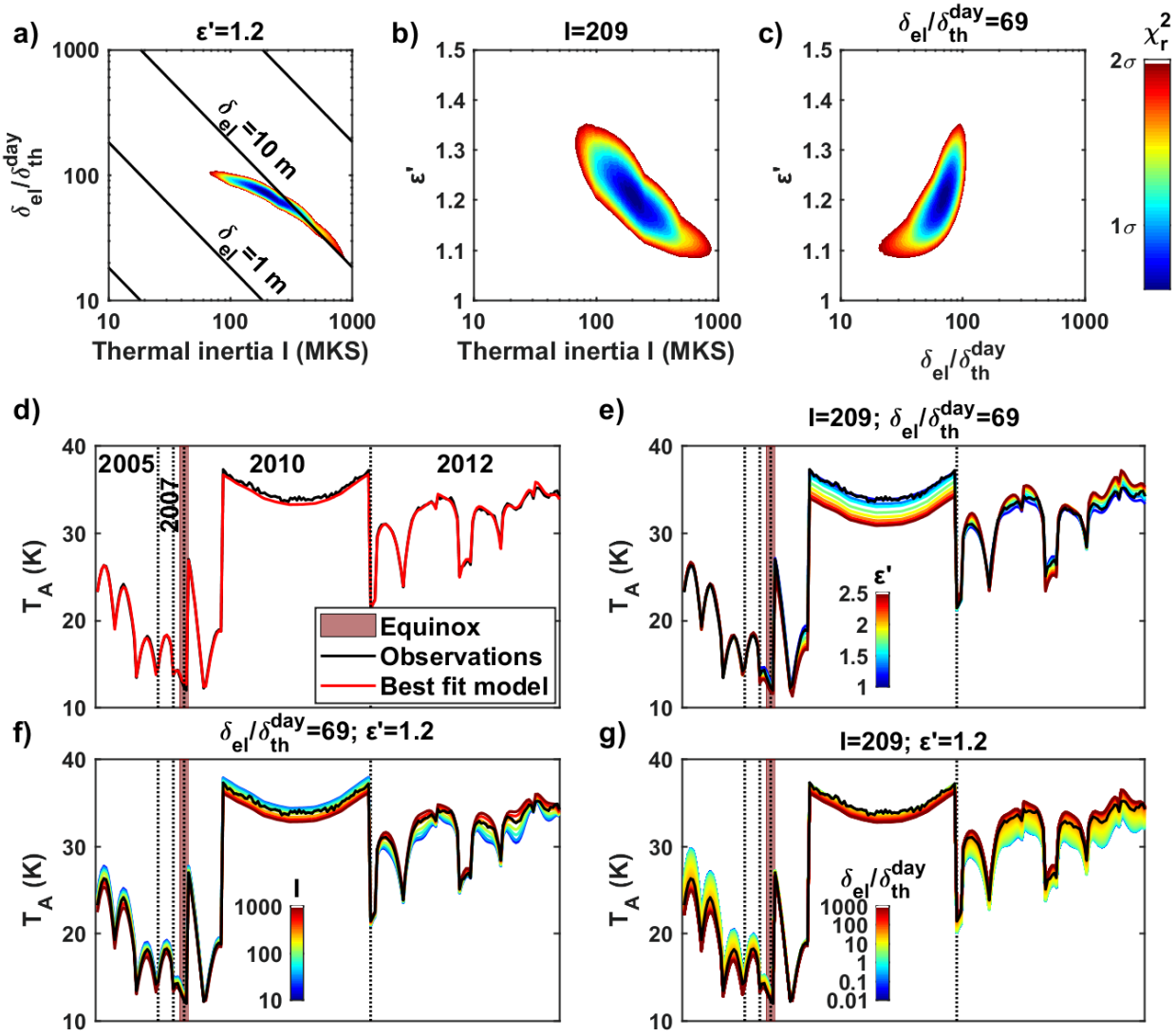

Figure 6.15 – Results of the fitting procedure in the South pole of Rhea (>50°S), assuming a uniform emissivity map and a bolometric Bond albedo of $A_B = 0.72$. (a) 2-σ best fitting ellipses in the (I,r) domain. (b) 2-σ best fitting ellipses in the (I,ε'_r) domain. (c) 2-σ best fitting ellipses in the (r,ε'_r) domain. (d) Observed and best-fit modeled antenna temperatures T_A, given as a time sequence. Vertical dotted lines separate the data from different flybys, in order: RH011 (July 2005), RH045 (May 2007), RH049 (August 2007), RH127 distant then resolved (March 2010), and RH177 (December 2012). The southern fall equinox occurred in August 2009, between the RH049 and RH127 flybys, as indicated. Note that the 2005 temperatures (RH011) are the lowest even though they are in summer, because the resolution of this dataset is among the worse of all. (e) Modeled T_A for I and r constant, and ε'_r varying. (f) Modeled T_A for ε'_r and r constant, and I varying. (g) Modeled T_A for ε'_r and I constant, and r varying. Note that both the thermal inertia and the skin depth ratio are reasonably well constrained due to the observations at different seasons, whereas the dielectric constant is determined from the higher-resolution datasets (RH127 and RH177).

6.2.3 Interpretations and discussion

In this section, we examine the implications of the results of fitting the simulated antenna temperatures to Rhea radiometry observations. We look first at global compositional and structural characteristics derived for Rhea, then at regional variability.

Global results: composition

As a general result, we find that the Cassini radiometer is observing Rhea's subsurface down to depths of $\delta_{el} = 6 - 13$ m, with variable error bars. At the South pole, excluding Inktomi and for all considered albedo values, the minimum electrical skin depth is 3.8 m, which is 170 times the radiometer wavelength (2.2 cm). Large penetration depths indicate a low loss tangent ($\tan\delta < 1.1\times10^{-3}$ at the South pole; $\tan\delta < 4.7 \times 10^{-3}$ elsewhere) and a correspondingly small imaginary part of the electrical permittivity, pointing to a very transparent, non-absorbing medium. This further implies that the near subsurface of Rhea is composed of very pure water ice. As vacuum is even more transparent than water ice, high porosities would further decrease the loss tangent of the medium, and their presence is therefore also a likely explanation for the low observed loss tangents. Impurities, such as organics or silicates originating from impacts or dust from the Saturn system, would tend to reduce the transparency of the medium.

This interpretation is consistent with the high recorded backscattering coefficients and disk-integrated radar albedos (Chapter 3 and Le Gall et al., 2019) which are both indicative of ultra-clean water ice in the top few meters. The upper crust of Rhea was already suspected to be composed of pure water ice down to a depth of a few km based on the strong H_2O spectral signature identified by Cassini VIMS in the trailing hemisphere tectonic scarps and in the walls of recent craters (Stephan et al., 2012). The trailing hemisphere darkening and the leading hemisphere reddening apparent in visible and near-infrared data (Schenk et al., 2011) must then be due to a thin (i.e., at most a few centimeters) layer of contaminants, through which the radar/radiometer can easily see. Indeed, a non-icy layer tens centimeters thick would increase the emissivity and reduce the probed depth, as on the dark side of Iapetus (Le Gall et al., 2014).

Iapetus, the only other icy satellite of Saturn where the same method was applied, shows a lower radar brightness ($A^{disk}_{SL-2} = 0.3 - 1.0$; Section 3.2.2 and Le Gall et al., 2019), higher emissivities ($e = 0.74 - 0.87$), and shallower depths probed by the radiometer ($\delta_{el} = 1.2 - 4.1$ m) than on Rhea (Le Gall et al., 2014, 2019). These values are explained by the presence of absorbing contaminants, especially on Iapetus's leading side, introduced by the incoming Phoebe ring particles. Meanwhile, at Rhea, fluxes from Saturn's Phoebe ring, E ring, charged particles from the magnetosphere, and other solid impactors are expected to be very small (Verbiscer et al., 2009; Schenk et al., 2011; Howett et al., 2018; Hendrix et al., 2018), in agreement with a thin non-icy coating. An almost pure water ice upper crust suggests a relatively young surface; however, to accurately determine the age of the surface, a model of the micrometeoroid and large impactor flux and composition would be necessary, which is particularly difficult given the multiple sources of impactors (Kirchoff et al., 2018, and references therein). Moreover, these fluxes are expected to be different in different regions of Rhea (polar/equatorial, leading/trailing, sub-Saturn/anti-Saturn), so the well-constrained polar loss tangent is not applicable to all of Rhea.

Global results: structure

For very diffuse scattering surfaces such as those of the icy satellites, the effective dielectric constant is mostly a measure of the degree of depolarization of the incident waves by the regolith. It thus provides insight into the subsurface structure (porosity, heterogeneity) rather than composition

(although a pure water ice regolith will favor scattering in the subsurface volume by allowing large penetration depths). This is why very low effective dielectric constants are possible for a depolarized water ice medium, even though the bulk dielectric constant of water ice is 3.13 at cm wavelengths (e.g., Mätzler, 1996; Paillou et al., 2008). The low derived ε'_r values ($\varepsilon'_r = 1.07 - 1.5$, close to that of vacuum) indicate that little to no increase of the emissivity is detected at the Brewster angles: the near-surface mainly consists in an unpolarized regolith. Subsurface scattering by pores and/or inhomogeneities is the most likely cause of this depolarization of the outgoing signal.

We recall that diffuse scattering in the subsurface was modeled when calculating the emissivity as $f \times (\sigma^0(\theta, \phi))/(2n \cos^n \theta_{\text{eff}})$. Thus when σ^0 is held constant (i.e., everywhere except near Inktomi), the parameter $f = (1 + \mu_L)/f_{\text{CBE}}$ represents the amount of scattering. As discussed in Section 5.3.2, f should theoretically lie between 0.5 and 2, and more likely be > 1 since the derived very low ε'_r points to a highly depolarizing subsurface and therefore to a linear polarization ratio μ_L close to 1. Instead, we find $f = 0.21-0.42$ for a bolometric Bond albedo of $A_B = 0.72$, and $f = 0.39-0.60$ for $A_B = 0.42$. For $\mu_L = 1$ and $A_B = 0.55$, this would imply a coherent backscattering factor $f_{\text{CBE}} = 3.6-6$ while this latter parameter should remain below the theoretical value of 2 (Hapke, 1990). This further means that the coherent backscattering effect is not sufficient to explain the radar backscatter recorded on Rhea. This result is consistent with the analysis of the disk-integrated radar albedo measured by the Cassini radar in the Saturnian inner system (Chapter 3 and Le Gall et al., 2019). It suggests that some exotic scattering processes are at play in the subsurface of Rhea (as well as on Saturn's other moons including in some regions on Titan, Janssen et al., 2011), likely triggered by the presence of structures of centimetric size (i.e., of the order of the wavelength; Hapke, 1990) very efficient at returning the radar waves in the backscattering direction.

The thermal inertia values derived from the Cassini microwave radiometry dataset also provide insights into the state of the regolith, especially by comparison to values inferred from measurements in the infrared which are sensitive to shallower depths (a few millimeters against few meters). The thermal inertias we derive on Rhea at 2.2 cm (best fits around $50 - 300$ MKS, Table 6.1) are higher than those measured in the infrared ($1 - 50$ MKS; Howett et al., 2014; Howett et al., 2016), implying compaction of the medium with depth, as also found on Iapetus by Le Gall et al. (2014). Yet these thermal inertia values remain low compared to the bulk thermal inertia of water ice (2000 MKS). Low thermal inertias have been measured at infrared and millimeter wavelengths on outer Solar System bodies, including Jupiter's satellites ($I = 50 - 70$ MKS, Spencer et al., 1999), Saturn's icy satellites ($I = 1.5 - 70$ MKS, Howett et al., 2010), and trans-Neptunian objects ($I = 0.1 - 10$ MKS, Lellouch et al., 2013). These values have been generally interpreted as primarily caused by high porosities in the top few mm–cm of the surface, though several studies showed a dependence on grain size, grain arrangement, the presence of amorphous water ice, and temperature (if heat transfer by radiation is important) (e.g., Gundlach and Blum, 2013; Ferrari and Lucas, 2016). Amorphous water ice has a lower bulk thermal inertia (dependent on temperature) and a lower thermal conductivity than crystalline water ice. Based on the heliocentric distance variation of the thermal inertia in outer Solar System objects, Ferrari and Lucas (2016) favor the presence of amorphous ice at cm depths, under a thin crystalline coating, both for Mimas and TNOs. VIMS data indicate the coexistence of amorphous and crystalline ice on Rhea's surface (Dalle Ore et al., 2015). Thus our observations are in general agreement with the interpretations of Ferrari and Lucas (2016), additionally pointing to an increase of thermal inertia with depth, consistent with decreasing porosity and/or amorphous ice fraction with depth.

South pole

Because the South pole was observed at different seasons, the thermal inertia I and skin depth ratio r are well determined, while also providing an excellent fit ($\chi^2_{r,\min} \sim 1$). For a bolometric Bond albedo of $A_B = 0.72$ (Howett et al., 2016), when Inktomi is masked, we find a thermal inertia of $I = 209^{+662}_{-140}$ MKS, an electrical skin depth of $\delta_{\rm el} = 7.9^{+4.0}_{-4.1}$ m (i.e., $4 - 12$ m), and a dielectric constant of $\varepsilon'_r = 1.2^{+0.15}_{-0.11}$. These values can be compared to the ones found by Howett et al. (2016): assuming that both poles share the same thermal properties and combining CIRS northern winter and southern summer observations, they inferred a bolometric Bond albedo $A_B = 0.70 - 0.74$ and a thermal inertia $I = 1 - 46$ MKS. They interpreted these low thermal inertias as indicative of a meter-deep unconsolidated regolith at Rhea's poles. The larger thermal inertias derived from Cassini radiometry imply a gradient in thermal inertia with depth: while the upper tens of cm of the polar surface may be a very fluffy, snow-like medium, at meter depths the subsurface is more compacted. Specifically, the thermal inertia may increase from $I \sim 25$ MKS in the first meter to $I \sim 210$ MKS at $5 - 10$ m depths.

The real part of the permittivity, ε'_r, depends primarily on the structure of the subsurface, whereas the imaginary part ε''_r is very sensitive to the amount of non-icy contaminants and can thus offer constraints on the composition. To deduce the plausible volume fraction of contaminants, we assume a ternary mixture composed of water ice, vacuum, and tholins, which are a possible relatively low-loss component of the optically dark material seen on Rhea's leading and trailing hemisphere (Schenk et al., 2011). We use the bulk permittivity values measured by Paillou et al. (2008): $\varepsilon'_{r,\rm tholin} = 2.33 + j20.6 \times 10^{-3}$ and $\varepsilon'_{r,\rm water\ ice} = 3.13 + j1.3 \times 10^{-3}$. The Hashin-Shtrikman bounds, derived from the Maxwell-Garnett mixing laws, allow us to constrain the volume fraction of each constituent (Hashin and Shtrikman, 1962; Sihvola, 2000). Since we assumed only losses through absorption when deriving the loss tangent and it is known that scattering is important on Rhea, only a maximal volume fraction of tholins can be obtained, with the actual value likely being significantly smaller. The loss tangent is inversely proportional to the electrical skin depth (Eq. 5.21), itself equal to the product of the ratio and the diurnal thermal skin depth, which is inversely proportional to $(1 - p)$, where p is the medium's porosity (Eq. 5.11). The ternary diagram was therefore made for several porosities, two of which are illustrated in Fig. 6.16.

The compositional constraints inferred from the imaginary part of the permittivity at the South pole are shown in the ternary diagram of Fig. 6.16. The low loss tangent indicates that the average porosity over the probed depths is necessarily >10%. We also find that tholin compounds can only be present in small quantities (<10%) at the South pole. While ferrous oxides or silicates are also candidate components for this dark material, their loss tangent is at least two orders of magnitude higher than that of tholins, implying that they can only be present in even smaller quantities.

Equatorial vs polar regions

The interpretation of the radiometry dataset collected in Rhea's equatorial regions suffers from several limitations: i) all data were collected during the local night, ii) while some data were acquired 5 years apart, seasonal temperature variations are small near the equator, iii) the equatorial region is not homogeneous: the residuals shown in Fig. 6.12 reveal cold and warm spots, at the +/-2 K level, that the model is unable to explain, even after masking or mapping the IEBR. These are the reasons why the fits obtained at the Equator ($\chi^2_{r,\min} > 1.7$) are never as good as those obtained in the South pole ($\chi^2_{r,\min} \sim 1$), and are associated with large error bars (Table 6.1, Fig. 6.10).

Nevertheless, it appears that the equatorial regions tend to have lower thermal inertias (and correspondingly higher skin depth ratios, keeping the electrical skin depth of the same order) than the South Polar region (Table 6.1, Fig. 6.10). This could indicate higher equatorial porosities, larger

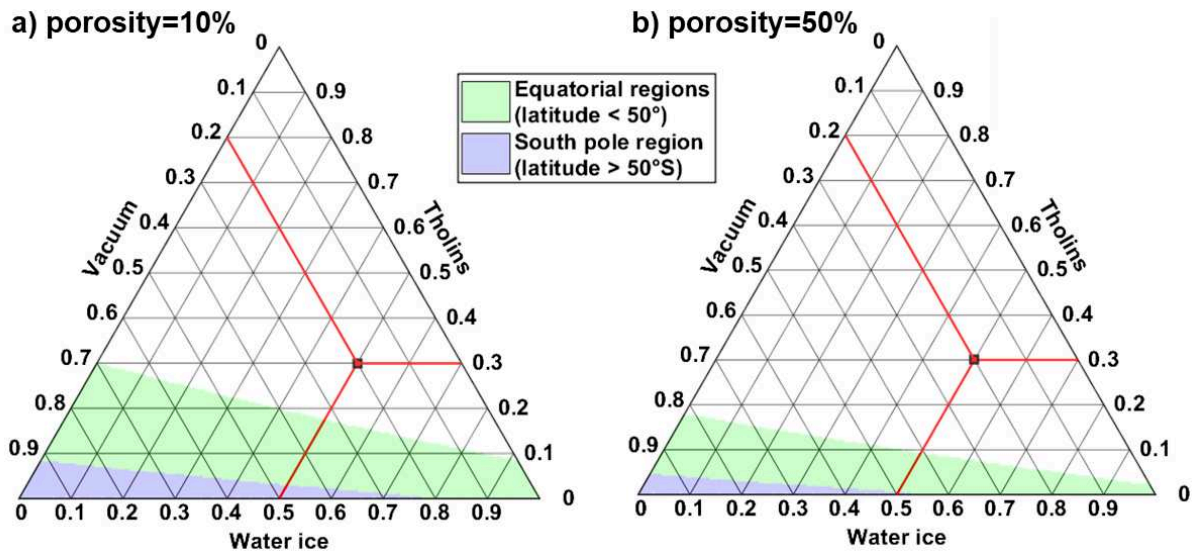

Figure 6.16 – Ternary diagram showing the compositional constraints for Rhea's near-subsurface, assuming that it consists in porous water ice with tholin inclusions. The maximum values for ε_r'' include the effect of the albedo range ($A_B = 0.42-0.72$). The imaginary component of the permittivity is calculated assuming a) 10% and b) 50% porosity. The region corresponding to acceptable values of the imaginary components of the permittivity is shaded in green for the equatorial regions and in blue for the South pole region. To help read this diagram, an example composition is shown in red, corresponding to a mixture of 20% vacuum, 30% tholins, and 50% water ice.

amounts of amorphous water ice, larger grain sizes, and/or looser contacts between grains (Ferrari and Lucas, 2016) near the Equator. Most of these explanations could result from the enhanced intensity of impact gardening at low latitudes.

The real part of the dielectric constant, while still low (1.20 – 1.50 including 2-σ error bars), tends to be larger at the Equator than at the South pole (1.08 – 1.30), which can be explained by a smaller porosity, a larger concentration of scattering and depolarizing structures in the subsurface, or more contamination by non-ice compounds at low latitudes. In addition, the resolved scatterometry data do not show any significant increase in scattering near the South pole which argues in favor of more contamination by impurities in the Equatorial region. Such impurities may have been introduced by impact gardening. Unfortunately, the loss tangent cannot provide complementary information on the relative polar and equatorial impurity content, as no lower bounds can be constrained. Another explanation for the decrease in dielectric constant with increasing latitude would be the deposition of CO_2 frost at the poles as suggested by Teolis and Waite (2016) (CO_2 has a lower dielectric constant than water ice; Paillou et al., 2008).

Sub-Saturn anomaly

On Rhea, two distant scans centered on the sub-Saturn side have been acquired: RH018 (November 2005) and RH049 (August 2007). These data can be compared to the observations in other regions of Rhea, including 3 southern high-latitude flybys and 2 anti-Saturn flybys. The disk-integrated emissivities from the two sub-Saturn flybys are larger than for the rest of Rhea, with all other parameters equal (Section 6.1.4 and Fig. 6.8). The emissivity map derived assuming a constant albedo (Fig. 6.14) also shows a locally high emissivity on the sub-Saturn side, especially at high northern latitudes. Indeed, if the albedo is kept constant at $A_B = 0.55$, the sub-Saturn side has a slightly higher emissivity (0.70 vs 0.67 with an error bar of about 0.01) than the anti-Saturn side (Table 6.1), especially in the

northern mid-latitudes (Fig. 6.14). Finally, fitting all the data at once leaves a 1–3 K residual on the sub-Saturn side (Fig. 6.12). These different representations of the same dataset therefore all show that the simulated antenna temperatures are unable to reproduce the high observed sub-Saturn temperatures. Yet, no albedo, compositional, or thermal inertia anomaly has been detected at this location at other wavelengths (e.g., Schenk et al., 2011; Scipioni et al., 2014; Howett et al., 2014).

A possible explanation is that the trailing hemisphere terrain is affecting the sub-Saturn side; indeed, one of the two sub-Saturn observations is centered at 15°E, i.e., within the optically dark trailing region, whereas all of the anti-Saturn observations are centered between -136°E and -167°E, i.e., within the optically brighter leading hemisphere. Assuming that e varies with bolometric Bond albedo A_B as $(1-A_B)^{-1/4}$, we find that, in order to have the same emissivity on both sides, the albedos of the sub-Saturn/trailing and of the anti-Saturn/leading must be, respectively, 0.55 and 0.62, or 0.46 and 0.55, depending upon which side is imposed an albedo of 0.55. This albedo contrast is of the same order as those measured between the trailing and leading by Howett et al. (2010) ($0.57^{+0.20}_{-0.26}$ and $0.63^{+0.11}_{-0.12}$) and by Pitman et al. (2010) (0.42 ± 0.10 and 0.55 ± 0.08).

Nevertheless, it remains puzzling that, in the emissivity map derived from dividing Rhea into 45° latitude/longitude regions and in the residual maps, the positive emissivity anomaly is on the sub-Saturn side, and not strictly on the trailing side. The very strong sub-Saturn anomaly found on Dione (see Section 6.3) has led us to consider an alternate hypothesis: Saturn itself might be heating the sub-Saturn side. Indeed, the effects of both the thermal IR flux from Saturn and the visible flux reflected by Saturn were assumed negligible in the thermal model (Section 5.1.1), even though they contribute a yearly average of almost 3% of the total absorbed flux at the sub-Saturn point. It is therefore conceivable that we are detecting a local increase in temperature at the sub-Saturn side due to these additional incident fluxes from Saturn.

The absorbed fluxes, including those from Saturn, are shown in Fig. 6.17 for three days around the RH018 sub-Saturn side observation. The thermal infrared emission from Saturn, while it is small, is constantly reaching the same regions. The visible flux reflected off Saturn, meanwhile, is only active during the local night of the sub-Saturn side, when Saturn is illuminated. Thus, Saturn's contribution is particularly significant for night-time observations, which is the time at which all radiometry scans of Rhea were undergone. Similarly, high winter latitudes receive little to no flux from the Sun, whereas they are affected by Saturnshine and Saturn thermal emission. This would explain why during the RH018 and RH049 observations, the northern hemisphere, which is in winter, displays high residuals (Fig. 6.12): Saturn contributes a larger fraction of the total incident flux in this region.

To test this hypothesis, Saturn's contribution to the flux has been included in the thermal model, and simulated temperatures were re-computed. The resulting temperature profile during the RH018 flyby is shown in Fig. 6.18 for three different latitudes and two values of the thermal inertia (I = 10 and 1000 MKS). Because this is a night-time observation, the surface temperature is low, and a small peak occurs at the diurnal skin depth, as discussed in Section 5.1.4. More complex temperature variations occur at depth, caused by temporal changes in flux due primarily to seasons and variations in the solar distance (see Section 5.1.1). The added contribution of Saturn to the temperature is inversely correlated to the subsurface temperature, due to the way temperature is derived non-linearly from absorbed flux, from the heat equation and assuming radiative equilibrium at the surface (see Section 5.1.2). As a consequence, the winter hemisphere (Northern, in this case) should be heated more than the summer hemisphere by incident fluxes from Saturn.

All fits on Rhea have been re-calculated while including Saturn's contribution to the flux. The quality of the fits is slightly improved (minimum χ^2 values are lower by about 0.1), while all results

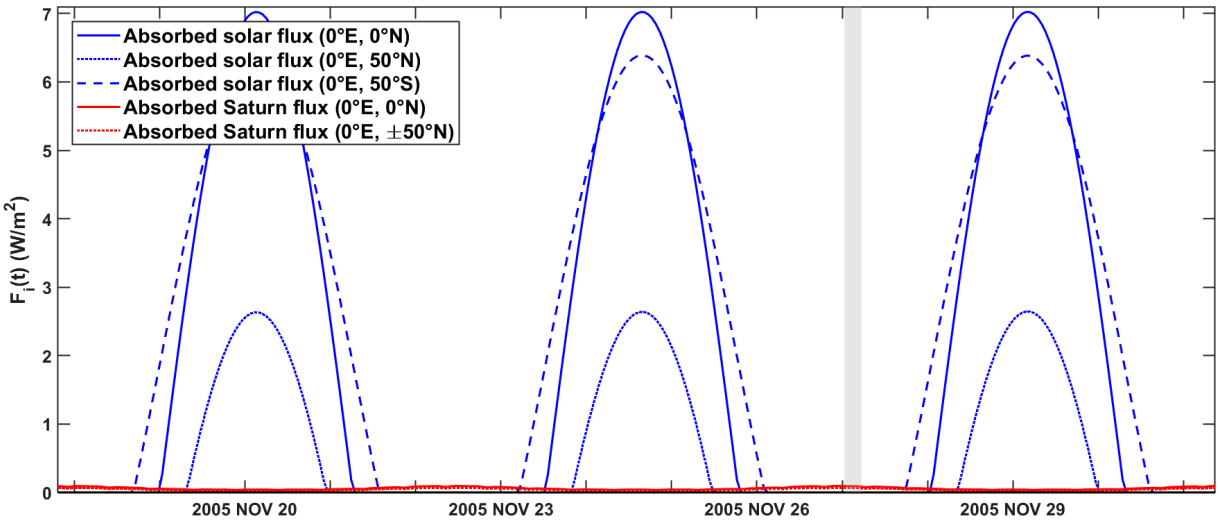

Figure 6.17 – Absorbed solar and Saturn fluxes over three Rhea days, including during the RH018 flyby on 27 November 2005 (gray shaded line). Fluxes are shown for ±50°N and for the equator, on the sub-Saturn side; the absorbed Saturn flux is the same at 50°N and 50°S. The Saturn flux shown here includes both thermal infrared emission from Saturn, and solar radiation reflected on the illuminated part of Saturn. Absorbed fluxes were calculated for a Rhea bolometric Bond albedo of 0.55.

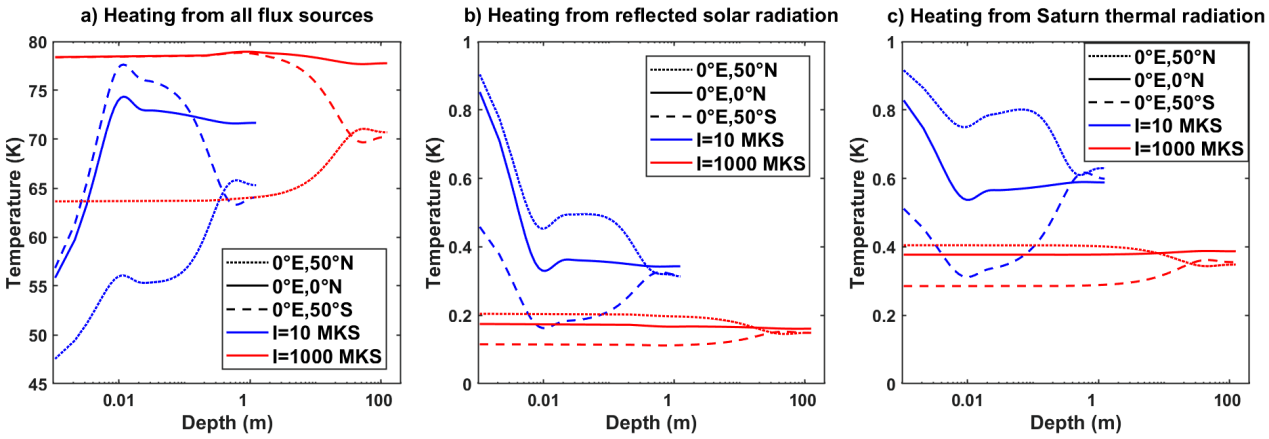

Figure 6.18 – (a) Modeled temperature variations with depth on Rhea's sub-Saturn side on 27 November 2005 (during the RH018 flyby), for low (I = 10 MKS) and high (I = 1000 MKS) thermal inertias, down to six seasonal thermal skin depths. As in Fig. 6.17, results at 50°S, 0°N, and 50°N are shown. (b) Contribution to the temperature from solar radiation reflected by Saturn, calculated as the difference between the temperature profiles with and without accounting for this flux. (c) Contribution to the temperature from Saturn's thermal infrared radiation, calculated as the difference between the temperature profiles with and without accounting for this flux. Absorbed fluxes were calculated for a Rhea bolometric Bond albedo of 0.55. Note that, even though Saturn's flux is latitudinally symmetric around the equator, Saturn's net contribution to the temperature is not. Instead, Saturn's IR and visible contributions to the temperature are both roughly inversely correlated to the temperature, because temperature depends non-linearly on flux. The infrared component is generally more significant, except near the surface during the local night, when Saturn's IR and visible fluxes are equivalent.

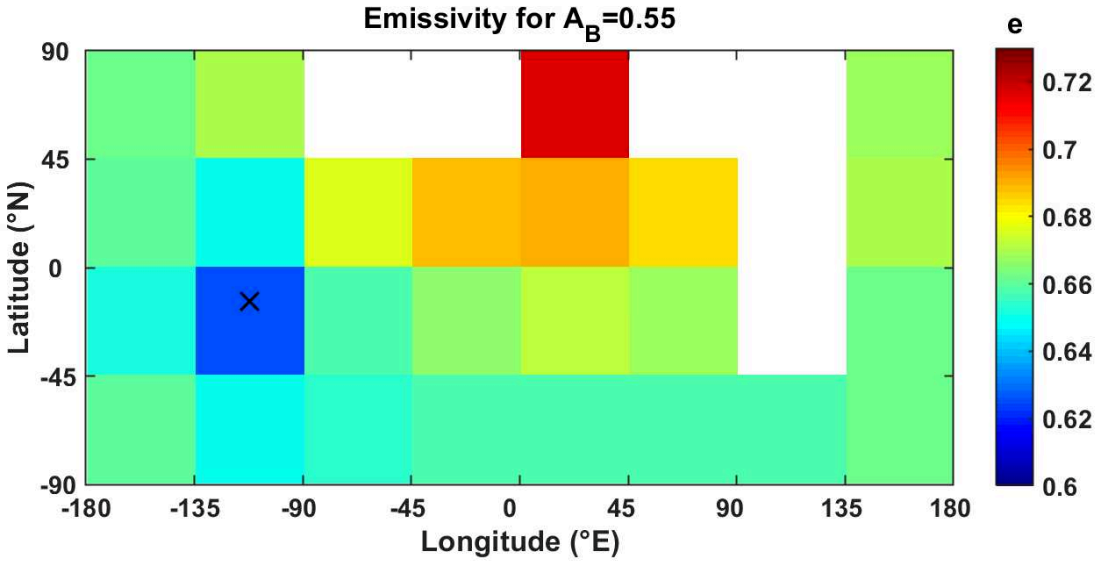

Figure 6.19 – Same as Fig. 6.14, except Saturn's contribution to the incoming flux is now accounted for in the model. Note that, while the sub-Saturn anomaly remains, its amplitude is decreased.

remain substantially the same. Only the values of the scattering factor f and the emissivity e on the sub-Saturn side are changed, but remain within uncertainty of the values given in Table 6.2. The residuals of the global fit are decreased by at most $\sim$ 0.5 K on the sub-Saturn side, which goes in the right direction but is insufficient to fully account for the 1–3 K sub-Saturn hot spot (Fig. 6.12). This is also apparent in the emissivity map, which has been updated while correctly modeling Saturn's flux, as shown in Fig. 6.19: the emissivity of the sub-Saturn side is decreased, but remains present. Thus, Saturn's contribution to the flux is noticeable, but is too small to account for the anomaly detected at the sub-Saturn side.

Inktomi crater

Based on the CIRS instrument, which probes the top millimeters of the surface, Howett et al. (2014) detected a locally higher thermal inertia in the IEBR ($\sim$19 MKS instead of the $\sim$10 MKS equatorial thermal inertia), but no local variation in albedo. The authors attributed this detection to either larger grain sizes, or large blocks of icy ejecta among a small grain-sized surface. VIMS spectra of Inktomi and its surroundings similarly suggest larger grain sizes nearer to Inktomi, while the rest of Rhea's leading hemisphere is covered by a processed, fine-grained regolith (Stephan et al., 2012). VIMS spectra also indicate a lower amorphous to crystalline ice ratio near recent craters, especially Inktomi (Dalle Ore et al., 2015), which would increase the thermal inertia in agreement with CIRS results.

While there is too little spatial and temporal coverage to derive parameters from the IEBR alone, the emissivity map clearly shows a low emissivity/high albedo anomaly in the IEBR (Fig. 6.14). This feature is actually already visible in the deconvolved data prior to any modeling (Fig. 4.6). In addition, we find that masking and including the IEBR lead to the same derived thermal and dielectric parameters for all regions (Table 6.1 and Fig. 6.10), implying that the IEBR does not have any highly unusual (beyond the error bars) thermal or dielectric properties at the depths sensed by the radiometer (6 – 13 m). However, small amplitude (within the error bars) and/or localized (e.g., only very close to the crater) thermal and permittivity anomalies remain possible. Using the same relationship between emissivity and albedo as above ($e \propto (1-A_B)^{-1/4}$), we find that the emissivity over the IEBR (Fig. 6.14) would be the same as over its surroundings if it had an albedo $\sim$ 0.08 higher, which is within the range

of albedo variations on Rhea. Nonetheless, the high radar brightness measured during the scatterometry experiment (Fig. 3.11) strongly suggests that the IEBR, at metric depths, is associated with a strong emissivity anomaly. Both the thermal inertia and the albedo may be different in this region, conceivably contributing to the behavior shown in Fig. 6.14, but the high scattering properties of the IEBR provide a more natural explanation to its apparently low radiometric emissivity.

Even assuming that the IEBR anomaly is only caused by a locally lower emissivity, the precise magnitude of this emissivity anomaly cannot be measured, as both radiometry and scatterometry have footprint sizes larger than the crater ejecta, and the emissivity difference decreases with distance to its center. An estimate can nonetheless be obtained as follows. Averaged over a 45° region, the emissivity is about 6% lower in the IEBR (Fig. 6.14). The better resolved scatterometry map (Fig. 3.11) shows a peak increase in the backscatter of 37% at Inktomi compared to its surroundings, which would lead to a 20% peak decrease in emissivity ($e = 1 - R - f \times \sigma^0$ from Eq. 5.15). Such high scattering, as well as the very high radar albedo of the IEBR (2.13 ± 0.06; Fig. 3.8) would be explained by the presence of subsurface structures back-scattering the signal to the Cassini spacecraft, more than in the rest of Rhea (see Section 2.5). Both a high 2.2-cm radar brightness and a low emissivity are likely caused by wavelength-scale inhomogeneities, such as multiple fractures in the ice blocks forming the ejecta, or large pores or grain sizes (~a few cm).

6.2.4 Summary and conclusion

The thermal inertia values obtained from Cassini radiometry are generally higher (> 69 MKS on the South pole, best fitting values of 50-300 MKS everywhere) than those inferred from IR measurements ($1 - 46$ MKS; Howett et al., 2014; Howett et al., 2016, indicating an increasing degree of compaction in the regolith with depth. At the South pole, where it is better determined, the low loss tangent ($< 1 \times 10^{-3}$) indicates at most 10% of contaminants and > 10% porosity averaged over the top $5 - 10$ m. Very high backscatter is measured on Rhea during the resolved scatterometry observation, yielding high radar albedos of ~ 1.7, consistent with those found from distant disk-integrated observations by Le Gall et al. (2019), using the same instrument. Rhea's inferred emissivities ($e = 0.65 - 0.70$ for $A_B = 0.55$) seem to be not small enough to correspond to such high backscatter when invoking common random scattering mechanisms, suggesting more exotic backscattering processes associated to subsurface structures (see Chapter 3 and Le Gall et al., 2019).

Regional variations suggest higher thermal inertias and smaller dielectric constants at the South pole, while there does not seem to be a significant difference in scattering properties between the high southern latitudes and the Equator. Our best interpretation is that exogenous processes such as (micro)meteoroid impacts, incoming dust from the E-ring and Phoebe ring, and electron and ionized particle impacts, which preferentially affect lower latitudes, are introducing small amounts of material with a slightly higher dielectric constant than porous water ice while also loosening the structure of the subsurface (hence a lower thermal inertia). The radiometry and scatterometry data have also shown that the Inktomi crater ejecta blanket is a low-emissivity and high-backscatter region, but these data are too limited in resolution and local time sampling to detect a thermal inertia or dielectric constant anomaly. It could be that increased scattering in the subsurface of this region is caused by numerous and organized cm-scale inhomogeneities and/or a very high density of randomly oriented fractures in the ice blocks of the ejecta blanket, consistent with the interpretations of VIMS and CIRS data (Stephan et al., 2012; Howett et al., 2014). High water ice purity near Inktomi (observed by VIMS: Stephan et al., 2012; Scipioni et al., 2014) would also increase the probed depth, and thus increase the number of opportunities for the signal to be scattered, leading to lower emissivity and higher radar brightness. As over the rest of Rhea, it is unclear which subsurface structures and organization would lead to sufficiently strong backscatter while keeping the emissivity high.

6.3 Preliminary results for Dione

As detailed in Section 1.5.2, Dione, though smaller and closer to Saturn than Rhea, presents many similarities with it, including a leading/trailing dichotomy, fractured "wispy" terrain across the trailing hemisphere, and a young crater (Creusa) analogous to Inktomi crater. Cassini radar and radiometry data suggest that Dione and/or Rhea break the trend of decreasing radar albedo and increasing brightness temperature with distance to Enceladus (Chapters 3 and 4; especially Figs. 3.6 and 4.5). Dione's near-subsurface is especially interesting to compare to Rhea's, as they should both be affected by similar processes but to different degrees (e.g., more incoming E-ring material and more high-energy electron impacts on Dione than on Rhea). After the detailed study of Rhea's subsurface from Cassini radiometry, I therefore began a preliminary analysis of the Dione's subsurface.

Radiometry scans were only acquired during 4 Dione flybys, two of which (DI016 and DI177) were unresolved. As shown in Fig. 6.6, only the sub-Saturn side was observed at more than one instance. Given the small dataset, its coarse resolution, and its poor temporal sampling, the subsurface properties of Dione cannot be as well constrained as those of Rhea. Nonetheless, this preliminary study already suggests new results, including the notable contribution of Saturn's heating to the incoming flux and the lack of a leading/trailing dichotomy, encouraging future work.

6.3.1 Method

Unlike Rhea, Dione's bolometric Bond albedo has been partially mapped (Section 5.1.3 and Blackburn et al., 2012) and is included in the model. The emissivities derived below for Dione are therefore independent from albedo variations. We apply the method described in Section 5.4.3 to derive the parameter f within $45 \times 45°$ latitude and longitude bins. As explained in Section 5.3.3, because there is only partial scatterometry coverage and the pointing offset is uncertain, we assume a uniform $\sigma^0_{\text{map}} = (\sigma^0(\theta,\phi))/(2ncos^n\theta_{\text{eff}}) = 0.529$ (the average value on Dione) when calculating f. The backscatter is not actually uniform but exhibits a leading/trailing dichotomy: we therefore expect the derived emissivity map to also feature this dichotomy.

The fits of simulated antenna temperatures to the observations have also been conducted assuming a uniform emissivity. As shown in Table 4.1 and mentioned in Section 6.1.4, the sub-Saturn side has been observed both before and after the vernal equinox, at different local times. Furthermore, the preliminary analysis presented in Section 6.1.4 shows an anomaly on the sub-Saturn side of Dione. We therefore apply the fitting method i) to all data then separately ii) to the sub-Saturn region (defined as the 0°E sub-Saturn point ±45° in longitude) and iii) to the rest of Dione (excluding 0 ± 70°E). The transition region ($\pm 45 - 70$°E), which features rapid temperature changes with longitude, is not fitted. There is too little coverage and temporal sampling on regions of Dione other than the sub-Saturn for accurate determination of their thermal and structural parameters.

6.3.2 Results

The results obtained from fitting the modeled antenna temperatures to the data in all three regions (all of Dione, sub-Saturn region, and all of Dione except the sub-Saturn region) are given in Table 6.3, and the 2-σ confidence regions in (I,r) space are illustrated in Fig. 6.21. The residuals from fitting all the data assuming a uniform and then a variable emissivity are shown in Fig. 6.20 a) & b); the resulting emissivity map is shown in Fig. 6.22. For comparison, the residuals from the fit using only sub-Saturn data, and using all except the sub-Saturn data are shown in Fig. 6.20c) & d.

Table 6.3 – Best-fit parameters and associated 2-σ error bars in different regions of **Dione**. When the error bars reach the boundaries of the range of tested values for the thermal inertia ($10 < I < 1000$) or the ratio ($0.01 < r < 1000$), the actual error bars cannot be known, and *MIN* or *MAX* are indicated instead. As in Table 6.2, the skin depths and loss tangents were calculated assuming zero porosity. The uncertainties on the parameters derived from thermal inertia and ratio are calculated for the minimum and/or maximum values of I and r, but may actually be larger. Note that the fits are considerably less good for Dione than for Rhea (Table 6.2), and the parameters are less well constrained.

Region	$\chi^2_{\mathrm{r,min}}$	I **(MKS)**	$r = \frac{\delta_{\mathrm{el}}}{\delta_{\mathrm{th}}^{\mathrm{day}}}$	ε'_r	$f = \frac{1+\mu_L}{f_{\mathrm{CBE}}}$	δ_{el} [c] **(m)**	e **(at nadir)**	$\delta_{\mathrm{th}}^{\mathrm{day}}$ [c] **(cm)**	$\delta_{\mathrm{th}}^{\mathrm{season}}$ [c] **(m)**	$\tan\delta$ [c] **$\times 10^{-3}$**
All data[a]	3.3	50^{+132}_{-MIN}	692^{+MAX}_{-473}	$1.56^{+0.2}_{-0.12}$	$0.33^{+0.04}_{-0.10}$	$14.7^{+49.5}_{-13.1}$	$0.81^{+0.05}_{-0.01}$	$2.1^{+5.6}_{-1.7}$	$1.3^{+3.5}_{-1.1}$	< 1.7[b]
Sub-Saturn 0°E±45°	3.6	20^{+327}_{-MIN}	363^{+MAX}_{-258}	$1.72^{+0.16}_{-0.22}$	$0.21^{+0.07}_{-0.06}$	$6.1^{+41.4}_{-2.1}$	$0.87^{+0.03}_{-0.03}$	$0.8^{+13.9}_{-0.4}$	$0.5^{+8.7}_{-0.3}$	< 2.8[b]
All except sub-Saturn 180°E±110°	3.0	20^{+220}_{-MIN}	417^{+MAX}_{-188}	$1.16^{+0.16}_{-0.12}$	$0.41^{+0.07}_{-0.07}$	$3.5^{+66.9}_{-2.4}$	$0.78^{+0.04}_{-0.03}$	$0.9^{+9.3}_{-0.4}$	$0.5^{+5.9}_{-0.3}$	< 2.9[b]

[a] For the global fit, we calculate the factor f separately in bins of 45 by 45° before fitting all data jointly. The value given here is the global average.

[b] The upper bound for $\tan\delta$ was calculated from the electrical skin depth, itself computed from the ratio assuming a thermal inertia of 10 MKS.

[c] The values given herein were calculated for a bulk density of $\rho_0 = 992\mathrm{kg/m^3}$. The correct value for crystalline water ice is $\rho_0 = 918\mathrm{kg/m^3}$, leading to an 8% underestimation of depths, and overestimation of $\tan\delta$.

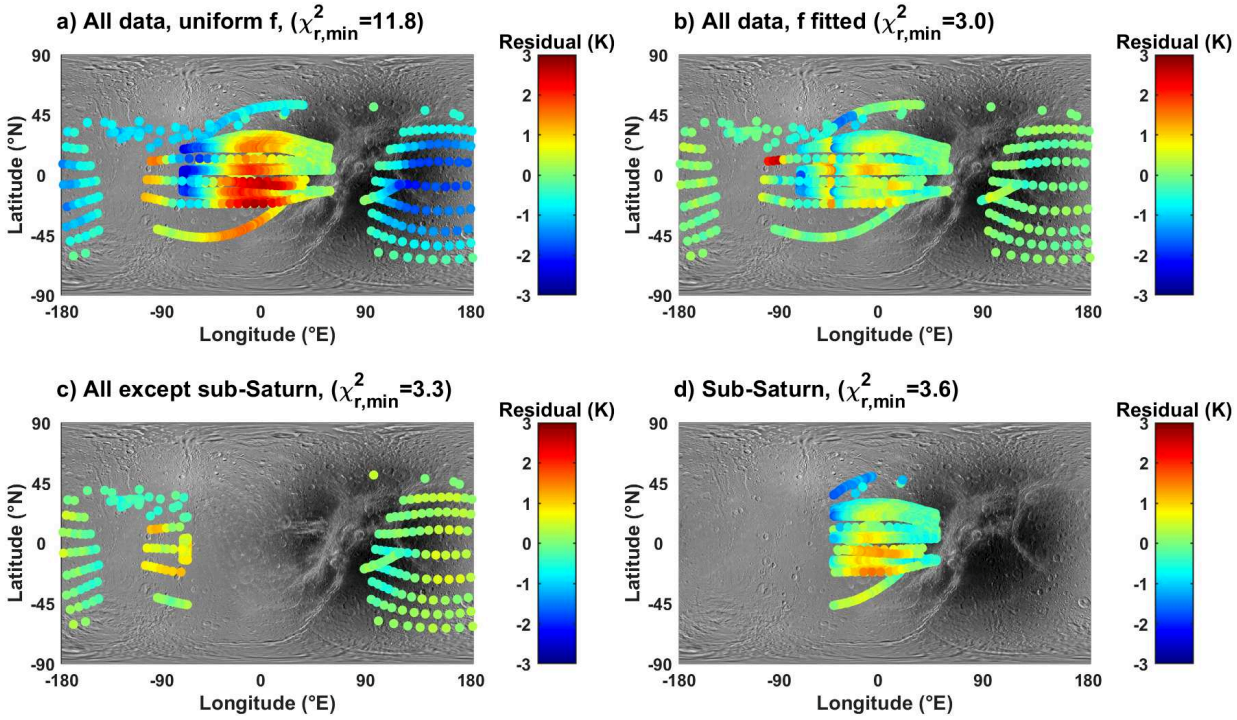

Figure 6.20 – Residual maps after fitting the model to all Dione data, (a) assuming the emissivity is uniform over the whole satellite and (b) dividing f (and therefore the emissivity) into 45° latitude and longitude bins. (c) Residual map assuming uniform emissivity, but fitting only the data at longitudes below -70°E or above 70°E, thus masking the sub-Saturn region. (d) Same as (c), but fitting only the data within the sub-Saturn region (0°E±45°).

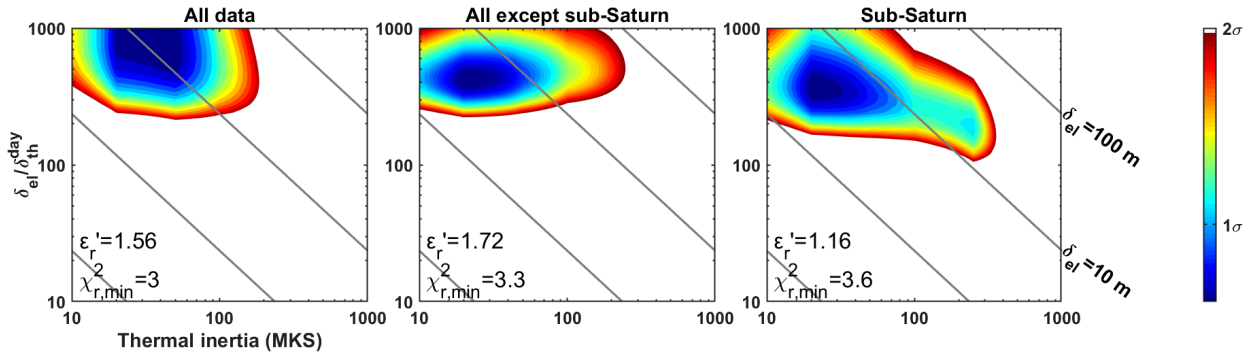

Figure 6.21 – 2-σ best fitting ellipses in the (I,r) domain, for the best-fit values of ε'_r (see Table 6.3 for the other parameters) for each of the 3 regions where the fitting method was applied on Dione. The minimum reduced χ^2_r value ($\chi^2_{r,\min}$) is indicated for each fit.

The residual brightness temperature varies very quickly with distance to the sub-Saturn point. Consequently, the fit in this fairly small region is poor ($\chi^2_r > 3.6$), even though this region is the only part of Dione observed twice by the Cassini radiometer, at different seasons and local times. Similarly, dividing f into 45° latitude and longitude bins does not yield a perfect fit, as large variations in the residual remain (Fig. 6.20c). The most reliable parameter constraints on Dione should therefore be obtained when fitting all data except the sub-Saturn side. This leaves us with flybys DI050 (8 PM in September 2007) and DI177 (7 AM in December 2012), as well as part of the resolved DI163 flyby (9 PM in March 2012). Primarily because of the small number of observations and the insufficient temporal sampling, the parameters are not as well constrained as on Rhea. Moreover, the fit is poor ($\chi^2_r > 3.0$), even without including the sub-Saturn side. The model simplifications (see Chapter 5.4.6), necessary to avoid excessive degeneracy between parameters, may not be applicable to Dione. In particular, it is likely that the thermal, structural, and compositional properties of Dione vary both regionally and with depth. However, both independent datasets (sub-Saturn and all except sub-Saturn) give similar ranges for all parameters except e and f (Fig. 6.21 and Table 6.3). This consistency lends some confidence to these preliminary results in spite of the poor quality of the fits.

The emissivity derived ranges from $0.78^{+0.04}_{-0.03}$ on most of Dione, to $0.87^{+0.03}_{-0.03}$ on the sub-Saturn side. While these values are consistent with the results discussed in Section 6.1.4, they are much larger than the emissivity of 0.65 found by Ostro et al. (2006) using only one flyby (DI016). The low emissivities they derived are most likely due i) to the low disk-integrated brightness temperature they found (50.8 K whereas we find $T_B^{\rm disk} = 55.6 \pm 0.7$ K for the same flyby; see Table 4.1) and ii) to the equilibrium temperature model they used: $T_{\rm eq} = 91.4(1 - A_B)^{1/4}$, with a bolometric Bond albedo $A_B = 0.45$, whereas Blackburn et al. (2012) find a bolometric Bond albedo above 0.6 over most of Dione (see Fig. 5.3).

As already seen in the disk-integrated emissivity values (Section 6.1.4), the sub-Saturn side features a higher emissivity than the rest of Dione. This is apparent both in the regional fits whose results are shown in Table 6.3 and in the emissivity map of Fig. 6.20d. If the emissivity is assumed uniform over all Dione, then a residual of up to +3 K is found on the sub-Saturn side leading to a very poor fit (Fig. 6.20a). The sub-Saturn hot spot also displays latitudinal asymmetry: it is very significant at southern high latitudes, but seems to disappear at northern high latitudes (Fig. 6.20). The sub-Saturn results are further discussed below.

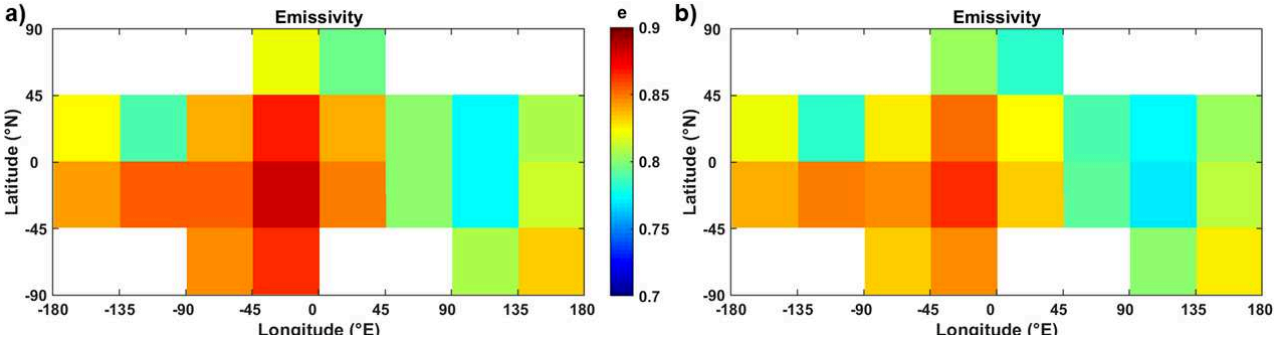

Figure 6.22 – Dione emissivity map, using all available data, corresponding to the residual shown in Fig. 6.20. The emissivity is assumed constant in every 45×45°latitude/longitude bin. There is no data available in the white regions. Note that the high emissivity at -135 to -90°E and -45 to 0°N is most likely caused by the poor fit of flyby DI163, causing underestimated daytime temperatures; it is unlikely to be an emissivity anomaly. High emissivities are linked to the high positive residuals found in Fig. 6.20. The emissivity map is shown both (a) without and (b) with Saturn's contribution to the incoming flux accounted for.

6.3.3 Preliminary interpretations

Comparison with Rhea

The fit on all Dione data except that in the sub-Saturn region, though far from perfect ($\chi^2_r > 3.0$) leads to the most reliable parameter constraints, which we propose to compare to Rhea's subsurface properties (Table 6.2).

The thermal inertia is in average lower on Dione than on Rhea, although both values are consistent within error. Meanwhile, the value of the skin depth ratio r on Dione ($r_{\mathrm{Dione}} > 229$) is at least twice as large as on Rhea (best fitting ratios around 70 – 130 for most regions). These low thermal inertias (leading to low diurnal skin depths) and high ratios combine to yield very similar electrical skin depth on both satellites ($\delta_{\mathrm{el,Dione}} = 3.5^{+66.9}_{-2.4}$ and $\delta_{\mathrm{el,Rhea}}$ is of the order of 5 – 15 meters). These electrical skin depths, which give a maximal value of the loss tangent of the same order ($< 2.9 \times 10^{-3}$ on Dione; $< 0.6 - 4.7 \times 10^{-3}$ on Rhea, depending on bolometric Bond albedo), point to low contamination by non-icy impurities on both satellites. Nonetheless, the large uncertainties associated to the subsurface parameters allow for differences in the degree of purity of water ice on these two satellites.

Such a difference is supported by Dione's lower radar brightness ($A^{\mathrm{disk}}_{\mathrm{SL-2}} = 1.65 \pm 0.29$, versus $A^{\mathrm{disk}}_{\mathrm{SL-2}} = 1.88 \pm 0.38$ for Rhea; Section 3.3 and Le Gall et al., 2019) and higher emissivities ($e = 0.78^{+0.04}_{-0.03}$, versus $e = 0.62$ to 0.76 for $A_B = 0.55$ for all regions of Rhea), following the anti-correlation between radar albedo and emissivity expected from Kirchhoff's law of thermal radiation. Possible explanations for the lower radar brightness of Dione have already been discussed in Section 3.4.2.

Both the dielectric constant and the scattering factor f are very similar on Dione ($\varepsilon'_r = 1.16^{+0.16}_{-0.12}$; $f = 0.41^{+0.07}_{-0.07}$) and on Rhea ($\varepsilon'_r = 1.07$ to 1.5 and $f = 0.21$ to 0.60 for $A_B = 0.42$ to 0.72 and for all regions of Rhea). The conclusions drawn for the structure of Rhea's near subsurface are therefore also valid for Dione's: it likely consists in an unpolarized, porous regolith with numerous scattering structures. As on Rhea, the coherent backscattering effect and high radar albedo would predict lower emissivities than observed.

Sub-Saturn anomaly

The sub-Saturn side of Dione has been observed during two flybys: DI016 (October 2005), which is unresolved, and DI163 (March 2012), which includes the resolved concurrent scatterometry and radiometry data. As on Rhea, these two observations are associated with higher disk-integrated temperatures/emissivities than the rest of the satellite (Section 6.1.5 and Fig. 6.6). Global fits yield either very high (~3 K) residuals in the sub-Saturn region (Fig. 6.20a) or locally high emissivities if f is divided into a 45×45 grid (Fig. 6.20d). High sub-Saturn temperatures were already apparent in the deconvolved image (Fig. 4.6), although the contrast with their surroundings could be attributed to limb darkening.

The high residuals seen during the resolved DI163 scan are focused near 0°E, and are more important at southern than northern latitudes. This geographic distribution is not consistent with the leading/trailing dichotomy seen in the scatterometry data (Fig. 3.12): it is therefore unlikely to be caused by true geographical emissivity variations. No sub-Saturn albedo or thermal inertia anomaly has been detected by other instruments (e.g., Schenk et al., 2011; Scipioni et al., 2013; Howett et al., 2014). As on Rhea, we conclude that a reasonable explanation for the high sub-Saturn temperatures is Saturnshine and thermal infrared emission from Saturn. Because Dione is closer to Saturn than Rhea, Saturn's angular size is larger, and the planet is expected to contribute more to the incident flux than on Rhea, consistent with the higher amplitude of the sub-Saturn anomaly at Dione. Furthermore, the DI163 observation was acquired during the southern fall, when high southern latitudes receive little sunlight. During this season, Saturn's contribution is then at its peak at southern latitudes, explaining the distribution of residuals.

As on Rhea (Section 6.2.3), Saturn's contribution to the flux has been added to the thermal model. The fluxes around the DI163 sub-Saturn observation are shown in Fig. 6.23, and the resulting temperature profiles are given for two different thermal inertias in Fig. 6.24. As expected, Dione, which is closer to Saturn than Rhea, receives more flux from Saturn. However, due to its higher sub-Saturn bolometric Bond albedo, Dione absorbs a small fraction of the visible flux from Saturn (Saturnshine), whose contribution to the temperature is consequently less than half the contribution from Saturn thermal emission (Fig. 6.24b and c). Due primarily to Saturn's thermal emission, Saturn contributes more to the temperature on Dione than on Rhea: ~ 1.2 K (for I = 1000 MKS) to ~ 1.7 K (for I = 10 MKs), versus ~ 0.5 K and ~ 1 K on Rhea for the same values of I. At the surface, however, Saturn's contribution varies significantly with time and location, and can sometimes be higher on Rhea than on Dione. A temperature increase of 1 to 2 K on the sub-Saturn side is of the right order of magnitude, although it appears insufficient to explain the residuals of up to 3 K (Fig. 6.20).

Once simulated temperatures are fitted to the data while accounting for Saturn's contribution, the amplitude of the sub-Saturn anomaly is visibly decreased (see Fig. 6.22). An anomaly may still remain, suggesting that, as on Rhea, Saturn's flux may be insufficient to account fully for the derived high sub-Saturn emissivity. However, uncertainties in the pointing offset of the DI163 flyby of the sub-Saturn side make a precise assessment of the anomaly difficult.

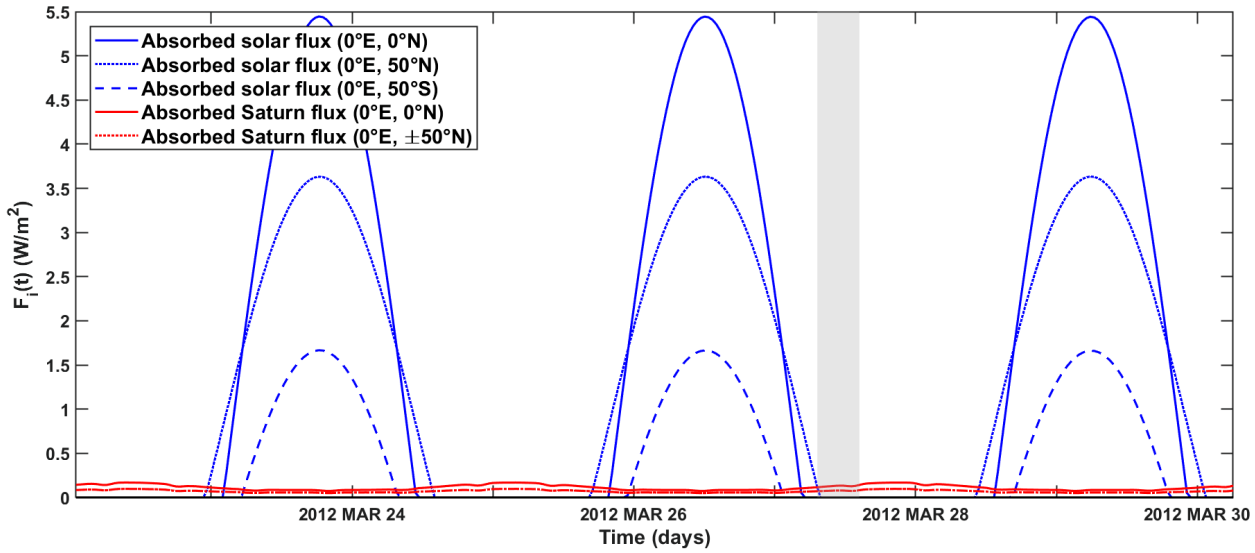

Figure 6.23 – Absorbed solar and Saturn fluxes over three Dione days, including during the DI163 flyby on 27 March 2012. Fluxes are shown for ±50°N and for the equator, on the sub-Saturn side; the absorbed Saturn flux is the same at 50°N and 50°S. The Saturn flux shown here includes both thermal infrared emission from Saturn, and solar radiation reflected on the illuminated part of Saturn. Absorbed fluxes were calculated following the Dione bolometric Bond albedo map provided in Fig. 5.3 (Blackburn et al., 2012).

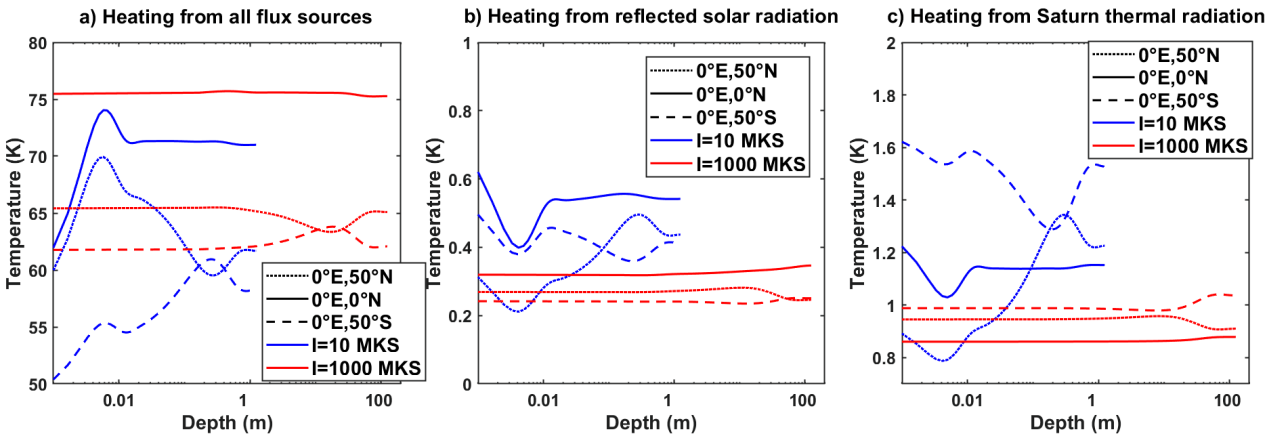

Figure 6.24 – (a) Modeled temperature variations with depth on Dione's sub-Saturn side on 27 March 2012 (during the DI163 flyby), for low (I = 10 MKS) and high (I = 1000 MKS) thermal inertias, down to six seasonal thermal skin depths. As in Fig. 6.23, results at 50°S, 0°N, and 50°N are shown. (b) Contribution to the temperature from solar radiation reflected by Saturn, calculated as the difference between the temperature profiles with and without accounting for this flux. (c) Contribution to the temperature from Saturn's thermal infrared radiation, calculated as the difference between the temperature profiles with and without accounting for this flux. Absorbed fluxes were calculated following the Dione bolometric Bond albedo map provided in Fig. 5.3 (Blackburn et al., 2012). The infrared component is much more significant than the visible component, except near the surface during the local night, when Saturn's IR and visible fluxes are equivalent.

Leading vs trailing hemispheres

We expected a clear leading/ trailing dichotomy in the emissivities, as in the radar backscatter (Fig. 3.12), with a high-emissivity trailing side. No such pattern is found in the emissivity map (Fig. 6.20d), nor in the residuals of the fit without the abnormal sub-Saturn side (Fig. 6.20b). If anything, the trailing hemisphere appears to have a lower emissivity than the leading hemisphere, as apparent in Fig. 6.22. However, a small change in the antenna pointing offset of the DI163 sub-Saturn flyby is enough to change this pattern significantly. Due to the uncertainty in the pointing offset, the scarcity of data on Dione, and the presence of a sub-Saturn anomaly, we can not conclude on the existence of an emissivity difference between the leading and trailing sides. Nevertheless, the absence of any trailing hemisphere increase in temperature in flyby DI050 (including in the deconvolved image shown in Fig. 4.6) indicates that such a dichotomy, if it exists, must be of low amplitude.

The hemispheric backscatter dichotomy may be due to i) a centimeter-thick layer of optically dark and 2.2-cm absorbing material on the trailing hemisphere decreasing the backscatter and/or ii) a centimeter-thick layer of E-ring icy, scattering material on the leading hemisphere increasing the backscatter. As discussed in Section 3.4.2, current models predict a very thin layer of E-ring particles on both Rhea and Dione (of the order of millimeters). The trailing hemisphere dark material, whose identity and origin is unknown, is also unlikely to be very thick (e.g., Hendrix et al., 2018; see Section 1.7). If further analysis of the Cassini 2.2 cm radiometry can confirm that the trailing side of Dione is either less emissive than or similar to its leading side, then both of these layers must be less than tens of centimeters thick. Indeed, the Cassini radiometer measured the one-way signal emitted by the subsurface, whereas the radar signal had to travel both ways through the subsurface: the radiometer thus probed about twice as deep as the radar. On Enceladus, the longer depths probed by the radiometer led to the detection of a buried anomaly on the leading side (Ries and Janssen, 2015), whereas on Dione it might be able to probe a uniform subsurface underneath a heterogeneous superficial layer.

6.4 Preliminary results for Iapetus

Le Gall et al. (2014) performed an in-depth analysis of the resolved radiometry data gathered during flyby IA049-3, and also included a disk-integrated analysis of the emissivities of other Iapetus radiometry observations. However, a joint fit to successive observations of the same regions has never been undergone on Iapetus. In this section, a preliminary application to Iapetus of the same method used above on Rhea and Dione is presented.

Although Iapetus is almost the same size as Rhea, its history has followed a very different path (Section 1.4.2). Even if its density points to an icy interior, the leading hemisphere of Iapetus is covered by an optically dark, non-icy material, most likely originating from the Phoebe ring (Spencer and Denk, 2010). We therefore expect different subsurface properties on Iapetus than on Rhea.

6.4.1 Method

The resolved IA049-3 scan is not used in this analysis. Indeed, its high resolution (beam-size <0.1 Iapetus diameter) reveals important small-scale heterogeneity, which requires an emissivity model for an accurate fit. Such a model has already been applied to the IA049-3 scan by Le Gall et al. (2014), including information from concurrent scatterometry. Instead of re-analyzing the same data, we propose for this preliminary analysis to examine the other, independent observations. Nonetheless, re-calibration and analysis of the resolved Iapetus scatterometry and radiometry, including an

adjustment of the pointing offset, would be very useful and should be conducted in future work.

As for Dione, the bolometric Bond albedo map of Iapetus (Blackburn et al., 2011) has been included in the thermal model, and the emissivity map derived by dividing f in $30 \times 30°$ regions is free from albedo variations. As detailed in Section 5.3.3, we assume that $\sigma^0(\theta,\phi)/(2ncos^n\theta_{\rm eff}) = 0.1$ is uniform, although it corresponds to the value found in Cassini Regio. Thus, the values of $f = (1+\mu_L)/f_{\rm CBE}$ should only be valid in the leading hemisphere, and be overestimated elsewhere.

The 4 flybys of Iapetus (listed in Table 4.1) include repeated observations of both the leading and trailing hemispheres, allowing us to fit both of these regions separately, by mapping Cassini Regio and calculating its contribution to the measured signal, as detailed in Section 5.4.5. Four scans (IA00B_2u, IA00C_2u, IA00C_3u, and IA017_2u) have been centered near 40°N, and therefore imaged the North polar region, as seen in Fig 4.6. However, the relatively low resolution (beam size of 0.7 to 1.8 Iapetus diameters) and low sub-spacecraft latitude mean that no observation was obtained at high latitudes exclusively: instead, all polar observations include a mixture of polar terrain and leading or trailing hemisphere terrain. Thus, in spite of the data near the North pole, we cannot derive its properties independently from those of other regions.

To summarize, the fitting method is applied i) to all equatorial data, without any emissivity model, ii) to all equatorial data, deriving f and the emissivity e in $30 \times 30°$ regions, iii) to the leading hemisphere terrain, i.e., data with >70% contribution from Cassini Regio, and iv) to the trailing hemisphere terrain, i.e., data with <30% contribution from Cassini Regio.

6.4.2 Results

The best-fitting parameters found within each region, and the skin depths, emissivity, and loss tangent derived, are provided in Table 6.4. The residuals found from each fit are shown in Fig. 6.26, and the 2-σ confidence regions in (I,r) space are illustrated in Fig. 6.25. Assuming uniform emissivity (Fig. 6.26a) leads to a catastrophically bad fit ($\chi^2_r > 47.8$), with a strong positive residual on the leading side and a negative residual on the trailing side. Allowing the emissivity to vary in $30\times30°$ regions greatly improves the situation, with a minimum χ^2_r of 1.71.

The resulting emissivity map, shown in Fig. 6.27, exposes a very strong leading/trailing dichotomy. From this map, the average leading and trailing hemisphere emissivities are, respectively, $e_{\rm LH} = 0.87^{+0.05}_{-0.02}$ and $e_{\rm TH} = 0.74^{+0.04}_{-0.02}$, where the uncertainties are the average of the leading and trailing hemisphere minimum and maximum emissivity values allowed within the 2-σ confidence region. These values are very close to those derived by Le Gall et al. (2014) and in Section 6.1.2, with finer constraints.

However, problems arise once the bright and dark terrains are separated. Indeed, the fit on the trailing hemisphere is not as good as one might hope ($\chi^2_r > 2.3$), and the parameters, especially the thermal inertia, are poorly constrained (Table 6.4 and Fig. 6.25). The residuals, of the order of ±1 K, are the highest near the equator (Fig. 6.26c), pointing to warmer equatorial regions than modeled.

Within Cassini Regio on the leading side, the problems are different: the fit is "too good", with a minimum χ^2_r value of 0.72. Such a low χ^2_r can be the consequence of either over-estimated error bars, or insufficient constraints from the data. In the first case, the solution is to adjust the uncertainties such that $\chi^2_{r,min} = 1$, thus obtaining the uncertainties presented in Table 6.4 and Fig . 6.25c. However, most derived values of the emissivity e within the 2-σ confidence region are above unity, which is not physical. We therefore favor the second hypothesis: that the data are insufficient to accurately

Table 6.4 – Best-fit parameters and associated 2-σ error bars in different regions of **Iapetus**. When the error bars reach the boundaries of the range of tested values for the thermal inertia ($10 < I < 1000$) or the ratio ($0.01 < r < 1000$), the actual error bars cannot be known, and *MIN* or *MAX* are indicated instead. As in Table 6.2, the skin depths and loss tangents were calculated assuming zero porosity. The uncertainties on the parameters derived from thermal inertia and ratio are calculated for the minimum and/or maximum values of I and r, but may actually be larger if the parameter space is not wide enough. f is calculated assuming that $\sigma^0/(2n\cos^n\theta_{\rm eff}) = 0.1$, the average value in Cassini Regio: it is therefore only valid in the leading hemisphere.

Region	$\chi^2_{\rm r,min}$	I **(MKS)**	$r = \frac{\delta_{\rm el}}{\delta^{\rm day}_{\rm th}}$	ε'_r	$f = \frac{1+\mu_L}{f_{\rm CBE}}$	$\delta_{\rm el}$ [c] **(m)**	e **(at nadir)**	$\delta^{\rm day}_{\rm th}$ [c] **(m)**	$\delta^{\rm season}_{\rm th}$ [c] **(m)**	$\tan\delta$ [c] **$\times 10^{-3}$**
Equatorial[a] (<50° lat)	1.71	501^{+MAX}_{-381}	$4.2^{+9.0}_{-2.7}$	$1.12^{+0.24}_{-0.12}$	$1.96^{+1.11}_{-1.37}$	$4.8^{+7.2}_{-2.2}$	$0.80^{+0.14}_{-0.11}$	$1.2^{+1.1}_{-0.9}$	$13.3^{+13.3}_{-10.1}$	< 1.3[b]
Trailing Hemisphere Terrain	2.34	200^{+MAX}_{-MIN}	17^{+34}_{-14}	$1.04^{+0.14}_{-0.04}$	$2.40^{+0.31}_{-1.52}$	$7.6^{+24.0}_{-7.1}$	$0.76^{+0.15}_{-0.03}$	$0.46^{+1.8}_{-0.4}$	$5.0^{+21.3}_{-5.0}$	< 7.0[b]
Leading Hemisphere Terrain[d]	0.72 > 0.74	15^{+167}_{-MIN} > 52	28^{+68}_{-20} > 7.9	$1.72^{+0.28}_{-0.26}$ same	$-1.01^{+1.57}_{-0.40}$ > 0	$1.0^{+4.0}_{-0.5}$ > 1.6	$1.08^{+0.03}_{-0.15}$ < 1	$0.03^{+0.38}_{-0.01}$ > 0.12	$0.4^{+4.4}_{-0.1}$ > 1.4	< 5.9[b] < 1.8

[a] For the global fit, we calculate the factor f separately in bins of 30 by 30° before fitting all data jointly. The values provided here give the full range of f.

[b] The upper bound for $\tan\delta$ was calculated assuming a thermal inertia of 10 MKS.

[c] The values given herein were calculated for a bulk density of $\rho_0 = 992\text{kg/m}^3$. The correct value for crystalline water ice is $\rho_0 = 918\text{kg/m}^3$, leading to an 8% underestimation of depths, and overestimation of $\tan\delta$.

[d] The best fit yields unphysical values of $e > 1$ and $f < 0$. The values of each parameter beyond which $e < 1$ and $f > 0$ are indicated. If the range of values is not affected, "same" is indicated.

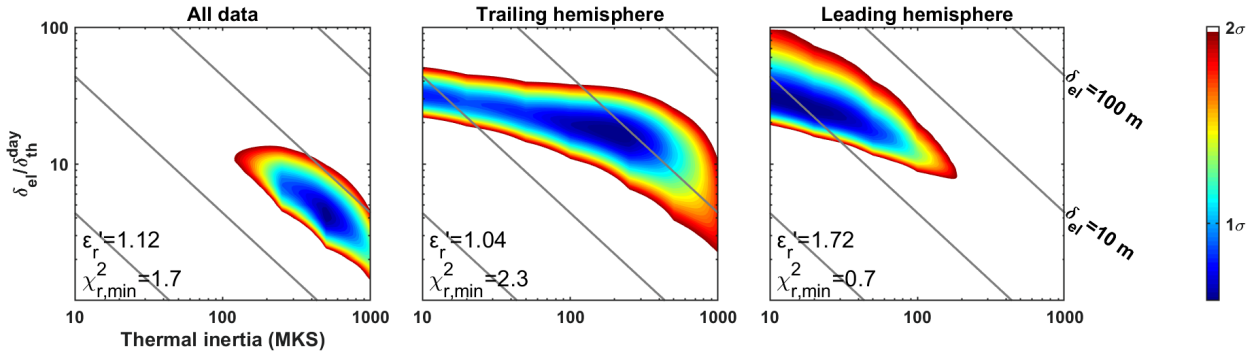

Figure 6.25 – 2-σ best fitting ellipses in the (I,r) domain, for the best-fit values of ε'_r (see Table 6.4 for the other parameters) for each of the 3 regions where the fitting method was applied on Iapetus. The minimum χ^2_r value ($\chi^2_{r,\rm min}$) is indicated for each fit. Before mapping these ellipses, the uncertainties on the data are adjusted such that the minimum χ^2_r value is equal to unity: this is inaccurate on the leading hemisphere, where the parameters are not well constrained.

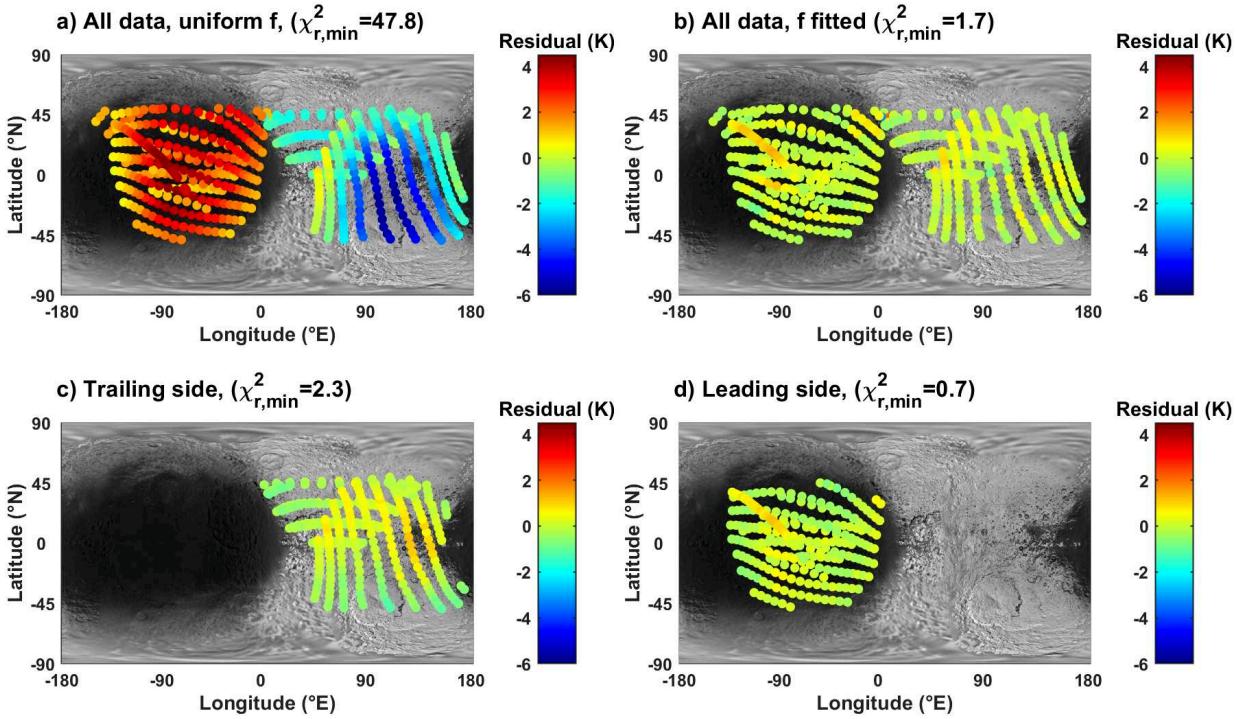

Figure 6.26 – Residual maps after fitting the model to all Iapetus data below 50° latitude, (a) assuming the emissivity is uniform over the whole satellite and b) dividing f (and therefore the emissivity) into 30° latitude and longitude bins, obtaining the emissivity map provided in Fig. 6.27. High-latitude data is not included because, at the radiometry resolutions, it observes a mixture of bright and dark terrains, and is not representative of the poles. (c) Residual map assuming uniform emissivity, but fitting only the data within the trailing hemisphere terrain. (d) Residual map assuming uniform emissivity, but fitting only the data within the leading hemisphere terrain.

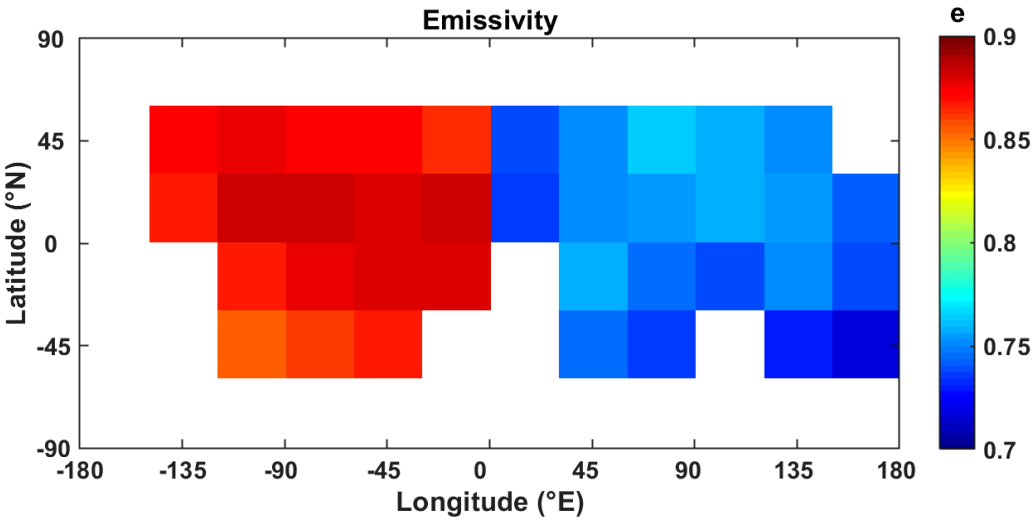

Figure 6.27 – Iapetus emissivity map, using all available data below 50° latitude, corresponding to the residual shown in Fig. 6.26. The emissivity is assumed constant in every 30×30°latitude/longitude bin. Uncertainties on the emissivities are of the order of ±0.04. The leading/trailing boundary, at 0°E, is only observed near the limbs of observations centered on each hemisphere; a more progressive transition in leading and trailing emissivities is therefore possible.

constrain the model parameters. Indeed, the leading hemisphere was observed on two different dates: December 2004 (14:30 local time) and Septembre 2007 (22:00 local time). The first of these two observations was acquired at a high latitude (40°N) and a relatively coarse resolution (beam size of 0.7 Iapetus diameters): it therefore does not sample the leading hemisphere independently from the pole. We are thus left with only one observation, insufficient to constrain the model parameters. If we do not adjust the minimum χ^2_r value to 1, then practically the full range of parameters with $\delta_{\rm el} > 1$ m and $I > 52$ MKS are within the 2-σ confidence region; only the dielectric constant remains constrained within 1.3 and 2.0. Consequently, these are the only constraints that can be reliably derived from the distant leading hemisphere scans alone.

6.4.3 Preliminary interpretations

The leading/trailing hemisphere dichotomy in emissivity derived from the global equatorial fit confirms the results of Section 6.1.2 and Le Gall et al. (2014). The emissivity values found from fitting the trailing hemisphere alone are less well constrained than in the global fit. On the leading hemisphere fits the best-fitting emissivities are non physical and the best-fitting scattering factor $f = (1 + \mu_l)/f_{\rm CBE}$ is below zero, due to insufficiently sampled data. Similarly, the leading hemisphere scattering factor $f = (1 + \mu_l)/f_{\rm CBE}$ is mostly below zero. On the trailing side and in the global fit, f is over-estimated, because it was derived using a very low backscattering cross-section only characteristic of Cassini Regio. No new interpretations can therefore be made for the degree of scattering in the subsurface of Iapetus.

Trailing hemisphere

The low-quality fit, poorly constrained parameters, and non-random residuals found on the trailing hemisphere of Iapetus are all consistent with important spatial heterogeneity within the optically bright trailing hemisphere terrain. Although bolometric Bond albedo variations were accounted for in the model, both emissivity and thermal inertia were assumed constant, even though latitudinal variations in subsurface properties are expected. Indeed, the trailing hemisphere equatorial regions receive more incoming Phoebe ring material than the poles (though much less than the leading hemisphere), as witnessed by the global distribution of dark material. Furthermore, water ice is expected to migrate to colder regions, especially the poles of Iapetus, thereby increasing latitudinal heterogeneity (Palmer and Brown, 2008; Spencer and Denk, 2010; Kimura et al., 2011). The trailing hemisphere emissivity values shown in Fig. 6.27 do not show an obvious latitudinal dependence, possibly due to inhomogeneous coverage, large uncertainties, and large region sizes (30°).

Leading hemisphere

On the leading hemisphere, an electrical skin depth >1 m and a thermal inertia >52 MKS are very similar to the lower bounds determined for these parameters by Le Gall et al. (2014) (Table 6.1), thus showing consistency between independent observations. Finer constraints on these parameters cannot be derived from the distant scans alone.

The effective dielectric constant is higher on the leading side ($1.3 < \varepsilon'_r < 2.0$) than averaged globally ($1.0 < \varepsilon'_r < 1.36$) or on only the trailing side ($1.0 < \varepsilon'_r < 1.28$). VIMS observations have found that CO_2 ($\varepsilon'_r = 1.55$) ice is more abundant on the leading than trailing hemisphere (Buratti et al., 2005), and tholins ($\varepsilon'_r = 2.03 - 2.33$) or other complex hydrocarbons with similarly low ε'_r are a favored dark material component (Cruikshank et al., 2008; Dalle Ore et al., 2012; Cruikshank et al., 2014; Le Gall et al., 2014).

We recall that the derived values of ε'_r are a combination of the intrinsic properties of the material, and its degree of depolarization, which is highest for "fluffy", unconsolidated materials. There are thus two possible explanations for the discrepancy between expected and derived leading/trailing differences in dielectric constants. Firstly, materials with higher ε'_r, such as iron oxides, may be present in large quantities within the Cassini Regio dark material (Clark et al., 2012). Secondly, the leading hemisphere's subsurface could be much more compact and less depolarizing than the trailing hemisphere's, enough to invert a dielectric constant difference. This hypothesis is particularly likely given that higher backscatter (Le Gall et al., 2014) and lower emissivities are seen on the trailing hemisphere, indicating important subsurface volume scattering, which is often associated with porous, depolarized media.

6.5 Conclusion

We have presented, reduced, and analyzed all available resolved and unresolved Cassini radiometry observations of Saturn's largest icy satellites Rhea, and performed a preliminary analysis of the Cassini radiometry dataset on Dione and Iapetus. With a combination of thermal, radiative transfer, and emissivity models, we have simulated antenna temperatures for each observation.

The Cassini radiometer is found to probe the subsurface down to at least $6-13$ m below the surface of Rhea and likely similar depths on Dione. Overall, the microwave dataset points to a very transparent (and therefore rich in pure water ice) and unpolarized (resulting in efficient multiple/volume scattering) subsurface on both satellites, with an increasingly compacted regolith with depth. As observed on Enceladus (Le Gall et al., 2017) and in the radar-bright Xanadu region on Titan (Janssen et al., 2011), the emissivities of both Dione and Rhea are not low enough compared to their very high backscatter, when compared to expectations based on the Kirchhof law of thermal radiation and classical models of random subsurafce scattering. In particular, the CBE (e.g., Hapke, 1990; Black et al., 2001b) predicts insufficient backscatter or much lower emissivities. The presence of (maybe organized) scattering cm-scale structures in the subsurface of Rhea, Dione, and likely Saturn's other inner icy satellites may be at the origin of both the high recorded radar backscattering coefficients and, by depolarizing the signal, of the very low inferred effective dielectric constants ($\varepsilon'_r = 1.1-1.5$). The structure of the subsurface remains to be fully investigated, as the nature and formation mechanism of these scattering subsurface structures is as yet unknown.

Subsurface scattering models exist for radar modeling (independent from microwave emission), such as the CBE model developed by Peters (1992) and applied to Galilean satellites by Black et al. (2001b). Microwave emission models of snow on Earth, such as the MEMLS3&a (Proksch et al., 2015) and the SMRT (Picard et al., 2018) may be applicable to snow-like media on Saturn's icy satellites, and should be investigated. Applying these models to outer Solar System surfaces is challenging due to the large number of unconstrained parameters, but can be helpful, as found by Ries (2012). Similarly, numerical models of the interactions between and electromagnetic waves and subsurface inhomogeneities have been developed, including the TEMSI-FD code (Le Gall et al., 2008); such models have been applied to radar observations of Titan (Le Gall et al., 2010) and to the preparation of the operation of a ground-penetrating radar on Mars (e.g., Ciarletti et al., 2017). Different subsurface scattering models should therefore be applied to Saturn's icy satellites in order to conciliate the Cassini radar (high backscatter) and radiometry (emissivities not low enough) results.

A preliminary analysis on Dione detected little to no hemispheric dichotomy in the radiometry data, although it seems to be present in the active radar data (Chapter 3). This result, which would

point to a likely shallow layer of both leading hemisphere E-ring deposit and trailing hemisphere dark material, must be confirmed by future work. A positive temperature anomaly is found on the sub-Saturn side of both Rhea and Dione, which is only partially accounted for by including Saturn's contribution to incident fluxes.

On Iapetus, preliminary analysis of only distant scans (excluding the resolved scan examined by Le Gall et al., 2014) leads to results consistent with previous work, but poorly constrained. Including the resolved data with the distant scans, using Le Gall et al. (2014)'s Combined Emissivity-Backscatter (CEB) model including a quasi-specular backscattering component, should lead to improved constraints on the leading hemisphere. This analysis would help constrain the dielectric constant, which preliminary results indicate is higher on the leading than trailing side.

The simplifications of the thermal model allow for a small number of parameters, which are well constrained in the case of Rhea, where the most and highest-quality Cassini radiometry data is available. However, our results point toward inhomogeneous properties with depth (at least thermal inertia, and therefore likely porosity and dielectric properties) and regionally (latitudinal and near Inktomi crater). Le Gall et al. (2014) has shown this to be the case for Iapetus also, and it is reasonable to assume that all Saturn's airless icy satellite surfaces include a loose, porous regolith over a more compact subsurface. In consequence, it is necessary to focus on both modeling and observing variations in thermo-physical subsurface properties with depth.

Chapter 7

Radiotelescope observations of Iapetus and Phoebe

Because longer wavelengths probe deeper into the subsurface, observing a surface at a variety of wavelengths can bring to light changes in thermal, compositional, and physical properties with depth. At an orbital radius of 61.1R_{Saturn}, the maximum elongation of Iapetus from Saturn is about 8 to 9 arc minutes: its flux can be separated from the planet's. Furthermore, at 1460 km in diameter, Iapetus is a fairly bright target at millimeter to centimeter wavelengths, making it observable from Earth at multiple microwave frequencies. Using the NIKA2 instrument on the IRAM 30-meter telescope and the VLA, new observations of the leading and trailing sides of Iapetus have been acquired and calibrated. In combination with pre-existing datasets from Cassini and other ground-based telescopes, the newly derived brightness temperatures reveal distinct leading and trailing hemisphere physical properties, with unexpected behaviors at millimeter wavelengths.

7.1 The hemispherical dichotomy of Iapetus in the microwaves

As described in Section 4.1, the leading and trailing sides of Iapetus interact differently with their orbital environment and, in particular, with the vast and diffuse ring around Phoebe (hereafter referred to as "Phoebe ring"). Indeed, an optically dark material progressively covers the leading side of Iapetus as it travels through the Phoebe ring (Verbiscer et al., 2009), and thermal segregation further enhances the resulting albedo contrast (Spencer and Denk, 2010). This albedo dichotomy is also apparent in the microwaves (Section 6.4).

7.1.1 Radar observations

Iapetus and Phoebe have both been observed by the Cassini radar (Chapter 3.2; Ostro et al., 2006; Ostro et al., 2010; Le Gall et al., 2019), and by the Arecibo radar system (Section 2.5.5 and Black et al., 2004). The radar albedos resulting from these observations, already provided in Tables 2.2 and 3.2, are summarized in Table 7.1 for convenience.

Table 7.1 – Arecibo (13 cm) and Cassini (2.2 cm) radar observations of Iapetus and Phoebe

	Iapetus Leading	**Iapetus Trailing**	**Phoebe**
$A^{\text{disk}}_{\text{TP}-2.2}$	0.34 ± 0.05	0.80 ± 0.13	0.30 ± 0.01
$A^{\text{disk}}_{\text{TP}-13}$	0.13 ± 0.04	0.17 ± 0.04	

Both Phoebe and Iapetus radar echoes are dominated by diffuse scattering rather than specular reflections, indicating the presence of at least some subsurface volume scattering (Ostro et al., 2006). At 2.2 cm, the Trailing Hemisphere (TH) of Iapetus has a higher radar albedo than the Leading Hemisphere (LH), whose radar albedo is very close to Phoebe's. This result is consistent with a deposit of low-reflectivity non-icy material originating on Phoebe and depositing preferentially on the leading side of Iapetus (Ostro et al., 2010; Le Gall et al., 2019). At 13 cm, however, the dichotomy disappears, with the LH and TH radar albedos being the same within error. The presence of a dichotomy at 2.2 cm but not at 13 cm points to a layer of low reflectivity material tens of centimeters thick, but less than a few meters thick (Ostro et al., 2010; Le Gall et al., 2014, 2019), slightly larger than the 7- to 16-cm thickness estimated by Rivera-Valentin et al. (2011) from CIRS data using a two-layer model, but consistent with predictions from dynamical and thermal migration models (Spencer and Denk, 2010; Tamayo et al., 2011).

7.1.2 Ground-based microwave radiometry

Radiometry observations, by informing on the brightness temperature and therefore the thermal properties of the subsurface, are complimentary to radar data. The Cassini radiometry of Iapetus, which has been described in Chapters 4 and analyzed by Ostro et al. (2006) and Le Gall et al. (2014) and in Chapter 6, includes both resolved and unresolved observations of various regions. However, this dataset remains limited in local time (with only three daytime observations) and only samples a single wavelength.

The FP1 long-wavelength detector (20 to 600 cm^{-1}; 17 to 500 μm) of the Composite Infrared Spectrometer (CIRS) instrument aboard Cassini also observed both Iapetus and Phoebe, allowing for the derivation of the thermal inertia by Flasar et al. (2005) and Howett et al. (2010) shown in Table 5.2. Yet even the long-wavelength detector likely only probes a few millimeters and at most a few centimeters in the subsurface (e.g., Howett et al., 2010). At these shallow depths, the surface is expected to be a loose, porous regolith, probably very different from the more compact meter-deep layer probed by the Cassini radiometer.

Ground-based radiometry, possible at multiple wavelengths from telescopes and interferometers around the world, can bridge the gap between Cassini CIRS and radiometry observations.

Advantages and disadvantages of ground-based microwave radiometry

Because long wavelengths (low frequencies) probe deeper than short wavelengths (high frequencies), observing at multiple wavelengths can inform both on the vertical structure of the regolith and on the propagation of the diurnal and seasonal thermal waves with depth. Furthermore, the efficiency of scattering, including the coherent backscatter effect, is wavelength-dependent. Thus, building the microwave spectrum of a solid body can reveal the characteristic size of possible scattering structures.

Earth-based radiometry of Saturn's icy satellites, though crucial to the understanding of their subsurfaces, is plagued by technical difficulties. Indeed, these small, cold bodies are at small angular distances from Saturn, as seen from the Earth: the very high flux of Saturn, present in the side lobes of the antenna beam pattern, often contaminates the signal from the inner icy satellites. However, these problems are not too serious for Iapetus, whose orbital radius (61 R_{Saturn}) is large enough that, near maximal elongation, there is generally little contamination from Saturn. Phoebe has an orbital radius almost four times that of Iapetus (221 R_{Saturn}), and also does not suffer from contamination by the planet's flux. Yet, it is a small object (212 km in diameter), which at Saturn's distance from Earth

makes it a very faint source, whose microwave flux lies at tens to hundreds of μJy (depending on the frequency). Fortunately, large radio telescopes and interferometers are sensitive enough to detect such a faint object, and have the resolution to separate Iapetus from Saturn. This is especially true of the upgraded Karl G. Jansky Very Large Array (VLA) and Atacama Large Millimeter/submillimeter Array (ALMA) interferometers, which, with their small synthetic beam, can even resolve features on Iapetus.

Deriving brightness temperatures

As detailed in Section 2.4.3, radiotelescopes generally obtain, at a frequency ν, a flux density S_ν (in units of Jansky, where 1Jy = 10^{-26}W m^{-2} Hz^{-1}), equal to the product of the spectral radiance B_ν^{target} of the target and its solid angle as seen from the observer Ω^{target}. The flux density of a target is measured in contrast to the sky's background microwave radiation B_ν^{CMB}. The CMB must then be subtracted as follows, especially at longer (centimeter) wavelengths where it contributes a larger fraction of the measured flux:

$$S_\nu = (B_\nu^{\text{target}} - B_\nu^{\text{CMB}}) \times \Omega^{\text{target}} \tag{7.1}$$

By inserting the formula for solid angle and Planck's equation for spectral radiance (Eq. 2.28), we find:

$$S_\nu = \frac{2h\nu^3}{c^2}\left(\frac{1}{e^{h\nu/k_B T_B^{\text{disk}}} - 1} - \frac{1}{e^{h\nu/k_B T_{\text{CMB}}} - 1}\right) \times \frac{\pi R_{eq} R'_p}{D^2} \tag{7.2}$$

where $T_{\text{CMB}} = 2.725$ K is the temperature of the CMB, D is the distance (in km) from the telescope to the target, R_{eq} is the equatorial radius (747.4 km in the case of Iapetus), and ν is the effective frequency, found by convolving the receiving bandwidth with the atmospheric transmission. R'_p is the projected polar radius of Iapetus, which depends on the sub-Earth latitude ϕ and the polar radius R_p (712.4 km in the case of Iapetus):

$$R'_p = \sqrt{R_{eq}^2 \sin^2\phi + R_p^2 \cos^2\phi} \tag{7.3}$$

The disk-integrated brightness temperature T_B^{disk} can then be derived from Eq. 7.2.

7.1.3 Iapetus ground-based radiometry: pre-existing observations and interpretations

Green Bank Telescope (GBT) observations

Ries (2012) partially bridged the gap between CIRS and Cassini radiometry by observing Iapetus's two faces at wavelengths varying from 3.3 to 10.8 mm using the Green Bank Telescope (GBT), a 100-meter single dish radiotelescope located in Green Bank, West Virginia (USA). At 3.3 mm (90 GHz; W band), the MUSTANG (MUltiplexed Squid Transition-edge sensor Array at Ninety Gigahertz) imaging bolometer array acquired observations on the LH and at 30°E (mixed dark and bright terrains, but dominantly TH). At 7.8, 8.6, 9.6, and 10.8 mm (38.25, 34.75, 31.25, and 27.75 GHz), the CCB (Caltech Continuum Backend) Ka-band receiver observed a variety of regions of Iapetus on 11 different occasions, four of which failed due to bad weather. Three observations had the best weather and are considered reliable; two of these are on the LH and one on the TH. The main characteristics of the data gathered with the GBT are presented in Table 7.2 and shown in Fig. 7.1; for further detail, including on the calibration, atmosphere removal, and sidelobe mitigation techniques, see Ries (2012). Ries (2012) then used an empirical thermal model with sub-solar heating to derive the emissivity.

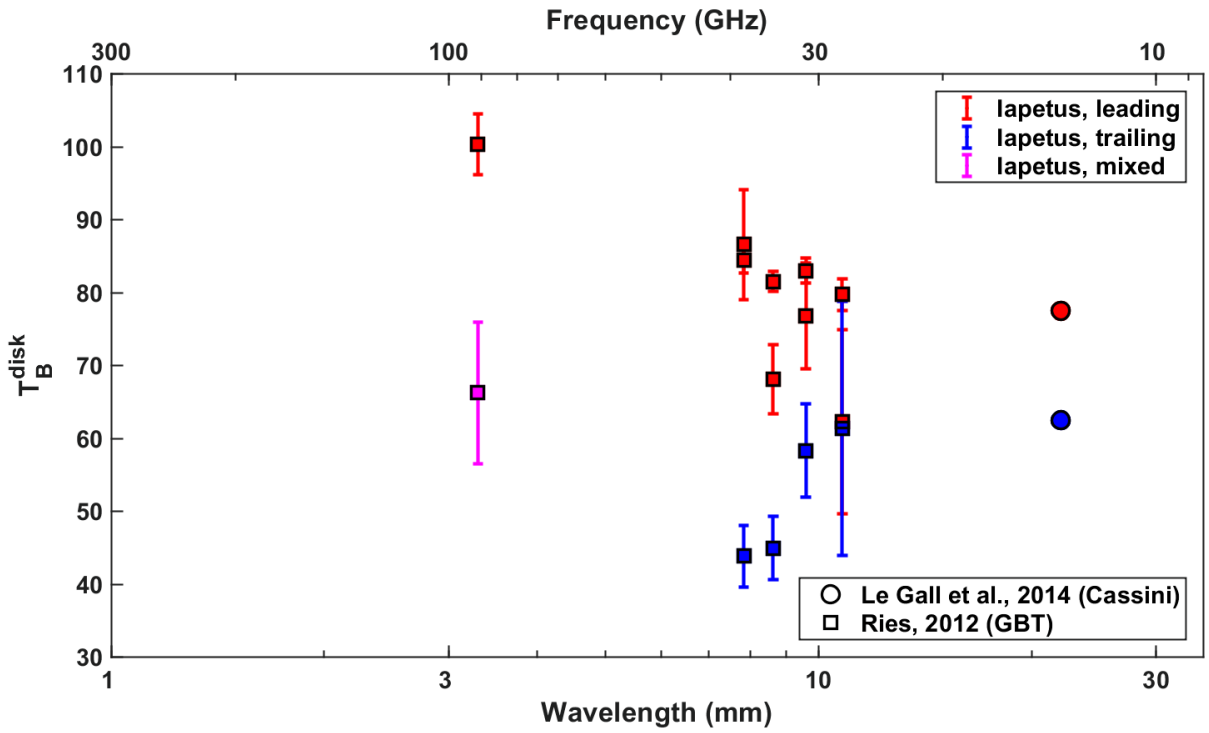

Figure 7.1 – Iapetus brightness temperatures found using the Green Bank Telescope (GBT) by Ries (2012) and using the Cassini radiometer (Le Gall et al., 2014 and Table 4.1). Only the three days with the best weather are shown for the GBT dataset. Only two Cassini radiometry observations were selected, representative of the leading (IA049-2) and trailing (IA049-4) hemispheres and acquired near 22h and 10h local time, respectively (whereas all Earth-based data is near local noon).

We re-calculated the brightness temperature from the fluxes found by Ries (2012), using the method described in Section 7.1.2. Because contribution from the CMB and polar flattening are now taken into account, the values of derived T_B^{disk} (shown in Table 7.2 and Fig. 7.1) are higher than those found by Ries (2012). Nonetheless, their interpretations remain valid.

On the leading side, Ries (2012) observed decreasing brightness temperatures and emissivities with increasing wavelength, especially compared to the surface temperature of ~100 K. At first glance, this observation appears consistent with a thermal depth effect, as longer wavelengths are probing deeper into the dayside's cold subsurface, below the diurnal skin depth. However, Ries (2012) point out that this explanation is insufficient to justify the very steep temperature drop from 3 mm to 7.8 mm. Instead, we suggest an alternate explanation, already proposed by Le Gall et al. (2014) to explain Cassini radiometry observations: at long wavelengths, radiometers probe increasingly into the low-emissivity icy substrate underlying the high-emissivity LH material. This idea is consistent with a dark material layer thickness of several decimeters, through which centimetric wavelengths would probe more easily than millimetric wavelengths (Black et al., 2004; Ostro et al., 2006; Le Gall et al., 2014).

The trailing side is less emissive than the leading side at all observed wavelengths. Further, it shows a putative large "absorption" feature, as suggested by the re-increase in T_B^{disk} with wavelength beyond 8 mm. The 3.3 mm "mixed" observation, which included signal from both LH and TH, leads to a fairly low brightness temperature (66.2 ± 9.7 K), implying that the value on the TH alone would be even lower: Ries (2012) extracted a 3.3-mm trailing side temperature of 42 K using a simplified temperature map (including three different values for the LH, TH, and polar regions). Ries, 2012 therefore deduced that the dip in T_B^{disk} is centered at about 3 millimeters. By comparison with outputs

from the semi-empirical Microwave Emission Model for Layered Snowpacks (MEMLS) developed for and tested on snow on Earth (Wiesmann et al., 1998), Ries (2012) attributed this feature to diffuse scattering by 1–2-mm ice particles. However, Ries (2012) points out that the MEMLS is restricted to grain sizes < 3 mm, a size large enough to model most snowpacks on Earth (Wiesmann et al., 1998; Wiesmann and Mätzler, 1999; Mätzler and Wiesmann, 1999), but possibly too small for some planetary ices.

Sub-Millimeter Array (SMA) observations

The Sub-Millimeter Array (SMA) is a joint project between the Smithsonian Astrophysical Observatory and the Academia Sinica Institute of Astronomy and Astrophysics and is funded by the Smithsonian Institution and the Academia Sinica. A series of observations of Iapetus were conducted with the SMA in Hawaii in 2012, in order to characterize the emissivity of the leading and trailing hemisphere terrains at a wavelength of 1.3 mm (225 GHz frequency). Four of these observations were calibrated and presented by Hagen et al. (2014), again showing a warmer LH than TH. Comparing the extracted brightness temperatures to two different thermal models, keeping the emissivity constant at $e = 0.9$ requires bolometric Bond albedo values inconsistent with the literature. This led the authors to the conclusion that a LH emissivity of $e_{\mathrm{LH}}^{1.3\ \mathrm{mm}} = 0.759$ and a TH emissivity of $e_{\mathrm{TH}}^{1.3\ \mathrm{mm}} = 0.602$ would be consistent with Cassini CIRS data (Hagen et al., 2014).

The remaining SMA observations of Iapetus have since been calibrated (M. Gurwell and A. Moullet, 2020, personal communication); Titan was used as a primary calibrator. The brightness temperatures were then derived using the method detailed in Section 7.1.2. These data are presented in Table 7.2 and shown in Fig. 7.2. The leading/trailing dichotomy is clearly visible in the resulting lightcurve, yielding average LH (−90 ± 50°E) and TH (+90 ± 50°E) disk-integrated brightness temperatures of $< T_B^{\mathrm{disk}} >_{\mathrm{LH}} = 84.2 \pm 1.9$ K and $< T_B^{\mathrm{disk}} >_{\mathrm{TH}} = 63.9 \pm 2.1$ K, respectively. These values are consistent with those found by Hagen et al. (2014) from a subsection of the same dataset.

Fig. 7.3 adds these observations to the LH and TH spectra obtained from Cassini radiometry and GBT observations. On the leading side, the 1.3 mm brightness temperatures are 15 K lower than measured by the GBT at 3.3 mm, but are within uncertainties of the 7.8 mm measurements. While a thermal depth effect may still be decreasing T_B^{disk} at the longer wavelengths, another process must be causing the 3.3-mm peak. Meanwhile, on the trailing side, T_B^{disk} is higher at 1.3 mm than at 7.8, 8.6, and probably 3.3 mm.

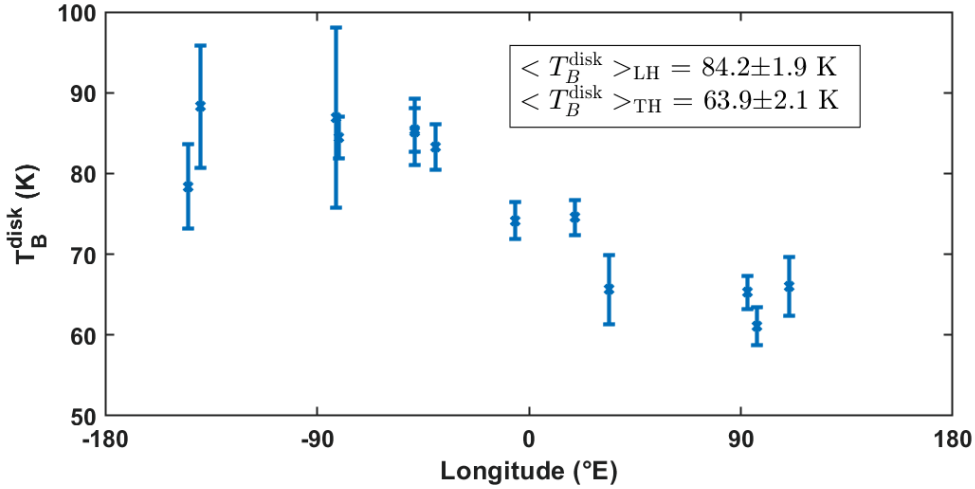

Figure 7.2 – SMA 1.3 mm (225 GHz) brightness temperatures $T_B^{\rm disk}$ found on Iapetus. The average leading and trailing hemisphere values are indicated. These data were gathered and calibrated by Hagen et al. (2014) and Gurwell and Moullet (2020, personal communication).

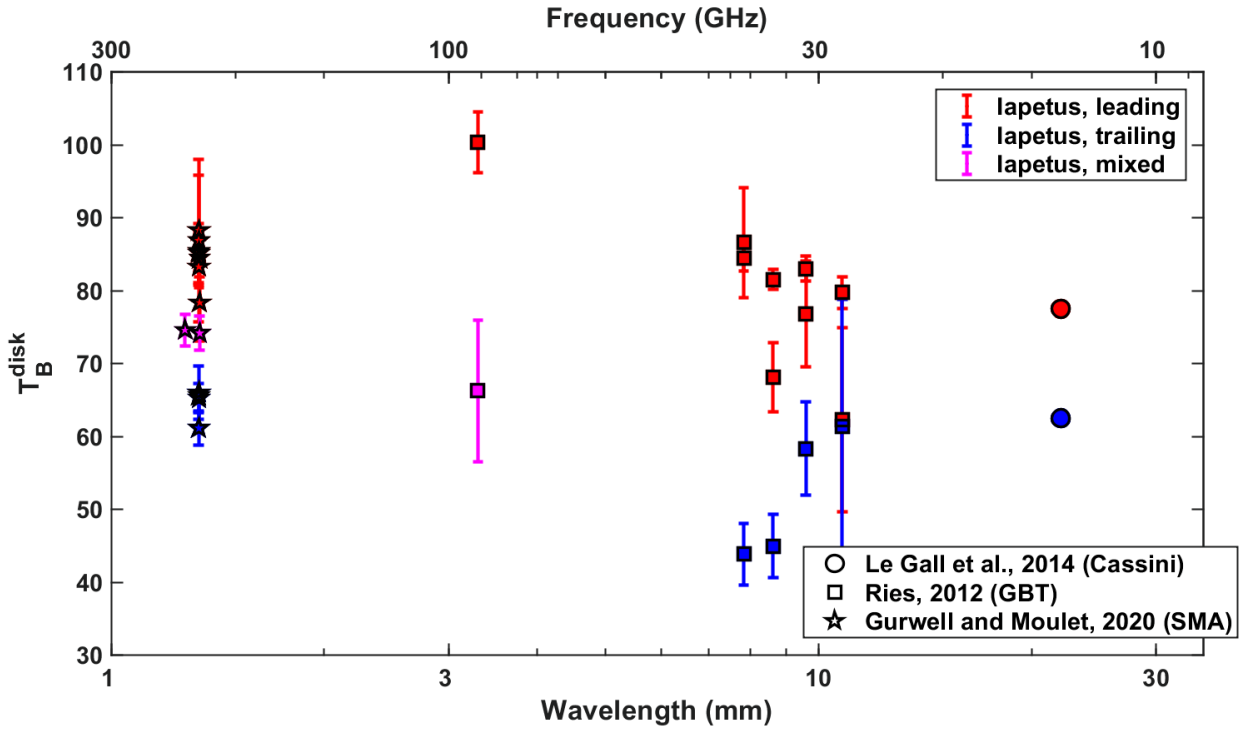

Figure 7.3 – Compilation of Iapetus brightness temperatures found before 2017 using the SMA by Hagen et al. (2014) and recalibrated by Gurwell and Moullet (2020, personal communication), the GBT by Ries (2012), and the Cassini radiometer (Le Gall et al., 2014 and Table 4.1).

Table 7.2 – Ground-based radiotelescope observations of Iapetus pre-dating the work presented herein, from Ries (2012), Hagen et al. (2014), and Gurwell and Moullet (2020, personal communication). All sub-Earth coordinates and disk-integrated brightness temperatures were re-calculated from the fluxes provided by these references.

Date	**λ (mm)**	**Lat. (°N)**	**Long. (°E)**	**Observed side**	**Flux (mJy)**	**T_B^{disk} (K)**	**Reference**
03 Mar 2010	3.33	10	30	Mixed	16.5 ± 2.5	66.2 ± 9.7	Ries (2012)
16 Feb 2011	3.33	13	-104	Leading	23.1 ± 1.0	100.4 ± 4.2	Ries (2012)
04 Dec 2010	10.8	13	-131	Leading	1.04 ± 0.22	62.3 ± 12.6	Ries (2012)
	9.6				1.64 ± 0.16	76.8 ± 7.2	Ries (2012)
	8.6				1.79 ± 0.13	68.1 ± 4.7	Ries (2012)
	7.8				2.78 ± 0.25	86.6 ± 7.5	Ries (2012)
06 May 2011	10.8	12	-108	Leading	1.77 ± 0.05	79.7 ± 2.2	Ries (2012)
	9.6				2.34 ± 0.05	83.0 ± 1.7	Ries (2012)
	8.6				2.84 ± 0.05	81.5 ± 1.4	Ries (2012)
	7.8				3.57 ± 0.08	84.5 ± 1.8	Ries (2012)
19 Nov 2011	10.8	14	91	Trailing	0.94 ± 0.28	61.38 ± 17.6	Ries (2012)
	9.6				1.13 ± 0.13	58.3 ± 6.4	Ries (2012)
	8.6				1.06 ± 0.11	44.9 ± 4.4	Ries (2012)
	7.8				1.25 ± 0.13	43.8 ± 4.3	Ries (2012)
23 Feb 2011[a]	1.33	13	-140	Leading	124.0 ± 10.7	88.3 ± 7.2	Gurwell and Moullet (2020)
28 Feb 2012	1.33	15	-6	Mixed	97.1 ± 1.4	74.2 ± 1.0	Gurwell and Moullet (2020)
11 May 2012	1.27	14	20	Mixed	112.4 ± 1.1	74.6 ± 0.7	Gurwell and Moullet (2020)
24 May 2012	1.33	14	-40	Leading	113.1 ± 2.4	83.3 ± 1.7	Gurwell and Moullet (2020)
26 May 2012	1.33	14	-48	Leading	115.5 ± 4.8	85.1 ± 3.3	Gurwell and Moullet (2020)
26 May 2012	1.33	14	-49	Leading	115.8 ± 1.8	85.4 ± 1.2	Gurwell and Moullet (2020)
02 Jun 2012	1.33	14	-80	Leading	112.2 ± 1.5	84.5 ± 1.1	Gurwell and Moullet (2020)
16 Jun 2012	1.33	14	-144	Leading	99.7 ± 6.5	78.4 ± 4.8	Gurwell and Moullet (2020)
09 Jul 2012[b]	1.33	14	111	Trailing	76.9 ± 1.0	66.0 ± 0.8	Gurwell and Moullet (2020)
12 Jul 2012	1.33	14	97	Trailing	69.9 ± 2.1	61.1 ± 1.7	Gurwell and Moullet (2020)
13 Jul 2012	1.33	14	93	Trailing	74.8 ± 1.2	65.3 ± 1.0	Hagen et al. (2014)
26 Jul 2012[b]	1.33	14	34	Mixed	71.7 ± 2.9	65.6 ± 2.4	Gurwell and Moullet (2020)
21 Aug 2012[a]	1.33	14	-81	Leading	89.9 ± 12.0	86.9 ± 11.1	Hagen et al. (2014)

[a] Due to poor weather, these observations are less reliable.
[b] Due to the proximity of Titan to Saturn, calibration was difficult and a 5% error should be added.

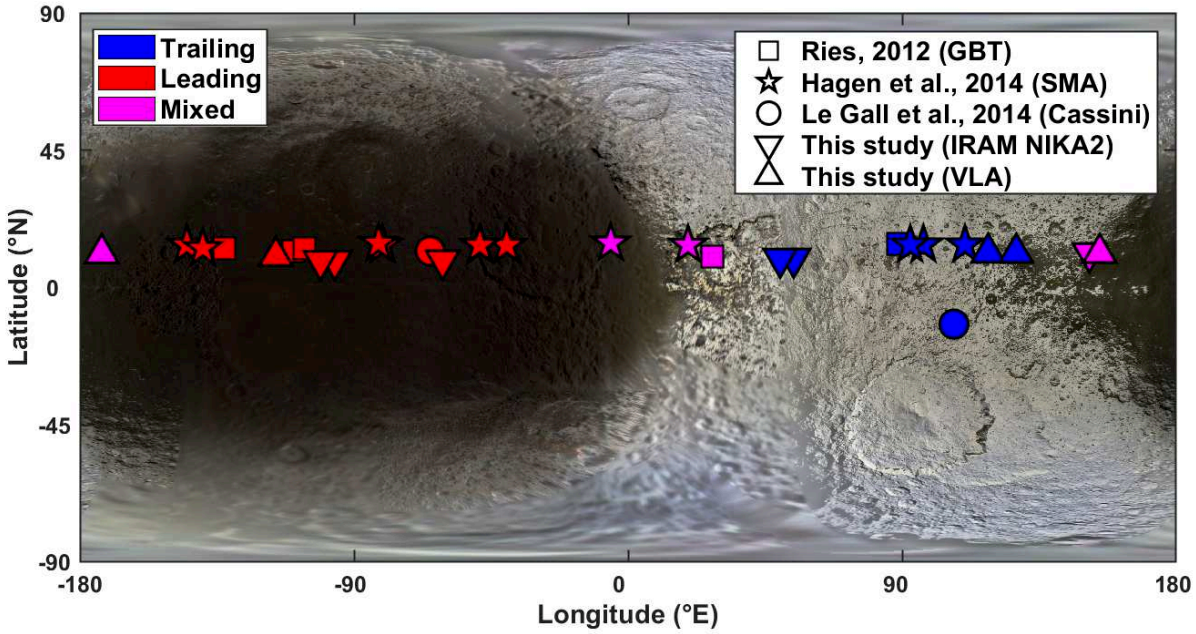

Figure 7.4 – Map of Iapetus with the sub-Earth point indicated for each date of observation acquired both before (Ries, 2012; Hagen et al., 2014, Gurwell and Moullet 2020, personal communication) and during the present study (triangles). The sub-spacecraft point of the two Cassini radiometry observations used herein is also shown. LH, TH, and mixed locations are shown in red, blue, and magenta, respectively. All Earth-based observations were acquired during the local day, whereas the two Cassini radiometry scans represented here have a local time of 21:49 UTC (IA049-2, on the leading side) and 09:54 UTC (IA049-4, on the trailing side) (see Table 4.1). The background image is the ISS 3-color composite of Iapetus (PIA18436).

7.1.4 Outstanding questions and motivations for the present study

The microwave radiometry data gathered by Ries (2012) and Hagen et al. (2014) reveals likely compositional and structural variations with depth, on both sides of Iapetus. However, these observations also pose new questions. If confirmed, what is the cause behind the increasing 1.3 – 3.3 mm values of T_B^{disk} on the leading side? Can further observations help quantify the particle size causing the trailing hemisphere mm-wavelength dip in T_B^{disk}? At what wavelength, if any, do the leading and trailing hemispheres have the same temperature and emissivity? Does microwave radiometry support the hypothesis that the Phoebe ring is the source of the leading hemisphere dark material?

In order to help answer these questions and complete a missing part of Iapetus's microwave spectrum, we conducted a microwave observation campaign. We observed the two faces of Iapetus at 1.15 and 2.0 mm using the NIKA2 camera (Catalano et al., 2014; Calvo et al., 2016; Adam et al., 2018) at the IRAM-30 m telescope at Pico Veleta in Spain; these data are described in Section 7.2. In parallel, centimetric data were acquired on Iapetus and Phoebe using the VLA interferometer in New Mexico, USA, as detailed in Section 7.3. The sub-Earth coordinates of all reliable existing microwave

observations of Iapetus to date, including those gathered with the VLA and the IRAM NIKA2 camera and described hereafter, are indicated in Fig. 7.4.

7.2 Disk-integrated observations of Iapetus from the IRAM 30 meter telescope

A preliminary analysis of the Institut de Radioastronomie Millimétrique (IRAM) 30 meter telescope observations of Iapetus has been presented at the mm Universe @ NIKA2 conference in June 2019, and published in the peer-reviewed conference proceedings (Bonnefoy et al., 2020b). The present section details the updated analysis and exposes the results.

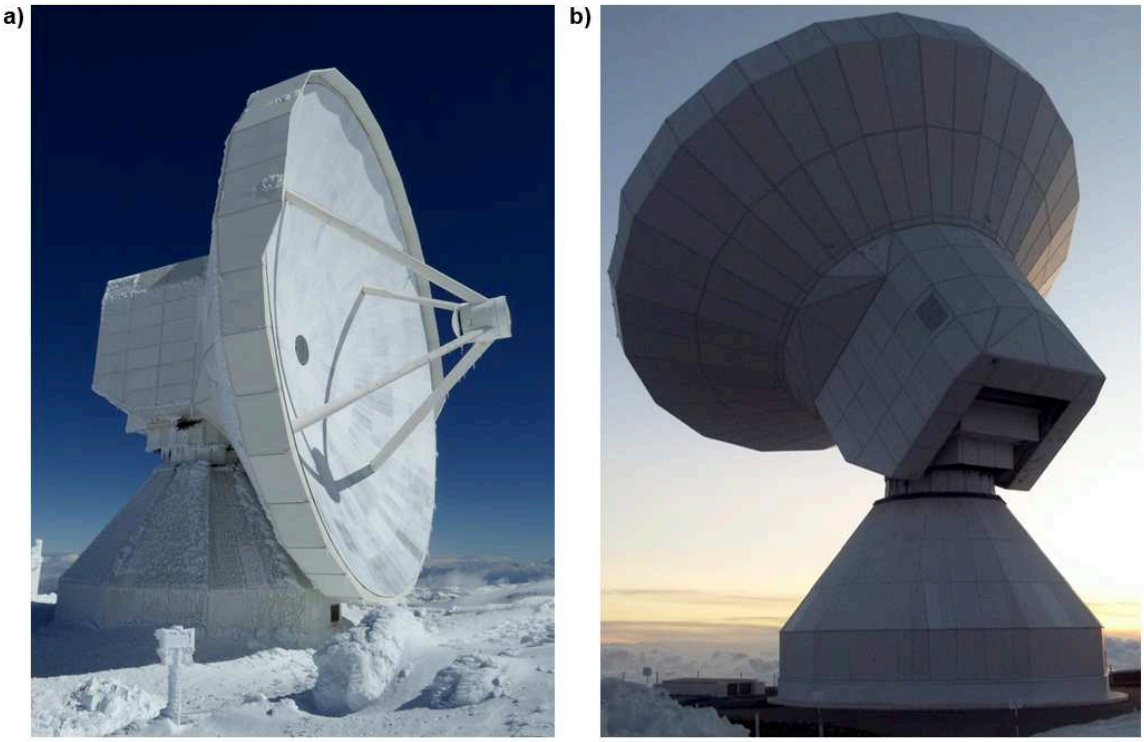

Figure 7.5 – a) IRAM 30-m telescope in March 2018, during an unsuccessful observation run. In spite of good atmospheric conditions, observations were impossible as the secondary mirror was covered in ice and the primary was fused to the ground by a thick icicle. b) IRAM 30-m telescope on the morning of 28 May 2018, after the first successful detection of Iapetus at 1.2 and 2.0 mm.

7.2.1 The NIKA2 camera on the IRAM 30-meter telescope

The New IRAM KIDs Array (NIKA2) camera mounted on the IRAM-30 m telescope (pictured in Fig. 7.5) can image a field of view of 6.5 arcmin at 150 GHz (2.0 mm) and 260 GHz (1.2 mm) simultaneously (Monfardini et al., 2014; Calvo et al., 2016; Adam et al., 2018; Perotto et al., 2020). It uses three kilopixel arrays of kinetic inductance detectors (KIDs): two at 260 GHz, which are averaged to obtain the 1.2 mm image, and one at 150 GHz. The transmission of each array is shown in Fig. 7.6, along with the Uranus and Titan spectra (used here as calibrators).

The 1.2 and 2.0 mm beam patterns of the IRAM 30-m telescope have been characterized by Kramer et al. (2013), Catalano et al. (2014), Adam et al. (2018), and Perotto et al. (2020). The main

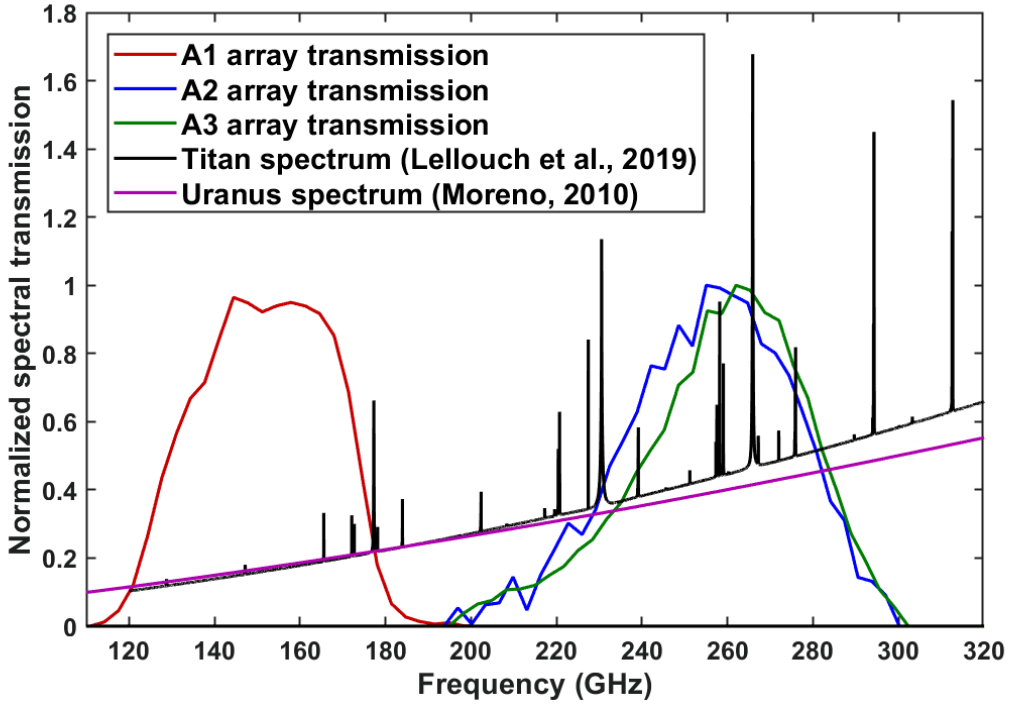

Figure 7.6 – Spectral transmission of the three NIKA2 arrays, from Adam et al. (2018) and Perotto et al. (2020). We also show the modeled spectra of Uranus (Moreno, 2010) and Titan (Lellouch et al., 2019), the two sources used for calibration, with arbitrary normalization. Note that Titan has numerous emission lines at these frequencies, which are accounted for in the calibration.

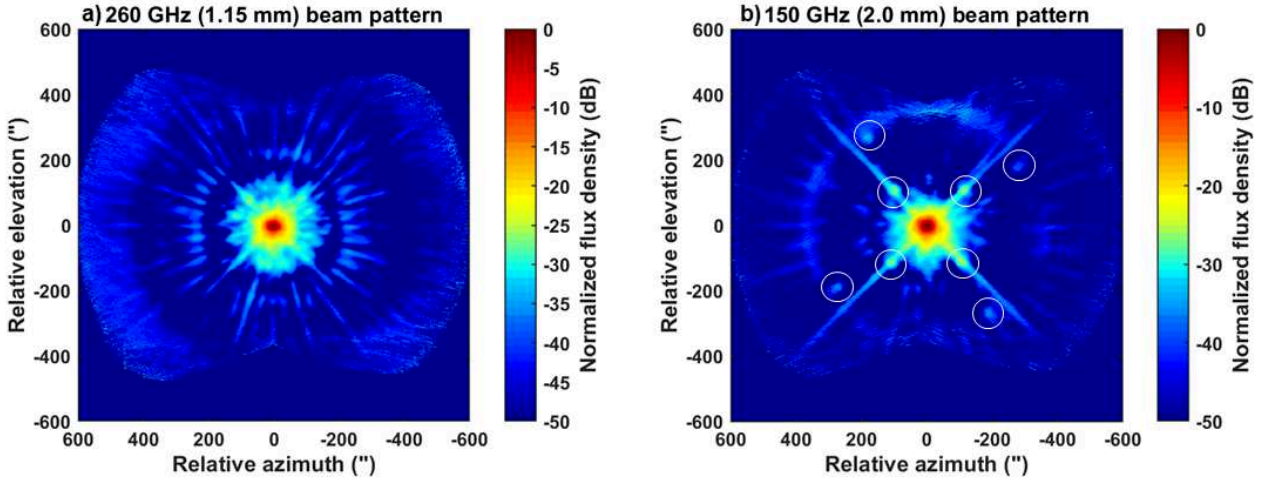

Figure 7.7 – Extended IRAM NIKA2 beam pattern in decibels at a) 260 GHz and b) 150 GHz, derived from averaging 2.5 hours of observations on Saturn on 14 February 2019. Iapetus and Titan have been masked on each individual scan constituting these maps. This figure is similar to the beam maps in Adam et al. (2018) and Perotto et al. (2020), but exposes additional structure because the source (Saturn) is brighter here than in previous analyses (Uranus). At 1.2 mm, numerous spokes are apparent, as well as a ring at ~200", which is likely caused by diffraction. At 2.0 mm, the quadrupod support structure causes an obvious ×-shape, and a likely diffraction ring is apparent at ~350". There are also eight 2.0-mm-bright spots (circled in white), whose positions can vary with respect to the rest of the beam. Finally, the bright circle at > 400" at 1.2 mm is most likely an artifact created by applying the atmospheric correction to a very bright source.

beam is a circular Gaussian of FWHM 10.8 ± 0.2" at 260 GHz and 17.4 ± 0.6" at 150 GHz, although the ellipticity and size of the main beam can increase at low elevations and during sunrise and late afternoon (Adam et al., 2018; Perotto et al., 2020). The beam pattern also includes an error beam decomposed into three Gaussians (from deformations of the primary mirror) as well as diffraction rings, spokes, and spikes, described by Kramer et al. (2013), Adam et al. (2018), and Perotto et al. (2020) and shown in Fig. 7.7.

7.2.2 Observation strategy

Given the small FWHM of the main beam, we were originally hoping to detect some of the inner moons of Saturn, whose maximum elongations vary from 25.5" for Mimas to 70" for Rhea; Iapetus was assumed to be far enough from Saturn to be always detected. Our first proposal (project number 087-17) therefore imaged a large field of view centered on Saturn and including both Titan and Iapetus. An example of the resulting map, on 28 May 2018, is illustrated in Fig. 7.8. It quickly became clear that, due to Saturn's contribution to the side lobes, the inner moons could not be detected. Indeed, flux densities of the order of 1 Jy are seen out to about 100" of Saturn at 1.2 mm and 2.0 mm, making it impossible to detect targets whose expected flux is of the order of tens to a hundred mJy (Fig. 7.8). Iapetus, however, can already be seen within this map, at 250" elongation. It was therefore decided to concentrate on Iapetus for the following proposal (project number 111-18), more specifically, on observing the leading and trailing hemispheres.

In order to measure the flux densities of the trailing and leading hemispheres of Iapetus independently, observations of the satellite had to occur near maximum elongation. Given that Iapetus orbits around Saturn in 79 days, the most appropriate dates to observe during the winter 2019 pools were January 31 to February 15 for the trailing side, and March 12 to March 26 for the leading side. Data were acquired on the trailing side on two occasions (14 and 15 February 2019) and on the leading side on three different days (12, 20, and 21 March 2019). On each day, we used the NIKA2 camera to image a field of view centered on Saturn and extending at least 100" beyond the position of Iapetus, which lies 200" to 500" away from Saturn depending on the date. Scans were centered on Saturn to keep the beam pattern symmetrical. Indeed, the atmosphere subtraction also removes some sidelobes: this processing becomes asymetrical if images are not centered on Saturn, and the side lobes become warped, which can affect the flux at Iapetus.

The characteristics of the IRAM observations of Iapetus are summarized in Table 7.3, and their sub-Earth coordinates are shown on a map of Iapetus in Fig. 7.4, along with the sub-Earth coordinates of the other Iapetus observations. Note that on May 23, 2018 Iapetus was too close to Saturn and on May 27 the sky opacity was too high: on both of these dates, Iapetus was not detected. The calibration of the remaining 7 observations is detailed hereafter.

7.2.3 Calibration and flux derivation

Individual scans, which each complete a map of Saturn and its surroundings, are often too noisy to detect Iapetus, and are thus averaged by series of six to increase the SNR. For the 2018 scans, which were smaller (extending about 400" from Saturn) and therefore faster to obtain, this corresponds to an average over 20 minutes; in 2019, scans are averaged over 36 minutes (the field scanned is larger to capture Iapetus); however, the integration time over Iapetus is similar because it is not within NIKA2's field of view (of 390") when imaging the other side of Saturn. On each day, three to eight series of six scans were acquired; for each, the flux from Iapetus and Titan was measured and is provided in Table 7.3.

Table 7.3 – NIKA2 observations of Iapetus. The latitude and longitude given are for the sub-Earth point on Iapetus. The sky opacity τ at zenith is measured with a 225 GHz (1.33 mm) taumeter. The Earth–Saturn distance is given in astronomical units (AU).

Date	**Time (UTC)**	**Elevation (°)**	τ	**Lat. (°N)**	**Long. (°E)**	**Iapetus elong.**	**Titan elong.**	**Int. time**	**Earth dist. (AU)**
23 May 2018[a]	01:18–02:56	27.6-30.7	0.28	11.2	179	95"	186"	1.5h	9.21
27 May 2018[a]	01:20–02:02	28.7-30.4	0.56	11.3	161	212"	106"	0.7h	9.17
28 May 2018[b]	00:01–04:26	22.2-30.7	0.21	11.3	157	250"	153"	3.9h	9.16
29 May 2018[b]	01:26–04:42	21.5-30.7	0.20	11.3	152	291"	185"	1.5h	9.16
14 Feb 2019	08:12–10:51	27.4-31.0	0.13	9.5	55	432"	92"	2.4h	10.82
15 Feb 2019	08:20–10:56	28.1-30.9	0.21	9.5	50	412"	132"	2.4h	10.81
12 Mar 2019	07:16–09:05	29.7-31.3	0.10	8.9	-61	412"	156"	1.8h	10.49
20 Mar 2019	04:58–07:47	20.2-31.3	0.13	8.8	-96	495"	163"	2.4h	10.35
21 Mar 2019	06:18–08:53	28.5-31.3	0.17	8.8	-101	491"	179"	2.4h	10.33

[a] Due to poor weather and the proximity of Iapetus to Saturn, Iapetus was not detected at these dates.
[b] Due to the proximity of Iapetus to Saturn and the non-ideal opacity, accurate measurement of the Iapetus flux was difficult, especially at 2.0 mm.

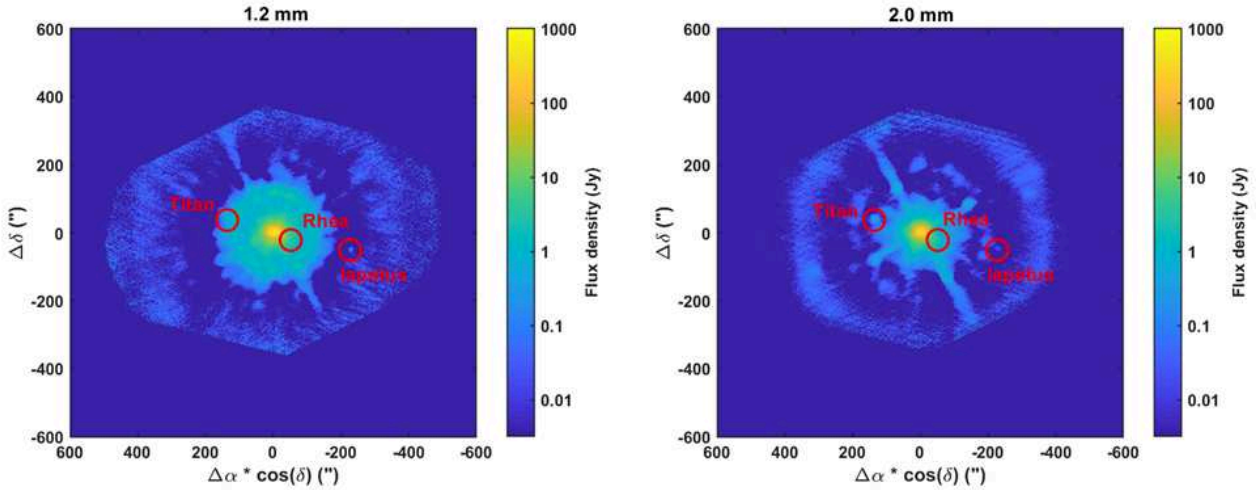

Figure 7.8 – Observation of Saturn and its satellites on 28 May, 2018. Data is integrated over 22 minutes, from 1:04 to 1:26 UTC. The positions of Rhea, Iapetus, and Titan are indicated; Saturn is in the center. Other rings, lines, and spots up to ~300" from the center reflect the extended beam pattern of the IRAM 30 m telescope and NIKA2. Rhea and the other mid-sized satellites of Saturn are too close to Saturn to separate.

The data was reduced and calibrated on Uranus by Jean-François Lestrade, astrophysicist at the Observatoire de Paris. For each day, I then attempted a re-calibration on Titan, which was observed under the same atmospheric conditions and at the same time and elevation as Iapetus but suffers from confusion with Saturn flux. For each day, the calibration source (Uranus or Titan) yielding the most consistent results was chosen.

Standard NIKA2 calibration on Uranus

The details of the NIKA2 calibration steps are provided in Perotto et al. (2020). Uranus and the secondary calibrators CL2688, NGC7027, and MWC349, were observed before or after each Iapetus observation. For each one-week observation run, the response of each individual pixel of all three kids arrays is defined, based on beam maps conducted each day on Uranus. Ideally several times a day, skydips are also performed in order to calibrate the response of the NIKA2 instrument with respect to changing atmospheric conditions (sky opacity). All data within a week-long observation run can thus be calibrated in a uniform way, depending on the recorded atmospheric conditions. To correct for second-order day-to-day inaccuracies in the calibration, the fluxes measured on the calibration sources at times close to the Iapetus observations are examined. This comparison results in an additional adjustment factor of up to 5%. The resulting flux densities are accurate to within 5% (Perotto et al., 2020).

Calibration on Titan

When Titan is sufficiently far from Saturn, it can also be used as a calibration source. Indeed, Titan's brightness temperature spectrum is well known (<5% uncertainty in flux; Lellouch et al., 2019), and more importantly it was observed at the same time and under the same atmospheric conditions as Iapetus, owing to the large field of view of NIKA2 and the map sizes. The caveat of using Titan as a calibrator is that it is always affected, to some degree, by Saturn contamination. Calibration on Titan imposes further timing constraints for the observations, as it is only possible to accurately measure the flux from Titan near its maximum elongation (~180" away from Saturn), when it is more easily separable from Saturn. Thus the 14 February 2019 observation cannot be calibrated on Titan, which was < 100" away from Saturn at that time.

The flux from both Titan and Iapetus is measured using the method described below. We then perform an absolute calibration on Titan using the spectrum from Lellouch et al. (2019), shown in Fig. 7.6. Titan's fluxes at 1.2 and 2.0 mm are predicted, and the Iapetus flux is adjusted correspondingly. Ideally, if the atmospheric conditions are stable, this adjustment should remain below 5%.

Extracting the flux

The observations on Saturn, a particularly bright source, reveal the structure of the extended beam pattern, which I mapped for each day. All daily observations were co-added in azimuth, elevation coordinates (in which the beam does not move), while Titan and Iapetus were masked. The resulting beam map on 14 February 2019 is shown in Fig. 7.7. Because we are using a brighter source (Saturn rather than Uranus) than Adam et al. (2018) and Perotto et al. (2020) to build this beam map, more structure is apparent. More specifically, we note previously undetected putative diffraction rings at 1.2 mm (~200" from the source) and 2.0 mm (~350" from the source), as well as four extra bright spots ~ 300" from the source at 2.0 mm, circled in white in Fig. 7.7.

As mentioned above (Section 7.2.2), the measurement of both Titan's and Iapetus's flux density is complicated by the proximity of Saturn, which, at ~1200 Jy at 1.2 mm and ~500 Jy at 2.0 mm, is

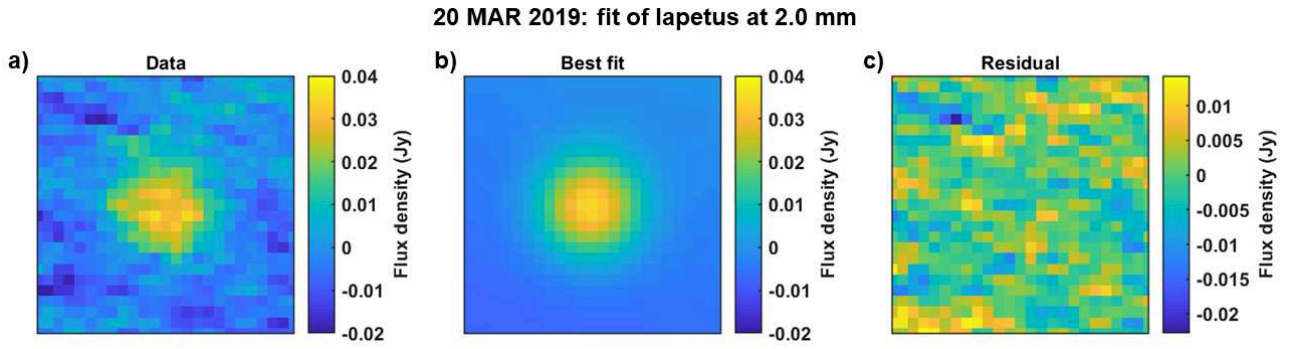

Figure 7.9 – a) View of Iapetus on 20 March, 2019. Data is integrated over 36 minutes, from 4:58 to 5:40 UTC. Image is shown for the 25x25" window where the fit is applied at 2.0 mm. b) Best fit to the data. The model fitted is a Gaussian over a tilted plane; in this case, the Iapetus flux found is 0.039 ± 0.002 Jy. c) Residual map, with a mean of 0 and a standard deviation of 0.005 Jy.

over 10000 times brighter than Iapetus (~0.1 Jy at 1.2 mm and ~0.03 Jy at 2.0 mm) and 1000 times brighter than Titan (~1.2 Jy at 1.2 mm and ~0.4 Jy at 2.0 mm) at mm wavelengths. The large-scale structures of the beam pattern, such as the error beam (Kramer et al., 2013), are filtered out along with the atmospheric fluctuations in the data reduction pipeline (Ruppin et al., 2018). Residual structures remain, which affect the data out to at least 350" from Saturn. Most of these sidelobes are fixed relative to the antenna; however, they also appear to change in amplitude, shape, and general appearance with elevation, time, and atmospheric conditions. Due to this time variability, the extended beam cannot be simply subtracted from the data. Instead, multiple observations at different times, parallactic angles, and on different days allow us to detect and average out the flux variability caused by the sidelobes.

Indeed, as the telescope follows Saturn in the sky over the 1.5 to 4 hours of observation, the parallactic angle changes. In practice, this means that the orientation of the beam pattern changes relative to the position of the satellites (this fact permitted the construction of the beam maps in Fig. 7.7 by masking the satellites). Over the hours of observation, both Titan and Iapetus move in and out of local peaks within the sidelobes. Our method consists in dividing the observations into 20 to 36-minute segments, which is a time span short enough that the position of the satellites within the beam varies little, and long enough that we have a clear detection. The positions of Saturn, Titan, and Iapetus are known precisely at each time from the SPICE NAIF toolkit (Acton et al., 2018). For each segments of 6 individual scans, we select the data over a small region (19x19" at 1.2 mm; 23x23" at 2.0 mm) centered on the satellite; these sizes have been optimised to properly separate the Gaussian parameters and the background. Within this small region, we fit a 2-dimensional Gaussian with a tilted plane in the background; the amplitude of the Gaussian is the satellite's flux. The tilted plane accounts for variations in the background flux caused by Saturn contamination and by the negative rebound introduced by the atmosphere subtraction on such a strong source. An example of the fitting method is shown in Fig. 7.9.

Iapetus flux is finally converted to brightness temperature following the method described in Section 7.1.2. The angular size of Iapetus is around 0.19" to 0.22" and varies with the Earth–Iapetus distance.

Uncertainties

Individual values for each segment are shown in Fig. 7.10 and Table 7.4. Uncertainties are derived from the 95% confidence interval of the 2-D Gaussian fits to the fluxes of Iapetus and Titan; residual errors due to the extended beam are most likely the cause of the observed scatter within each day (see Fig. 7.10). Estimating the uncertainty on each fit with a Monte Carlo method yields very similar error bars, except when the residual noise is not Gaussian, in which case a Monte Carlo method underestimates the uncertainty. The leading and trailing values are given in Table 7.5; error bars are propagated from the uncertainty on individual measurements while also taking into account the 5% uncertainty on the Titan model, if calibration on Titan is used.

7.2.4 Results

The disk-integrated brightness temperatures derived using the standard calibration and calibrating on Titan are shown in Fig. 7.10 and provided in Table 7.4, with the fluxes measured on Titan and Iapetus.

On 28 and 29 May 2018, Iapetus lies within the sidelobes at 2.0 mm, and cannot be accurately detected: the 2.0 mm "mixed" region brightness temperature should not be used. At 1.2 mm, Iapetus is detected, but both types of calibration appear problematic. Indeed, on 28 May, the fluxes measured on Titan and on Iapetus ($F^{\mathrm{obs}}_{\mathrm{Titan}}$ and F^{U}_{Iapetus} in Table 7.4) are correlated, and both increase with time. However, if we calibrate on Titan, the extracted values of T_B^{disk} are higher than on the leading hemisphere, leading us to believe that the calibration is at cause. On 29 May, the two methods of calibration give very different results at 1.2 mm; it is impossible to determine which one is correct. The poorly determined fluxes of May 2018 are primarily a consequence of the low elongation of Iapetus, though calibration issues are also likely. Since these results are unreliable and do not represent either the leading or trailing hemisphere, they are not included in the interpretations.

In 2019, only LH and TH observations were desired, both for scientific interest and for greater separation from Saturn. These observations were much more successful, and allow us to constrain the leading and trailing hemisphere fluxes. On 15 February and 12 March, calibration on Titan introduces noise (from the extraction of Titan's flux) with little to no change in the average T_B^{disk}: consequently, we use the calibration on Uranus instead. On 14 February, Titan is very close to Saturn, and using it as a calibrator is impossible. On March 20 and 21, imperfect calibration files were used in the standard NIKA2 pipeline. These data will be re-reduced with updated calibration files. Until then, calibration on Titan is necessary to bring the derived brightness temperatures to values consistent with the ones measured on 12 March.

The 1.2- and 2.0-mm brightness temperatures are averaged on each day, using the inverse variance as weights; the uncertainties are the weighted standard deviation. The resulting daily values are provided in Table 7.5 and shown in Fig. 7.11 alongside those found in previous studies (Ries, 2012; Hagen et al., 2014; Le Gall et al., 2014). As expected, the leading side, which is covered by the optically dark material, has significantly higher brightness temperatures than the trailing side.

On the trailing side, the 1.2-mm, 1.3-mm (from the SubMillimeter Array (SMA), Hagen et al., 2014), and 2.0-mm brightness temperatures are all similar within error bars. On the leading side, we observe a very steep spectral slope from 1 to 3 mm, unlike the decreasing temperatures with depth that would normally be expected for daytime observations. Either this steep spectral slope is a property intrinsic to the optically dark material covering the leading side, or it indicates that the subsurface properties change very quickly with depth in the top few cm of the subsurface. These results are

further discussed in Section 7.4.

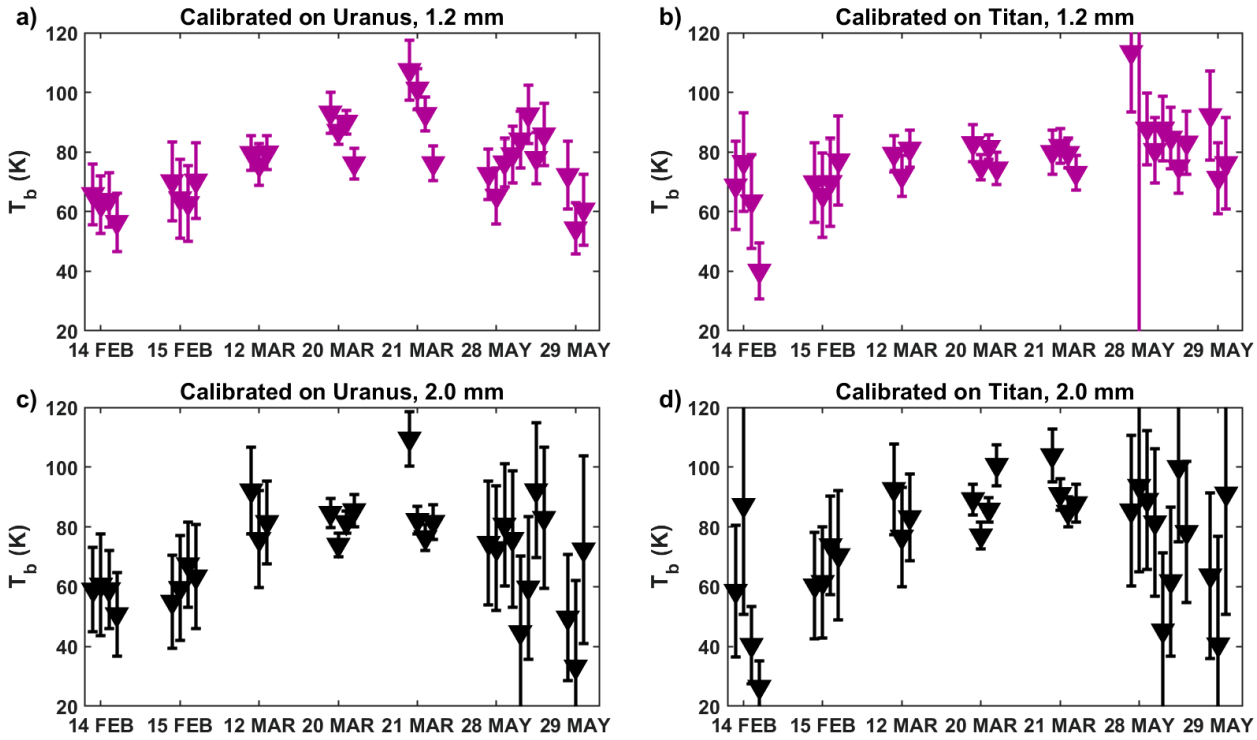

Figure 7.10 – Brightness temperatures derived for Iapetus at (top) 1.2 and (bottom) 2.0 mm, with (left) absolute calibration on Uranus, which is uncontaminated by Saturn but observed at a different time than Iapetus, and (right) absolute calibration on Titan, which is observed at the same time as Iapetus but is noisy due to contamination by Saturn's flux. On February 14, Titan was very close to Saturn and introduces a lot of noise: we prefer to keep the calibration on Uranus. On February 15 and March 12, calibration on Titan only introduces noise without changing the average values significantly: we therefore keep the calibration on Uranus. On March 20 and 21, calibration on Titan is more appropriate, as it strongly affects the derived brightness temperatures, bringing them to values very close to those of March 12. The values shown here are also provided in Table 7.4.

Table 7.4 – IRAM NIKA2 observations: results. Fluxes on Titan, observed using calibration on Uranus ($F^{\rm obs}_{\rm Titan}$) and predicted ($F^{\rm pred}_{\rm Titan}$) using the Titan spectrum from Lellouch et al. (2019) shown in Fig. 7.6 are given at 1.2 and 2.0 mm. Observed fluxes on Iapetus are given both with the default calibration on Uranus ($F^{U}_{\rm Iapetus}$) and with additional absolute calibration on Titan ($F^{T}_{\rm Iapetus}$). Similarly, derived brightness temperatures are provided with calibration on Uranus ($T_B^{\rm disk,U}$) and on Titan ($T_B^{\rm disk,T}$). Uncertainties are derived from the quality of the 2-D Gaussian fit of Titan's and Iapetus's fluxes. The brightness temperatures with the more reliable calibration method are in bold; these are interpreted in the following sections.

Date	$F^{\rm pred}_{\rm Titan}$	$F^{\rm obs}_{\rm Titan}$ (mJy)		$F^{U}_{\rm Iapetus}$ (mJy)		$F^{T}_{\rm Iapetus}$ (mJy)		$T_B^{\rm disk,U}$ (K)		$T_B^{\rm disk,T}$ (K)	
	(mJy)	1.2 mm	2.0 mm	1.2 mm	2.0 mm	1.2 mm	2.0 mm	1.2 mm	2.0 mm	1.2 mm	2.0 mm
28 May 2018	1581	996.6 ± 135.6	488.3 ± 47.3	122.7 ± 15.7	43.4 ± 12.7	198.1 ± 37.0	50.0 ± 15.5	72.6 ± 8.5	74.6 ± 20.7	113.5 ± 20.0	85.5 ± 25.2
(Mixed)	557	–	432.4 ± 45.4	109.2 ± 17.3	42.3 ± 12.8	–	55.1 ± 17.6	65.3 ± 9.4	72.8 ± 20.8	–	93.7 ± 28.7
		1385.7 ± 124.8	508.5 ± 29.6	129.8 ± 15.1	47.1 ± 12.6	150.7 ± 22.2	52.2 ± 14.3	76.5 ± 8.2	80.7 ± 20.5	87.8 ± 12.0	89.0 ± 23.2
		1578.4 ± 110.4	523.1 ± 20.8	134.8 ± 17.5	44.2 ± 14.0	137.5 ± 20.2	47.6 ± 15.2	79.2 ± 9.5	75.9 ± 22.8	80.6 ± 11.0	81.5 ± 24.7
		1537.0 ± 78.9	555.5 ± 22.6	144.0 ± 17.7	25.0 ± 15.8	150.7 ± 20.1	25.4 ± 16.0	84.1 ± 9.6	44.7 ± 25.7	87.8 ± 10.9	45.3 ± 26.1
		1769.9 ± 118.9	542.9 ± 27.6	159.6 ± 18.0	34.2 ± 14.7	145.1 ± 19.1	35.5 ± 15.3	92.6 ± 9.8	59.7 ± 23.9	84.7 ± 10.3	61.8 ± 24.9
		1674.0 ± 73.2	517.7 ± 25.4	132.5 ± 16.0	54.2 ± 13.9	127.4 ± 16.4	59.0 ± 15.4	77.9 ± 8.7	92.2 ± 22.6	75.1 ± 8.9	100.0 ± 25.0
		1666.4 ± 64.3	599.3 ± 63.1	147.1 ± 19.4	48.5 ± 14.5	142.1 ± 19.5	45.6 ± 14.5	85.8 ± 10.5	83.0 ± 23.6	83.1 ± 10.6	78.2 ± 23.6
29 May 2018	1585	1237.5 ± 43.9	431.4 ± 21.3	122.2 ± 20.8	28.1 ± 13.0	159.3 ± 27.7	36.7 ± 17.1	72.2 ± 11.3	49.6 ± 21.1	92.3 ± 15.0	63.7 ± 27.7
(Mixed)	559	1193.6 ± 49.8	450.3 ± 19.1	89.2 ± 15.8	18.0 ± 17.8	120.5 ± 22.0	22.5 ± 22.3	54.3 ± 8.6	33.2 ± 29.0	71.3 ± 11.9	40.7 ± 36.3
		1255.7 ± 31.0	443.4 ± 21.7	100.8 ± 21.8	42.1 ± 19.4	129.5 ± 28.2	53.6 ± 24.8	60.6 ± 11.8	72.4 ± 31.5	76.2 ± 15.3	91.1 ± 40.3
14 Feb 2019	1145	1111.7 ± 182.8	411.3 ± 127.5	79.0 ± 13.4	24.2 ± 6.2	82.8 ± 19.6	24.0 ± 9.7	**65.8 ± 10.2**	**59.0 ± 14.1**	68.7 ± 14.8	58.5 ± 21.9
(Trailing)	404	929.4 ± 149.3	277.5 ± 88.8	74.4 ± 12.8	24.9 ± 7.4	93.3 ± 22.0	36.7 ± 16.1	**62.3 ± 9.7**	**60.6 ± 16.9**	76.6 ± 16.6	87.3 ± 36.4
		1175.3 ± 265.3	616.3 ± 159.7	76.5 ± 12.1	24.3 ± 5.8	75.8 ± 20.9	16.1 ± 5.6	**63.9 ± 9.1**	**59.1 ± 13.1**	63.4 ± 15.8	40.5 ± 12.8
		1720.8 ± 331.0	848.0 ± 211.4	66.7 ± 12.9	20.6 ± 6.2	45.1 ± 12.3	9.9 ± 3.9	**56.5 ± 9.8**	**50.7 ± 14.0**	40.1 ± 9.4	26.4 ± 8.8
15 Feb 2019	1147	1173.5 ± 39.7	369.2 ± 29.1	84.9 ± 17.5	22.5 ± 6.8	84.4 ± 17.7	24.9 ± 7.8	**70.1 ± 13.3**	**54.9 ± 15.5**	69.8 ± 13.4	60.4 ± 17.8
(Trailing)	404	1145.7 ± 75.7	394.6 ± 28.3	77.3 ± 17.6	24.5 ± 7.7	78.7 ± 18.6	25.4 ± 8.2	**64.4 ± 13.3**	**59.5 ± 17.5**	65.5 ± 14.1	61.5 ± 18.6
		1037.8 ± 68.6	371.2 ± 23.7	75.1 ± 16.8	28.0 ± 6.3	84.5 ± 19.7	30.8 ± 7.2	**62.8 ± 12.7**	**67.4 ± 14.3**	69.9 ± 14.9	73.8 ± 16.4
		1056.1 ± 73.4	365.0 ± 49.6	85.2 ± 16.8	26.2 ± 7.7	94.1 ± 19.7	29.3 ± 9.5	**70.4 ± 12.7**	**63.4 ± 17.5**	77.1 ± 14.9	70.5 ± 21.6

Table 7.4 – (continued)

Date	$F^{\text{pred}}_{\text{Titan}}$	$F^{\text{obs}}_{\text{Titan}}$ (mJy)		F^{U}_{Iapetus} (mJy)		F^{T}_{Iapetus} (mJy)		$T_B^{\text{disk,U}}$ (K)		$T_B^{\text{disk,T}}$ (K)	
	(mJy)	1.2 mm	2.0 mm	1.2 mm	2.0 mm	1.2 mm	2.0 mm	1.2 mm	2.0 mm	1.2 mm	2.0 mm
12 Mar 2019	1217	1242.8 ± 27.6	431.4 ± 19.4	103.5 ± 8.2	41.3 ± 6.8	103.2 ± 8.5	41.5 ± 7.1	**79.6 ± 5.8**	**92.1 ± 14.6**	79.4 ± 6.0	92.6 ± 15.2
(Leading)	409	1308.5 ± 39.2	429.0 ± 16.6	98.0 ± 9.8	33.7 ± 7.6	92.8 ± 9.7	34.1 ± 7.8	**75.7 ± 7.0**	**75.9 ± 16.2**	72.0 ± 6.9	76.7 ± 16.6
		1217.4 ± 35.6	424.8 ± 18.3	103.8 ± 8.1	36.4 ± 6.5	105.6 ± 8.8	37.1 ± 6.8	**79.8 ± 5.8**	**81.6 ± 13.8**	81.1 ± 6.3	83.2 ± 14.5
20 Mar 2019	1247	1438.6 ± 26.3	420.6 ± 4.9	125.8 ± 9.8	38.8 ± 2.3	111.0 ± 8.9	41.0 ± 2.5	93.2 ± 6.8	84.6 ± 4.8	**82.9 ± 6.1**	**89.2 ± 5.2**
(Leading)	440	1493.2 ± 41.3	425.7 ± 9.0	117.0 ± 6.5	33.7 ± 1.9	99.4 ± 6.1	35.1 ± 2.1	87.0 ± 4.5	74.0 ± 4.0	**74.9 ± 4.3**	**77.1 ± 4.4**
		1411.4 ± 32.9	421.6 ± 5.8	121.4 ± 5.7	37.3 ± 1.8	109.2 ± 5.7	39.3 ± 2.0	90.1 ± 4.0	81.5 ± 3.7	**81.6 ± 4.0**	**85.7 ± 4.1**
		1300.9 ± 31.7	374.7 ± 9.5	101.2 ± 7.5	39.2 ± 2.6	98.8 ± 7.7	46.5 ± 3.3	76.1 ± 5.2	85.5 ± 5.4	**74.4 ± 5.4**	**100.7 ± 6.8**
21 Mar 2019	1250	1746.5 ± 33.5	470.4 ± 9.5	147.0 ± 14.6	50.9 ± 4.4	107.1 ± 10.9	48.3 ± 4.3	107.4 ± 10.1	109.5 ± 9.1	**79.9 ± 7.5**	**103.9 ± 8.9**
(Leading)	441	1594.4 ± 34.3	401.1 ± 6.7	137.9 ± 10.0	37.8 ± 2.2	110.1 ± 8.3	42.0 ± 2.6	101.2 ± 6.9	82.3 ± 4.6	**82.0 ± 5.7**	**90.9 ± 5.3**
		1498.7 ± 28.8	398.8 ± 6.3	125.5 ± 8.2	35.0 ± 2.1	106.6 ± 7.2	39.1 ± 2.4	92.7 ± 5.6	76.5 ± 4.3	**79.6 ± 5.0**	**85.0 ± 5.0**
		1334.2 ± 35.5	412.5 ± 5.3	101.6 ± 8.5	37.5 ± 2.8	96.9 ± 8.5	40.5 ± 3.1	76.2 ± 5.8	81.6 ± 5.8	**72.9 ± 5.8**	**87.9 ± 6.4**

Table 7.5 – Daily average disk-integrated temperature for the three LH and two TH IRAM NIKA2 observations of Iapetus.

Date	Iapetus region	T_B^{disk} (K) at 1.2 mm	T_B^{disk} (K) at 2.0 mm
14 FEB 2019	Trailing side	62.1 ± 3.4	57.2 ± 3.9
15 FEB 2019	Trailing side	66.9 ± 3.4	61.6 ± 4.9
12 MAR 2019	Leading side	78.7 ± 1.7	83.6 ± 6.6
20 MAR 2019	Leading side	78.5 ± 2.4	88.2 ± 2.4
21 MAR 2019	Leading side	78.6 ± 2.9	91.9 ± 3.0

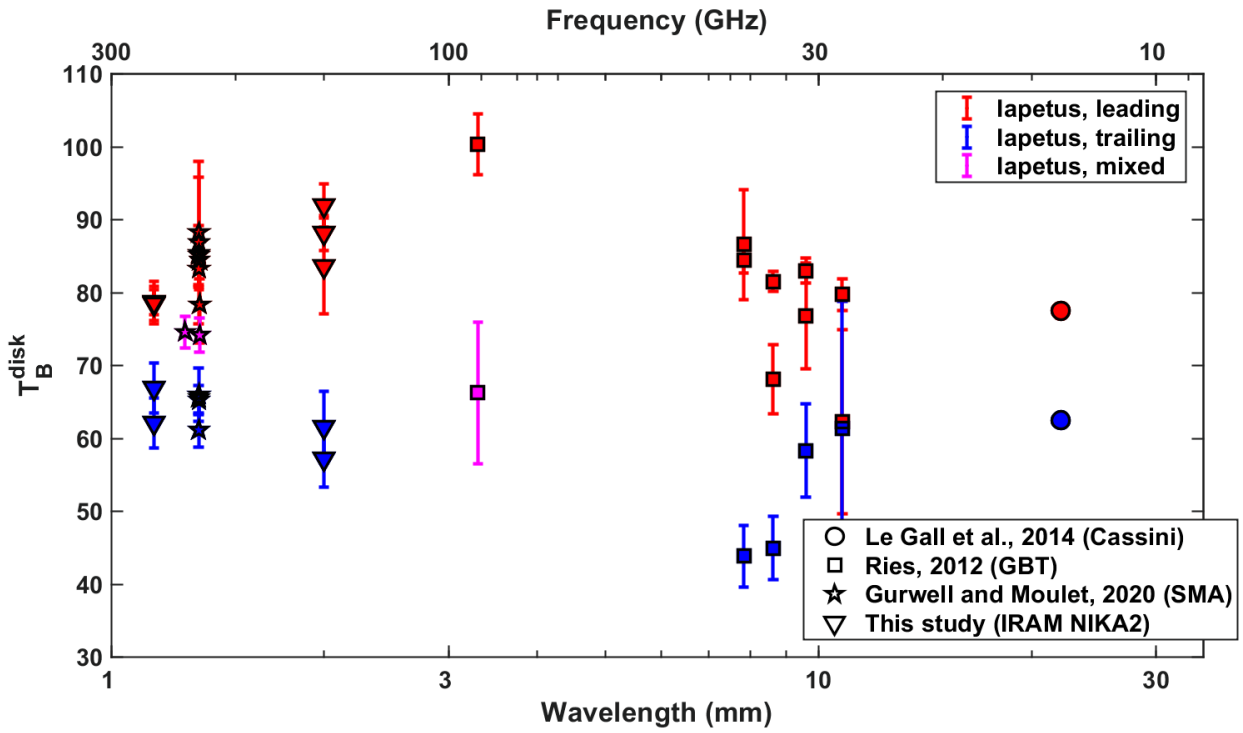

Figure 7.11 – Iapetus microwave spectra, including the 1.2- and 2.0-mm values found with the NIKA2 system as well as brightness temperatures found in previous studies (Ries, 2012; Hagen et al., 2014; Le Gall et al., 2014, ; Gurwell and Moullet, 2020, personal communication). Our error bars are derived from the 5% absolute calibration uncertainty and the 95% confidence interval of the fits, as detailed in Section 7.2.2.

7.3 Observations of Iapetus and Phoebe from the VLA

7.3.1 The Karl G. Jansky Very Large Array (VLA) interferometer

Interferometry, which consists in combining the incoming signal from multiple antennas (see Section 2.1.2), can achieve spatial resolutions much better than the largest single-dish radio telescopes. The NSF's Karl G. Jansky Very Large Array (VLA) is a radio interferometer of 27 25-meter parabolic antennas, located in the desert near Socorro, New Mexico (USA). It belongs to the National Radio Astronomy Observatory (NRAO), which is a facility of the National Science Foundation operated under cooperative agreement by Associated Universities, Inc. The VLA was constructed in the 1970s and underwent several upgrades, the last of which ended in 2012 and significantly improved its sensitivity, resolution, and frequency coverage (Perley et al., 2011). The individual antennas of the VLA can move along the Y-shaped tracks into four distinct configurations. With a maximum baseline length of 36 km, the A configuration is the most extended and therefore offers the highest resolution, as shown in Table 7.6. Given that the angular size of Iapetus is around 0.21", the highest possible resolution is required to resolve it, while also helping to separate its signal from Saturn's. Consequently, all the Iapetus VLA data discussed herein was acquired in the A configuration. Phoebe (0.03") is unresolved even in A configuration, and was observed in the B configuration instead.

Table 7.6 – Frequencies observable by the Karl G. Jansky Very Large Array (VLA), and the corresponding synthesized beam widths θ^{A}_{HPBW} and θ^{B}_{HPBW} in A and B configuration. Bands for which observations of Iapetus and/or Phoebe have been aquired are in bold.

Band	4	P	L	S	C	**X**	**Ku**	**K**	**Ka**	**Q**
Frequency (GHz)	0.075	0.350	1.5	3.0	6.0	10	15	22	33	45
Wavelength (cm)	4050	86	23	10	5	3	2	1.4	0.9	0.7
θ^{A}_{HPBW} (")	24	5.6	1.3	0.65	0.33	0.20	0.13	0.089	0.059	0.043
θ^{B}_{HPBW} (")	80	18.5	4.3	2.1	1.0	0.60	0.42	0.28	0.19	0.14

7.3.2 Observations and calibration

A total of three successive proposals of VLA observations of Iapetus and Phoebe have been accepted, two of which (project codes 18A-090 and 19A-093) led to the observations described herein. The latest proposal, 20B-290, should be observed in the winter of 2020-2021 and complete the centimetric spectra of Iapetus and Phoebe. Indeed, observing the leading and trailing side of Iapetus, which are visible alternately for a few days each month, imposes strong timing constraints, which could not always be met in previous proposals.

As detailed in Tables 7.7 and 7.8, data have been acquired on the trailing, anti-Saturn, and leading sides of Iapetus, as well as on Phoebe, which was detected for the first time from Earth at centimeter wavelengths. Table 7.7 summarizes the observing conditions, more specifically the wind and the phase fluctuations caused by turbulence in the troposphere (measured by the atmospheric phase interferometer, or API).

Table 7.7 – VLA observations of Iapetus and Phoebe. The frequency and wavelength within in each band is provided in Tables 7.6 and 7.8. The region observed at each data is given in Table 7.8. The image resolution is optimized to show features as small as possible while keeping a reasonable SNR.

Target	**Date**	**Time (UTC)**	**API (°)**	**Wind (m/s)**	**Band**	**Resolution (milliarcsec)**	**Target size (milliarcsec)**
Iapetus	21 May 2018	08:15–10:42	12.2–46.2	6.6–9.2	X	271 × 158	213
Iapetus	28 May 2018	07:54–10:21	1.0–3.2	0.5–4.9	Ka	91 × 48	215
Iapetus	03 Jun 2018	07:24–09:19	3.0–4.1	2.1–6.7	K	149 × 77	216
Iapetus	05 Jun 2018	07:21–09:17	2.2–5.1	4.0–7.0	Ku	223 × 114	216
Iapetus	29 Aug 2019	02:17–03:46	4.4–16.8	3.9–6.9	X	312 × 163	210
Phoebe	12 May 2019	10:02–12:38	1.7–3.8	2.8–6.3	K	360 × 350	30
Phoebe	31 May 2019	08:06–11:24	2.2–6.3	0.4–3.9	Q	300 × 200	31
Phoebe	01 Jun 2019	08:12–11:41	2.8–11.1	0.6–2.5	Ka	400 × 240	31
Phoebe	22 Jun 2019	07:23–09:59	1.9–4.4	0.3–6.1	K	610 × 340	31

The VLA observations of Iapetus and Phoebe were scheduled, verified, calibrated, and reduced by Bryan Butler, staff scientist at the National Radio Astronomy Observatory (NRAO), who also extracted the target fluxes and brightness temperatures. Bryan Butler spent a month at the LESIA in June 2019, where he reduced this dataset. The quasar 3C286 was used to calibrate for delay, bandpass, and flux density scale, whereas the complex gain was determined from either J1820-2528 or J1911-2006 (both quasars), which were close to Saturn at the time of the observations. The initial reduction and

calibration of the data used the VLA calibration pipeline.

Data were acquired in spectral windows of 128 MHz bandwidth, each composed of 64 2-MHz channels which are averaged together. In order to reduce the noise inherent to narrow bandwidths, data were averaged over 3 GHz (for the Ku band) or 4 GHz (for the X, K, and Ka bands). The decorrelation caused by tropospheric turbulence is corrected using the atmospheric phase interferometer (API) measurements (Butler and Desai, 1999; Carilli and Holdaway, 1999). The target's flux is derived by fitting a limb-darkened disk of the appropriate dimensions (taking into account polar flattening and sub-Earth latitude), on the visibilities (in the spatial frequency plane) rather than in the image plane. Finally, the final brightness temperatures are derived using the method described in Section 7.1.2.

During the 21 May 2018 X-band observation, Saturn was in the antenna primary beam, overwhelming the flux from Iapetus. In order to extract Saturn's flux, the limb-darkened planet and its rings were modeled and their contributions were subtracted from the visibilities. Most of the Saturn contribution was thus successfully removed, and the flux and brightness temperatures could be calculated from the resulting data.

We further note that Phoebe is a smaller and therefore fainter source than Iapetus, leading to much higher uncertainties in the derived brightness temperature values. To minimize noise, data was averaged over the whole bandwidth rather than over only 3 or 4 GHz. Phoebe was observed on four occasions, including twice in the K-band (13.6 mm); these two data points are averaged to obtain a more reliable measurement.

7.3.3 Results

The fluxes and brightness temperatures derived for Iapetus and Phoebe are provided in Table 7.8 and shown in Fig. 7.12, with all other Iapetus microwave daytime observations. The May and June 2019 K-band observations of Phoebe are averaged.

The VLA values of T_B^{disk} on the trailing hemisphere in the K and Ku bands are consistent with both the GBT data of Ries (2012) and the Cassini radiometry data of Le Gall et al. (2014). The Ku band temperature is stable, whereas at higher frequencies (shorter wavelengths), it appears to decrease, perhaps as a follow up of the trailing hemisphere scattering feature identified by Ries (2012).

As expected, the Ka band observation, which was centered near the anti-Saturn side and thus includes a mixture of leading and trailing hemisphere terrains, has an intermediate brightness temperature, lying between the leading and trailing side values measured by Ries (2012).

At 3.0 cm (X band), the leading hemisphere T_B^{disk} is above that of the "mixed" anti-Saturn observation. This indicates that, at this wavelength, the leading and trailing hemispheres must still be distinct. Nonetheless, on the leading side, T_B^{disk} decreases from 77.5 ± 0.9 K at 2 cm (IA049-2_1u in Table 4.1) to 70.9 ± 2.0 K at 3 cm. Because the Cassini 2.2 cm observation was acquired during the local night (at 21:49 UTC, as opposed to near noon for all Earth-based observations), the 2.2 cm daytime brightness temperature may be even higher (depending on the thermal inertia). A steep 2.2–3.0 cm decreasing slope on the trailing hemisphere suggests an abrupt change in subsurface properties.

Finally, the brightness temperatures measured on Phoebe are within error of those found by Ries (2012) on the leading side of Iapetus. Ka to Ku band VLA observations of the LH of Iapetus (accepted proposal 20B-290) and thermal modeling of both Iapetus and Phoebe are necessary before

we can conclude on the possible similarity in emissivity between these two bodies.

Table 7.8 – Fluxes and and brightness temperatures derived from VLA observations of Iapetus and Phoebe. The latitude and longitude given are for the sub-Earth point; the region observed is indicated for Iapetus but not for Phoebe, which is not in synchronous rotation.

Target	Date	Band	ν (GHz)	$\nu_{\rm eff}$ (GHz)	λ (mm)	Lat. (°N)	Long. (°E)	Observed side	Flux (µJy)	$T_B^{\rm disk}$ (K)
Iapetus	21 May 2018	X	8–12	10.07	29.8	11	-171	Mixed	172 ± 4.8	66.6 ± 1.8
Iapetus	28 May 2018	Ka	33–37	35.02	8.6	11	157	Mixed	2008 ± 16.9	62.7 ± 0.5
Iapetus	28 May 2018	Ka	29–33	31.02	9.7	11	157	Mixed	1597 ± 15.0	63.5 ± 0.6
Iapetus	03 Jun 2018	K	22–26	24.03	12.5	11	129	Trailing	830 ± 20.7	54.9 ± 1.3
Iapetus	03 Jun 2018	K	18–22	20.03	15.0	11	129	Trailing	645 ± 16.7	61.0 ± 1.5
Iapetus	05 Jun 2018	Ku	15–18	16.52	18.1	11	120	Trailing	454 ± 6.8	62.9 ± 0.9
Iapetus	05 Jun 2018	Ku	12–15	13.53	22.2	11	120	Trailing	304 ± 5.6	62.8 ± 1.1
Iapetus	29 Aug 2019	X	8–12	10.07	29.8	10	-115	Leading	178 ± 5.2	70.9 ± 2.0
Phoebe	12 May 2019	K	18–26	22.12	13.6	18	27	–	27.5 ± 5.8	110.5 ± 22.8
Phoebe	22 Jun 2019	K	18–26	22.00	13.6	19	-15	–	20.4 ± 5.1	74.5 ± 17.9
Phoebe	averaged	K	18–26	22.09	13.6	–	–	–	22.5 ± 4.1	90.8 ± 16.0
Phoebe	01 Jun 2019	Ka	29–37	34.0	9.4	19	-36	–	44.8 ± 5.8	76.6 ± 9.4
Phoebe	31 May 2019	Q	40–50	44.0	6.8	19	112	–	81.8 ± 18.5	78.9 ± 17.2

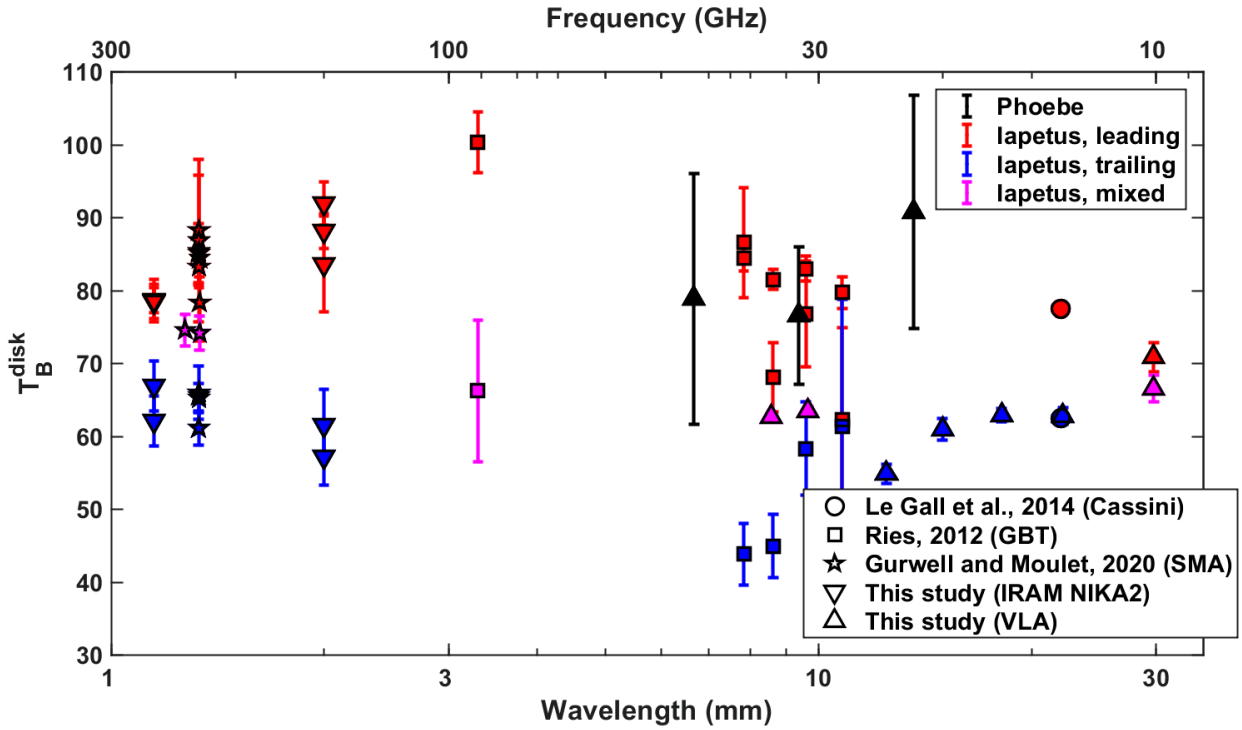

Figure 7.12 – Iapetus microwave spectrum, including the IRAM NIKA2 results, the VLA results, and brightness temperatures found in previous studies (Ries, 2012; Hagen et al., 2014; Le Gall et al., 2014, ; Gurwell and Moullet, 2020, personal communication). VLA observations of Phoebe are included for comparison.

7.4 Discussion and interpretations

7.4.1 The LH and TH microwave spectra of Iapetus

As shown in Fig. 7.12, the brightness temperature difference between the LH and TH of Iapetus is apparent at all observed millimeter to centimeter wavelengths. As expected from the leading/trailing albedo dichotomy, the leading side (with a lower albedo) is always warmer than the trailing side, at least during daytime. In order to determine whether an albedo difference is sufficient to account for this dichotomy or if other properties such as emissivity must also vary on either side of Iapetus, a thermal model is required. Comparison to such a model is discussed in Sections 7.4.2 and 7.4.3.

Disk-integrated brightness temperatures measured on the leading side by the IRAM NIKA2 camera at 1.2 and 2.0 mm, the SMA 1.3 mm, and the GBT at 3.3 mm are all consistent with a steep slope, with $T_B^{\rm disk}$ increasing with wavelength (from 78.5 ± 3.3 K at 1.2 mm to 100.4 ± 4.2 K at 3.3 mm). Such a steep positive slope is unlikely to be due only to variations of the effective temperature at the depths probed; more likely, they indicate structural and/or compositional changes with depth. At longer wavelengths and up to 3 cm, the brightness temperature steadily decreases, probably as the contribution of a lower emissivity layer increases.

The variations of $T_B^{\rm disk}$ on the trailing side of Iapetus appear to be, coincidentally, roughly anti-correlated to those on the leading side. $T_B^{\rm disk}$ may decrease with wavelength from 1.2 to a little beyond 3.3 mm, then progressively increase at longer wavelengths. The SMA 1.3 mm and IRAM NIKA2 1.2 and 2.0 mm brightness temperatures are all equal within uncertainties, although they seem to be dropping at 2.0 mm. Around a $\sim$ 1 cm wavelength, an increase in $T_B^{\rm disk}$ with wavelength is seen by both the GBT and the VLA, confirming the presence of a low-$T_B^{\rm disk}$ feature at wavelengths of $\sim 3-10$ mm, as detected by Ries (2012). Both the leading and trailing hemisphere features are discussed in more detail in Section 7.4.3.

7.4.2 Comparison with a thermal model

Thermal model

The thermal and radiative transfer models described in Chapter 5, which have been applied to the Cassini 2.2 cm radiometry of Iapetus by Le Gall et al. (2014) and in Chapter 6, can also be applied to observations at other wavelengths. We recall that the model uses the bolometric Bond albedo map of Iapetus (Fig. 5.3; Blackburn et al., 2011) and the time-varying incident solar fluxes as input, while the parameters are the thermal inertia I and the ratio of electric to thermal (diurnal) skin depth $r = \delta_{\rm el}/\delta_{\rm th}^{\rm day}$. We can thus obtain effective temperature maps at the epoch of the ground-based observations, from which the disk-integrated effective temperature $T_{\rm eff}^{\rm disk}$ is calculated (as in Section 6.1.1).

When applying the radiative transfer model to other wavelengths, we kept the 2.2-cm skin depth ratio, hereafter called $r_{\rm 2cm}$, as a parameter, rather than calculate the skin depth ratio for each wavelength. The electrical skin depth, which, assuming the dielectric constant and loss tangent are wavelength-independent, is proportional to the wavelength λ (Eq. 2.13), can be derived from $r_{\rm 2cm}$ and $\delta_{\rm th}^{\rm day}$ (itself calculated for each thermal inertia I from Eq. 5.11) as follows:

$$\delta_{\rm el}^{\lambda} = \frac{\lambda}{2.2\ {\rm cm}} \times r_{\rm 2cm} \times \delta_{\rm th}^{\rm day} \tag{7.4}$$

Fitting the 1.3-mm (SMA) lightcurve

Disk-integrated effective temperatures were simulated for seven values of the thermal inertia I from 10 MKS to 1000 MKS, and for nine values of the 2.2-cm skin depth ratio $r_{2\mathrm{cm}}$ from 0.1 to 1000 (leading to electrical skin depths between 0.1 mm and 120 m). The global emissivity is derived by performing a weighted average of the disk-integrated emissivities of each observations, themselves calculated from the Rayleigh-Jeans law as in Eq. 6.1.

We first attempted fitting all 1.3-mm SMA observations while keeping the emissivity, thermal inertia, and skin depth ratio constant over Iapetus, thereby supposing that the leading/trailing dichotomy is primarily caused by an albedo difference accounted for in the model. The global emissivity is calculated as the average of the ratio of observed brightness temperatures T_B^{disk} to disk-averaged effective temperatures $T_{\mathrm{eff}}^{\mathrm{disk}}(I, r_{2\mathrm{cm}})$, with the inverse of the squared uncertainties over T_B^{disk} (from Table 7.1) used as weights. The resulting emissivities are multiplied by $T_{\mathrm{eff}}^{\mathrm{disk}}(I, r_{2\mathrm{cm}})$, providing the simulated brightness temperatures shown in black in Fig. 7.13. The poor fit to the data at all values of $(I, r_{2\mathrm{cm}})$ demonstrates that an albedo dichotomy alone is insufficient to account for the 1.3-mm brightness temperature dichotomy, consistent with the results of Hagen et al. (2014) from an analysis of a subset of these data.

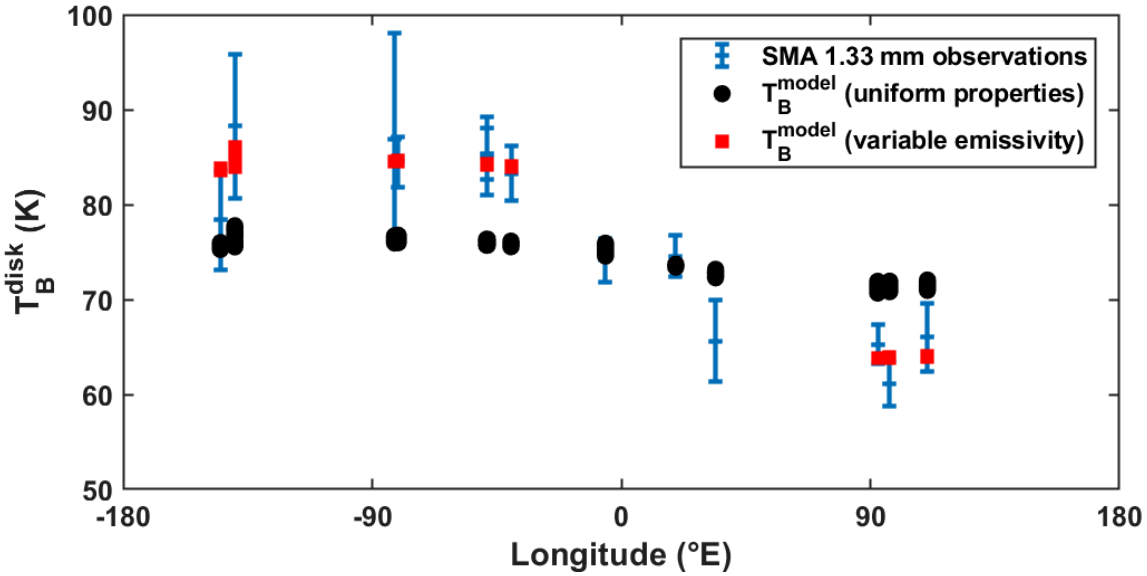

Figure 7.13 – SMA 1.3 mm (225 GHz) brightness temperatures T_B^{disk} measured on Iapetus, acquired and calibrated by Hagen et al. (2014) and Gurwell and Moullet (2020, personal communication). The modeled brightness temperatures are shown for all tested thermal inertias and ratios, while keeping the emissivity constant (black circles) or allowing it to vary between the leading and trailing hemispheres (red squares). Attempting to fit all data while keeping all parameters uniform over Iapetus is unsuccessful: the leading/trailing albedo anomaly must therefore be associated with an emissivity and/or a thermal inertia and ratio dichotomy.

The emissivity was then derived separately for the LH (-90 ± 50°E) and TH ($+90 \pm 50$°E), averaging only the data acquired in those regions. The LH and TH 1.3-mm emissivities thus obtained are mapped in Fig. 7.14 and lead to the brightness temperatures shown in red in Fig. 7.13. If the thermal inertia and the skin depth ratio remain uniform on all of Iapetus, then the emissivity must be at least 0.14 and up to 0.23 higher on the LH than on the TH. However, it is possible that thermal inertia and skin depth ratio are also different on either side. Indeed, the LH and TH emissivities may be much

closer or even identical if the LH has a lower electrical skin depth than the TH (requiring I and/or r to be lower on the LH). For example, emissivities near 0.75 are allowed on both hemispheres for $I = 10$ if the electrical skin depth is about 100 times deeper on the trailing hemisphere.

The most likely scenario is that thermal inertia, electrical skin depth, and emissivity all vary from leading to trailing sides. Indeed, these parameters are all closely related to the composition and structure of the near subsurface. On the trailing side, a low e and high $\delta_{\rm el}$ would be consistent with a low-loss, icy, and unconsolidated medium (e.g., Ferrari and Lucas, 2016; Howett et al., 2016). Meanwhile, the leading hemisphere's higher emissivity points to a more compact medium (lower porosity and fewer scattering losses), and/or a lower dielectric constant ε'_r. VIMS infrared spectra have detected a variety of materials on the LH of Iapetus, including iron oxides, CO_2 ice, and complex hydrocarbons (see Section 1.4.2 and Clark et al., 2012; Cruikshank et al., 2014). The SMA data suggest that fine-grained tholins, which have low dielectric constants ($\varepsilon'_r = 2.03 - 2.33$ at 13.78 GHz, compared to $\varepsilon'_r \sim 3.13$ for solid water ice; Paillou et al., 2008), and which cannot form large crystals like water ice, are a good candidate for the leading hemisphere dark material. Silicates and iron oxides are less ideal due to their high dielectric constants and loss tangents, but cannot be discarded from this dataset alone.

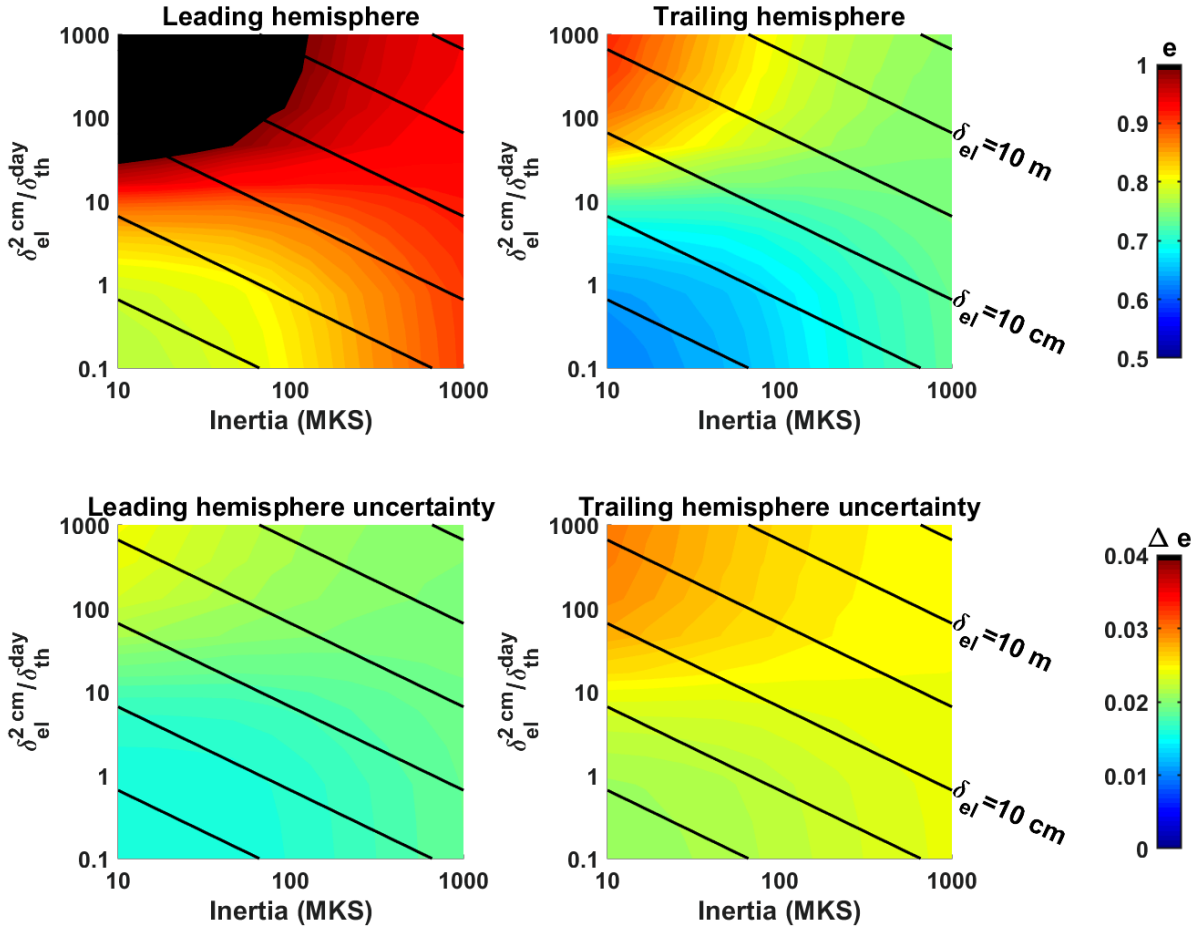

Figure 7.14 – Top: leading (left) and trailing (right) hemisphere 1.3-mm emissivities for all tested combinations of thermal inertia and skin depth ratio. Bottom: Uncertainty on the emissivities derived. For uniform I and $r_{2\rm cm}$, the leading hemisphere emissivity must be at least 0.14 higher than on the trailing side. However, the emissivity could be similar on both hemispheres if I and r are very low on the LH, while I is high on the TH.

7.4.3 Emissivity variations with wavelength

As for the 1.3 mm SMA data, the effective temperatures have also been simulated for all other microwave observations of Iapetus described above, to obtain simulated temperature profiles at their epochs of measurement. Assuming that the thermal inertia, loss tangent, and dielectric constant are constant with depth, we can derive the leading and trailing hemisphere emissivity spectra. For this first derivation, we chose $I = 100$ MKS and $r^{2cm} = 5$, near the values derived by Le Gall et al. (2014) from Cassini 2.2-cm radiometry (see Table 6.1); the electrical skin depth at each wavelength can be found using Eq. 7.4. The emissivities derived for this vertically uniform model are shown in Fig. 7.15; approximate leading and trailing emissivity spectra are hand-drawn for reference.

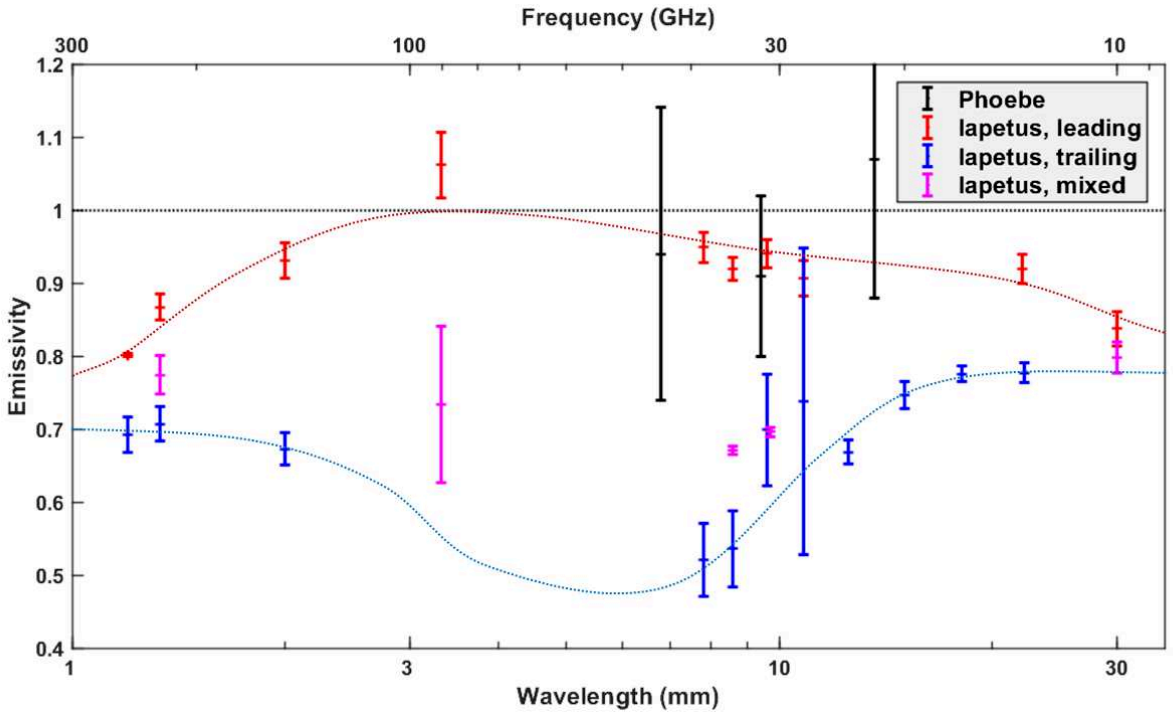

Figure 7.15 – Extracted emissivities assuming a constant thermal inertia of $I = 100$ MKS and 2.2-cm ratio of $r^{2cm} = 5$, values derived by Le Gall et al. (2014) from Cassini 2.2-cm radiometry. All data available within each region (LH, TH, or mixed) is averaged for each wavelength. The maximum possible emissivity of 1 is marked with a black dashed line; values above this point are unphysical, likely indicating different thermal inertia and skin depth ratio then assumed here. A hand-drawn line approximately adjusted to the leading and trailing hemisphere data is added for reference, but does not represented any physical model. Note that, in reality, both the thermal inertia and the skin depth are expected to change with depth. As seen in Section 7.4.3, variations in I and r^{2cm} cannot eliminate the trends apparent here.

However, as seen above with the SMA data, it is likely that the thermal and electric properties of the medium vary with the probed depth, and therefore with the observation wavelength. The emissivities as a function of thermal inertia I and skin depth ratio r_{2cm} have been calculated for both hemispheres at all possible microwave wavelengths, and are shown for the leading and trailing hemispheres in Fig. 7.16 and Fig. 7.17, respectively. Our preferred interpretations are detailed hereafter and summarized in Fig. 7.18.

Leading hemisphere

The high 3.3-mm brightness temperature of $T_B^{\rm disk} = 100.4 \pm 4.2$ K constrains the maximum electrical skin depth to $\delta_{\rm el}^{\lambda<3.3{\rm mm}} < 10$ cm, using the minimum value of the emissivity allowed by the uncertainties. More plausible values (with emissivities around 0.95) lie around 1 to 10 mm, as seen in the 3.3 mm emissivity map of Fig. 7.16. Even if we assume that the derived 3.3 mm brightness temperature is too high to be real (possibly due to calibration uncertainties), the 2.0 mm emissivities also point to relatively low skin depths, which must remain $\delta_{\rm el}^{2{\rm mm}} < 10$ cm if the emissivity is to be kept below 0.93 and to allow thermal inertia values below 100 MKS.

Using Eq. 5.21 and assuming negligible scattering losses, the loss tangent can be derived from the electrical skin depths. Electrical skin depths of $\delta_{\rm el}^{3.3{\rm mm}} = 10$ mm would lead to loss tangents of the order of $\tan\delta \approx 20 - 50 \times 10^{-3}$, depending on the dielectric constant (loss tangent is inversely proportional to electrical skin depth). These values are several times larger than those expected for tholins (generally < 0.01; Paillou et al., 2008; Lethuillier et al., 2018), but lie within the range observed for silicates and hematite (e.g., Campbell and Ulrichs, 1969; Nelson et al., 1989; He et al., 2015). A 3.3-mm electrical skin depth near 10 cm (unlikely from the 3.3 mm emissivities) would bring the loss tangent to $2 - 5 \times 10^{-3}$. Water ice and CO_2 both have loss tangents of the order of 10^{-4}, and therefore cannot be the dominant component of the leading hemisphere material. We recall that the loss tangent calculated here only accounts for losses by absorption; accounting also for scattering losses would yield lower values of $\tan\delta$. From the 3.3 mm observation, plausible compositions include a tholin-like material, an unconsolidated iron oxide, or a mixture of these and other components (Clark et al., 2012; Dalle Ore et al., 2012; Le Gall et al., 2014). The high emissivity of the dark material favors materials with a low dielectric constant, e.g. tholins, CO_2 ice, or a high-porosity material. This material must be fine-grained, such that its scattering efficiency at 3.3 mm is very low.

Because this result is based primarily on one data point (the 3.3 mm observation from the GBT by Ries, 2012), it must be confirmed or refuted by further observations at 3 to 6 mm wavelengths.

The steeply increasing 1.2 to 3.3 mm slope in emissivity (see Fig. 7.15) persists for all values of thermal inertia and ratio. Although the electrical properties can vary with wavelength independently of the depth, the variations we observe are most likely due to variations of the subsurface compositionnal and structural properties with depth. Keeping the electrical properties constant with wavelength, variations in thermal inertia or ratio cannot account for the rapidly changing brightness temperature from 1.2 to 3.3 mm: a changing emissivity is necessary, as seen in Fig. 7.16. For $I = 50$ MKS and $\delta_{\rm el}^{1.2{\rm mm}} = 1$ cm ($\delta_{\rm el}^{3.3{\rm mm}} = 2.78$ cm), the emissivity would have to rise from $e = 0.76 \pm 0.01$ at 1.2 mm to $e = 0.95 \pm 0.04$ at 3.3 mm. High degrees of mm-scale surface roughness would be insufficient to account for the low millimiter-wavelength emissivities, and are unlikely for a surface coated by fine-grained regolith. Instead, this emissivity slope must be caused by changes in the composition and/or structure in the top few centimeters. Compositional changes would involve a low-emissivity (at millimeter wavelengths) layer overlying the high emissivity material. This thin superficial veneer would also have to be optically dark; no obvious material fits this description.

Structural changes would have to cause enhanced subsurface scattering at 1.2 mm, which would necessarily be less active at longer wavelengths/larger depths. We can think of four possible explanations for such a rapid gradient in scattering over the top few centimeters of the subsurface. i) The dark material particle size is of the order of $a \approx \lambda/2\pi < 200$ µm, where $\lambda \leq 1.2$ mm is the wavelength at which scattering is most active. ii) Scattering is less efficient at longer wavelengths both because of the restricted particle sizes, and because increasing compaction with depth prevents the wave from probing much deeper at longer wavelength, thereby decreasing the number of opportunities for scattering. iii) Scattering may also be caused by empty pores themselves rather than grain sizes. As the porosity rapidly decreases with depth, scattering quickly becomes less efficient. iv) These empty pores near the surface create a dielectric contrast with the surrounding dark material. At depth, these

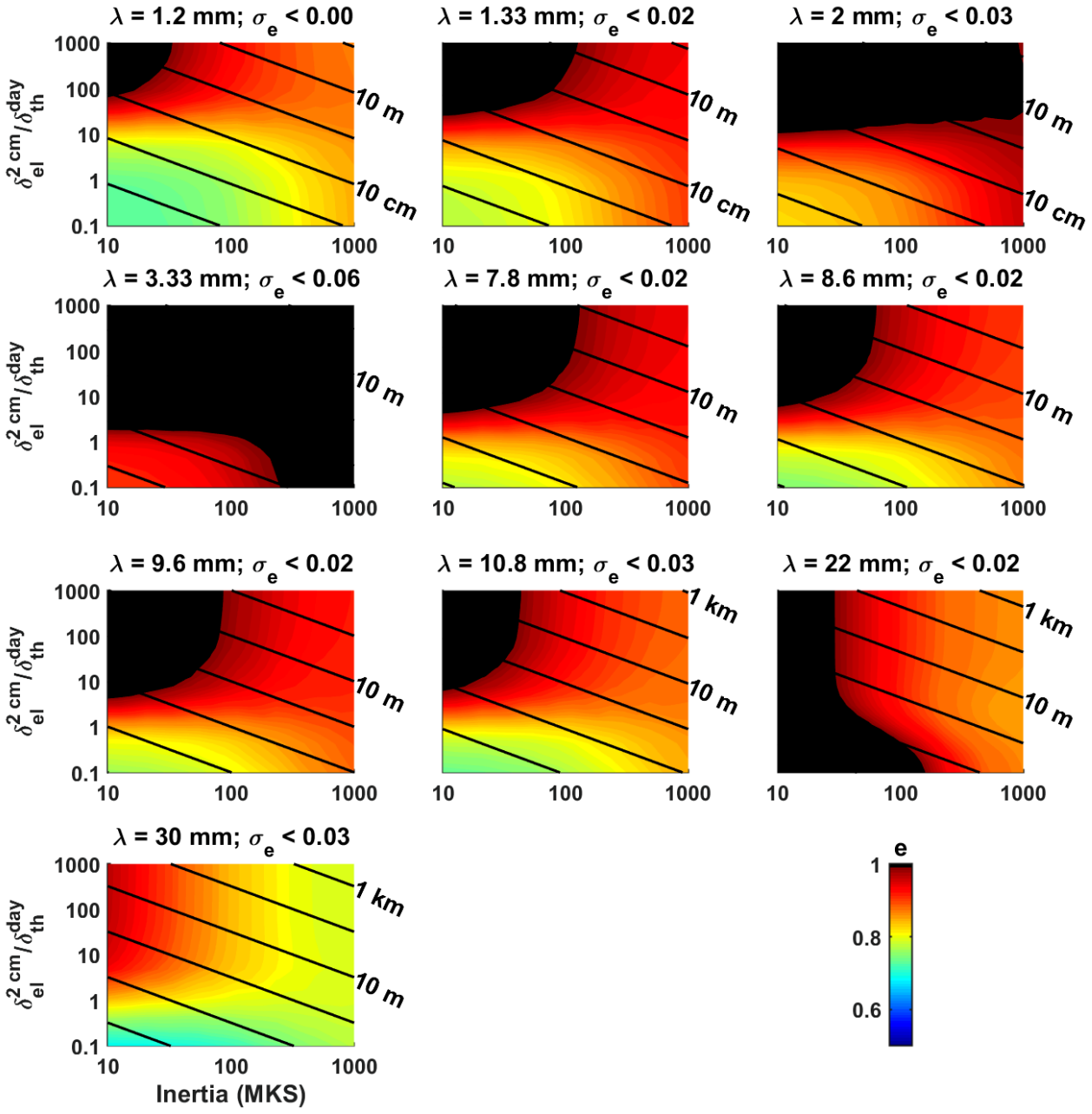

Figure 7.16 – Leading hemisphere emissivities for all tested combinations of thermal inertia and skin depth ratio, for each wavelengths where observations exist. The maximum uncertainty on the emissivity is given for each wavelength.

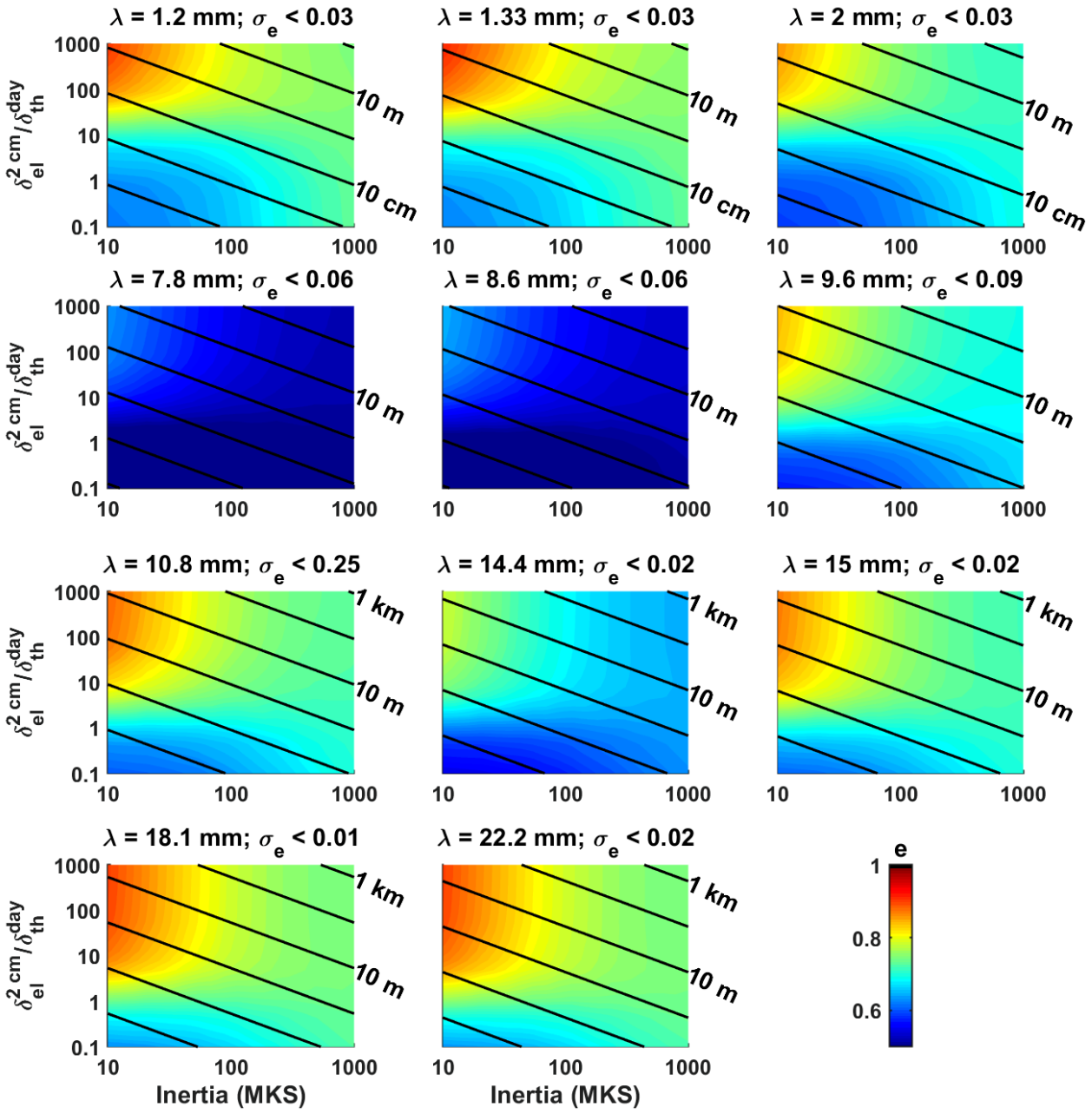

Figure 7.17 – Trailing hemisphere emissivities for all tested combinations of thermal inertia and skin depth ratio, for each wavelengths where observations exist. The color bar is the same as in Fig. 7.16: emissivities are generally lower on the TH than on the LH. The electrical skin depths outlined in black are calculated for each wavelength from Eq. 7.4.

pores may be filled with water ice, leading to a lower dielectric contrast and therefore less scattering, and a higher emissivity. These four hypotheses are not mutually exclusive, and are all consistent with a rapidly increasing degree of compaction of the regolith with depth. Fig. 7.18 only displays this increasing compaction in the top few centimeters, without showing the < 200 μm grain sizes or pores. An increasingly compact subsurface would also increase the thermal inertia, consistent with the low sub-millimeter value found by CIRS ($I = 14^{+7}_{-8}$ MKS; Howett et al., 2010) and the higher 2.2-cm value found by the Cassini radiometer ($I > 50$ MKS; Le Gall et al., 2014); this increase in compaction may occur primarily within the top few centimeters. Note also that increasing the thermal inertia at larger depths would imply a further enhancement of the spectral variation of the emissivity, as pictured in Fig. 7.16.

The decreasing 3.3 to 30 mm brightness temperatures can only be partly accounted for by decreasing temperatures at depth. Indeed, Fig. 7.16 shows that the emissivity may remain roughly constant between 7.8 and 22 mm, but it must drop on two occasions: from 3.3 to 7.8 mm, and from 22 to 30 mm. Even without the very high 3.3 emissivity, the values found at 7.8 mm are also lower than those at 2.0 mm. Our interpretations is that, beyond 3.3 mm wavelengths, radiometers are beginning to probe the icy substrate underlying the high-emissivity layer. Thus the probed depth (estimated above at 1 to 10 mm, and strictly below 10 cm) at 3.3 mm indicates a minimal thickness of the leading hemisphere high-emissivity material. At 7.8 mm to 22 mm, most of the material probed still consists in the same high-emissivity material, but the icy substrate is increasingly detected, possibly pointing to existence of a mixed transition layer between the two materials. At 30 mm, a sharp drop in emissivity occurs, likely indicating that a significant part of the signal now originates from the water ice layer. These results are generally consistent with a leading hemisphere high-emissivity material thickness of the order of decimeters, with the likely existence of a mixed transition zone, as pictured in Fig. 7.15.

Note also that both thermal inertia and 2.2-cm ratio likely increase with depth, as found by Le Gall et al. (2014). Indeed, the 3.3 mm skin depth is restricted to at most 10 cm (i.e., <30 times the wavelength), whereas Le Gall et al. (2014) constrained the 2.2 cm skin depth to be $\delta_{\rm el}^{\rm 2cm} > 1.2$ m (i.e., >54 times the wavelength). This non-linearity of $\delta_{\rm el}^{\lambda}$ with wavelength is likely caused by a decreasing loss tangent with depth. The loss tangent of solid water ice (0.41×10^{-3} at 13 GHz; Paillou et al., 2008) being lower than that of both tholins ($8.8 - 10.8 \times 10^{-3}$ at 13 GHz; Paillou et al., 2008) and hematite ($\sim 50 \times 10^{-3}$ at 13 GHz; Nelson et al., 1989; He et al., 2015), this result is consistent with the 2.2 cm radiometry data probing the icy substrate.

Trailing hemisphere

Plausible variations in emissivity from 1.2 to 2.0 mm depend upon the thermal inertia I and electrical skin depth $\delta_{\rm el}$. For equal I and $\delta_{\rm el}$ with wavelength and depth, the emissivity drops by only about 0.02, which remains within the error bars. It is possible that all parameters (I, $\delta_{\rm el}$ and e) remain constant at the depths probed by 1.2 to 2.0 mm wavelengths, while the slight decrease in $T_B^{\rm disk}$ in Fig. 7.12 would be due to cooler temperatures in the subsurface than near the dayside surface. The emissivity then drops to very low 7.8 and 8.6 mm values (e<0.7), and at longer (centimetric) wavelengths, there is likely a slow increase in emissivity, assuming I and $\delta_{\rm el}$ vary little with depth. In all cases, the 1.2 to 2 mm and centimetric emissivity is unambiguously higher than at 7.8 and 8.6 mm.

This result is mostly consistent with the 1- to 2-mm grain size constrained by Ries (2012) from the data then available. Indeed, Mie scattering is expected to peak at a particle size near $\lambda/2\pi$ (Section 2.2.4), and the Coherent Backscattering Effect (CBE) is most efficient for inhomogeneity sizes of the order of the wavelength (Hapke, 1990; Hapke and Blewett, 1991; Black et al., 2001b). If the peak in scattering occurs near 5 to 6 mm, then 1- to 2-mm grain sizes fall in between those

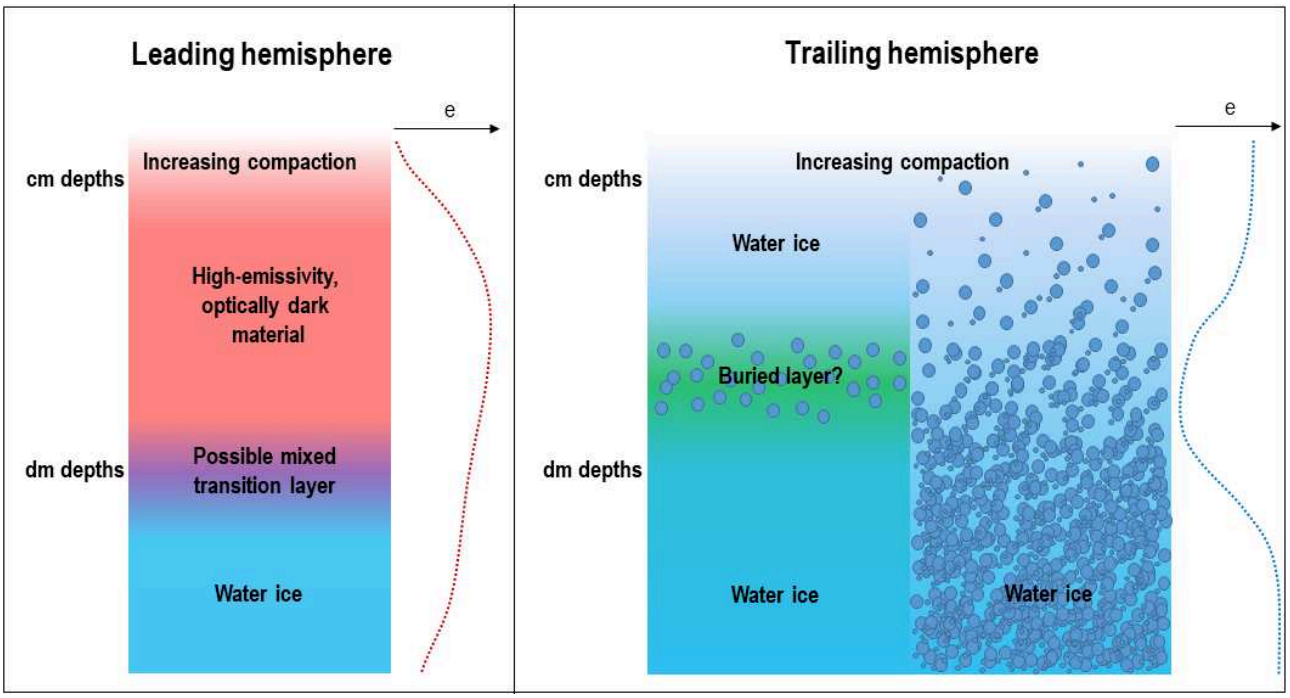

Figure 7.18 – Schematic representation of our interpretation of the subsurface of the leading (left) and trailing (right) hemispheres of Iapetus. For each, an outline of the emissivity variations with depth is drawn for reference, assuming that the probed depth is directly proportional to wavelength (from Fig. 7.15). On both hemispheres, the degree of compaction is expected to increase with depth. On the LH, the high-emissivity, optically dark material extends to decimeter depths, under which the water ice substrate is present. On the TH, the low-emissivity 3–8 mm feature can be explained either by a buried low-emissivity layer, or mm-sized particles, pores, or inhomogeneities throughout the subsurface. Interpretations are further detailed in the text.

expected from Mie scattering and from the CBE, due to the use of a more sophisticated and probably more realistic model. The particles or inhomogeneities causing the low millimetric emissivities may either exist at all depths, with the wavelength dependence being primarily controlled by the grain size. The scattering millimeter-sized grains may alternately be buried under a fine-grained regolith, adding to their undetectability at short wavelengths (see Fig. 7.18 for an illustration). This subsurface layer of larger particle sizes or buried fractures could be the bedrock underlying the highly processed regolith, or could be the signature of a past event having affected the surface. In all cases, the thermal inertia derived at 2.2 cm (48 – 560 MKS) by Le Gall et al. (2014) is higher than in the infrared (15 – 30 MKS) by Howett et al. (2010) and Rivera-Valentin et al. (2011), indicating that the degree of compaction of the regolith must increase with depth.

Comparison with Phoebe

Phoebe is not in synchronous rotation, and has a fairly short day of 0.39 Earth days (i.e., 9.36 hours). The thermal model described above would need a very short time step to correctly sample such a short day, leading to very large computation times. Instead, we simply calculate the equilibrium temperature T_{eq} of Phoebe at the date of each observation, a simple model which is generally appropriate for a fast rotator such as Phoebe:

$$T_{\mathrm{eq}} = \left(\frac{F_{\odot}}{D} \frac{(1 - A_B)}{4\sigma} \right)^{1/4} \tag{7.5}$$

where $F_\odot$ = 1370 W/m^2 is the solar constant, D is the Phoebe-Sun distance in AU, A_B = 0.1 is Phoebe's bolometric Bond albedo (Flasar et al., 2005; Howett et al., 2010), and σ is the Stefan-Boltzmann constant. For the four dates on which Phoebe was observed by the VLA, its equilibrium temperature is T_{eq} = 85.4 K. This value is lower than the 12 May 2019 K-band brightness temperature (110.5 ± 22.8 K), indicating that either the physical temperature should be much higher, or this unusually high T_B^{disk} value is caused by noise (a likely hypothesis, as it is an outlier with respect to the three other Phoebe brightness temperatures shown in Table 7.8).

Emissivity is then derived, as usual, as the ratio of disk-integrated brightness temperatures (available in Table 7.8) to physical temperature. The emissivities found for Phoebe are provided in Table 7.9. Apart from the unphysical value (above 1) derived for 12 May 2019, Phoebe's emissivity appears constant within error, at $e = 0.8 - 1$, very consistent with the emissivity of 0.92 found by Ostro et al. (2006) from early Cassini radiometry measurements. These values are also close to those found on the LH of Iapetus at the same wavelengths (Fig. 7.16), but are higher than the TH emissivities for most values of the thermal inertia and skin depth (Fig. 7.17). These results support the presence of a high-emissivity material in the near subsurface of both Phoebe and the LH of Iapetus. This is consistent with the hypothesis that the optically dark material covering the LH of Iapetus originates from the Phoebe ring, which likely originates from Phoebe itself (Tosi et al., 2010; Spencer and Denk, 2010; Hamilton et al., 2015).

Table 7.9 – Phoebe disk-integrated emissivities, extracted assuming the physical temperature at the depth probed is equal to the equilibrium temperature.

	13.6 mm (K-band)	**13.6 mm (K-band)**	**13.6 mm (K-band)**	**9.4 mm (Q-band)**	**6.8 mm (Ka-band)**
Day	12 May 2019	22 Jun 2019	12 May & 22 Jun 2019	31 May 2019	01 Jun 2019
Emissivity	1.30 ± 0.27	0.88 ± 0.11	1.07 ± 0.19	0.91 ± 0.11	0.94 ± 0.20

7.5 Conclusion and perspectives

By complementing the pre-existing radiometry data acquired by the Cassini radiometer, the SMA, and the GBT with millimetric IRAM NIKA2 and centimetric VLA observations, this work adds to the microwave spectra of the two faces of Iapetus. These new data have led to the detection of variations of thermal, structural, and/or compositional properties with depth on the leading hemisphere, better characterization of the trailing hemisphere scattering feature, and further support the Phoebe origin its dark cover.

7.5.1 Future observations

Yet, the microwave spectra of Iapetus are still not complete. More specifically, VLA data has only been acquired on the trailing side of Iapetus at 1 to 2 cm wavelengths, while at 3 cm only the leading and anti-Saturn sides have been observed. This gap in observations will be filled in the winter of 2020–2021, with VLA LH observations (accepted proposal 20B-290). Furthermore, on both hemispheres, we will acquire C-band (6 cm) data, a crucial wavelength to further constrain the depth of the leading hemisphere material. Indeed, at this wavelength, the radiometer should probe several decimeters into the subsurface, deep enough to sense the icy substrate and maybe record a thermal emission that is dominated by contribution from this layer rather than by that of the dark cover. If

this is the case, we expect to find similar emissivities on both the leading and trailing hemispheres. Finally, Q-band (6.7 mm) data on the leading and trailing sides will be key to confirm or infirm the low TH and high LH values of T_B^{disk} found by Ries (2012).

There is another important gap in the microwave spectra of Iapetus, at 3–6 mm. Further 3 mm data would allow us to verify the very high brightness temperature of the LH 3.3 mm GBT observation. On the trailing side, 3–6 mm data would permit a more complete characterization of the scattering or absorption feature, although observations at 5 mm are impossible from Earth due to an oxygen absorption line. The Atacama Large Millimeter/submillimeter Array (ALMA) in Chile, to which we have already submitted three unsuccessful proposals, is the ideal instrument to bridge the gap between millimetric and centimetric observations, especially within the ALMA 2.6–3.6 mm band (and in the 6–8.5 mm band, which is under construction). Furthermore, ALMA would be able to resolve Iapetus, detecting variations in temperature with latitude and longitude. Such temperature maps can be compared to a thermal model to better constrain the thermal inertia and emissivity of both sides of Iapetus, similar to previous work on Europa and Ganymede (Trumbo et al., 2017, 2018; de Kleer et al., 2019; Rathbun and Spencer, 2020). Other radio telescopes than ALMA can also gather disk-integrated observations of Iapetus at 3 mm, such as the GBT used by Ries (2012), the Northern Extended Millimeter Array (NOEMA), or the Combined Array for Research in Millimeter-wave Astronomy (CARMA).

7.5.2 Towards a resolved analysis of VLA observations

In the Ka (29 to 37 GHz) and K (18 to 26 GHz) bands, the VLA is able to resolve Iapetus. The resulting maps, reduced and calibrated by Bryan Butler, are shown in Fig. 7.19. The Ka band observation, which was acquired on the anti-Saturn side and therefore features the LH to the East, clearly shows a difference in longitudinal variation in flux density. The K band image, which has a lower resolution and was obtained closer to the leading side of Iapetus, nonetheless also exhibits a longitudinal gradient in flux density. While it is tempting to attribute the high eastern fluxes to the detection of the higher leading hemisphere emissivity, it may also be at least partly caused by differences in local time. Indeed, during this observation, a sunny morning was beginning on the TH, whereas the day was nearing its end on the LH.

Comparing the observed flux densities to those predicted by the thermal and radiative transfer model is the logical next step of the analysis of the resolved VLA observations. The effective temperature maps modeled for a thermal inertia of 50 MKS and a 2 cm skin depth ratio of $r^{2\text{cm}} = 5$ are shown at the time of both resolved observations in Fig. 7.19. The next step will be to convolve these maps with the synthetic beam, after which they can be directly compared to those obtained by the VLA. Future observations at 6.8 mm (Q-band) should also be able to resolve Iapetus.

7.5.3 Need for a multi-layer thermal model

The radar and radiometry data are consistent with decimeter depths of exogenous dark material, with centimeter wavelengths beginning to probe the icy subtrate below (Black et al., 2004; Ostro et al., 2006; Ostro et al., 2010; Ries, 2012; Le Gall et al., 2014, and present work). A two-layer model would permit testing of this result and finer constraining of the thickness and thermo-physical properties of the dark material, as suggested e.g. by Le Gall et al. (2014).

In addition to the transition between the absorbing/emissive LH material and the underlying icy substrate at decimeter depths, there are also probably rapid changes in the thermo-physical properties within the top few millimeters of the subsurface, as discussed in Section 7.4.3. In order to confirm that

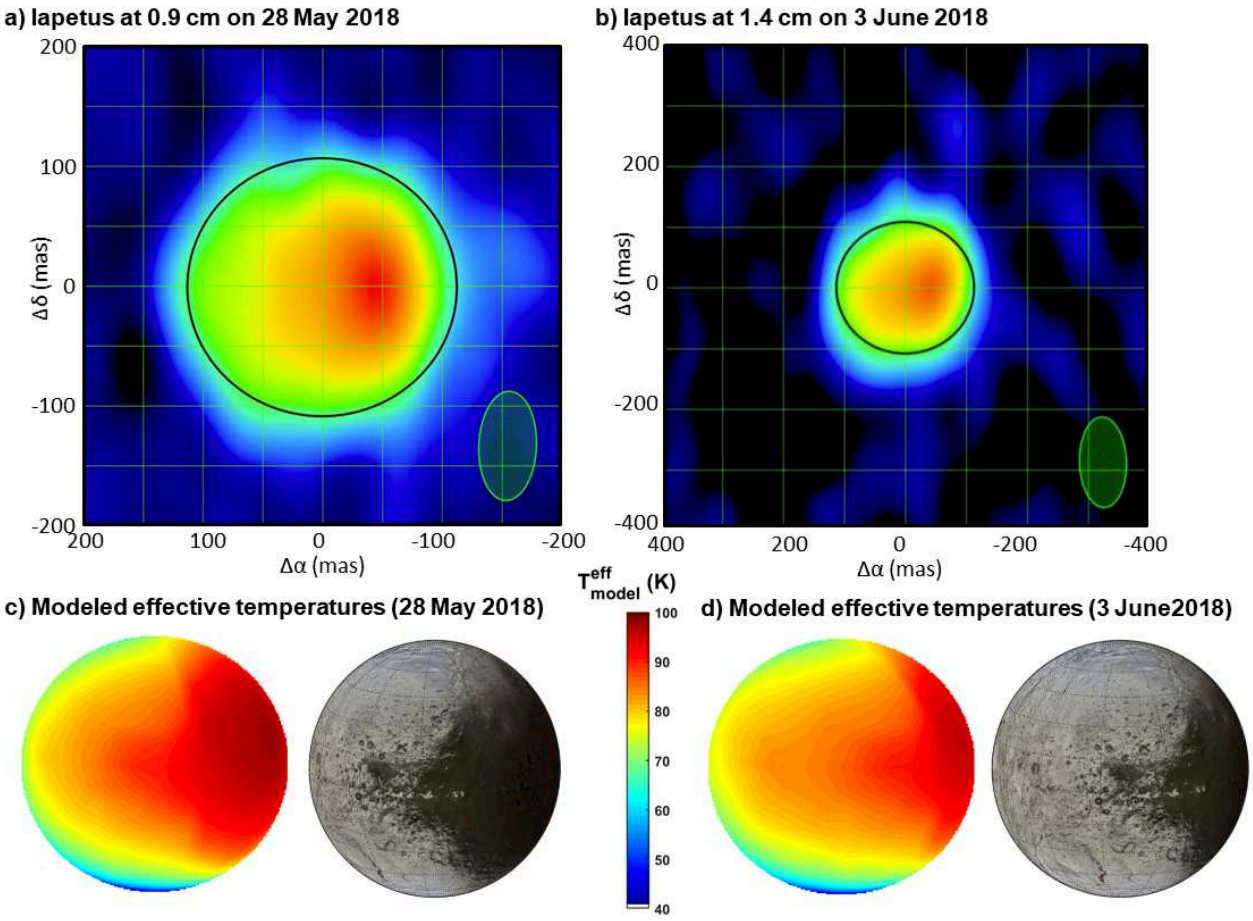

Figure 7.19 – a) Ka band (0.9 cm) observation of Iapetus acquired on 28 May 2018, centered at 157°E,11°N (anti-Saturn side). The peak flux density is 3.18×10^{-4} Jy/beam. b) K band (1.4 cm) observation of Iapetus acquired on 3 June 2018, centered at 129°E,11°N (mostly trailing side). The peak flux density is 2.34×10^{-4} Jy/beam. The dimensions of the synthetic beam is indicated with a green ellipse. Both observations were acquired in the extended A configuration of the VLA; the resolution is better at the shorter wavelength. Credit: Bryan Butler.
Bottom: modeled effective temperatures for $I = 50$ MKS and $r^{2\mathrm{cm}} = 5$ during (c) the 0.9 cm observation and (d) the 1.4 cm observation. The appearance of Iapetus as seen from Earth is shown for each date. On both observations, in both the observed flux and the modeled T_{eff} of the eastern side of Iapetus is warmer: this is both the location of the leading hemisphere (lower albedo) and of late afternoon local times.

the steep 1 to 3 mm rise in brightness temperature is caused by an increased degree of compaction of the regolith with depth, a thermal model with varying thermal inertia with depth would be necessary, similar to the one used by Howett et al. (2016) on Rhea.

7.5.4 Emissivity modeling

A drop in brightness temperatures and emissivities is seen on the trailing hemisphere of Iapetus at 3 to 8 mm wavelengths, which can be attributed either to subsurface scattering (Ries, 2012) or absorption by a buried layer. Assuming that subsurface scattering is the cause, it should be possible to constrain the grain size from the emissivity spectrum (Ries, 2012).

However, constraining grain sizes from emissivities is not straightforward. Indeed, the emissivity of the TH of Iapetus cannot be well constrained unless the thermal inertia and probed depth are well known. Even assuming good constraints on the emissivity, a subsurface scattering process and model should be chosen. Ries (2012) applied a semi-empirical snow model (the MEMLS model), which is limited in grain size (to 3 mm) and makes certain assumptions on the vertical layering and subsurface structure (Wiesmann and Mätzler, 1999; Ries, 2012).

Since the analysis conducted by Ries (2012), the MEMLS has been upgraded (e.g., to include backscattering for active radar modeling; Proksch et al., 2015). Several other models have also been developed to simulate microwave emission from snow, such as the Helsinki University of Technology (HUT) model (Pulliainen et al., 1999), and several Dense Media Radiative transfer theory models (DMRT-ML; Picard et al., 2013 and DMRT-QMS; Tsang et al., 2007; Liang et al., 2008). These models have recently been all integrated into the Snow Microwave Radiative Transfer (SMRT) model, which can simulate both active and passive observations of snow of varying properties (Picard et al., 2018). Future work should apply these new snow models to Iapetus, to better derive the characteristics of the trailing hemisphere's subsurface causing its enigmatic drop in emissivity at 3 to 8 mm.

Conclusion and perspectives

The Cassini radar and radiometry observations of Saturn's icy satellites have been calibrated and analyzed. On Rhea, Dione, and Iapetus, all radiometry data were analyzed jointly and compared to simulated temperatures, derived from a combination of thermal, radiative transfer, and emissivity models. On Dione, a leading/trailing dichotomy is observed in the Cassini scatterometry and at optical and infrared wavelengths, but is not obvious in the passive radiometry, pointing to centimetric depths of clean water ice on the Leading Hemisphere (LH) and/or non-icy contaminants on the Trailing Hemisphere (TH). On Rhea, no such dichotomy is observed in the 2.2 cm dataset, indicating that the LH E-ring ice and the TH dark material apparent at optical and IR wavelengths must be superficial (<cm depths). These interpretations are represented schematically in parts a) and b) of Fig. 7.20. Meanwhile, on Iapetus, the famous leading/trailing dichotomy was further investigated with the Cassini 2.2 cm radiometry ($e_{\mathrm{LH}} = 0.87^{+0.05}_{-0.02}$ and $e_{\mathrm{TH}} = 0.74^{+0.04}_{-0.02}$), implying that the optically dark, radar-absorbing, and high-emissivity material of the LH must extend deeper than the exogenous material layers on Rhea and Dione (Fig. 7.20c). Microwave observations can therefore provide new information to better constrain the depths affected by incoming exogenous fluxes of icy and non-icy material.

Microwave radiometry has also brought to light new structural information on Saturn's icy satellite subsurfaces. On Dione, Rhea, and Iapetus, higher thermal inertias ($I > 50$ MKS) were found from 2.2 cm radiometry than from previous analyses of infrared data ($I < 50$ MKS), pointing to an increased degree of compaction of the regolith with depth, confirming the result of Le Gall et al. (2014) on Iapetus. A likely explanation is that micrometeorite gardening is creating a loose, mixed regolith, as represented schematically in Fig. 7.20d. Impacts modify both the composition and structure of the near subsurface by excavating water ice from the crust and projecting blocks of icy ejecta up to hundreds of km away from the impact site. This process, which has been evidenced by the low emissivity and high radar albedo of the Inktomi crater ejecta blanket region on Rhea, is represented in Fig. 7.20e. Globally, very low effective dielectric constants ($\varepsilon'_r < 2$) were derived, especially on Rhea ($\varepsilon'_r < 1.5$) implying a depolarized subsurface. Low emissivities were found on Rhea ($e = 0.59 - 0.84$ on Rhea) and Dione ($e = 0.75 - 0.9$). Yet, according to current scattering models such as the coherent backscattering effect, the emissivities measured on Rhea and Dione are not low enough to justify the very high radar albedos measured by the Cassini radar. Well-constrained electrical skin depths on Rhea are very large, of the order of several hundred times the wavelength (5–10 m), pointing to high purity of the icy regolith. Low dielectric constants, high backscatter, and comparably insufficiently low emissivity all indicate the existence of very efficient scattering structures in the subsurface (Fig. 7.20f).

Although great progress has been made from Cassini radar/radiometry data, several paths of analysis remain to be explored. More specifically, no radiometry simulations of the existing data have yet been undergone for Mimas and Tethys, and only disk-integrated emissivities have been derived for Enceladus. Applying the same method used on Rhea, Dione, and Iapetus to Enceladus would be especially useful in order to better understand its present and past activity, for example through the possible detection of endogenic heat in different flybys, the study of the young leading and trailing hemisphere terrains, and the characterization of plume particle deposition patterns.

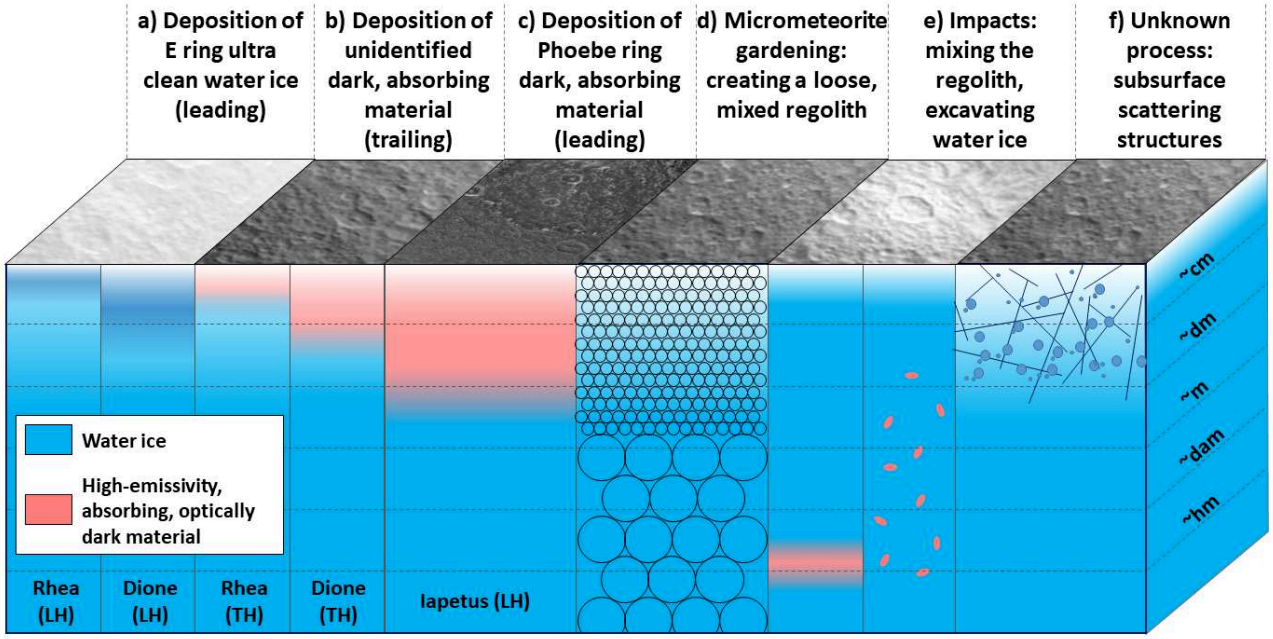

Figure 7.20 – Schematic representation of the processes causing the subsurface properties observed by Cassini radar and radiometry of Saturn's icy satellites Rhea, Dione, and Iapetus. See text for further details.

On the leading side of Iapetus, new 1.2 and 2.0 mm observations acquired with the NIKA2 instrument on the Institut de Radioastronomie Millimétrique (IRAM) 30-m telescope, associated with observations from the Green Bank Telescope (GBT) and the Sub-Millimeter Array (SMA), point to very fast changes in emissivity within the top few centimeters of the subsurface; the explanation we favor is rapidly decreasing porosity with depth. At wavelengths longer than 3.3 mm, GBT, Karl G. Jansky Very Large Array (VLA), and Cassini radiometry data all indicate a decreasing brightness temperature, particularly at 30 mm. This result is consistent with the presence of an icy substrate below decimeters of emissive material, which is increasingly probed as the wavelength increases. On the trailing side, multi-wavelength microwave radiometry confirms low brightness temperatures within wavelengths between ~3 and ~8 mm. The cause of this dip in the microwave spectrum is likely very efficient scattering by millimeter-sized particles.

To investigate further the puzzling microwave properties of Saturn's satellites' icy regolith, both theoretical and numerical modeling of the cm-wavelength scattering properties of porous, fractured, or otherwise inhomogeneous media is necessary. For example, the TEMSI-FD code designed to simulate individual interactions of electromagnetic waves with simulated media can be applied to radar observations icy moons (see Section 6.5). Meanwhile, radiometry data can be simulated by microwave emissivity model such as the MEMLS (Microwave Emission Model for Layered Snowpacks) or the Snow Microwave Radiative Transfer (SMRT), though particular care should be taken when applying models tested on Earth to the very different conditions existing on Saturn's moons.

In parallel, microwave radar and radiometry field studies of the thermal, dielectric, and scattering properties of ices and snows of varying porosity and grain size on Earth could provide the ground truth both to constrain the models and to interpret the observations. Of course, such an approach is not straightforward either. Naturally occurring ices and snows on Earth are affected by processes that do not take place on atmosphere-less icy moons, including high enough temperatures and pressures to melt ice. Liquid water has a very high dielectric constant and loss tangent, and its

presence even in small quantities dominates microwave radar/radiometry signals. Even in very cold conditions, ices and snows on Earth have complicated vertical structure associated with varying temperatures and precipitation. Nonetheless, a lot could be learned from the vast literature of radar and radiometry observations of ices on Earth, especially when using the emissivity models based on them.

Escaping the complexity of the natural world, laboratory simulations of planetary environments in controlled conditions can give more precise information on the interdependence of subsurface properties. Re-creating the environment of Saturn's icy satellites in a laboratory is difficult, as it would ideally involve meters-thick ice with varying controlled properties (grain size, porosity, non-icy contaminant composition and amount...) at very low temperatures (about 30 to 100 K), in quasi-vacuum. Yet, similar experiments have been undergone and continue today, e.g. at the Ice Laboratory at the University of Bern in Germany for the study of cometary ices, and at ESAC (the European Space Astronomy Centre) in Spain, to measure the dielectric and thermal properties of ices in preparation for the JUICE mission. The results of such studies can greatly improve our understanding of Solar System ices, and may be of great help in the interpretation of the results presented herein.

Another crucial tool for the analysis Saturn's icy moons is a multi-layer thermal model. Indeed, our simulations have used thermal models in which the thermal inertia is independent of depth; yet the ensemble of our and past results, especially from CIRS, point to an increase of the thermal inertia with depth. On Iapetus, the icy substrate below the non-icy optically dark material should also be modeled, implying the use of a 2-layer model at the least. Varying the thickness of the overlying layer and the dielectric and its thermal properties may help determine these parameters, although the data may not be sufficient in number and diversity to accurately constrain multiple parameters simultaneously.

Therein lies the ultimate *caveat* of outer Solar System science: more data is needed. Fortunately, in this case, more data can be acquired. Chapter 7 has already detailed the advantages of ground-based multi-wavelength microwave radiometry of Iapetus, and the future VLA observations that are planned for next winter. Resolved analysis of the data already acquired and of the future VLA observations will be undergone by comparison with simulated temperature maps. Atacama Large Millimeter/submillimeter Array (ALMA) data would be extremely useful, both to complete Iapetus's millimeter-wavelength spectrum, and to resolve longitudinal and latitudinal variations. However, other radio telescopes around the world can also be considered for millimeter-wavelength disk-integrated observations of Iapetus, including for example the Northern Extended Millimeter Array (NOEMA) in France, the Combined Array for Research in Millimeter-wave Astronomy (CARMA) in the USA, the Nobeyama Radio Observatory in Japan (NAOJ), the Sardinia Radio Telescope (SRT) in Italy, or the enhanced Multi Element Remotely Linked Interferometer Network (e-MERLIN) in the UK. Such observations would help confirm the results presented herein and refine the Iapetus spectrum with data at multiple wavelengths. Moreover, Saturn is occasionally used as a calibration source: data which includes its icy satellites may have already been gathered, and examining telescope observation archives may prove to be helpful. At longer (decimeter to meter) wavelengths, Iapetus becomes increasingly difficult to separate from Saturn, while at the same time the brightness of Iapetus decreases: such observations may not be possible. Nonetheless, high-sensitivity and resolution arrays exist, such as the Giant Metrewave Radio Telescope (GMRT) in India, while the worldwide Square Kilometre Array (SKA) will be finished in 2025, leading to improved resolutions and sensitivities at wavelengths comparable to the VLA's.

Of course, Iapetus is not the only icy moon that can be observed from Earth-based radiotelescopes. Rhea, which is the same size as Iapetus but much closer to Saturn, may be possible to detect with the ALMA and VLA telescope, and in the future with the SKA. Ku-band radiometry from

the Earth would provide crucial daytime data to complement the Cassini night-time observations, enabling better constraints of the thermal inertia in Rhea's equatorial regions. Saturn's icy satellites can also be compared to those of the other planets. Very little is know about the microwave properties of the satellites of Uranus, even though they could likely be detected from the most powerful radio telescopes. Oberon and Titania, especially, have maximum elongations of about 60" and 80", which should be sufficient to separate them from Uranus. Meanwhile, the Galilean moons, larger, closer to Earth, and further from their planet than Saturn's moons, are much easier to observe in the microwaves: a multi-frequency observation campaign is currently being conducted by a team at CalTech in preparation for the upcoming missions to the Jupiter system. The Jupiter, Saturn, and Uranus systems are vastly different in terms of heliocentric distance, inclination, magnetosphere, tides, and rings. Comparing the microwave properties of icy moons in these varied environments can help us understand the ways in which different processes shape icy subsurfaces.

Finally, radars and radiometers on spacecraft provide unique coverage and (often) resolutions. Although no future spacecraft are planned to explore Saturn's icy satellites, the Juno spacecraft currently orbiting Jupiter will likely conduct microwave radiometry observations of Europa, and two missions to the Galilean satellites are planned: NASA's Europa Clipper mission, and ESA's JUpiter ICy moons Explorer (JUICE) mission. Subsurface characterization is a key goal of both of these missions. The Galilean moons share several features with Rhea, Dione and Iapetus, especially concerning their microwave properties (see Section 2.5). Finally, the Dragonfly mission to Titan's surface will examine a surface which, in spite of undeniable differences with Rhea due to the abundance of organics and erosional processes, is also an icy surface where microwaves observations show the key role of volume scattering. The knowledge gained in the next few decades on Europa, Ganymede, and Titan will teach us about icy moons in general.

Bibliography

Abramov, O. and Spencer, J. R. (2009). "Endogenic heat from Enceladus' south polar fractures: New observations, and models of conductive surface heating". *Icarus* 199.1, pp. 189–196. doi: 10.1016/j.icarus.2008.07.016.

Acton, C., Bachman, N., Semenov, B., and Wright, E. (2018). "A look towards the future in the handling of space science mission geometry". *Planetary and Space Science* 150. Enabling Open and Interoperable Access to Planetary Science and Heliophysics Databases and Tools, pp. 9–12. doi: 10.1016/j.pss.2017.02.013.

Acton, C. H. (1996). "Planetary data system ancillary data services of NASA's Navigation and Ancillary Information Facility". *Planetary and Space Science* 44.1, 65–70. doi: 10.1016/0032-0633(95)00107-7.

Adam, R., Adane, A., Ade, P. A. R., André, P., Andrianasolo, A., Aussel, H., Beelen, A., Benoît, A., Bideaud, A., Billot, N., Bourrion, O., Bracco, A., Calvo, M., Catalano, A., Coiffard, G., Comis, B., De Petris, M., Désert, F.-X., Doyle, S., Driessen, E. F. C., Evans, R., Goupy, J., Kramer, C., Lagache, G., Leclercq, S., Leggeri, J.-P., Lestrade, J.-F., Macías-Pérez, J. F., Mauskopf, P., Mayet, F., Maury, A., Monfardini, A., Navarro, S., Pascale, E., Perotto, L., Pisano, G., Ponthieu, N., Revéret, V., Rigby, A., Ritacco, A., Romero, C., Roussel, H., Ruppin, F., Schuster, K., Sievers, A., Triqueneaux, S., Tucker, C., and Zylka, R. (2018). "The NIKA2 large-field-of-view millimetre continuum camera for the 30 m IRAM telescope". *A&A* 609, A115. doi: 10.1051/0004-6361/201731503.

Aharonson, O., Hayes, A. G., Lunine, J. I., Lorenz, R. D., Allison, M. D., and Elachi, C. (2009). "An asymmetric distribution of lakes on Titan as a possible consequence of orbital forcing". *Nature Geosci* 2, pp. 851–854. doi: 10.1038/ngeo698.

Altenhoff, W. J., Chini, R., Hein, H., Kreysa, E., Mezger, P. G., Salter, C., and Schraml, J. B. (1988). "First radio astronomical estimate of the temperature of Pluto". *Astronomy and Astrophysics* 190.1-2, pp. L15–L17.

Altobelli, N., Postberg, F., Fiege, K., Trieloff, M., Kimura, H., Sterken, V. J., Hsu, H.-W., Hillier, J., Khawaja, N., Moragas-Klostermeyer, G., Blum, J., Burton, M., Srama, R., Kempf, S., and Gruen, E. (2016). "Flux and composition of interstellar dust at Saturn from Cassini's Cosmic Dust Analyzer". *Science* 352.6283, pp. 312–318. doi: 10.1126/science.aac6397.

Alvarellos, J. L., Zahnle, K. J., Dobrovolskis, A. R., and Hamill, P. (2005). "Fates of satellite ejecta in the Saturn system". *Icarus* 178.1, pp. 104–123. doi: 10.1016/j.icarus.2005.04.017.

Alvarellos, J. L., Dobrovolskis, A. R., Zahnle, K. J., Hamill, P., Dones, L., and Robbins, S. (2017). "Fates of satellite ejecta in the Saturn system, II". *Icarus* 284, pp. 70–89. doi: 10.1016/j.icarus.2016.10.028.

Anderson, J. D. and Schubert, G. (2007). "Saturn's satellite Rhea is a homogeneous mix of rock and ice". *Geophysical Research Letters* 34.2. doi: 10.1029/2006GL028100.

Asphaug, E. and Reufer, A. (2013). "Late origin of the Saturn system". *Icarus* 223.1, pp. 544–565. doi: 10.1016/j.icarus.2012.12.009.

Baragiola, R. A. (2003). "Water ice on outer solar system surfaces: Basic properties and radiation effects". *Planetary and Space Science* 51.14. Surfaces and Atmospheres of the Outer Planets their Satellites and Ring Systems, pp. 953–961. doi: 10.1016/j.pss.2003.05.007.

Baron, J. E., Tyler, G. L., and Simpson, R. A. (2003). "Three-dimensional numerical modeling of refraction and reflection scattering from icy galilean satellites". *Icarus* 164.2, pp. 404–417. doi: 10.1016/S0019-1035(03)00124-6.

Beddingfield, C. B., Burr, D. M., and Dunne, W. M. (2015). "Shallow normal fault slopes on Saturnian icy satellites". *Journal of Geophysical Research: Planets* 120.12, pp. 2053–2083. doi: 10.1002/2015JE004852.

Beuthe, M., Rivoldini, A., and Trinh, A. (2016). "Enceladus's and Dione's floating ice shells supported by minimum stress isostasy". *Geophysical Research Letters* 43.19, pp. 10,088–10,096. doi: 10.1002/2016GL070650.

Běhounková, M., Tobie, G., Choblet, G., and Čadek, O. (2012). "Tidally-induced melting events as the origin of south-pole activity on Enceladus ". *Icarus* 219.2, 655–664. doi: 10.1016/j.icarus.2012.03.024.

Bierhaus, E. B., McEwen, A. S., Robbins, S. J., Singer, K. N., Dones, L., Kirchoff, M. R., and Williams, J.-P. (2018). "Secondary craters and ejecta across the solar system: Populations and effects on impact-crater–based chronologies". *Meteoritics & Planetary Science* 53.4, pp. 638–671. doi: 10.1111/maps.13057.

Bierhaus, E. B., Dones, L., Alvarellos, J. L., and Zahnle, K. (2012). "The role of ejecta in the small crater populations on the mid-sized saturnian satellites". *Icarus* 218.1, pp. 602–621. doi: 10.1016/j.icarus.2011.12.011.

Biver, N., Bockelée-Morvan, D., Hofstadter, M., Lellouch, E., Choukroun, M., Gulkis, S., Crovisier, J., Schloerb, F. P., Rezac, L., von Allmen, P., Lee, S., Leyrat, C., Ip, W. H., Hartogh, P., Encrenaz, P., Beaudin, G., and the MIRO team (2019). "Long-term monitoring of the outgassing and composition of comet 67P/Churyumov-Gerasimenko with the Rosetta/MIRO instrument". *A&A* 630, A19. doi: 10.1051/0004-6361/201834960.

Black, G. J., Campbell, D. B., and Ostro, S. J. (2001a). "Icy Galilean Satellites: 70 cm Radar Results from Arecibo". *Icarus* 151.2, pp. 160–166. doi: 10.1006/icar.2001.6615.

Black, G. J., Campbell, D. B., and Nicholson, P. D. (2001b). "Icy Galilean Satellites: Modeling Radar Reflectivities as a Coherent Backscatter Effect". *Icarus* 151.2, pp. 167–180. doi: 10.1006/icar.2001.6616.

Black, G. J., Campbell, D. B., and Carter, L. M. (2007). "Arecibo radar observations of Rhea, Dione, Tethys, and Enceladus". *Icarus* 191.2, pp. 702–711. doi: 10.1016/j.icarus.2007.06.009.

Black, G. J., Campbell, D. B., and Carter, L. M. (2011). "Ground-based radar observations of Titan: 2000–2008". *Icarus* 212.1, pp. 300–320. doi: 10.1016/j.icarus.2010.10.025.

Black, G. J., Campbell, D. B., Carter, L. M., and Ostro, S. J. (2004). "Radar Detection of Iapetus". *Science* 304.5670, pp. 553–553. doi: 10.1126/science.1096470.

Blackburn, D. G., Buratti, B. J., and Rivera-Valentin, E. G. (2012). "Exploring the Impact of Thermal Segregation on Dione Through a Bolometric Bond Albedo Map". In: *Lunar and Planetary Science Conference*. 1536.

Blackburn, D. G., Buratti, B. J., and Ulrich, R. (2011). "A bolometric Bond albedo map of Iapetus: Observations from Cassini VIMS and ISS and Voyager ISS". *Icarus* 212.1, pp. 329–338. doi: 10.1016/j.icarus.2010.12.022.

Bland, M. T., McKinnon, W. B., and Schenk, P. M. (2015). "Constraining the heat flux between Enceladus' tiger stripes: Numerical modeling of funiscular plains formation". *Icarus* 260, pp. 232–245. doi: 10.1016/j.icarus.2015.07.016.

Blankenship, D. D., Young, D. A., Moore, W. B., Moore, J. C., Pappalardo, R. T., McKinnon, W. B., and Khurana, K. K. (2009). "Radar sounding of Europa's subsurface properties and processes: The view from Earth". In: *Europa*. Univ. of Ariz. Press Tucson, pp. 631–654.

Boissier, J., Groussin, O., Jorda, L., Lamy, P., Bockelée-Morvan, D., Crovisier, J., Biver, N., Colom, P., Lellouch, E., and Moreno, R. (2011). "Earth-based detection of the millimetric thermal emission from the nucleus of comet 8P/Tuttle". *A&A* 528, A54. doi: 10.1051/0004-6361/201016060.

Bond, W. C. (1848). "Discovery of a new satellite of Saturn". *Monthly Notices of the Royal Astronomical Society* 9.1, 1–2. doi: 10.1093/mnras/9.1.1.

Bonnefoy, L. E., Le Gall, A., Lellouch, E., Leyrat, C., Janssen, M., and Sultana, R. (2020a). "Rhea's subsurface probed by the Cassini radiometer: Insights into its thermal, structural, and compositional properties". *Icarus*. doi: 10.1016/j.icarus.2020.113947.

Bonnefoy, L. E., Lestrade, Jean-François, Lellouch, Emmanuel, Le Gall, A., Leyrat, Cédric, Ponthieu, Nicolas, and Ladjelate, Bilal (2020b). "Probing the subsurface of the two faces of Iapetus". *EPJ Web Conf.* 228, p. 00006. doi: 10.1051/epjconf/202022800006.

Braga-Ribas, F., Sicardy, B., Ortiz, J. L., Snodgrass, C., Roques, F., Vieira-Martins, R., Camargo, J. I. B., Assafin, M., Duffard, R., Jehin, E., Pollock, J., Leiva, R., Emilio, M., Machado, D. I., Colazo, C., Lellouch, E., Skottfelt, J., Gillon, M., Ligier, N., Maquet, L., Benedetti-Rossi, G., Gomes, A. R., Kervella, P., Monteiro, H., Sfair, R., Moutamid, M. E., Tancredi, G., Spagnotto, J., Maury, A., Morales, N., Gil-Hutton, R., Roland, S., Ceretta, A., Gu, S. h., Wang, X. b., Harpsøe, K., Rabus, M., Manfroid, J., Opitom, C., Vanzi, L., Mehret, L., Lorenzini, L., Schneiter, E. M., Melia, R., Lecacheux, J., Colas, F., Vachier, F., Widemann, T., Almenares, L., Sandness, R. G., Char, F., Perez, V., Lemos, P., Martinez, N., Jorgensen, U. G., Dominik, M., Roig, F., Reichart, D. E., LaCluyze, A. P., Haislip, J. B., Ivarsen, K. M., Moore, J. P., Frank, N. R., and Lambas, D. G. (2014). "A ring system detected around the Centaur (10199) Chariklo". *Nature* 508, pp. 72–75. doi: 10.1038/nature13155.

Brown, M. E. and Butler, B. J. (2017). "The Density of Mid-sized Kuiper Belt Objects from ALMA Thermal Observations". *The Astronomical Journal* 154.1, p. 19. doi: 10.3847/1538-3881/aa6346.

Brown, R. H., Baines, K. H., Bellucci, G., Bibring, J.-P., Buratti, B. J., Capaccioni, F., Cerroni, P., Clark, R. N., Coradini, A., Cruikshank, D. P., Drossart, P., Formisano, V., Jaumann, R., Langevin, Y., Matson, D. L., Mccord, T. B., Mennella, V., Miller, E., Nelson, R. M., Nicholson, P. D., Sicardy, B., and Sotin, C. (2004). "The Cassini Visual and Infrared Mapping Spectrometer (VIMS) Investigation". *Space Sci Rev* 115, pp. 111–168. doi: 10.1007/s11214-004-1453-x.

Bruzzone, L., Plaut, J. J., Alberti, G., Blankenship, D. D., Bovolo, F., Campbell, B. A., Ferro, A., Gim, Y., Kofman, W., Komatsu, G., McKinnon, W., Mitri, G., Orosei, R., Patterson, G. W., Plettemeier, D., and Seu, R. (2013). "RIME: Radar for Icy Moon Exploration". In: *2013 IEEE International Geoscience and Remote Sensing Symposium - IGARSS*, pp. 3907–3910.

Buratti, B. and Veverka, J. (1984). "Voyager photometry of Rhea, Dione, Tethys, Enceladus and Mimas". *Icarus* 58.2, pp. 254–264. doi: 10.1016/0019-1035(84)90042-3.

Buratti, B. J., Cruikshank, D. P., Brown, R. H., Clark, R. N., Bauer, J. M., Jaumann, R., McCord, T. B., Simonelli, D. P., Hibbitts, C. A., Hansen, G. B., Owen, T. C., Baines, K. H., Bellucci, G., Bibring, J.-P., Capaccioni, F., Cerroni, P., Coradini, A., Drossart, P., Formisano, V., Langevin, Y., Matson, D. L., Mennella, V., Nelson, R. M., Nicholson, P. D., Sicardy, B., Sotin, C., Roush, T. L., Soderlund, K., and Muradyan, A. (2005). "Cassini Visual and Infrared Mapping Spectrometer observations of Iapetus: Detection of CO_2". *The Astrophysical Journal* 622.2, pp. L149–L152. doi: 10.1086/429800.

Buratti, B. J., Soderlund, K., Bauer, J., Mosher, J. A., Hicks, M. D., Simonelli, D. P., Jaumann, R., Clark, R. N., Brown, R. H., Cruikshank, D. P., and Momary, T. (2008). "Infrared (0.83–5.1μm) photometry of Phoebe from the Cassini Visual Infrared Mapping Spectrometer". *Icarus* 193.2. Saturn's Icy Satellites from Cassini, 309–322. doi: 10.1016/j.icarus.2007.09.014.

Buratti, B. J., Hansen, C. J., Hendrix, A. R., Esposito, L. W., Mosher, J. A., Brown, R. H., Clark, R. N., Baines, K. H., and Nicholson, P. D. (2018). "The Search for Activity on Dione and Tethys With Cassini VIMS and UVIS". *Geophysical Research Letters* 45.12, pp. 5860–5866. doi: 10.1029/2018GL078165.

Buratti, B. J. (1988). "Enceladus: Implications of its unusual photometric properties". *Icarus* 75.1, pp. 113–126. doi: 10.1016/0019-1035(88)90130-3.

Buratti, B. J., Mosher, J. A., and Johnson, T. V. (1990). "Albedo and color maps of the Saturnian satellites". *Icarus* 87.2, pp. 339–357. doi: 10.1016/0019-1035(90)90138-Y.

Burns, J. A., Hamilton, D. P., Mignard, F., and Soter, S. (1996). "The Contamination of Iapetus by Phoebe Dust". In: *IAU Colloq. 150: Physics, Chemistry, and Dynamics of Interplanetary Dust*. Ed. by B. A. S. Gustafson and M. S. Hanner. Vol. 104. Astronomical Society of the Pacific Conference Series, p. 179.

Butler, B. and Desai, K. (1999). *Phase Fluctuations at The VLA Derived From One Year of Site Testing Interferometer Data*. VLA Test Memo. No. 222. National Radio Astronomy Observatory.

Butler, B. (1993). "The 3.5-cm radar investigation of Mars and Mercury: Planetological implications".

Butler, B. (2012). *ALMA Memo 594*. Tech. rep.

Butler, B. J., Steffes, P. G., Suleiman, S. H., Kolodner, M. A., and Jenkins, J. M. (2001). "Accurate and Consistent Microwave Observations of Venus and Their Implications". *Icarus* 154.2, pp. 226–238. doi: 10.1006/icar.2001.6710.

Calvo, M., Benoît, A., Catalano, A., Goupy, J., Monfardini, A., Ponthieu, N., Barria, E., Bres, G., Grollier, M., Garde, G., Leggeri, J.-P., Pont, G., Triqueneaux, S., Adam, R., Bourrion, O., Macías-Pérez, J.-F., Rebolo, M., Ritacco, A., Scordilis, J.-P., Tourres, D., Adane, A., Coiffard, G., Leclercq, S., Désert, F.-X., Doyle, S., Mauskopf, P., Tucker, C., Ade, P., André, P., Beelen, A., Belier, B., Bideaud, A., Billot, N., Comis, B., D'Addabbo, A., Kramer, C., Martino, J., Mayet, F., Pajot, F., Pascale, E., Perotto, L., Revéret, V., Ritacco, A., Rodriguez, L., Savini, G., Schuster, K., Sievers, A., and Zylka, R. (2016). "The NIKA2 Instrument, A Dual-Band Kilopixel KID Array for Millimetric Astronomy". *Journal of Low Temperature Physics* 184.3, pp. 816–823. doi: 10.1007/s10909-016-1582-0.

Campbell, B. A., Campbell, D. B., Margot, J. L., Ghent, R. R., Nolan, M., Chandler, J., Carter, L. M., and Stacy, N. J. S. (2007). "Focused 70-cm Wavelength Radar Mapping of the Moon". *IEEE Transactions on Geoscience and Remote Sensing* 45.12, pp. 4032–4042. doi: 10.1109/TGRS.2007.906582.

Campbell, B. A. (1994). "Merging Magellan emissivity and SAR data for analysis of Venus surface dielectric properties". *Icarus* 112.1, pp. 187–203. doi: 10.1006/icar.1994.1177.

Campbell, B. A., Ray Hawke, B., Morgan, G. A., Carter, L. M., Campbell, D. B., and Nolan, M. (2014). "Improved discrimination of volcanic complexes, tectonic features, and regolith properties in Mare Serenitatis from Earth-based radar mapping". *Journal of Geophysical Research: Planets* 119.2, pp. 313–330. doi: 10.1002/2013JE004486.

Campbell, B. A., Campbell, D. B., Morgan, G. A., Carter, L. M., Nolan, M. C., and Chandler, J. F. (2015). "Evidence for crater ejecta on Venus tessera terrain from Earth-based radar images". *Icarus* 250, pp. 123–130. doi: 10.1016/j.icarus.2014.11.025.

Campbell, D. B., Chandler, J. F., Ostro, S. J., Pettengill, G. H., and Shapiro, I. I. (1978). "Galilean satellites: 1976 radar results". *Icarus* 34.2, pp. 254–267. doi: 10.1016/0019-1035(78)90166-5.

Campbell, D. B., Black, G. J., Carter, L. M., and Ostro, S. J. (2003). "Radar Evidence for Liquid Surfaces on Titan". *Science* 302.5644, pp. 431–434. doi: 10.1126/science.1088969.

Campbell, M. J. and Ulrichs, J. (1969). "Electrical properties of rocks and their significance for lunar radar observations". *Journal of Geophysical Research (1896-1977)* 74.25, pp. 5867–5881. doi: 10.1029/JB074i025p05867.

Canup, R. (2010). "Origin of Saturn's rings and inner moons by mass removal from a lost Titan-sized satellite". *Nature* 468, pp. 943–946. doi: 10.1038/nature09661.

Canup, R. and Ward, W. (2006). "A common mass scaling for satellite systems of gaseous planets". *Nature* 441, pp. 834–839. doi: 10.1038/nature04860.

Carilli, C. L. and Holdaway, M. A. (1999). "Tropospheric phase calibration in millimeter interferometry". *Radio Science* 34.4, pp. 817–840. doi: 10.1029/1999RS900048.

Carter, L. M., Campbell, D. B., and Campbell, B. A. (2004). "Impact crater related surficial deposits on Venus: Multipolarization radar observations with Arecibo". *Journal of Geophysical Research: Planets* 109.E6. doi: 10.1029/2003JE002227.

Carter, L. M., Neish, C. D., Bussey, D. B. J., Spudis, P. D., Patterson, G. W., Cahill, J. T., and Raney, R. K. (2012). "Initial observations of lunar impact melts and ejecta flows with the Mini-RF radar". *Journal of Geophysical Research: Planets* 117.E12. doi: 10.1029/2011JE003911.

Castillo-Rogez, J. C., Matson, D. L., Sotin, C., Johnson, T. V., Lunine, J. I., and Thomas, P. C. (2007). "Iapetus' geophysics: Rotation rate, shape, and equatorial ridge". *Icarus* 190.1, pp. 179–202. doi: 10.1016/j.icarus.2007.02.018.

Castillo-Rogez, J. C., Hemingway, D., Rhoden, A., Tobie, G., and McKinnon, W. B. (2018). "Origin and Evolution of Saturn's Mid-Sized Moons". In: *Enceladus and the Icy Moons of Saturn*. Ed. by P. M. Schenk, R. N. Clark, C. J. A. Howett, A. J. Verbiscer, and J. H. Waite, p. 285. doi: 10.2458/azu_uapress_9780816537075-ch014.

Catalano, A., Calvo, M., Ponthieu, N., Adam, R., Adane, A., Ade, P., André, P., Beelen, A., Belier, B., Benoît, A., Bideaud, A., Billot, N., Boudou, N., Bourrion, O., Coiffard, G., Comis, B., D´Addabbo, A., Désert, F.-X., Doyle, S., Goupy, J., Kramer, C., Leclercq, S., Macías-Pérez, J. F., Martino, J., Mauskopf, P., Mayet, F., Monfardini, A., Pajot, F., Pascale, E., Perotto, L., Revéret, V., Rodriguez, L., Savini, G., Schuster, K., Sievers, A., Tucker, C., and Zylka, R. (2014). "Performance and calibration of the NIKA camera at the IRAM 30 m telescope". *A&A* 569, A9. doi: 10.1051/0004-6361/201423557.

Charnoz, S., Crida, A., Castillo-Rogez, J. C., Lainey, V., Dones, L., Karatekin, Özgür, Tobie, G., Mathis, S., Poncin-Lafitte], C. L., and Salmon, J. (2011). "Accretion of Saturn's mid-sized moons during the viscous spreading of young massive rings: Solving the paradox of silicate-poor rings versus silicate-rich moons". *Icarus* 216.2, pp. 535–550. doi: 10.1016/j.icarus.2011.09.017.

Choblet, G., Tobie, G., Sotin, C., Běhounková, M., Čadek, O., Postberg, F., and Souček, O. (2017). "Powering prolonged hydrothermal activity inside Enceladus". *Nat Astron* 1, pp. 841–847. doi: 10.1038/s41550-017-0289-8.

Choukroun, M., Keihm, S., Schloerb, F. P., Gulkis, S., Lellouch, E., Leyrat, C., von Allmen, P., Biver, N., Bockelée-Morvan, D., Crovisier, J., Encrenaz, P., Hartogh, P., Hofstadter, M., Ip, W.-H., Jarchow, C., Janssen, M., Lee, S., Rezac, L., Beaudin, G., Gaskell, B., Jorda, L., Keller, H. U., and Sierks, H. (2015). "Dark side of comet 67P/Churyumov-Gerasimenko in Aug.-Oct. 2014 - MIRO/Rosetta continuum observations of polar night in the southern regions". *A&A* 583, A28. doi: 10.1051/0004-6361/201526181.

Ciarletti, V., Levasseur-Regourd, A. C., Lasue, J., Statz, C., Plettemeier, D., Hérique, A., Rogez, Y., and Kofman, W. (2015). "CONSERT suggests a change in local properties of 67P/Churyumov-Gerasimenko's nucleus at depth". *A&A* 583, A40. doi: 10.1051/0004-6361/201526337.

Ciarletti, V., Clifford, S., Plettemeier, D., Le Gall, A., Hervé, Y., Dorizon, S., Quantin-Nataf, C., Benedix, W.-S., Schwenzer, S., Pettinelli, E., Heggy, E., Herique, A., Berthelier, J.-J., Kofman, W., Vago, J. L., Hamran, S.-E., and WISDOM Team, the (2017). "The WISDOM Radar: Unveiling the Subsurface Beneath the ExoMars Rover and Identifying the Best Locations for Drilling". *Astrobiology* 17.6-7, pp. 565–584. doi: 10.1089/ast.2016.1532.

Ciarniello, M., Capaccioni, F., Filacchione, G., Clark, R. N., Cruikshank, D. P., Cerroni, P., Coradini, A., Brown, R. H., Buratti, B. J., Tosi, F., and Stephan, K. (2011). "Hapke modeling of Rhea surface properties through Cassini-VIMS spectra". *Icarus* 214.2, pp. 541–555. doi: 10.1016/j.icarus.2011.05.010.

Clark, R. N., Brown, R. H., Owensby, P. D., and Steele, A. (1984). "Saturn's satellites: Near-infrared spectrophotometry (0.6–2.5 μm) of the leading and trailing sides and compositional implications". *Icarus* 58.2, pp. 265–281. doi: 10.1016/0019-1035(84)90043-5.

Clark, R. N., Brown, R. H., Jaumann, R., Cruikshank, D. P., Nelson, R. M., Buratti, B. J., McCord, T. B., Lunine, J., Baines, K. H., Bellucci, G., Bibring, J.-P., Capaccioni, F., Cerroni, P., Coradini, A., Formisano, V., Langevin, Y., Matson, D. L., Mennella, V., Nicholson, P. D., Sicardy, B., Sotin, C., Hoefen, T. M., Curchin, J. M., Hansen, G., Hibbits, K., and Matz, K.-D. (2005). "Compositional maps of Saturn's moon Phoebe from imaging spectroscopy". *Nature* 435, 66–69. doi: 10.1038/nature03558.

Clark, R. N., Curchin, J. M., Jaumann, R., Cruikshank, D. P., Brown, R. H., Hoefen, T. M., Stephan, K., Moore, J. M., Buratti, B. J., Baines, K. H., Nicholson, P. D., and Nelson, R. M. (2008). "Compositional mapping of Saturn's satellite Dione with Cassini VIMS and implications of dark material in the Saturn system". *Icarus* 193.2. Saturn's Icy Satellites from Cassini, pp. 372–386. doi: 10.1016/j.icarus.2007.08.035.

Clark, R. N., Cruikshank, D. P., Jaumann, R., Brown, R. H., Stephan, K., Ore, C. M. D., Livo, K. E., Pearson, N., Curchin, J. M., Hoefen, T. M., Buratti, B. J., Filacchione, G., Baines, K. H., and Nicholson, P. D. (2012). "The surface composition of Iapetus: Mapping results from Cassini VIMS". *Icarus* 218.2, pp. 831–860. doi: 10.1016/j.icarus.2012.01.008.

Combe, J.-P., McCord, T. B., Matson, D. L., Johnson, T. V., Davies, A. G., Scipioni, F., and Tosi, F. (2019). "Nature, distribution and origin of CO_2 on Enceladus". *Icarus* 317, pp. 491–508. doi: 10.1016/j.icarus.2018.08.007.

Coradini, A., Tosi, F., Gavrishin, A. I., Capaccioni, F., Cerroni, P., Filacchione, G., Adriani, A., Brown, R. H., Bellucci, G., Formisano, V., D'Aversa, E., Lunine, J. I., Baines, K. H., Bibring, J.-P., Buratti, B. J., Clark, R. N., Cruikshank, D. P., Combes, M., Drossart, P., Jaumann, R., Langevin, Y., Matson, D. L., McCord, T. B., Mennella, V., Nelson, R. M., Nicholson, P. D., Sicardy, B., Sotin, C., Hedman, M. M., Hansen, G. B., Hibbitts, C. A., Showalter, M., Griffith, C., and Strazzulla, G. (2008). "Identification of spectral units on Phoebe". *Icarus* 193.1, 233–251. doi: 10.1016/j.icarus.2007.07.023.

Corlies, P., Hayes, A. G., Kelland, J., Ádámkovics, M., Rodriguez, S., Rojo, P., P.Turtle, E., Lora, J., Mitchell, J., Lunine, J., and Perry, J. E. (2019). "Ongoing Monitoring of Clouds on Titan". In:

Crow-Willard, E. N. and Pappalardo, R. T. (2015). "Structural mapping of Enceladus and implications for formation of tectonized regions". *Journal of Geophysical Research: Planets* 120.5. 2015JE004818, pp. 928–950. doi: 10.1002/2015JE004818.

Cruikshank, D. P., Dalton, J. B., Ore, C. M. D., Bauer, J., Stephan, K., Filacchione, G., Hendrix, A. R., Hansen, C. J., Coradini, A., Cerroni, P., Tosi, F., Capaccioni, F., Jaumann, R., Buratti, B. J., Clark, R. N., Brown, R. H., Nelson, R. M., McCord, T. B., Baines, K. H., Nicholson, P. D., Sotin, C., Meyer, A. W., Bellucci, G., Combes, M., Bibring, J.-P., Langevin, Y., Sicardy, B., Matson, D. L., Formisano, V., Drossart, P., and Mennella, V. (2007). "Surface composition of Hyperion". *Nature* 448, pp. 54–56. doi: 10.1038/nature05948.

Cruikshank, D. P., Owen, T. C., Ore, C. D., Geballe, T. R., Roush, T. L., Bergh], C. [de, Sandford, S. A., Poulet, F., Benedix, G. K., and Emery, J. P. (2005). "A spectroscopic study of the surfaces of Saturn's large satellites: H_2O ice, tholins, and minor constituents". *Icarus* 175.1, pp. 268–283. doi: 10.1016/j.icarus.2004.09.003.

Cruikshank, D. P., Wegryn, E., Dalle Ore, C. M., Brown, R. H., Bibring, J.-P., Buratti, B. J., Clark, R. N., McCord, T. B., Nicholson, P. D., Pendleton, Y. J., Owen, T. C., Filacchione, G., Coradini, A., Cerroni, P., Capaccioni, F., Jaumann, R., Nelson, R. M., Baines, K. H., Sotin, C., Bellucci, G., Combes, M., Langevin, Y., Sicardy, B., Matson, D. L., Formisano, V., Drossart, P., and Mennella, V. (2008). "Hydrocarbons on Saturn's satellites Iapetus and Phoebe". *Icarus* 193.2. Saturn's Icy Satellites from Cassini, pp. 334–343. doi: 10.1016/j.icarus.2007.04.036.

Cruikshank, D. P., Ore, C. M. D., Clark, R. N., and Pendleton, Y. J. (2014). "Aromatic and aliphatic organic materials on Iapetus: Analysis of Cassini VIMS data". *Icarus* 233, pp. 306–315. doi: 10.1016/j.icarus.2014.02.011.

Ćuk, M., Dones, L., and Nesvorný, D. (2016). "Dynamical evidence for a late formation of Saturn's moons". *The Astrophysical Journal* 820.2, p. 97. doi: 10.3847/0004-637x/820/2/97.

Cuzzi, J. N. and Muhleman, D. O. (1972). "The microwave spectrum and nature of the subsurface of Mars". *Icarus* 17.2, pp. 548–560. doi: 10.1016/0019-1035(72)90019-X.

Cuzzi, J. N. and Pollack, J. B. (1978). "Saturn's rings: Particle composition and size distribution as constrained by microwave observations: I. Radar observations". *Icarus* 33.2, pp. 233–262. doi: 10.1016/0019-1035(78)90145-8.

Cuzzi, J. N., Pollack, J. B., and Summers, A. L. (1980). "Saturn's rings: Particle composition and size distribution as constrained by observations at microwave wavelengths: II. Radio interferometric observations". *Icarus* 44.3, pp. 683–705. doi: 10.1016/0019-1035(80)90137-2.

Dalle Ore, C. M., Cruikshank, D. P., Mastrapa, R. M. E., Lewis, E., and White, O. L. (2015). "Impact craters: An ice study on Rhea". *Icarus* 261, pp. 80–90. doi: 10.1016/j.icarus.2015.08.008.

Dalle Ore, C. M., Cruikshank, D. P., and Clark, R. N. (2012). "Infrared spectroscopic characterization of the low-albedo materials on Iapetus". *Icarus* 221.2, pp. 735–743. doi: 10.1016/j.icarus.2012.09.010.

Dalton, J. B., Cruikshank, D. P., and Clark, R. N. (2012). "Compositional analysis of Hyperion with the Cassini Visual and Infrared Mapping Spectrometer". *Icarus* 220.2, pp. 752–776. doi: 10.1016/j.icarus.2012.05.003.

de Kleer, K., Butler, B., de Pater, I., Gurwell, M., and Moullet, A. (2019). "Thermal properties of Europa and Ganymede from spatially resolved ALMA observations". In: *EPSC-DPS Joint Meeting 2019*. Vol. 2019, EPSC–DPS2019–917.

de Pater, I., Brown, R. A., and Dickel, J. R. (1984). "VLA observations of the Galilean satellites". *Icarus* 57.1, pp. 93–101. doi: 10.1016/0019-1035(84)90011-3.

de Pater, I., Ulich, B. L., Kreysa, E., and Chini, R. (1989). "Planetary observations at a wavelenght of 355 μm". *Icarus* 79.1, pp. 190–195. doi: 10.1016/0019-1035(89)90115-2.

de Pater, I. and Dickel, J. R. (1991). "Multifrequency radio observations of Saturn at ring inclination angles between 5 and 26 degrees". *Icarus* 94.2, pp. 474–492. doi: 10.1016/0019-1035(91)90242-L.

de Pater, I., Forster, J. R., Wright, M., Butler, B. J., Palmer, P., Veal, J. M., A'Hearn, M. F., and Snyder, L. E. (1998). "BIMA and VLA Observations of Comet Hale-Bopp at 22–115 GHz". *The Astronomical Journal* 116.2, pp. 987–996. doi: 10.1086/300470.

Denk, T., Mottola, S., Tosi, F., Bottke, W., and Hamilton, D. (2018). "The Irregular Satellites of Saturn". In: doi: 10.2458/azu_uapress_9780816537075-ch020.

Dlugach, J. M., Mishchenko, M. I., and Mackowski, D. W. (2011). "Numerical simulations of single and multiple scattering by fractal ice clusters". *Journal of Quantitative Spectroscopy and Radiative Transfer* 112.11. Electromagnetic and Light Scattering by Nonspherical Particles XII, pp. 1864–1870. doi: 10.1016/j.jqsrt.2011.01.038.

Dobrovolskis, A. R., Alvarellos, J. L., Zahnle, K. J., and Lissauer, J. J. (2010). "Exchange of ejecta between Telesto and Calypso: Tadpoles, horseshoes, and passing orbits". *Icarus* 210.1, pp. 436–445. doi: 10.1016/j.icarus.2010.06.023.

Dollfus, A. (1968). "La découverte du 10e satellite de Saturne". *L'Astronomie* 82, p. 253.

Dong, Z., Fang, G., Ji, Y., Gao, Y., Wu, C., and Zhang, X. (2017). "Parameters and structure of lunar regolith in Chang'E-3 landing area from lunar penetrating radar (LPR) data". *Icarus* 282, pp. 40–46. doi: 10.1016/j.icarus.2016.09.010.

Dougherty, M. K., Kellock, S., Southwood, D. J., Balogh, A., Smith, E. J., Tsurutani, B. T., Gerlach, B., Glassmeier, K.-H., Gleim, F., Russell, C. T., Erdos, G., Neubauer, F. M., and Cowley, S. W. H. (2004). "The Cassini Magnetic Field Investigation". *Space Sci Rev* 114, pp. 331–383. doi: 10.1007/s11214-004-1432-2.

Dougherty, M. K., Khurana, K. K., Neubauer, F. M., Russell, C. T., Saur, J., Leisner, J. S., and Burton, M. E. (2006). "Identification of a Dynamic Atmosphere at Enceladus with the Cassini Magnetometer". *Science* 311.5766, pp. 1406–1409. doi: 10.1126/science.1120985.

Dyce, B. R., Pettengill, G. H., and Shapiro, I. I. (1967). "Radar determination of the rotations of Venus and Mercury". *Astrophysical Journal* 72, p. 351. doi: 10.1086/110231.

Elachi, C., Kobrick, M., Roth, L., Tiernan, M., and Brown, W. E. (1976). "Local lunar topography from the Apollo 17 Alse radar imagery and altimetry". *The Moon* 15, pp. 119–131. doi: 10.1007/BF00562476.

Elachi, C., Allison, M. D., Borgarelli, L., Encrenaz, P., Im, E., Janssen, M. A., Johnson, W. T. K., Kirk, R. L., Lorenz, R. D., Lunine, J. I., Muhleman, D. O., Ostro, S. J., Picardi, G., Posa, F., Rapley, C. G., Roth, L. E., Seu, R., Soderblom, L. A., Vetrella, S., Wall, S. D., Wood, C. A., and Zebker, H. A. (2004). "Radar: The Cassini Titan Radar Mapper". English. *Space Science Reviews* 115.1-4, pp. 71–110. doi: 10.1007/s11214-004-1438-9.

Elachi, C., Wall, S., Allison, M., Anderson, Y., Boehmer, R., Callahan, P., Encrenaz, P., Flamini, E., Franceschetti, G., Gim, Y., Hamilton, G., Hensley, S., Janssen, M., Johnson, W., Kelleher, K., Kirk, R., Lopes, R., Lorenz, R., Lunine, J., Muhleman, D., Ostro, S., Paganelli, F., Picardi, G., Posa, F., Roth, L., Seu, R., Shaffer, S., Soderblom, L., Stiles, B., Stofan, E., Vetrella, S., West, R., Wood, C., Wye, L., and Zebker, H. (2005). "Cassini Radar Views the Surface of Titan". *Science* 308.5724, pp. 970–974. doi: 10.1126/science.1109919.

Eshleman, V. R. (1986). "Radar Glory from Buried Craters on Icy Moons". *Science* 234.4776, pp. 587–590. doi: 10.1126/science.234.4776.587.

Esposito, L. W., Barth, C. A., Colwell, J. E., Lawrence, G. M., McClintock, W. E., Stewart, A. I. F., Keller, H. U., Korth, A., Lauche, H., Festou, M. C., Lane, A. L., Hansen, C. J., Maki, J. N., West, R. A., Jahn, H., Reulke, R., Warlich, K., Shemansky, D. E., and Yung, Y. L. (2004). "The Cassini Ultraviolet Imaging Spectrograph Investigation". *Space Sci Rev* 115, pp. 299–361. doi: 10.1007/s11214-004-1455-8.

Fa, W. and Jin, Y.-Q. (2010). "A primary analysis of microwave brightness temperature of lunar surface from Chang-E 1 multi-channel radiometer observation and inversion of regolith layer thickness". *Icarus* 207.2, pp. 605–615. doi: 10.1016/j.icarus.2009.11.034.

Fang, G.-Y., Zhou, B., Ji, Y.-C., Zhang, Q.-Y., Shen, S.-X., Li, Y.-X., Guan, H.-F., Tang, C.-J., Gao, Y.-Z., Lu, W., Ye, S.-B., Han, H.-D., Zheng, J., and Wang, S.-Z. (2014). "Lunar Penetrating Radar onboard the Chang'E-3 mission". *Research in Astronomy and Astrophysics* 14.12, pp. 1607–1622. doi: 10.1088/1674-4527/14/12/009.

Ferrari, C. and Leyrat, C. (2006). "Thermal emission of spherical spinning ring particles - The standard model". *A&A* 447.2, pp. 745–760. doi: 10.1051/0004-6361:20052953.

Ferrari, C. and Lucas, A. (2016). "Low thermal inertias of icy planetary surfaces - Evidence for amorphous ice?" *A&A* 588, A133. doi: 10.1051/0004-6361/201527625.

Filacchione, G., Capaccioni, F., Clark, R. N., Cuzzi, J. N., Cruikshank, D. P., Coradini, A., Cerroni, P., Nicholson, P. D., McCord, T. B., Brown, R. H., Buratti, B. J., Tosi, F., Nelson, R. M., Jaumann, R., and Stephan, K. (2010). "Saturn's icy satellites investigated by Cassini–VIMS: II. Results at the end of nominal mission". *Icarus* 206.2. Cassini at Saturn, pp. 507–523. doi: 10.1016/j.icarus.2009.11.006.

Filacchione, G., Capaccioni, F., Ciarniello, M., Clark, R. N., Cuzzi, J. N., Nicholson, P. D., Cruikshank, D. P., Hedman, M. M., Buratti, B. J., Lunine, J. I., Soderblom, L. A., Tosi, F., Cerroni, P., Brown, R. H., McCord, T. B., Jaumann, R., Stephan, K., Baines, K. H., and Flamini, E. (2012). "Saturn's icy satellites and rings investigated by Cassini–VIMS: III – Radial compositional variability". *Icarus* 220.2, pp. 1064–1096. doi: 10.1016/j.icarus.2012.06.040.

Fink, U., Larson, H. P., Gautier T. N., I., and Treffers, R. R. (1976). "Infrared spectra of the satellites of Saturn: identification of water ice on Iapetus, Rhea, Dione, and Tethys." *Astrophys. J* 207, pp. L63–L67. doi: 10.1086/182180.

Flasar, F, Achterberg, R., Conrath, B., Pearl, J., Bjoraker, G., Jennings, D, Romani, P., Simon, A., Kunde, V, Nixon, C., Bézard, B, Orton, G., Spilker, L, Spencer, J, Irwin, P., Teanby, N., Owen, T, Brasunas, J, Segura, M, and Wishnow, E (2005). "Temperatures, Winds, and Composition in the Saturnian System". *Science (New York, N.Y.)* 307, pp. 1247–51. doi: 10.1126/science.1105806.

Flasar, F. M., Kunde, V. G., Abbas, M. M., Achterberg, R. K., Ade, P., Barucci, A., B'ezard, B., Bjoraker, G. L., Brasunas, J. C., Calcutt, S., Carlson, R., C'esarsky, C. J., Conrath, B. J., Coradini, A., Courtin, R., Coustenis, A., Edberg, S., Edgington, S., Ferrari, C., Fouchet, T., Gautier, D., Gierasch, P. J., Grossman, K., Irwin, P., Jennings, D. E., Lellouch, E., Mamoutkine, A. A., Marten, A., Meyer, J. P., Nixon, C. A., Orton, G. S., Owen, T. C., Pearl, J. C., Prang'e, R., Raulin, F., Read, P. L., Romani, P. N., Samuelson, R. E., Segura, M. E., SHOWALTER, M. R., Simon-Miller, A. A., Smith, M. D., Spencer, J. R., Spilker, L. J., and Taylor, F. W. (2004). "Exploring The Saturn System In The Thermal Infrared: The Composite Infrared Spectrometer". *Space Sci Rev* 115, pp. 169–297. doi: 10.1007/s11214-004-1454-9.

Fornasier, S., Lellouch, E., Müller, T., Santos-Sanz, P., Panuzzo, P., Kiss, C., Lim, T., Mommert, M., Bockelée-Morvan, D., Vilenius, E., Stansberry, J., Tozzi, G. P., Mottola, S., Delsanti, A., Crovisier, J., Duffard, R., Henry, F., Lacerda, P., Barucci, A., and Gicquel, A. (2013). "TNOs are Cool: A survey of the trans-Neptunian region - VIII. Combined Herschel PACS and SPIRE observations of nine bright targets at 70–500 μm". *A&A* 555, A15. doi: 10.1051/0004-6361/201321329.

Fouchet, T., Moreno, R., Lellouch, E., Formisano, V., Giuranna, M., and Montmessin, F. (2011). "Interferometric millimeter observations of water vapor on Mars and comparison with Mars Express measurements". *Planetary and Space Science* 59.8, pp. 683–690. doi: 10.1016/j.pss.2011.01.017.

Fountain, J. W. and Larson, S. M. (1977). "A New Satellite of Saturn?" *Science* 197.4306, pp. 915–917. doi: 10.1126/science.197.4306.915.

Gerdes, D. W., Sako, M., Hamilton, S., Zhang, K., Khain, T., Becker, J. C., Annis, J., Wester, W., Bernstein, G. M., Scheibner, C., Zullo, L., Adams, F., Bergin, E., Walker, A. R., Mueller, J. H., Abbott, T. M. C., Abdalla, F. B., Allam, S., Bechtol, K., Benoit-Lévy, A., Bertin, E., Brooks, D., Burke, D. L., Carnero Rosell, A., Carrasco Kind, M., Carretero, J., Cunha, C. E., da Costa, L. N., Desai, S., Diehl, H. T., Eifler, T. F., Flaugher, B., Frieman, J., García-Bellido, J., Gaztanaga, E., Goldstein, D. A., Gruen, D., Gschwend, J., Gutierrez, G., Honscheid, K., James, D. J., Kent, S., Krause, E., Kuehn, K., Kuropatkin, N., Lahav, O., Li, T. S., Maia, M. A. G., March, M., Marshall, J. L., Martini, P., Menanteau, F., Miquel, R., Nichol, R. C., Plazas, A. A., Romer, A. K., Roodman, A., Sanchez, E., Sevilla-Noarbe, I., Smith, M., Smith, R. C., Soares-Santos, M., Sobreira, F., Suchyta, E., Swanson, M. E. C., Tarle, G., Tucker, D. L., and Zhang, Y. (2017). "Discovery and Physical Characterization of a Large Scattered Disk Object at 92 au". *The Astrophysical Journal* 839.1, p. L15. doi: 10.3847/2041-8213/aa64d8.

Ghail, R., Wilson, C., Widemann, T., Bruzzone, L., Dumoulin, C., Helbert, J., Herrick, R., Marcq, E., Mason, P., and Rosenblatt, P. (2017). "EnVision: understanding why our most Earth-like neighbour is so different". *arXiv e-prints, arXiv:1703.09010*.

Giese, B., Wagner, R., Neukum, G., Helfenstein, P., and Thomas, P. C. (2007). "Tethys: Lithospheric thickness and heat flux from flexurally supported topography at Ithaca Chasma". *Geophysical Research Letters* 34.21. doi: 10.1029/2007GL031467.

Giese, B., Denk, T., Neukum, G., Roatsch, T., Helfenstein, P., Thomas, P. C., Turtle, E. P., McEwen, A., and Porco, C. C. (2008). "The topography of Iapetus' leading side". *Icarus* 193.2. Saturn's Icy Satellites from Cassini, pp. 359–371. doi: 10.1016/j.icarus.2007.06.005.

Glein, C. R., Postberg, F., and Vance, S. D. (2018). "The Geochemistry of Enceladus: Composition and Controls". In: *Enceladus and the Icy Moons of Saturn*. Ed. by P. M. Schenk, R. N.

Clark, C. J. A. Howett, A. J. Verbiscer, and J. H. Waite, p. 39. doi: 10.2458/azu_uapress_9780816537075-ch003.

Goguen, J. D., Buratti, B. J., Brown, R. H., Clark, R. N., Nicholson, P. D., Hedman, M. M., Howell, R. R., Sotin, C., Cruikshank, D. P., Baines, K. H., Lawrence, K. J., Spencer, J. R., and Blackburn, D. G. (2013). "The temperature and width of an active fissure on Enceladus measured with Cassini {VIMS} during the 14 April 2012 South Pole flyover ". *Icarus* 226.1, pp. 1128–1137. doi: 10.1016/j.icarus.2013.07.012.

Goldstein, R. M. and Morris, G. A. (1973). "Radar Observations of the rings of Saturn". *Icarus* 20.3, pp. 260–262. doi: 10.1016/0019-1035(73)90002-X.

Goldstein, R. M. and Green, R. R. (1980). "Ganymede: Radar Surface Characteristics". *Science* 207.4427, pp. 179–180. doi: 10.1126/science.207.4427.179.

Gong, X., Paige, D. A., Siegler, M. A., and Jin, Y. (2015). "Inversion of Dielectric Properties of the Lunar Regolith Media With Temperature Profiles Using Chang'e Microwave Radiometer Observations". *IEEE Geoscience and Remote Sensing Letters* 12.2, pp. 384–388.

Gulkis, S., Frerking, M., Crovisier, J., Beaudin, G., Hartogh, P., Encrenaz, P., Koch, T., Kahn, C., Salinas, Y., Nowicki, R., Irigoyen, R., Janssen, M., Stek, P., Hofstadter, M., Allen, M., Backus, C., Kamp, L., Jarchow, C., Steinmetz, E., Deschamps, A., Krieg, J., Gheudin, M., Bockelée-Morvan, D., Biver, N., Encrenaz, T., Despois, D., Ip, W., Lellouch, E., Mann, I., Muhleman, D., Rauer, H., Schloerb, P., and Spilker, T. (2007). "Microwave Instrument for Rosetta Orbiter". *Space Sci Rev*. doi: 10.1007/s11214-006-9032-y.

Gulkis, S., Keihm, S., Kamp, L., Backus, C., Janssen, M., Lee, S., Davidsson, B., Beaudin, G., Biver, N., Bockelée-Morvan, D., Crovisier, J., Encrenaz, P., Encrenaz, T., Hartogh, P., Hofstadter, M., Ip, W., Lellouch, E., Mann, I., Schloerb, P., Spilker, T., and Frerking, M. (2010). "Millimeter and submillimeter measurements of asteroid (2867) Steins during the Rosetta fly-by". *Planetary and Space Science* 58.9, pp. 1077–1087. doi: 10.1016/j.pss.2010.02.008.

Gundlach, B. and Blum, J. (2013). "A new method to determine the grain size of planetary regolith". *Icarus* 223.1, pp. 479–492. doi: 10.1016/j.icarus.2012.11.039.

Hagen, N. R., Moullet, A., and Gurwell, M. A. (2014). "Interpreting the Thermal Lightcurve of Iapetus at 1.3mm". In: *American Astronomical Society Meeting Abstracts #223*. Vol. 223. American Astronomical Society Meeting Abstracts, p. 247.17.

Hagfors, T., Gold, T., and lerkic, H. M. (1985). "Refraction scattering as origin of the anomalous radar returns of Jupiter's satellites". *Nature* 315, pp. 637–640. doi: 10.1038/315637a0.

Hagfors, T., Dahlstrøm, I., Gold, T., Hamran, S.-E., and Hansen, R. (1997). "Refraction Scattering in the Anomalous Reflections from Icy Surfaces". *Icarus* 130.2, pp. 313–322. doi: 10.1006/icar.1997.5844.

Haldemann, A. F. C. and Muhleman, D. O. (1999). "Circular-polarization radar properties of high-altitude ice: Western Kunlun Shan and central Andes". *Journal of Geophysical Research: Planets* 104.E10, pp. 24075–24094. doi: 10.1029/1999JE900023.

Hamilton, D. P. and Burns, J. A. (1994). "Origin of Saturn's E Ring: Self-Sustained, Naturally". *Science* 264.5158, pp. 550–553. doi: 10.1126/science.264.5158.550.

Hamilton, D. P., Skrutskie, M. F., Verbiscer, A. J., and Masci, F. J. (2015). "Small particles dominate Saturn's Phoebe ring to surprisingly large distances". *Nature* 522, 185–187. doi: 10.1038/nature14476.

Hammond, N. P., Phillips, C. B., Nimmo, F., and Kattenhorn, S. A. (2011). "Stereo Topography of Fault Systems and Crater-Fault Interactions on Rhea". In: *AGU Fall Meeting Abstracts*. Vol. 2011, P43D–1714.

Hammond, N. P., Phillips, C. B., Nimmo, F., and Kattenhorn, S. A. (2013). "Flexure on Dione: Investigating subsurface structure and thermal history". *Icarus* 223.1, pp. 418–422. doi: 10.1016/j.icarus.2012.12.021.

Hamran, S., Berger, T., Brovoll, S., Damsgård, L., Helleren, Øyan, M. J., Amundsen, H. E., Carter, L., Ghent, R., Kohler, J., Mellon, M., Paige, D., Plettemeier, D., and Eide, J. (2015). "RIMFAX: A GPR for the Mars 2020 rover mission". In: *2015 8th International Workshop on Advanced Ground Penetrating Radar (IWAGPR)*, pp. 1–4. doi: 10.1109/IWAGPR.2015.7292690.

Hanel, R. A., Conrath, B. J., Kunde, V. G., Pearl, J. C., and Pirraglia, J. A. (1983). "Albedo, internal heat flux, and energy balance of Saturn". *Icarus* 53.2, pp. 262–285. doi: 10.1016/0019-1035(83)90147-1.

Hapke, B. and Blewett, D. (1991). "Coherent backscatter model for the unusual radar reflectivity of icy satellites". *Nature* 352.46-47. doi: 10.1038/352046a0.

Hapke, B. (1990). "Coherent backscatter and the radar characteristics of outer planet satellites". *Icarus* 88.2, pp. 407–417. doi: 10.1016/0019-1035(90)90091-M.

Harcke, L. J. (2005). "Radar imaging of solar system ices". PhD thesis. Stanford University.

Harland, D. M. (2007). *Cassini at Saturn-Huygens Results*.

Harmon, J. K., Perillat, P. J., and Slade, M. A. (2001). "High-Resolution Radar Imaging of Mercury's North Pole". *Icarus* 149.1, pp. 1–15. doi: 10.1006/icar.2000.6544.

Harmon, J. K., Slade, M. A., and Rice, M. S. (2011). "Radar imagery of Mercury's putative polar ice: 1999–2005 Arecibo results". *Icarus* 211.1, pp. 37–50. doi: 10.1016/j.icarus.2010.08.007.

Harmon, J. K., Nolan, M. C., Husmann, D. I., and Campbell, B. A. (2012). "Arecibo radar imagery of Mars: The major volcanic provinces". *Icarus* 220.2, pp. 990–1030. doi: 10.1016/j.icarus.2012.06.030.

Harmon, J. K. and Nolan, M. C. (2017). "Arecibo radar imagery of Mars: II. Chryse–Xanthe, polar caps, and other regions". *Icarus* 281, pp. 162–199. doi: 10.1016/j.icarus.2016.08.015.

Hartogh, P., Barabash, S., Beaudin, G., Börner, P., Bockeleé-Morvan, D., Boogaerts, W., Cavalié, T., Christensen, U. R., Dannenberg, A., Eriksson, P., Fränz, M., Fouchet, T., Frisk, U., Hocke, K., Janssen, C., Jarchow, C., Kasai, Y., Kikuchi, K., Krieg, J. M., Krupp, N., Kuroda, T., Lellouch, E., Loose, A., Maestrini, A., Manabe, T., Medvedev, A. S., Mendrok, J., Miettinen, E. P., Moreno, R., Murk, A., Murtagh, D., Nishibori, T., Rengel, M., Rezac, L., Sagawa, H., Steinmetz, E., Thomas, B., Urban, J., and Wicht, J. (2013). "The Submillimetre Wave Instrument on JUICE". In: *European Planetary Science Congress*, EPSC2013–710.

Hashin, Z. and Shtrikman, S. (1962). "A Variational Approach to the Theory of the Effective Magnetic Permeability of Multiphase Materials". *Journal of Applied Physics* 33.10, pp. 3125–3131. doi: 10.1063/1.1728579.

Hayes, A. G., Birch, S. P. D., Dietrich, W. E., Howard, A. D., Kirk, R. L., Poggiali, V., Mastrogiuseppe, M., Michaelides, R. J., Corlies, P. M., Moore, J. M., Malaska, M. J., Mitchell, K. L., Lorenz, R. D., and Wood, C. A. (2017). "Topographic Constraints on the Evolution and Connectivity of Titan's Lacustrine Basins". *Geophysical Research Letters* 44.23, pp. 11,745–11,753. doi: 10.1002/2017GL075468.

He, C. L., Ma, S. J., Su, X. J., Mo, Q. H., and Yang, J. L. (2015). "Comparison of the Microwave Absorption Characteristics of Hematite, Magnetite and Pyrite". *Journal of Microwave Power and Electromagnetic Energy* 49.3, pp. 131–146. doi: 10.1080/08327823.2015.11689903.

Heggy, E., Scabbia, G., Bruzzone, L., and Pappalardo, R. T. (2017). "Radar probing of Jovian icy moons: Understanding subsurface water and structure detectability in the JUICE and Europa missions". *Icarus* 285, pp. 237–251. doi: 10.1016/j.icarus.2016.11.039.

Heiles, C. E. and Drake, F. D. (1963). "The polarization and intensity of thermal radiation from a planetary surface". *Icarus* 2, pp. 281–292. doi: 10.1016/0019-1035(63)90023-X.

Helfenstein, P. and Porco, C. C. (2015). "Enceladus' geysers: Relation to geological features". *The Astronomical Journal* 150.3, p. 96. doi: 10.1088/0004-6256/150/3/96.

Hemingway, D., Iess, L., Tajeddine, R., and Tobie, G. (2018). "The Interior of Enceladus". In: *Enceladus and the Icy Moons of Saturn*. Ed. by P. M. Schenk, R. N. Clark, C. J. A. Howett, A. J. Verbiscer, and J. H. Waite, p. 57. doi: 10.2458/azu_uapress_9780816537075-ch004.

Hemingway, D. J., Zannoni, M., Tortora, P., Nimmo, F., and Asmar, S. W. (2016). "Dione's Internal Structure Inferred from Cassini Gravity and Topography". In: *Lunar and Planetary Science Conference*. Lunar and Planetary Science Conference, p. 1314.

Hendrix, A. R., Buratti, B. J., Cruikshank, D. P., Clark, R. N., Scipioni, F., and Howett, C. J. A. (2018). "Surface Composition of Saturn's Icy Moons". In: *Enceladus and the Icy Moons of Saturn*. Ed. by P. M. Schenk, R. N. Clark, C. J. A. Howett, A. J. Verbiscer, and J. H. Waite, p. 307. doi: 10.2458/azu_uapress_9780816537075-ch015.

Hendrix, A. R. and Hansen, C. J. (2008a). "The albedo dichotomy of Iapetus measured at UV wavelengths". *Icarus* 193.2. Saturn's Icy Satellites from Cassini, pp. 344–351. doi: 10.1016/j.icarus.2007.07.025.

Hendrix, A. R. and Hansen, C. J. (2008b). "Ultraviolet observations of Phoebe from the Cassini UVIS". *Icarus* 193.2. Saturn's Icy Satellites from Cassini, pp. 323–333. doi: 10.1016/j.icarus.2007.06.030.

Hendrix, A. R., Cassidy, T. A., Buratti, B. J., Paranicas, C., Hansen, C. J., Teolis, B., Roussos, E., Todd Bradley, E., Kollmann, P., and Johnson, R. E. (2012). "Mimas' far-UV albedo: Spatial variations". *Icarus* 220.2, pp. 922–931. doi: 10.1016/j.icarus.2012.06.012.

Hendrix, A. R., Filacchione, G., Paranicas, C., Schenk, P., and Scipioni, F. (2018). "Icy Saturnian satellites: Disk-integrated UV-IR characteristics and links to exogenic processes". *Icarus* 300, pp. 103–114. doi: 10.1016/j.icarus.2017.08.037.

Hensley, S., Smrekar, S., Shaffer, S., Paller, M., Figueroa, H., Freeman, A., Hodges, R., and Walkemeyer, P. (2015). "VISAR: A next generation interferometric radar for venus exploration". In: *2015 IEEE 5th Asia-Pacific Conference on Synthetic Aperture Radar (APSAR)*, pp. 362–366.

Herschel, W. (1790). "I. Account of the discovery of a sixth and seventh satellite of the planet Saturn; with remarks on the construction of its ring, its atmosphere, its rotation on an axis, and its spheroidical figure". *Philosophical Transactions of the Royal Society of London* 80, pp. 1–20. doi: 10.1098/rstl.1790.0001.

Hewison, T. J. and English, S. J. (1999). "Airborne retrievals of snow and ice surface emissivity at millimeter wavelengths". *IEEE Transactions on Geoscience and Remote Sensing* 37.4, pp. 1871–1879. doi: 10.1109/36.774700.

Hill, T. W. (1984). "Saturn's E ring". *Advances in Space Research* 4.9, pp. 149–157. doi: 10.1016/0273-1177(84)90020-6.

Hinson, D. P., Linscott, I. R., Young, L. A., Tyler, G. L., Stern, S. A., Beyer, R. A., Bird, M. K., Ennico, K., Gladstone, G. R., Olkin, C. B., Pätzold, M., Schenk, P. M., Strobel, D. F., Summers, M. E., Weaver, H. A., and Woods, W. W. (2017). "Radio occultation measurements of Pluto's neutral atmosphere with New Horizons". *Icarus* 290, pp. 96–111. doi: 10.1016/j.icarus.2017.02.031.

Hirata, N. (2016a). "Differential impact cratering of Saturn's satellites by heliocentric impactors". *Journal of Geophysical Research: Planets* 121.2, pp. 111–117. doi: 10.1002/2015JE004940.

Hirata, N. (2016b). "Timing of the faulting on the Wispy Terrain of Dione based on stratigraphic relationships with impact craters". *Journal of Geophysical Research: Planets* 121.11, pp. 2325–2334. doi: 10.1002/2016JE005176.

Hirata, N., Miyamoto, H., and Showman, A. P. (2014). "Particle deposition on the saturnian satellites from ephemeral cryovolcanism on Enceladus". *Geophysical Research Letters* 41.12, pp. 4135–4141. doi: 10.1002/2014GL060470.

Hirata, N. and Miyamoto, H. (2016). "Rayed craters on Dione: Implication for the dominant surface alteration process". *Icarus* 274, pp. 116–121. doi: 10.1016/j.icarus.2016.03.021.

Hofgartner, J. D., Hayes, A. G., Campbell, D. B., Lunine, J. I., Black, G. J., MacKenzie, S. M., Birch, S. P. D., Elachi, C., Kirk, R. D., Le Gall, A., Lorenz, R. D., and Wall, S. D. (2020). "The root of anomalously specular reflections from solid surfaces on Saturn's moon Titan". *Nat Commun* 11.2829. doi: 10.1038/s41467-020-16663-1.

Howard, A. D., Moore, J. M., Schenk, P. M., White, O. L., and Spencer, J. (2012). "Sublimation-driven erosion on Hyperion: Topographic analysis and landform simulation model tests". *Icarus* 220.1, pp. 268–276. doi: 10.1016/j.icarus.2012.05.013.

Howett, C. J. A., Spencer, J. R., Pearl, J., and Segura, M. (2010). "Thermal inertia and bolometric Bond albedo values for Mimas, Enceladus, Tethys, Dione, Rhea and Iapetus as derived from Cassini/CIRS measurements ". *Icarus* 206.2, pp. 573–593. doi: 10.1016/j.icarus.2009.07.016.

Howett, C. J. A., Spencer, J. R., Schenk, P., Johnson, R. E., Paranicas, C., Hurford, T. A., Verbiscer, A., and Segura, M. (2011a). "A high-amplitude thermal inertia anomaly of probable magnetospheric origin on Saturn's moon Mimas". *Icarus* 216.1, pp. 221–226. doi: 10.1016/j.icarus.2011.09.007.

Howett, C. J. A., Spencer, J. R., Pearl, J., and Segura, M. (2011b). "High heat flow from Enceladus' south polar region measured using 10-600 cm^{-1} Cassini/CIRS data". *Journal of Geophysical Research: Planets* 116.E3. E03003. doi: 10.1029/2010JE003718.

Howett, C. J. A., Spencer, J. R., Hurford, T., Verbiscer, A., and Segura, M. (2012). "PacMan returns: An electron-generated thermal anomaly on Tethys ". *Icarus* 221.2, pp. 1084–1088. doi: 10.1016/j.icarus.2012.10.013.

Howett, C. J. A., Spencer, J. R., Hurford, T., Verbiscer, A., and Segura, M. (2014). "Thermophysical property variations across Dione and Rhea ". *Icarus* 241, pp. 239–247. doi: 10.1016/j.icarus.2014.05.047.

Howett, C. J. A., Spencer, J. R., Hurford, T., Verbiscer, A., and Segura, M. (2016). "Thermal properties of Rhea's poles: Evidence for a meter-deep unconsolidated subsurface layer". *Icarus* 272, pp. 140–148. doi: 10.1016/j.icarus.2016.02.033.

Howett, C. J. A., Hendrix, A. R., Nordheim, T. A., Paranicas, C., Spencer, J. R., and Verbiscer, A. J. (2018). "Ring and Magnetosphere Interactions with Satellite Surfaces". In: *Enceladus and the Icy Moons of Saturn*. Ed. by P. M. Schenk, R. N. Clark, C. J. A. Howett, A. J. Verbiscer, and J. H. Waite, p. 343. doi: 10.2458/azu_uapress_9780816537075-ch017.

Howett, C. J. A., Spencer, J. R., Hurford, T., Verbiscer, A., and Segura, M. (2019). "Maps of Tethys' thermophysical properties". *Icarus* 321, pp. 705–714. doi: 10.1016/j.icarus.2018.12.018.

Howett, C. J. A., Spencer, J. R., and Nordheim, T. (2020). "Bolometric bond albedo and thermal inertia maps of Mimas". *Icarus*, p. 113745. doi: 10.1016/j.icarus.2020.113745.

Howett, C. J. A., Spencer, J. R., Hurford, T., Verbiscer, A., and Segura, M. (2018). "Limits on Dione's Activity Using Cassini/CIRS Data". *Geophysical Research Letters* 45.12, pp. 5876–5898. doi: 10.1029/2018GL078161.

Hsu, H.-W., Postberg, F., Sekine, Y., Shibuya, T., Kempf, S., Horányi, M., Juhász, A., Altobelli, N., Suzuki, K., Masaki, Y., Kuwatani, T., Tachibana, S., Sirono, S. iti, Moragas-Klostermeyer, G., and Srama, R. (2015). "Ongoing hydrothermal activities within Enceladus". *Nature* 519, pp. 207–210. doi: 10.1038/nature14262.

Huygens, C. (1659). *Systema Saturnium*. https://archive.org/details/CristianiHugeni00Huyg/page/n5/mode/2up: Hagae-Comitis : Ex typographia Adriani Vlacq.

Hyodo, R. and Charnoz, S. (2017). "Dynamical Evolution of the Debris Disk after a Satellite Catastrophic Disruption around Saturn". *The Astronomical Journal* 154.1, p. 34. doi: 10.3847/1538-3881/aa74c9.

Iess, L., Militzer, B., Kaspi, Y., Nicholson, P., Durante, D., Racioppa, P., Anabtawi, A., Galanti, E., Hubbard, W., Mariani, M. J., Tortora, P., Wahl, S., and Zannoni, M. (2019). "Measurement

and implications of Saturn's gravity field and ring mass". *Science* 364.6445. doi: 10.1126/science.aat2965.

Janssen, M. A., Lorenz, R. D., West, R., Paganelli, F., Lopes, R. M. C., Kirk, R. L., Elachi, C., Wall, S. D., Johnson, W. T. K., Anderson, Y., Boehmer, R. A., Callahan, P., Gim, Y., Hamilton, G. A., Kelleher, K. D., Roth, L., Stiles, B., and Le Gall, A. (2009). "Titan's surface at 2.2-cm wavelength imaged by the Cassini {RADAR} radiometer: Calibration and first results". *Icarus* 200.1, pp. 222–239. doi: 10.1016/j.icarus.2008.10.017.

Janssen, M. A., Le Gall, A., and Wye, L. C. (2011). "Anomalous radar backscatter from Titan's surface?" *Icarus* 212.1, pp. 321–328. doi: 10.1016/j.icarus.2010.11.026.

Janssen, M. A., Ingersoll, A. P., Allison, M. D., Gulkis, S., Laraia, A. L., Baines, K. H., Edgington, S. G., Anderson, Y. Z., Kelleher, K., and Oyafuso, F. A. (2013). "Saturn's thermal emission at 2.2-cm wavelength as imaged by the Cassini {RADAR} radiometer". *Icarus* 226.1, pp. 522–535. doi: 10.1016/j.icarus.2013.06.008.

Janssen, M. A., Le Gall, A., Lopes, R. M. C., Lorenz, R. D., Malaska, M. J., Hayes, A. G., Neish, C. D., Solomonidou, A., Mitchell, K. L., Radebaugh, J., Keihm, S. J., Choukroun, M., Leyrat, C., Encrenaz, P. J., and Mastrogiuseppe, M. (2016). "Titan's surface at 2.18-cm wavelength imaged by the Cassini {RADAR} radiometer: Results and interpretations through the first ten years of observation". *Icarus* 270. Titan's Surface and Atmosphere, pp. 443–459. doi: 10.1016/j.icarus.2015.09.027.

Janssen, M. A., Oswald, J. E., Brown, S. T., Gulkis, S., Levin, S. M., Bolton, S. J., Allison, M. D., Atreya, S. K., Gautier, D., Ingersoll, A. P., Lunine, J. I., Orton, G. S., Owen, T. C., Steffes, P. G., Adumitroaie, V., Bellotti, A., Jewell, L. A., Li, C., Li, L., Misra, S., Oyafuso, F. A., Santos-Costa, D., Sarkissian, E., Williamson, R., Arballo, J. K., Kitiyakara, A., Ulloa-Severino, A., Chen, J. C., Maiwald, F. W., Sahakian, A. S., Pingree, P. J., Lee, K. A., Mazer, A. S., Redick, R., Hodges, R. E., Hughes, R. C., Bedrosian, G., Dawson, D. E., Hatch, W. A., Russell, D. S., Chamberlain, N. F., Zawadski, M. S., Khayatian, B., Franklin, B. R., Conley, H. A., Kempenaar, J. G., Loo, M. S., Sunada, E. T., Vorperion, V., and Wang, C. C. (2017). "MWR: Microwave Radiometer for the Juno Mission to Jupiter". *Space Sci Rev* 213, pp. 139–185. doi: 10.1007/s11214-017-0349-5.

Jaumann, R., Stephan, K., Hansen, G. B., Clark, R. N., Buratti, B. J., Brown, R. H., Baines, K. H., Newman, S. F., Bellucci, G., Filacchione, G., Coradini, A., Cruikshank, D. P., Griffith, C. A., Hibbitts, C. A., McCord, T. B., Nelson, R. M., Nicholson, P. D., Sotin, C., and Wagner, R. (2008). "Distribution of icy particles across Enceladus' surface as derived from Cassini-VIMS measurements". *Icarus* 193.2. Saturn's Icy Satellites from Cassini, pp. 407–419. doi: 10.1016/j.icarus.2007.09.013.

Johnson, J. B. (1928). "Thermal Agitation of Electricity in Conductors". *Phys. Rev.* 32 (1), pp. 97–109. doi: 10.1103/PhysRev.32.97.

Johnson, R. E., Famá, M., Liu, M., Baragiola, R. A., Sittler, E. C., and Smith, H. T. (2008). "Sputtering of ice grains and icy satellites in Saturn's inner magnetosphere". *Planetary and Space Science* 56.9, pp. 1238–1243. doi: 10.1016/j.pss.2008.04.003.

Johnson, T. V. and Lunine, J. I. (2005). "Saturn's moon Phoebe as a captured body from the outer Solar System". *Nature* 435, pp. 69–71. doi: 10.1038/nature03384.

Jordan, R., Picardi, G., Plaut, J., Wheeler, K., Kirchner, D., Safaeinili, A., Johnson, W., Seu, R., Calabrese, D., Zampolini, E., Cicchetti, A., Huff, R., Gurnett, D., Ivanov, A., Kofman, W., Orosei, R., Thompson, T., Edenhofer, P., and Bombaci, O. (2009). "The Mars express MARSIS sounder instrument". *Planetary and Space Science* 57.14, pp. 1975–1986. doi: 10.1016/j.pss.2009.09.016.

Juhasz, A. and Horanyi, M. (2015). "Dust Delivery from Enceladus to the Moons of Saturn". In: *AGU Fall Meeting Abstracts*. Vol. 2015.

Kaku, T., Haruyama, J., Miyake, W., Kumamoto, A., Ishiyama, K., Nishibori, T., Yamamoto, K., Crites, S. T., Michikami, T., Yokota, Y., Sood, R., Melosh, H. J., Chappaz, L., and Howell, K. C. (2017). "Detection of intact lava tubes at Marius Hills on the Moon by SELENE (Kaguya) Lunar Radar Sounder". *Geophysical Research Letters* 44.20, pp. 10,155–10,161. doi: 10.1002/2017GL074998.

Kalousová, K., Schroeder, D. M., and Soderlund, K. M. (2017). "Radar attenuation in Europa's ice shell: Obstacles and opportunities for constraining the shell thickness and its thermal structure". *Journal of Geophysical Research: Planets* 122.3, pp. 524–545. doi: 10.1002/2016JE005110.

Keihm, S., Kamp, L., Gulkis, S., Hofstadter, M., Lee, S., Janssen, M., and Choukroun, M. (2013). "Reconciling main belt asteroid spectral flux density measurements with a self-consistent thermophysical model". *Icarus* 226.1, pp. 1086–1102. doi: 10.1016/j.icarus.2013.07.005.

Kempf, S., Horányi, M., Hsu, H. W., Hill, T. W., Juhász, A., and Smith, H. T. (2018). "Saturn's Diffuse E Ring and Its Connection with Enceladus". In: *Enceladus and the Icy Moons of Saturn*. Ed. by P. M. Schenk, R. N. Clark, C. J. A. Howett, A. J. Verbiscer, and J. H. Waite, p. 195. doi: 10.2458/azu_uapress_9780816537075-ch010.

Kempf, S., Beckmann, U., and Schmidt, J. (2010). "How the Enceladus dust plume feeds Saturn's E ring". *Icarus* 206.2. Cassini at Saturn, pp. 446–457. doi: 10.1016/j.icarus.2009.09.016.

Kimura, J., Kawamura, T., Morito, H., Morota, T., Honda, C., Kuramoto, K., and Okada, T. (2011). "Sublimation's impact on temporal change of albedo dichotomy on Iapetus". *Icarus* 214.2, pp. 596–605. doi: 10.1016/j.icarus.2011.06.015.

Kirchoff, M. R., Bierhaus, E. B., Dones, L., Robbins, S. J., Singer, K. N., Wagner, R. J., and Zahnle, K. J. (2018). "Cratering Histories in the Saturnian System". In: *Enceladus and the Icy Moons of Saturn*. Ed. by P. M. Schenk, R. N. Clark, C. J. A. Howett, A. J. Verbiscer, and J. H. Waite, p. 267. doi: 10.2458/azu_uapress_9780816537075-ch013.

Kirchoff, M. R. and Schenk, P. (2009). "Crater modification and geologic activity in Enceladus' heavily cratered plains: Evidence from the impact crater distribution". *Icarus* 202.2, pp. 656–668. doi: 10.1016/j.icarus.2009.03.034.

Kirchoff, M. R. and Schenk, P. (2010). "Impact cratering records of the mid-sized, icy saturnian satellites". *Icarus* 206.2. Cassini at Saturn, pp. 485–497. doi: 10.1016/j.icarus.2009.12.007.

Kirchoff, M. R. and Schenk, P. (2015). "Dione's resurfacing history as determined from a global impact crater database". *Icarus* 256, pp. 78–89. doi: 10.1016/j.icarus.2015.04.010.

Klinger, J. (1981). "Some consequences of a phase transition of water ice on the heat balance of comet nuclei". *Icarus* 47.3, pp. 320–324. doi: 10.1016/0019-1035(81)90179-2.

Kofman, W., Herique, A., Goutail, J.-P., Hagfors, T., Williams, I. P., Nielsen, E., Barriot, J.-P., Barbin, Y., Elachi, C., Edenhofer, P., Levasseur-Regourd, A.-C., Plettemeier, D., Picardi, G., Seu, R., and Svedhem, V. (2007). "The Comet Nucleus Sounding Experiment by Radiowave Transmission (CONSERT): A Short Description of the Instrument and of the Commissioning Stages". *Space Sci Rev*. doi: 10.1007/s11214-006-9034-9.

Kofman, W., Orosei, R., and Pettinelli, E. (2010). "Radar Signal Propagation and Detection Through Ice". *Space Sci Rev* 153, pp. 249–271. doi: 10.1007/s11214-010-9642-2.

Kofman, W., Herique, A., Barbin, Y., Barriot, J.-P., Ciarletti, V., Clifford, S., Edenhofer, P., Elachi, C., Eyraud, C., Goutail, J.-P., Heggy, E., Jorda, L., Lasue, J., Levasseur-Regourd, A.-C., Nielsen, E., Pasquero, P., Preusker, F., Puget, P., Plettemeier, D., Rogez, Y., Sierks, H., Statz, C., Svedhem, H., Williams, I., Zine, S., and Van Zyl, J. (2015). "Properties of the 67P/Churyumov-Gerasimenko interior revealed by CONSERT radar". *Science* 349.6247. doi: 10.1126/science.aab0639.

Kostylev, V. I. (2007). "Scattering Fundamentals". In: *Bistatic Radar*. John Wiley & Sons, Ltd. Chap. 10, pp. 193–223. doi: 10.1002/9780470035085.ch10.

Kramer, C., Peñalver, J., and Greve, A. (2013). “Improvement of the IRAM 30 m telescope beam pattern”. *Tech. Rep. 2013-1*.

Kuga, Y., Ulaby, F. T., Haddock, T. F., and DeRoo, R. D. (1991). “Millimeter-wave radar scattering from snow 1. Radiative transfer model”. *Radio Science* 26.2, pp. 329–341. doi: 10.1029/90RS02560.

Kuzmin, A. D. (1983). “Venus”. In: *Venus*. University of Arizona Press. Chap. Radio astronomical studies of Venus. Pp. 36–44.

Lainey, V., Karatekin, Özgür, Desmars, J., Charnoz, S., Arlot, J.-E., Emelyanov, N., Poncin-Lafitte, C. L., Mathis, S., Remus, F., Tobie, G., and Zahn, J.-P. (2012). “Strong tidal dissipation in Saturn and constraints on Enceladus’ thermal state from astrometry”. *The Astrophysical Journal* 752.1, p. 14. doi: 10.1088/0004-637x/752/1/14.

Lassell, W. (1848). “Discovery of a new satellite of Saturn”. *Monthly Notices of the Royal Astronomical Society* 8.9, pp. 195–197. doi: 10.1093/mnras/8.9.195a.

Le Gall, A., Ciarletti, V., Berthelier, J., Reineix, A., Guiffaut, C., Ney, R., Dolon, F., and Bonaime, S. (2008). “An Imaging HF GPR Using Stationary Antennas: Experimental Validation Over the Antarctic Ice Sheet”. *IEEE Transactions on Geoscience and Remote Sensing* 46.12, pp. 3975–3986. doi: 10.1109/TGRS.2008.2000718.

Le Gall, A., Janssen, M. A., Paillou, P., Lorenz, R. D., and Wall, S. D. (2010). “Radar-bright channels on Titan”. *Icarus* 207.2, pp. 948–958. doi: 10.1016/j.icarus.2009.12.027.

Le Gall, A., Leyrat, C., Janssen, M. A., Keihm, S., Wye, L. C., West, R., Lorenz, R. D., and Tosi, F. (2014). “Iapetus’ near surface thermal emission modeled and constrained using Cassini {RADAR} Radiometer microwave observations”. *Icarus* 241, pp. 221–238. doi: 10.1016/j.icarus.2014.06.011.

Le Gall, A., Leyrat, C., Janssen, M. A., Choblet, G., Tobie, G., Bourgeois, O., Lucas, A., Sotin, C., Howett, C., Kirk, R., Lorenz, R. D., West, R. D., Stolzenbach, A., Massé, M., Hayes, A. H., Bonnefoy, L. E., Veyssière, G., and Paganelli, F. (2017). “Thermally anomalous features in the subsurface of Enceladus’s south polar terrain”. *Nature Astronomy* 1.0063. doi: 10.1038/s41550-017-0063.

Le Gall, A., West, R. D., and Bonnefoy, L. E. (2019). “Dust and Snow Cover on Saturn’s Icy Moons”. *Geophysical Research Letters* 46.21, pp. 11747–11755. doi: 10.1029/2019GL084218.

Le Mouélic, S., Cornet, T., Rodriguez, S., Sotin, C., Seignovert, B., Barnes, J. W., Brown, R. H., Baines, K. H., Buratti, B. J., Clark, R. N., Nicholson, P. D., Lasue, J., Pasek, V., and Soderblom, J. M. (2019). “The Cassini VIMS archive of Titan: From browse products to global infrared color maps”. *Icarus* 319, pp. 121–132. doi: 10.1016/j.icarus.2018.09.017.

Lecacheux, J., Laques, P., Vapillon, L., Auge, A., and Despiau, R. (1980). “A new satellite of Saturn: Dione B”. *Icarus* 43.1, pp. 111–115. doi: 10.1016/0019-1035(80)90093-7.

Leliwa-Kopystynski, J., Banaszek, M., and Wlodarczyk, I. (2012). “Longitudinal asymmetry of craters’ density distributions on the icy satellites”. *Planetary and Space Science* 60.1. Titan Through Time: A Workshop on Titan’s Formation, Evolution and Fate, pp. 181–192. doi: 10.1016/j.pss.2011.08.002.

Lellouch, E., Paubert, G., Moreno, R., and Schmitt, B. (2000). “Search for Variations in Pluto’s Millimeter-Wave Emission”. *Icarus* 147.2, pp. 580–584. doi: 10.1006/icar.2000.6491.

Lellouch, E., Santos-Sanz, P., Lacerda, P., Mommert, M., Duffard, R., Ortiz, J. L., Müller, T. G., Fornasier, S., Stansberry, J., Kiss, C., Vilenius, E., Mueller, M., Peixinho, N., Moreno, R., Groussin, O., Delsanti, A., and Harris, A. W. (2013). “"TNOs are Cool": A survey of the trans-Neptunian region - IX. Thermal properties of Kuiper belt objects and Centaurs from combined Herschel and Spitzer observations”. *A&A* 557, A60. doi: 10.1051/0004-6361/201322047.

Lellouch, E., Santos-Sanz, P., Fornasier, S., Lim, T., Stansberry, J., Vilenius, E., Kiss, Cs., Müller, T., Marton, G., Protopapa, S., Panuzzo, P., and Moreno, R. (2016). “The long-wavelength ther-

mal emission of the Pluto-Charon system from Herschel observations. Evidence for emissivity effects". *A&A* 588, A2. doi: 10.1051/0004-6361/201527675.

Lellouch, E., Gurwell, M., Butler, B., Fouchet, T., Lavvas, P., Strobel, D. F., Sicardy, B., Moullet, A., Moreno, R., Bockelée-Morvan, D., Biver, N., Young, L., Lis, D., Stansberry, J., Stern, A., Weaver, H., Young, E., Zhu, X., and Boissier, J. (2017a). "Detection of CO and HCN in Pluto's atmosphere with ALMA". *Icarus* 286, pp. 289–307. doi: 10.1016/j.icarus.2016.10.013.

Lellouch, E., Moreno, R., Müller, T., Fornasier, S., Santos-Sanz, P., Moullet, A., Gurwell, M., Stansberry, J., Leiva, R., Sicardy, B., Butler, B., and Boissier, J. (2017b). "The thermal emission of Centaurs and trans-Neptunian objects at millimeter wavelengths from ALMA observations". *A&A* 608, A45. doi: 10.1051/0004-6361/201731676.

Lellouch, E., Gurwell, M. A., Moreno, R., Vinatier, S., Strobel, D. F., Moullet, A., Butler, B., Lara, L., Hidayat, T., and Villard, E. (2019). "An intense thermospheric jet on Titan". *Nat Astron* 3, pp. 614–619. doi: 10.1038/s41550-019-0749-4.

Lethuillier, A., Le Gall, A., Hamelin, M., Caujolle-Bert, S., Schreiber, F., Carrasco, N., Cernogora, G., Szopa, C., Brouet, Y., Simões, F., Correia, J. J., and Ruffié, G. (2018). "Electrical Properties of Tholins and Derived Constraints on the Huygens Landing Site Composition at the Surface of Titan". *Journal of Geophysical Research: Planets* 123.4, pp. 807–822. doi: 10.1002/2017JE005416.

Levenberg, K. (1944). "A method for the solution of certain problems in least-squares". *Q. Appl. Math* 2, pp. 164–168. doi: 10.1090/qam/10666.

Leyrat, C., Coradini, A., Erard, S., Capaccioni, F., Capria, M. T., Drossart, P., De Sanctis, M. C., Tosi, F., and Team, VIRTIS (2011). "Thermal properties of the asteroid (2867) Steins as observed by VIRTIS/Rosetta". *A&A* 531, A168. doi: 10.1051/0004-6361/201116529.

Leyrat, C., Barucci, A., Mueller, T., O´Rourke, L., Valtchanov, I., and Fornasier, S. (2012). "Thermal properties of (4) Vesta derived from Herschel measurements". *A&A* 539, A154. doi: 10.1051/0004-6361/201117793.

Leyrat, C., Lorenz, R. D., and Le Gall, A. (2016). "Probing Pluto's underworld: Ice temperatures from microwave radiometry decoupled from surface conditions". *Icarus* 268, pp. 50–55. doi: 10.1016/j.icarus.2015.12.016.

Leyrat, C. (2006). "Thermal properties of Saturn's rings : from CAMIRAS to the CASSINI mission." Theses. Université Paris-Diderot - Paris VII.

Leyrat, C., Erard, S., Capaccioni, F., Tosi, F., Filacchione, G., Bockelee-Morvan, D., Capria, T., De Sanctis, M. C., Drossart, P., Schmitt, B., and Arnold, G. (2015). "Surface thermal properties of 67/P inferred by VIRTIS/Rosetta". In:

Li, C., Ingersoll, A., Janssen, M., Levin, S., Bolton, S., Adumitroaie, V., Allison, M., Arballo, J., Bellotti, A., Brown, S., Ewald, S., Jewell, L., Misra, S., Orton, G., Oyafuso, F., Steffes, P., and Williamson, R. (2017). "The distribution of ammonia on Jupiter from a preliminary inversion of Juno microwave radiometer data". *Geophysical Research Letters* 44.11, pp. 5317–5325. doi: 10.1002/2017GL073159.

Li, C., Su, Y., Pettinelli, E., Xing, S., Ding, C., Liu, J., Ren, X., Lauro, S. E., Soldovieri, F., Zeng, X., Gao, X., Chen, W., Dai, S., Liu, D., Zhang, G., Zuo, W., Wen, W., Zhang, Z., Zhang, X., and Zhang, H. (2020). "The Moon's farside shallow subsurface structure unveiled by Chang'E-4 Lunar Penetrating Radar". *Science Advances* 6.9. doi: 10.1126/sciadv.aay6898.

Liang, D., Xu, X., Tsang, L., Andreadis, K. M., and Josberger, E. G. (2008). "The Effects of Layers in Dry Snow on Its Passive Microwave Emissions Using Dense Media Radiative Transfer Theory Based on the Quasicrystalline Approximation (QCA/DMRT)". *IEEE Transactions on Geoscience and Remote Sensing* 46.11, pp. 3663–3671. doi: 10.1109/TGRS.2008.922143.

Lopes, R. M. C., Wall, S. D., Elachi, C., Birch, S. P. D., Corlies, P., Coustenis, A., Hayes, A. G., Hofgartner, J. D., Janssen, M. A., Kirk, R. L., Le Gall, A., Lorenz, R. D., Lunine, J. I., Malaska, M. J., Mastroguiseppe, M., Mitri, G., Neish, C. D., Notarnicola, C., Paganelli, F., Paillou, P.,

Poggiali, V., Radebaugh, J., Rodriguez, S., Schoenfeld, A., Soderblom, J. M., Solomonidou, A., Stofan, E. R., Stiles, B. W., Tosi, F., Turtle, E. P., West, R. D., Wood, C. A., Zebker, H. A., Barnes, J. W., Casarano, D., Encrenaz, P., Farr, T., Grima, C., Hemingway, D., Karatekin, O., Lucas, A., Mitchell, K. L., Ori, G., Orosei, R., Ries, P., Riccio, D., Soderblom, L. A., and Zhang, Z. (2019). "Titan as Revealed by the Cassini Radar". *Space Sci Rev*. doi: 10.1007/s11214-019-0598-6.

Lorenz, R. D., Wall, S., Radebaugh, J., Boubin, G., Reffet, E., Janssen, M., Stofan, E., Lopes, R., Kirk, R., Elachi, C., Lunine, J., Mitchell, K., Paganelli, F., Soderblom, L., Wood, C., Wye, L., Zebker, H., Anderson, Y., Ostro, S., Allison, M., Boehmer, R., Callahan, P., Encrenaz, P., Ori, G. G., Francescetti, G., Gim, Y., Hamilton, G., Hensley, S., Johnson, W., Kelleher, K., Muhleman, D., Picardi, G., Posa, F., Roth, L., Seu, R., Shaffer, S., Stiles, B., Vetrella, S., Flamini, E., and West, R. (2006). "The Sand Seas of Titan: Cassini RADAR Observations of Longitudinal Dunes". *Science* 312.5774, pp. 724–727. doi: 10.1126/science.1123257.

Lorenz, R. D., Turtle, E. P., Barnes, J. W., Trainer, M. G., Adams, D. S., Hibbard, K., Sheldon, C. Z., Zacny, K., Peplowski, P. N., Lawrence, D. J., Ravine, M. A., McGee, T. G., Sotzen, K. S., MacKenzie, S. M., Langelaan, J., Schmitz, S., Wolfarth, L. S., and Bedini, P. D. (2018). "Dragonfly: A rotorcraft lander concept for scientific exploration at Titan". *Johns Hopkins APL Technical Digest (Applied Physics Laboratory)* 34, pp. 374–387.

Lorenz, R. D. and Lunine, J. I. (1997). "Titan's surface reviewed: the nature of bright and dark terrain". *Planetary and Space Science* 45.8, pp. 981–992. doi: 10.1016/S0032-0633(97)00087-1.

Lorenz, R. D., Brown, M. E., and Flasar, F. M. (2010). "Seasonal Change on Titan". In: *Titan from Cassini-Huygens*. Ed. by R. H. Brown, J.-P. Lebreton, and J. H. Waite. Dordrecht: Springer Netherlands, pp. 353–372. doi: 10.1007/978-1-4020-9215-2_14.

MacKenzie, S. M., Barnes, J. W., Sotin, C., Soderblom, J. M., Mouélic], S. L., Rodriguez, S., Baines, K. H., Buratti, B. J., Clark, R. N., Nicholson, P. D., and McCord, T. B. (2014). "Evidence of Titan's climate history from evaporite distribution". *Icarus* 243, pp. 191–207. doi: 10.1016/j.icarus.2014.08.022.

MacKintosh, F. C. and John, S. (1988). "Coherent backscattering of light in the presence of time-reversal-noninvariant and parity-nonconserving media". *Phys. Rev. B* 37 (4), pp. 1884–1897. doi: 10.1103/PhysRevB.37.1884.

Malaska, M., Radebaugh, J., Lorenz, R., Mitchell, K., Farr, T., and Stofan, E. (2010). "Identification of Karst-like Terrain on Titan from Valley Analysis". In:

Marquardt, D. (1963). "An algorithm for least-squares estimation of nonlinear parameters". *SIAM J. Appl. Math* 11, pp. 431–444. doi: 10.1137/0111030.

Martens, H. R., Ingersoll, A. P., Ewald, S. P., Helfenstein, P., and Giese, B. (2015). "Spatial distribution of ice blocks on Enceladus and implications for their origin and emplacement". *icarus* 245, pp. 162–176. doi: 10.1016/j.icarus.2014.09.035.

Martin, E. S., Kattenhorn, S. A., Collins, G. C., Michaud, R. L., Pappalardo, R. T., and Wyrick, D. Y. (2017). "Pit chains on Enceladus signal the recent tectonic dissection of the ancient cratered terrains". *Icarus* 294, pp. 209–217. doi: 10.1016/j.icarus.2017.03.014.

Mastrogiuseppe, M., Hayes, A., Poggiali, V., Seu, R., Lunine, J. I., and Hofgartner, J. D. (2016). "Radar Sounding Using the Cassini Altimeter: Waveform Modeling and Monte Carlo Approach for Data Inversion of Observations of Titan's Seas". *IEEE Transactions on Geoscience and Remote Sensing* 54.10, pp. 5646–5656. doi: 10.1109/TGRS.2016.2563426.

Mastrogiuseppe, M., Hayes, A. G., Poggiali, V., Lunine, J. I., Lorenz, R. D., Seu, R., Le Gall, A., Notarnicola, C., Mitchell, K. L., Malaska, M., and Birch, S. P. D. (2018). "Bathymetry and composition of Titan's Ontario Lacus derived from Monte Carlo-based waveform inversion of Cassini RADAR altimetry data". *Icarus* 300, pp. 203–209. doi: 10.1016/j.icarus.2017.09.009.

Mastrogiuseppe, M., Poggiali, V., Hayes, A., Lorenz, R., Lunine, J., Picardi, G., Seu, R., Flamini, E., Mitri, G., Notarnicola, C., Paillou, P., and Zebker, H. (2014). "The bathymetry of a Titan sea". *Geophysical Research Letters* 41.5, pp. 1432–1437. doi: 10.1002/2013GL058618.

Matson, D. L., Castillo-Rogez, J. C., Schubert, G., Sotin, C., and McKinnon, W. B. (2009). "The Thermal Evolution and Internal Structure of Saturn's Mid-Sized Icy Satellites". In: *Saturn from Cassini-Huygens*. Ed. by M. K. Dougherty, L. W. Esposito, and S. M. Krimigis. Dordrecht: Springer Netherlands, pp. 577–612. doi: 10.1007/978-1-4020-9217-6_18.

Matthews, R. A. J. (1992). "The Darkening of Iapetus and the Origin of Hyperion". *Quarterly Journal of the Royal Astronomical Society* 33, p. 253.

McKay, C. P., Davila, A., Glein, C. R., Hand, K. P., and Stockton, A. (2018). "Enceladus Astrobiology, Habitability, and the Origin of Life". In: *Enceladus and the Icy Moons of Saturn*. Ed. by P. M. Schenk, R. N. Clark, C. J. A. Howett, A. J. Verbiscer, and J. H. Waite, p. 437. doi: 10.2458/azu_uapress_9780816537075-ch021.

Miller, C., Verbiscer, A. J., Chanover, N. J., Holtzman, J. A., and Helfenstein, P. (2011). "Comparing Phoebe's 2005 opposition surge in four visible light filters". *Icarus* 212.2, pp. 819–834. doi: 10.1016/j.icarus.2010.12.024.

Mishchenko, M. I. (1992). "Enhanced backscattering of polarized light from discrete random media: calculations in exactly the backscattering direction". *J. Opt. Soc. Am. A* 9.6, pp. 978–982. doi: 10.1364/JOSAA.9.000978.

Mishchenko, M. I., Dlugach, J. M., Yanovitskij, E. G., and Zakharova, N. T. (1999). "Bidirectional reflectance of flat, optically thick particulate layers: an efficient radiative transfer solution and applications to snow and soil surfaces". *Journal of Quantitative Spectroscopy and Radiative Transfer* 63.2, pp. 409–432. doi: 10.1016/S0022-4073(99)00028-X.

Mishchenko, M. I. and Dlugach, J. M. (2017). "Electromagnetic scattering by spheroidal volumes of discrete random medium". *Journal of Quantitative Spectroscopy and Radiative Transfer* 200, pp. 244–248. doi: 10.1016/j.jqsrt.2017.06.021.

Mitchell, D. L. and de Pater, I. (1994). "Microwave Imaging of Mercury's Thermal Emission at Wavelengths from 0.3 to 20.5 cm". *Icarus* 110.1, pp. 2–32. doi: 10.1006/icar.1994.1105.

Mitchell, K. L., West, R. D., Stiles, B. W., Pappalardo, R. T., Anderson, Y., Lopes, R. M. C., Wall, S. D., Janssen, M. A., and the Cassini RADAR Team (2012). "The First High-Resolution SAR Observation of Enceladus by Cassini Radar". In: *Lunar and Planetary Science Conference*. Lunar and Planetary Science Conference, p. 2760.

Moeckel, C., Janssen, M. A., and Pater], I. [de (2019). "A re-analysis of the Jovian radio emission as seen by Cassini-RADAR and evidence for time variability". *Icarus* 321, pp. 994–1012. doi: 10.1016/j.icarus.2018.12.013.

Monfardini, A., Adam, R., Adane, A., Ade, P., André, P., Beelen, A., Belier, B., Benoit, A., Bideaud, A., Billot, N., Bourrion, O., Calvo, M., Catalano, A., Coiffard, G., Comis, B., D'Addabbo, A., Désert, F.-X., Doyle, S., Goupy, J., Kramer, C., Leclercq, S., Macias-Perez, J., Martino, J., Mauskopf, P., Mayet, F., Pajot, F., Pascale, E., Ponthieu, N., Revéret, V., Rodriguez, L., Savini, G., Schuster, K., Sievers, A., Tucker, C., and Zylka, R. (2014). "Latest NIKA Results and the NIKA-2 Project". *J Low Temp Phys* 176, pp. 787–795. doi: doi.org/10.1007/s10909-013-0985-4.

Moore, J. M. (1984). "The tectonic and volcanic history of Dione". *Icarus* 59.2, pp. 205–220. doi: 10.1016/0019-1035(84)90024-1.

Moore, J. M. and Ahern, J. L. (1983). "The geology of Tethys". *Journal of Geophysical Research: Solid Earth* 88.S02, A577–A584. doi: 10.1029/JB088iS02p0A577.

Moore, J. M., Horner, V. M., and Greeley, R. (1985). "The geomorphology of Rhea: Implications for geologic history and surface processes". *Journal of Geophysical Research: Solid Earth* 90.S02, pp. C785–C795. doi: 10.1029/JB090iS02p0C785.

Moreno, R. (2010). *Neptune and Uranus planetary brightness temperature tabulation*. Tech. rep. ESA Herschel Science Center. url: ftp://ftp.sciops.esa.int/pub/hsc-calibration/PlanetaryModels/ESA2.

Moroz, A. (2005). "Improvement of Mishchenko's T-matrix code for absorbing particles". *Appl. Opt.* 44.17, pp. 3604–3609. doi: 10.1364/AO.44.003604.

Morrison, D. (1969). "Thermal models and microwave temperatures of the planet Mercury".

Morrison, D., Sagan, C., and Pollack, J. B. (1969). "Martian temperatures and thermal properties". *Icarus* 11.1, pp. 36–45. doi: 10.1016/0019-1035(69)90113-4.

Morrison, D., Owen, T., and Soderblom, L. A. (1986). "The satellites of Saturn". In: *IAU Colloq. 77: Some Background about Satellites*. Ed. by J. A. Burns and M. S. Matthews, pp. 764–801.

Mosqueira, I. and Estrada, P. R. (2003a). "Formation of the regular satellites of giant planets in an extended gaseous nebula I: subnebula model and accretion of satellites". *Icarus* 163.1, pp. 198–231. doi: 10.1016/S0019-1035(03)00076-9.

Mosqueira, I. and Estrada, P. R. (2003b). "Formation of the regular satellites of giant planets in an extended gaseous nebula II: Satellite migration and survival". *Icarus* 163.1, pp. 232–255. doi: 10.1016/S0019-1035(03)00077-0.

Mosqueira, I., Estrada, P. R., and Charnoz, S. (2010). "Deciphering the origin of the regular satellites of gaseous giants – Iapetus: The Rosetta ice-moon". *Icarus* 207.1, pp. 448–460. doi: 10.1016/j.icarus.2009.10.018.

Mätzler, C. (1996). "Microwave permittivity of dry snow". *IEEE Transactions on Geoscience and Remote Sensing* 34.2, pp. 573–581. doi: 10.1109/36.485133.

Mätzler, C., ed. (2006). *Thermal Microwave Radiation: Applications for Remote Sensing*. Electromagnetic Waves. Institution of Engineering and Technology. doi: 10.1049/PBEW052E.

Mätzler, C. and Wiesmann, A. (1999). "Extension of the Microwave Emission Model of Layered Snowpacks to Coarse-Grained Snow". *Remote Sensing of Environment* 70.3, pp. 317–325. doi: 10.1016/S0034-4257(99)00047-4.

Muhleman, D. O., Butler, B. J., Grossman, A. W., and Slade, M. A. (1991). "Radar Images of Mars". *Science* 253.5027, pp. 1508–1513. doi: 10.1126/science.253.5027.1508.

Muhleman, D. O. and Clancy, R. T. (1995). "Microwave spectroscopy of the Mars atmosphere". *Appl. Opt.* 34.27, pp. 6067–6080. doi: 10.1364/AO.34.006067.

Muhleman, D. O. and Berge, G. L. (1991). "Observations of Mars, Uranus, Neptune, Io, Europa, Ganymede, and Callisto at a wavelength of 2.66 mm". *Icarus* 92.2, pp. 263–272. doi: 10.1016/0019-1035(91)90050-4.

Muhleman, D. O., Grossman, A. W., and Butler, B. J. (1995). "Radar Investigation of Mars, Mercury, and Titan". *Annual Review of Earth and Planetary Sciences* 23.1, pp. 337–374. doi: 10.1146/annurev.ea.23.050195.002005.

Neish, C. D., Blewett, D. T., Bussey, D. B. J., Lawrence, S. J., Mechtley, M., and Thomson, B. J. (2011). "The surficial nature of lunar swirls as revealed by the Mini-RF instrument". *Icarus* 215.1, pp. 186–196. doi: 10.1016/j.icarus.2011.06.037.

Neish, C. D. and Carter, L. M. (2014). "Chapter 53 - Planetary Radar". In: *Encyclopedia of the Solar System (Third Edition)*. Ed. by T. Spohn, D. Breuer, and T. V. Johnson. Third Edition. Boston: Elsevier, pp. 1133 –1159. doi: 10.1016/B978-0-12-415845-0.00053-0.

Nelson, S., Lindroth, D., and Blake, R. (1989). "Dielectric Properties of Selected and Purified Minerals At 1 to 22 GHz". *Journal of Microwave Power and Electromagnetic Energy* 24.4, pp. 213–220. doi: 10.1080/08327823.1989.11688096.

Newman, S. F., Buratti, B., Brown, R., Jaumann, R., Bauer, J., and Momary, T. (2009). "Water ice crystallinity and grain sizes on Dione". *Icarus* 203.2, pp. 553–559. doi: 10.1016/j.icarus.2009.04.034.

Nicholson, P. D., French, R. G., Campbell, D. B., Margot, J.-L., Nolan, M. C., Black, G. J., and Salo, H. J. (2005). "Radar imaging of Saturn's rings". *Icarus* 177.1, pp. 32–62. doi: 10.1016/j.icarus.2005.03.023.

Nimmo, F., Barr, A. C., Běhounková, M., and McKinnon, W. B. (2018). "The Thermal and Orbital Evolution of Enceladus: Observational Constraints and Models". In: *Enceladus and the Icy Moons of Saturn*. Ed. by P. M. Schenk, R. N. Clark, C. J. A. Howett, A. J. Verbiscer, and J. H. Waite, p. 79. doi: 10.2458/azu_uapress_9780816537075-ch005.

Nordheim, T. A., Hand, K. P., Paranicas, C., Howett, C. J. A., Hendrix, A. R., Jones, G. H., and Coates, A. J. (2017). "The near-surface electron radiation environment of Saturn's moon Mimas". *Icarus* 286, pp. 56–68. doi: 10.1016/j.icarus.2017.01.002.

Nozette, S., Spudis, P., Bussey, B., Jensen, R., Raney, K., Winters, H., Lichtenberg, C. L., Marinelli, W., Crusan, J., Gates, M., and Robinson, M. (2010). "The Lunar Reconnaissance Orbiter Miniature Radio Frequency (Mini-RF) Technology Demonstration". *Space Sci Revs* 150, pp. 285–302. doi: 10.1007/s11214-009-9607-5.

Nyquist, H. (1928). "Thermal Agitation of Electric Charge in Conductors". *Phys. Rev.* 32 (1), pp. 110–113. doi: 10.1103/PhysRev.32.110.

Olhoeft, G. and Strangway, D. W. (1975). "Dielectric properties of the first 100 meters of the Moon". *Earth and Planetary Science Letters* 24, pp. 394–404. doi: 10.1016/0012-821X(75)90146-6.

Ono, T., Kumamoto, A., Yamaguchi, Y., Yamaji, A., Kobayashi, T., Kasahara, Y., and Oya, H. (2008). "Instrumentation and observation target of the Lunar Radar Sounder (LRS) experiment onboard the SELENE spacecraft". *Earth Planet Sp* 60, pp. 321–332. doi: 10.1186/BF03352797.

Ortiz, J. L., Santos-Sanz, P., Sicardy, B., Benedetti-Rossi, G., Bérard, D., Morales, N., Duffard, R., Braga-Ribas, F., Hopp, U., Ries, C., Nascimbeni, V., Marzari, F., Granata, V., Pál, A., Kiss, C., Pribulla, T., Komžík, R., Hornoch, K., Pravec, P., Bacci, P., Maestripieri, M., Nerli, L., Mazzei, L., Bachini, M., Martinelli, F., Succi, G., Ciabattari, F., Mikuz, H., Carbognani, A., Gaehrken, B., Mottola, S., Hellmich, S., Rommel, F. L., Fernández-Valenzuela, E., Bagatin, A. C., Cikota, S., Cikota, A., Lecacheux, J., Vieira-Martins, R., Camargo, J. I. B., Assafin, M., Colas, F., Behrend, R., Desmars, J., Meza, E., Alvarez-Candal, A., Beisker, W., Gomes-Junior, A. R., Morgado, B. E., Roques, F., Vachier, F., Berthier, J., Mueller, T. G., Madiedo, J. M., Unsalan, O., Sonbas, E., Karaman, N., Erece, O., Koseoglu, D. T., Ozisik, T., Kalkan, S., Guney, Y., Niaei, M. S., Satir, O., Yesilyaprak, C., Puskullu, C., Kabas, A., Demircan, O., Alikakos, J., Charmandaris, V., Leto, G., Ohlert, J., Christille, J. M., Szakáts, R., Farkas, A. T., Varga-Verebélyi, E., Marton, G., Marciniak, A., Bartczak, P., Santana-Ros, T., Butkiewicz-Bąk, M., Dudziński, G., Alí-Lagoa, V., Gazeas, K., Tzouganatos, L., Paschalis, N., Tsamis, V., Sánchez-Lavega, A., Pérez-Hoyos, S., Hueso, R., Guirado, J. C., Peris, V., and Iglesias-Marzoa, R. (2017). "The size, shape, density and ring of the dwarf planet Haumea from a stellar occultation". *Nature* 550, pp. 219–223. doi: 10.1038/nature24051.

Ostro, S. J. (1985). "Radar observations of asteroids and comets". *Publications of the Astronomical Society of the Pacific* 97, p. 877. doi: 10.1086/131619.

Ostro, S. J., Campbell, D. B., Simpson, R. A., Hudson, R. S., Chandler, J. F., Rosema, K. D., Shapiro, I. I., Standish, E. M., Winkler, R., Yeomans, D. K., Velez, R., and Goldstein, R. M. (1992). "Europa, Ganymede, and Callisto: New radar results from Arecibo and Goldstone". *Journal of Geophysical Research: Planets* 97.E11, pp. 18227–18244. doi: 10.1029/92JE01992.

Ostro, S. J., West, R. D., Wye, L. C., Zebker, H. A., Janssen, M. A., Stiles, B., Kelleher, K., Anderson, Y. Z., Boehmer, R. A., Callahan, P., Gim, Y., Hamilton, G. A., Johnson, W. T. K., Veeramachaneni, C., and Lorenz, R. D. (2010). "New Cassini {RADAR} results for Saturn's icy satellites ". *Icarus* 206.2. Cassini at Saturn, pp. 498–506. doi: 10.1016/j.icarus.2009.07.041.

Ostro, S. J. and Pettengill, G. H. (1978). "Icy craters on the Galilean satellites?" *Icarus* 34.2, pp. 268–279. doi: 10.1016/0019-1035(78)90167-7.

Ostro, S. J., Pettengill, G. H., and Campbell, D. B. (1980). "Radar observations of Saturn's rings at intermediate tilt angles". *Icarus* 41.3, pp. 381–388. doi: 10.1016/0019-1035(80)90222-5.

Ostro, S. J., West, R. D., Janssen, M. A., Lorenz, R. D., Zebker, H. A., Black, G. J., Lunine, J. I., Wye, L. C., Lopes, R. M., Wall, S. D., Elachi, C., Roth, L., Hensley, S., Kelleher, K., Hamilton, G. A., Gim, Y., Anderson, Y. Z., Boehmer, R. A., and Johnson, W. T. K. (2006). "Cassini {RADAR} observations of Enceladus, Tethys, Dione, Rhea, Iapetus, Hyperion, and Phoebe". *Icarus* 183.2, pp. 479–490. doi: 10.1016/j.icarus.2006.02.019.

Paillou, P., Lunine, J., Ruffié, G., Encrenaz, P., Wall, S., Lorenz, R., and Janssen, M. (2008). "Microwave dielectric constant of Titan-relevant materials". *Geophysical Research Letters* 35.18. doi: 10.1029/2008GL035216.

Palmer, E. E. and Brown, R. H. (2008). "The stability and transport of carbon dioxide on Iapetus". *Icarus* 195.1, pp. 434–446. doi: 10.1016/j.icarus.2007.11.020.

Paranicas, C., Roussos, E., Decker, R. B., Johnson, R. E., Hendrix, A. R., Schenk, P., Cassidy, T. A., Dalton, J. B., Howett, C. J. A., Kollmann, P., Patterson, W., Hand, K. P., Nordheim, T. A., Krupp, N., and Mitchell, D. G. (2014). "The lens feature on the inner saturnian satellites". *Icarus* 234, pp. 155–161. doi: 10.1016/j.icarus.2014.02.026.

Patterson, G. W., Kattenhorn, S. A., Helfenstein, P., Collins, G. C., and Pappalardo, R. T. (2018). "The Geology of Enceladus". In: *Enceladus and the Icy Moons of Saturn*. Ed. by P. M. Schenk, R. N. Clark, C. J. A. Howett, A. J. Verbiscer, and J. H. Waite, p. 95. doi: 10.2458/azu_uapress_9780816537075-ch006.

Patthoff, D. A. and Kattenhorn, S. A. (2011). "A fracture history on Enceladus provides evidence for a global ocean". *Geophysical Research Letters* 38.18. doi: 10.1029/2011GL048387.

Peake, W. (1959). "Interaction of electromagnetic waves with some natural surfaces". *IRE Transactions on Antennas and Propagation* 7.5, pp. 324–329. doi: 10.1109/TAP.1959.1144736.

Penzias, A. A. and Wilson, R. W. (1965). "A Measurement of Excess Antenna Temperature at 4080 Mc/s." *Astrophysical Journal* 142, pp. 419–421. doi: 10.1086/148307.

Perley, R. A., Chandler, C. J., Butler, B. J., and Wrobel, J. M. (2011). "The expanded Very Large Array: a new telescope for new science". *The Astrophysical Journal* 739.1. doi: 10.1088/2041-8205/739/1/l1.

Perotto, L., Ponthieu, N., Macías-Pérez, J. F., Adam, R., Ade, P., André, P., Andrianasolo, A., Aussel, H., Beelen, A., Benoît, A., Berta, S., Bideaud, A., Bourrion, O., Calvo, M., Catalano, A., Comis, B., De Petris, M., Désert, F.-X., Doyle, S., Driessen, E. F. C., García, P., Gomez, A., Goupy, J., John, D., Kéruzoré, F., Kramer, C., Ladjelate, B., Lagache, G., Leclercq, S., Lestrade, J.-F., Maury, A., Mauskopf, P., Mayet, F., Monfardini, A., Navarro, S., Peñalver, J., Pierfederici, F., Pisano, G., Revéret, V., Ritacco, A., Romero, C., Roussel, H., Ruppin, F., Schuster, K., Shu, S., Sievers, A., Tucker, C., and Zylka, R. (2020). "Calibration and performance of the NIKA2 camera at the IRAM 30-m Telescope". *A&A* 637, A71. doi: 10.1051/0004-6361/201936220.

Peters, K. J. (1992). "Coherent-backscatter effect: A vector formulation accounting for polarization and absorption effects and small or large scatterers". *Phys. Rev. B* 46 (2), pp. 801–812. doi: 10.1103/PhysRevB.46.801.

Pettengill, G. H., Ford, P. G., and Wilt, R. J. (1992). "Venus surface radiothermal emission as observed by Magellan". *Journal of Geophysical Research: Planets* 97.E8, pp. 13091–13102. doi: 10.1029/92JE01356.

Phillips, R. J., Zuber, M. T., Smrekar, S. E., Mellon, M. T., Head, J. W., Tanaka, K. L., Putzig, N. E., Milkovich, S. M., Campbell, B. A., Plaut, J. J., Safaeinili, A., Seu, R., Biccari, D., Carter, L. M., Picardi, G., Orosei, R., Mohit, P. S., Heggy, E., Zurek, R. W., Egan, A. F., Giacomoni, E., Russo, F., Cutigni, M., Pettinelli, E., Holt, J. W., Leuschen, C. J., and Marinangeli, L. (2008). "Mars North Polar Deposits: Stratigraphy, Age, and Geodynamical Response". *Science* 320.5880, pp. 1182–1185. doi: 10.1126/science.1157546.

Picard, G., Brucker, L., Roy, A., Dupont, F., Fily, M., Royer, A., and Harlow, C. (2013). "Simulation of the microwave emission of multi-layered snowpacks using the Dense Media Radiative transfer theory: the DMRT-ML model". *Geoscientific Model Development* 6.4, pp. 1061–1078. doi: 10.5194/gmd-6-1061-2013.

Picard, G., Sandells, M., and Löwe, H. (2018). "SMRT: an active–passive microwave radiative transfer model for snow with multiple microstructure and scattering formulations (v1.0)". *Geoscientific Model Development* 11.7, pp. 2763–2788. doi: 10.5194/gmd-11-2763-2018.

Pickering, W. H. (1905). "Phoebe, the ninth satellite of Saturn". *Annals of Harvard College Observatory* 53, pp. 85–100.

Piddington, J. H. and Minnett, H. C. (1949). "Microwave Thermal Radiation from the Moon". *Australian Journal of Chemistry* 2, pp. 63–77. doi: 10.1071/CH9490063.

Pinilla-Alonso, N., Roush, T. L., Marzo, G. A., Cruikshank, D. P., and Dalle Ore, C. M. (2011). "Iapetus surface variability revealed from statistical clustering of a VIMS mosaic: The distribution of CO_2". *Icarus* 215.1, pp. 75–82. doi: 10.1016/j.icarus.2011.07.004.

Pitman, K. M., Buratti, B. J., and Mosher, J. A. (2010). "Disk-integrated bolometric Bond albedos and rotational light curves of saturnian satellites from Cassini Visual and Infrared Mapping Spectrometer". *Icarus* 206.2. Cassini at Saturn, pp. 537–560. doi: 10.1016/j.icarus.2009.12.001.

Pitman, K. M., Kolokolova, L., Verbiscer, A. J., Mackowski, D. W., and Joseph, E. C. S. (2017). "Coherent backscattering effect in spectra of icy satellites and its modeling using multi-sphere T-matrix (MSTM) code for layers of particles". *Planetary and Space Science* 149. Special Issue: Cosmic Dust IX, pp. 23–31. doi: 10.1016/j.pss.2017.08.005.

Pollack, J. B. and Sagan, C. (1965). "The microwave phase effect of Venus". *Icarus* 4.1, pp. 62–103. doi: 10.1016/0019-1035(65)90018-7.

Pollack, J. B. and Sagan, C. (1967). "An Analysis of the Mariner 2 Microwave Observations of Venus". *Astrophys Journal* 150, p. 327. doi: 10.1086/149334.

Pollack, J. B. and Morrison, D. (1970). "Venus: Determination of atmospheric parameters from the microwave spectrum". *Icarus* 12.3, pp. 376–390. doi: 10.1016/0019-1035(70)90006-0.

Pollack, J. B., Burns, J. A., and Tauber, M. E. (1979). "Gas drag in primordial circumplanetary envelopes: A mechanism for satellite capture". *Icarus* 37.3, pp. 587–611. doi: 10.1016/0019-1035(79)90016-2.

Pommerol, A., Kofman, W., Audouard, J., Grima, C., Beck, P., Mouginot, J., Herique, A., Kumamoto, A., Kobayashi, T., and Ono, T. (2010). "Detectability of subsurface interfaces in lunar maria by the LRS/SELENE sounding radar: Influence of mineralogical composition". *Geophysical Research Letters* 37.3. doi: 10.1029/2009GL041681.

Porco, C. C., Baker, E., Barbara, J., Beurle, K., Brahic, A., Burns, J. A., Charnoz, S., Cooper, N., Dawson, D. D., Del Genio, A. D., Denk, T., Dones, L., Dyudina, U., Evans, M. W., Giese, B., Grazier, K., Helfenstein, P., Ingersoll, A. P., Jacobson, R. A., Johnson, T. V., McEwen, A., Murray, C. D., Neukum, G., Owen, W. M., Perry, J., Roatsch, T., Spitale, J., Squyres, S., Thomas, P. C., Tiscareno, M., Turtle, E., Vasavada, A. R., Veverka, J., Wagner, R., and West, R. (2005). "Cassini Imaging Science: Initial results on Phoebe and Iapetus". *Science* 307.5713, pp. 1237–1242. doi: 10.1126/science.1107981.

Porco, C. C., Helfenstein, P., Thomas, P. C., Ingersoll, A. P., Wisdom, J., West, R., Neukum, G., Denk, T., Wagner, R., Roatsch, T., Kieffer, S., Turtle, E., McEwen, A., Johnson, T. V., Rathbun, J., Veverka, J., Wilson, D., Perry, J., Spitale, J., Brahic, A., Burns, J. A., DelGenio, A. D., Dones, L., Murray, C. D., and Squyres, S. (2006). "Cassini Observes the Active South pole of Enceladus". *Science* 311.5766, pp. 1393–1401. doi: 10.1126/science.1123013.

Porco, C., DiNino, D., and Nimmo, F. (2014). "How the geysers, tidal stresses, and thermal emission across the South Polar Terrain of Enceladus are related". *The Astronomical Journal* 148.3, p. 45. doi: 10.1088/0004-6256/148/3/45.

Porco, C. C., West, R. A., Squyres, S., Mcewen, A., Thomas, P., Murray, C. D., Delgenio, A., Ingersoll, A. P., Johnson, T. V., Neukum, G., Veverka, J., Dones, L., Brahic, A., Burns, J. A., Haemmerle, V., Knowles, B., Dawson, D., Roatsch, T., Beurle, K., and Owen, W. (2004). "Cassini Imaging Science: Instrument Characteristics And Anticipated Scientific Investigations At Saturn". *Space Sci Rev* 115, pp. 363–497. doi: 10.1007/s11214-004-1456-7.

Postberg, F., Schmidt, J., Hillier, J., Kempf, S., and Srama, R. (2011). "A salt-water reservoir as the source of a compositionally stratified plume on Enceladus". *Nature* 474.7353, pp. 620–622.

Postberg, F., Clark, R. N., Hansen, C. J., Coates, A. J., Dalle Ore, C. M., Scipioni, F., Hedman, M. M., and Waite, J. H. (2018). "Plume and Surface Composition of Enceladus". In: *Enceladus and the Icy Moons of Saturn*. Ed. by P. M. Schenk, R. N. Clark, C. J. A. Howett, A. J. Verbiscer, and J. H. Waite, p. 129. doi: 10.2458/azu_uapress_9780816537075-ch007.

Proksch, M., Mätzler, C., Wiesmann, A., Lemmetyinen, J., Schwank, M., Löwe, H., and Schneebeli, M. (2015). "MEMLS3&a: Microwave Emission Model of Layered Snowpacks adapted to include backscattering". *Geoscientific Model Development* 8.8, pp. 2611–2626. doi: 10.5194/gmd-8-2611-2015.

Pulliainen, J. T., Grandell, J., and Hallikainen, M. T. (1999). "HUT snow emission model and its applicability to snow water equivalent retrieval". *IEEE Transactions on Geoscience and Remote Sensing* 37.3, pp. 1378–1390. doi: 10.1109/36.763302.

Radebaugh, J., Lorenz, R. D., Kirk, R. L., Lunine, J. I., Stofan, E. R., Lopes, R. M. C., and Wall, S. D. (2007). "Mountains on Titan observed by Cassini Radar". *Icarus* 192.1, pp. 77–91. doi: 10.1016/j.icarus.2007.06.020.

Rathbun, J. A. and Spencer, J. R. (2020). "Proposed plume source regions on Europa: No evidence for endogenic thermal emission". *Icarus* 338, p. 113500. doi: 10.1016/j.icarus.2019.113500.

Redman, R. O., Feldman, P. A., Matthews, H. E., Halliday, I., and Creutzberg, F. (1992). "Millimeter and Submillimeter Observations of the Asteroid 4 Vesta". *The Astronomical Journal* 104, p. 405. doi: 10.1086/116248.

Redman, R. O., Feldman, P. A., and Matthews, H. E. (1998). "High-Quality Photometry of Asteroids at Millimeter and Submillimeter Wavelengths". *The Astronomical Journal* 116.3, pp. 1478–1490. doi: 10.1086/300495.

Rhoden, A. R., Henning, W., Hurford, T. A., Patthoff, D. A., and Tajeddine, R. (2017). "The implications of tides on the Mimas ocean hypothesis". *Journal of Geophysical Research: Planets* 122.2, pp. 400–410. doi: 10.1002/2016JE005097.

Ries, P. A. (2012). "High Frequency Observation of Iapetus on the Green Bank Telescope Aided by Improvements in Understanding the Telescope Response to Wind". PhD thesis. University of Virginia, USA. doi: 10.18130/V3TV9S.

Ries, P. A. and Janssen, M. (2015). "A large-scale anomaly in Enceladus' microwave emission". *Icarus* 257, pp. 88–102. doi: 10.1016/j.icarus.2015.04.030.

Rignot, E. J., Ostro, S. J., Zyl, J. J. van, and Jezek, K. C. (1993). "Unusual Radar Echoes from the Greenland Ice Sheet". *Science* 261.5129, pp. 1710–1713. doi: 10.1126/science.261.5129.1710.

Rignot, E. (1995). "Backscatter model for the unusual radar properties of the Greenland Ice Sheet". *Journal of Geophysical Research: Planets* 100.E5, pp. 9389–9400. doi: 10.1029/95JE00485.

Rivera-Valentin, E. G., Blackburn, D. G., and Ulrich, R. (2011). "Revisiting the thermal inertia of Iapetus: Clues to the thickness of the dark material". *Icarus* 216.1, pp. 347–358. doi: 10.1016/j.icarus.2011.09.006.

Roatsch, T., Jaumann, R., Stephan, K., and Thomas, P. C. (2009). "Cartographic Mapping of the Icy Satellites Using ISS and VIMS data". In: *Saturn from Cassini-Huygens*. Ed. by M. K. Dougherty, L. W. Esposito, and S. M. Krimigis. Dordrecht: Springer Netherlands, pp. 763–781. doi: 10.1007/978-1-4020-9217-6_24.

Robuchon, G., Choblet, G., Tobie, G., Čadek, O., Sotin, C., and Grasset, O. (2010). "Coupling of thermal evolution and despinning of early Iapetus". *Icarus* 207.2, pp. 959–971. doi: 10.1016/j.icarus.2009.12.002.

Rodriguez, S., Mouélic, S. L., Barnes, J. W., Kok, J. F., Rafkin, S. C. R., Lorenz, R. D., Charnay, B., Radebaugh, J., Narteau, C., Cornet, T., Bourgeois, O., Lucas, A., Rannou, P., Griffith, C. A., Coustenis, A., Appéré, T., Hirtzig, M., Sotin, C., Soderblom, J. M., Brown, R. H., Bow, J., Vixie, G., Maltagliati, L., Courrech du Pont, S., Jaumann, R., Stephan, K., Baines, K. H., Buratti, B. J., Clark, R. N., and Nicholson, P. D. (2018). "Observational evidence for active dust storms on Titan at equinox". *Nature Geosci* 11, pp. 727–732. doi: 10.1038/s41561-018-0233-2.

Royer, E. M. and Hendrix, A. R. (2014). "First far-ultraviolet disk-integrated phase curve analysis of Mimas, Tethys and Dione from the Cassini-UVIS data sets". *Icarus* 242, pp. 158–171. doi: 10.1016/j.icarus.2014.07.026.

Ruppin, F., Mayet, F., Pratt, G., Adam, R., Ade, P., André, P., Arnaud, M., Aussel, H., Bartalucci, I., Beelen, A., Benoît, A., Bideaud, A., Bourrion, O., Calvo, M., Catalano, A., Comis, B., De Petris, M., Désert, F.-X., Doyle, S., Driessen, E. F. C., Goupy, J., Kramer, C., Lagache, G., Leclercq, S., Lestrade, J.-F., Macías-Pérez, J. F., Mauskopf, P., Monfardini, A., Perotto, L., Pisano, G., Pointecouteau, E., Ponthieu, N., Revéret, V., Ritacco, A., Romero, C., Roussel, H., Schuster, K., Sievers, A., Tucker, C., and Zylka, R. (2018). "First Sunyaev-Zel´dovich mapping with the NIKA2 camera: Implication of cluster substructures for the pressure profile and mass estimate". *A&A* 615, A112. doi: 10.1051/0004-6361/201732558.

Saunders, R. S., Spear, A. J., Allin, P. C., Austin, R. S., Berman, A. L., Chandlee, R. C., Clark, J., Decharon, A. V., De Jong, E. M., Griffith, D. G., Gunn, J. M., Hensley, S., Johnson, W. T. K., Kirby, C. E., Leung, K. S., Lyons, D. T., Michaels, G. A., Miller, J., Morris, R. B., Morrison, A. D., Piereson, R. G., Scott, J. F., Shaffer, S. J., Slonski, J. P., Stofan, E. R., Thompson, T. W., and Wall, S. D. (1992). "Magellan mission summary". *Journal of Geophysical Research: Planets* 97.E8, pp. 13067–13090. doi: 10.1029/92JE01397.

Schaible, M. J., Johnson, R. E., Zhigilei, L. V., and Piqueux, S. (2017). "High energy electron sintering of icy regoliths: Formation of the PacMan thermal anomalies on the icy Saturnian moons". *Icarus* 285, pp. 211–223. doi: 10.1016/j.icarus.2016.08.033.

Schenk, P., White, O. L., Byrne, P. K., and Moore, J. M. (2018). "Saturn's Other Icy Moons: Geologically Complex Worlds in Their Own Right". In: *Enceladus and the Icy Moons of Saturn*. Ed. by P. M. Schenk, R. N. Clark, C. J. A. Howett, A. J. Verbiscer, and J. H. Waite, p. 237. doi: 10.2458/azu_uapress_9780816537075-ch012.

Schenk, P. M. and Moore, J. M. (2009). "Eruptive Volcanism on Saturn's Icy Moon Dione". In: *Lunar and Planetary Science Conference*. Lunar and Planetary Science Conference, p. 2465.

Schenk, P., Hamilton, D. P., Johnson, R. E., McKinnon, W. B., Paranicas, C., Schmidt, J., and Showalter, M. R. (2011). "Plasma, plumes and rings: Saturn system dynamics as recorded in global color patterns on its midsize icy satellites". *Icarus* 211.1, pp. 740–757. doi: 10.1016/j.icarus.2010.08.016.

Schloerb, F. P., Keihm, S., von Allmen, P., Choukroun, M., Lellouch, E., Leyrat, C., Beaudin, G., Biver, N., Bockelée-Morvan, D., Crovisier, J., Encrenaz, P., Gaskell, R., Gulkis, S., Hartogh, P., Hofstadter, M., Ip, W.-H., Janssen, M., Jarchow, C., Jorda, L., Keller, H. U., Lee, S., Rezac, L., and Sierks, H. (2015). "MIRO observations of subsurface temperatures of the nucleus of 67P/Churyumov-Gerasimenko". *A&A* 583, A29. doi: 10.1051/0004-6361/201526152.

Schroeder, D. M., Romero-Wolf, A., Carrer, L., Grima, C., Campbell, B. A., Kofman, W., Bruzzone, L., and Blankenship, D. D. (2016). "Assessing the potential for passive radio sounding of Europa and Ganymede with RIME and REASON". *Planetary and Space Science* 134, pp. 52–60. doi: 10.1016/j.pss.2016.10.007.

Scipioni, F., Tosi, F., Stephan, K., Filacchione, G., Ciarniello, M., Capaccioni, F., and Cerroni, P. (2013). "Spectroscopic classification of icy satellites of Saturn I: Identification of terrain units on Dione". *Icarus* 226.2, pp. 1331–1349. doi: 10.1016/j.icarus.2013.08.008.

Scipioni, F., Tosi, F., Stephan, K., Filacchione, G., Ciarniello, M., Capaccioni, F., and Cerroni, P. (2014). "Spectroscopic classification of icy satellites of Saturn II: Identification of terrain units on Rhea". *Icarus* 234, pp. 1–16. doi: 10.1016/j.icarus.2014.02.010.

Scipioni, F., Schenk, P., Tosi, F., D'Aversa, E., Clark, R., Combe, J.-P., and Dalle Ore, C. M. (2017). "Deciphering sub-micron ice particles on Enceladus surface". *Icarus* 290, pp. 183–200. doi: 10.1016/j.icarus.2017.02.012.

Seidelmann, P. K., Harrington, R. S., Pascu, D., Baum, W. A., Currie, D. G., Westphal, J. A., and Danielson, G. E. (1981). "Saturn satellite observations and orbits from the 1980 ring plane crossing". *Icarus* 47.2, pp. 282–287. doi: 10.1016/0019-1035(81)90172-X.

Sekine, Y. and Genda, H. (2012). "Giant impacts in the Saturnian system: A possible origin of diversity in the inner mid-sized satellites". *Planetary and Space Science* 63-64. Advances in Planetary Atmospheres and Exploration, pp. 133–138. doi: 10.1016/j.pss.2011.05.015.

Selvans, M. M., Plaut, J. J., Aharonson, O., and Safaeinili, A. (2010). "Internal structure of Planum Boreum, from Mars advanced radar for subsurface and ionospheric sounding data". *Journal of Geophysical Research: Planets* 115.E9. doi: 10.1029/2009JE003537.

Seu, R., Phillips, R. J., Biccari, D., Orosei, R., Masdea, A., Picardi, G., Safaeinili, A., Campbell, B. A., Plaut, J. J., Marinangeli, L., Smrekar, S. E., and Nunes, D. C. (2007). "SHARAD sounding radar on the Mars Reconnaissance Orbiter". *Journal of Geophysical Research: Planets* 112.E5. doi: 10.1029/2006JE002745.

Shah, K. P., Muhleman, D. O., and Berge, G. L. (1991). "Measurement of winds in Venus' upper mesosphere based on doppler shifts of the 2.6-mm 12CO line". *Icarus* 93.1, pp. 96–121. doi: 10.1016/0019-1035(91)90167-R.

Shapiro, I. I., Pettengill, G. H., Ash, M. E., Stone, M. L., Smith, W. B., Ingalls, R. P., and Brockelman, R. A. (1968). "Fourth Test of General Relativity: Preliminary Results". *Phys. Rev. Lett.* 20 (22), pp. 1265–1269. doi: 10.1103/PhysRevLett.20.1265.

Sihvola, A. (2000). "Mixing Rules with Complex Dielectric Coefficients". *Subsurface Sensing Technologies and Applications* 1, pp. 393–415. doi: 10.1023/A:1026511515005.

Simmons, G. (1974). "Final Technical Report on the Surface Electrical Properties Experiment". *Apollo Lunar Surface Experiment Package (ALSEP) Documents*.

Simon, S., Kriegel, H., Saur, J., Wennmacher, A., Neubauer, F. M., Roussos, E., Motschmann, U., and Dougherty, M. K. (2012). "Analysis of Cassini magnetic field observations over the poles of Rhea". *Journal of Geophysical Research: Space Physics* 117.A7. doi: 10.1029/2012JA017747.

Simonelli, D. P., Kay, J., Adinolfi, D., Veverka, J., Thomas, P. C., and Helfenstein, P. (1999). "Phoebe: Albedo Map and Photometric Properties". *Icarus* 138.2, pp. 249–258. doi: 10.1006/icar.1999.6077.

Smith, B. A., Soderblom, L., Beebe, R., Boyce, J., Briggs, G., Bunker, A., Collins, S. A., Hansen, C. J., Johnson, T. V., L., M. J., Terrile, R. J., Carr, M., Cook, A., Cuzzi, J., Pollack, J. B., Danielson, G. E., Ingersoll, A. P., Davies, M. E., Hunt, G. E., Masursky, H., Shoemaker, E., Morrison, D., Owen, T., Sagan, C., Veverka, J., Strom, R., and Suomi, V. E. (1981). "Encounter with Saturn: Voyager 1 Imaging Science Results". *Science* 212.4491, pp. 163–191. doi: 10.1126/science.212.4491.163.

Smith, B. A., Soderblom, L., Batson, R., Bridges, P., Inge, J., Masursky, H., Shoemaker, E., Beebe, R., Boyce, J., Briggs, G., Bunker, A., Collins, S. A., Hansen, C. J., Johnson, T. V., L., M. J., Terrile, R. J., Cook, A. F., Cuzzi, J., Pollack, J. B., Danielson, G. E., Ingersoll, A. P., Davies, M. E., Hunt, G. E., Morrison, D., Owen, T., Sagan, C., Veverka, J., Strom, R., and Suomi, V. E. (1982). "A New Look at the Saturn System: The Voyager 2 Images". *Science* 215.4532, pp. 504–537. doi: 10.1126/science.215.4532.504.

Soter, S. (1974). “Brightness asymmetry of Iapetus”. In: *IAU colloquium No. 28*. Ithaca, NY.

Southworth, B. S., Kempf, S., and Spitale, J. (2019). “Surface deposition of the Enceladus plume and the zenith angle of emissions”. *Icarus* 319, pp. 33–42. doi: 10.1016/j.icarus.2018.08.024.

Spencer, J. R., Pearl, J. C., Segura, M., and Cassini Cirs Team (2005). “Cassini CIRS Observations of Iapetus’ Thermal Emission”. In: *36th Annual Lunar and Planetary Science Conference*. Ed. by S. Mackwell and E. Stansbery. Lunar and Planetary Science Conference, p. 2305.

Spencer, J. R., Pearl, J. C., Segura, M., Flasar, F. M., Mamoutkine, A., Romani, P., Buratti, B. J., Hendrix, A. R., Spilker, L. J., and Lopes, R. M. C. (2006). “Cassini Encounters Enceladus: Background and the Discovery of a South Polar Hot Spot”. *Science* 311.5766, pp. 1401–1405. doi: 10.1126/science.1121661.

Spencer, J. R., Lebofsky, L. A., and Sykes, M. V. (1989). “Systematic biases in radiometric diameter determinations”. *Icarus* 78.2, pp. 337–354. doi: 10.1016/0019-1035(89)90182-6.

Spencer, J. R., Tamppari, L. K., Martin, T. Z., and Travis, L. D. (1999). “Temperatures on Europa from Galileo Photopolarimeter-Radiometer: Nighttime Thermal Anomalies”. *Science* 284, p. 1514. doi: 10.1126/science.284.5419.1514.

Spencer, J. R., Barr, A. C., Esposito, L. W., Helfenstein, P., Ingersoll, A. P., Jaumann, R., McKay, C. P., Nimmo, F., and Waite, J. H. (2009). “Enceladus: An Active Cryovolcanic Satellite”. In: *Saturn from Cassini-Huygens*. Ed. by M. K. Dougherty, L. W. Esposito, and S. M. Krimigis. Dordrecht: Springer Netherlands, pp. 683–724. doi: 10.1007/978-1-4020-9217-6_21.

Spencer, J. R. and Denk, T. (2010). “Formation of Iapetus’ Extreme Albedo Dichotomy by Exogenically Triggered Thermal Ice Migration”. *Science* 327.5964, pp. 432–435. doi: 10.1126/science.1177132.

Spencer, J. R. and Nimmo, F. (2013). “Enceladus: An Active Ice World in the Saturn System”. *Annual Review of Earth and Planetary Sciences* 41.1, pp. 693–717. doi: 10.1146/annurev-earth-050212-124025.

Spudis, P. D., Bussey, D. B. J., Baloga, S. M., Cahill, J. T. S., Glaze, L. S., Patterson, G. W., Raney, R. K., Thompson, T. W., Thomson, B. J., and Ustinov, E. A. (2013). “Evidence for water ice on the Moon: Results for anomalous polar craters from the LRO Mini-RF imaging radar”. *Journal of Geophysical Research: Planets* 118.10, pp. 2016–2029. doi: 10.1002/jgre.20156.

Spudis, P., Nozette, S., Bussey, B., Raney, K., Winters, H., Lichtenberg, C. L., Marinelli, W., Crusan, J. C., and Gates, M. M. (2009). “Mini-SAR: an imaging radar experiment for the Chandrayaan-1 mission to the Moon”. *Current Science* 96.4, pp. 533–539.

Squyres, S. W., Buratti, B., Veverka, J., and Sagan, C. (1984). “Voyager photometry of Iapetus”. *Icarus* 59.3, pp. 426–435. doi: 10.1016/0019-1035(84)90111-8.

Srama, R., Ahrens, T. J., Altobelli, N., Auer, S., Bradley, J. G., Burton, M., Dikarev, V. V., Economou, T., Fechtig, H., Görlich, M., Grand e, M., Graps, A., Grün, E., Havnes, O., Helfert, S., Horanyi, M., Igenbergs, E., Jessberger, E. K., Johnson, T. V., Kempf, S., Krivov, A. V., Krüger, H., Mocker-Ahlreep, A., Moragas-Klostermeyer, G., Lamy, P., Landgraf, M., Linkert, D., Linkert, G., Lura, F., McDonnell, J. A. M., Möhlmann, D., Morfill, G. E., Müller, M., Roy, M., Schäfer, G., Schlotzhauer, G., Schwehm, G. H., Spahn, F., Stübig, M., Svestka, J., Tschernjawski, V., Tuzzolino, A. J., Wäsch, R., and Zook, H. A. (2004). “The Cassini Cosmic Dust Analyzer”. *Space Sci Rev* 114.1-4, pp. 465–518. doi: 10.1007/s11214-004-1435-z.

Srama, R., Kempf, S., Moragas-Klostermeyer, G., Helfert, S., Ahrens, T. J., Altobelli, N., Auer, S., Beckmann, U., Bradley, J. G., Burton, M., Dikarev, V. V., Economou, T., Fechtig, H., Green, S. F., Grande, M., Havnes, O., Hillier, J. K., Horanyi, M., Igenbergs, E., Jessberger, E. K., Johnson, T. V., Krüger, H., Matt, G., McBride, N., Mocker, A., Lamy, P., Linkert, D., Linkert, G., Lura, F., McDonnell, J. A. M., Möhlmann, D., Morfill, G. E., Postberg, F., Roy, M., Schwehm, G. H., Spahn, F., Svestka, J., Tschernjawski, V., Tuzzolino, A. J., Wäsch, R., and Grün, E.

(2006). “In situ dust measurements in the inner Saturnian system”. *Planetary and Space Science* 54.9. Physics of Dusty Rings, pp. 967–987. doi: 10.1016/j.pss.2006.05.021.

Stephan, K., Jaumann, R., Wagner, R., Clark, R. N., Cruikshank, D. P., Hibbitts, C. A., Roatsch, T., Hoffmann, H., Brown, R. H., Filiacchione, G., Buratti, B. J., Hansen, G. B., McCord, T. B., Nicholson, P. D., and Baines, K. H. (2010). “Dione’s spectral and geological properties”. *Icarus* 206.2, pp. 631–652. doi: 10.1016/j.icarus.2009.07.036.

Stephan, K., Jaumann, R., Wagner, R., Clark, R. N., Cruikshank, D. P., Giese, B., Hibbitts, C. A., Roatsch, T., Matz, K.-D., Brown, R. H., Filacchione, G., Cappacioni, F., Scholten, F., Buratti, B. J., Hansen, G. B., Nicholson, P. D., Baines, K. H., Nelson, R. M., and Matson, D. L. (2012). “The Saturnian satellite Rhea as seen by Cassini VIMS”. *Planetary and Space Science* 61.1, pp. 142–160. doi: 10.1016/j.pss.2011.07.019.

Stiles, B. W., Hensley, S., Gim, Y., Bates, D. M., Kirk, R. L., Hayes, A. G., Radebaugh, J., Lorenz, R. D., Mitchell, K. L., Callahan, P. S., Zebker, H., Johnson, W. T. K., Wall, S. D., Lunine, J. I., Wood, C. A., Janssen, M. A., Pelletier, F., West, R. D., and Veeramacheneni, C. (2009). “Determining Titan surface topography from Cassini SAR data”. *Icarus* 202.2, pp. 584–598. doi: https://doi.org/10.1016/j.icarus.2009.03.032.

Stofan, E. R., Elachi, C., Lunine, J. I., Lorenz, R. D., Stiles, B., Mitchell, K. L., Ostro, S., Soderblom, L., Wood, C., Zebker, H., Wall, S., Janssen, M., Kirk, R., Lopes, R., Paganelli, F., Radebaugh, J., Wye, L., Anderson, Y., Allison, M., Boehmer, R., Callahan, P., Encrenaz, P., Flamini, E., Francescetti, G., Gim, Y., Hamilton, G., Hensley, S., Johnson, W. T. K., Kelleher, K., Muhleman, D., Paillou, P., Picardi, G., Posa, F., Roth, L., Seu, R., Shaffer, S., Vetrella, S., and West, R. (2007). “The lakes of Titan”. *Nature* 445, pp. 61–64. doi: 10.1038/nature05438.

Szalay, J. R., Poppe, A. R., Agarwal, J., Britt, D., Belskaya, I., Horányi, M., Nakamura, T., Sachse, M., and Spahn, F. (2018). “Dust Phenomena Relating to Airless Bodies”. *Space Sci Rev* 214.98. doi: 10.1007/s11214-018-0527-0.

Tajeddine, R., Rambaux, N., Lainey, V., Charnoz, S., Richard, A., Rivoldini, A., and Noyelles, B. (2014). “Constraints on Mimas’ interior from Cassini ISS libration measurements”. *Science* 346.6207, pp. 322–324. doi: 10.1126/science.1255299.

Tamayo, D., Burns, J. A., Hamilton, D. P., and Hedman, M. M. (2011). “Finding the trigger to Iapetus’ odd global albedo pattern: Dynamics of dust from Saturn’s irregular satellites”. *Icarus* 215.1, pp. 260–278. doi: 10.1016/j.icarus.2011.06.027.

Tamayo, D., Markham, S. R., Hedman, M. M., Burns, J. A., and Hamilton, D. P. (2016). “Radial profiles of the Phoebe ring: A vast debris disk around Saturn”. *Icarus* 275, pp. 117–131. doi: 10.1016/j.icarus.2016.04.009.

Teolis, B., Tokar, R., Cassidy, T., Khurana, K., and Nordheim, T. (2018). “Exospheres and Magnetospheric Currents at Saturn’s Icy Moons: Dione and Rhea”. In: *Enceladus and the Icy Moons of Saturn*. Ed. by P. M. Schenk, R. N. Clark, C. J. A. Howett, A. J. Verbiscer, and J. H. Waite, p. 361. doi: 10.2458/azu_uapress_9780816537075-ch018.

Teolis, B. D., Jones, G. H., Miles, P. F., Tokar, R. L., Magee, B. A., Waite, J. H., Roussos, E., Young, D. T., Crary, F. J., Coates, A. J., Johnson, R. E., Tseng, W.-L., and Baragiola, R. A. (2010). “Cassini Finds an Oxygen–Carbon Dioxide Atmosphere at Saturn’s Icy Moon Rhea”. *Science* 330.6012, pp. 1813–1815. doi: 10.1126/science.1198366.

Teolis, B. D. and Waite, J. H. (2016). “Dione and Rhea seasonal exospheres revealed by Cassini CAPS and INMS”. *Icarus* 272, pp. 277–289. doi: 10.1016/j.icarus.2016.02.031.

Thomas, B. (2004). “Etude et réalisation d’une tête de réception hétérodyne en ondes submillimétriques pour l’étude des atmosphères et surfaces de planètes”. PhD thesis. Observatoire de Paris; Université Pierre et Marie Curie - Paris VI, 2.

Thomas, P. C. (2010). “Sizes, shapes, and derived properties of the saturnian satellites after the Cassini nominal mission”. *Icarus* 208.1, pp. 395–401. doi: 10.1016/j.icarus.2010.01.025.

Thomas, P. C., Armstrong, J. W., Asmar, S. W., Burns, J. A., Denk, T., Giese, B., Helfenstein, P., Iess, L., Johnson, T. V., McEwen, A., Nicolaisen, L., Porco, C., Rappaport, N., Richardson, J., Somenzi, L., Tortora, P., Turtle, E. P., and Veverka, J. (2007a). "Hyperion's sponge-like appearance". *Nature* 448, pp. 50–53. doi: 10.1038/nature05779.

Thomas, P. C., Burns, J. A., Helfenstein, P., Squyres, S., Veverka, J., Porco, C., Turtle, E. P., McEwen, A., Denk, T., Giese, B., Roatsch, T., Johnson, T. V., and Jacobson, R. A. (2007b). "Shapes of the saturnian icy satellites and their significance". *Icarus* 190.2. Deep Impact Mission to Comet 9P/Tempel 1, Part 2, pp. 573–584. doi: 10.1016/j.icarus.2007.03.012.

Thomas, P. C., Burns, J. A., Hedman, M., Helfenstein, P., Morrison, S., Tiscareno, M. S., and Veverka, J. (2013). "The inner small satellites of Saturn: A variety of worlds". *Icarus* 226.1, pp. 999–1019. doi: 10.1016/j.icarus.2013.07.022.

Thomas, P. C., Tiscareno, M. S., and Helfenstein, P. (2018). "The Inner Small Satellites of Saturn, and Hyperion". In: *Enceladus and the Icy Moons of Saturn*. Ed. by P. M. Schenk, R. N. Clark, C. J. A. Howett, A. J. Verbiscer, and J. H. Waite, p. 387. doi: 10.2458/azu_uapress_9780816537075-ch019.

Tokar, R. L., Johnson, R. E., Thomsen, M. F., Sittler, E. C., Coates, A. J., Wilson, R. J., Crary, F. J., Young, D. T., and Jones, G. H. (2012). "Detection of exospheric O_2^+ at Saturn's moon Dione". *Geophysical Research Letters* 39.3. doi: 10.1029/2011GL050452.

Tomasko, M. G., Archinal, B., Becker, T., Bézard, B., Bushroe, M., Combes, M., Cook, D., Coustenis, A., Bergh, C. de, Dafoe, L. E., Doose, L., Douté, S., Eibl, A., Engel, S., Gliem, F., Grieger, B., Holso, K., Howington-Kraus, E., Karkoschka, E., Keller, H. U., Kirk, R., Kramm, R., Küppers, M., Lanagan, P., Lellouch, E., Lemmon, M., Lunine, J., McFarlane, E., Moores, J., Prout, G. M., Rizk, B., Rosiek, M., Rueffer, P., Schröder, S. E., Schmitt, B., See, C., Smith, P., Soderblom, L., Thomas, N., and West, R. (2005). "Rain, winds and haze during the Huygens probe's descent to Titan's surface". *Nature* 438, pp. 765–778. doi: 10.1038/nature04126.

Tortora, P., Zannoni, M., Hemingway, D., Nimmo, F., Jacobson, R. A., Iess, L., and Parisi, M. (2016). "Rhea gravity field and interior modeling from Cassini data analysis". *Icarus* 264, pp. 264–273. doi: 10.1016/j.icarus.2015.09.022.

Tosi, F., Turrini, D., Coradini, A., and Filacchione, G. a. (2010). "Probing the origin of the dark material on Iapetus". *Monthly Notices of the Royal Astronomical Society* 403.3, pp. 1113–1130. doi: 10.1111/j.1365-2966.2010.16044.x.

Trumbo, S. K., Brown, M. E., and Butler, B. J. (2017). "ALMA Thermal Observations of a Proposed Plume Source Region on Europa". *The Astronomical Journal* 154.4, p. 148. doi: 10.3847/1538-3881/aa8769.

Trumbo, S. K., Brown, M. E., and Butler, B. J. (2018). "ALMA Thermal Observations of Europa". *The Astronomical Journal* 156.4, p. 161. doi: 10.3847/1538-3881/aada87.

Tsang, L., Pan, J., Liang, D., Li, Z., Cline, D. W., and Tan, Y. (2007). "Modeling Active Microwave Remote Sensing of Snow Using Dense Media Radiative Transfer (DMRT) Theory With Multiple-Scattering Effects". *IEEE Transactions on Geoscience and Remote Sensing* 45.4, pp. 990–1004. doi: 10.1109/TGRS.2006.888854.

Turtle, E. P., Perry, J. E., McEwen, A. S., DelGenio, A. D., Barbara, J., West, R. A., Dawson, D. D., and Porco, C. C. (2009). "Cassini imaging of Titan's high-latitude lakes, clouds, and south-polar surface changes". *Geophysical Research Letters* 36.2. doi: 10.1029/2008GL036186.

Turtle, E. P., Perry, J. E., Hayes, A. G., Lorenz, R. D., Barnes, J. W., McEwen, A. S., West, R. A., Del Genio, A. D., Barbara, J. M., Lunine, J. I., Schaller, E. L., Ray, T. L., Lopes, R. M. C., and Stofan, E. R. (2011). "Rapid and Extensive Surface Changes Near Titan's Equator: Evidence of April Showers". *Science* 331.6023, pp. 1414–1417. doi: 10.1126/science.1201063.

Tyler, G. L., Linscott, I. R., Bird, M. K., Hinson, D. P., Strobel, D. F., Pätzold, M., Summers, M. E., and Sivaramakrishnan, K. (2009). "The New Horizons Radio Science Experiment (REX)". In: *New Horizons: Reconnaissance of the Pluto-Charon System and the Kuiper Belt*. Ed. by C. T.

Russell. New York, NY: Springer New York, pp. 217–259. doi: 10.1007/978-0-387-89518-5_10.

Ulaby, F. and Long, D. (2015). *Microwave radar and radiometric remote sensing*. Artech House.

Ulich, B. L., Duckel, J. R., and de Pater, I. (1984). "Planetary observations at a wavelength of 1.32 mm". *Icarus* 60.3, pp. 590–598. doi: 10.1016/0019-1035(84)90166-0.

Verbiscer, A. J., Helfenstein, P., Buratti, B. J., and Royer, E. (2018). "Surface Properties of Saturn's Icy Moons from Optical Remote Sensing". In: *Enceladus and the Icy Moons of Saturn*. Ed. by P. M. Schenk, R. N. Clark, C. J. A. Howett, A. J. Verbiscer, and J. H. Waite, p. 323. doi: 10.2458/azu_uapress_9780816537075-ch016.

Verbiscer, A., French, R., Showalter, M., and Helfenstein, P. (2007). "Enceladus: Cosmic Graffiti Artist Caught in the Act". *Science* 315.5813, pp. 815–815. doi: 10.1126/science.1134681.

Verbiscer, A. J., Skrutskie, M. F., and Hamilton, D. P. (2009). "Saturn's largest ring". *Nature* 461, 1098–1100. doi: 10.1038/nature08515.

Wagner, R. J., Neukum, G., Wolf, U., Schmedemann, N., Denk, T., Stephan, K., Roatsch, T., and Porco, C. C. (2011). "Bright Ray Craters on Rhea and Dione". In: *Lunar and Planetary Science Conference*. Lunar and Planetary Science Conference, p. 2249.

Waite., J. H., Lewis, W. S., Kasprzak, W. T., Anicich, V. G., Block, B. P., Cravens, T. E., Fletcher, G. G., Ip, W.-H., Luhmann, J. G., Mcnutt, R. L., Niemann, H. B., Parejko, J. K., Richards, J. E., Thorpe, R. L., Walter, E. M., and Yelle, R. V. (2004). "The Cassini ion and neutral mass spectrometer (INMS)". *Space Sci Rev* 114, pp. 113–231. doi: 10.1007/s11214-004-1408-2.

Waite, J. H., Glein, C. R., Perryman, R. S., Teolis, B. D., Magee, B. A., Miller, G., Grimes, J., Perry, M. E., Miller, K. E., Bouquet, A., Lunine, J. I., Brockwell, T., and Bolton, S. J. (2017). "Cassini finds molecular hydrogen in the Enceladus plume: Evidence for hydrothermal processes". *Science* 356.6334, pp. 155–159. doi: 10.1126/science.aai8703.

Webster, W. J. and Johnston, K. J. (1989). "On the wavelength dependence of apparent emissivity of asteroid microwave emissions - Ceres and Vesta". *Publications of the Astronomical Society of the Pacific* 101, p. 122. doi: 10.1086/132410.

West, R. D., Anderson, Y., Boehmer, R., Borgarelli, L., Callahan, P., Elachi, C., Gim, Y., Hamilton, G., Hensley, S., Janssen, M. A., Johnson, W. T. K., Kelleher, K., Lorenz, R., Ostro, S., Roth, L., Shaffer, S., Stiles, B., Wall, S., Wye, L. C., and Zebker, H. A. (2009). "Cassini RADAR Sequence Planning and Instrument Performance". *IEEE Transactions on Geoscience and Remote Sensing* 47.6, pp. 1777–1795. doi: 10.1109/TGRS.2008.2007217.

White, O. L., Schenk, P. M., and Dombard, A. J. (2013). "Impact basin relaxation on Rhea and Iapetus and relation to past heat flow". *Icarus* 223.2, pp. 699–709. doi: 10.1016/j.icarus.2013.01.013.

White, O. L., Schenk, P. M., Bellagamba, A. W., Grimm, A. M., Dombard, A. J., and Bray, V. J. (2017). "Impact crater relaxation on Dione and Tethys and relation to past heat flow". *Icarus* 288, pp. 37–52. doi: 10.1016/j.icarus.2017.01.025.

White, T. L. and Cogdell, J. R. (1973). "Lunar polarization studies at 3.1 mm wavelength". *Earth, Moon, and Planets* 6.3-4, pp. 235–249. doi: 10.1007/BF00562205.

Wiesmann, A., Mätzler, C., and Weise, T. (1998). "Radiometric and structural measurements of snow samples". *Radio Science* 33.2, pp. 273–289. doi: 10.1029/97RS02746.

Wiesmann, A. and Mätzler, C. (1999). "Microwave Emission Model of Layered Snowpacks". *Remote Sensing of Environment* 70.3, pp. 307–316. doi: 10.1016/S0034-4257(99)00046-2.

Wye, L. C. (2011). "Radar scattering from Titan and Saturn's icy satellites using the Cassini spacecraft". PhD thesis. Stanford University.

Xiao, L., Zhu, P., Fang, G., Xiao, Z., Zou, Y., Zhao, J., Zhao, N., Yuan, Y., Qiao, L., Zhang, X., Zhang, H., Wang, J., Huang, J., Huang, Q., He, Q., Zhou, B., Ji, Y., Zhang, Q., Shen, S., Li, Y., and Gao, Y. (2015). "A young multilayered terrane of the northern Mare Imbrium revealed by Chang'E-3 mission". *Science* 347.6227, pp. 1226–1229. doi: 10.1126/science.1259866.

Yin, A. and Pappalardo, R. T. (2015). "Gravitational spreading, bookshelf faulting, and tectonic evolution of the South Polar Terrain of Saturn's moon Enceladus". *Icarus* 260, pp. 409–439. doi: 10.1016/j.icarus.2015.07.017.

Young, D. T., Berthelier, J. J., Blanc, M., Burch, J. L., Coates, A. J., Goldstein, R., Grande, M., Hill, T. W., Johnson, R. E., Kelha, V., Mccomas, D. J., Sittler, E. C., Svenes, K. R., Szegö, K., Tanskanen, P., Ahola, K., Anderson, D., Bakshi, S., Baragiola, R. A., Barraclough, B. L., Black, R. K., Bolton, S., Booker, T., Bowman, R., Casey, P., Crary, F. J., Delapp, D., Dirks, G., Eaker, N., Funsten, H., Furman, J. D., Gosling, J. T., Hannula, H., Holmlund, C., Huomo, H., Illiano, J. M., Jensen, P., Johnson, M. A., Linder, D. R., Luntama, T., Maurice, S., Mccabe, K. P., Mursula, K., Narheim, B. T., Nordholt, J. E., Preece, A., Rudzki, J., Ruitberg, A., Smith, K., Szalai, S., Thomsen, M. F., Viherkanto, K., Vilppola, J., Vollmer, T., Wahl, T. E., Wüest, M., Ylikorpi, T., and Zinsmeyer, C. (2004). "Cassini Plasma Spectrometer Investigation". *Space Sci Rev* 114, pp. 1–112. doi: 10.1007/s11214-004-1406-4.

Zahnle, K., Schenk, P., Levison, H., and Dones, L. (2003). "Cratering rates in the outer Solar System". *Icarus* 163.2, pp. 263–289. doi: 10.1016/S0019-1035(03)00048-4.

Zhang, Z., Hayes, A. G., Janssen, M. A., Nicholson, P. D., Cuzzi, J. N., de Pater, I., Dunn, D. E., Estrada, P. R., and Hedman, M. M. (2017a). "Cassini microwave observations provide clues to the origin of Saturn's C ring". *Icarus* 281, pp. 297–321. doi: 10.1016/j.icarus.2016.07.020.

Zhang, Z., Hayes, A. G., Janssen, M. A., Nicholson, P. D., Cuzzi, J. N., de Pater, I., and Dunn, D. E. (2017b). "Exposure age of Saturn's A and B rings, and the Cassini Division as suggested by their non-icy material content". *Icarus* 294, pp. 14–42. doi: 10.1016/j.icarus.2017.04.008.

Zhang, Z., Hayes, A. G., de Pater, I., Dunn, D. E., Janssen, M. A., Nicholson, P. D., Cuzzi, J. N., Butler, B. J., Sault, R. J., and Chatterjee, S. (2019). "VLA multi-wavelength microwave observations of Saturn's C and B rings". *Icarus* 317, pp. 518–548. doi: 10.1016/j.icarus.2018.08.014.

Zhu, Y., Zheng, Y., Fang, S., Zou, Y., and Pearson, S. (2019). "Analysis of the brightness temperature features of the lunar surface using 37 GHz channel data from the Chang'E-2 microwave radiometer". *Advances in Space Research* 63.1, pp. 750–765. doi: 10.1016/j.asr.2018.10.014.